Implications of in situ zircon U-Pb, Lu-Hf, oxygen-isotope, and trace element geochemistry on the petrogenetic history of the northern Hogem batholith in the Quesnel terrane, north-central British Columbia, Canadian Cordillera

by

Gabrielle Jones

A thesis submitted in partial fulfillment of the requirements for the degree of

Master of Science

Department of Earth and Atmospheric Sciences
University of Alberta

Abstract

The Cordilleran orogen of western Canada is a type example of accretionary tectonism and thus an ideal location to study continental growth by oceanic and continental arc magmatism and terrane accretion. Cordilleran Intermontane terranes are interpreted as accreted oceanic arcs that contributed significant crustal material to the western North American margin during the Mesozoic; however, uncertainties regarding the pre-accretionary history and basement of these terranes hinder understanding the relative roles of new juvenile crust and reworked crust in the building of this major orogeny. An improved understanding of these issues also has broader implications for models of Phanerozoic juvenile crustal growth and accretionary tectonics. The Hogem batholith in north-central Quesnel terrane, British Columbia comprises Triassic to Cretaceous-aged intrusions. It provides a natural laboratory to better understand the magma sources, nature and antiquity of the batholith, the basement to the Quesnel terrane, and the tectonic history in this area through time.

This study presents new combined zircon U-Pb/Hf, $\delta^{18}O$ and trace element data for 13 intrusive plutonic rocks from the Hogem batholith, supplemented by apatite and titanite U-Pb+Sm-Nd and whole rock major oxide and trace element geochemical data. New zircon U-Pb dates coincide with previous geochronology results and expand the crystallization age range of four intrusive suites, from 206.8±0.9 to 127.1±1.6 Ma, revealing the batholith's composite and protracted 80-million-year magmatic history. Notably, the age range of the Mesilinka intrusive suite, 135.4±0.9 to 127.1±1.6 Ma, corresponds with a period otherwise marked by magmatic quiescence across the Cordillera. The crystallization ages of the Thane Creek (207 to 194 Ma) and Duckling Creek (182 to 174 Ma) intrusive suites overlap with prolific periods of porphyry Cu±Au-Mo mineralization in the Canadian Cordillera. Zircon trace element geochemistry results

($Eu/Eu_N^* \geq 0.4$, $Ce/Ce_C^* > 100$, $\Delta FMQ > 0$) suggest zircon crystallized in oxidized and hydrous magma conditions at near-solidus temperatures (750 to 650°C), which indicates potentially favourable magma conditions for porphyry mineralization in the Thane and Duckling Creek suites. Zircon Hf-O isotope results are consistent with a predominantly juvenile, mantle-derived source for the pre- to syn-accretionary Thane Creek and Duckling Creek suites. Xenocrystic zircons from the post-accretionary Osilinka suite (ca. 160 Ma) reveal an inherited juvenile Hf-O signature from the melt source, while zircon Hf-O results from the Mesilinka suite (135 to 127 Ma) suggest a mix of juvenile mantle- and recycled supracrustal-derived magma sources. There is no indication that the magmas that formed the Hogem batholith experienced significant interaction with ancient North American continental basement.

Overall, the generally juvenile Hf-O signatures of zircon from plutonic rocks studied here contrast with previous isotope studies of plutonic rocks in southern and northern Quesnellia and suggest disparate basement compositions and accretionary styles across the Quesnel terrane during the Mesozoic. These findings form the basis of a model for the production and preservation of juvenile crust in the Quesnellia arc, which supports the overall trend to juvenile Hf isotope compositions in Phanerozoic circum-Pacific accretionary belts. This model may be applied to better understanding juvenile crustal growth and orogen-craton interactions in other accreted terranes in the North American Cordillera as well as within global Phanerozoic accretionary orogens.

Preface

This thesis is an original work by Gabrielle Jones. Sections of Chapter 3 (Mineral Geochronology and Geochemistry Analytical Methods and Results) of this thesis have been published as:

> L. Ootes, G. Jones, P. Schiarizza, D. Milidragovic, R. Friedman, A. Camacho, Y. Luo, A. Vezinet, D.G. Pearson, and S. Zhang, "Geochronologic and geochemical data from northern Hogem batholith and its surroundings, north-central British Columbia", British Columbia Geological Survey Geofile 2020-01.
>
> G.O. Jones, D.G. Pearson, A. Vezinet, Y. Luo, R.A. Stern, D. Milidragovic, and L.O. Ootes, "Preliminary Zircon Geochemistry of Northern Hogem Batholith, Quesnel Terrane, North-Central British Columbia", Geoscience BC Report 2021-01, pp. 105-120.
>
> G. Jones, L. Ootes, D. Milidragovic, R. Friedman, A. Camacho, Y. Luo, A. Vezinet, D.G. Pearson, and P. Schiarizza, "Geochronology of northern Hogem batholith, Quesnel terrane, north-central British Columbia", British Columbia Geological Survey Paper 2021-01, pp. 37-56.

I was responsible for the data collection, analysis, and manuscript composition. Y. Luo, R.A. Stern, and A. Vezinet assisted with data collection and analysis. L. Ootes and D.G. Pearson were the supervisory authors and were involved in concept formation and manuscript composition.

The data repository for the mineral geochronology and geochemistry results (Chapter 3.2) of this thesis study will be published as a British Columbia Geological Survey Geofile.

Acknowledgements

This project was supported by the British Columbia Geological Survey (BCGS), the Diamond Exploration Training School (DERTS) at University of Alberta, and a Geoscience BC scholarship and NSERC Canada Graduate Scholarship awarded to the author.

I thank my supervisors, Graham Pearson and Luke Ootes, for their mentorship, feedback and guidance in the field, research, and entire thesis writing process. Adrien Vezinet was invaluable in guiding me through research planning, sample preparation, and LA-ICP-MS analyses at the University of Alberta. Mark Labbe is thanked for his help with sample and grain mount preparation. Yan Luo helped with LA-ICP-MS analyses at the University of Alberta and was patient with all my questions. Richard Stern facilitated SIMS analyses at the Canadian Centre for Isotopic Microanalysis (CCIM) at the University of Alberta and was always welcoming for insightful discussions.

The entire BCGS Hogem crew are thanked for their contributions to bedrock mapping and sample collection, as well as camaraderie in the field. Dejan Milidragovic was a wealth of knowledge throughout the project and provided insight on this study.

Thanks to the friends I made during my time in Edmonton for their good company and conversation, as well as the remote discussions we continued to have during a global pandemic. Thanks to my family, JN, RN, and KZ, who have supported me through my endeavours.

Table of Contents

List of Tables

List of Figures

Abbreviations

AFM	alkalies-FeO*-MgO
ASI	alumina saturation-index
BCGS	British Columbia Geological Survey
BSE	back scattered electron
CA-ID-TIMS	chemical abrasion-isotope dilution-thermal ionization mass spectrometry
CCIM	Canadian Centre for Isotopic Microanalysis
CHUR	chondritic uniform reservoir
CL	cathodoluminescence
CMB	Coast Mountains Batholith
cps	counts per second
DM	depleted mantle
DRS	data reduction scheme
FMQ	fayalite-magnetite-quartz
fO_2	oxygen fugacity
g	gram
HFSE	high field strength element
HREE	heavy rare earth element
IMF	instrumental mass fractionation
km	kilometer
LA-ICP-MS	laser ablation-inductively coupled plasma-mass spectrometry
LASS	laser ablation split stream
LILE	large ion lithophile element
LOI	loss on ignition
LOD	limit of detection
LOQ	limit of quantification
LREE	light rare earth element
m	meter

Ma	mega annum
MALI	modified alkali-lime index
MASH	melting, assimilation, storage, and homogenization
MORB	mid ocean ridge basalt
MREE	middle rare earth element
MSWD	mean squared weighted deviation
ppm	parts per million
$p(\chi)^2$	probability of fit
REE	rare earth element
REE_N	chondrite normalized rare earth element
RM	reference material
RSD	relative standard deviation
s	second
SCLM	sub-continental lithospheric mantle
SE	standard error
SEM	scanning electron microscope
SIMS	secondary ion mass spectrometry
syn-COLG	syn-collisional granite
TAS	total alkalis – silica
TE	trace element
µm	micrometer
VAG	volcanic arc granite
VSMOW	Vienna standard mean ocean water
YTT	Yukon Tanana terrane

1 Introduction

1.1 Geologic Background and Thesis Objectives

The Canadian Cordillera is a type example of major Phanerozoic accretionary orogenesis and provides an opportunity to study continental growth via terrane accretion and arc magmatism (Cawood et al., 2009). During the Mesozoic, western North America experienced extensive magmatic activity, which stitched together accreted terranes and formed the plutonic hosts to Cu±Au-Mo-Ag porphyry mineralization in British Columbia, Yukon, and Alaska. Characterizing the non-mineralized, background magmatic phases is key to better understanding the petrogenesis of these porphyry-hosting intrusions, as alteration haloes enveloping porphyry deposits may significantly affect whole rock and mineral chemistry interpretations.

The Hogem batholith is located in north-central British Columbia, within the Quesnel terrane of the Canadian Cordillera (Figure 1.1.1). Mapping and geochemical studies of the Hogem batholith and the surrounding geology have improved knowledge of field relationships, petrography, geochronology, and mineralization in the area (e.g., Lord, 1948; Woodsworth, 1976; Garnett, 1978; Devine et al., 2014). Despite a long history of studies focused on the Hogem batholith, there is uncertainty about the nature, antiquity and longevity of magmatism, the tectonic evolution of the batholith, and the relationship of these parameters to potential mineralization.

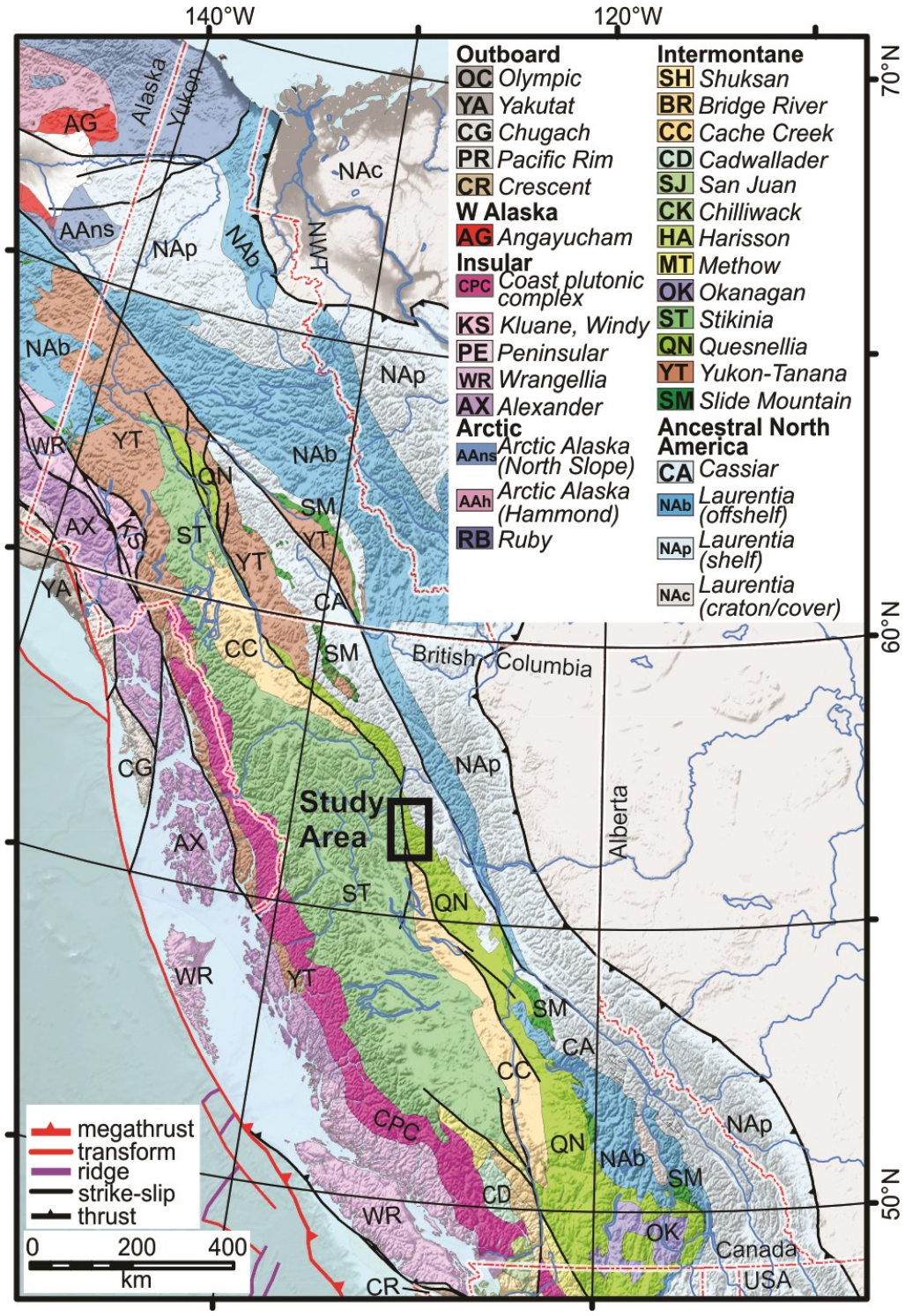

Figure 1.1.1. Terrane map of the Canadian Cordillera, northwestern United States, and eastern Alaska, modified after Colpron and Nelson (2020). The black square indicates the location of this thesis study area.

This study aims to address the lack of modern isotopic and trace element data for the plutonic rocks of the Hogem batholith and to better understand the magmatic phases within four mappable intrusive suites identified in the northern Hogem batholith, through:

- Characterization of the intrusive suites using whole rock major oxide and trace element geochemistry.
- Interpretation of magmatic crystallization ages using igneous zircon and titanite laser ablation-inductively coupled plasma-mass spectrometry (LA-ICP-MS) U-Pb geochronology.
- Estimation of the relative crust and mantle contributions to Hogem batholith magmas using combined zircon LA-ICP-MS Lu-Hf and secondary ion mass spectrometry (SIMS) oxygen-isotope ($\delta^{18}O$) data.
- Comparison of zircon tracer isotope (Lu-Hf, $\delta^{18}O$) geochemistry results to Quesnel terrane basement, Yukon Tanana terrane, and Paleoproterozoic North America (Hottah terrane) detrital zircon geochemistry data to evaluate whether ancient crust was involved in Hogem batholith magmatism.
- Determination of the temporal evolution and petrogenesis of the Hogem batholith, and possible implications for juvenile crust formation and Phanerozoic accretionary tectonic models.
- Estimation of relative magma temperatures, oxygen fugacities, and fluid contents using zircon trace element concentrations, and the implication of these factors for the mineralization potential of the magmas.

1.2 Regional Geology and Previous Work

1.2.1 Canadian Cordillera Geology

The Cordilleran orogen of western Canada has a protracted evolution that spans from the Paleoproterozoic to present. Many works have synthesized the tectonic history and structural framework of the Canadian Cordillera (e.g., Monger, 1977; Jones et al., 1977; Davis et al., 1978; Coney et al., 1980; Monger et al., 1982; Jones et al., 1983; Wheeler et al., 1991; Mihalynuk et al., 1994; Monger and Price, 2002; Evenchick et al., 2005; Nelson and Colpron, 2007; Colpron et al., 2007; Evenchick et al., 2007; Johnston, 2008; Nelson et al., 2013). These works are partially

summarized here in relation to the formation of the Intermontane superterrane, Quesnel terrane, and host rocks to the Hogem batholith.

Rifting and break-up of ancestral North America (Laurentia) from Rodinia from ca. 750 to 540 Ma led to the opening of the proto-Pacific Ocean (Panthalassa; Monger and Price, 2002). Beginning in the Middle Devonian, a convergent boundary formed in eastern Panthalassa, outboard of the western Laurentian margin. Chains of volcanic island arcs developed above an eastward-dipping subduction zone and were separated from Laurentia by the Slide Mountain Ocean (Figure 1.2.1.1; Monger and Price, 2002; Nelson et al. 2013).

At the end of the Triassic, the Slide Mountain Ocean closed after a reversal in subduction polarity, eventually leading to the accretion of the island arcs onto the western Laurentian margin, which formed discrete, fault-bounded terranes (Figures 1.2.1.2 and 1.2.1.3; Monger and Price, 2002; Nelson et al., 2013). The extent of North American basement beneath these accreted terranes remains a point of contention; however, it is thought the basement may extend as far west as the exposed Cache Creek terrane in the northern Canadian Cordillera and to the Fraser Fault in the southern Canadian Cordillera (Cook et al., 2004; Clowes et al., 2005; Evenchick et al., 2007; Nelson et al., 2013).

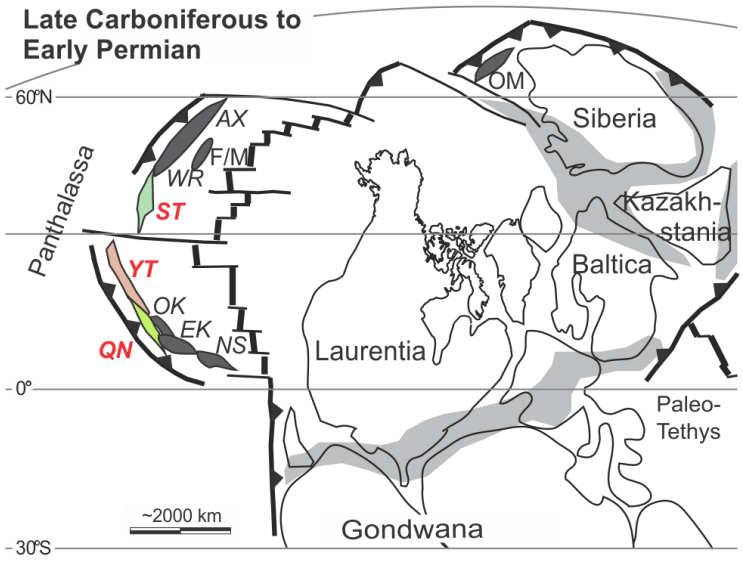

Figure 1.2.1.1. Reconstruction of the accreted terranes during the Late Carboniferous to Early Permian, prior to closure of the Slide Mountain Ocean and accretion onto the western Laurentian continental margin. Modified after Nelson et al. (2013), based on Belasky and Stevens (2006), Bradley et al. (2003), Nokleberg et al. (2005), and Malkowski and Hampton (2014). AX=Alexander terrane, WR=Wrangellia, F/M=Farewell/Mystic terrane, ST=Stikine terrane, YT=Yukon-Tanana terrane, QN=Quesnel terrane, OK=Okanagan subterrane, EK=Eastern Klamaths, NS=Northern Sierras, OM=Omulevka Ridge.

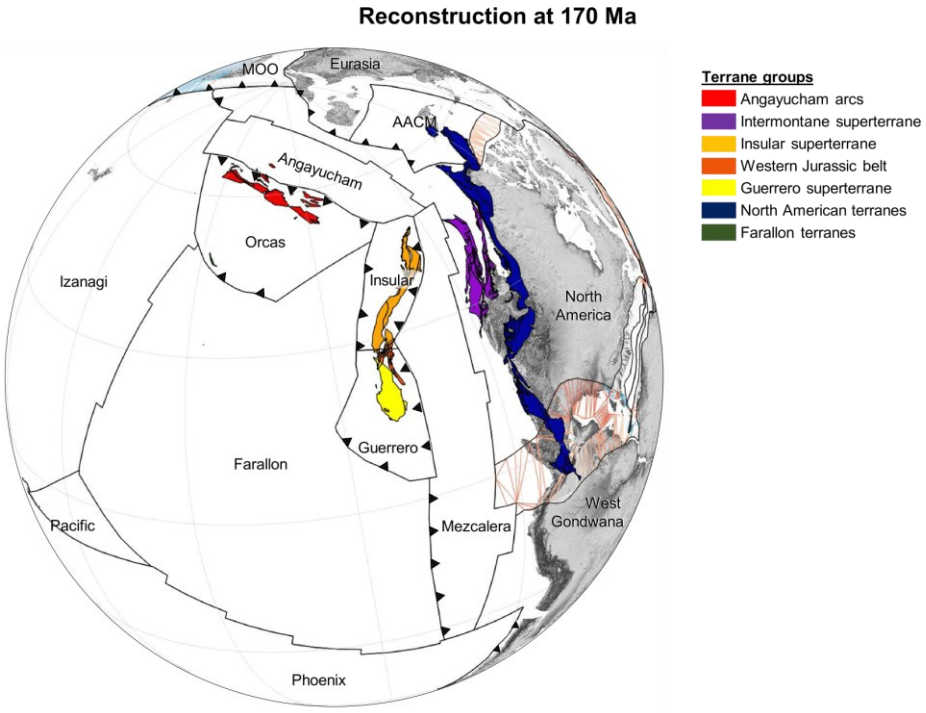

Figure 1.2.1.2. Plate and Cordilleran terrane reconstruction model at 170 Ma, modified after Clennett et al. (2020). Ongoing accretion of the Intermontane superterrane (purple) to the western North American (Laurentian) margin began at ca. 185 Ma.

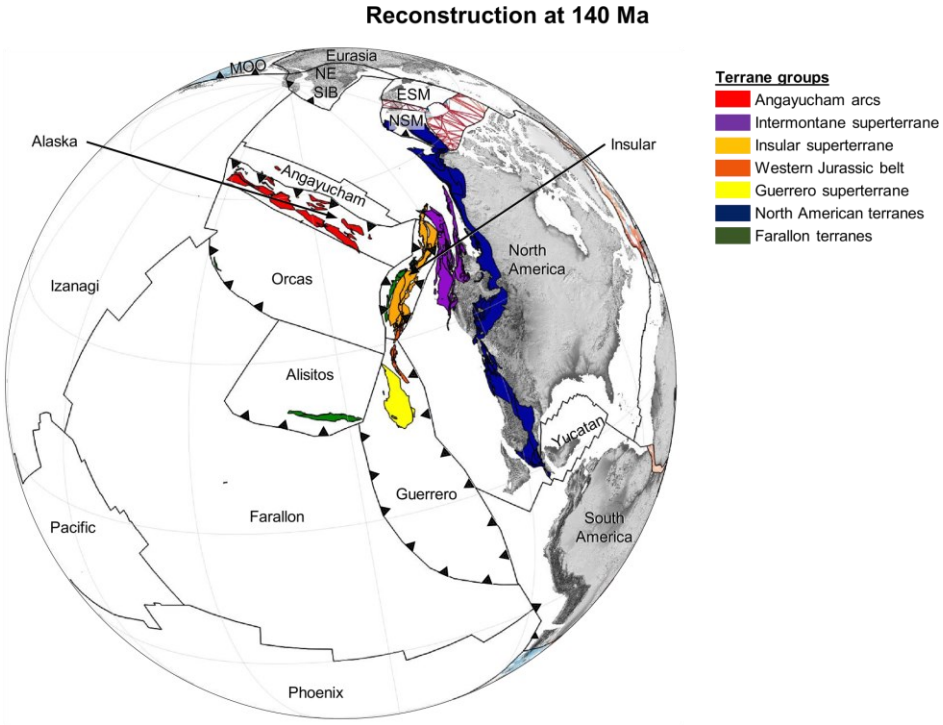

Figure 1.2.1.3. Plate and Cordilleran terrane reconstruction model at 140 Ma, modified after Clennett et al. (2020). Accretion of the Intermontane superterrane (purple) to the western North American (Laurentian) margin was complete by this time.

1.2.2 Development of the Intermontane terranes

The Intermontane superterrane is made up by the Stikine (Stikinia), Quesnel (Quesnellia), Cache Creek, and Yukon-Tanana terranes (Figure 1.2.2.1; Monger et al., 1982; Rusmore et al., 1988). It has been proposed these terranes were volcanic island arcs originally built upon rifted craton or pericratonic fragments, which were separated from one another by an ocean or back-arc that formed the Cache Creek terrane (Colpron et al., 2006; Nelson et al., 2006; Colpron et al., 2007; Zagorevski, 2015). Some suggest these Intermontane island arcs were amalgamated and evolved together, prior to accretion (Monger et al., 1982; Colpron et al., 2007), while others cite evidence that the individual arcs were accreted separately and simultaneously across the continental margin (Mortimer, 1986; Cordey et al., 1987; Rusmore et al., 1988). By the Middle Jurassic (ca. 174 Ma), accretion of the Intermontane superterrane onto the western North American continental margin was essentially complete, however, minor syn-accretion related magmatism continued until ~160 Ma (Nelson et al., 2013; Monger, 2014). Across the Cordillera, magmatism during the period 155 to 125 Ma was rare, representing a post-accretionary setting in the Intermontane terranes (Armstrong, 1988).

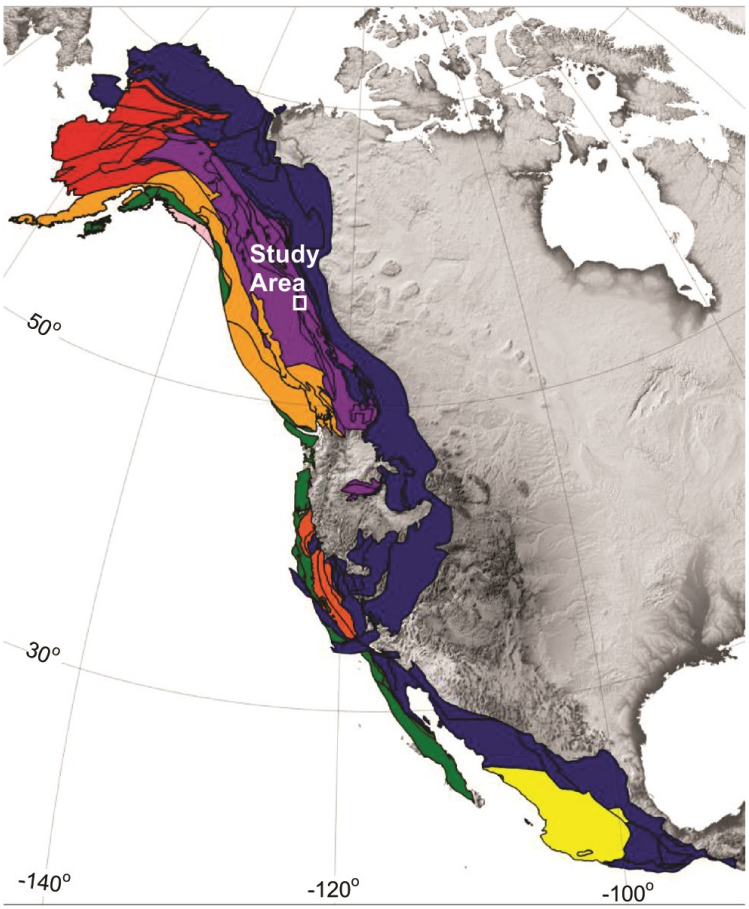

Figure 1.2.2.1. Terrane and superterrane configurations within the North American Cordillera at present, modified after Clennett et al. (2020). The white square represents this thesis study area within the Intermontane superterrane (purple). Other terranes and superterranes include: Angayucham (red), Insular (orange), Guerrero (yellow), Western Jurassic belt (dark orange), North America (dark blue), Farallon (green), and Kula (pink).

1.2.3 Quesnel terrane background

Quesnel terrane forms discontinuous exposures spanning from north-central Washington state to south-central Yukon (Figure 1.1.1). It is exposed between Cache Creek and Stikine terranes to the west, and Slide Mountain terrane and pericratonic sedimentary rocks to the east (Monger et al., 1991; Wheeler et al., 1991; Schiarizza, 2019). Two major stratigraphic divisions make up Quesnel terrane: upper Paleozoic volcanic and sedimentary strata and lower to middle Mesozoic volcanic and sedimentary strata with temporally associated plutonic rocks (Monger et al., 1991).

1.2.4 Quesnel terrane basement

Upper Paleozoic strata comprise the basement to Quesnel terrane, including the Mississippian to Permian Lay Range assemblage in north-central Quesnel terrane, which is correlative to the Harper Ranch subterrane in the south (Monger et al., 1991; Nelson and Bellefontaine, 1996; Ferri, 1997; Colpron et al., 2007). The upper Paleozoic Lay Range assemblage consists of two main stratigraphic units, a lower sedimentary and upper mafic tuff division. The lower sedimentary division comprises Middle Mississippian to Middle Pennsylvanian chert, tuff, carbonate, and clastic sedimentary rocks (Ferri et al., 1993; Ferri, 1997). These sedimentary rocks are unconformably overlain by the Permian upper mafic tuff division, consisting of tuff, agglomerate, and mafic volcanic flows (Ferri et al., 1993; Ferri, 1997). The Lay Range assemblage is exposed on the eastern edge of north-central Quesnel terrane, while correlative rocks of the Nina Creek Group, which are assigned to Slide Mountain terrane, extend further south. This strip of Lay Range assemblage and Nina Creek Group Paleozoic rocks extends over 200 km along strike of the Cordillera and separates Mesozoic Quesnel terrane rocks from pericratonic rocks to the east (Ferri, 1997).

1.2.5 Quesnel Terrane Mesozoic Rocks

An angular unconformity divides Paleozoic basement rocks from overlying Mesozoic strata in Quesnellia (Read and Okulitch, 1977). The lower Mesozoic volcano-sedimentary strata mostly consist of the upper Triassic to lower Jurassic Nicola Group in the southern Quesnel terrane, which is temporally, lithologically, and geochemically correlated to the Takla Group in north-central Quesnel terrane (Monger et al., 1991). The Nicola and Takla Groups are predominantly expressed as clinopyroxene- and feldspar-phyric basalts with inter-bedded volcanogenic sandstones and argillites (Monger et al., 1991; Dostal et al., 2009).

The Takla Group is also present in the more outboard Stikine terrane and is separated from the Quesnel Takla Group by dextral strike-slip faults or high-pressure accretionary complex rocks of the Cache Creek terrane (Lord, 1948; Dostal et al., 2009). The Nicola and Takla Group volcano-sedimentary rocks are thought to represent a volcanic island arc; however, it is uncertain whether these groups represent a single arc or separate arcs (Monger et al., 1991; Dostal et al., 2009). Dostal et al. (2009) inferred that upper Triassic volcanic strata across Quesnellia and Stikinia may be correlated, including the Nicola and Takla Groups, and the Stuhini Group of

Stikine terrane. All three of these groups share similar lithologies, stratigraphy, and Nd and Sr isotopic compositions (Dostal et al., 2009).

Quesnellia and Stikinia volcanic and sedimentary strata were intruded by co-magmatic Late Triassic to Early Jurassic calc-alkaline and alkaline plutons (Monger et al., 1991; Logan and Mihalynuk, 2014). These plutons represent an important period of magmatism in the Canadian Cordillera, as they are major hosts to porphyry Cu±Au-Mo-Ag mineralization in British Columbia (Figure 1.2.5.1) and Yukon (e.g., Guichon, Iron Mask, Copper Mountain, Texas Creek, and Granite Mountain batholiths; Christopher and Carter, 1976; Armstrong, 1988). Most of the Quesnel-Stikine terrane porphyry mineralization occurred within a 15-million-year period, and approximately 90% of known mineralization occurred from approximately 208 to 202 Ma (Logan and Mihalynuk, 2014).

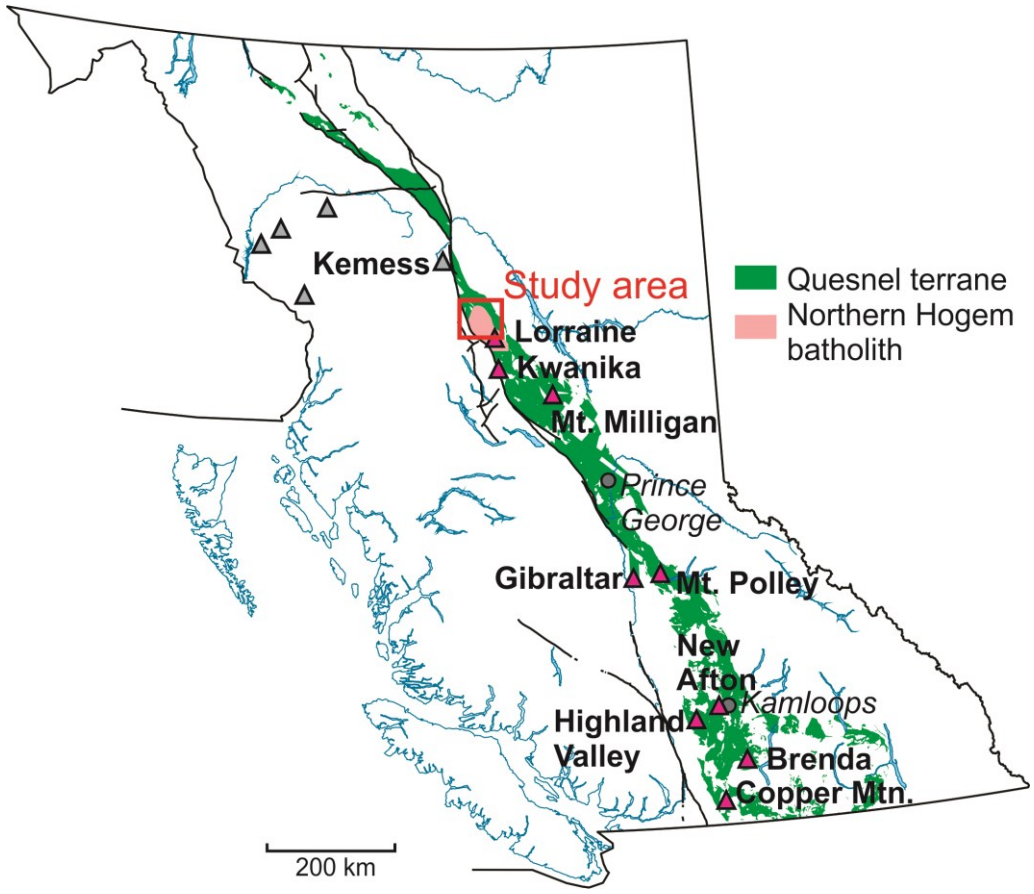

Figure 1.2.5.1. Geographic distribution of the Quesnel terrane and major Triassic-Jurassic porphyry deposits in British Columbia. Pink triangles are select Quesnel terrane-hosted porphyry deposits. Grey triangles are select Stikine terrane-hosted porphyry deposits. The northern Hogem batholith is highlighted in pink and the study area is indicated by the red square. Geology from BC Geological Survey (2020).

1.2.6 Relationship of Quesnel terrane with Yukon-Tanana and Stikine terranes

Several authors have proposed that Quesnellia and Stikinia share a genetic history because of the lithological, geochemical, and age similarities between the volcano-sedimentary rocks (Lord, 1948; Church, 1975; Monger, 1977; Monger and Church, 1977; Dostal et al., 2009). Additionally, the Asitka Group basement rocks underlying the Takla Group in Stikinia are similar in age, stratigraphy, and geochemistry to the upper Lay Range assemblage in Quesnellia and suggest the two terranes may share a basement (Dostal et al., 2009). A similar relationship exists between Quesnellia and the Yukon-Tanana terrane (YTT). Close correspondence in stratigraphy, age, and geochemistry between the Lay Range assemblage (and Harper Ranch Group) and the Late Mississippian to Early Permian Klinkit assemblage in the YTT support a shared pre-accretionary history between the two terranes (Simard et al., 2003; Colpron et al., 2007). Late Triassic to Early Jurassic plutonic suites intruded and crosscut the boundaries of Quesnellia, Stikinia, and YTT, implying the Intermontane terranes were amalgamated by the time of this intrusive event (Nelson and Friedman, 2004; Colpron et al., 2007).

Several tectonic models attempt to explain the affiliation of Quesnellia, Stikinia, and YTT. One model involves the development of a single arc that was later offset by strike-slip faulting (Wernicke and Klepacki, 1988; Beck, 1991, 1992; Irving et al., 1996). Another involves large-scale thrusting, imbrication, and synformal folding of the accreted terranes onto the continental margin (Samson et al., 1991; Gehrels et al., 1991; Dostal et al., 2009). Others have suggested a model of syn-collisional oroclinal bending of the YTT around Quesnellia, Stikinia, and Cache Creek terrane (Nelson and Mihalynuk, 1993; Mihalynuk et al., 1994; Nelson et al., 2006). Johnston (2008) suggested that the Intermontane terranes, in part, constituted an exotic composite ribbon continent that experienced oroclinal bending in the Late Cretaceous during collision with autochthonous North America.

1.3 Hogem Batholith Geology and Previous Work

1.3.1 Geology

The Hogem batholith is made up of Triassic to Cretaceous-aged intrusions within Quesnel terrane in north-central British Columbia (Figure 1.1.1). These intrusions consist of calc-alkalic to alkalic plutonic rocks that were emplaced into upper Triassic Takla Group

volcano-sedimentary strata, which are exposed to the north and east of the Hogem batholith (Figure 1.3.1.1; Garnett, 1972). To the west, the Hogem batholith is juxtaposed against Stikine and Cache Creek terranes along the Pinchi-Ingenika dextral strike-slip fault system (Figure 1.3.1.1; Garnett, 1972). Lay Range assemblage basement is exposed to the northeast of Hogem batholith and Takla Group rocks (not shown on map).

Four petrologically distinct intrusive suites sub-divide the Hogem batholith (Figure 1.3.1.1). From oldest to youngest, these are the Thane Creek, Duckling Creek, Osilinka, and Mesilinka suites (Woodsworth, 1976; Woodsworth et al., 1991; Ootes et al., 2019a,b, 2020a,b). The intrusive Thane Creek suite predominantly consists of diorite to quartz monzodiorite, which crosscut and co-mingled with minor hornblendite (Figure 1.3.1.2). Rocks of the Thane Creek suite vary from undeformed to strongly deformed and locally mylonitic (Ootes et al., 2019b). Mineralization is variably present as disseminated copper-sulphides and rare veinlets, with blue-green copper staining in outcrop. Copper sulphide minerals occur in both the dioritic and hornblendite phases.

The Duckling Creek suite is made up of syenites to monzonites, which intruded older biotite clinopyroxenite. Rhythmic magmatic layering visible in outcrop separates felsic syenites from mafic, biotite- and clinopyroxenite-rich syenites (Figure 1.3.1.3). In northern Hogem batholith, these rocks are weakly deformed (Ootes et al., 2019b, 2020a,b); however, in the south and more proximal to the Lorraine Cu-Au deposit (Figure 1.2.5.1), Duckling Creek rocks are moderately to strongly deformed (e.g., Devine et al., 2014). Mineralization of the Duckling Creek suite typically occurs as disseminated, porphyry-style copper-sulphides, with copper staining visible in outcrop.

Leucocratic, medium-grained granites comprise the Osilinka suite (Figure 1.3.1.4), which are crosscut by feldspar porphyry dykes. Osilinka granites have low mafic mineral contents (<5%), which makes deformation in these rocks cryptic; however, cross-cutting mafic dykes locally contain shear fabrics (Ootes et al., 2019b).

Four intrusive phases are recognized in the Mesilinka suite. These include older tonalite and granodiorite phases, which were intruded by equigranular granite and K-feldspar porphyritic granite phases (Figure 1.3.1.5). All the Mesilinka suite phases have a foliation defined by biotite

(Ootes et al., 2019b, 2020a,b). Younger pegmatite dykes cross-cut the Mesilinka suite intrusions (Figure 1.3.1.5).

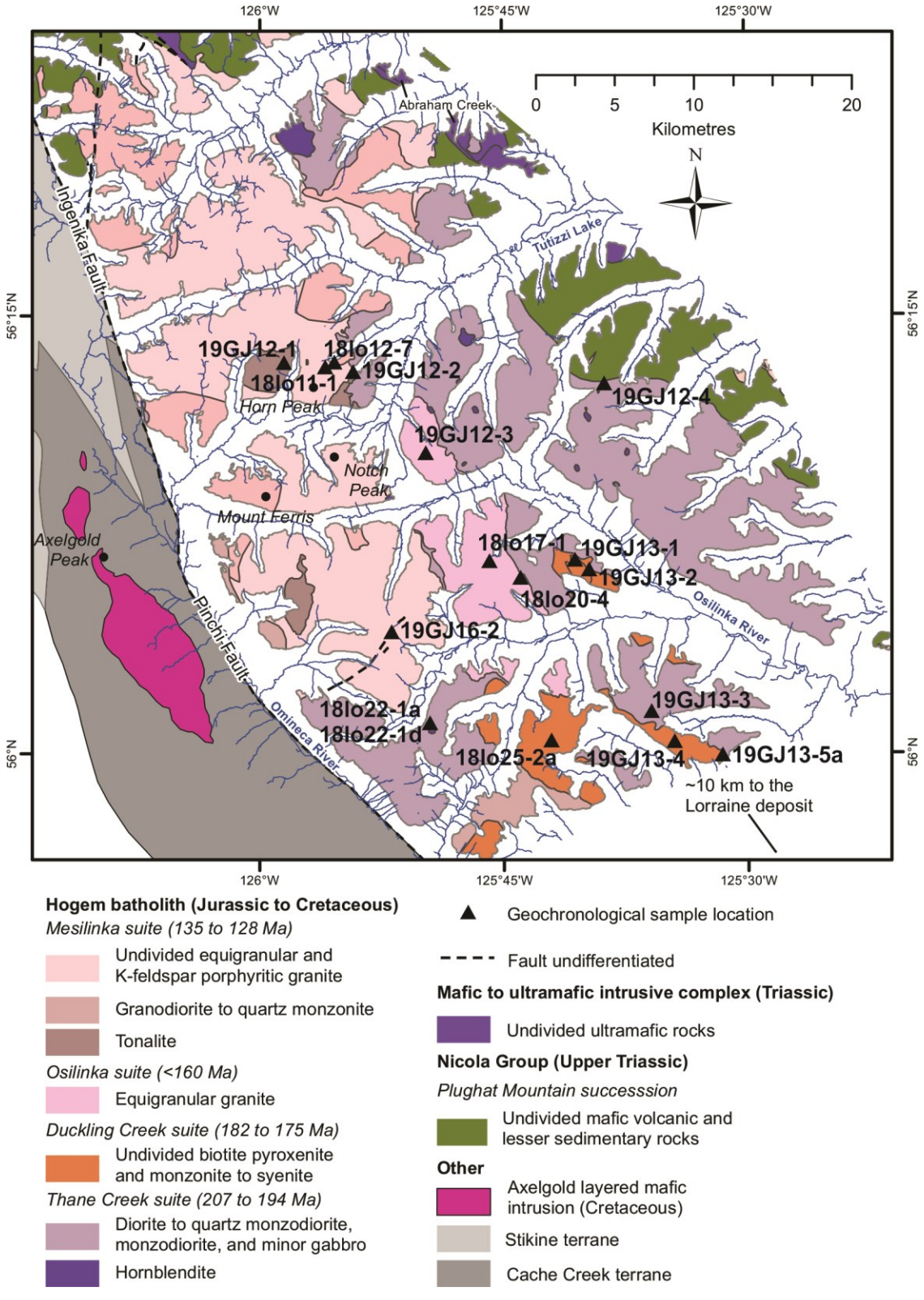

Figure 1.3.1.1. Bedrock geology map of northern Hogem batholith, modified after Ootes et al. (2020a) with sample locations after Jones et al. (2021). Black triangles represent geochronology and geochemistry intrusive rock samples taken for this thesis study.

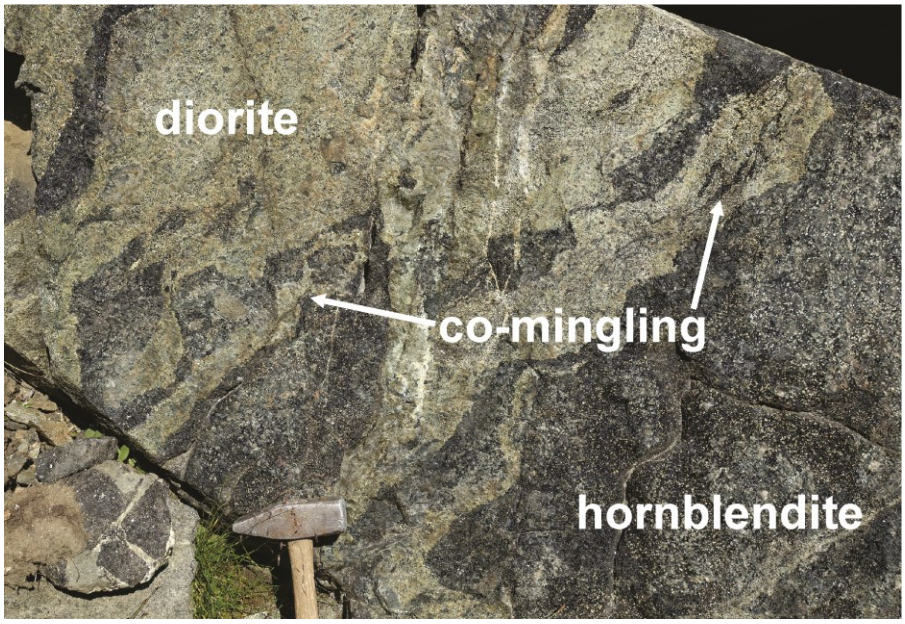

Figure 1.3.1.2. Outcrop photograph of crosscutting and co-mingling magmatic textures between the Thane Creek diorite and hornblendite.

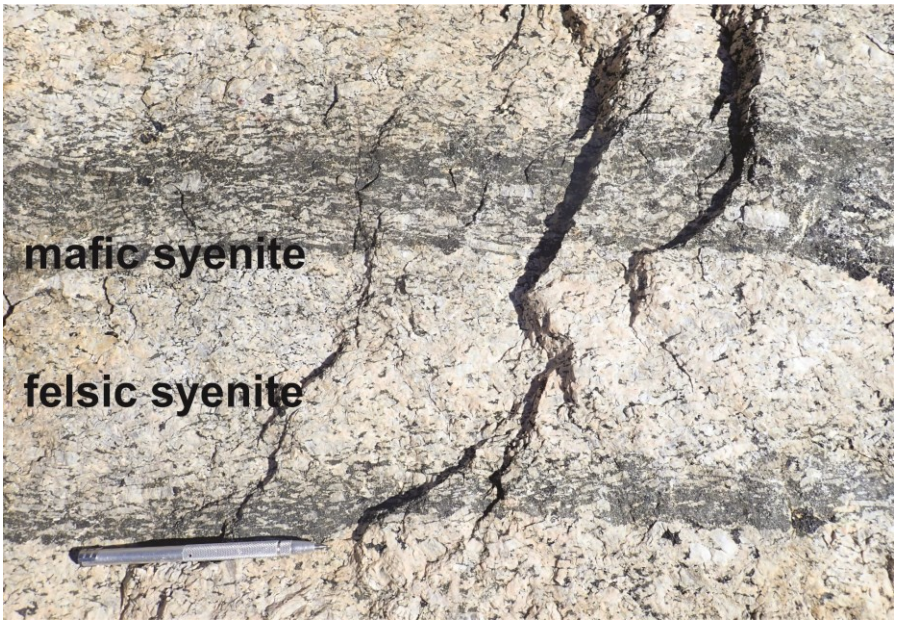

Figure 1.3.1.3. Rhythmic magmatic layering of the Duckling Creek felsic and mafic syenite in outcrop.

Figure 1.3.1.4. Outcrop photograph of the Osilinka suite leucocratic granite. Deformation in this lithology is cryptic due to the lack of mafic minerals.

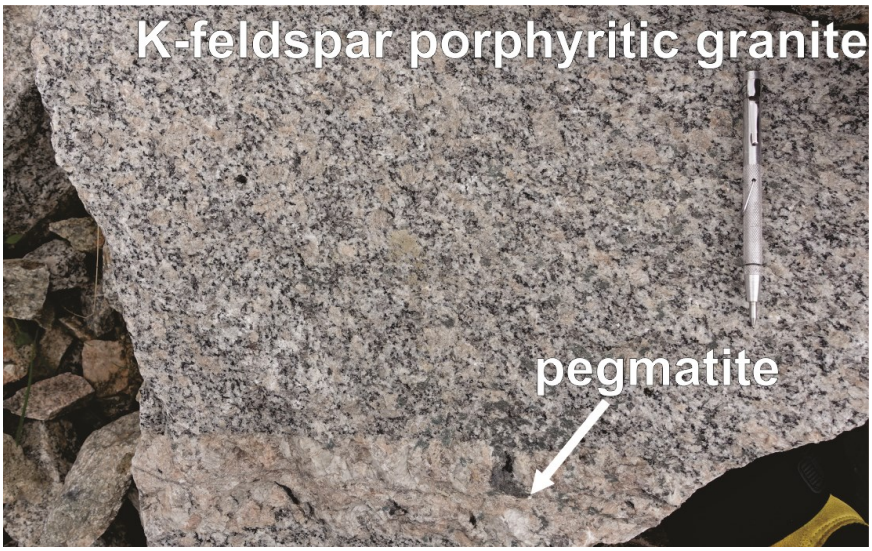

Figure 1.3.1.5. Outcrop photograph of the Mesilinka suite K-feldspar porphyritic granite that is cut sharply by a late granitic pegmatite dyke. Black biotite defines a tectonic foliation in the K-feldspar porphyritic granite.

1.3.2 Previous Work

1948 to 1954

The Hogem batholith area was originally mapped by Lord (1948), with the most recent map updates to northern Hogem batholith by Ootes et al. (2019a,b, 2020a,b). Lord (1948) identified the Hogem batholith as part of the Omineca intrusions and briefly described the field relationships and mineralogy of the main lithologies. Lord (1948) constrained the relative age of emplacement of the Omineca intrusions from late Lower Jurassic to upper Lower Cretaceous. Armstrong (1949) identified the largest known body of the Omineca intrusions as the Hogem batholith. It was inferred that Hogem batholith differentiated in place into a granodiorite-granite core bordered by more mafic phases (Armstrong, 1949). Armstrong (1949) sub-divided the Duckling Creek syenite, suggesting it may be younger than the Hogem batholith. Roots (1954) described the Hogem batholith as a composite intrusive body composed of many plutons, which represent a prolonged period of magmatism. Roots (1954) divided the batholith into lesser older 'melanocratic' rocks and major younger 'leucocratic' rocks.

1968 to 1978

The BSc thesis of Koo (1968) on the geology and mineralization of the Lorraine deposit, hosted by the Duckling Creek syenites of the Hogem batholith, proposed that the syenites formed by metasomatism of Hogem batholith diorites. A biotite K-Ar date of 170±8 Ma (confidence level not stated) was thought to represent the minimum age of syenite crystallization and the maximum age of mineralization (Koo, 1968). Irvine (1971) reported a biotite K-Ar date of 122±6 (2σ) Ma for a Hogem batholith granite sample. Irvine (1971) stated this was the first geochronological date reported for the Hogem batholith and suggested the age was correlative with geochronology results from the Cassiar batholith.

Garnett (1972) grouped the syenitic phases into the Duckling Creek Syenite Complex and described copper mineralization within this complex in southern Hogem batholith. Garnett (1972) described two types of copper mineralization in the Hogem area, with one found as stringers within volcanic rocks at the Hogem batholith-Takla Group contact zone, and the other as disseminated sulphide minerals within the Duckling Creek Syenite Complex (Garnett, 1972).

Woodsworth (1976) grouped the Hogem batholith into four tectonic units with distinct rock types and structural characteristics. The predominantly diorite to monzodiorite intrusive body in eastern Hogem batholith was named the 'Thane Creek pluton' (Woodsworth, 1976). In western Hogem batholith, foliated, quartz-rich, quartz monzodiorite to granodiorites were grouped as the 'Mesilinka pluton'. Woodsworth (1976) interpreted the Thane Creek and Mesilinka plutons as the oldest intrusive rocks in Hogem batholith. Woodsworth (1976) determined the timing of magmatism of the Thane Creek and Mesilinka plutons to between deposition of the Takla Group (Late Triassic) and emplacement of the Duckling Creek Syenite Complex (Early Jurassic). The PhD thesis of Meade (1977) described lithologies and interpreted geochemistry of the Takla Group volcanic rocks and intrusive rocks of the Germansen and Hogem batholiths.

Garnett (1978) studied part of the southern Hogem batholith and determined three distinct phases of magmatism based on geochronology and geochemistry. Phase 1 includes the 'Hogem basic suite' and 'Hogem granodiorite' and was constrained to 203±9 to 175±5 Ma using K-Ar biotite and hornblende geochronology (Garnett, 1978). Phase 2 represents the Duckling Creek syenite, with magmatism dated between 177±5 and 170±8 Ma (K-Ar biotite and hornblende; Garnett, 1978; Koo, 1968). Phase 3 includes leucocratic granites with a K-Ar biotite date of 112±4 Ma (Garnett, 1978).

1991 to 2005

Woodsworth et al. (1991) compared the Hogem batholith to other Quesnel terrane intrusions and called the leucocratic granite intrusions in Hogem the 'Osilinka stocks'. The Osilinka stocks were correlated to the Cretaceous Cassiar batholith to the north. Ferri et al. (1993) and Ferri (1997) mapped and described stratigraphy of the Takla Group volcanics and Lay Range assemblage surrounding the Hogem batholith area. Nixon and Peatfield (2003) described the geology and interpreted the magmatic setting of the Duckling Creek Syenite Complex around the Lorraine Cu-Au deposit.

Nelson et al. (2003) referred to the leucocratic granite phase as the Osilinka pluton. Mortensen et al. (1995) determined a zircon TIMS U-Pb age of 204.0±0.4 Ma on the CAT monzonite of the Thane Creek pluton (Table 1.3.2.1). Schiarizza and Tan (2005a,b) mapped part

of northern Hogem batholith and determined preliminary Early Cretaceous U-Pb zircon and titanite ages from the Mesilinka pluton (ca. 135 Ma).

2014 to Present

Devine et al. (2014) and Bath et al. (2014) studied the Duckling Creek Syenite Complex-hosted Lorraine Cu-Au deposit in the central Hogem batholith (Figure 1.2.5.1). Isotopic ages reported in these studies constrained crystallization and mineralization ages within the Duckling Creek Complex (Table 1.3.2.1). Ootes et al. (2019a,b, 2020a,b) updated and refined mapping in northern Hogem batholith. Ootes et al. (2019a,b) sub-divided the plutons into Thane Creek, Duckling Creek, Mesilinka, and Osilinka intrusive suites based on previous studies (Woodsworth, 1976; Woodsworth et al., 1991). Ootes et al. (2020b) determined preliminary U-Pb zircon and Ar-Ar biotite, hornblende, and muscovite geochronology (Table 1.3.2.1). Ootes et al. (2020c) and Jones et al. (2021) summarized new and previously unpublished geochronological data from northern Hogem batholith and constrained the crystallization ages of the four intrusive suites. A portion of the zircon LA-ICP-MS U-Pb data reported in Ootes et al. (2020c) and Jones et al. (2021) were collected for this thesis study (section 3.2.1.1).

Table 1.3.2.1. Summary of previously published northern Hogem batholith mineral U-Pb and Ar-Ar geochronology, modified after Table 1 from Jones et al. (2021). Ages are quoted at 95% (2σ) uncertainty. Bt: biotite; ttn: titanite; zr: zircon; hbl: hornblende.

Intrusive Suite	Lithology	Method	Age (Ma)	Source
Mesilinka	Tonalite	Ar-Ar (bt)	108±2	Jones et al. (2021)
Mesilinka	Tonalite	Ar-Ar (bt)	111±3	Jones et al. (2021)
Mesilinka	Granodiorite	Ar-Ar (bt)	123±2	Jones et al. (2021)
Mesilinka	Equigranular granite	TIMS U-Pb (ttn)	133.9±0.3	Jones et al. (2021)
Mesilinka	Porphyritic granite	TIMS U-Pb (ttn)	134.5±0.3	Jones et al. (2021)
Mesilinka	Porphyritic granite	TIMS U-Pb (zr)	135.0±0.3	Jones et al. (2021)
Duckling Creek	Vein: biotite-albite-apatite	Ar-Ar (bt)	175.2±0.9	Devine et al. (2014)
Duckling Creek	Leucosyenite dyke	TIMS U-Pb (zr)	176.8±0.2	Devine et al. (2014)
Duckling Creek	Syenite	Ar-Ar (hbl)	177±5	Jones et al. (2021)
Duckling Creek	Vein: biotite-K-feldspar-albite-magnetite	Ar-Ar (bt)	177.1±0.9	Devine et al. (2014)
Duckling Creek	Syenite	TIMS U-Pb (zr)	177.3±0.4	Bath et al. (2014)
Duckling Creek	Pegmatite dyke	TIMS U-Pb (zr)	177.6±0.2	Devine et al. (2014)
Duckling Creek	Syenite	TIMS U-Pb (zr)	178.4±0.3	Bath et al. (2014)
Duckling Creek	Pseudoleucite bearing feldspathic pyroxenite	TIMS U-Pb (zr)	178.4±0.3	Bath et al. (2014)
Duckling Creek	Rhythmically layered syenite	TIMS U-Pb (zr)	178.6±0.2	Bath et al. (2014)
Duckling Creek	Syenite	TIMS U-Pb (zr)	178.7±0.3	Bath et al. (2014)
Duckling Creek	K-feldspar megacrystic porphyry	TIMS U-Pb (zr)	178.8±0.2	Devine et al. (2014)
Duckling Creek	Equigranular monzonite	TIMS U-Pb (zr)	179.7±2.5	Devine et al. (2014)
Duckling Creek	Fine-grained, equigranular syenite	TIMS U-Pb (zr)	180.2±0.3	Devine et al. (2014)
Duckling Creek	Biotite pyroxenite	Ar-Ar (bt)	181.7±1.0	Devine et al. (2014)
Thane Creek	Diorite	Ar-Ar (hbl)	124±2	Jones et al. (2021)
Thane Creek	Diorite	Ar-Ar (bt)	124±1	Jones et al. (2021)
Thane Creek	Diorite	Ar-Ar (bt)	126±2	Jones et al. (2021)
Thane Creek	Diorite	CA-TIMS U-Pb (zr)	196.6±0.9	Ootes et al. (2020b)
Thane Creek	Hornblendite	CA-TIMS U-Pb (zr)	197.6±0.1	Ootes et al. (2020b)
Thane Creek	Rhonda Gabbro	TIMS U-Pb (zr)	200.9±0.2	Bath et al. (2014)
Thane Creek	Quartz monzodiorite	Ar-Ar (hbl)	202±5	Jones et al. (2021)
Thane Creek	CAT monzonite	TIMS U-Pb (zr)	204.0±0.4	Mortensen et al. (1995)

1.4 Field Work and Sample Collection

Plutonic rock samples were collected over the course of the 2018 and 2019 field seasons with the British Columbia Geological Survey. This thesis makes up a portion of the larger Hogem batholith study, which is a multi-year regional bedrock mapping program in the northern Hogem batholith and surrounding area (Ootes et al., 2019a,b, 2020a,b). The samples collected specifically for this thesis were obtained in the 2019 field season over 3 days via helicopter, after identifying the main lithologies and locations to be studied. These are supplemented by samples collected during bedrock mapping in 2018 (denoted by sample names with the prefix '18'; Figure 1.3.1.1). This thesis focuses on the geochronology and isotopic tracing of the batholith and hence geochronology samples taken here supplement a much larger whole rock dataset constructed in the 2018 and 2019 field seasons. The outcrop locations for geochronology samples were chosen to represent the main intrusive suites within the Hogem batholith, providing a representative distribution across the mapping area to account for any geochemical heterogeneity (Appendix A1). Care was taken to ensure that the samples are as fresh as possible, not showing evidence of extensive alteration or veining. Samples were collected away from porphyry-related alteration, as this can significantly affect the geochemistry of samples.

1.5 Sample Descriptions and Petrography

Hand sample and petrographic descriptions of samples collected for whole rock and mineral geochemistry are summarized below. Sample locations are in Appendix A1. Complete modal abundances and petrographic details are in Appendix A2.

Thane Creek suite

Hornblendite: 18lo22-1a

Hornblendite sample 18lo22-1a of the Thane Creek suite is from 18.6 km south-southeast of Mount Ferris (Figure 1.3.1.1). The rock is a coarse-grained to pegmatitic plagioclase-bearing hornblendite (Figure 1.5.1A-B). Pegmatitic white amphibole-plagioclase segregations (~7%) are interstitial to predominantly green amphibole (~72%). Amphibole is commonly overgrown by brown or green biotite, with biotite making up ~10% of the sample. The sample contains ~5% magnetite that is interstitial to amphibole and is concentrated with accessory titanite (1%) and apatite (trace). Coarse, subhedral accessory epidote (2%) occurs in pegmatitic plagioclase

segregations. Euhedral, ~100 to 200 μm long zircon (trace) grains occur within patches of intercumulus feldspar and epidote. Trace fine-grained chalcopyrite is disseminated through the sample.

Quartz diorite: 18lo22-1d

Quartz diorite sample 18lo22-1d of the Thane Creek suite is from 18.6 km south-southeast of Mount Ferris, approximately 100 m east of hornblendite sample 18lo22-1a (Figure 1.3.1.1). The rock is a "salt and pepper", medium-grained equigranular quartz diorite (Figure 1.5.1C-D). The rock is deformed and contains a moderate foliation defined by plagioclase, biotite, and amphibole. The sample is mostly clay-altered plagioclase (65%), biotite (12%), and amphibole (6%). Minor clay-altered alkali feldspar (7%) and quartz (1-2%) are present and interstitial to plagioclase. Accessory anhedral to subhedral, fine-grained epidote, apatite, magnetite, and zircon spatially occur with biotite. Trace fine-grained chalcopyrite is disseminated through the sample.

Quartz diorite: 19GJ12-4

Quartz diorite sample 19GJ12-4 of the Thane Creek suite is from 17.9 km east-northeast of Notch Peak (Figure 1.3.1.1). The rock is a white and black, medium-grained, equigranular quartz diorite, and is composed of mostly plagioclase (~62%), with about 25% equal parts green amphiboles with corroded clinopyroxene cores, and brown (metamorphic?) and green biotite (Figure 1.5.1E-F). The sample contains minor quartz (~6%) and alkali feldspar (~7%), with accessory magnetite, apatite, titanite, zircon, and epidote. Titanite occurs as rims on magnetite grains. Euhedral, fine-grained apatite (trace) are included in feldspar, magnetite, and amphibole. Epidote occurs as fine-grained patches that occur with altered feldspar. Anhedral to euhedral, fine-grained magnetite (1%) are disseminated throughout the sample and as an alteration product within amphibole. Zircon (trace) occurs as euhedral, ~50 to 100 μm long inclusions in amphibole and clinopyroxene. Trace fine-grained chalcopyrite is disseminated and occurs as inclusions in magnetite.

Quartz monzodiorite: 19GJ13-3

Quartz monzodiorite sample 19GJ13-3 of the Thane Creek suite is from 25.9 km southeast of Notch Peak (Figure 1.3.1.1). The rock is a "salt and pepper", fine- to medium-

grained, equigranular quartz monzodiorite, composed of ~40% euhedral plagioclase, ~30% poikilitic alkali feldspar, and ~15% anhedral, strained quartz (Figure 1.5.1G-H). Mafic minerals make up ~10% of the sample, mainly subhedral amphibole (8%) with lesser biotite (2%). Anhedral magnetite and titanite, and euhedral apatite and zircon are accessory. Titanite occurs as ~1 mm poikilitic grains and as fine rims on magnetite.

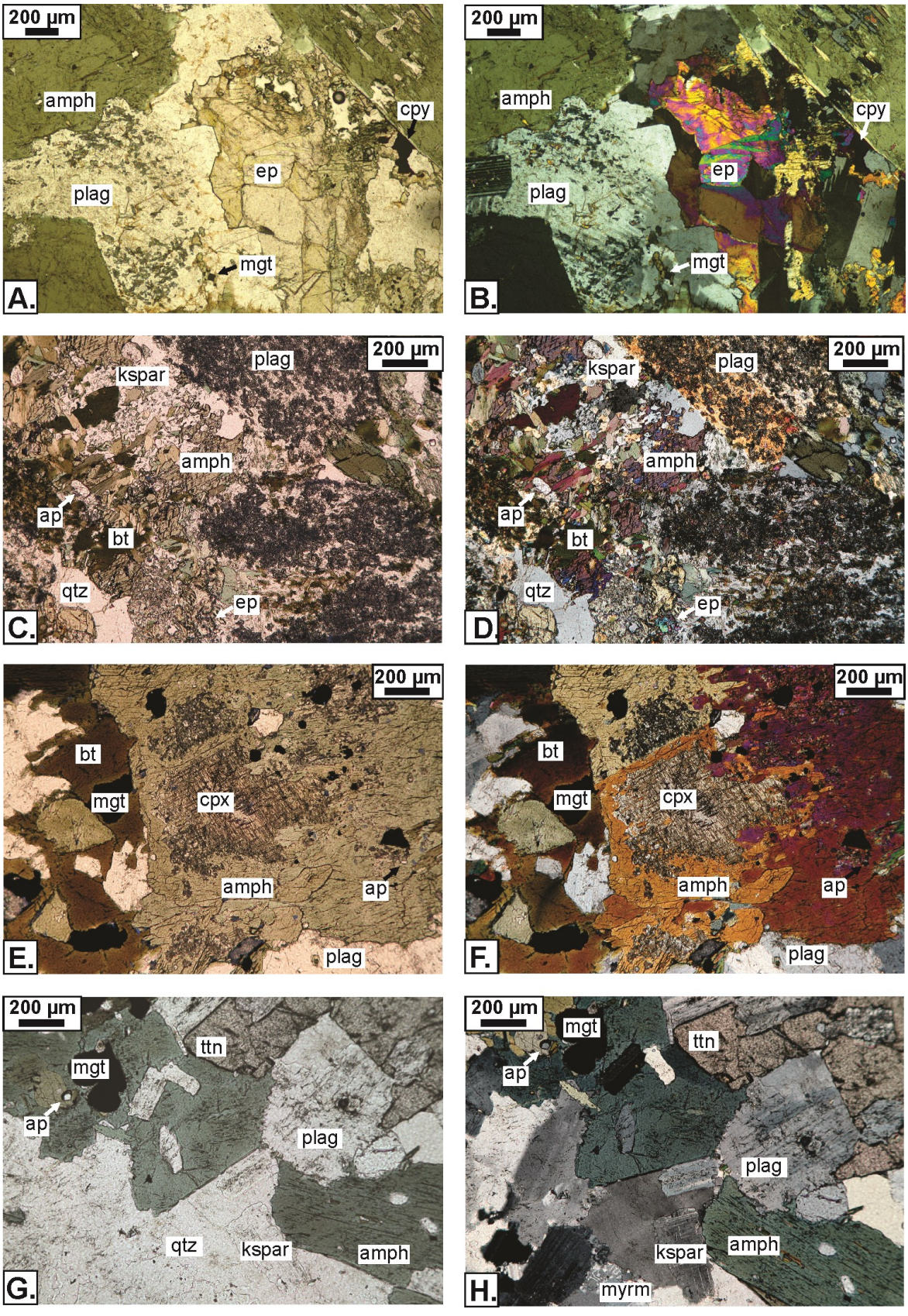
200 µm
amph
cpy
ep
plag
mgt
A.
200 µm
amph
cpy
ep
plag
mgt
B.
200 µm
kspar
plag
amph
ap
bt
qtz
ep
C.
200 µm
kspar
plag
amph
ap
bt
qtz
ep
D.
200 µm
bt
mgt
cpx
amph
ap
plag
E.
200 µm
bt
mgt
cpx
amph
ap
plag
F.
200 µm
ttn
mgt
ap
plag
qtz
kspar
amph
G.
200 µm
mgt
ttn
ap
plag
kspar
amph
myrm
H.

Figure 1.5.1. Photomicrographs of Thane Creek suite intrusive rock samples: **A)** Sample 18lo22-1a (PPL): Intercumulus patch of plagioclase, epidote, and magnetite with chalcopyrite, surrounded by cumulate amphibole in a hornblendite. **B)** Cross-polarized image of sample 18lo22-1a. **C)** Sample 18lo22-1d (PPL): Intergrown altered plagioclase and amphibole, with lesser quartz and K-feldspar, and accessory apatite, biotite, magnetite, and epidote in a quartz diorite. **D)** Cross-polarized image of 18lo22-1d. **E)** Sample 19GJ12-4 (PPL): Relict clinopyroxene core surrounded by later amphibole with inclusions of apatite and magnetite, and interstitial biotite, magnetite, and plagioclase in a quartz diorite. **F)** Cross-polarized image of sample 19GJ12-4. **G)** Sample 19GJ13-3 (PPL): intergrown plagioclase, K-feldspar, myrmekitic quartz, titanite, and amphibole, with apatite and magnetite inclusions in a quartz monzodiorite. **H)** Cross-polarized image of 19GJ13-3. Cpx: clinopyroxene, amph: amphibole, bt: biotite, mgt: magnetite, ap: apatite, plag: plagioclase, ep: epidote, cpy: chalcopyrite, kspar: K-feldspar, ttn: titanite, qtz: quartz.

Duckling Creek suite

Syenite: 18lo25-2a

Syenite sample 18lo25-2a of the Duckling Creek suite is from 22.7 km southeast of Notch Peak (Figure 1.3.1.1). The rock is a pink-white, medium-grained, equigranular syenite (Figure 1.5.2A-B). The sample consists of ~90% two alkali feldspars (K- and Na-bearing), with lesser clinopyroxene (~5%). Magnetite (2%), titanite (1%), chlorite (1%), and zircon (<1%) are accessory minerals. Titanite occurs as ~1 mm wide euhedral, wedge-shaped grains with clinopyroxene.

Biotite clinopyroxenite: 19GJ13-1

Biotite clinopyroxenite sample 19GJ13-1 of the Duckling Creek suite is from 18.2 km southeast of Notch Peak (Figure 1.3.1.1). The rock is a black, medium-grained, equigranular clinopyroxenite (Figure 1.5.2C-D). The sample consists of ~82% cumulate clinopyroxenite, with lesser subpoikilitic biotite (~10%), disseminated magnetite (~5%), and trace anhedral amphibole. Apatite (~3%), titanite (<1%), and epidote (<1%) are accessory. Apatite is bimodal and occurs as ~0.1 to 2 mm wide subhedral to anhedral, mostly interstitial to clinopyroxene and as inclusions in magnetite. The coarser grained apatite fraction is visible in hand sample.

Syenite: 19GJ13-2

Syenite sample 19GJ13-2 of the Duckling Creek suite is from 18.2 km southeast of Notch Peak (Figure 1.3.1.1). The rock is a pink-white and greenish-black, coarse-grained, K-feldspar phenocrystic syenite (Figure 1.5.2E-F). It is mostly made up of >2cm long alkali feldspar phenocrysts (~85%). Muscovite (10%), epidote (2%), magnetite (1%), biotite (1%), and quartz (trace) occur as fine-grained intergrown patches interstitial to K-feldspar phenocrysts. Subhedral

fine-grained titanite (trace) occurs with magnetite. Rare, disseminated, fine-grained chalcopyrite grains are spatially associated with biotite inclusions within K-feldspar.

Syenite: 19GJ13-4

Duckling Creek suite syenite sample 19GJ13-4 is from 28.9 km southeast of Notch Peak (Figure 1.3.1.1). The rock is a pink and greenish-black, medium-grained, foliated syenite (Figure 1.5.2G-H). The sample consists of ~80% anhedral, clay-altered alkali feldspar with lesser anhedral clinopyroxene (~8%) and amphibole (~5%). Biotite (2%) occurs as fine grains along clinopyroxene grain boundaries, has magnetite inclusions within cleavage, and is spatially associated with chlorite (2%). Magnetite (1%), muscovite (1%), apatite (1%), epidote (trace), and titanite (trace) are accessory minerals. Subhedral magnetite is generally very fine-grained and disseminated throughout the sample and concentrated with other mafic minerals. Muscovite is very fine-grained and occurs with epidote, biotite, and chlorite. Fine-grained euhedral apatite and anhedral titanite are spatially associated and occur interstitially to K-feldspar.

Syenite: 19GJ13-5a

Syenite sample 19GJ13-5a of the Duckling Creek suite is from 31.1 km southwest of Notch Peak (Figure 1.3.1.1). The sample was collected next to the Slide Cu-Au porphyry prospect, and 7 m south of a grab sample with chalcopyrite that yielded 0.07 wt.% Cu (19GJ13-5b; Ootes et al., 2020b). The rock is a pink-white and greenish-black, medium-grained, equigranular syenite (Figure 1.5.2I-J). It contains alkali feldspar (~70%), with lesser amphibole (9%), plagioclase (8%), and clinopyroxene (5%). Biotite, chlorite, and magnetite combine to make up ~5% of the sample, while fine-grained apatite, titanite, epidote, and zircon are trace (<1%) accessory minerals. Chalcopyrite occurs as rare fine, disseminated grains, and may be rimmed by titanite.

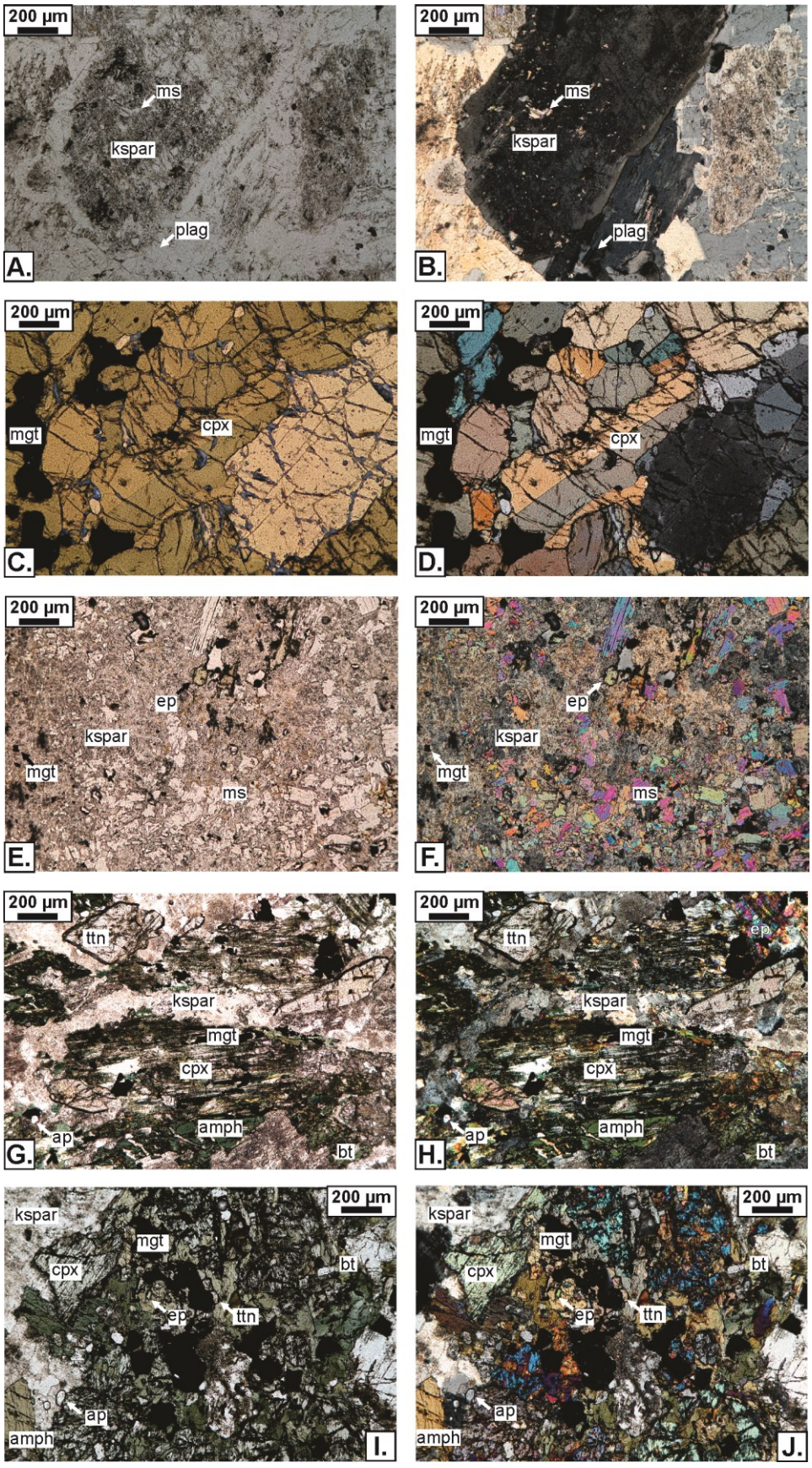
200 µm
ms
kspar
plag
A.
200 µm
ms
kspar
plag
B.
200 µm
mgt
cpx
C.
200 µm
mgt
cpx
D.
200 µm
ep
kspar
mgt
ms
E.
200 µm
ep
kspar
mgt
ms
F.
200 µm
ttn
kspar
mgt
cpx
ap
amph
bt
G.
200 µm
ttn
ep
kspar
mgt
cpx
ap
amph
bt
H.
kspar
200 µm
mgt
bt
cpx
ep
ttn
ap
amph
I.
kspar
mgt
bt
cpx
ep
ttn
ap
amph
J.

Figure 1.5.2. Photomicrographs of Duckling Creek suite samples. **A)** Sample 18lo25-2a (PPL): Coarse K-feldspar grains with minor muscovite alteration and plagioclase in a syenite. **B)** Cross-polarized image of 18lo25-2a. **C)** Sample 19GJ13-1 (PPL): Cumulate clinopyroxene and magnetite grains in a biotite clinopyroxenite. **D)** Cross-polarized image of sample 19GJ13-1. **E)** Sample 19GJ13-2 (PPL): Interstitial muscovite and epidote alteration in a K-feldspar phenocrystic syenite. **F)** Cross-polarized image of sample 19GJ13-2. **G)** Sample 19GJ13-4 (PPL): Clinopyroxene core with magnetite inclusions concentrated along cleavage, rimmed by amphibole and biotite, and surrounded by K-feldspar and titanite in a syenite. **H)** Cross-polarized image of 19GJ13-4. **I)** Sample 19GJ13-5a (PPL): Mafic clot of intergrown clinopyroxene, amphibole, biotite, and magnetite rimmed with titanite, and lesser apatite, surrounded by K-feldspar in a syenite. **J)** Cross-polarized image of 19GJ13-5a. Cpx: clinopyroxene, amph: amphibole, bt: biotite, mgt: magnetite, ap: apatite, kspar: K-feldspar, plag: plagioclase, ep: epidote, ttn: titanite.

Osilinka suite

Granite: 18lo17-1

Granite sample 18lo17-1 of the Osilinka suite is from 11.9 km southeast of Notch Peak (Figure 1.3.1.1). The rock is a white (leucocratic), medium-grained, equigranular granite (Figure 1.5.3A-B). Strained quartz (~37%), subhedral alkali feldspar (32%), and subhedral plagioclase (26%) comprise most of the sample. Rare accessory biotite, muscovite, and magnetite constitute less than 5% of the rock. Fine-grained biotite and magnetite occur interstitial to feldspar grains, whereas muscovite and sericite are present within feldspar cores and along grain boundaries. Trace euhedral zircon grains are found as inclusions within quartz.

Porphyry Sheet: 18lo20-4

Porphyry sheet sample 18lo20-4 is from a flat-lying dyke that cuts the Osilinka suite, 14.0 km southeast of Notch Peak (Figure 1.3.1.1). The dyke is at least 4 m thick. Fine-grained plagioclase and quartz make up most of the groundmass, with plagioclase phenocrysts up to 0.5 cm (Figure 1.5.3C-D). Magnetite, chlorite, epidote, and calcite are accessory groundmass minerals. Rare ~2.5 mm wide euhedral chalcopyrite grains also occur in the groundmass. A ~0.5 mm wide calcite-filled vein cuts the sample.

Granite: 19GJ12-3

Granite sample 19GJ12-3 of the Osilinka suite is from 6.1 km east of Notch Peak (Figure 1.3.1.1). The rock is a white (leucocratic), medium-grained, equigranular granite (Figure 1.5.3E-F). Strained quartz (~30%), subhedral alkali feldspar (29%), and subhedral plagioclase (35%) comprise most of the sample. Muscovite/sericite (5%), biotite (1%), epidote (trace), magnetite (trace), pyrite (trace), and zircon (trace) are accessory minerals. Muscovite/sericite is fine-

grained, anhedral and occurs as an alteration product of feldspar. Biotite and magnetite are spatially associated, very fine-grained, and disseminated. Epidote is fine-grained, anhedral, fractured, and disseminated through the sample. Rare, anhedral pyrite occurs as fine, disseminated grains rimmed by hematite. Rare, euhedral ~100 μm long zircon grains are found as inclusions in feldspar and quartz.

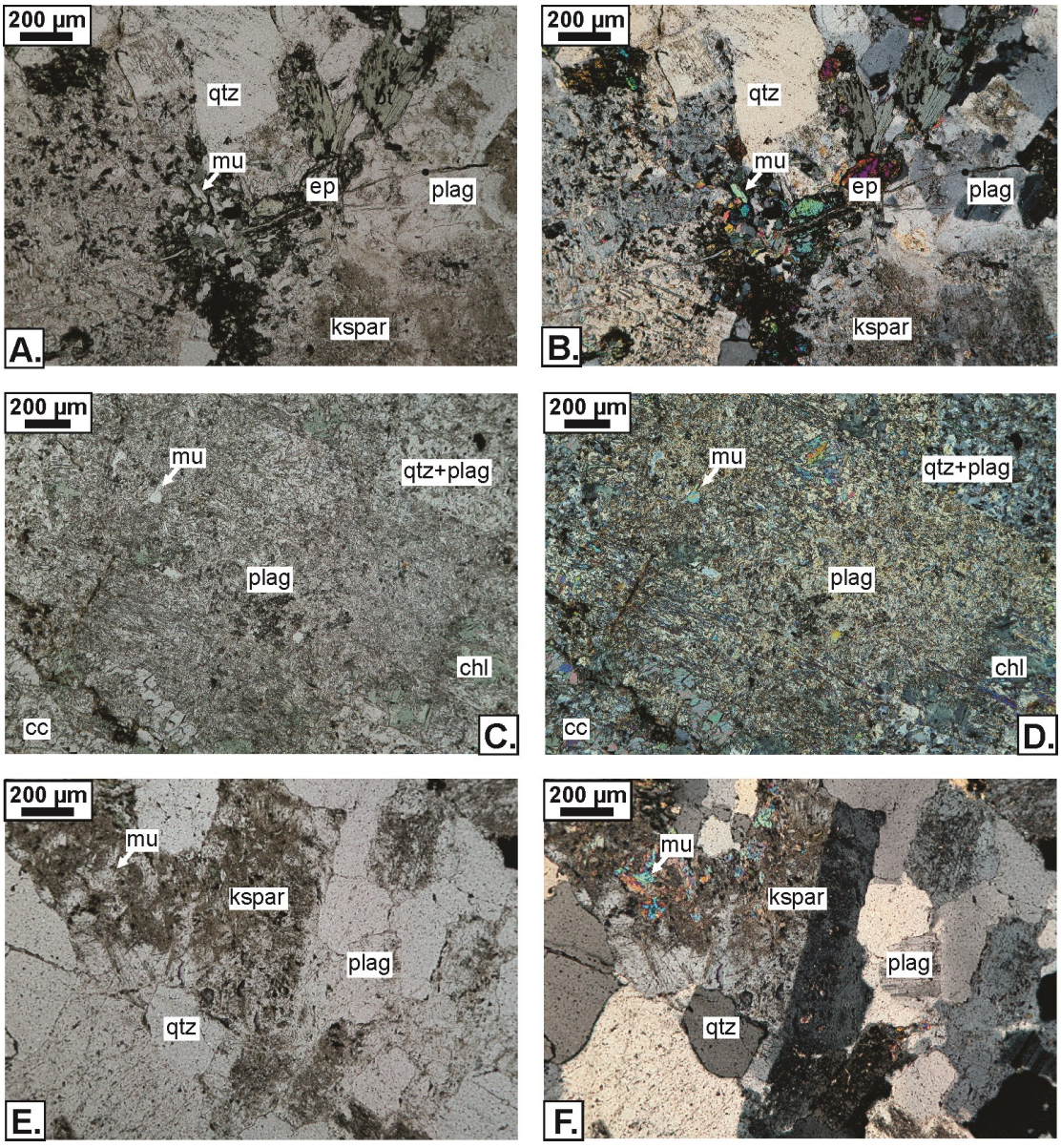

Figure 1.5.3. Photomicrographs of Osilinka suite samples. **A)** Sample 18lo17-1 (PPL): Intergrown quartz, plagioclase, and K-feldspar, with interstitial clot of biotite, epidote, and muscovite in a granite. **B)** Cross-polarized image of sample 18lo17-1. **C)** Sample 18lo20-4 (PPL): Muscovite alteration in plagioclase phenocryst, surrounded by quartz and plagioclase dominated matrix with lesser chlorite, crosscut by a calcite vein in a feldspar porphyry sheet. **D)** Cross-polarized image of sample 18lo20-4. **E)** Sample 19GJ12-3 (PPL): Intergrown K-feldspar, quartz, and plagioclase, with muscovite alteration in a granite. **F)** Cross-polarized image of 19GJ12-3. Qtz: quartz, plag: plagioclase, kspar: K-feldspar, ep: epidote, mu: muscovite, bt: biotite, chl: chlorite, cc: calcite.

Mesilinka suite

Equigranular granite: 18lo11-1

Equigranular granite sample 18lo11-1 of the Mesilinka suite is from 1.5 km northeast of Horn Peak (Figure 1.3.1.1). The rock is an equigranular, fine to medium-grained granite with a foliation defined by biotite (Figure 1.5.4A-B). The sample is mostly strained fine-grained quartz (40%), anhedral medium-grained alkali feldspar (30%), and clay-altered plagioclase (25%). Accessory minerals include zircon, fine-grained muscovite, biotite, and magnetite. Magnetite may be rimmed by titanite.

K-feldspar porphyritic granite: 18lo12-7

K-feldspar porphyritic granite sample 18lo12-7 of the Mesilinka suite is from 2.1 km northeast of Horn Peak (Figure 1.3.1.1). The rock is a medium-grained K-feldspar porphyritic granite with a foliation defined by biotite (Figure 1.5.4C-D). Clay-altered alkali feldspar phenocrysts up to 5 cm (38%), strained anhedral quartz (28%), and myrmekitic plagioclase (22%) comprise most of the sample. Biotite (10%) is 1 to 2 mm wide and interstitial to feldspar and quartz. Accessory minerals include zircon, magnetite, apatite, epidote, and allanite with epidote rims.

Tonalite: 19GJ12-1

Tonalite sample 19GJ12-1 of the Mesilinka suite is from 2.4 km northwest of Horn Peak (Figure 1.3.1.1). The rock is a grey, medium-grained, equigranular biotite-rich tonalite with a foliation defined by biotite (Figure 1.5.4E-F). Equigranular granite dykes cut the tonalite in outcrop ~50 m away. The sample is composed of slightly clay-altered, subhedral plagioclase (~50%), with lesser anhedral, strained quartz (~30%) and brown and green biotite (~15%). Subhedral amphibole (2%) and magnetite (trace) are spatially associated with biotite. Trace fine-grained anhedral epidote and titanite, and euhedral apatite and zircon occur with and as inclusions in biotite.

Tonalite: 19GJ12-2

Tonalite sample 19GJ12-2 of the Mesilinka suite is from 2.5 km northeast of Horn Peak (Figure 1.3.1.1). The rock is a grey, fine-grained, equigranular biotite-rich tonalite (Figure

1.5.4G-H). The sample is composed of slightly clay-altered, subhedral plagioclase (~48%), with myrmekitic quartz (~33%), and euhedral, bimodal (very fine- and fine-grained) biotite (~16%). Minor subhedral, fine-grained amphibole (2%) occurs with biotite and epidote. Apatite, epidote, magnetite, and titanite are accessory. Apatite (trace) occurs as very fine-grained, euhedral inclusions within feldspar, quartz, and biotite. Fine, anhedral epidote (1%) grains are spatially associated with biotite and may have rare allanite cores. Trace, fine-grained subhedral magnetite (trace) and anhedral titanite occur with biotite.

Equigranular granite: 19GJ16-2

Equigranular granite sample 19GJ16-2 of the Mesilinka suite is from 11.8 km southeast of Mount Ferris (Figure 1.3.1.1). The rock is a pinkish-white and black, fine to medium-grained, equigranular granite (Figure 1.5.4I-J). The sample is composed of slightly altered, anhedral K-feldspar (~40%), with subhedral, variably myrmekitic plagioclase (~32%), and anhedral, strained quartz (~22%). Minor anhedral, fine-grained brown biotite (2%) occurs interstitially to the main minerals and is variably altered to chlorite (1%). Apatite, epidote, magnetite, titanite, allanite, muscovite, zircon, chalcopyrite, and bornite are accessory. Apatite (1%) occurs as very fine-grained, euhedral inclusions within biotite. Subhedral, very fine- magnetite (1%), fine-, anhedral epidote (trace), and fine-, anhedral titanite (trace) grains are spatially associated with biotite. Rare, euhedral, fine-grained zoned allanite (trace) are rimmed by epidote. Euhedral, ~50 to 60 μm long zircon (trace) grains are inclusions in biotite, quartz, and feldspar. Chalcopyrite and bornite are rare, very fine-grained inclusions in magnetite.

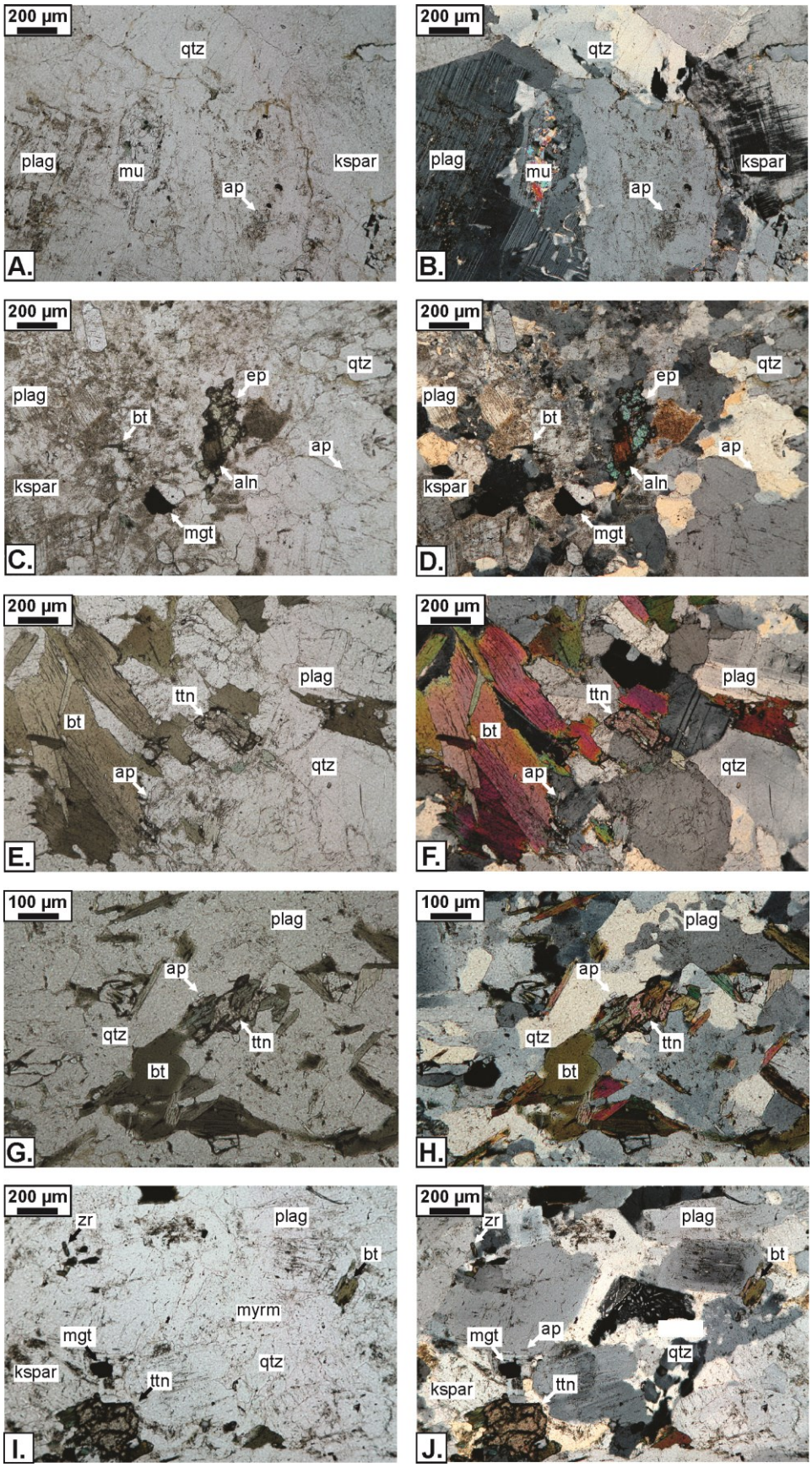
200 µm
qtz
plag
mu
ap
kspar
A.
200 µm
qtz
plag
mu
ap
kspar
B.
200 µm
qtz
ep
plag
bt
ap
kspar
aln
mgt
C.
200 µm
qtz
ep
plag
bt
ap
kspar
aln
mgt
D.
200 µm
plag
ttn
bt
ap
qtz
E.
200 µm
plag
ttn
bt
ap
qtz
F.
100 µm
plag
ap
qtz
ttn
bt
G.
100 µm
plag
ap
qtz
ttn
bt
H.
200 µm
zr
plag
bt
myrm
mgt
kspar
qtz
ttn
I.
200 µm
zr
plag
bt
mgt
ap
qtz
kspar
ttn
J.

Figure 1.5.4. Photomicrographs of Mesilinka suite samples. **A)** Sample 18lo11-1 (PPL): Intergrown K-feldspar, quartz, and plagioclase, with minor apatite inclusions and muscovite alteration in a granite. **B)** Cross-polarized image of 18lo11-1. **C)** Sample 18lo12-7 (PPL): Intergrown quartz, plagioclase, and K-feldspar, with lesser magnetite, biotite, apatite, and allanite rimmed by epidote in a granite. **D)** Cross-polarized image of 18lo12-7. **E)** Sample 19GJ12-1 (PPL): Intergrown quartz and plagioclase with biotite, titanite, and minor apatite inclusions in a tonalite. **F)** Cross-polarized image of sample 19GJ12-1. **G)** Sample 19GJ12-2 (PPL): Intergrown quartz and plagioclase with interstitial biotite and titanite, with minor apatite inclusions in a tonalite. **H)** Cross-polarized image of sample 19GJ12-2. **I)** Sample 19GJ16-2 (PPL): Intergrown quartz, plagioclase, and K-feldspar, with minor myrmekite, and inclusions of zircon, magnetite, titanite, and biotite. **J)** Cross-polarized image of 19GJ16-2. Qtz: quartz, plag: plagioclase, kspar: K-feldspar, myrm: myrmekite, ap: apatite, mu: muscovite, bt: biotite, ttn: titanite, mgt: magnetite, ep: epidote, aln: allanite, zr: zircon.

1.6 Data collection workflow

In situ isotopic and trace element data collection of minerals (zircon, apatite, titanite) for this study involve secondary ion mass spectrometry (SIMS) and laser ablation-inductively coupled plasma-mass spectrometry (LA-ICP-MS) analytical techniques. With the goal to collect multiple datasets from the same zircon grains, a strategic workflow was planned to preserve sufficient material for multiple analyses (Figure 1.6.1). Intrusive rock samples were split into separate portions for whole-rock and mineral geochemistry. After mineral separation, selection, and mounting (section 3.1.1), zircon oxygen-isotope data were collected first using SIMS, as it is the least destructive technique. A combination of destructive single stream and split stream LA-ICP-MS techniques were used to collect zircon U-Pb, Lu-Hf, and trace element data. Due to zircon grain size limitations and larger analytical spot sizes required for split stream, single stream LA-ICP-MS techniques were preferred to collect U-Pb data after SIMS oxygen-isotope analyses. For the remaining zircon Lu-Hf and trace element data collection, single stream or split stream LA-ICP-MS techniques were used depending on zircon grain sizes and the laboratory set up at the time.

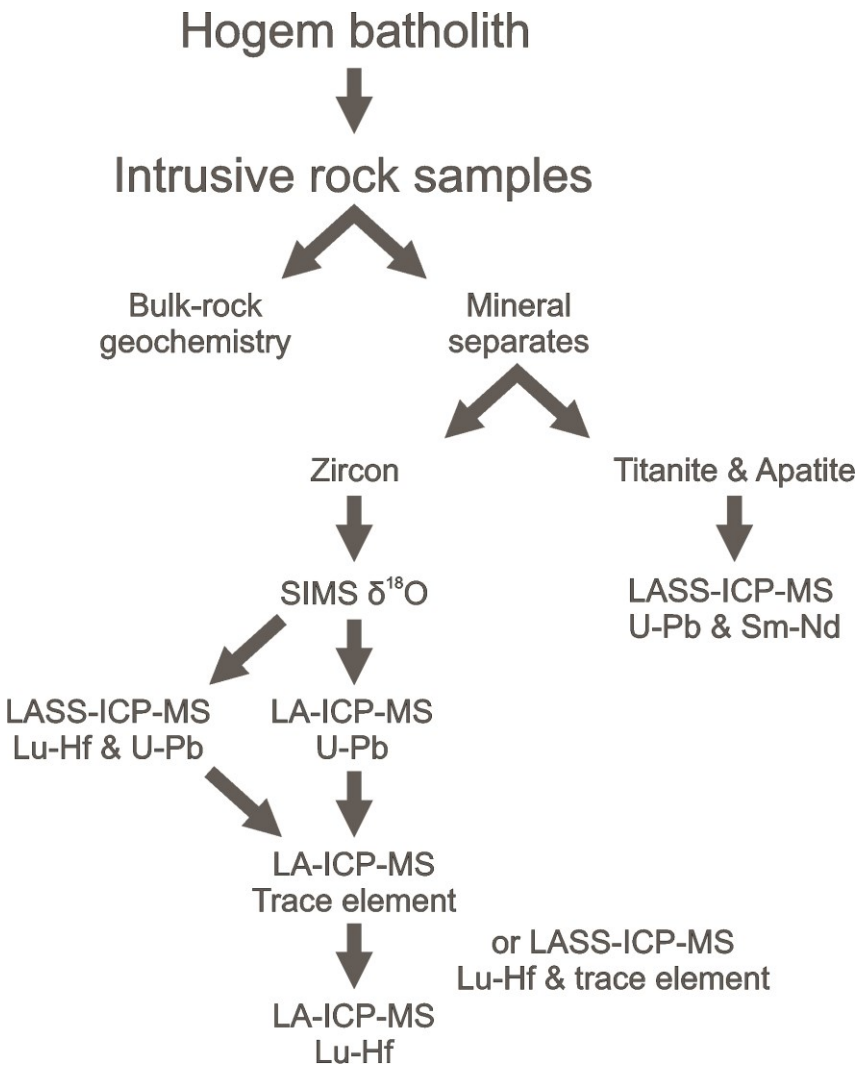

Figure 1.6.1. Sample preparation and data collection workflow for this study. Planning was required to maximize zircon material for multiple analyses on the same grains.

2 Whole Rock Geochemistry

2.1 Analytical Methods

One hundred and seventy-seven (110 in 2018 and 67 in 2019) fist-sized samples (approximately 200 g) were first cut using a rock saw to ensure no visible weathering, alteration, or veining was present. Where required, some of the samples were then cut into several centimetre-sized pieces using a rock saw and washed. These samples were then submitted to Actlabs in Ancaster, Ontario for whole rock major, minor, and trace element geochemical analysis. At Actlabs, samples were crushed to pass 2 mm, mechanically split using a rifle splitter, and pulverized using mild steel to 95% passing 105 µm (Code RX-2). Lithium metaborate/tetraborate fusion was performed on the resulting pulp to produce a molten bead, which was rapidly digested in nitric acid solution. Major element oxides were determined using inductively coupled plasma optical emission spectroscopy (ICP-OES) and trace element concentrations were determined using inductively coupled plasma mass spectrometry (ICP-MS), with 56 elements quantified in total (Code 4 Lithoresearch/WRA+Trace analytical package). Measurement accuracy was determined using certified reference materials (RMs) provided by Actlabs. Additionally, blind samples of the RMs SY-4, GSP-2, and TDB-1 and an in-house BCGS till standard were submitted for analysis with the unknown samples. Accepted values, if not provided by Actlabs, were determined from the GeoReM website (Jochum et al., 2005). Duplicate samples were inserted every 10-20 measurements to ensure precision throughout the analysis.

Measurement accuracy was estimated by comparing the measured value of the RMs to the certified reference value (Appendix B1 and B2). Major element accuracy was determined to generally be within 5% error. Major element concentrations which had greater than 5% error were either within the uncertainty of the standard, were in low concentration (< 1 wt.%), or both. Oxides MnO, TiO_2, K_2O, and P_2O_5 suffered higher uncertainties due to the low concentration of these elements in the RMs. Major element precision was usually better than 5% relative standard deviation (RSD), and often better than 2% RSD (Appendix B1 and B2). P_2O_5 was the least precise major element oxide, as it was higher than 5% RSD in 4 out of 10 duplicate measurements.

Minor and trace element accuracy was determined to generally be within 10% error (Appendix B1 and B2). Accuracy often improved to within 5% error with increased elemental concentrations. Minor and trace elements which had greater than 10% error were either within the uncertainty of the RM, lower in concentration (< 10 ppm), or present at concentrations outside the limit of detection. Exceptions to this include the elements Zr, Ba, and Ni, which consistently yielded results greater than 10% error. Hafnium, Nb, Y, Cs, Cu, As, Th, and Cr were each off-set by >10% only once in the sample batch. The rare earth elements (REEs) were determined to be within 10% of the accepted RM values, except where the RMs had elemental concentrations too high to quantify (Appendix B1 and B2). Minor, trace, and REE precision was generally 5% RSD or better (Appendix B1 and B2). Duplicate measurements with RSD higher than 10% were more common in the 2018 analysis than 2019.

In addition to determining the analytical accuracy and precision, the geochemical uncertainty introduced during sampling was estimated using the EXCEL spreadsheet developed by Stanley (2003). This spreadsheet provides an estimate of the 1 SD absolute sampling error (wt %) and relative sampling error (CV%) using mineral grain sizes, mineral modal percentages, and mass of a sample. Representative samples from each mappable lithology in the four Hogem suites were input into the spreadsheet, using the modal compositions and grain sizes determined from petrographic analysis. An estimated mass of 2 kg was used from the original sample weights, which varied from 2 to 5 kg. The average 1σ relative sampling error (CV%) for whole rock oxides of the representative lithologies is summarized in Table 2.1.1. Outside of analytical uncertainty, the whole rock geochemical results can be no more accurate than these sampling uncertainties.

Table 2.1.1. Average 1σ relative sampling error (CV%) for whole rock oxides of representative Hogem batholith lithologies, calculated after the approach of Stanley (2003).

	Oxide	**SiO_2**	**TiO_2**	**Al_2O_3**	**Fe_2O_3**	**FeO**	**MnO**	**MgO**	**CaO**	**Na_2O**	**K_2O**	**H_2O**	**P_2O_5**	**ZrO_2**	**Ce_2O_3**
Intrusive Suite	**Lithology**	**Average 1 Std. Dev. Relative Sampling Error (CV%)**													
Thane Creek	Hornblendite	1.03	2.03	0.91	0.89	0.80	0.00	1.16	1.11	1.05	0.50	1.01	0.63	1.08	0.00
	Diorite	0.19	2.49	0.23	0.06	0.61	0.00	1.02	0.62	0.22	0.45	0.83	0.11	0.17	0.00
Duckling Creek	Syenite	0.61	0.16	0.56	0.26	0.24	0.00	0.43	0.27	0.65	0.65	0.19	0.09	0.05	0.00
	Clinopyroxenite	0.25	0.00	0.32	0.30	0.17	0.00	0.26	0.25	9.23	0.12	0.27	0.42	0.00	0.00
Osilinka	Granite	0.17	0.00	0.22	1.43	0.10	0.00	0.11	0.35	0.31	0.31	0.07	0.00	0.36	0.00
Mesilinka	Tonalite	0.09	0.38	0.16	0.33	0.35	0.00	0.35	0.14	0.18	0.41	0.34	0.03	0.08	0.00
	Granite	0.16	0.76	0.11	0.49	0.24	0.00	0.34	0.15	0.18	0.07	0.31	0.03	2.93	2.99

2.2 Results

Whole rock major-, minor-, and trace-element geochemistry results are reported in Appendix B3. A total of 120 samples were analyzed from the four Hogem batholith intrusive suites. The results are summarized below according to intrusive suite. Major element data are reported on an LOI-free, anhydrous basis.

2.2.1 Major Element Variation

Thane Creek suite

Two fundamental groups can be subdivided from the Thane Creek suite based on field observations of mafic mineral content, which is supported by major element geochemistry. Hornblendites (high mafic mineral content) have relatively low SiO_2 (37 to 49 wt.%), Al_2O_3 (3 to 13 wt.%), Na_2O (0.4 to 3 wt.%), and relatively high, but variable, MgO (5 to 15 wt.%), FeO* (10 to 23 wt.%), CaO (8 to 15 wt.%), and TiO_2 (1.0 to 2.5 wt.%) (Figure 2.2.1.1). The Thane Creek suite 'diorites' (*sensu lato*: including granodiorites, quartz monzodiorites, quartz diorites, and diorites) have relatively lower mafic mineral contents and are higher in SiO_2 (48 to 70 wt.%), Al_2O_3 (15 to 20 wt.%), Na_2O (3 to 5 wt.%), and relatively low in MgO (1 to 6 wt.%), FeO* (3 to 10 wt.%), CaO (3 to 10 wt.%), and TiO_2 (0.3 to 1.0 wt.%) (Figure 2.2.1.1).

The Thane Creek suite samples range from mid-K to shoshonitic on a plot of SiO_2 versus K_2O (Figure 2.2.1.2), predominantly falling between mid-K and high-K. On the total alkalis – silica (TAS) diagram (Figure 2.2.1.3), the Thane Creek intrusive samples plot close to the subalkaline and alkaline fields boundary. 'Diorite' samples predominantly occur within the gabbro diorite and diorite compositional fields, while hornblendites plot within the peridotite and gabbro compositional fields (Figure 2.2.1.3).

Both hornblendites and diorites are mostly magnesian on the SiO_2 versus Fe* diagram (Figure 2.2.1.4). On the AFM ternary diagram, diorites scatter around the calc-alkaline trend, while the higher MgO hornblendites are tholeiitic (Figure 2.2.1.5). On the plot of SiO_2 versus modified alkali-lime index (MALI; Na_2O+K_2O-CaO), the Thane Creek suite rocks plot within the calc-alkalic to alkali-calcic fields (Figure 2.2.1.6). The Thane Creek suite is entirely metaluminous on the SiO_2 versus ASI plot (ASI <1.0), with the most SiO_2-rich samples plotting close to the metaluminous-peraluminous line (ASI=1.0) (Figure 2.2.1.7).

Overall, rocks of the Thane Creek suite range from ultramafic to felsic compositions and are predominantly characterized as calc-alkaline, metaluminous, and magnesian.

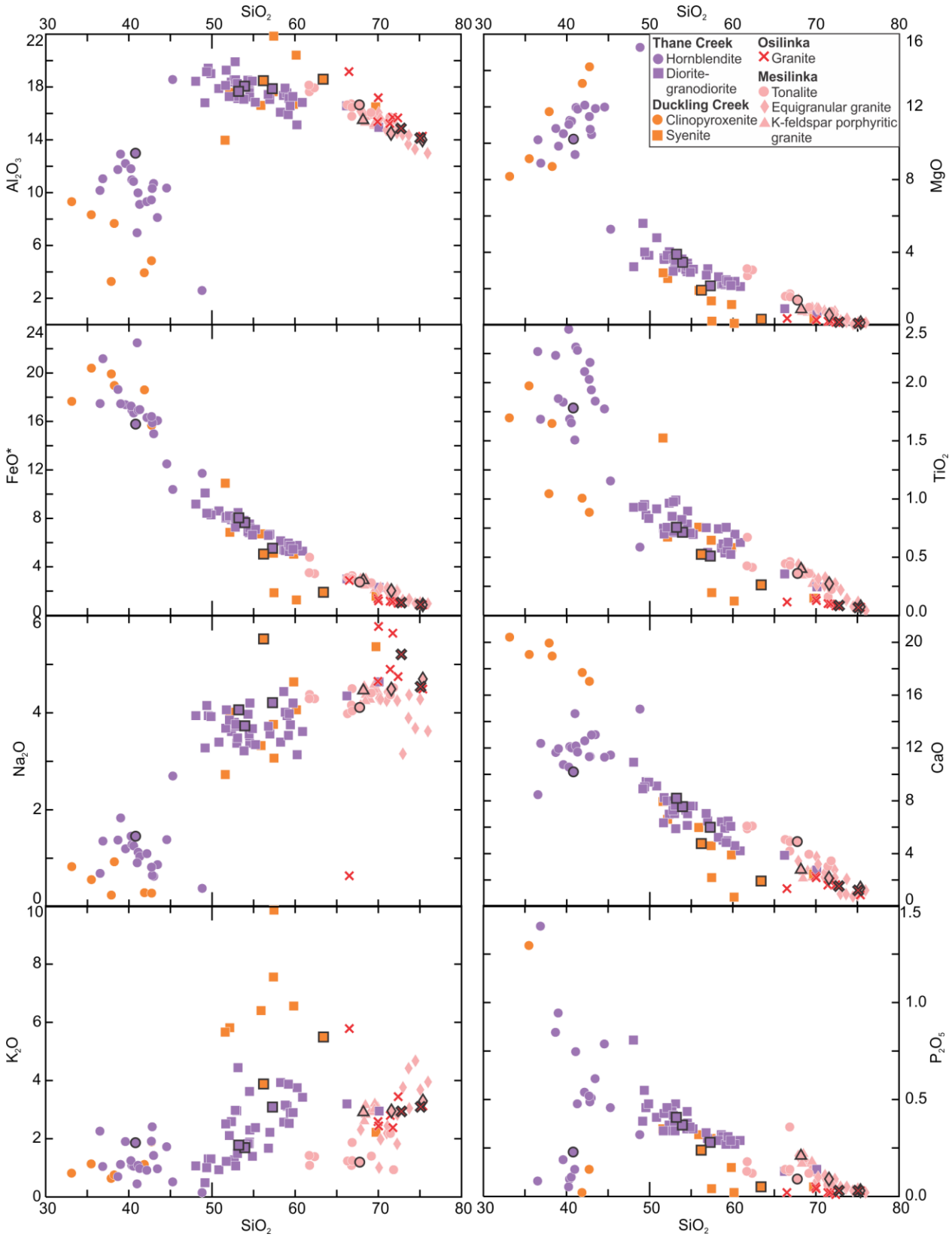

Figure 2.2.1.1. Major element oxide (wt. %) Harker plots of the four main intrusive suites of the Hogem batholith. Data points outlined in black are samples which were used for mineral isotopic analyses.

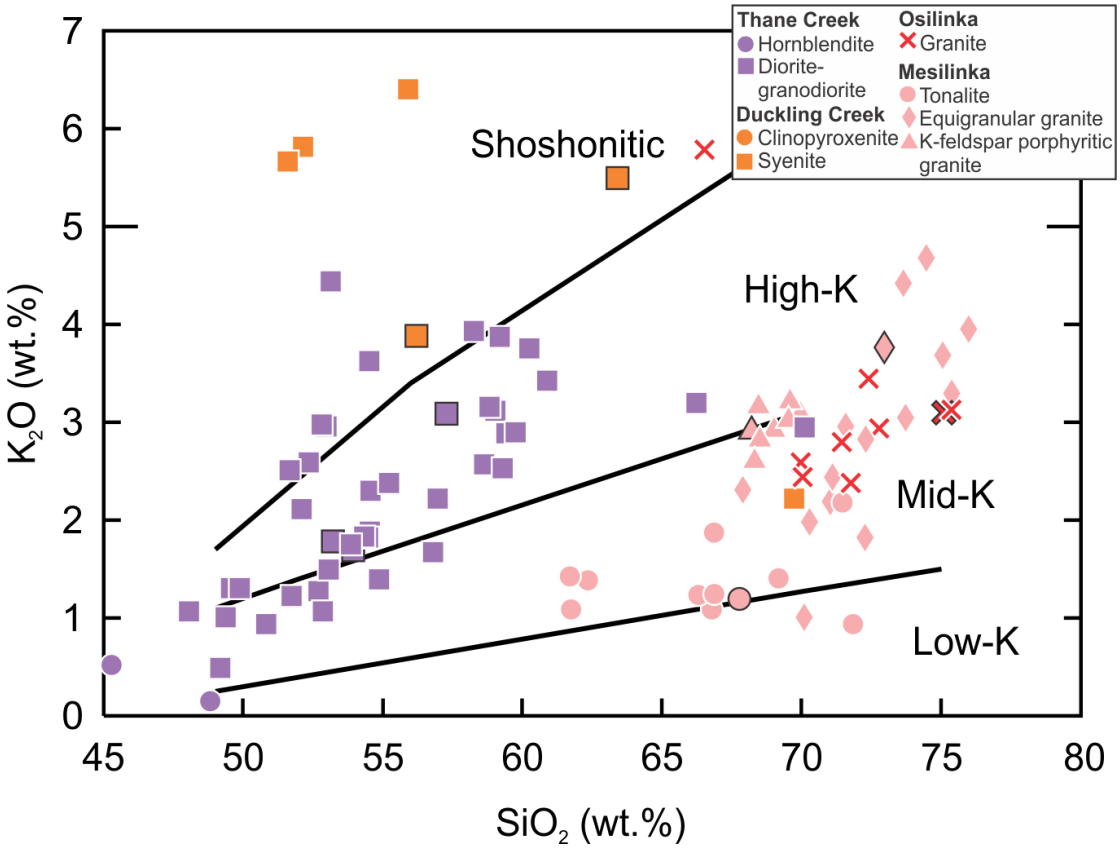

Figure 2.2.1.2. SiO_2 vs. K_2O plot of Peccerillo and Taylor (1976) showing low-, mid-, and high-K calc-alkaline and shoshonitic fields. Data points outlined in black are samples which were used for mineral isotopic analyses.

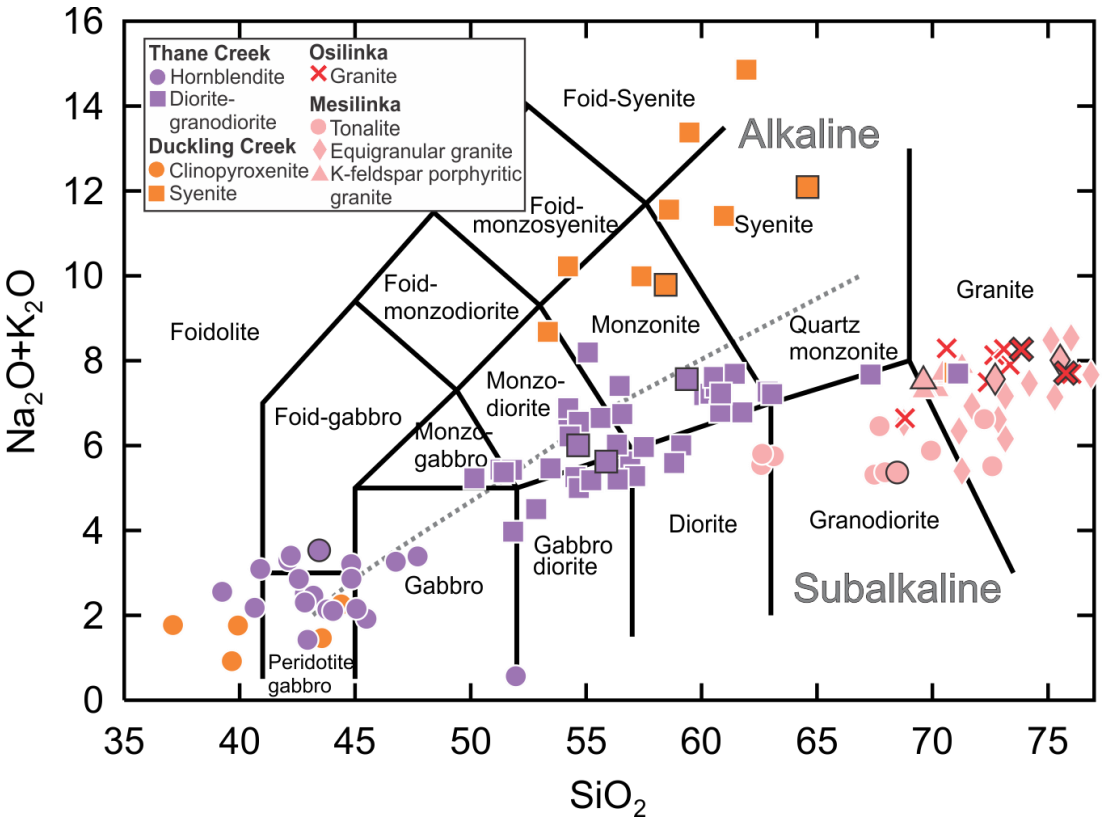

Figure 2.2.1.3. Total Alkali-Silica (TAS) diagram (wt.%) for the four main intrusive suites of the Hogem batholith, after LeBas et al. (1986). Intrusive grain size equivalent rock names after Middlemost (1994). Grey line dividing alkaline and subalkaline fields is from Irvine and Baragar (1971). Data outlined in black are samples which were used for mineral isotopic analyses.

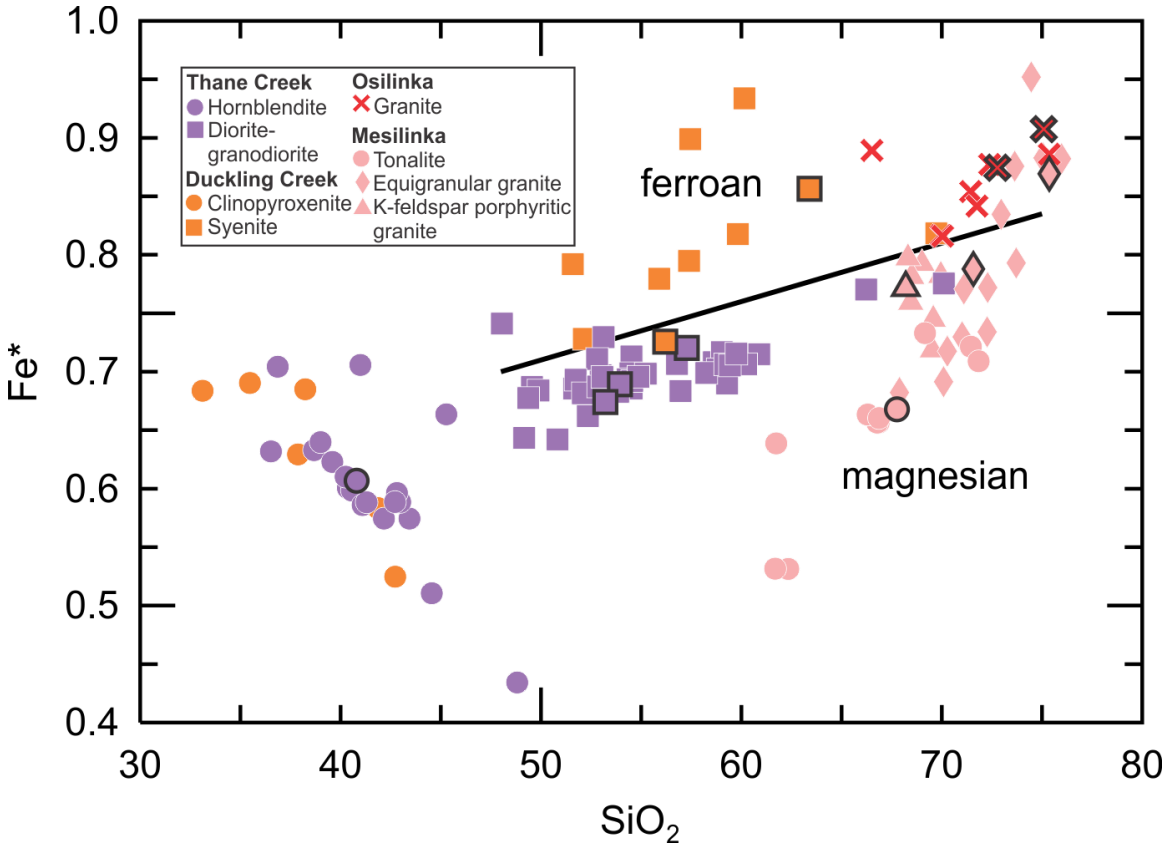

Figure 2.2.1.4. Fe-index versus SiO_2 (wt.%) from Frost and Frost (2008) for the four main intrusive suites of the Hogem batholith. Data points outlined in black are samples which were used for mineral isotopic analyses. Fe-index = FeO*/(FeO*+MgO).

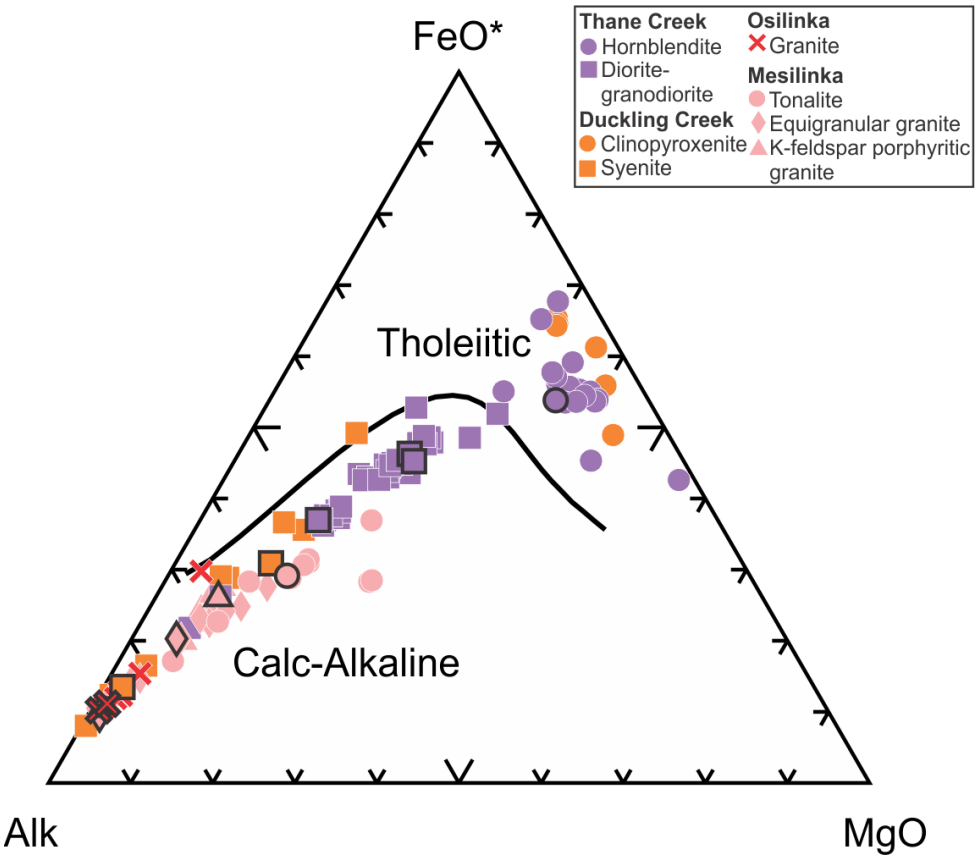

Figure 2.2.1.5. AFM (alkalies-FeO*-MgO) ternary plot of the four main intrusive suites of the Hogem batholith (Irvine and Baragar, 1971). Data outlined in black are samples which were used for mineral isotopic analyses.

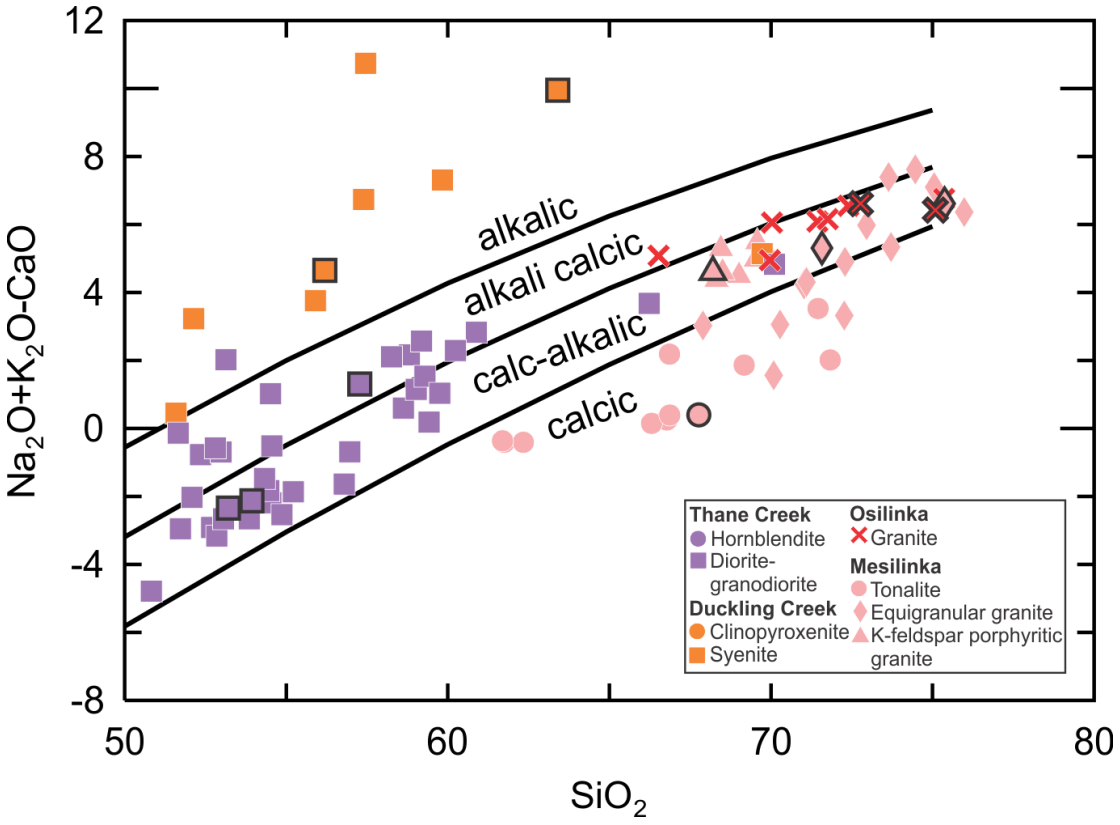

Figure 2.2.1.6. Modified alkali-lime index (MALI) versus SiO_2 (wt.%) from Frost and Frost (2008) of the four main intrusive suites of the Hogem batholith. Data points outlined in black are samples which were used for mineral isotopic analyses. MALI = molar Na_2O+K_2O-CaO.

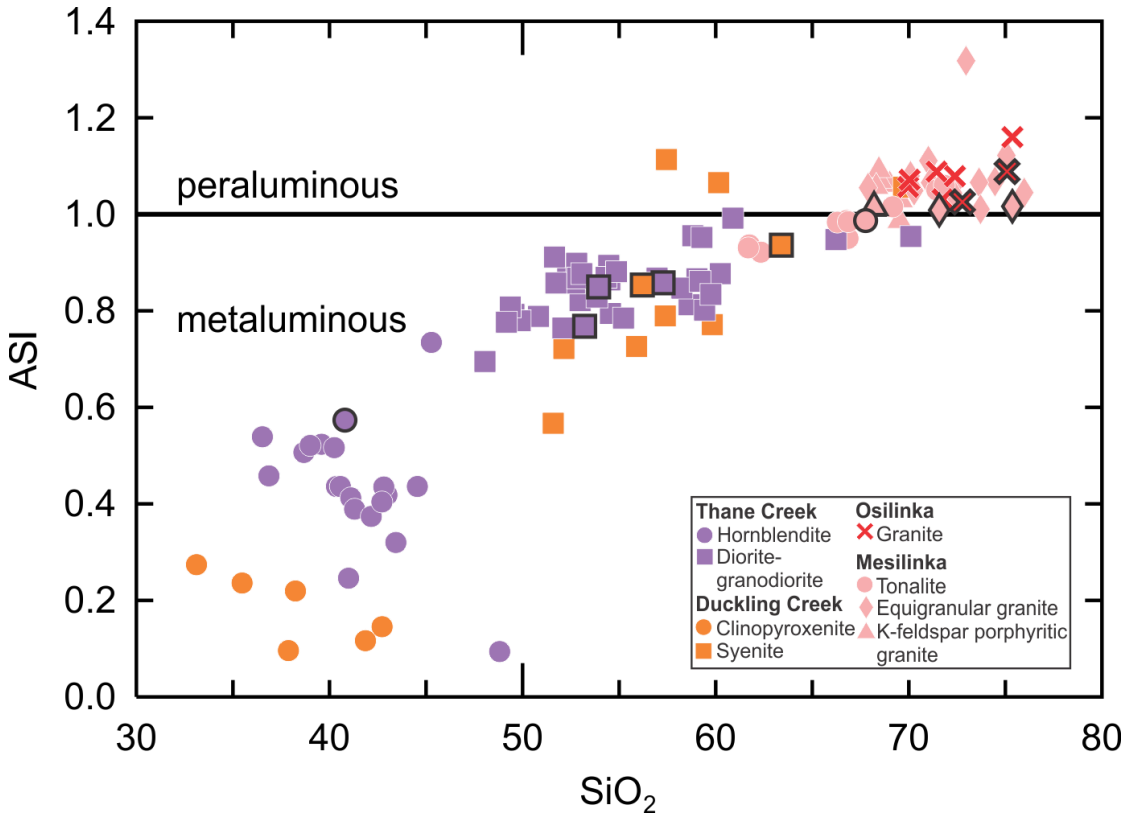

Figure 2.2.1.7. Alumina saturation-index (ASI) versus SiO_2 (wt.%) from Frost and Frost (2008) of the four main intrusive suites of the Hogem batholith. Data points outlined in black are samples which were used for mineral isotopic analyses. ASI = molar $Al_2O_3/(CaO+K_2O+Na_2O)$.

Duckling Creek suite

The Duckling Creek suite is subdivided into mafic pyroxenites and more felsic syenites to monzonites based on field observations of relative mafic mineral content, which is supported by whole rock geochemistry. Pyroxenites have low SiO_2 (33 to 43 wt.%), Al_2O_3 (3 to 9 wt.%), Na_2O (0.2 to 1 wt.%), K_2O (0.6 to 2 wt.%), and relatively high MgO (8 to 15 wt.%), FeO* (16 to 22 wt.%), CaO (17 to 20 wt.%), and TiO_2 (0.9 to 1.7 wt.%) (Figure 2.2.1.1). Duckling Creek 'syenites' (*sensu lato*: including monzonites and syenites) are higher in SiO_2 (52 to 70 wt.%), Al_2O_3 (14 to 20 wt.%), Na_2O (3 to 6 wt.%), K_2O (2 to 8 wt.%), and relatively low in MgO (0.4 to 3 wt.%), FeO* (2 to 11 wt.%), CaO (1 to 8 wt.%), and TiO_2 (0.1 to 1.5 wt.%) (Figure 2.2.1.1).

Nearly all the Duckling Creek syenite samples have compositions plotting within the shoshonitic field on the plot of SiO_2 versus K_2O (Figure 2.2.1.2). Clinopyroxenite samples are not plotted on this diagram, as the SiO_2 compositions are too low to be classified. On the TAS diagram, the Duckling Creek intrusive suite rocks mainly plot within the alkaline field (Figure 2.2.1.3). 'Syenite' samples predominantly range from the monzodiorite to syenite fields, while clinopyroxenites plot within the feldspathoidolite and peridotite gabbro compositional fields (Figure 2.2.1.3). The syenites mainly plot as ferroan on the SiO_2 versus Fe* diagram, while the pyroxenites are not classified due to their low SiO_2 contents (Figure 2.2.1.4). Syenites plot in the alkalic field on the SiO_2 versus MALI diagram (Figure 2.2.1.6). However, like the Thane Creek suite, on the AFM ternary plot, the Duckling Creek syenites plot as calc-alkaline, while the pyroxenites classify as tholeiitic, as this plot was not designed to differentiate alkaline rocks (Figure 2.2.1.5). Pyroxenites are distinctly metaluminous (ASI= 0.0-0.4), while syenites range from metaluminous to slightly peraluminous (ASI= 0.6-1.1) (Figure 2.2.1.7).

Overall, rocks of the Duckling Creek intrusive suite range from ultramafic to intermediate compositions and are predominantly characterized as alkaline, metaluminous, and ferroan.

Osilinka suite

The Osilinka suite rocks have relatively narrow major element compositional variations. Granites have high SiO_2 (67 to 75 wt.%), Al_2O_3 (14 to 19 wt.%), and Na_2O (0.6 to 6 wt.%), and low MgO (0.1 to 0.4 wt.%), FeO* (0.9 to 2.9 wt.%), TiO_2 (~0.1 wt.%), and CaO (0.9 to 2 wt.%) (Figure 2.2.1.1). Most Osilinka granite samples occur within the upper mid-K field on a plot of

SiO_2 versus K_2O (Figure 2.2.1.2). On the TAS diagram, the Osilinka samples plot within the subalkaline and granite compositional fields (Figure 2.2.1.3). The Osilinka granites plot as ferroan on the SiO_2 versus Fe* diagram (Figure 2.2.1.4). The Osilinka suite rocks are weakly peraluminous (ASI= 1.0-1.2) (Figure 2.2.1.7), and predominantly classify as calc-alkalic on both the SiO_2 versus MALI (Figure 2.2.1.6) and AFM plots (Figure 2.2.1.5).

Overall, the Osilinka suite rocks have felsic compositions, and are considered calc-alkaline, weakly peraluminous, and ferroan.

Mesilinka suite

Plutonic rocks of the Mesilinka suite generally form a continuous range of major element concentrations that span between tonalite and granite. Tonalites have the lowest SiO_2 (62 to 72 wt.%) and K_2O (0.9 to 2 wt.%), highest Al_2O_3 (16 to 18 wt.%), MgO (0.6 to 3 wt.%), FeO* (2 to 5 wt.%), TiO_2 (0.2 to 0.5 wt.%), and CaO (3 to 6 wt.%) (Figure 2.2.1.1). Equigranular granites have relatively high SiO_2 (68 to 76 wt.%) and Na_2O (3 to 5 wt.%), moderate K_2O (1 to 5 wt.%), Al_2O_3 (13 to 16 wt.%), and low MgO (0.1 to 1 wt.%), FeO* (1 to 3 wt.%), TiO_2 (0.04 to 0.4 wt.%), and CaO (0.7 to 4 wt.%) (Figure 2.2.1.1). The K-feldspar phenocrystic granite samples have narrower major element concentration ranges compared to equigranular granite samples. K-feldspar phenocrystic granites also have relatively high SiO_2 (68 to 69 wt.%) and Na_2O (~4 wt.%), moderate K_2O (~3 wt.%), Al_2O_3 (15 to 16 wt.%), and low MgO (0.6 to 1 wt.%), FeO* (2 to 3 wt.%), TiO_2 (0.3 to 0.4 wt.%), and CaO (2 to 3 wt.%) (Figure 2.2.1.1).

The Mesilinka suite intrusive rocks predominantly fall within the mid-K field on a plot of SiO_2 versus K_2O, but equigranular and K-feldspar phenocrystic granites range into the high-K field (Figure 2.2.1.2). The Mesilinka plutonic rocks have compositions that generally fall within the subalkaline field on the TAS diagram (Figure 2.2.1.3). Tonalite samples mostly plot within the diorite and granodiorite fields, while both equigranular and K-feldspar phenocrystic granites occur within the granodiorite and granite compositional fields (Figure 2.2.1.3). The tonalites and K-feldspar phenocrystic granites classify as magnesian on the Fe* versus SiO_2 plot, while equigranular granites classify as both magnesian and ferroan (Figure 2.2.1.4). On the AFM ternary, all three Mesilinka suite lithologies plot as calc-alkaline (Figure 2.2.1.5). On the SiO_2 versus MALI diagram, tonalites classify as calcic, K-feldspar phenocrystic granites classify as calc-alkalic, and equigranular granites classify as calcic to weakly alkali-calcic (Figure 2.2.1.6).

The Mesilinka tonalites plot across the metaluminous-peraluminous line (ASI= 0.9-1.1), while both equigranular granites (ASI= 1.0-1.3) and K-feldspar phenocrystic granites (ASI= 1.0-1.1) are weakly peraluminous (Figure 2.2.1.7).

Overall, Mesilinka suite rocks range in composition from intermediate to felsic, and are considered predominantly calcic to calc-alkalic, weakly peraluminous, and magnesian to ferroan.

2.2.2 Minor and Trace Element Variation

Thane Creek suite

On chondrite-normalized rare earth element plots, the Thane Creek suite plutonic rocks demonstrate low to moderate enrichment in LREE relative to HREE (La_N/Yb_N: 1.2-4.6) in hornblendites, and moderate enrichment (La_N/Yb_N: 4.5-11) in diorites (Figure 2.2.2.1-2.2.2.2). Hornblendite REE patterns are slightly concave downward to sigmoidal and diorite REE patterns are concave upward. Hornblendite samples have moderate negative Eu-anomalies (Eu/Eu_N^*=0.6-1.0), whereas diorite samples have moderate negative to positive Eu-anomalies (Eu/Eu_N^*=0.7-1.4; Figure 2.2.2.1 and 2.2.2.3).

The Thane Creek hornblendites show negative Nb-Ta and Zr signatures on primitive-mantle normalized trace element diagrams (Figure 2.2.2.4). Primitive-mantle normalized P and Ti are variable, resulting in both negative and positive anomalies. Lead anomalies range from absent to positive on normalised plots. Thane Creek diorites also display negative Nb-Ta anomalies and absent to positive Pb anomalies. However, Zr anomalies range from negative to positive and P and Ti are negative. Uranium and Th concentrations in Thane Creek plutonic rocks are relatively low (Figure 2.2.2.5). Hornblendites have U concentrations from 0.1 to 0.5 ppm and Th concentrations from 0.2 to 1.0 ppm. ‘Diorites’ are slightly more enriched, with U concentrations from 0.1 to 2.4 ppm and Th from 0.2 to 6.8 ppm. Thane Creek hornblendite samples yield the greatest ranges in Cu, Ni, and Cr concentrations. Hornblendites have Cu concentrations from <10 ppm (LOD) to 780 ppm, Ni concentrations from <10 ppm (LOD) to 110 ppm, and Cr concentrations from <10 ppm (LOD) to 340 ppm (Figures 2.2.2.6-2.2.2.8). Thane Creek diorites are significantly less enriched in Cu, Ni, and Cr than hornblendites. Diorites have Cu concentrations up to 220 ppm, Ni concentrations up to 30 ppm, and Cr concentrations up to 70 ppm.

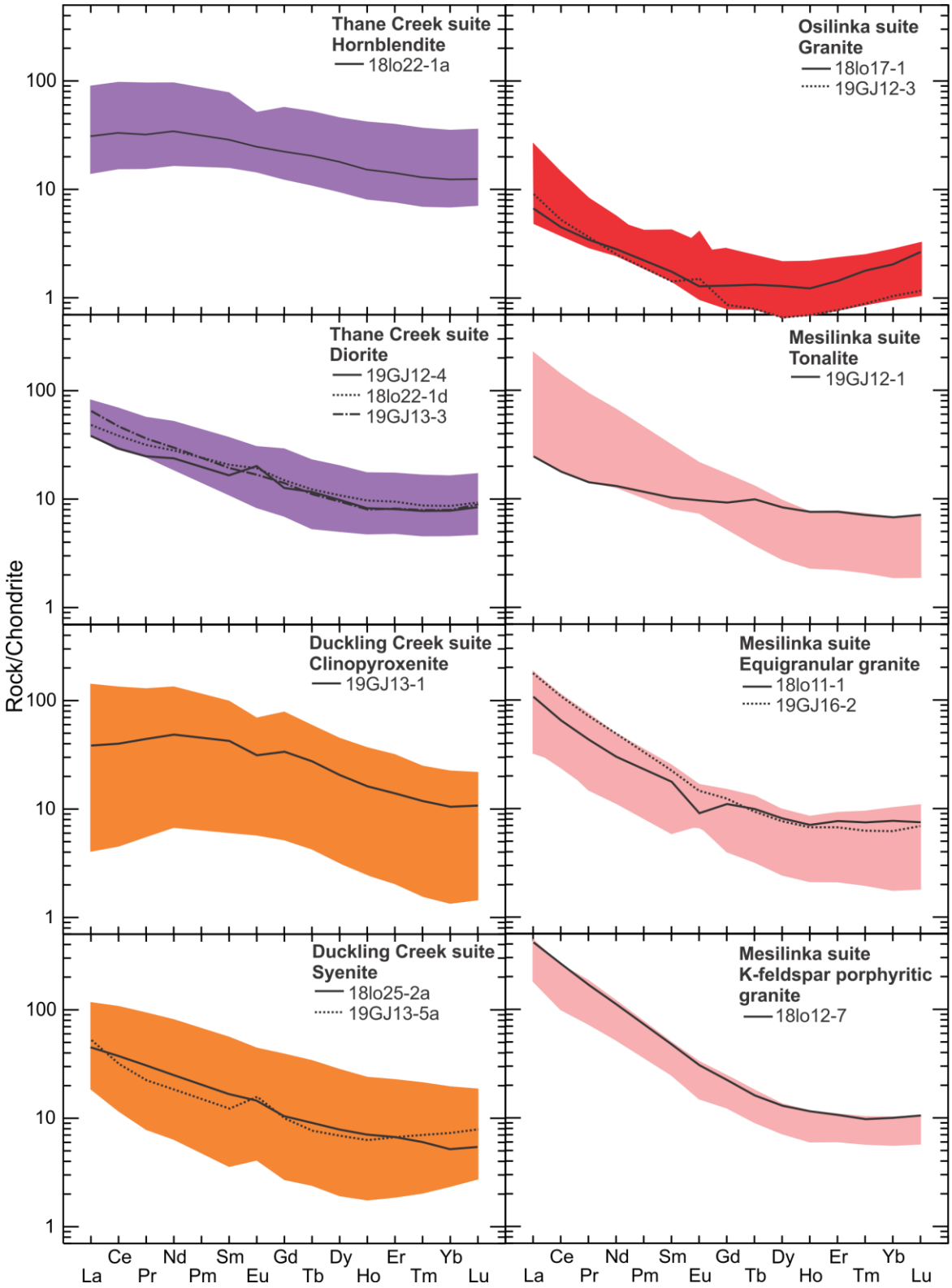

Figure 2.2.2.1. Chondrite-normalized rare earth element (REE) plot (Sun and McDonough, 1989) of the four Hogem batholith suites. The entire range of normalized REEs of the main phases within the suites are shown in colour, while black lines indicate the signatures of individual samples used in later zircon geochemical analyses.

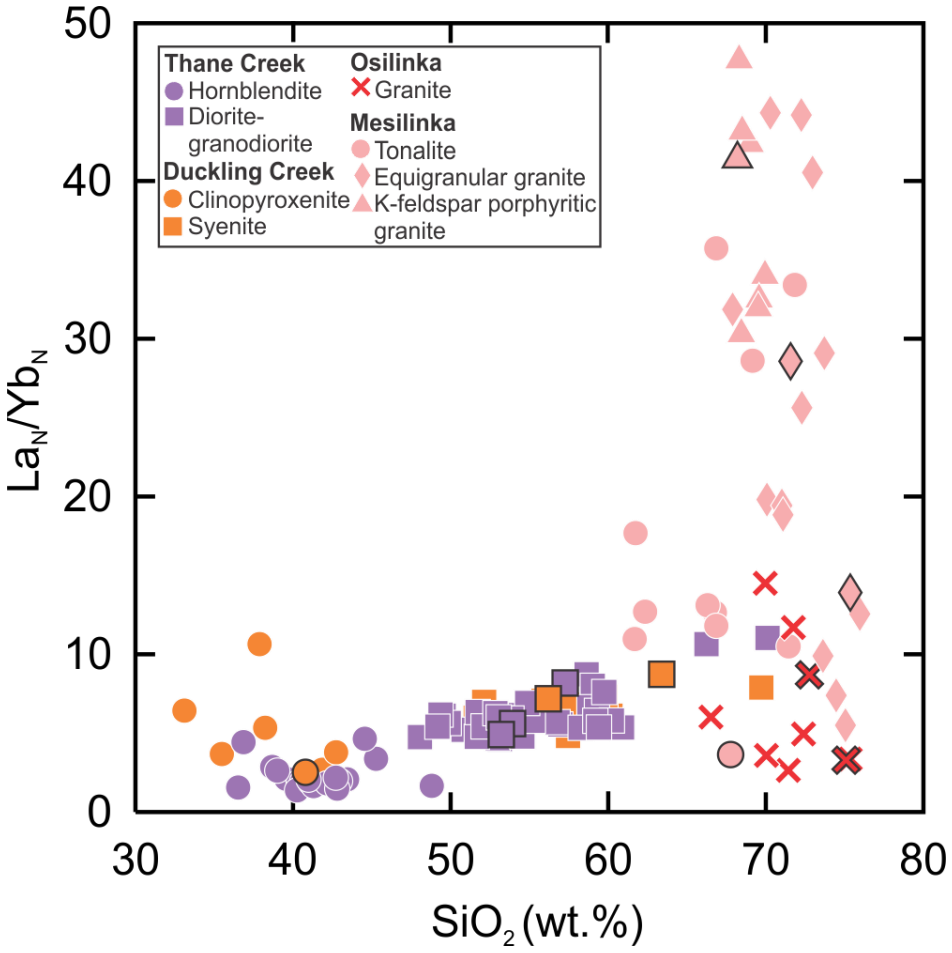

Figure 2.2.2.2. Chondrite-normalized La/Yb versus SiO_2 (wt.%). Chondrite values from Sun and McDonough (1989). Data points outlined in black indicate individual samples used in later mineral geochemical analyses.

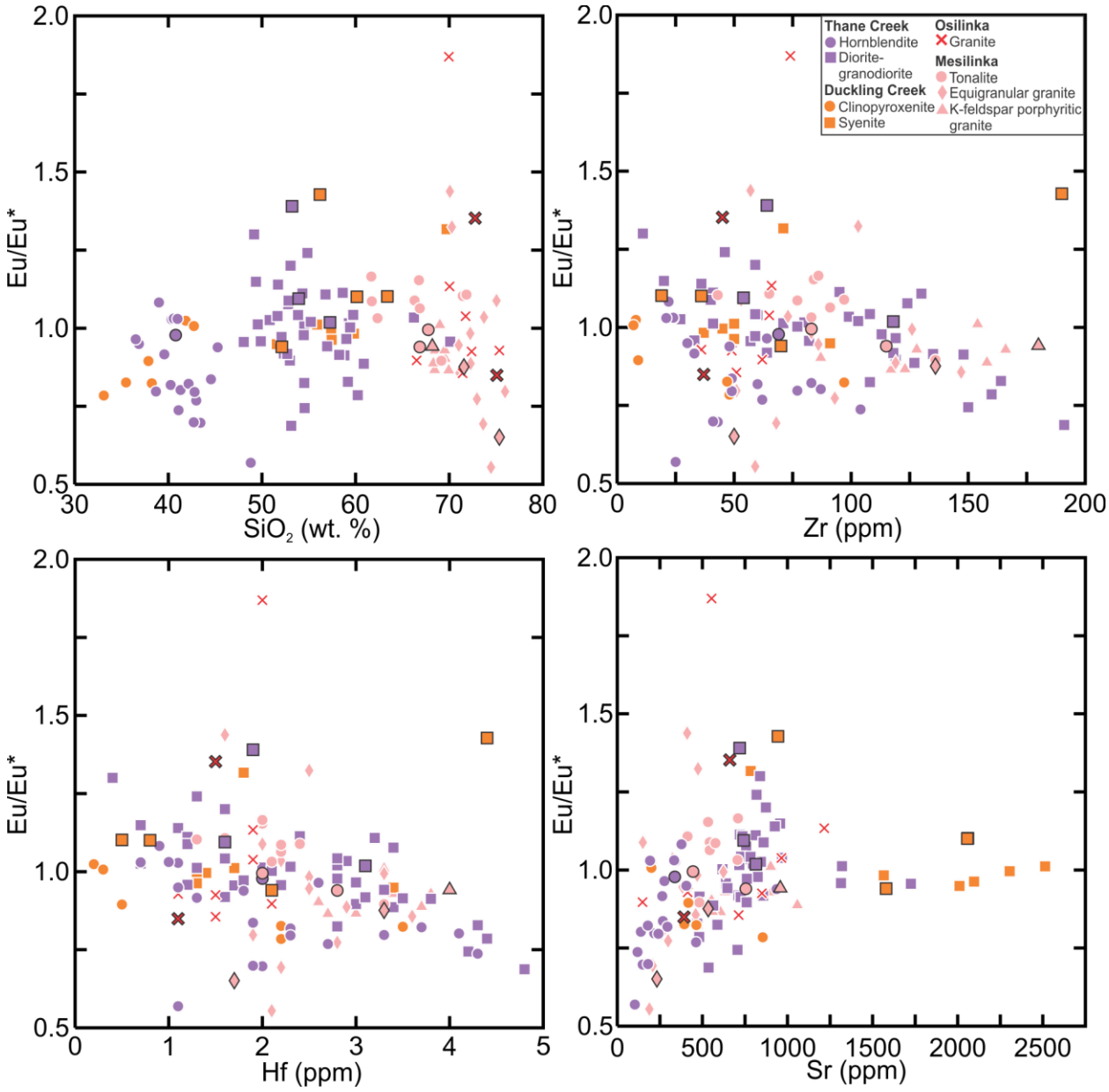

Figure 2.2.2.3. Whole rock chondrite-normalized Eu-anomalies versus SiO_2 (wt. %), Zr (ppm), Hf (ppm), and Sr (ppm). Chondrite values from Sun and McDonough (1989). Data points outlined in black indicate individual samples used in later mineral geochemical analyses. $Eu/Eu^* = Eu_N / (Sm_N * Gd_N)^{0.5}$.

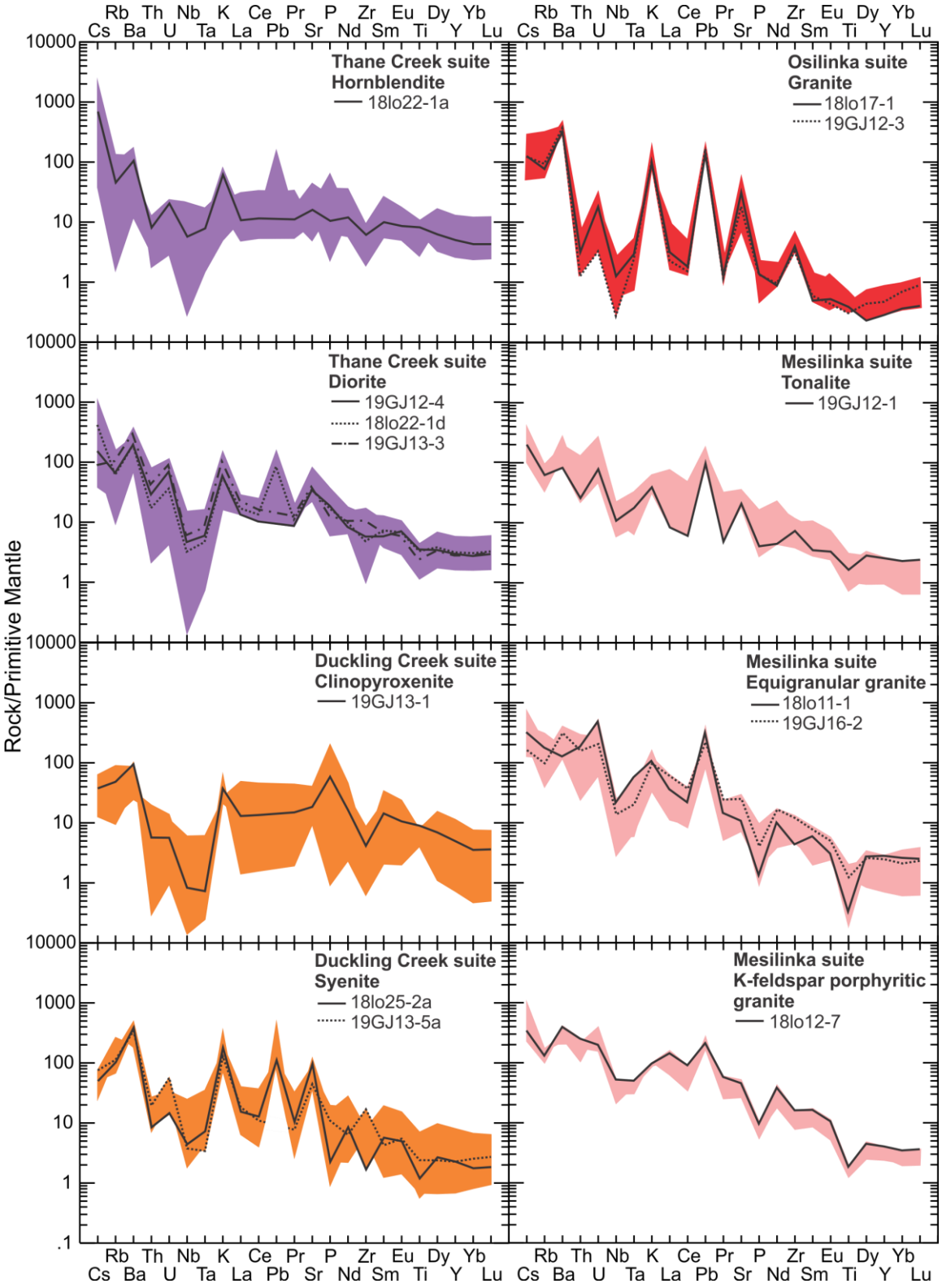

Figure 2.2.2.4. Primitive mantle normalized multi-element spidergrams (Sun and McDonough, 1989) of the four Hogem batholith suites. The entire range of normalized elements of the main phases within the suites are shown in colour, while black lines indicate the signatures of individual samples used for zircon geochemical analyses.

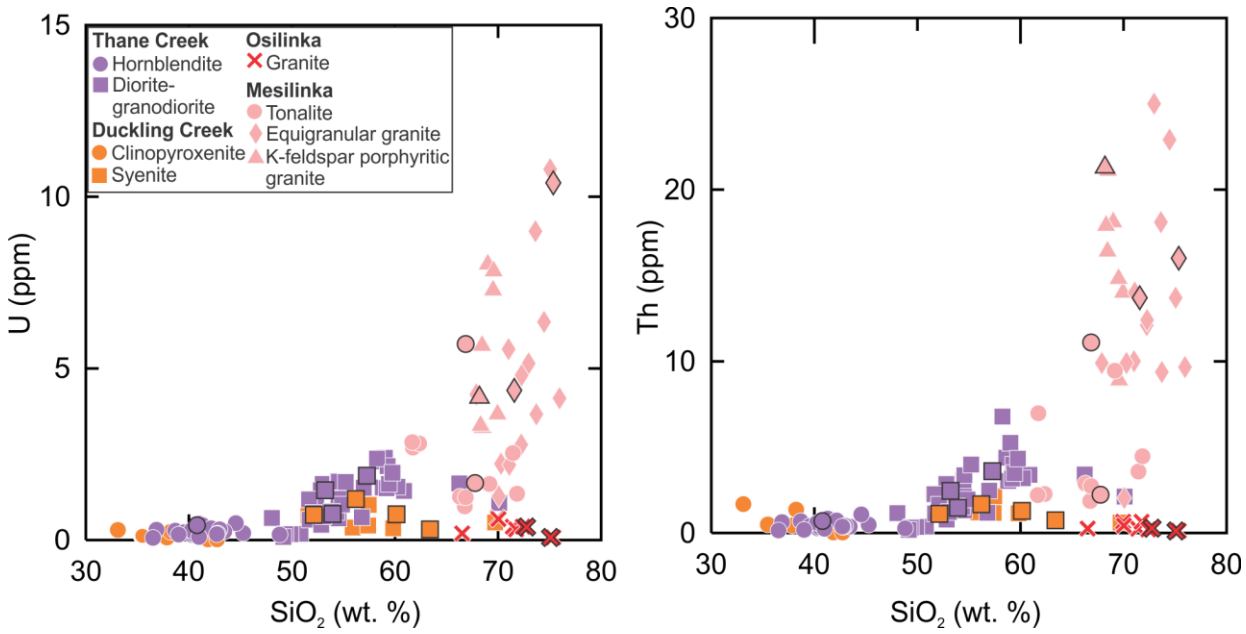

Figure 2.2.2.5. Whole rock Uranium and Thorium concentrations (ppm) versus SiO_2 (wt.%) for Hogem batholith intrusive samples. Data points outlined in black indicate individual samples used in later mineral geochemical analyses.

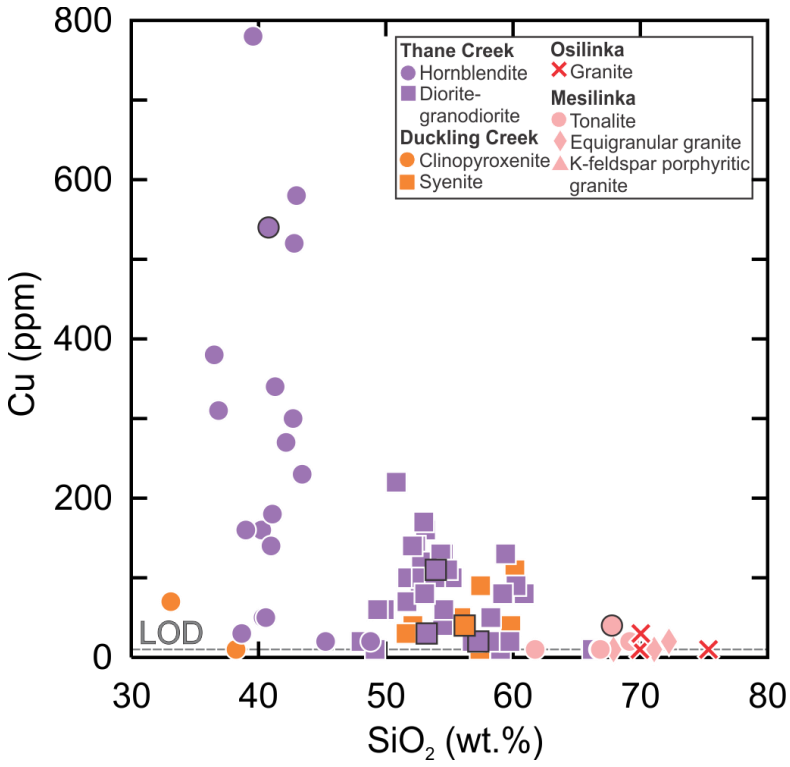

Figure 2.2.2.6. Copper concentration (ppm) versus SiO_2 (wt.%) for Hogem batholith whole rock intrusive samples. Limit of detection (LOD, 10 ppm) is indicated by the dashed grey line. Data points outlined in black indicate individual samples used in later mineral geochemical analyses.

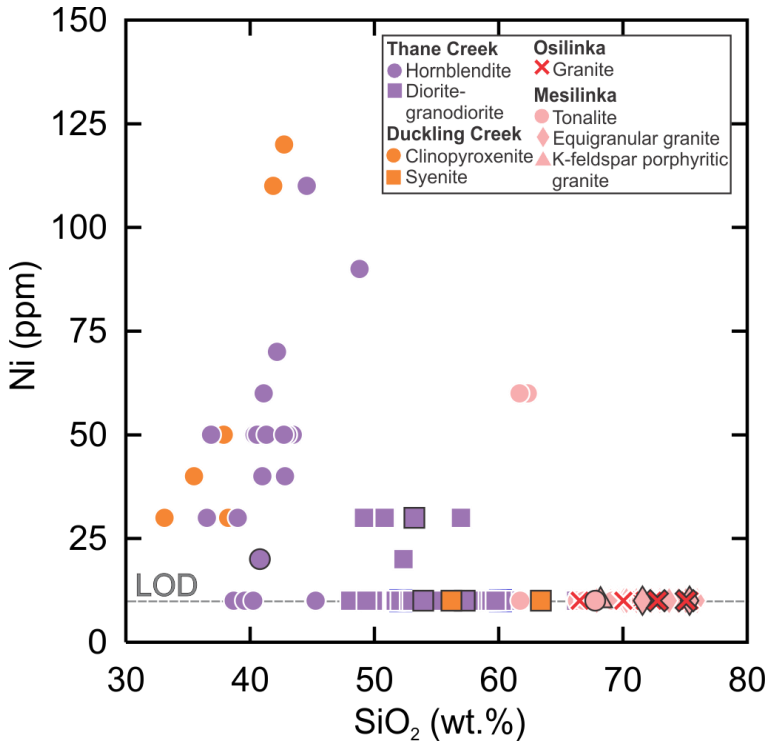

Figure 2.2.2.7. Nickel concentration (ppm) versus SiO_2 (wt.%) for Hogem batholith whole rock intrusive samples. Limit of detection (LOD, 10 ppm) is indicated by the dashed grey line. Data points outlined in black indicate individual samples used in later mineral geochemical analyses.

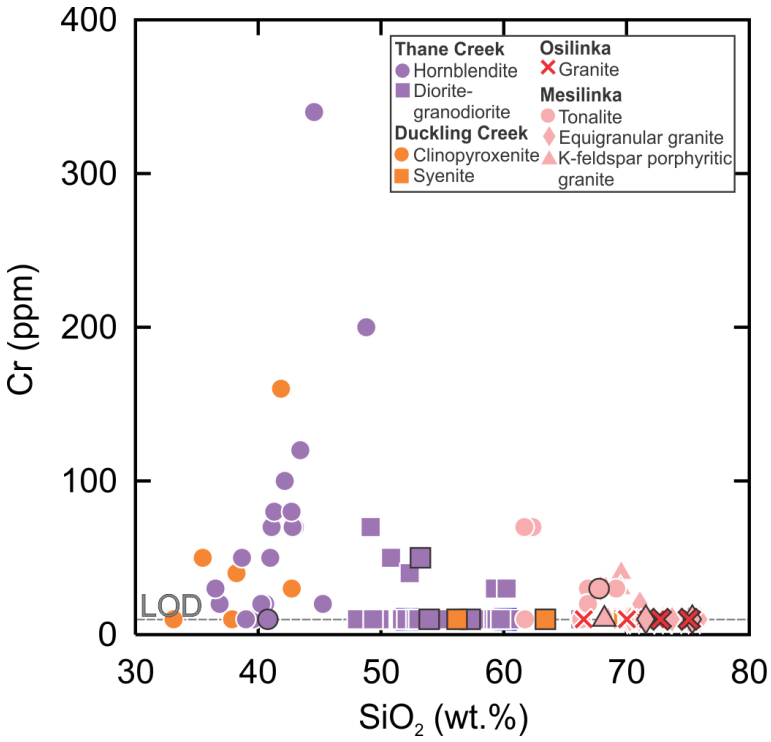

Figure 2.2.2.8. Chromium concentration (ppm) versus SiO_2 (wt.%) for Hogem batholith whole rock intrusive samples. Limit of detection (LOD, 10 ppm) is indicated by the dashed grey line. Data points outlined in black indicate individual samples used in later mineral geochemical analyses.

Trace element ratios Zr/Y and Th/Yb were used as a more robust method to distinguish calc-alkaline from tholeiitic rocks (Ross and Bedard, 2009). Thane Creek hornblendites plot as tholeiitic, however, diorites form a trend across the tholeiitic, transitional, and calc-alkaline fields, with the majority of samples plotting as calc-alkaline (Figure 2.2.2.9). This differs slightly from the AFM results (Figure 2.2.1.5), which separated tholeiitic hornblendite samples from calc-alkaline diorites. Thane Creek suite intrusive rocks predominantly fall within the volcanic arc granite (VAG) field on tectonomagmatic trace-element discrimination diagrams (Figure 2.2.2.10; Pearce et al., 1984). Pearce discrimination diagrams were modified by Whalen and Hildebrand (2019) to better discriminate granitoid rocks with SiO_2 compositions between 55 and 70 wt.% and to identify granitoids generated by slab break-off during subduction, referred to as "slab failure". On these modified discrimination diagrams, silica-rich Thane Creek diorite samples predominantly plot within the field defined by plutonic rocks that result from "slab failure", or on the boundary between arc and slab failure fields (Figure 2.2.2.11). Thane Creek hornblendite samples have SiO_2 compositions below 55 wt.% and thus are not discriminated using these plots.

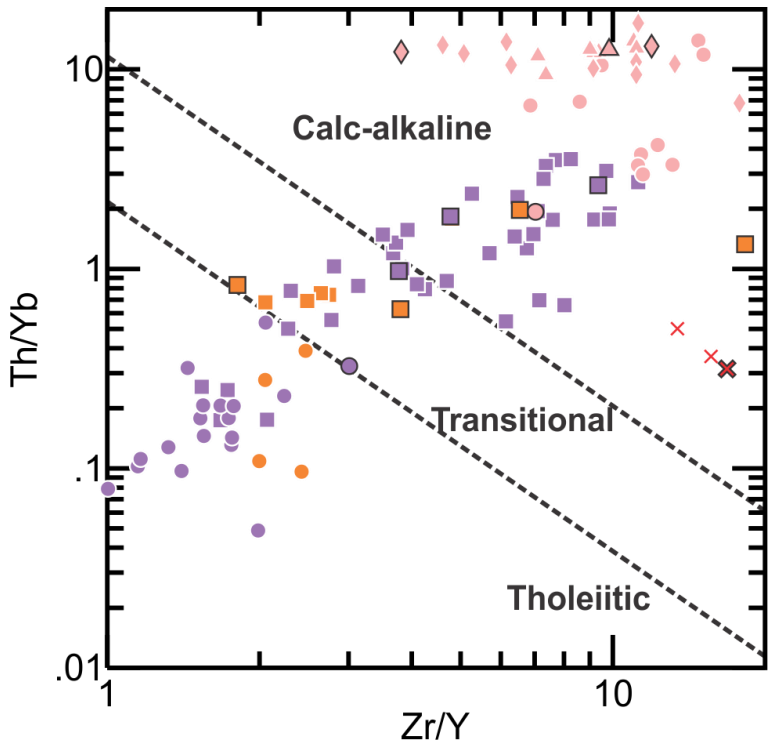

Figure 2.2.2.9. Trace element ratios Zr/Y versus Th/Yb results for the four Hogem batholith intrusive suites. "Tholeiitic", "Transitional", and "Calc-alkaline" fields are from Ross and Bedard (2009). Data points outlined in black indicate individual samples used in later mineral geochemical analyses.

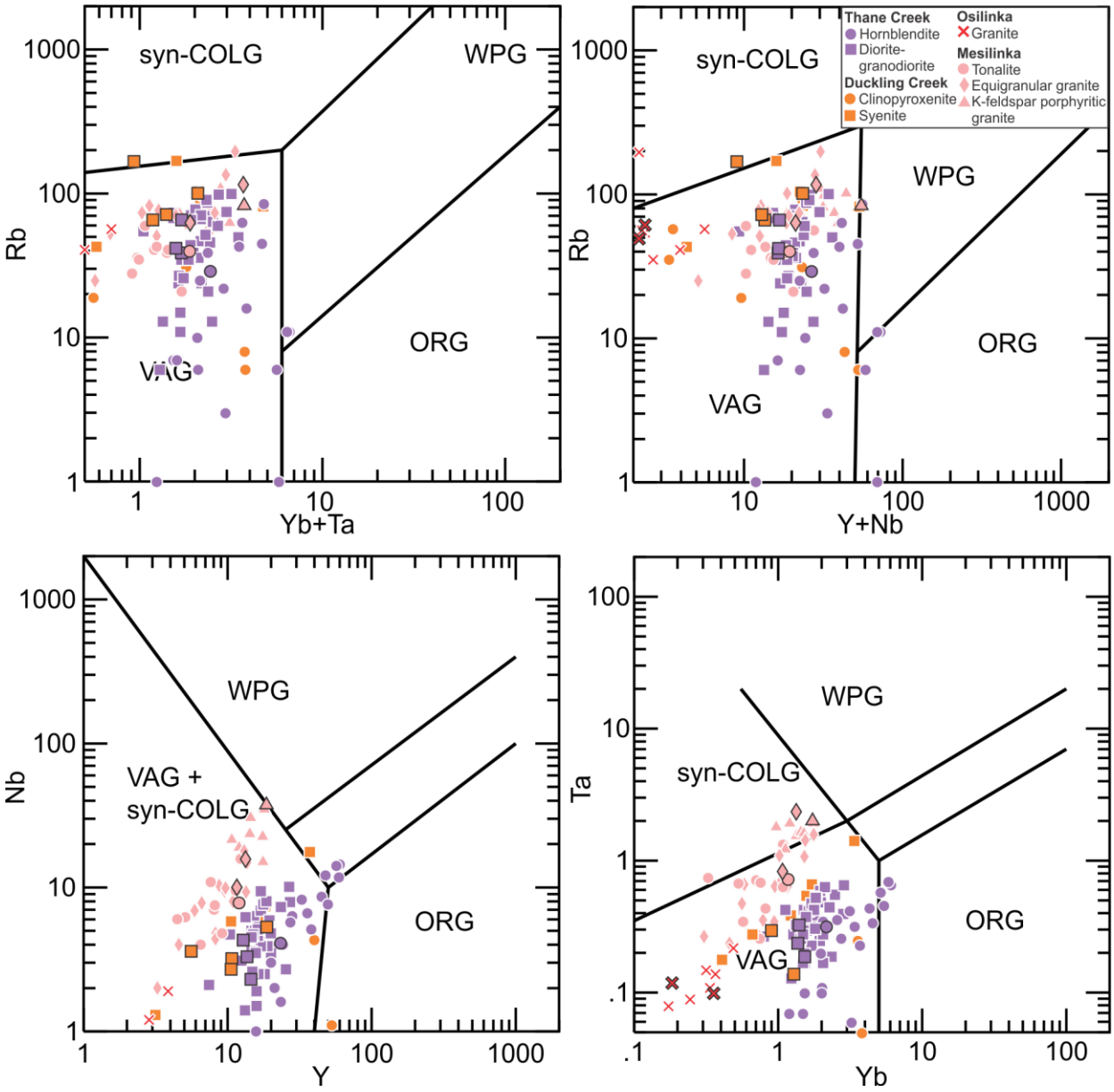

Figure 2.2.2.10. Tectonomagmatic discrimination diagrams (Pearce et al., 1984) for Hogem batholith samples. Data points outlined in black indicate individual samples used in later mineral geochemical analyses. WPG= within-plate granite, VAG= volcanic arc granite, ORG= ocean ridge granite, syn-COLG= syn-collisional granite.

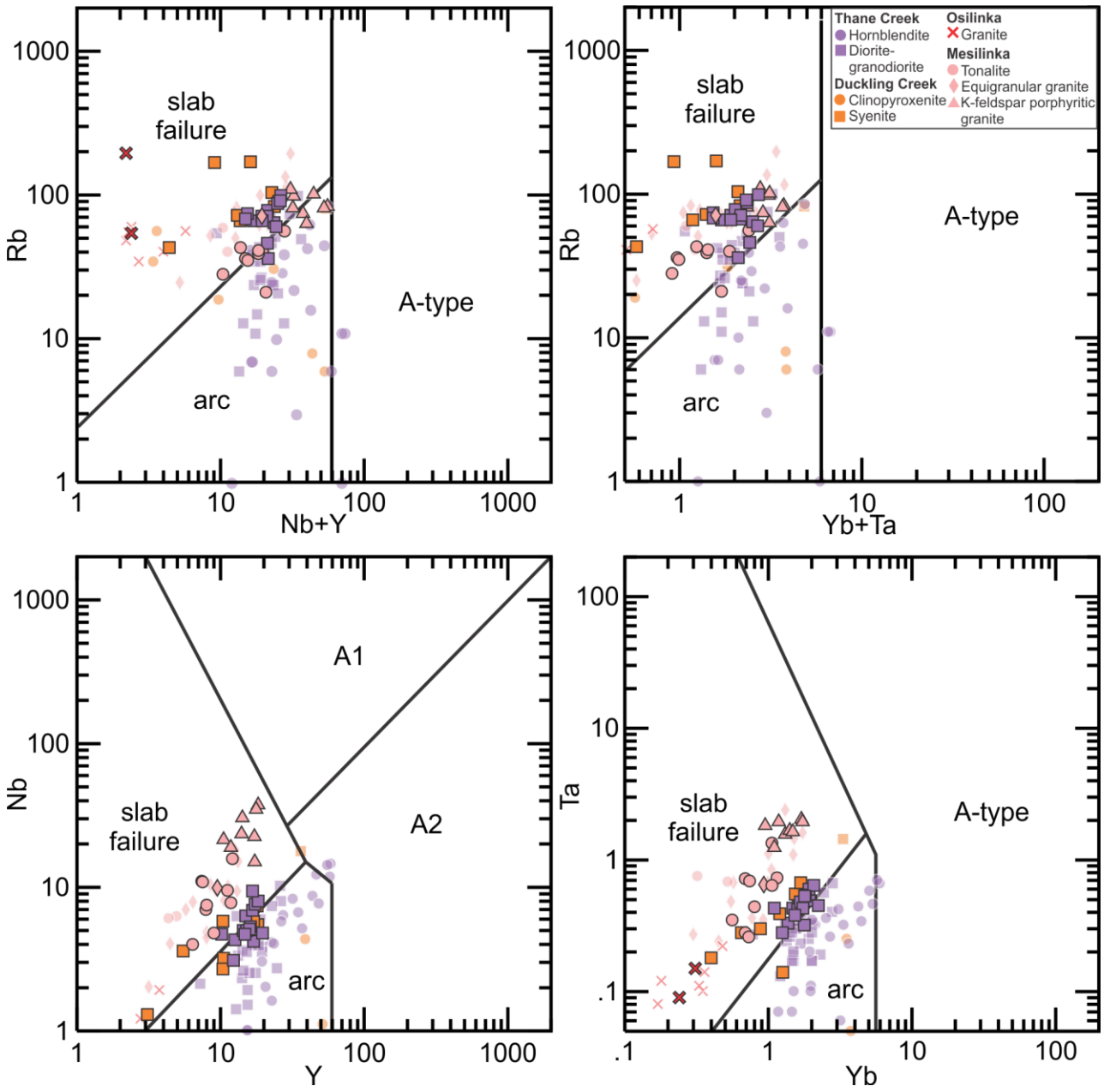

Figure 2.2.2.11. Modified Pearce et al. (1984) tectonomagmatic discrimination diagrams for Hogem batholith samples, with discriminant boundaries of Whalen and Hildebrand (2019). Transparent symbols represent samples with less than 55 wt. % or greater than 70 wt. % SiO_2 and are not used for discrimination. A-type indicates granitoids found in anorogenic settings. The A1 field is interpreted intraplate oceanic island and continental rift environments. The A2 field is interpreted as late stage collisional or extensional collapse environments. The arc field designates typical subduction-generated granitoids. Slab failure indicates granitoids generated by magmatism related to break off of the subducting slab (Whalen and Hildebrand, 2019).

Duckling Creek suite

The Duckling Creek suite samples have chondrite-normalized trace element patterns similar to Thane Creek patterns. Clinopyroxenites have low to moderate enrichment in LREE relative to HREE (La_N/Yb_N: 2.7-11), and syenite samples have moderate enrichment (La_N/Yb_N: 4.7-8.7) (Figures 2.2.2.1-2.2.2.2). Clinopyroxenite REE patterns are slightly concave downward and diorite REE patterns are concave upward. Clinopyroxenite samples have slight negative Eu-anomalies (Eu/Eu_N*=0.8-1.0), whereas syenites have positive Eu-anomalies (Eu/Eu_N*= 1.0-1.5; Figures 2.2.2.1 and 2.2.2.3).

The Duckling Creek clinopyroxenites have negative Nb-Ta and Zr anomalies on primitive mantle normalized trace element plots (Figure 2.2.2.4). Phosphorus and Ti anomalies are variable, ranging from negative to positive, and Pb anomalies are absent. The Duckling Creek syenites also display negative Nb-Ta signatures. However, Zr anomalies range from negative to positive, P and Ti anomalies are negative, and Pb is positive.

Uranium and Th concentrations in the Duckling Creek plutonic rocks are relatively low (Figure 2.2.2.5). Clinopyroxenites have U concentrations from 0.02 to 0.3 ppm, while 'syenites' range from 0.3 to 1.2 ppm. Th concentrations range from 0.03 to 1.7 ppm in clinopyroxenites and from 0.6 to 2.2 ppm in 'syenites'.

The Duckling Creek intrusive samples have intermediate Cu, Ni, and Cr concentrations relative to the Thane Creek suite. Pyroxenites have Cu concentrations up to 70 ppm, Ni concentrations from 30 ppm to 160 ppm, and Cr concentrations up to 160 ppm (Figure 2.2.2.6-Figure 2.2.2.8). The Duckling Creek syenites are more enriched in Cu and less enriched in Ni and Cr than pyroxenites. Syenites have Cu concentrations up to 90 ppm and Ni and Cr concentrations <10 ppm.

On the Zr/Y versus Th/Yb plot, the Duckling Creek clinopyroxenites classify as tholeiitic, while the syenites predominantly plot within the transitional field (Figure 2.2.2.9). This differs slightly from the AFM results (Figure 2.2.1.5), which separate tholeiitic clinopyroxenite samples from calc-alkaline syenites. However, neither of these plots were designed to differentiate alkaline rocks.

The Duckling Creek suite intrusive rocks predominantly classify within the VAG field on all Pearce et al. (1984) tectonomagmatic trace-element discrimination plots (Figure 2.2.2.10). On modified Pearce discrimination diagrams (Whalen and Hildebrand, 2019), silica-rich Duckling Creek syenites predominantly plot within the "slab failure" field (Figure 2.2.2.11). The Duckling Creek clinopyroxenites have SiO_2 compositions below 55 wt.%, so these samples are not discriminated using these plots.

Osilinka suite

The Osilinka granite samples are relatively depleted in chondrite-normalized REEs and have slight enrichment in LREE relative to HREE (La_N/Yb_N: 3 to 15; Figures 2.2.2.1-2.2.2.2). Europium-anomalies in the Osilinka granites range from slightly negative to positive (Eu_N/Eu^*= 0.9 to 1.9; Figures 2.2.2.1 and 2.2.2.3). On primitive-mantle normalized trace element plots (Figure 2.2.2.4), the Osilinka granites show negative Nb-Ta, P, and Ti anomalies. Zirconium and Pb anomalies are positive.

The Osilinka granites have anomalously low U and Th contents, with U concentrations ranging from 0.1 to 0.6 ppm and Th from 0.1 to 0.7 ppm (Figure 2.2.2.5). Additionally, the Osilinka suite granites are the least Cu, Ni, and Cr enriched samples, with only one sample above the LOD (Figures 2.2.2.6 and 2.2.2.8).

On the Zr/Y versus Th/Yb plot, the Osilinka granites plot within the calc-alkaline field (Figure 2.2.2.9), consistent with the AFM plot classification (Figure 2.2.1.5).

On tectonomagmatic trace-element discrimination diagrams (Pearce et al., 1984; Figure 2.2.2.10), the Osilinka suite granite samples predominantly plot within the VAG field on all plots. Only two Osilinka suite granite samples have SiO_2 compositions between 55 and 70 wt.%, the range used to discriminate granitoids on modified Pearce discrimination diagrams (Whalen and Hildebrand, 2019). These two samples occur within the "slab failure field" (Figure 2.2.2.11); However, caution should be used in discriminating these samples, as they may represent "S-type" granites, which the authors warn may share trace element characteristics (high La/Yb, Nb/Y) with granites plotting within the "slab failure" discrimination field (Whalen and Hildebrand, 2019). The Sr/Y ratio may be used as a rough discriminator between slab failure granitoids (>20) and S-type granites (<20), however, this parameter is also not definitive, as Sr is

fluid mobile (Whalen and Hildebrand, 2019). The Osilinka suite granites have Sr/Y ratios of approximately 100 to 900 ppm, indicating these granites may be “S-type” and not slab failure granites.

Mesilinka suite

Chondrite-normalized trace element patterns of the Mesilinka plutonic rocks demonstrate low to high enrichment in LREE relative to HREE in tonalites (La_N/Yb_N: 3.6-36) and equigranular granites (La_N/Yb_N: 5.5-44), and high enrichment (La_N/Yb_N: 30-48) in K-feldspar phenocrystic granites (Figures 2.2.2.1-2.2.2.2). The Mesilinka REE patterns are concave upward to steeply negatively sloped. Tonalites have slight negative to slight positive Eu anomalies (Eu_N/Eu^*= 0.9 to 1.2), while equigranular granites have a larger range between moderately negative and positive Eu anomalies (Eu_N/Eu^*= 0.6 to 1.4). K-feldspar phenocrystic granites generally lack an Eu-anomaly (Eu_N/Eu^*= 0.9 to 1.0; Figures 2.2.2.1 and 2.2.2.3)

On primitive-mantle normalized trace element plots, the Mesilinka tonalites, equigranular granites, and K-feldspar phenocrystic granites show negative Nb-Ta, P, Ti and positive Pb anomalies (Figure 2.2.2.4). Zirconium anomalies are positive in tonalites, absent to positive in equigranular granites, and negative in K-feldspar phenocrystic granites.

The Mesilinka suite plutonic rocks have the most enriched U and Th in the Hogem batholith (Figure 2.2.2.5). Tonalites have the lowest U and Th contents in the suite, with U concentrations from 1.0 to 2.9 ppm and Th from 1.9 to 9.5 ppm. Equigranular granites have U ranging from 1.3 to 10.8 ppm and Th from 2.0 to 23 ppm. K-feldspar phenocrystic granites have U concentrations from 3.3 to 8.0 ppm and Th from 8.9 to 21 ppm.

The Mesilinka suite samples have less enriched Cu, Ni, and Cr concentrations relative to the Thane Creek and Duckling Creek suites. Tonalites have Cu concentrations up to 40 ppm, Ni concentrations up to 60 ppm, and Cr concentrations up to 70 ppm (Figures 2.2.2.6 and 2.2.2.8). Mesilinka suite granites are less enriched in Cu, Ni, and Cr than the tonalites. Equigranular granites have Cu concentrations up to 20 ppm, Ni concentration < 10 ppm, and Cr up to 30 ppm. K-feldspar phenocrystic granites have Cu concentrations up to 40 ppm, Ni concentration < 10 ppm, and Cr up to 40 ppm.

On the Zr/Y versus Th/Yb plot, all the Mesilinka tonalites and granites plot within the calc-alkaline field (Figure 2.2.2.9), which does not differ from the AFM results (Figure 2.2.1.5).

On tectonomagmatic trace-element discrimination diagrams (Pearce et al., 1984; Figure 2.2.2.10), the Mesilinka suite rocks predominantly plot within the VAG field. On the Yb versus Ta discrimination diagram, a portion of the Mesilinka samples fall within the syn-collisional granite (syn-COLG) field. In contrast, the majority of the Mesilinka suite rocks plot within the slab failure field on modified Pearce discrimination diagrams (Figure 2.2.2.11).

3 Mineral Geochronology and Geochemistry

3.1 Analytical Methods

3.1.1 Grain Mount Preparation

Preparation for mineral geochemistry was completed at University of Alberta. Approximately 500 to 1000 grams of sample, with more material for coarser-grained samples, were cut into several centimetre-sized pieces using a diamond blade rock saw. These were disaggregated using the electronic pulse disaggregation system in the SELFRAG laboratory in the Canadian Centre for Isotopic Microanalysis (CCIM), University of Alberta, which fragments samples along grain boundaries to yield high quality mineral separates. The mineral separates were dried in a 20°C oven over night, or until dry, then sieved to pass 355 μm mesh to remove the coarser portion. The fine-grained fraction was panned to separate high density minerals, and this portion was then dried again in a 20°C oven over night, or until dry. A hand-held magnet was used to remove magnetic grains from the high-density mineral separates. The remaining grains were then examined using a stereoscope to select apatite, titanite, and zircon grains for epoxy mounting. Zircon separates from the 2018 batch of samples were picked by L. Ootes (British Columbia Geology Survey) and Dr. R. Friedman at the University of British Columbia.

Zircon grain mounts were prepared by the author, Dr. R. Stern, and R. Dokken at the CCIM, University of Alberta. Apatite and titanite grain mounts were prepared by the author and Mark Labbe at the Thin Section Laboratory, Department of Earth and Atmospheric Science, University of Alberta. Minerals were selected and placed onto a mount stage using fine-tipped tweezers, then set with epoxy resin within 25 mm round moulds. Once the epoxy was set, the minerals were polished using diamond grits to expose the grain mid-sections, while using a reflected microscope periodically to check the exposure of the grains.

3.1.2 SIMS Oxygen Isotope Analysis

Oxygen isotope ($^{18}O/^{16}O$) data for zircon was collected by secondary ion mass-spectrometry (SIMS), and this was completed first in the workflow cycle (Figure 1.6.1), as it is a non-destructive process. Zircon mounts (M1533, M1579, and M1623) were first coated with 25 nm of Au, then imaged using a Zeiss EVO MA15 scanning electron microscope (SEM) equipped

with cathodoluminescence (CL) and backscattered electron (BSE) detectors. Beam conditions were 15kV and 3-5 nA sample current. Following SEM imaging and before SIMS analysis, a further 100 nm of Au was coated on the grain mount. Zircon grains and individual spots were selected using CL and BSE images of the grains. Grains or zones with fractures, alteration, or metamictization were avoided as these may not yield representative $^{18}O/^{16}O$ signatures. Most zircons from the Hogem batholith display oscillatory zoning and commonly magmatic cores, while inherited cores are less common. When possible, multiple analytical spots were selected for both the core and rim of a single zircon grain.

$^{18}O/^{16}O$ compositions were measured on 488 spots on 397 zircon grains using a Cameca IMS 1280 multicollector ion microprobe. Analytical procedures followed those of Stern (2020). A $^{133}Cs^{+}$ beam was operated using an impact energy of 20 keV and beam current of approximately 2.0 nA. Prior to data acquisition, the 10 µm diameter was rastered (20 x 20 µm) for 30 seconds, over an area of 5 x 5 µm during analysis. The normal incidence electron gun was used for charge compensation. Negative secondary ions were extracted through 10 kV into the secondary (transfer) column. Transfer conditions included a 122 µm entrance slit, a 5 x 5 mm pre-ESA (field) aperture, and 100x (MA80) sample magnification at the field aperture, transmitting all regions of the sputtered area. No energy filtering was employed. The mass/charge separated oxygen ions were detected simultaneously in Faraday cups L'2 ($^{16}O^{-}$) and H'2 ($^{18}O^{-}$) as mass resolutions (m/Δm at 10%) of 1950 and 2250, respectively. Secondary ion count rates for $^{16}O^{-}$ and $^{18}O^{-}$ were approximately $2x10^{9}$ and $4x10^{6}$ counts per second using 10^{10} Ω and 10^{11} Ω amplifier circuits, respectively. Faraday cup baselines were determined at the beginning of the analytical run. A single analysis took 240 s in total, including pre-analysis rastering, automated secondary ion tuning, and 75 s of continuous peak counting.

Oxygen isotope results were presented as $\delta^{18}O_{VSMOW}$ and reported in permille, ‰, calculated as follows:

$$\delta^{18}O_{VSMOW} = \left(\frac{(^{18}O/^{16}O_{SAMPLE})}{(^{18}O/^{16}O_{VSMOW})} - 1 \right) \times 1000 ,$$

where $^{18}O/^{16}O_{VSMOW} = 0.0020052$ (Baertschi, 1976).

Instrumental mass fractionation (IMF) was monitored by repeated analysis of the zircon primary reference material (S0081 with $\delta^{18}O_{VSMOW} = +4.87‰$; R. Stern, unpublished laser

fluorination data, University of Oregon), once after every four unknowns. Additionally, a secondary zircon reference material, TEM2 ($\delta^{18}O_{VSMOW}$ = +8.2‰; Black et al., 2004) was analyzed after every 12 unknowns (Table 3.1.2.1). The collective $^{18}O^{-}/^{16}O^{-}$ data for S0081 for the single analytical session resulted in a standard deviation of 0.08‰, after correction for systematic within-session drift of +1.5‰. Uncertainties in $\delta^{18}O_{VSMOW}$ of individual spots for the unknowns have a median of ±0.20‰ at 95% confidence, including errors relating to within-spot counting statistics, between-spot (geometric) effects, and correction for IMF. Results for multiple spots on multiple grains of the secondary reference material (TEM2) yield a weighted mean of $\delta^{18}O$ within uncertainty to the accepted value (Figure 3.1.2.1).

Table 3.1.2.1. Summary of SIMS weighted mean δ18OVSMOW results for zircon reference material TEM2.

Sample run	Session	Date	$\delta^{18}O_{VSMOW}$ weighted mean, ‰ (2SE)	No. analyses; MSWD; $p(\chi^2)$	Difference from accepted (‰)
18lo11-1 18lo12-7 18lo17-1 18lo20-4 18lo25-2a	1	February 2019	8.19±0.04	20/21; 0.47; 0.97	0.01
18lo22-1a 19GJ12-1 19GJ12-4 19GJ13-3 19GJ13-5a	2	December 2019	8.20±0.04	24/26; 0.69; 0.86	0.00
18lo22-1d 19GJ16-2 19GJ12-3	3	September 2020	8.27±0.05	18/19; 0.77; 0.73	0.07

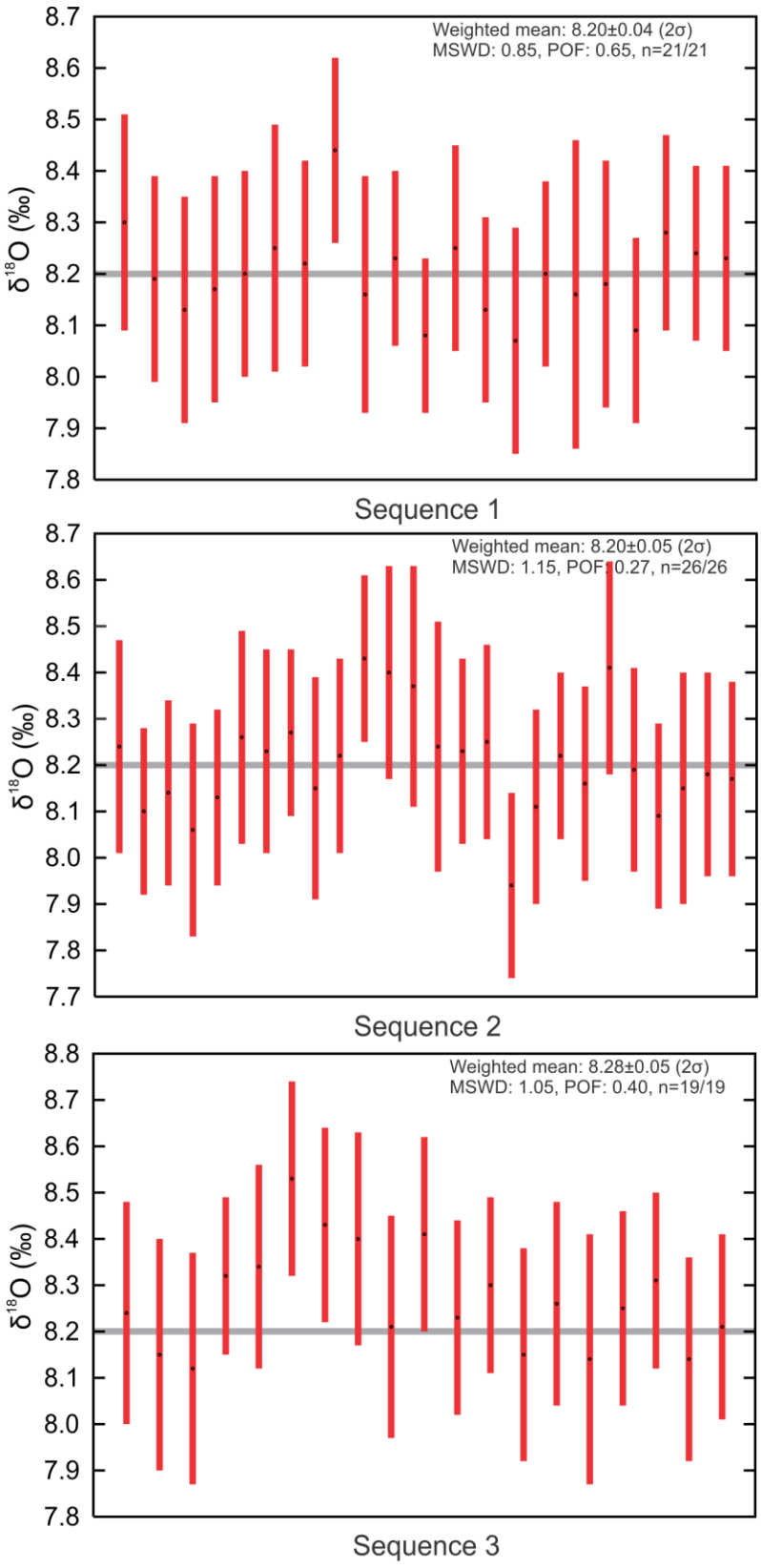

Figure 3.1.2.1. SIMS $\delta^{18}O$ results for secondary zircon reference material TEM2. The grey line indicates the published RM $\delta^{18}O_{VSMOW}$ value (+8.2‰; Black et al., 2004).

3.1.3 Zircon U-Pb Isotopes Geochronology LA-ICP-MS

Uranium-lead isotopes of zircon grains were determined following oxygen isotope (section 3.1.2) analyses on the same grains. Zircon U-Pb isotope data were collected using laser ablation coupled plasma mass spectrometry (LA-ICP-MS) with a RESOlution 193 nm ArF excimer laser, equipped with a 2-volume Laurin-Technic S-155 ablation cell, coupled with a Thermo Fisher Scientific Element II-XR single collector (SC)-sector field (SF)-ICP-MS at the University of Alberta in the Arctic Resources Geochemistry Laboratory. Analytical points were determined from CL and BSE images as described in section 3.1.2, and U-Pb spots were positioned on top of shallow SIMS analysis pits. A 33 µm (session 1-3), 40 µm (session 4), or 23 µm (session 5) diameter laser spot size was ablated using settings of 35 to 50 s of ablation, 50 s of background and washout, 6 Hz repetition rate, 120 mJ laser energy, 11%T attenuator value, and ca. 1.8 J/cm^2 fluence, measured at the ablation site. Masses 202, 204, 206, 207, 208, 232, and 238 were measured. Uranium-235 was calculated from ^{238}U results and the $^{238}U/^{235}U$ isotopic ratio (Jaffey et al., 1971). Data was processed and reduced offline using the Iolite version 3 software package (Paton et al., 2010; Paton et al., 2011), using the data reduction scheme (DRS) "X_U_Pb_Geochron". The decay constants of ^{235}U (9.485×10^{-10} year^{-1}), ^{238}U (1.55125×10^{-10} year^{-1}) and the $^{238}U/^{235}U$ isotopic ratio (137.88) used in age calculations are from Jaffey et al. (1971).

No common Pb correction was applied to the data. The $^{206}Pb/^{204}Pb$ ratio in the unknown zircons ranged from 200 to 1800000. The presence of significant common Pb in individual zircon analyses was indicated by calculating $f^{206}Pb_c$, in which the $^{206}Pb/^{204}Pb$ ratio was calculated using the method of Stacey and Kramers (1975) and divided by the measured $^{206}Pb/^{204}Pb$ ratio for each analysis (e.g., Vezinet et al., 2018). Measured ^{204}Pb was corrected for ^{204}Hg interference by subtracting the counts per second (cps) of ^{202}Hg multiplied by the natural ratio of ^{204}Hg to ^{202}Hg (6.87/29.86; Rosman and Taylor, 1998) from the cps of ^{204}Pb. Zircon with $f^{206}Pb_c$ results >1% were not included in age calculations.

$$f^{206}Pb_c\ \% = [(^{206}Pb/^{204}Pb)_{\text{Stacey \& Kramers, 1975}} / (^{206}Pb/^{204}Pb)_{\text{measured}}] * 100$$

Possible lead loss in zircon was determined by calculating the total alpha dose of single zircons, using U-Pb isotope analysis results and the equations of Murakami et al. (1991).

Total alpha-dose = ^{238}U alpha-dose + ^{235}U alpha-dose + ^{232}Th alpha-dose, in which:

^{238}U alpha-dose = $8*(U_{(ppm)}*\text{isotopic abundance } ^{238}U) *10e^{-6}*(6.022e^{23}/ \text{mass of } ^{238}U)*(e^{(\lambda 238U*\text{age of zircon})}-1)$

^{235}U alpha-dose = $7*(U_{(ppm)}*\text{natural ratio } ^{235}U/^{238}U)*10e^{-6}*(6.022e^{23}/ \text{mass of } ^{235}U)*(e^{(\lambda 235U*\text{age of zircon})}-1)$

^{232}Th alpha-dose = $6*Th_{(ppm)} *10e^{-6}*(6.022e^{23}/ \text{mass of } ^{232}Th)*(e^{(\lambda 232Th*\text{age of zircon})}-1)$.

Zircon with a total alpha-dose greater than $3x10^{15}$ α-decay events/mg indicates stage II zircon damage to the crystal structure may have occurred (Murakami et al., 1991). During stage II zircon damage, fluid mobile elements, including Pb, can be lost or gained from the crystal structure, which may affect the U-Pb isotopic ratios. Zircon analyses with total alpha-dose greater than $3x10^{15}$ α-decay events/mg were not used to filter data from weighted mean and concordia age calculations but were used to assess these age results. Only three intrusive samples (19GJ12-4, 18lo25-2a, 19GJ12-3) had zircons with total alpha-dose $>3x10^{15}$ α-decay events/mg.

Zircon grains with >5% discordance, determined using the individual zircon $^{206}Pb/^{238}U$ and $^{207}Pb/^{235}U$ ages, were rejected from intrusive sample age weighted means. In addition to U-Pb data filters, the internal structures of zircon were examined using CL and BSE images (Appendix C). Xenocrystic or antecrystic cores were identified by the degree of roundness and crosscutting growth zones, and these grains were not used toward calculating sample ages. Zircon grains with suspect age results (significantly younger or older than the main population) that passed the initial data filters were further filtered using trace element concentrations (section 3.1.5) of Ca >300 ppm, Fe >300 ppm, Ti >20 ppm, and La >1 ppm. Concentrations over these values may indicate altered zircon domains, or growth zones with mineral inclusions, which may affect the interpreted age of the sample. After data filtering, individual zircon $^{206}Pb/^{238}U$ ages were used to calculate a weighted mean $^{206}Pb/^{238}U$ age for each sample. Zircon $^{207}Pb/^{235}U$ and $^{206}Pb/^{238}U$ ratios were used to determine concordia ages. Weighted means and concordia plots were created using IsoplotR online (Vermeesch, 2018). All reported isotope ratios and age uncertainties are reported as 2σ standard error, or 95.4% confidence level, propagated by quadratic addition.

Uranium-lead isotopes of standard zircon reference material were determined throughout three analytical sessions. Three zircon reference materials were analyzed after every six analyses of unknowns. The zircon 91500 (Wiedenbeck et al., 1995, 2004) was used as the primary calibration reference material to monitor analytical reproducibility, U-Pb fractionation, and instrument drift during each analytical run. The Plešovice, 94-35, and Mud Tank zircons (Sláma et al., 2008; Klepeis et al., 1998; Gain et al., 2019) were used as secondary validation reference materials to monitor the accuracy of the primary correction. In sequence 5, Plešovice was used as the primary calibration reference material, as this yielded lower propagated U-Pb ratio analytical uncertainties. The weighted mean $^{206}Pb/^{238}U$ age results for the primary and secondary zircon reference materials were compared to the accepted values and summarized in Table 3.1.3.1-3.1.3.4.

The LA-ICP-MS $^{206}Pb/^{238}U$ dates determined on calibration material 91500 agreed within uncertainty of the published weighted $^{206}Pb/^{238}U$ age of 1062.4±0.8 Ma (ID-TIMS, 2σ; Wiedenbeck et al., 1995) for three analytical runs (Figure 3.1.3.1; Table 3.1.3.1).

Table 3.1.3.1. Summary of LA-ICP-MS weighted $^{206}Pb/^{238}U$ date results for primary zircon reference material 91500.

Sample run	Session	Date	$^{206}Pb/^{238}U$ date weighted mean (2SE)	No. analyses; MSWD; p(χ^2)	Difference from accepted age (%)
19GJ13-3	1	Feb. 19, 2020	1062.3±1.5	19/19; 0.22; 1.00	0.01
18lo22-1a 19GJ13-5a	2	Feb. 19, 2020	1062.2±3.6	27/27; 0.87; 0.65	0.02
19GJ12-1 19GJ12-4	3	Feb. 20, 2020	1062.4±2.3	27/27; 0.52; 0.98	0.00
18lo22-1d	4	Mar. 25, 2021	1062.3±2.4	15/15; 0.39; 0.98	0.01
19GJ12-3 19GJ16-2	5	Mar. 26, 2021	1060.7±3.5	24/24; 0.99; 0.47	0.16

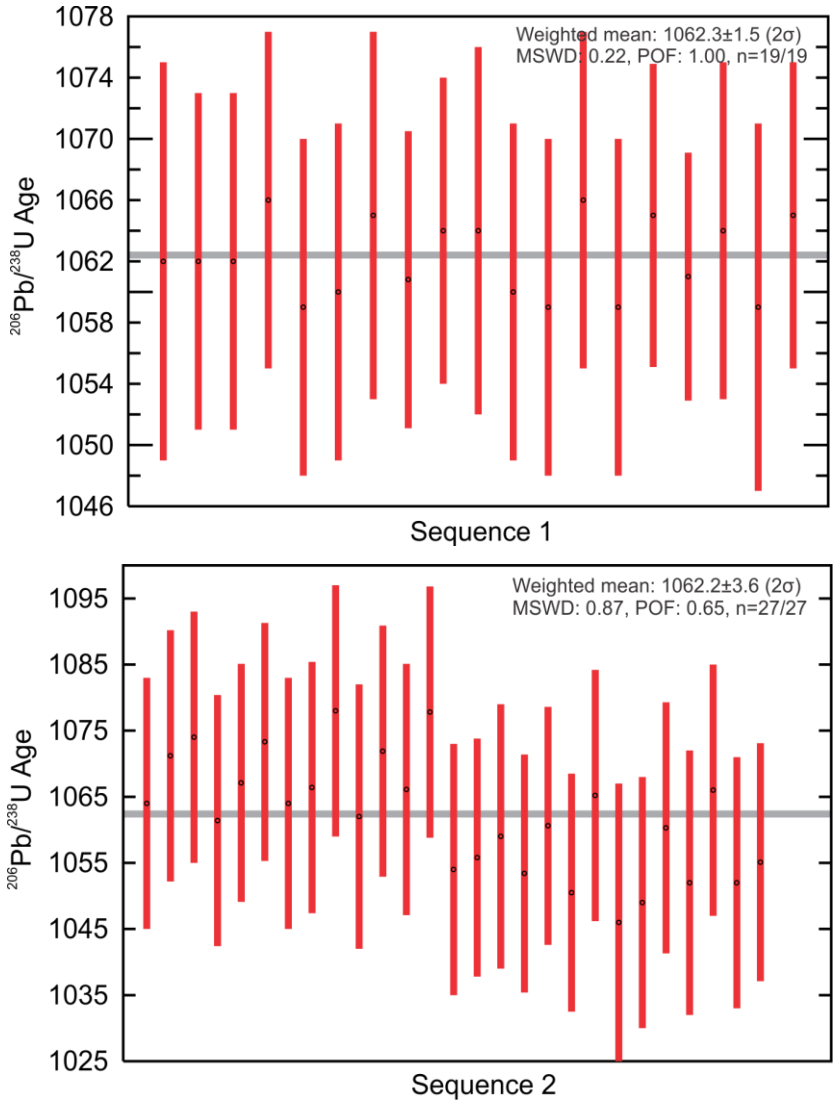

Figure 3.1.3.1. LA-ICP-MS $^{206}Pb/^{238}U$ age results for primary calibration zircon reference material 91500. The grey line indicates the published RM age (1062.4±0.8 Ma; Wiedenbeck et al., 1995).

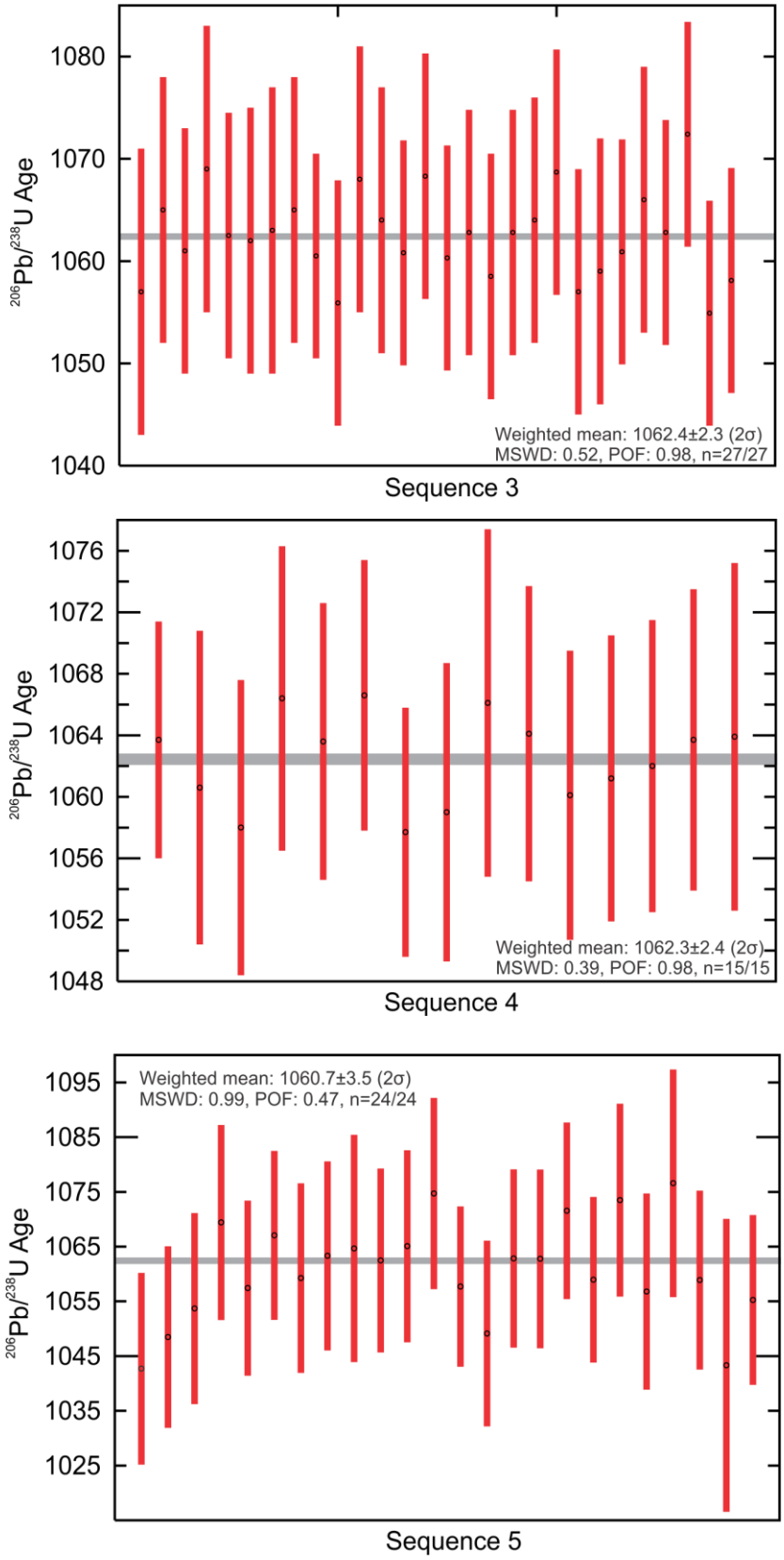

Figure 3.1.3.1 continued.

The LA-ICP-MS $^{206}Pb/^{238}U$ dates determined on validation material 94-35 agreed within uncertainty with the published concordia age of 55.5±1.5 Ma (ID-TIMS, 2σ; Klepeis et al., 1998) for three analytical runs (Figure 3.1.3.2; Table 3.1.3.2). The 94-35 $^{206}Pb/^{238}U$ dates yield less than 1% differences from the accepted age.

Table 3.1.3.2. Summary of LA-ICP-MS weighted $^{206}Pb/^{238}U$ date results for zircon reference material 94-35.

Sample run	Session	Date	$^{206}Pb/^{238}U$ date weighted mean (2SE)	No. analyses; MSWD; $p(\chi^2)$	Difference from accepted age (%)
19GJ13-3	1	Feb. 19, 2020	55.1±0.5	8/10; 1.9; 0.073	0.73
18lo22-1a 19GJ13-5a	2	Feb. 19, 2020	55.9±0.5	15/15; 1.02; 0.42	0.72
19GJ12-1 19GJ12-4	3	Feb. 20, 2020	55.9±0.4	13/13; 1.01; 0.44	0.72

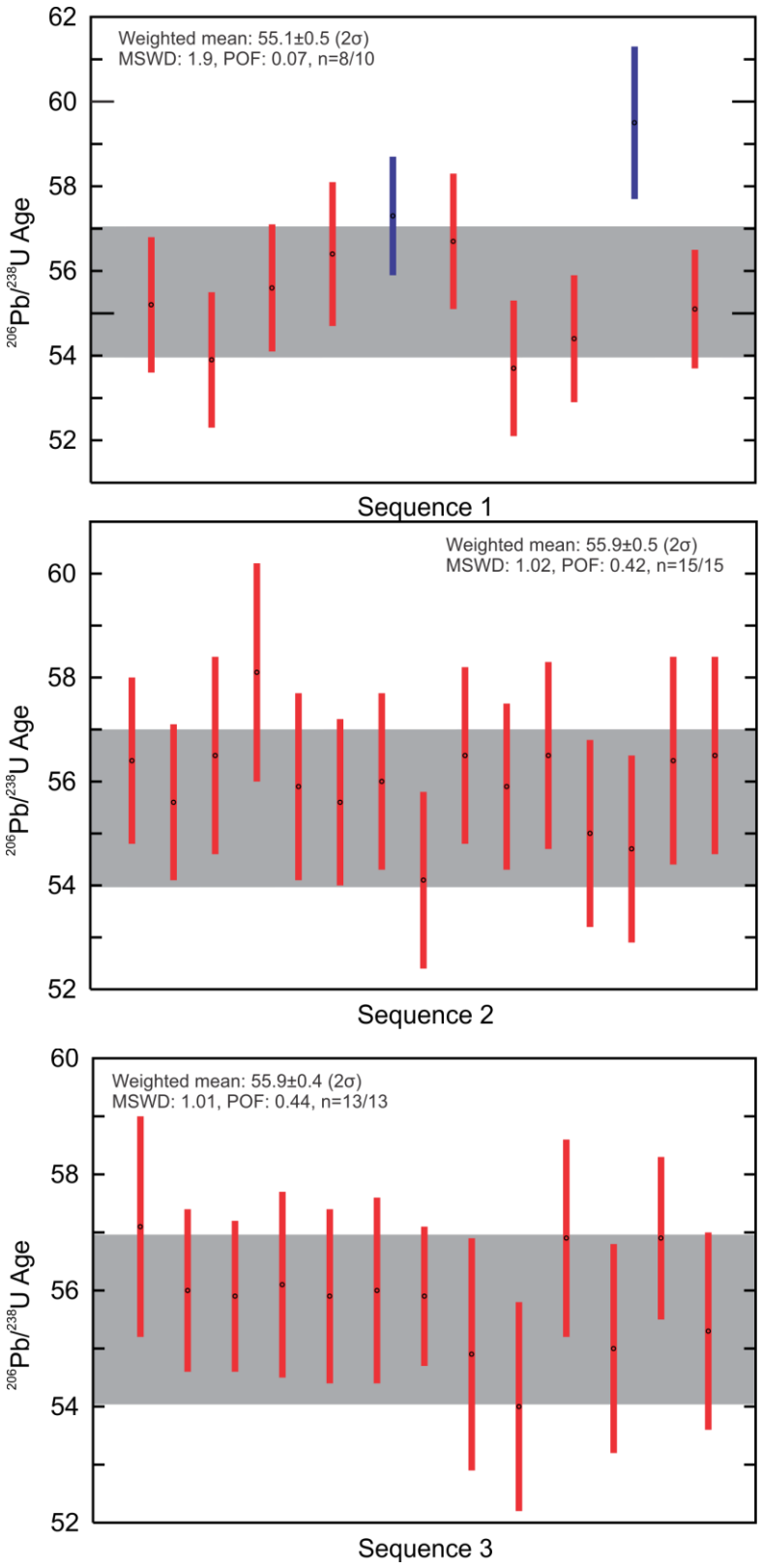

Figure 3.1.3.2. LA-ICP-MS $^{206}Pb/^{238}U$ age results for zircon reference material 94-35, analysed as a secondary standard. The grey line indicates the published RM age (55.5±1.5 Ma; Klepeis et al., 1998). Blue bars indicate analyses rejected from the weighted mean.

The validation material Plešovice yielded elevated $^{206}Pb/^{238}U$ ratios, resulting in $^{206}Pb/^{238}U$ dates older than the published age of 337.13±0.37 Ma (ID-TIMS, 2σ; Sláma et al., 2008) for four analytical runs (Figure 3.1.3.3; Table 3.1.3.3). Analytical session 1 yielded a spread in Plešovice $^{206}Pb/^{238}U$ dates resulting in a high MWSD and a ~1.5-2% difference from the accepted age. The difference in the measured $^{206}Pb/^{238}U$ ratios and ages from the accepted values may be attributed to heterogeneity in the Plešovice RM (e.g., Horstwood et al., 2016; Widmann et al., 2019). Although the results are older relative to the published age, the mean Plešovice dates are consistent between the analytical sessions.

Table 3.1.3.3. Summary of LA-ICP-MS weighted $^{206}Pb/^{238}U$ date results for zircon reference material Plešovice.

Sample run	Session	Date	$^{206}Pb/^{238}U$ date weighted mean (2SE)	No. analyses; MSWD; $p(\chi^2)$	Difference from accepted age (%)
19GJ13-3	1	Feb. 19, 2020	344.3±0.8	16/16; 6.4; 0.006	2.13
18lo22-1a 19GJ13-5a	2	Feb. 19, 2020	344.5±1.6	15/15; 0.39; 0.98	2.14
19GJ12-1 19GJ12-4	3	Feb. 20, 2020	342.4±0.9	24/24; 1.33; 0.13	1.45
18lo22-1d	4	Mar. 25, 2021	341.1±1.0	14/14; 0.83; 0.63	1.18
19GJ12-3 19GJ16-2	5	Mar. 26, 2021	337.1±1.1	21/21; 0.69; 0.84	0.01

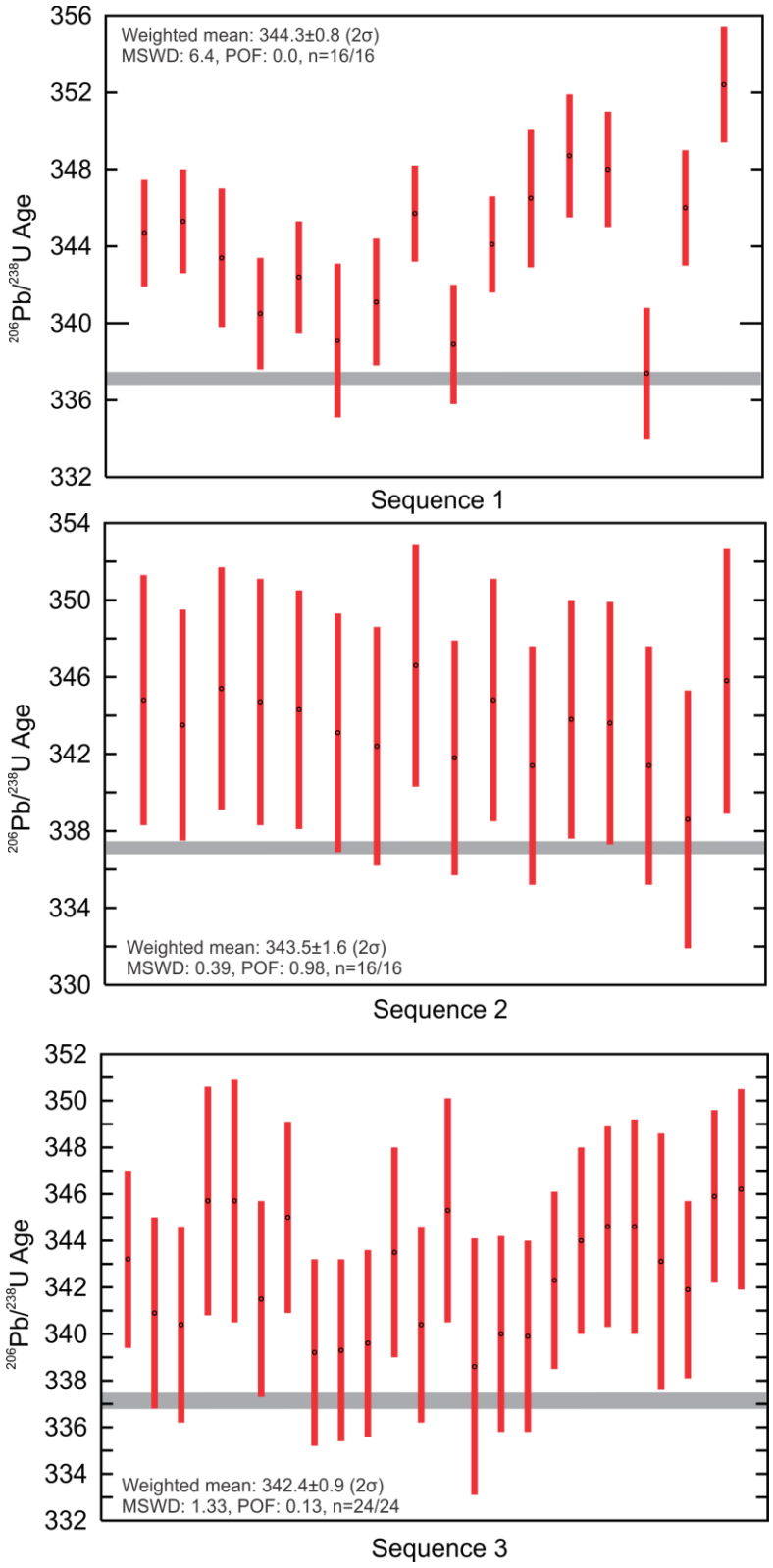

Figure 3.1.3.3. LA-ICP-MS $^{206}Pb/^{238}U$ age results for zircon reference material Plešovice, analysed as a secondary standard. The grey line indicates the published RM age (337.13±0.37 Ma; Sláma et al., 2008).

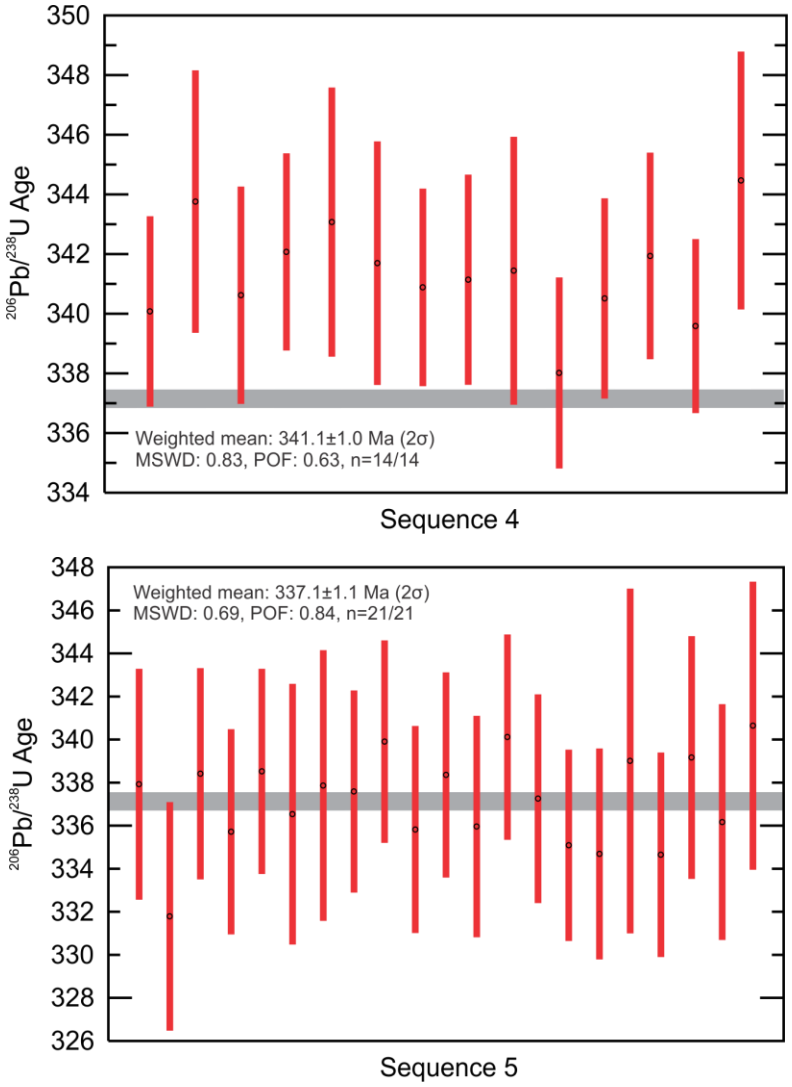

Figure 3.1.3.3 continued.

The validation material Mud Tank yielded low $^{206}Pb/^{238}U$ ratios, resulting in $^{206}Pb/^{238}U$ dates younger than the published age of 731.0±0.2 Ma (LA-ICP-MS, 2σ; Gain et al., 2019) for two analytical runs (Figure 3.1.3.4; Table 3.1.3.4). Analytical session 4 and 5 yielded Mud Tank $^{206}Pb/^{238}U$ dates ~3.0 to 4.5% younger than the accepted age. Although the results are younger relative to the published age, the Mud Tank dates are consistent, indicated by low MSWDs of the means.

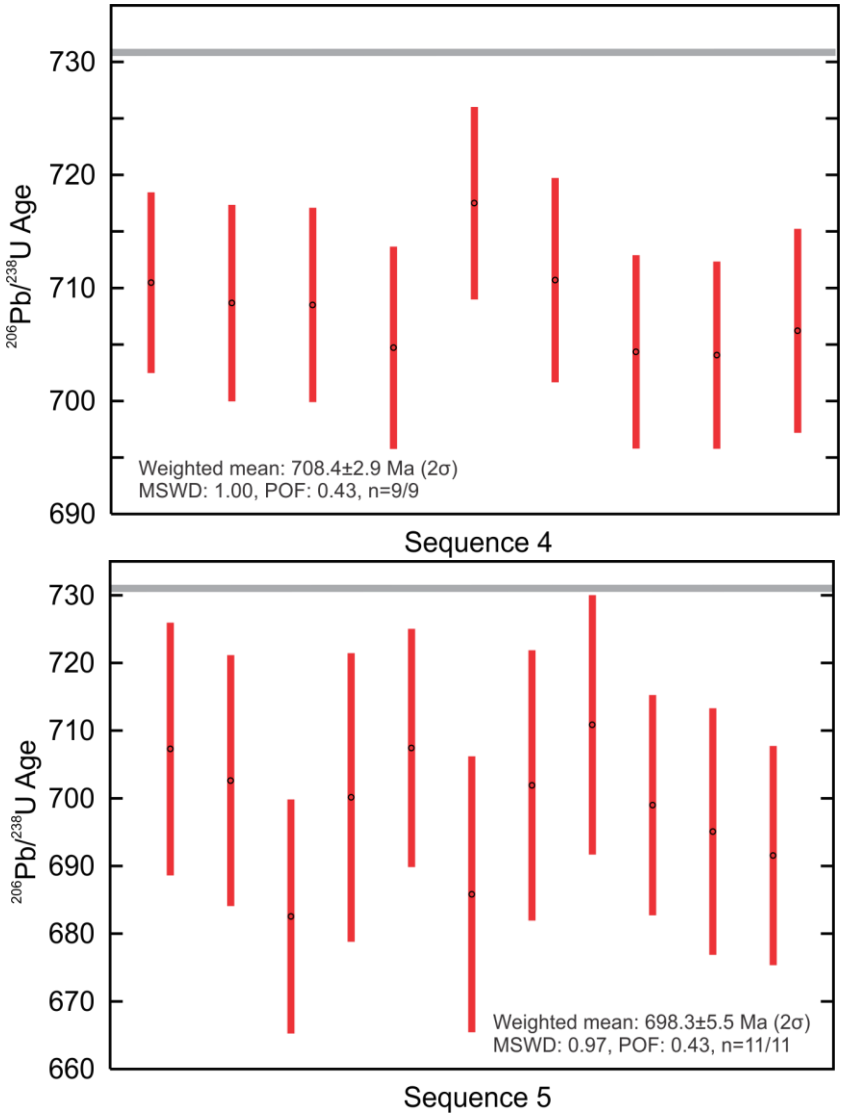

Figure 3.1.3.4. LA-ICP-MS $^{206}Pb/^{238}U$ age results for zircon reference material Mud Tank, analysed as a secondary standard. The grey line indicates the published RM age (731.0±0.2 Ma; Gain et al., 2019).

Table 3.1.3.4. Summary of LA-ICP-MS weighted $^{206}Pb/^{238}U$ date results for zircon reference material Mud Tank.

Sample run	Session	Date	$^{206}Pb/^{238}U$ date weighted mean (2SE)	No. analyses; MSWD; p(χ^2)	Difference from accepted age (%)
18lo22-1d	4	Mar. 25, 2021	708.4±2.9	9/9; 1.00; 0.43	3.09
19GJ12-3 19GJ16-2	5	Mar. 26, 2021	698.3±5.5	11/11; 0.97; 0.43	4.47

3.1.4 Zircon Lu-Hf Isotopes LA-ICP-MS

Lutetium-hafnium isotopes in zircon were analyzed by multi-collector (MC) LA- ICP-MS in the Arctic Resources Laboratory at the University of Alberta. The same zircon grains used for oxygen isotope (section 3.1.2) and U-Pb isotope (section 3.1.3) analyses were used for Lu-Hf isotope analysis, and the same analytical spots or magmatic zones were sampled. The same laser ablation system used for U-Pb isotope analyses (section 3.1.3) was utilized for Hf isotope analysis and coupled with a Thermo Fisher Scientific Neptune Plus MC-SF-ICP-MS using multiple Faraday detectors with 10^{11} Ω amplifiers operating in static collection mode. Masses 172, 173, 175, 176, 177, 178, 179, 180, and 181 were measured. A 33 µm diameter laser spot size was ablated using settings of 60 s of ablation, 60 s of background and washout, 8 Hz repetition rate, 120 mJ laser energy, 44%T attenuator value, and ca. 6.5 J/cm^2.

Data was processed and reduced offline using the Iolite version 3 software package (Paton et al., 2010; Paton et al., 2011), using the data reduction scheme (DRS) "Hf_Alberta". Due to the interferences of ^{176}Yb and ^{176}Lu on ^{176}Hf, a two-step correction was necessary to determine accurate Hf isotopic ratios. The Yb-mass bias factor (βYb) was determined using the peak-stripping method, by measuring the ratio of two interference-free isotopes of Yb, ^{172}Yb/^{173}Yb (Woodhead et al., 2004; Fisher et al., 2011), and calculated using the exponential mass fractionation law described in Russell et al. (1978). The measured ^{176}Yb/^{173}Yb was iteratively calibrated to optimize the Yb-interference correction, monitored by zircon reference materials with variable Yb contents (91500, MUN1, MUN3). The Lu interference correction was calculated in the same manner as the Yb interference, assuming Lu behaves similarly to Yb, using the ^{176}Lu/^{175}Lu ratio (e.g., Vezinet et al., 2018).

The corrected ^{176}Hf/^{177}Hf results of unknowns were converted to εHf(t), which is the ^{176}Hf/^{177}Hf ratio of at the time of crystallization (t) relative to the ^{176}Hf/^{177}Hf ratio of the chondritic uniform reservoir (CHUR):

$$\varepsilon Hf_{(t)} = \left(\frac{(^{176}Hf/^{177}Hf_{SAMPLE(t)})}{(^{176}Hf/^{177}Hf_{CHUR(t)})} - 1 \right) \times 10000$$, in which:

$$^{176}Hf/^{177}Hf_{(t)} = {}^{176}Hf/^{177}Hf_{(measured)} - {}^{176}Lu/^{177}Hf \times e^{[(\lambda 176Lu \times t) - 1]},$$

^{176}Hf/^{177}Hf$_{CHUR(measured)}$=0.282785±1, ^{176}Lu/^{177}Hf$_{CHUR}$=0.0336±1 (Bouvier et al., 2008), and λ^{176}Lu=1.867x10^{-11} (Söderlund et al., 2004).

The time of crystallization used in the εHf(t) for individual zircon analyses was either the single zircon $^{206}Pb/^{238}U$ age, or the interpreted crystallization age of the sample if a single zircon age was not available. Uncertainties on εHf(t) values were propagated using the calculations of Ickert (2013).

Hafnium isotopes of standard zircon reference material were determined throughout three analytical sessions. Four zircon reference materials were analyzed after every seven to twelve unknown analyses. The natural zircon Plešovice (Sláma et al., 2008) was used as the primary calibration reference material to monitor analytical reproducibility, Hf fractionation, and instrument drift during each analytical run. The natural zircon 91500 (Wiedenbeck et al., 1995; Blichert-Toft, 2008) and synthetic zircons MUN1 and MUN3 (Fisher et al., 2011) were used as secondary reference materials to verify the accuracy of the calibration. The weighted mean $^{176}Hf/^{177}Hf$ results for the primary and secondary zircon reference materials were compared to the accepted values and summarized in Tables 3.1.4.1-3.1.4.4.

The mean LA-MC-ICP-MS $^{176}Hf/^{177}Hf$ results of Plešovice for each analytical run (Table 3.1.4.1; Figure 3.1.4.1) agreed with published LA-ICP-MS and solution $^{176}Hf/^{177}Hf$ results (0.282482±13 (2σ); Sláma et al., 2008).

Table 3.1.4.1. Summary of LA-ICP-MS weighted $^{176}Hf/^{177}Hf$ ratio results for zircon reference material Plešovice.

Sample run	Session	Date	$^{176}Hf/^{177}Hf$ weighted mean (2SE)	No. analyses; MSWD; p(χ^2)	Difference from accepted $^{176}Hf/^{177}Hf$ (ppm)
18lo22-1a 19GJ12-1	1	Aug. 22, 2020	0.282482±0.000005	24/24; 1.33; 0.13	0
19GJ12-1 19GJ12-4	2	Aug. 22, 2020	0.282482±0.000008	12/12; 0.12; 1.00	0
19GJ12-4 19GJ13-3 19GJ13-5a	3	Aug. 23, 2020	0.282482±0.000005	27/27; 1.21; 0.22	0

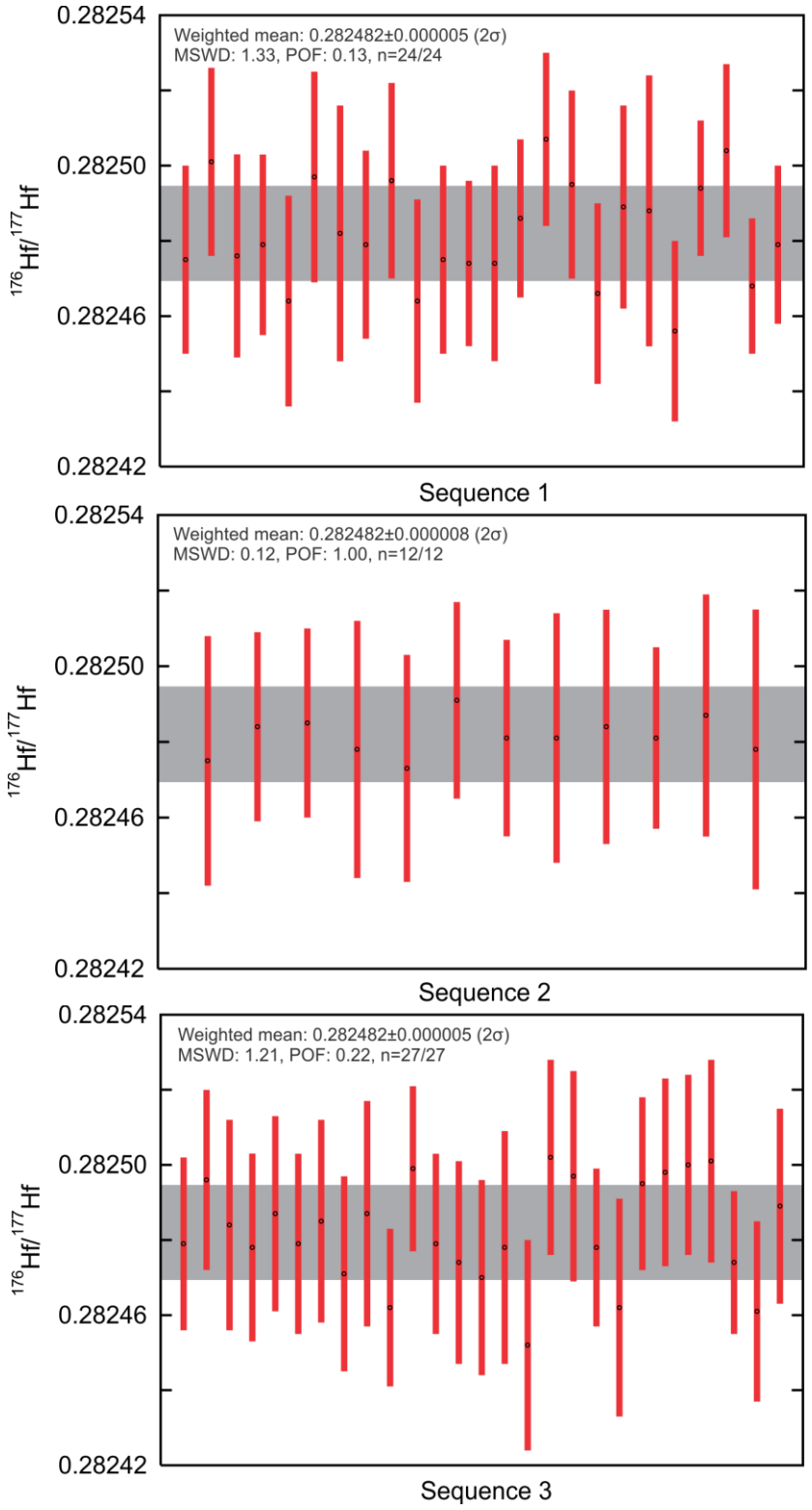

Figure 3.1.4.1. LA-ICP-MS $^{176}Hf/^{177}Hf$ ratio result for primary calibration zircon reference material Plešovice. The grey line indicates the published RM value (0.282482±13; Sláma et al., 2008).

The mean LA-MC-ICP-MS $^{176}Hf/^{177}Hf$ results of 91500 for each analytical run (Table 3.1.4.2; Figure 3.1.4.2) agreed with published solution $^{176}Hf/^{177}Hf$ results (0.282308±6 (2σ); Blichert-Toft, 2008). The measured 91500 $^{176}Hf/^{177}Hf$ ratios yield a less than a 35 ppm difference from the accepted ratio, on average.

Table 3.1.4.2. Summary of LA-ICP-MS weighted $^{176}Hf/^{177}Hf$ ratio results for zircon reference material 91500.

Sample run	Session	Date	$^{176}Hf/^{177}Hf$ weighted mean (2SE)	No. analyses; MSWD; p(χ^2)	Difference from accepted $^{176}Hf/^{177}Hf$ (ppm)
18lo22-1a 19GJ12-1	1	Aug. 22, 2020	0.282301±0.000010	14/14; 1.23; 0.25	25
19GJ12-1 19GJ12-4	2	Aug. 22, 2020	0.282307±0.000015	6/6; 1.38; 0.23	4
19GJ12-4 19GJ13-3 19GJ13-5a	3	Aug. 23, 2020	0.282298±0.000009	18/18; 0.83; 0.66	35

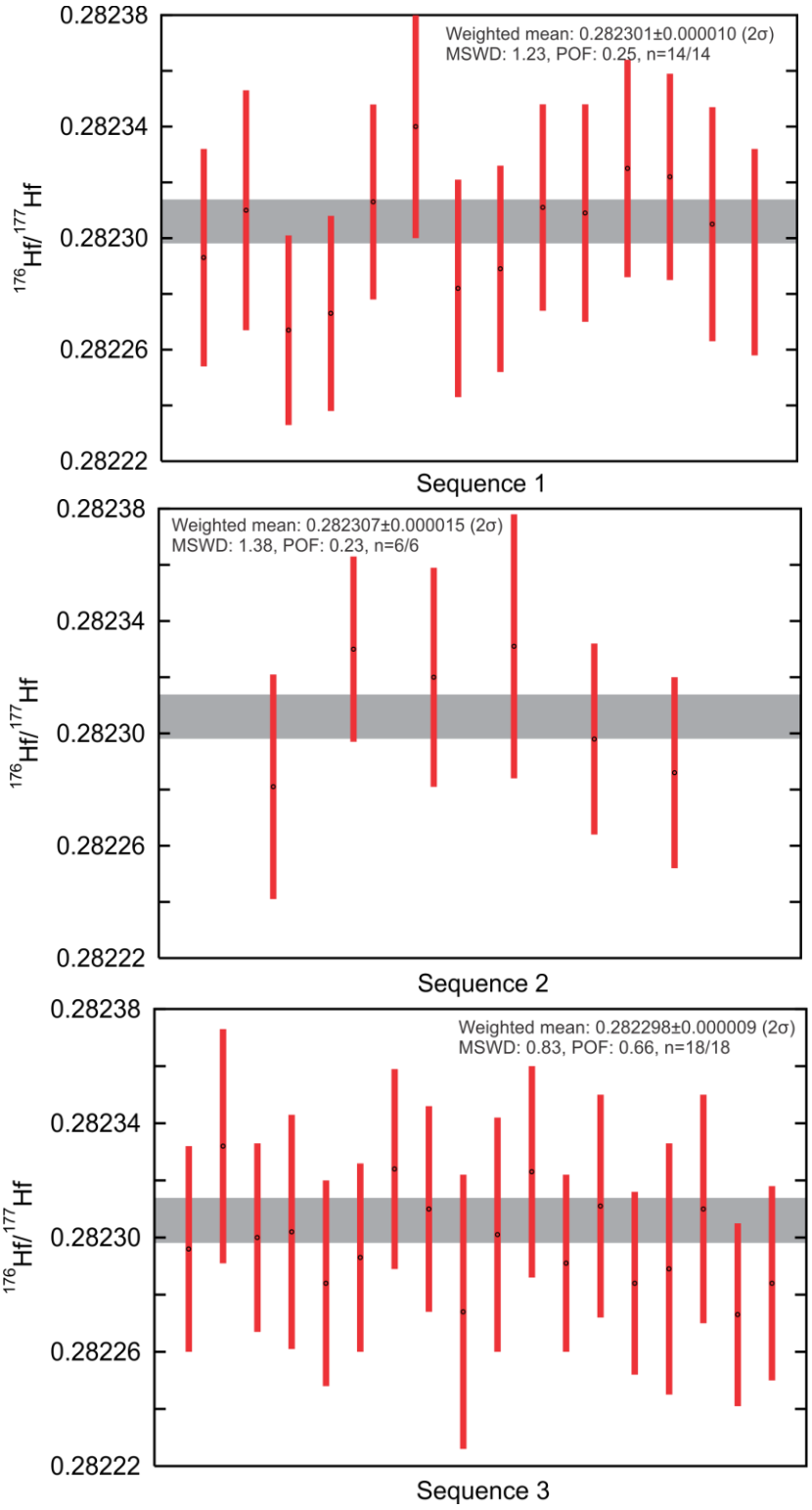

Figure 3.1.4.2. LA-ICP-MS $^{176}Hf/^{177}Hf$ ratio results for zircon reference material 91500, analysed as a secondary standard. The grey line indicates the published RM value (0.282308±6; Blichert-Toft., 2008).

The mean LA-MC-ICP-MS $^{176}Hf/^{177}Hf$ results of synthetic zircons MUN1 and MUN3 for each analytical run (Tables 3.1.4.3 and 3.1.4.4; Figures 3.1.4.3 and 3.1.4.4) agreed with published solution $^{176}Hf/^{177}Hf$ results (0.282135±7 (2σ); Fisher et al., 2011). The measured MUN1 and MUN3 $^{176}Hf/^{177}Hf$ ratios yielded less than a 50 ppm difference from the accepted ratios, on average.

Table 3.1.4.3. Summary of LA-ICP-MS weighted $^{176}Hf/^{177}Hf$ ratio results for synthetic zircon reference material MUN1.

Sample run	Session	Date	$^{176}Hf/^{177}Hf$ weighted mean (2SE)	No. analyses; MSWD; p(χ^2)	Difference from accepted $^{176}Hf/^{177}Hf$ (ppm)
18lo22-1a 19GJ12-1	1	Aug. 22, 2020	0.282132±0.000009	9/9; 1.34; 0.22	11
19GJ12-1 19GJ12-4	2	Aug. 22, 2020	0.282128±0.000018	3/3; 0.97; 0.38	25
19GJ12-4 19GJ13-3 19GJ13-5a	3	Aug. 23, 2020	0.282132±0.000009	9/9; 1.34; 0.22	11

Table 3.1.4.4. Summary of LA-ICP-MS weighted $^{176}Hf/^{177}Hf$ ratio results for synthetic zircon reference material MUN3.

Sample run	Session	Date	$^{176}Hf/^{177}Hf$ weighted mean (2SE)	No. analyses; MSWD; p(χ^2)	Difference from accepted $^{176}Hf/^{177}Hf$ (ppm)
18lo22-1a 19GJ12-1	1	Aug. 22, 2020	0.282149±0.000012	8/8; 1.85; 0.07	50
19GJ12-1 19GJ12-4	2	Aug. 22, 2020	0.282131±0.000024	3/3; 0.26; 0.77	14
19GJ12-4 19GJ13-3 19GJ13-5a	3	Aug. 23, 2020	0.282144 ±0.000012	9/9; 0.95; 0.47	32

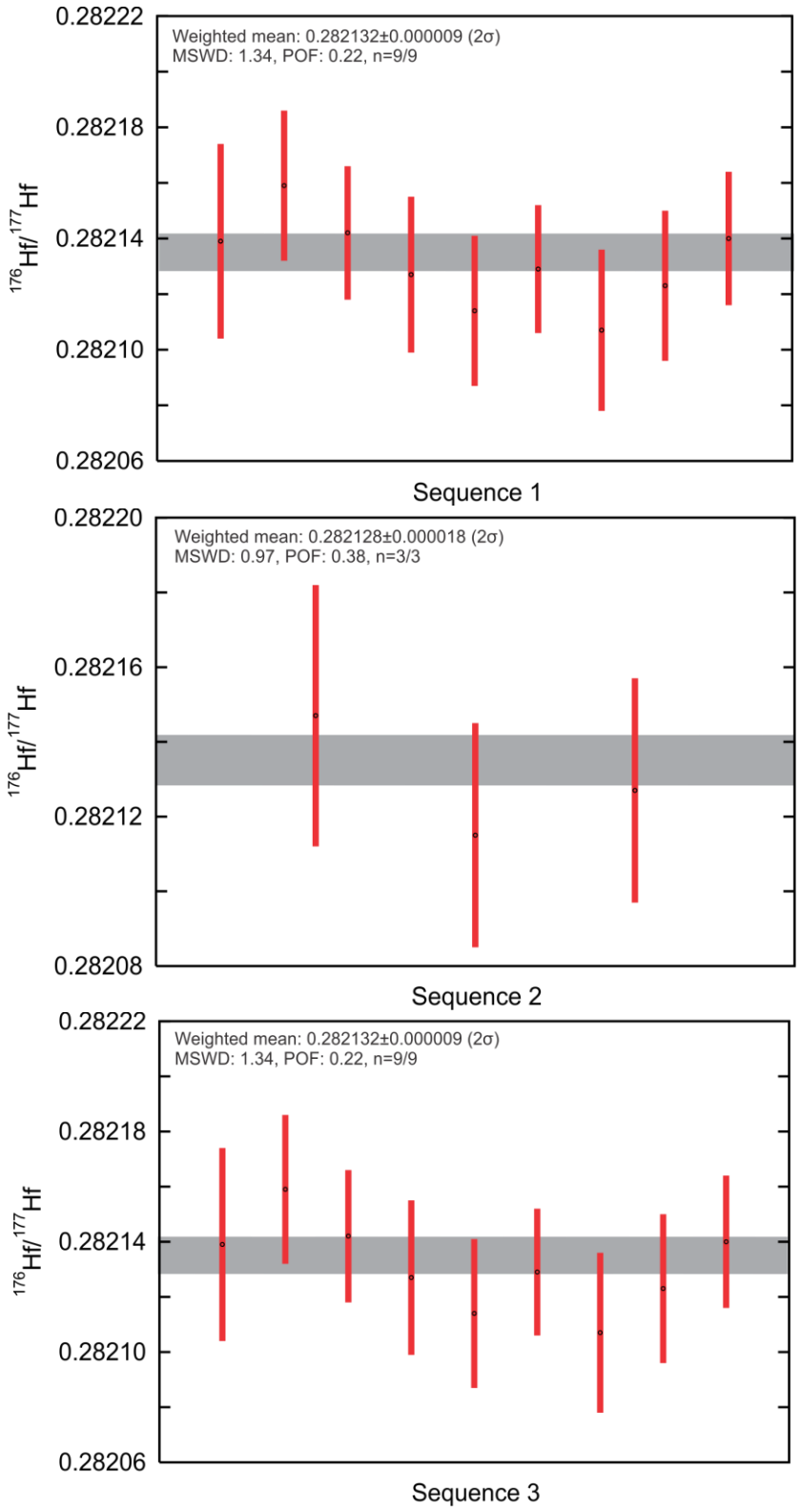

Figure 3.1.4.3. LA-ICP-MS $^{176}Hf/^{177}Hf$ ratio results for synthetic zircon reference material MUN1, analysed as a secondary standard. The grey line indicates the published RM value (0.282135±7; Fisher et al., 2011).

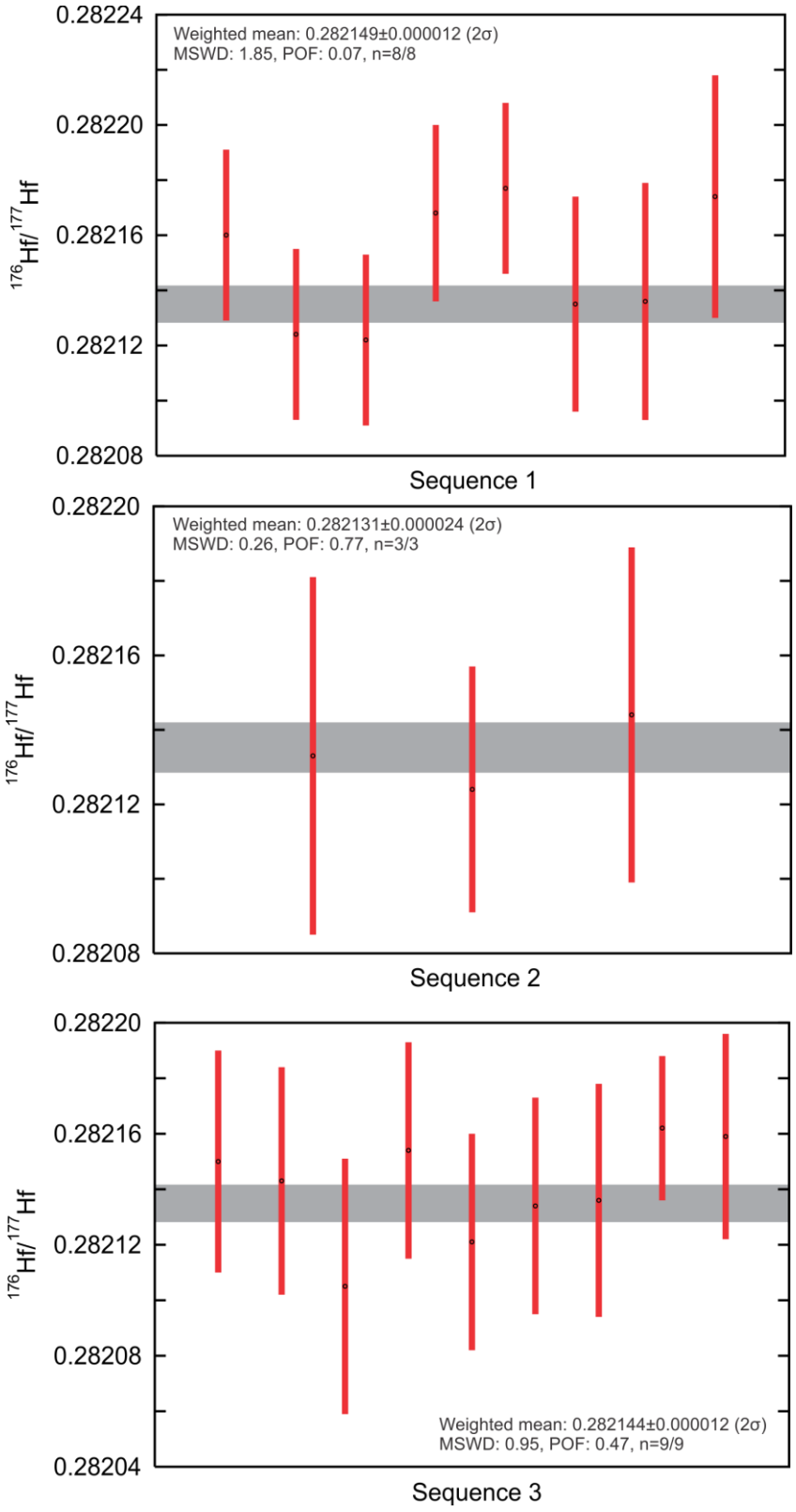

Figure 3.1.4.4. LA-ICP-MS $^{176}Hf/^{177}Hf$ ratio results for synthetic zircon reference material MUN3, analysed as a secondary standard. The grey line indicates the published RM value (0.282135±7; Fisher et al., 2011).

3.1.5 Zircon Trace Element LA-ICP-MS

Trace elements in zircon were analyzed by LA-SC-SF-ICP-MS using the same laser ablation and ICP-MS configuration as used for U-Pb isotope analysis, described in section 3.1.2. The same zircon grains used for oxygen isotope (section 3.1.2), U-Pb isotope (section 3.1.3), and Hf isotope (section 3.1.4) analyses were used for trace element analysis, and the same analytical spots or growth zones were sampled. A portion of the samples were analyzed for Hf isotopes prior to trace element analysis, while the other portion was analyzed for trace elements first. Concentrations for twenty-nine elements were acquired: ^{31}P, ^{43}Ca, ^{45}Sc, ^{49}Ti, ^{55}Mn, ^{57}Fe, ^{89}Y, ^{93}Nb, ^{137}Ba, ^{139}La, ^{140}Ce, ^{141}Pr, ^{146}Nd, ^{147}Sm, ^{153}Eu, ^{157}Gd, ^{159}Tb, ^{163}Dy, ^{165}Ho, ^{166}Er, ^{169}Tm, ^{172}Yb, ^{175}Lu, ^{177}Hf, ^{181}Ta, ^{232}Th, ^{204}Pb, ^{208}Pb, and ^{238}U. Samples were ablated for 40 or 50s, using a 33µm or 50 µm laser beam diameter, 60s of background and washout, 10 Hz repetition rate, 120mJ laser energy, 26%T attenuator value, and fluence of ca. 3.5 J/cm^2.

Data was processed and reduced offline using the Iolite version 4.3.7 software package (Paton et al., 2010; Paton et al., 2011), using the DRS "Trace Elements" (Longerich et al., 1996). Trace element reference materials were analyzed between every 8-10 unknowns. Glass standard reference material (SRM) NIST 612 was used as the primary calibration standard. NIST SRM 614 and zircon 91500 were used as secondary verification standards to monitor accuracy, instrumental drift, and matrix effects. The stoichiometric ^{29}Si content in zircon (15.32 wt.%) was used as an internal standard. Limits of detection (LOD= 3.29σ blank; Currie, 1968) were calculated in Iolite using the calculation of Pettke et al. (2012), based on Poisson statistics. For data to be quantitative it must exceed the limit of quantification (LOQ= 10σ blank; Currie, 1968), which was calculated and reported for each analysis. If unknown results were below the LOQ, but above LOD, the result for that analytical point was replaced with 0.5*LOQ in order to be plotted.

Table 3.1.5.1 summarizes the average concentration, uncertainty, LOD, and LOQ results for the three RMs, compared to accepted values. The NIST 612, NIST 614, and zircon 91500 reference values are from preferred GeoReM values (GeoReM 5211, Jochum et al., 2011; GeoReM 104, Wiedenbeck et al., 2004).

The trace element concentrations of NIST 612 from this study are within the 2 standard errors of GeoReM 5211 reported values (Figure 3.1.5.1; Jochum et al., 2011).

The NIST 614 results generally agree with the GeoReM 5211 values (Table 3.1.5.1, Figure 3.1.5.2; Jochum et al., 2011). Exceptions include ^{31}P, with a measured concentration of 61.2±5.3 ppm, significantly higher than the reported 11.4±3.9 ppm. ^{55}Mn and ^{57}Fe yielded concentrations below their respective limits of quantification (average LOQ=2.37 and 44.5 ppm). All rare earth elements (La through Lu) had concentrations lower than the values reported in GeoReM 5211 (Figure 3.1.5.2; Jochum et al., 2011).

Table 3.1.5.1. Summary of average trace element concentration, uncertainty, LOD, and LOQ results for glass standard reference materials NIST612 and NIST614 and zircon reference material 91500.

Reference Material	Element	^{31}P	^{43}Ca	^{45}Sc	^{49}Ti	^{55}Mn	^{57}Fe	^{89}Y	^{93}Nb	^{137}Ba
NIST612	Average concentration (ppm)	46.3	84942.8	39.9	44.0	38.7	51.7	38.3	38.9	39.3
	Uncertainty (2SE)	2.3	362.4	0.2	0.3	0.2	1.3	0.2	0.2	0.2
	Average LOD	-1.8	122.7	0.3	1.2	0.7	15.1	0.1	0.01	0.12
	Average LOQ	-6.0	408.9	0.9	4.1	2.2	50.2	0.2	0.04	0.41
	Reference Value	46.6	85049.0	39.9	44.0	38.7	51.0	38.3	38.9	39.3
	Uncertainty	6.9	0.1	2.5	2.3	0.9	2.0	1.4	2.1	0.9
NIST614	Average concentration (ppm)	61.2	82682.7	1.0	3.2	Below LOQ	Below LOQ	0.74	0.79	3.12
	Uncertainty (2SE)	5.3	749.4	0.0	0.1	0.1	1.8	0.01	0.02	0.07
	Average LOD	-9.3	115.9	0.3	0.9	0.7	13.3	0.04	0.01	0.09
	Average LOQ	-31.1	386.3	0.9	2.9	2.4	44.5	0.14	0.03	0.31
	Reference Value	11.4	85061.0	0.74	3.61	1.42	18.8	0.79	0.82	3.2
	Uncertainty	3.9	715.0		0.25	0.07	6	0.032	0.03	0.09
91500	Average concentration (ppm)	25.0	Below LOQ	769.6	4.2	Below LOQ	Below LOQ	115.2	0.99	Below LOQ
	Uncertainty (2SE)	1.8	10.4	3.0	0.2	0.08	1.3	0.4	0.01	0.01
	Average LOD	-1.3	99.2	0.2	1.0	0.5	12.1	0.04	0.01	0.09
	Average LOQ	-4.4	330.8	0.7	3.3	1.8	40.3	0.14	0.03	0.31
	Reference Value	13.9	1.9	1.17	4.73	0.19	3.4	145	2.03	0.06
	Uncertainty	4.1	1.2	0.12	0.3	0.1	0.4	38	0.12	0.03

Table 3.1.5.1 continued.

Reference Material	Element	^{139}La	^{140}Ce	^{141}Pr	^{146}Nd	^{147}Sm	^{153}Eu	^{157}Gd	^{159}Tb	^{163}Dy	^{165}Ho	^{166}Er
NIST612	Average concentration (ppm)	36.0	38.4	37.9	35.5	37.7	35.6	37.3	37.6	35.5	38.3	38.0
	Uncertainty (2SE)	0.2	0.2	0.2	0.2	0.2	0.2	0.2	0.2	0.2	0.2	0.2
	Average LOD	0.01	0.01	0.01	0.08	0.07	0.02	0.10	0.01	0.07	0.01	0.07
	Average LOQ	0.02	0.03	0.02	0.26	0.24	0.07	0.34	0.03	0.23	0.03	0.22
	Reference Value	36	38.4	37.9	35.5	37.7	35.6	37.3	37.6	35.5	38.3	38
	Uncertainty	0.7	0.7	1.00	0.7	0.8	0.8	0.9	1.1	0.7	0.8	0.9
NIST614	Average concentration (ppm)	0.68	0.74	0.72	0.71	0.71	0.74	0.71	0.71	0.70	0.70	0.71
	Uncertainty (2SE)	0.01	0.01	0.01	0.02	0.03	0.02	0.03	0.01	0.02	0.01	0.02
	Average LOD	0.004	0.01	0.01	0.06	0.06	0.02	0.07	0.01	0.05	0.01	0.05
	Average LOQ	0.01	0.03	0.02	0.20	0.20	0.05	0.24	0.02	0.18	0.03	0.16
	Reference Value	0.72	0.813	0.768	0.752	0.754	0.77	0.763	0.739	0.746	0.749	0.74
	Uncertainty	0.013	0.025	0.015	0.014	0.013	0.016	0.021	0.02	0.022	0.015	0.017
91500	Average concentration (ppm)	0.01	2.10	0.014	0.17	0.34	0.19	1.84	0.68	9.22	3.80	20.85
	Uncertainty (2SE)	0.001	0.01	0.001	0.01	0.01	0.01	0.03	0.01	0.07	0.02	0.11
	Average LOD	0.004	0.01	0.01	0.06	0.06	0.02	0.08	0.01	0.05	0.01	0.05
	Average LOQ	0.01	0.03	0.02	0.21	0.19	0.05	0.27	0.03	0.18	0.03	0.18
	Reference Value	0.015	2.6	0.019	0.23	0.38	0.2	1.8	0.83	10.4	4.6	24.1
	Uncertainty	0.02	0.4	0.012	0.02	0.06	0.04	0.8	0.16	1.8	1	5.6

Table 3.1.5.1 continued.

Reference Material	Element	^{169}Tm	^{172}Yb	^{175}Lu	^{177}Hf	^{181}Ta	^{204}Pb	^{208}Pb	^{Total}Pb*	^{232}Th	^{238}U
NIST612	Average concentration (ppm)	36.8	39.2	37.0	36.7	37.6	38.6	38.5		37.8	37.4
	Uncertainty (2SE)	0.2	0.2	0.2	0.2	0.2	0.4	0.1		0.2	0.2
	Average LOD	0.01	0.05	0.01	0.07	0.01	1.21	0.02		0.02	0.01
	Average LOQ	0.03	0.18	0.04	0.23	0.03	4.03	0.05		0.06	0.02
	Reference Value	36.8	39.2	37	36.7	37.6	38.57	38.57		37.79	37.38
	Uncertainty	0.6	0.9	0.9	1.2	1.9	0.20	0.20		0.08	0.08
NIST614	Average concentration (ppm)	0.68	0.75	0.70	0.67	0.72	Below LOQ	2.18		0.73	0.78
	Uncertainty (2SE)	0.01	0.03	0.01	0.03	0.01	0.21	0.03		0.02	0.01
	Average LOD	0.01	0.05	0.01	0.06	0.01	1.27	0.02		0.02	0.00
	Average LOQ	0.03	0.16	0.03	0.19	0.02	4.25	0.05		0.06	0.01
	Reference Value	0.732	0.777	0.732	0.711	0.808	2.32	2.32		0.748	0.823
	Uncertainty	0.02	0.021	0.018	0.022	0.026	0.04	0.04		0.006	0.002
91500	Average concentration (ppm)	5.11	54.8	10.87	5298.5	0.28	Below LOQ	2.52	16.67	24.3	68.2
	Uncertainty (2SE)	0.03	0.3	0.05	24.0	0.01	0.09	0.02		0.1	0.3
	Average LOD	0.01	0.04	0.01	0.06	0.01	1.00	0.01		0.02	0.00
	Average LOQ	0.03	0.14	0.03	0.18	0.03	3.34	0.04		0.05	0.01
	Reference Value	6.1	61.4	14.2	6030	0.54	0.11	1.76	15	28.6	81.3
	Uncertainty	1.2	18	3.8	640	0.1		2	2	0.1	9.2

*Total Pb determined using calculated average ^{206}Pb and ^{207}Pb from U-Pb LA-ICP-MS analyses

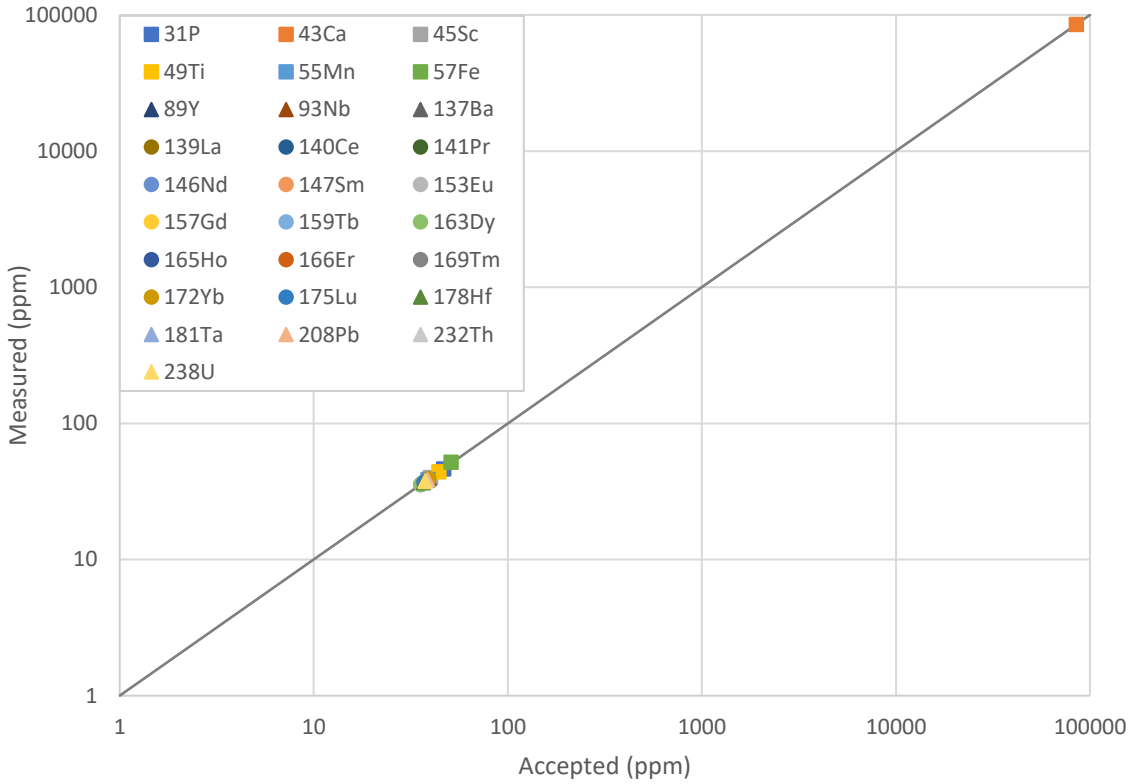

Figure 3.1.5.1. LA-ICP-MS trace elements results for primary calibration glass reference material NIST612. The grey line indicates a 1:1 ratio of measured concentrations to the accepted RM values (summarized in Table 3.1.5.1; Jochum et al., 2011). Deviation from this line indicates elements which do not agree with the accepted values.

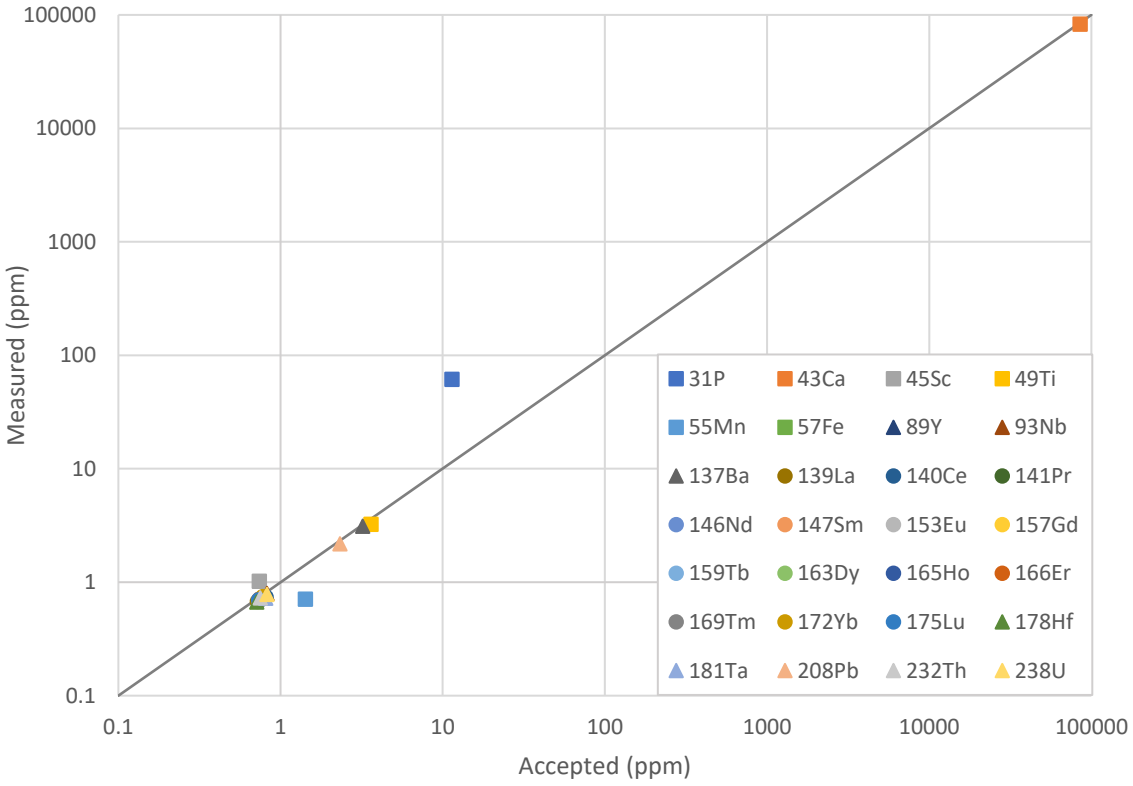

Figure 3.1.5.2. LA-ICP-MS trace elements results for secondary glass reference material NIST614. The grey line indicates a 1:1 ratio of measured concentrations to the accepted RM values (summarized in Table 3.1.5.1; Jochum et al., 2011). Deviation from this line indicates elements which do not agree with the accepted values.

The results of zircon 91500 are also generally within agreement of GeoReM 104 (Table 3.1.5.1, Figure 3.1.5.3; Wiedenbeck et al., 2004). Exceptions include ^{31}P and ^{45}Sc which had measured concentrations significantly greater than reported values (Table 3.1.5.1; Figure 3.1.5.3). The high concentrations of ^{45}Sc are likely due to interference with $^{29}Si^{16}O^{+}$ and Zr^{90++}, while ^{31}P has an interference with $^{15}N^{16}O$ and is difficult to ionize. ^{43}Ca, ^{55}Mn, ^{57}Fe, and ^{137}Ba yielded concentrations below the limit of detections (average LOD = 99.2, 0.54, 12.1, and 0.09 ppm). Most REEs (Ce, Tb, Dy, Er, Tm, Lu), Nb, and Ta were lower than the reported GeoReM values, while ^{208}Pb concentrations were greater than the GeoReM value (Figure 3.1.5.3; Wiedenbeck et al., 2004). Since ^{208}Pb values were greater than published values, the average total Pb concentration was determined for zircon 91500. The average total Pb was calculated using the average ^{206}Pb and ^{207}Pb concentrations determined from LA-ICP-MS U-Pb results and adding these averages to the average ^{204}Pb (<LOD) and ^{208}Pb concentrations from the LA-ICP-MS trace element analyses. The calculated average total Pb (16.67 ppm) for zircon 91500 was within uncertainty of the published value (15±2 ppm). The zircon 91500 La and Nd results were below the LOQ for this study (average LOQ= 0.01 and 0.21). The low concentrations of light rare earth elements (LREE) in zircon resulted in La, Pr, Nd, and Sm concentrations being below or close to the LOD in all unknown analyses. Figure 3.1.5.4 shows the proximity of all La, Pr, Nd, and Sm results to the LOD of these elements.

Europium- and Ce-anomalies were calculated for unknown zircons. The zircon Eu-anomaly is calculated as:

$Eu/Eu_N^* = Eu_N/(Sm_N*Gd_N)^{0.5}$, where N indicates the element concentration normalized to chondrite (Sun and McDonough, 1989).

However, due to low LODs in La and Pr in zircon, Ce-anomalies may be overestimated if calculated as:

$Ce/Ce_N^* = Ce_N/(La_N*Pr_N)^{0.5}$

Therefore, Ce-anomalies are instead calculated as Ce/Ce_C^*, which better estimates Ce* by using a curve fit line function through the zircon MREE and HREE concentrations (Zhong et al., 2019; Lee et al., 2020; Lee et al., 2021).

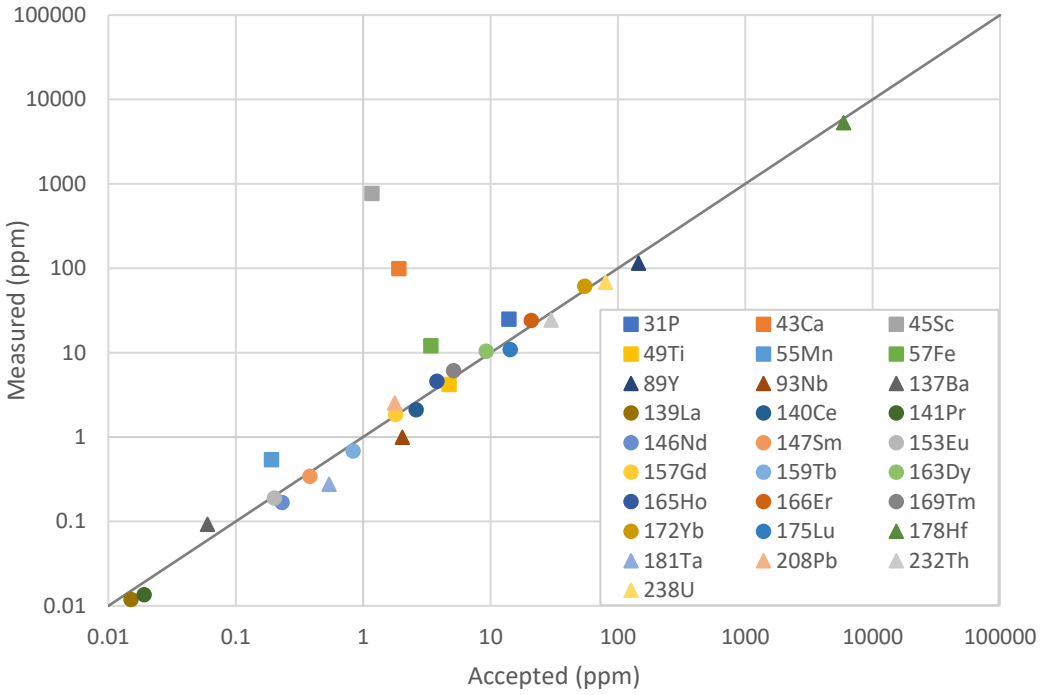

Figure 3.1.5.3. LA-ICP-MS trace elements results for secondary zircon reference material 91500. The grey line indicates a 1:1 ratio of measured concentrations to the accepted RM values (summarized in Table 3.1.5.1; Wiedenbeck et al., 2004). Deviation from this line in dictates elements which do not agree with the accepted values.

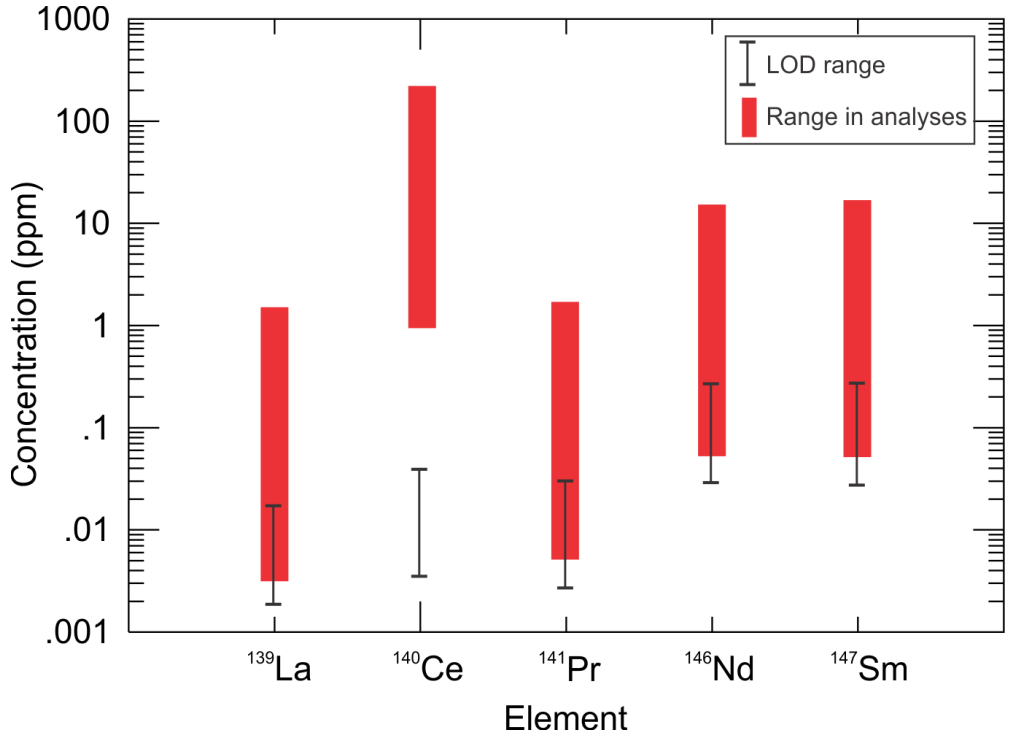

Figure 3.1.5.4. Range in LA-ICP-MS light rare earth element results in unknown zircons. Red boxes represent the range in concentrations from all unknown zircon analyses. Black lines represent the range in LODs for each LREE.

3.1.6 Laser Ablation Split Stream (LASS) ICP-MS

Apatite and titanite Sm-Nd and U-Pb

Samarium-neodymium and U-Pb isotopes in apatite and titanite were simultaneously measured using the laser ablation split-stream (LASS)-ICP-MS method (Yuan et al., 2004; Fisher et al., 2011; Fisher et al., 2014; Fisher et al., 2017). Concurrent Sm-Nd and U-Pb measurements were obtained at the University of Alberta Arctic Resources Laboratory, using the same laser and ICP-MS configurations as described in the U-Pb and Lu-Hf single stream LA-ICP-MS methods (Section 3.1.3 and 3.1.4). The U-Pb isotope measurements were acquired on a Thermo Fisher Element II XR SC-SF-ICP-MS. The Sm-Nd isotope measurements were obtained simultaneously, on a portion of the same material as analyzed for U-Pb, on a Thermo Fisher Scientific Neptune Plus MC-SF-ICP-MS using multiple Faraday detectors with 10^{11} Ω amplifiers operating in static collection mode. Masses 143, 144, 145, 148, and 150 were measured. The apatite and titanite samples were ablated using a RESOlution 193 nm ArF excimer laser using a 90 μm diameter spot size, 45s of ablation time, 60s of background and washout, 8 Hz repetition rate, and ca. 5-6 J/cm^2 fluence.

Data was processed and reduced offline using the Iolite version 3 software package (Paton et al., 2010; Paton et al., 2011) in multiple DRS mode, using the DRS "SmNd_Downhole" and "X_U_Pb_Geochron". The Nd mass bias corrections were calibrated using the Bear Lake titanite (TH-tnt-1 of Fisher et al., 2020 and BLR-1 of Aleinikoff et al., 2007) and Bancroft apatite (TH-ap-1 of Fisher et al., 2020) as primary reference materials. Verification of the Nd mass bias correction was determined using the MKED titanite (Spandler et al., 2016) and MAD apatite (Fisher et al., 2020). The U-Pb mass bias corrections were calibrated using the MKED titanite and Bancroft apatite and verified using the Bear Lake titanite and MAD apatite. The LASS-ICP-MS $^{143}Nd/^{144}Nd$ and U-Pb ages were compared to the reported values for each reference material, shown in Figures 3.1.6.1-3.1.6.7, and summarized in Tables 3.1.6.1-3.1.6.4.

The LASS-ICP-MS $^{143}Nd/^{144}Nd$ ratios and U-Pb discordia age results of titanite RM Bear Lake (Table 3.1.6.1; Figures 3.1.6.1 and 3.1.6.2) agreed with published $^{143}Nd/^{144}Nd$ ratio results of 0.512310±0.000005 (ID-TIMS, 2σ; Fisher et al., 2020) and age of 1047.1±0.4 Ma (TIMS, 2σ; Aleinikoff et al., 2007). The measured Bear Lake $^{143}Nd/^{144}Nd$ ratios yield a less than a 10 ppm

difference from the accepted ratio, on average. The Bear Lake discordia age yields a less than 1% difference from the accepted age.

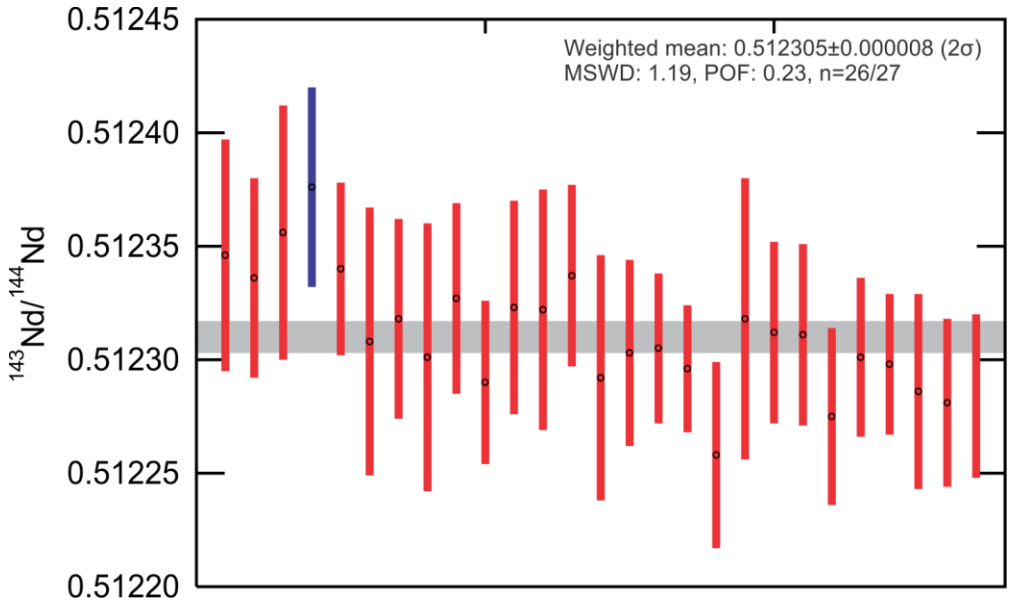

Figure 3.1.6.1. LASS-ICP-MS $^{143}Nd/^{144}Nd$ ratio results for primary calibration titanite reference material Bear Lake. The grey line indicates the published RM value (0.512310±5; Fisher et al., 2020).

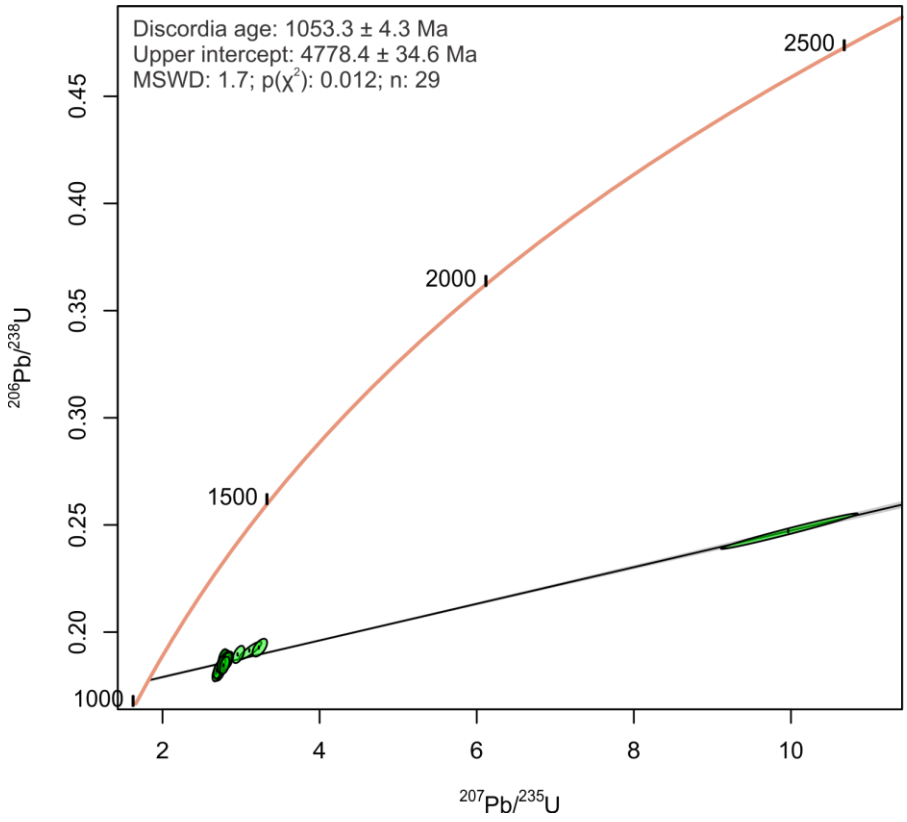

Figure 3.1.6.2. LASS-ICP-MS U-Pb concordia results for secondary U-Pb titanite reference material Bear Lake. The published RM age is 1047.1±0.4 Ma (Aleinikoff et al., 2007).

Table 3.1.6.1. Summary of LASS-ICP-MS weighted $^{143}Nd/^{144}Nd$ ratio and $^{206}Pb/^{238}U$-$^{207}Pb/^{235}U$ discordia age results for titanite reference material Bear Lake.

Sample run	Date	$^{143}Nd/^{144}Nd$ weighted mean (2SE)	No. analyses; MSWD; $p(\chi^2)$	$^{206}Pb/^{238}U$ - $^{207}Pb/^{235}U$ Discordia age (2SE)	No. analyses; MSWD; $p(\chi^2)$	Difference from accepted age (%); $^{143}Nd/^{144}Nd$ (ppm)
19GJ12-1 19GJ12-2 19GJ13-2 19GJ13-3 19GJ13-4	Jan. 31, 2020	0.512305 ±0.000008	26/27; 1.19; 0.23	1053.3 ±4.3 Ma	29/29; 1.7; 0.012	0.6; 10

The LASS-ICP-MS weighted mean $^{143}Nd/^{144}Nd$ ratios and $^{206}Pb/^{238}U$ age results of titanite RM MKED (Table 3.1.6.2; Figure 3.1.6.3 and 3.1.6.4) agreed with published $^{143}Nd/^{144}Nd$ ratio results of 0.511630±0.000003 (TIMS, 2σ; Spandler et al., 2016) and $^{206}Pb/^{238}U$ age of 1519.5±3.0 Ma (LA-ICP-MS, 2σ; Spandler et al., 2016). The measured MKED $^{143}Nd/^{144}Nd$ ratios yield a less than a 10 ppm difference from the accepted ratio, on average. The MKED $^{206}Pb/^{238}U$ weighted mean age yields a less than 1% difference from the accepted age.

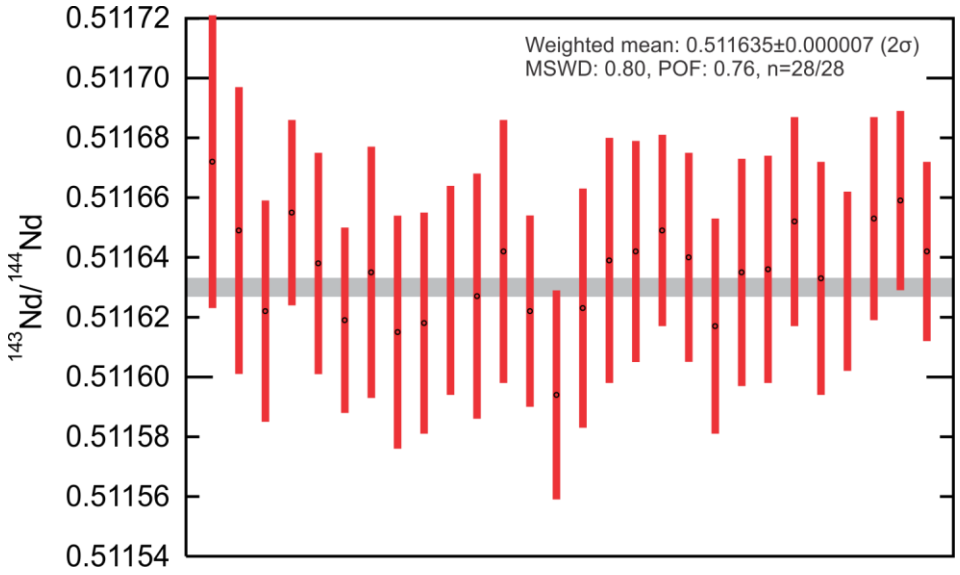

Figure 3.1.6.3. LASS-ICP-MS $^{143}Nd/^{144}Nd$ ratio results for titanite reference material MKED, analysed as a secondary standard. The grey line indicates the published RM value (0.511630±3; Spandler et al., 2016).

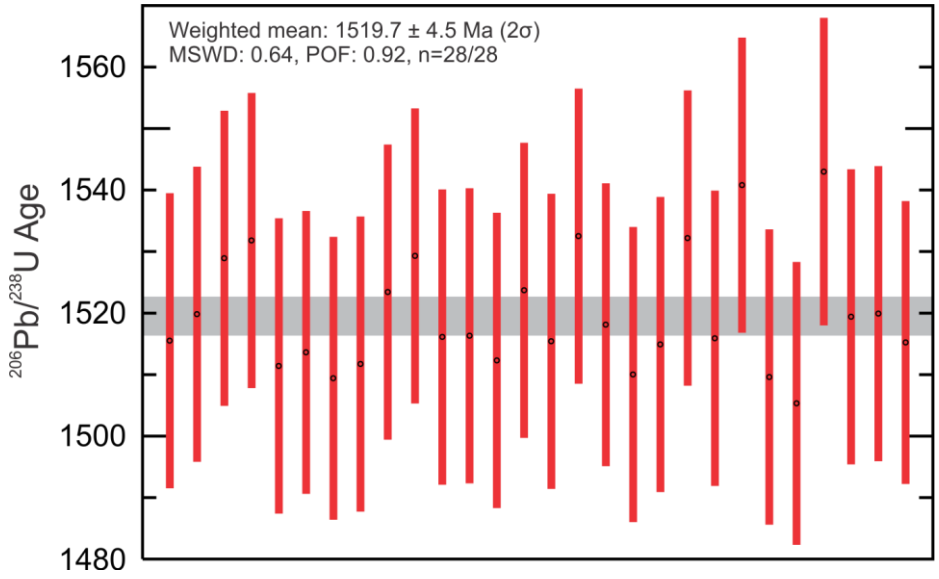

Figure 3.1.6.4. LASS-ICP-MS $^{206}Pb/^{238}U$ age results for primary U-Pb calibration titanite reference material MKED. The grey line indicates the published RM age (1519.5±3.0 Ma; Spandler et al., 2016)

Table 3.1.6.2. Summary of LASS-ICP-MS weighted $^{143}Nd/^{144}Nd$ ratio and $^{206}Pb/^{238}U$ age result for titanite reference material MKED.

Sample run	Date	$^{143}Nd/^{144}Nd$ weighted mean (2SE)	No. analyses; MSWD; p(χ^2)	$^{206}Pb/^{238}U$ weighted mean age (2SE)	No. analyses; MSWD; p(χ^2)	Difference from accepted age (%); $^{143}Nd/^{144}Nd$ (ppm)
19GJ12-1 19GJ12-2 19GJ13-2 19GJ13-3 19GJ13-4	Jan. 31, 2020	0.511635± 0.000007	28/28; 0.80; 0.76	1519.7± 4.5 Ma	28/28; 0.64; 0.92	0.01; 10

The LASS-ICP-MS weighted mean $^{143}Nd/^{144}Nd$ ratio results of apatite RM Bancroft (Table 3.1.6.3; Figures 3.1.6.5 and 3.1.6.6) agreed with published $^{143}Nd/^{144}Nd$ ratio results of 0.512048±0.000006 (ID-TIMS, 2σ; Fisher et al., 2020). The measured Bancroft $^{143}Nd/^{144}Nd$ ratios yield a 31 ppm difference from the accepted ratio, on average. However, the concordia age result of 964.8±4.1 Ma of the RM is significantly less than the published $^{207}Pb/^{206}Pb$ and $^{238}U/^{206}Pb$ intercept age of 1021±3 Ma (ID-TIMS, 2σ; Fisher et al., 2020). This Bancroft concordia age accounts for a ~5.5% difference from the accepted age.

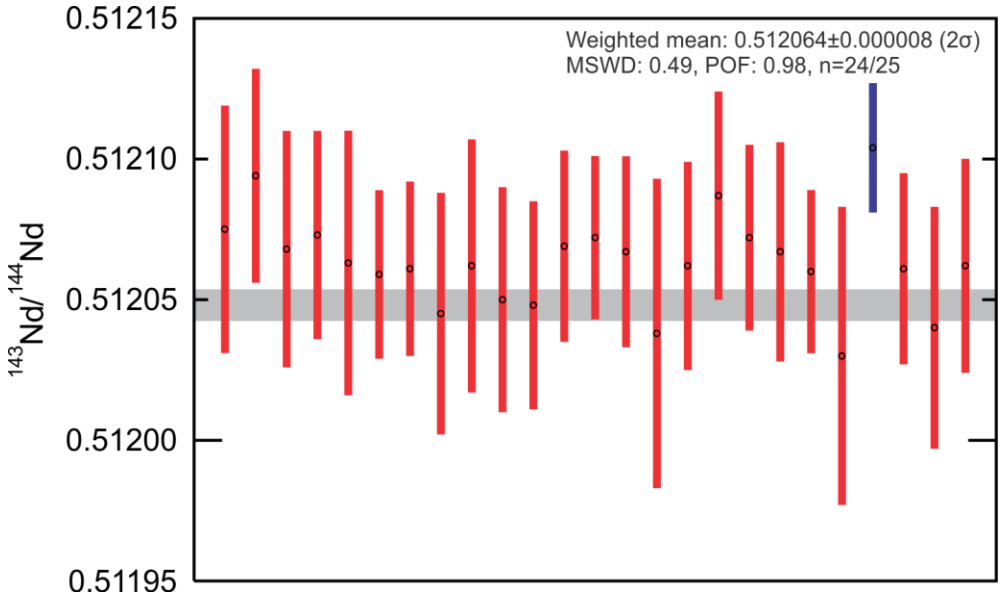

Figure 3.1.6.5. LASS-ICP-MS $^{143}Nd/^{144}Nd$ ratio results for apatite reference material Bancroft, analysed as a secondary standard. The grey line indicates the published RM value (0.512048±6; Fisher et al., 2020).

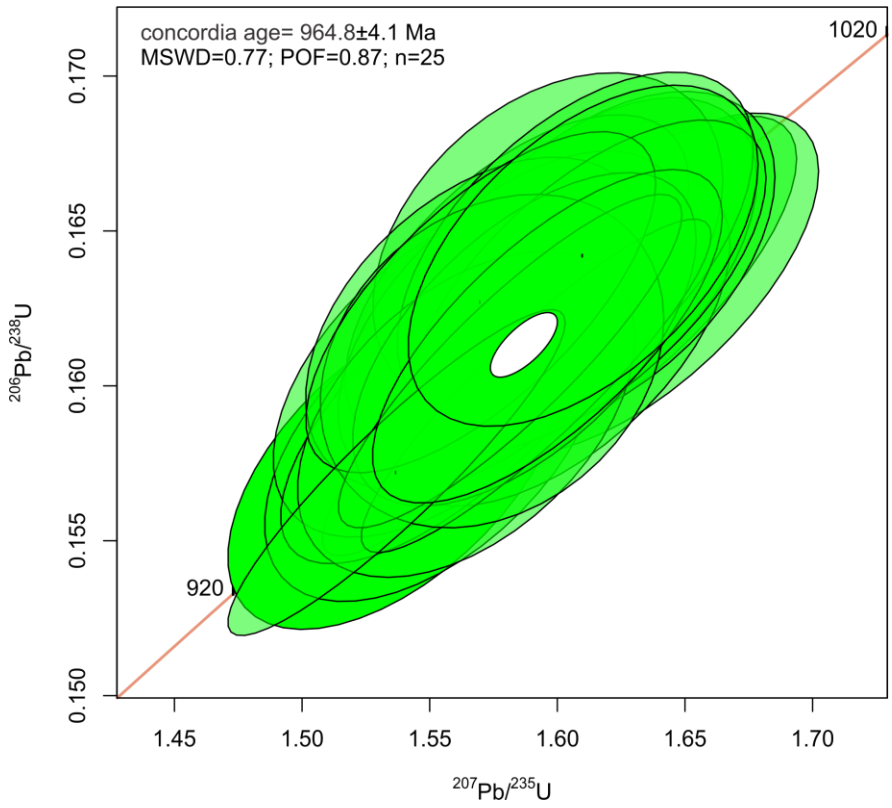

Figure 3.1.6.6. LASS-ICP-MS U-Pb concordia results for primary U-Pb calibration apatite reference material Bancroft. The published RM age is 1021±3 Ma (Fisher et al., 2020).

Table 3.1.6.3. Summary of LASS-ICP-MS weighted $^{143}Nd/^{144}Nd$ ratio and $^{206}Pb/^{238}U$-$^{207}Pb/^{235}U$ concordia age results for calibration apatite reference material Bancroft.

Sample run	Date	$^{143}Nd/^{144}Nd$ weighted mean (2SE)	No. analyses; MSWD; $p(\chi^2)$	$^{206}Pb/^{238}U$ - $^{207}Pb/^{235}U$ Concordia age (2SE)	No. analyses; MSWD; $p(\chi^2)$	Difference from accepted age (%); $^{143}Nd/^{144}Nd$ (ppm)
18lo22-1a 18lo22-1d 19GJ12-4 19GJ13-3 19GJ13-4 19GJ16-2	Jan. 30, 2020	0.512064 ±0.000008	24/25; 0.49; 0.98	964.8 ±4.1 Ma	25/25; 0.77; 0.87	5.5; 31

The LASS-ICP-MS weighted mean $^{143}Nd/^{144}Nd$ ratio results of apatite RM MAD (Table 3.1.6.4; Figure 3.1.6.7) agreed with published $^{143}Nd/^{144}Nd$ ratio results of 0.511304±0.000013 (ID-TIMS, 2σ; Fisher et al., 2020). The measured MAD $^{143}Nd/^{144}Nd$ ratios yield a 39 ppm difference from the accepted ratio, on average. However, U-Pb analyses did not yield any dates correlating to the published $^{206}Pb/^{238}U$ age of 475.4±1.8 Ma (ID-TIMS, 2σ; Fisher et al., 2020).

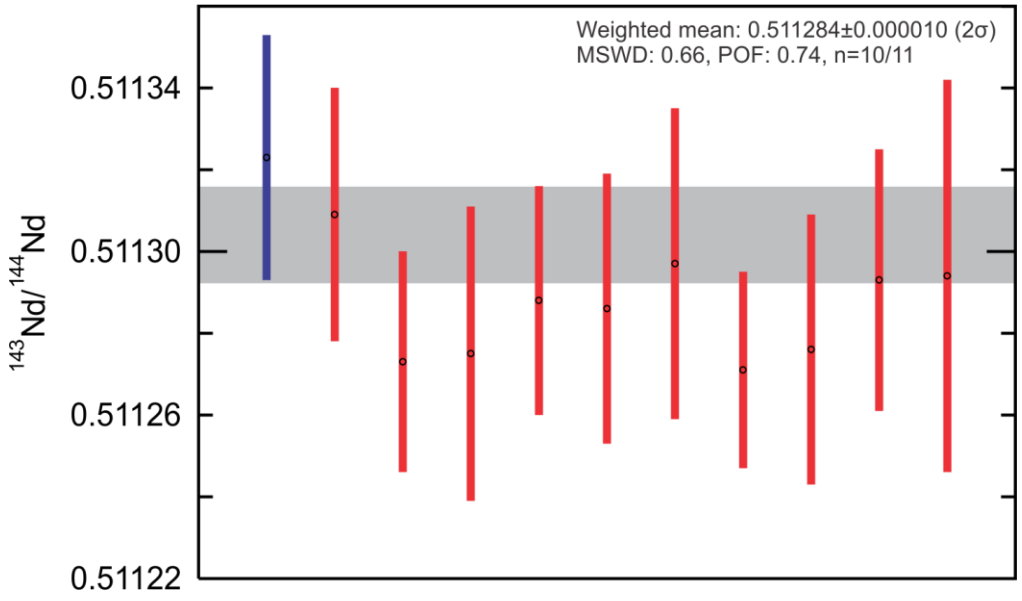

Figure 3.1.6.7. LASS-ICP-MS $^{143}Nd/^{144}Nd$ ratio results for primary calibration apatite reference material MAD. The grey line indicates the published RM value (0.511304±13; Fisher et al., 2020).

Table 3.1.6.4. Summary of LASS-ICP-MS weighted $^{143}Nd/^{144}Nd$ ratio and $^{206}Pb/^{238}U$-$^{207}Pb/^{235}U$ concordia age results for apatite reference material MAD, analysed as a secondary standard.

Sample run	Date	$^{143}Nd/^{144}Nd$ weighted mean (2SE)	No. analyses; MSWD; $p(\chi^2)$	$^{206}Pb/^{238}U$ - $^{207}Pb/^{235}U$ Concordia age (2SE)	No. analyses; MSWD; $p(\chi^2)$	Difference from accepted $^{143}Nd/^{144}Nd$ (ppm)
19GJ12-1 19GJ12-2 19GJ13-2 19GJ13-3 19GJ13-4	Jan. 30, 2020	0.511284± 0.000010	10/11; 0.66; 0.74	N/A	N/A	39

The $^{143}Nd/^{144}Nd$ results of unknown titanite and apatite grains were converted to εNd(t), which is the $^{143}Nd/^{144}Nd$ ratio of at the time of crystallization (t) relative to the $^{143}Nd/^{144}Nd$ ratio of the chondritic uniform reservoir (CHUR):

$$\varepsilon Nd_{(t)} = \left(\frac{(^{143}Nd/^{144}Nd_{SAMPLE(t)})}{(^{143}Nd/^{144}Nd_{CHUR(t)})} - 1\right) \times 10000$$

Where $^{143}Nd/^{144}Nd_{(t)} = {}^{143}Nd/^{144}Nd_{(measured)} - {}^{147}Sm/^{144}Nd \times e^{[(\lambda 147Sm \times t) - 1]}$, $^{143}Nd/^{144}Nd_{CHUR(measured)}=0.51263\pm11$, $^{147}Sm/^{144}Nd_{CHUR}=0.1960\pm4$ (Bouvier et al., 2008), and $\lambda^{147}Sm=6.54\times10^{-12}$ (Lugmair and Marti, 1979).

The interpreted titanite U-Pb discordia age was used for time of crystallization in the εNd(t) calculation for individual titanite analyses. Since apatite U-Pb analyses did not yield any ages, the interpreted zircon $^{206}Pb/^{238}U$ ages from the same samples were used to calculate εNd(t) of the apatite grains. Uncertainties on εNd(t) values were propagated using the calculations of Ickert (2013).

Additionally, titanite and apatite εNd(t) results were converted to εHf(t) using the calculation of Vervoort et al. (2011), which utilizes the linearity of the mantle Hf-Nd isotope array:

$$\varepsilon Hf(t) = [1.55 \times \varepsilon Nd(t)] + 1.21$$

Zircon Lu-Hf and U-Pb

Uranium-lead and Lu-Hf isotopes in a subset of zircon grains were simultaneously measured using the laser ablation split-stream (LASS)-ICP-MS method (e.g., Yuan et al., 2004; Fisher et al., 2011, 2014, 2017). Concurrent U-Pb and Lu-Hf measurements were obtained at the University of Alberta Arctic Resources Laboratory, using the same laser and ICP-MS configurations as described in U-Pb and Lu-Hf single stream LA-ICP-MS methods (Section 3.1.3 and 3.1.4). Analytical points were determined from CL and BSE images as described in section 3.1.2, and split stream spots were positioned on top of shallow SIMS analysis pits. The zircon samples were ablated using a RESOlution 193 nm ArF excimer laser using a 44 µm diameter laser spot size and settings of 60 s of ablation, 60 s of background and washout, 8 Hz repetition rate, 120 mJ laser energy, 44%T attenuator value, and ca. 6.0 J/cm^2.

Data was processed and reduced offline using the Iolite version 3 software package (Paton et al., 2010; Paton et al., 2011), using the same DRS as described in sections 3.1.3 and

3.1.4, in multiple DRS mode. For U-Pb data processing, the decay constants of ^{235}U (9.485 x 10^{-10} $year^{-1}$), ^{238}U (1.55125 x 10^{-10} $year^{-1}$) and the $^{238}U/^{235}U$ isotopic ratio (137.88) used in age calculations are from Jaffey et al. (1971). Weighted means and Concordia plots were created using IsoplotR online (Vermeesch, 2018). The same data correction as utilized for the single stream Lu-Hf measurements (section 3.1.4) were applied to the split-stream measurements. All reported isotope ratios and age uncertainties are reported as 2σ standard error, or 95.4% confidence level, and were propagated by quadratic addition.

Hafnium and U-Pb isotopes of standard zircon reference material were determined throughout four analytical sessions. Six zircon reference materials were analyzed after every eight to twelve unknown analyses. The natural zircon 91500 (Wiedenbeck et al., 1995, 2004; Blichert-Toft, 2008) was used as the primary calibration reference material to monitor analytical reproducibility, Hf and U-Pb fractionation, and instrument drift during each analytical run. The natural zircons Plešovice (Sláma et al., 2008) and GJ1 (Jackson et al., 2004; Morel et al., 2008) were used as secondary reference materials to verify accuracy of both U-Pb and Lu-Hf calibrations, while natural zircon R33 (Black et al., 2004) was only used to verify U-Pb calibrations and synthetic zircons MUN1 and MUN3 (Fisher et al., 2011) were only used to verify accuracy of Hf calibrations. The LASS-ICP-MS weighted mean $^{176}Hf/^{177}Hf$ and U-Pb ages were compared to the reported values for each reference material are shown in Figures 3.1.6.8-3.1.6.16 and summarized in Tables 3.1.6.5-3.1.6.10.

The mean LASS-MC-ICP-MS $^{176}Hf/^{177}Hf$ results of RM zircon 91500 for each analytical run (Table 3.1.6.5; Figures 3.1.6.8 and 3.1.6.9) agreed with the published $^{176}Hf/^{177}Hf$ ratio of 0.282308±6 (solution chemistry and MC-ICP-MS, 2σ; Blichert-Toft, 2008). The measured 91500 $^{176}Hf/^{177}Hf$ ratios yield a less than an 18 ppm difference from the accepted ratio, on average. However, three analytical runs yielded younger $^{206}Pb/^{238}U$ ages than the published $^{206}Pb/^{238}U$ age of 1062.4±0.8 Ma (ID-TIMS, 2σ; Wiedenbeck et al., 1995). These 91500 weighted mean $^{206}Pb/^{238}U$ dates yield 1.4% or less differences from the accepted age.

Table 3.1.6.5. Summary of LASS-ICP-MS weighted $^{206}Pb/^{238}U$ age and $^{176}Hf/^{177}Hf$ ratio results for zircon reference material 91500.

Sample run	Session	Date	$^{176}Hf/^{177}Hf$ weighted mean (2SE)	No. analyses; MSWD; $p(\chi^2)$	$^{206}Pb/^{238}U$ date weighted mean (2SE)	No. analyses; MSWD; $p(\chi^2)$	Difference from accepted age (%); $^{176}Hf/^{177}Hf$ (ppm)
18lo11-1 18lo12-7	1	Mar. 19, 2019	0.282306 ±0.000007	21/22; 1.53; 0.06	1047.3 ±2.3	22/22; 2.75; 0.00	1.4; 7
18lo12-7 18lo17-1	2	Mar. 20, 2019	0.282305 ±0.000009	12/12; 0.97; 0.47	1062.6 ±4.5	12/12; 0.77; 0.67	0.02; 11
18lo17-1 18lo20-4 18lo25-2a	3	Mar. 21, 2019	0.282313 ±0.000007	18/18; 1.48; 0.09	1050.3 ±3.8	16/18; 0.99; 0.46	1.1; 18
18lo25-2a	4	Mar. 21, 2019	0.282310 ±0.000009	12/12; 0.88; 0.56	1054.8 ±4.7	12/12; 0.58; 0.84	0.7; 7

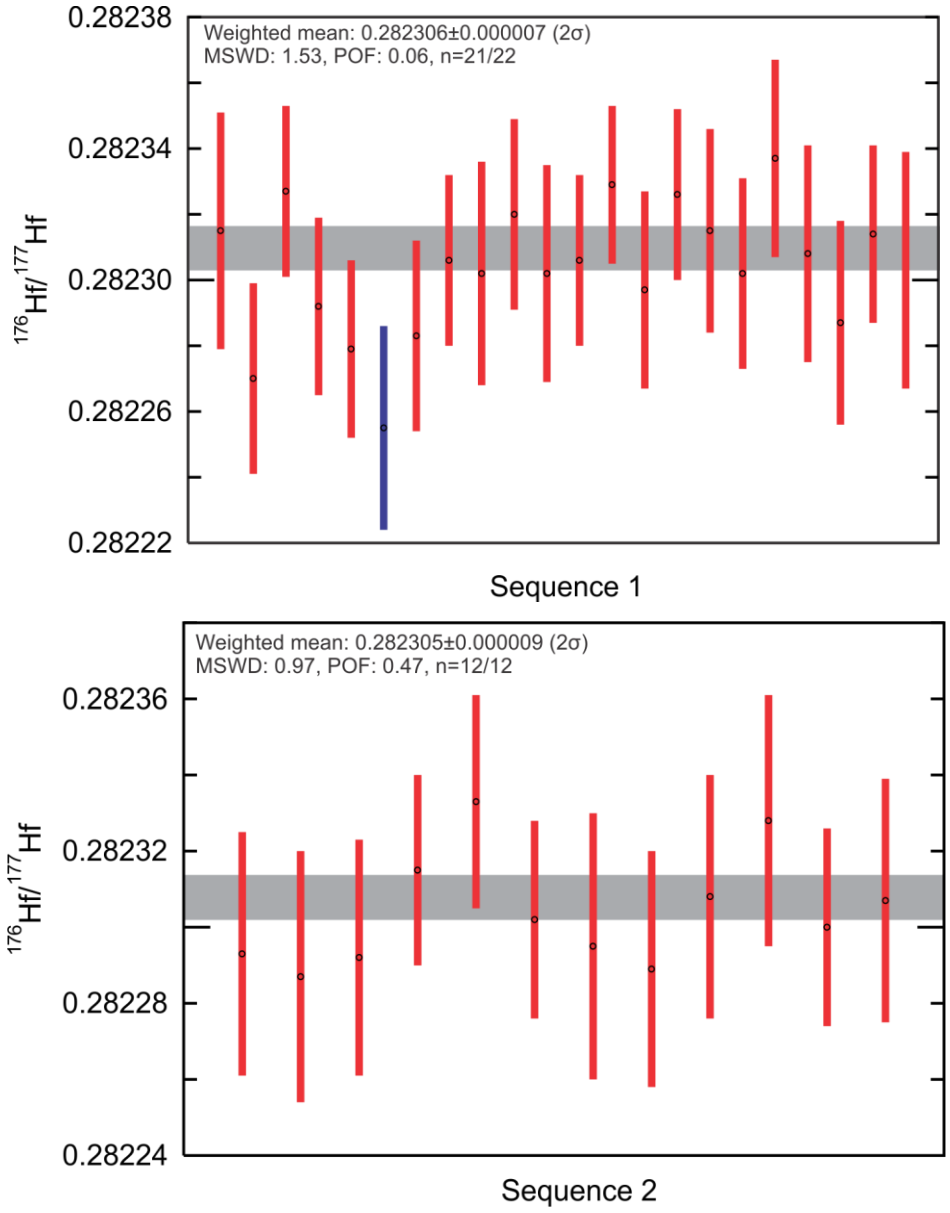

Figure 3.1.6.8. LASS-ICP-MS $^{176}Hf/^{177}Hf$ ratio results for primary calibration zircon reference material 91500. The grey line indicates the published RM value (0.282308±6; Blichert-Toft, 2008).

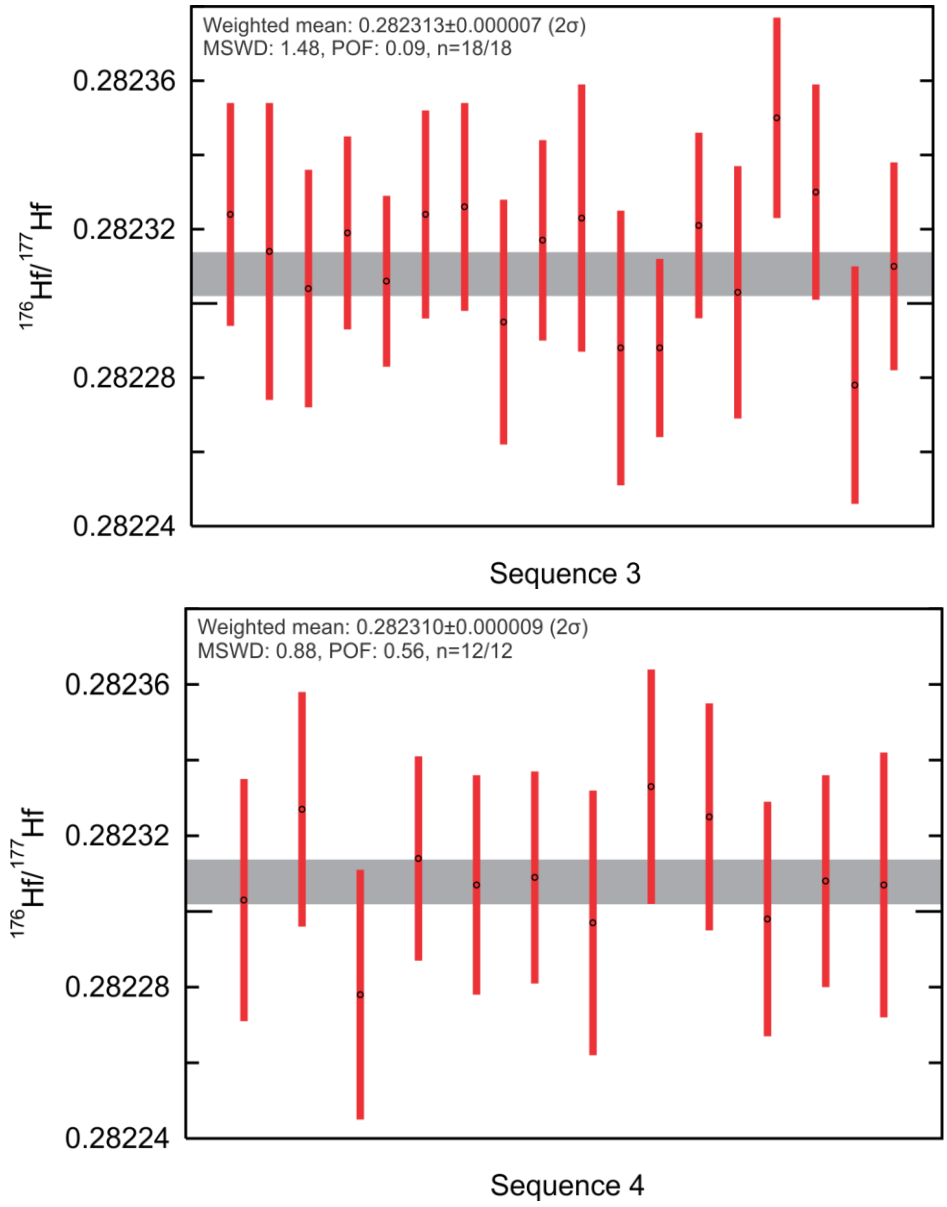

Figure 3.1.6.8 continued.

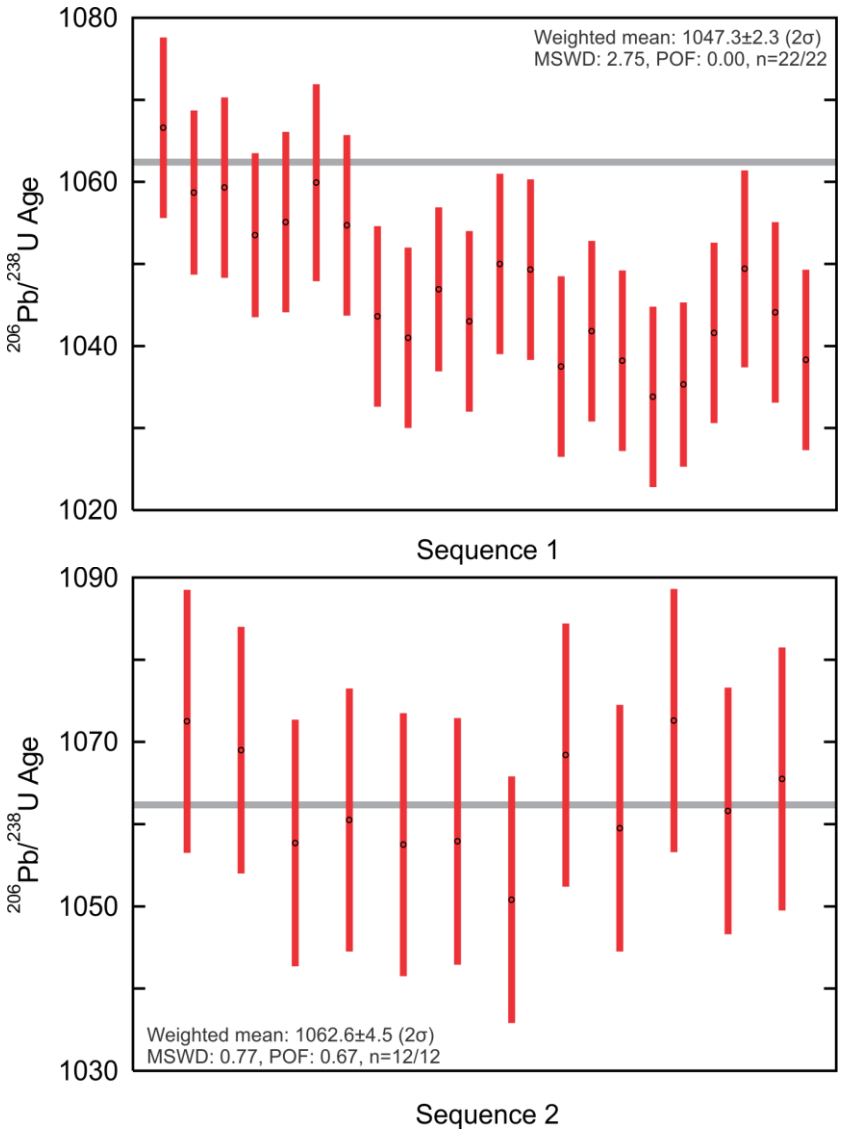

Figure 3.1.6.9. LASS-ICP-MS $^{206}Pb/^{238}U$ age results for primary calibration zircon reference material 91500. The grey line indicates the published RM age (1062.4±0.8 Ma; Wiedenbeck et al., 1995).

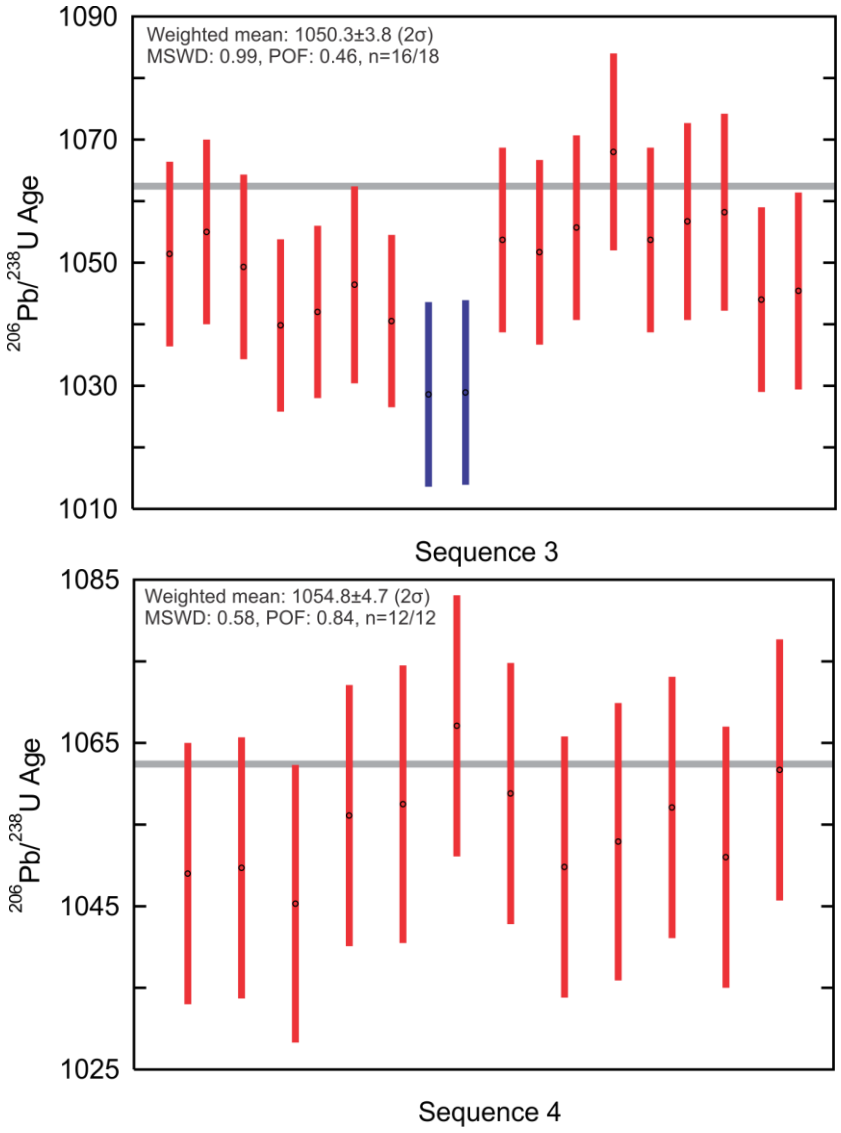

Figure 3.1.6.9 continued.

The mean LASS-MC-ICP-MS $^{176}Hf/^{177}Hf$ and $^{206}Pb/^{238}U$ results of RM Plešovice for each analytical run (Table 3.1.6.6; Figures 3.1.6.10 and 3.1.6.11) agreed with the published $^{176}Hf/^{177}Hf$ ratio of 0.282482±13 (solution and laser ablation MC-ICP-MS, 2σ) and $^{206}Pb/^{238}U$ age of 337.13±0.37 Ma (ID-TIMS, 2σ; Sláma et al., 2008). These 91500 weighted mean $^{206}Pb/^{238}U$ dates yield 1.4% or less differences from the accepted age. The measured Plešovice $^{176}Hf/^{177}Hf$ ratios yield a less than a 4 ppm difference from the accepted ratio, on average. The Plešovice weighted mean $^{206}Pb/^{238}U$ dates yield less than 1% differences from the accepted age.

Table 3.1.6.6. Summary of LASS-ICP-MS weighted $^{206}Pb/^{238}U$ age and $^{176}Hf/^{177}Hf$ ratio results for zircon reference material Plešovice.

Sample run	Session	Date	$^{176}Hf/^{177}Hf$ weighted mean (2SE)	No. analyses; MSWD; p(χ^2)	$^{206}Pb/^{238}U$ date weighted mean (2SE)	No. analyses; MSWD; p(χ^2)	Difference from accepted age (%); $^{176}Hf/^{177}Hf$ (ppm)
18lo11-1 18lo12-7	1	Mar. 19, 2019	0.282482 ±0.000006	17/17; 1.37; 0.15	337.0 ±0.9	16/16; 0.44; 0.97	0.03; 0
18lo12-7 18lo17-1	2	Mar. 20, 2019	0.282482 ±0.000005	13/13; 0.47; 0.94	338.8 ±1.6	13/13; 1.84; 0.04	0.5; 0
18lo17-1 18lo20-4 18lo25-2a	3	Mar. 21, 2019	0.282481 ±0.000004	23/24; 0.75; 0.79	337.2 ±1.1	23/23; 0.47; 0.98	0.02; 4
18lo25-2a	4	Mar. 21, 2019	0.282483 ±0.000005	17/17; 0.70; 0.80	336.1 ±1.6	15/16; 0.38; 0.98	0.3; 4

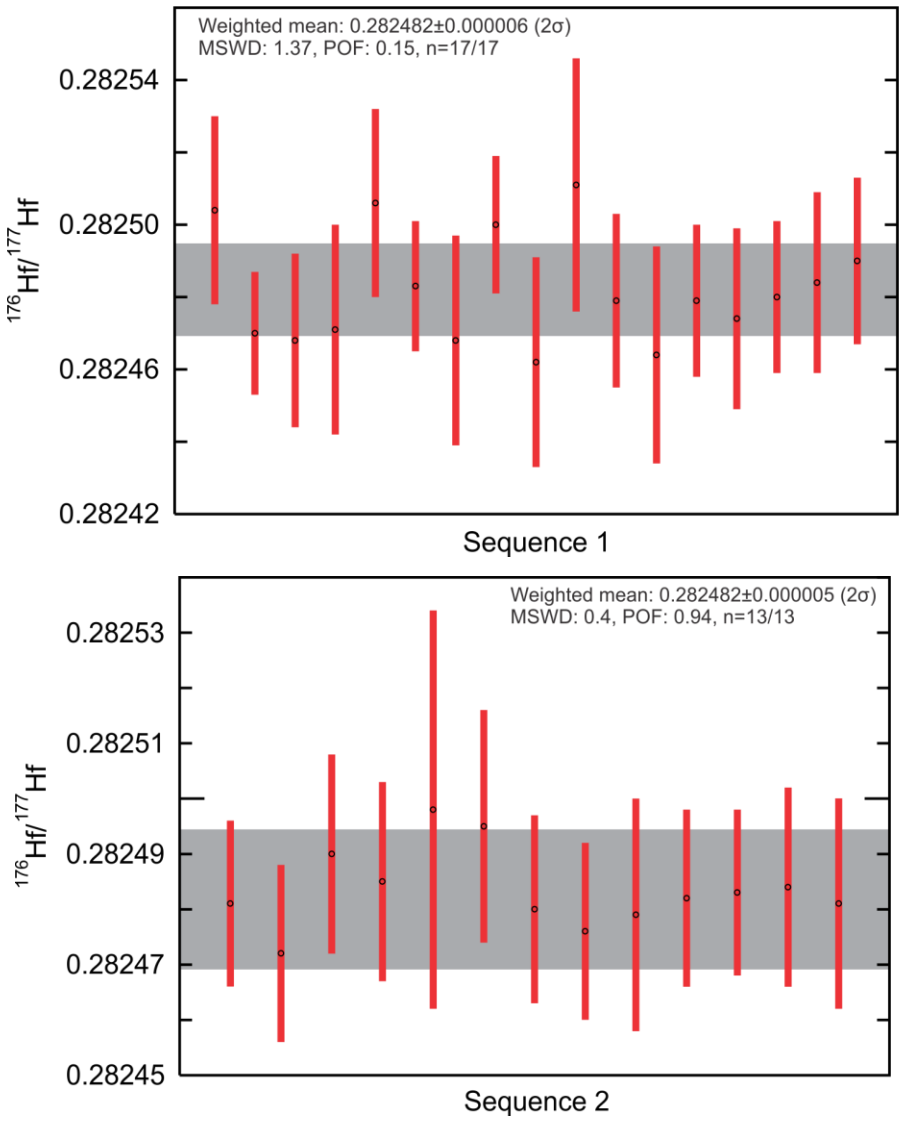

Figure 3.1.6.10. LASS-ICP-MS $^{176}Hf/^{177}Hf$ ratio results for zircon reference material Plešovice, analysed as a secondary standard. The grey line indicates the published RM value (0.282482±13; Sláma et al., 2008).

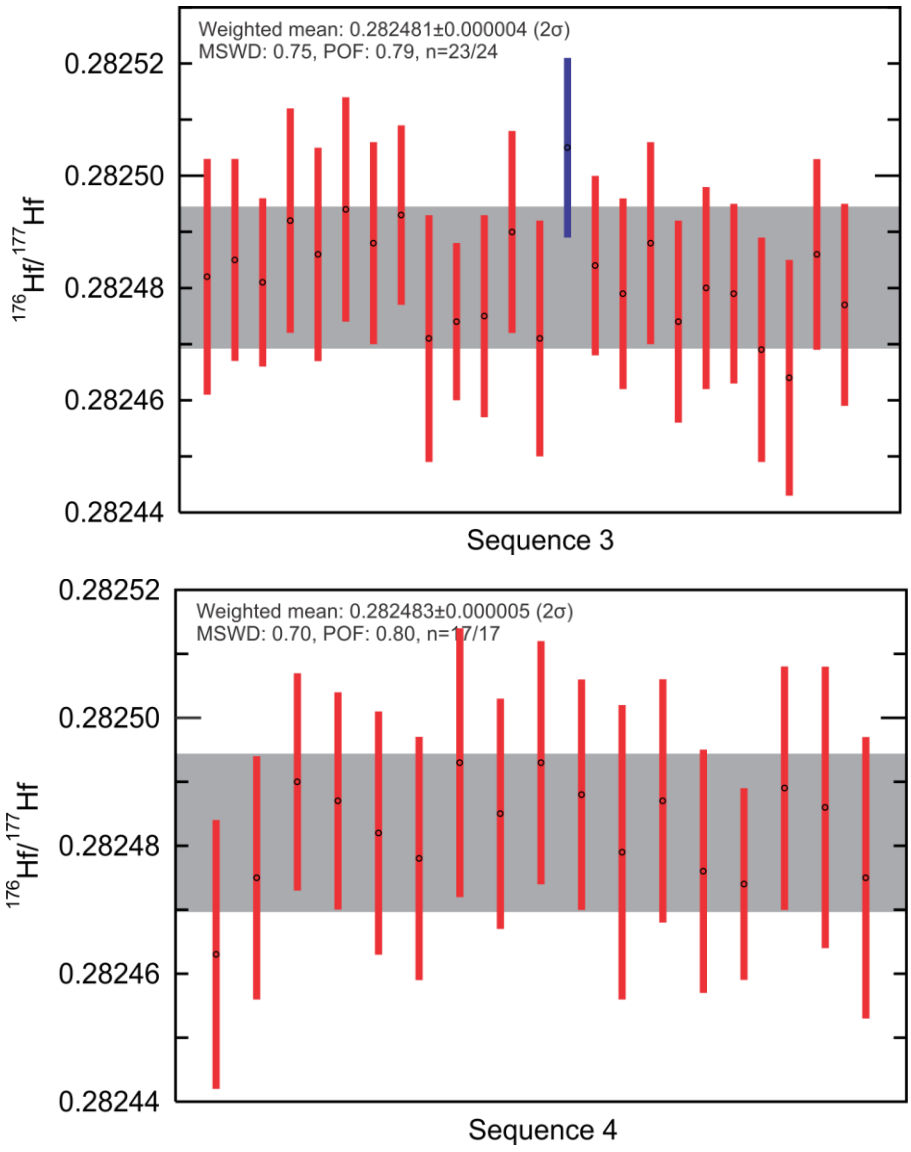

Figure 3.1.6.10 continued.

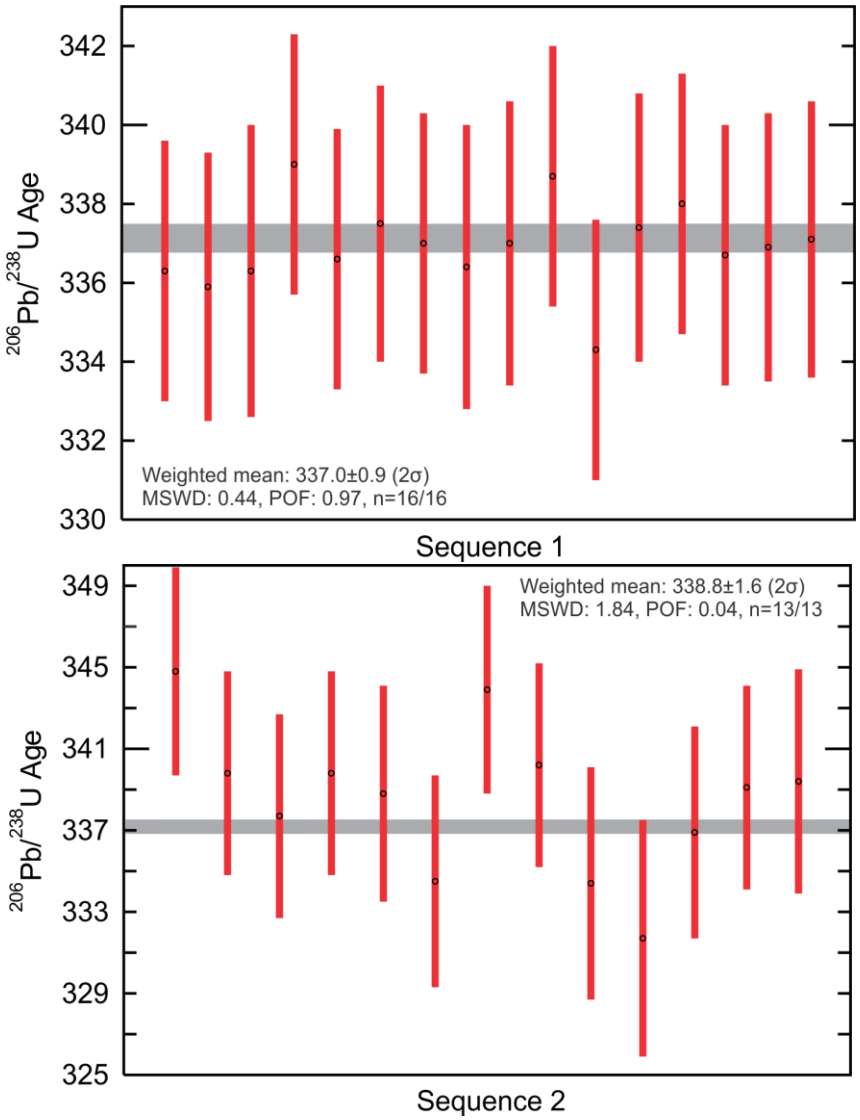

Figure 3.1.6.11. LASS-ICP-MS $^{206}Pb/^{238}U$ age results for zircon reference material Plešovice, analysed as a secondary standard. The grey line indicates the published RM age (337.13±0.37 Ma; Sláma et al., 2008).

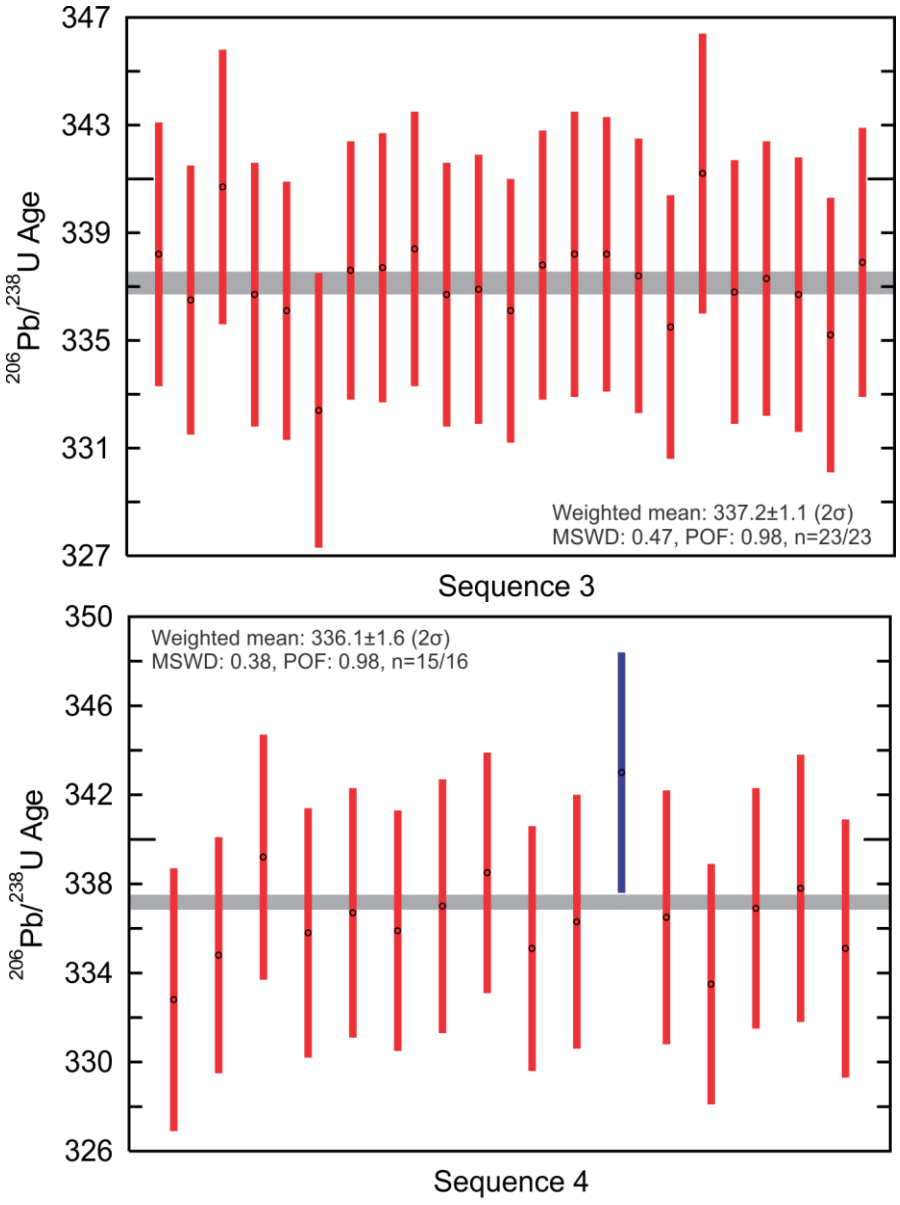

Figure 3.1.6.11 continued.

The mean LASS-MC-ICP-MS $^{176}Hf/^{177}Hf$ results of RM GJ1 for each analytical run (Table 3.1.6.7; Figure 3.1.6.12 and 3.1.6.13) agreed with the published $^{176}Hf/^{177}Hf$ ratio of 0.282013±5 (laser ablation MC-ICP-MS, 2σ; Morel et al., 2008). The measured GJ1 $^{176}Hf/^{177}Hf$ ratios yield a 39 ppm or less difference from the accepted ratio, on average. However, three analytical runs yielded younger $^{206}Pb/^{238}U$ ages than the published $^{207}Pb/^{206}U$ age of 608.5±0.4 Ma (TIMS, 2σ; Jackson et al., 2004). The GJ1 weighted mean $^{206}Pb/^{238}U$ dates yield 1.7 to 2.4% differences from the accepted age.

Table 3.1.6.7. Summary of LASS-ICP-MS weighted $^{206}Pb/^{238}U$ age and $^{176}Hf/^{177}Hf$ ratio results for zircon reference material GJ1.

Sample run	Session	Date	$^{176}Hf/^{177}Hf$ weighted mean (2SE)	No. analyses; MSWD; p(χ^2)	$^{206}Pb/^{238}U$ date weighted mean (2SE)	No. analyses; MSWD; p(χ^2)	Difference from accepted age (%); $^{176}Hf/^{177}Hf$ (ppm)
18lo11-1 18lo12-7	1	Mar. 19, 2019	0.282021 ±0.000008	10/10; 0.44; 0.92	594.8 ±1.9	10/10; 2.84; 0.00	2.3; 28
18lo12-7 18lo17-1	2	Mar. 20, 2019	0.282024 ±0.000011	5/5; 0.87; 0.48	597.9 ±4.1	5/5; 0.46; 0.77	1.7; 39
18lo17-1 18lo20-4 18lo25-2a	3	Mar. 21, 2019	0.282020 ±0.000008	8/8; 1.06; 0.39	594.2 ±3.2	8/8; 3.02; 0.004	2.4; 25
18lo25-2a	4	Mar. 21, 2019	N/A	N/A	N/A	N/A	

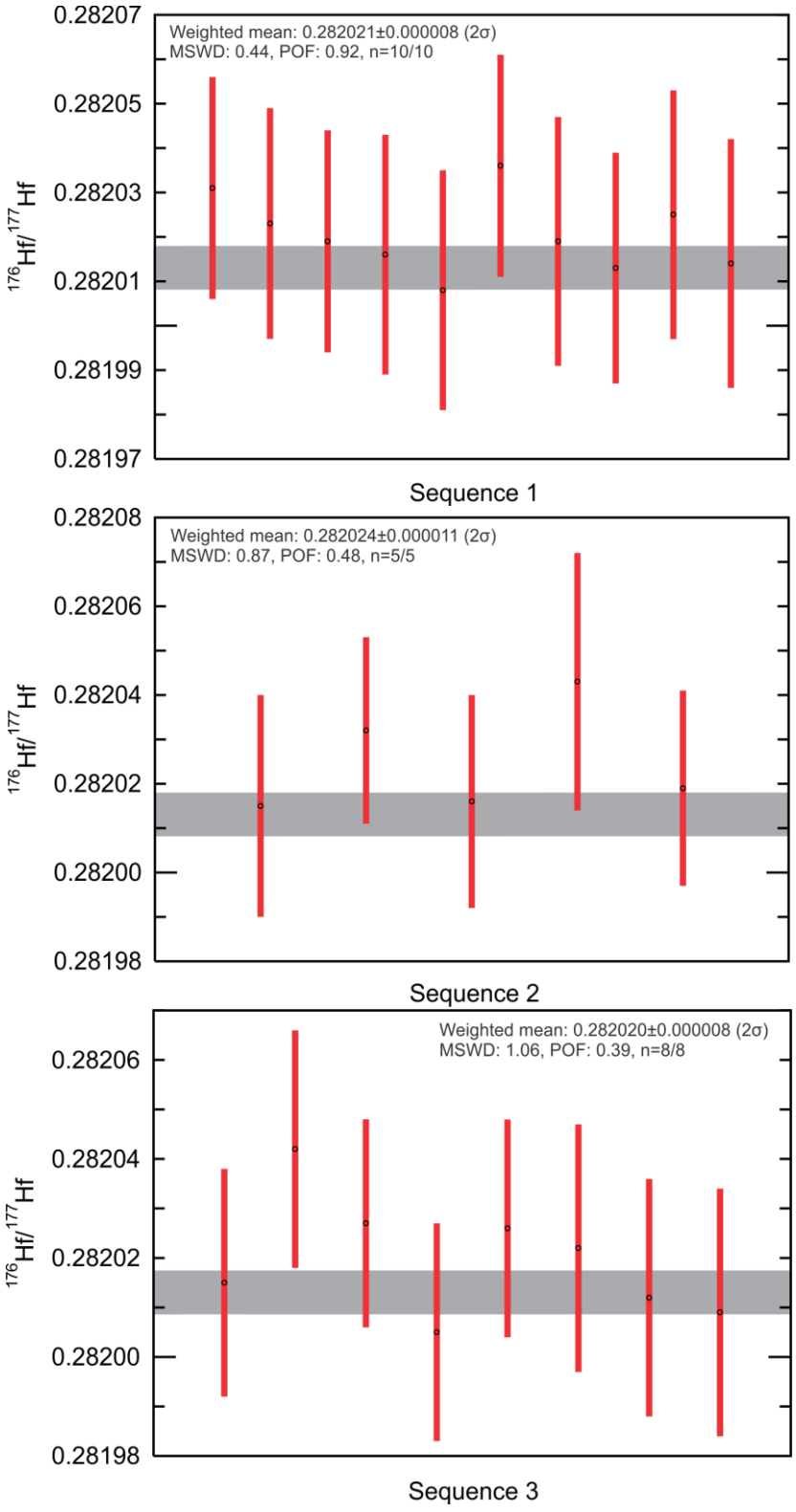

Figure 3.1.6.12. LASS-ICP-MS $^{176}Hf/^{177}Hf$ ratio results for zircon reference material GJ1, analysed as a secondary standard. The grey line indicates the published RM value (0.282013±5; Morel et al., 2008).

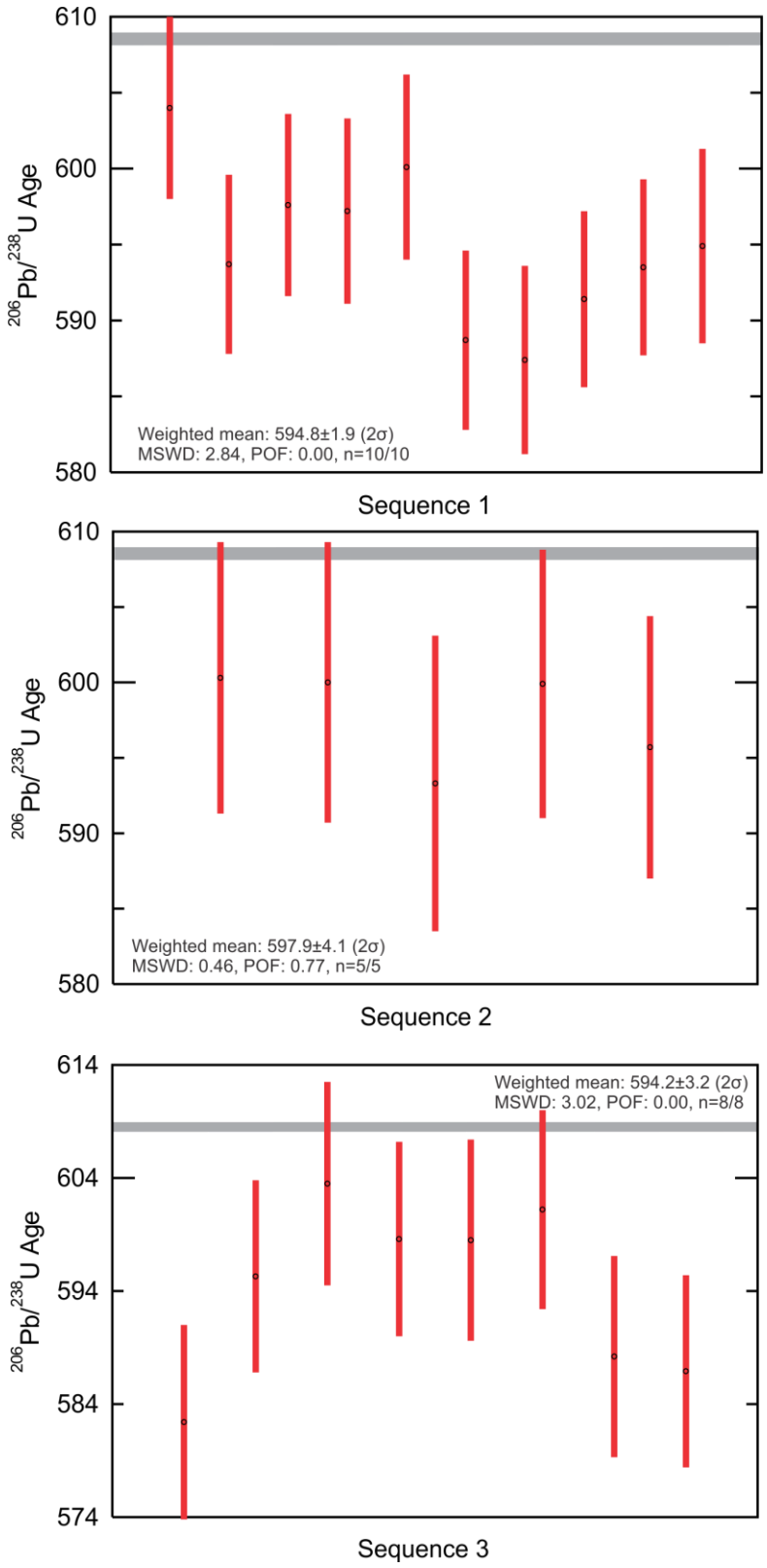

Figure 3.1.6.13. LASS-ICP-MS $^{206}Pb/^{238}U$ age results for zircon reference material GJ1, analysed as a secondary standard. The grey line indicates the published RM age (608.5±0.4 Ma; Jackson et al., 2004).

The mean LASS-MC-ICP-MS $^{206}Pb/^{238}U$ results of RM R33 for two analytical runs (Table 3.1.6.8; Figure 3.1.6.14) agreed with the published $^{206}Pb/^{238}U$ age of 418.9±0.4 Ma (ID-TIMS, 2σ; Black et al., 2004). One analytical run yielded a slightly younger weighted mean $^{206}Pb/^{238}U$ age result than the published age. The R33 weighted mean $^{206}Pb/^{238}U$ dates less than 1% differences from the accepted age.

Table 3.1.6.8. Summary of LASS-ICP-MS weighted $^{206}Pb/^{238}U$ age results for zircon reference material R33.

Sample run	Session	Date	$^{206}Pb/^{238}U$ date weighted mean (2SE)	No. analyses; MSWD; p(χ^2)	Difference from accepted age (%)
18lo11-1 18lo12-7	1	Mar. 19, 2019	419.3 ±1.8	7/10; 2.27; 0.03	0.1
18lo12-7 18lo17-1	2	Mar. 20, 2019	414.7 ±3.4	4/6; 4.52; 0.00	1.0
18lo17-1 18lo20-4 18lo25-2a	3	Mar. 21, 2019	417.9 ±3.3	4/4; 1.75; 0.15	0.2
18lo25-2a	4	Mar. 21, 2019	N/A	N/A	

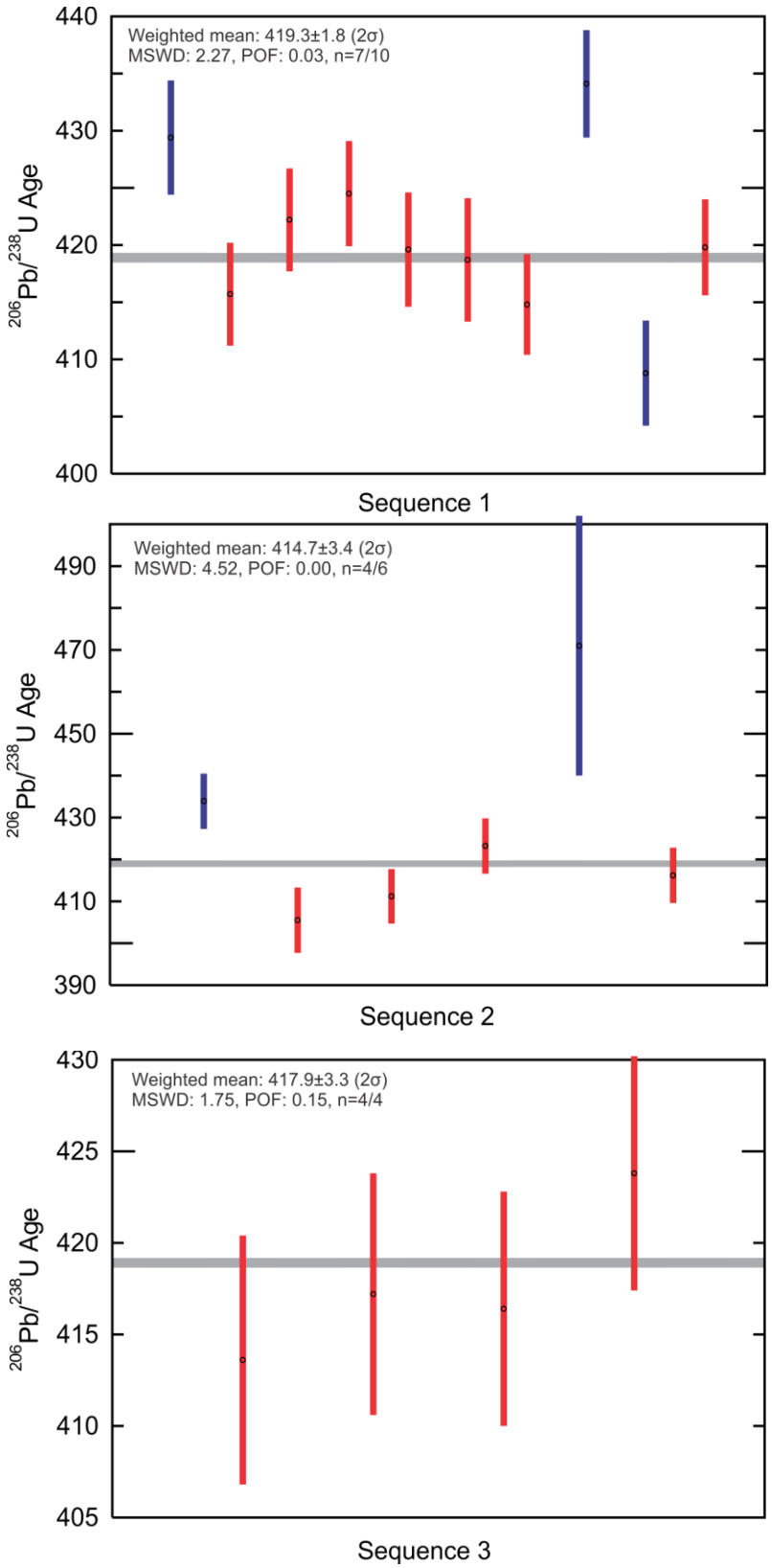

Figure 3.1.6.14. LASS-ICP-MS $^{206}Pb/^{238}U$ age results for zircon reference material R33, analysed as a secondary standard. The grey line indicates the published RM age (418.9±0.4 Ma; Black et al., 2004).

The mean LASS-MC-ICP-MS $^{176}Hf/^{177}Hf$ results of RMs MUN1 and MUN3 for each analytical run (Tables 3.1.6.9 and 3.1.6.10; Figures 3.1.6.15 and 3.1.6.16) agreed with the published $^{176}Hf/^{177}Hf$ ratio of 0.282135±7 (solution chemistry, 2σ; Fisher et al., 2011). The measured MUN1 and MUN3 $^{176}Hf/^{177}Hf$ ratios yield a 43 ppm or less difference from the accepted ratio, on average.

Table 3.1.6.9. Summary of LASS-ICP-MS weighted $^{176}Hf/^{177}Hf$ ratio results for synthetic zircon reference material MUN1.

Sample run	Session	Date	$^{176}Hf/^{177}Hf$ weighted mean (2SE)	No. analyses; MSWD; p(χ^2)	Difference from accepted $^{176}Hf/^{177}Hf$ (ppm)
18lo11-1 18lo12-7	1	Mar. 19, 2019	0.282137 ±0.000009	10/10; 1.40; 0.18	7
18lo12-7 18lo17-1	2	Mar. 20, 2019	0.282136 ±0.000010	6/6; 1.31; 0.26	4
18lo17-1 18lo20-4 18lo25-2a	3	Mar. 21, 2019	0.282123 ±0.000008	10/12; 1.54; 0.13	43
18lo25-2a	4	Mar. 21, 2019	0.282136 ±0.000012	3/3; 2.42; 0.09	4

Table 3.1.6.10. Summary of LASS-ICP-MS weighted $^{176}Hf/^{177}Hf$ ratio results for synthetic zircon reference material MUN3.

Sample run	Session	Date	$^{176}Hf/^{177}Hf$ weighted mean (2SE)	No. analyses; MSWD; p(χ^2)	Difference from accepted $^{176}Hf/^{177}Hf$ (ppm)
18lo11-1 18lo12-7	1	Mar. 19, 2019	0.282123 ±0.000009	8/9; 0.57; 0.78	43
18lo12-7 18lo17-1	2	Mar. 20, 2019	0.282125 ±0.000010	6/6; 1.36; 0.23	35
18lo17-1 18lo20-4 18lo25-2a	3	Mar. 21, 2019	0.282127 ±0.000009	8/8; 0.93; 0.48	28
18lo25-2a	4	Mar. 21, 2019	0.282123 ±0.000014	3/3; 0.45; 0.64	43

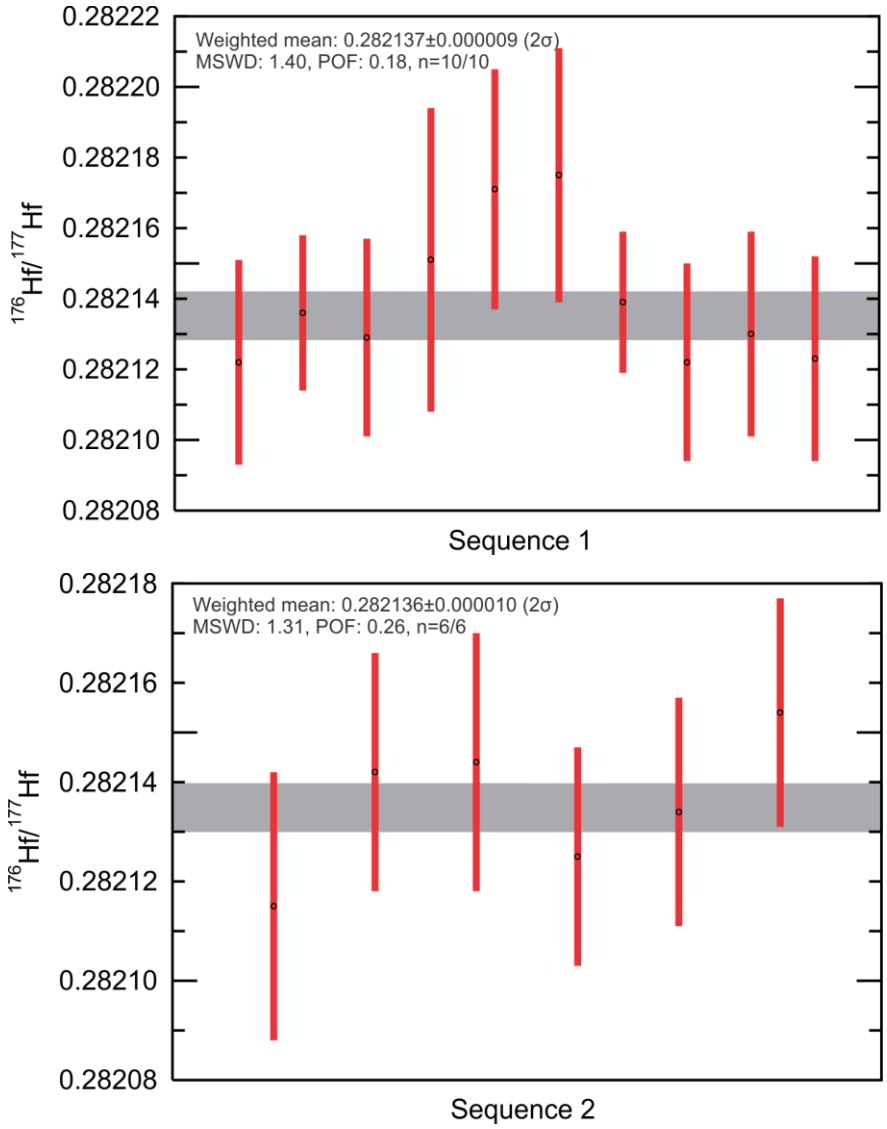

Figure 3.1.6.15. LASS-ICP-MS $^{176}Hf/^{177}Hf$ ratio results for zircon reference material MUN1, analysed as a secondary standard. The grey line indicates the published RM value (0.282135±7; Fisher et al., 2011).

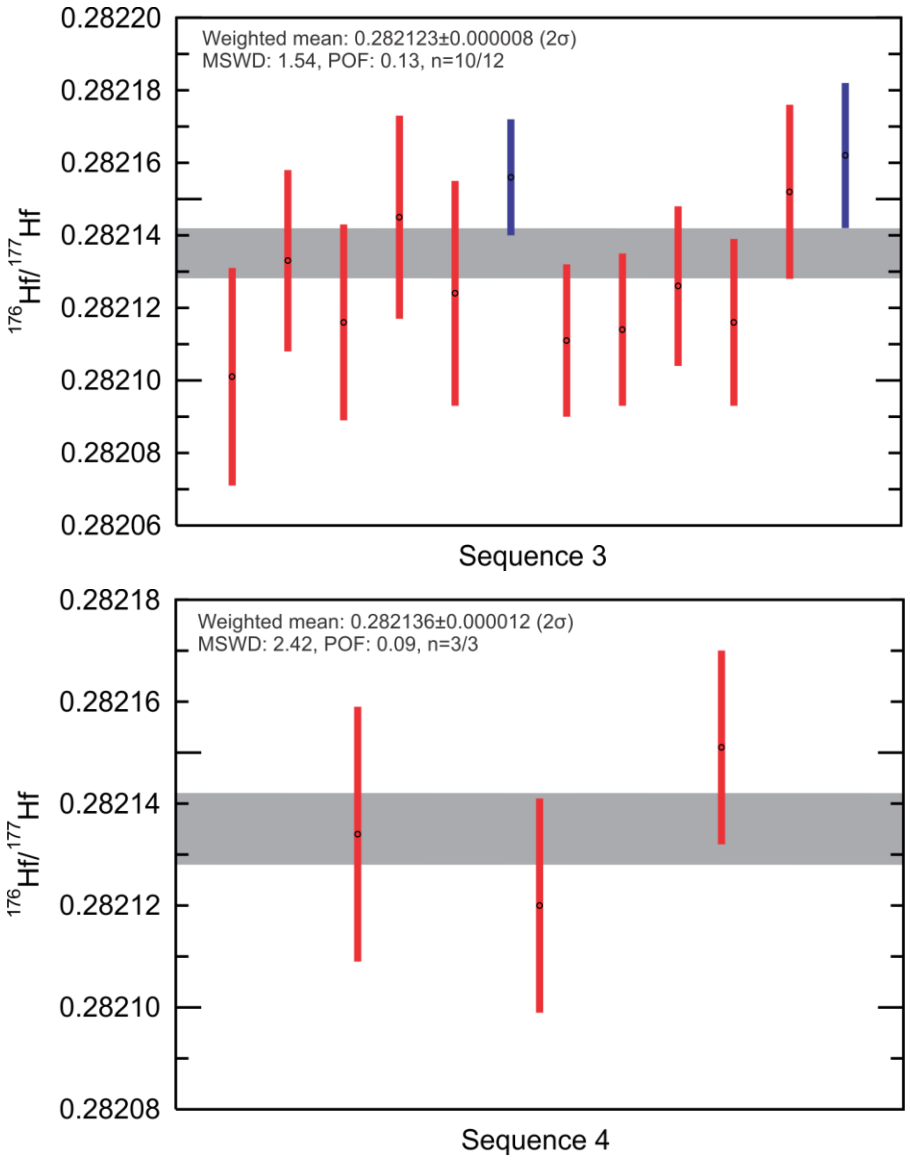

Figure 3.1.6.15 continued.

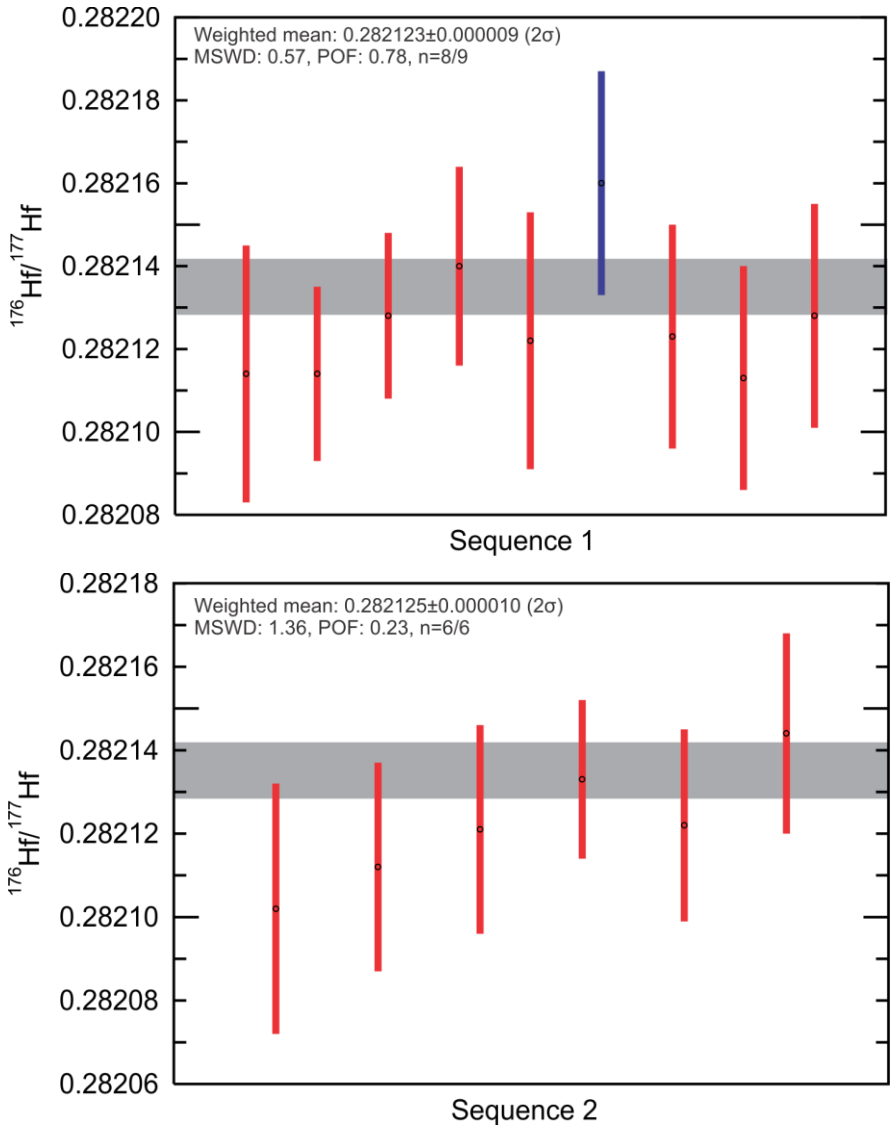

Figure 3.1.6.16. LASS-ICP-MS $^{176}Hf/^{177}Hf$ ratio results for zircon reference material MUN3, analysed as a secondary standard. The grey line indicates the published RM value (0.282135±7; Fisher et al., 2011).

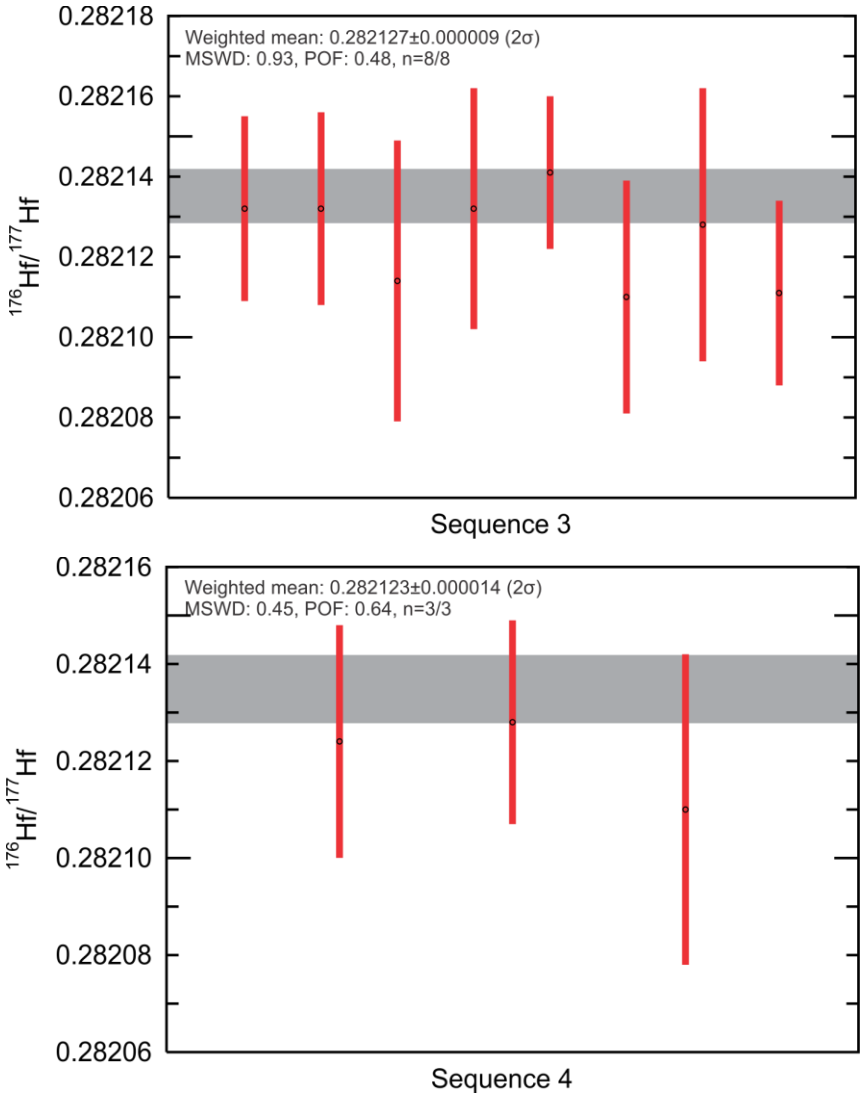

Figure 3.1.6.16 continued.

Zircon Lu-Hf and TE

Lutetium-Hafnium isotopes and trace elements in a subset of zircon grains were simultaneously measured using the laser ablation split-stream (LASS)-ICP-MS method (Yuan et al., 2004; Fisher et al., 2011, 2014, 2017). Concurrent Lu-Hf and TE measurements were obtained at the University of Alberta Arctic Resources Laboratory, using the same laser and ICP-MS configurations as described in Lu-Hf and TE single stream LA-ICP-MS methods (section 3.1.4 and 3.1.5). Analytical points were determined from CL and BSE images as described in section 3.1.2, and split stream spots were positioned on top of shallow SIMS analysis pits. The zircon samples were ablated using a RESOlution 193 nm ArF excimer laser using a 33 or 40 μm diameter laser spot size and settings of 60 s of ablation, 60 s of background and washout, 8 Hz repetition rate, 120 mJ laser energy, 44%T attenuator value, and ca. 6.0 J/cm^2.

Data were processed and reduced offline using the Iolite version 3 software package in multiple DRS mode (Paton et al., 2010, 2011), using the same Lu-Hf DRS as described in section 3.1.4 with the trace element DRS "X_Trace Elements_IS". The same data correction as utilized for the single stream Lu-Hf measurements (section 3.1.4) were applied to the split-stream measurements.

Lutetium-Hafnium isotopes and trace elements of standard reference materials were determined throughout two analytical sessions. Seven zircon reference materials were analyzed after every eight to twelve unknown analyses. The natural zircon Plešovice (Sláma et al., 2008), was used as the primary calibration reference material for Lu-Hf isotopes to monitor analytical reproducibility, Hf fractionation, and instrument drift during each analytical run. The natural zircon 91500 (Wiedenbeck et al., 1995, 2004; Blichert-Toft, 2008), and synthetic zircons MUN1 and MUN3 (Fisher et al., 2011) were used to verify accuracy of Hf calibrations. Glass standard reference material (SRM) NIST 612 was used as the primary calibration standard. NIST SRM 614 and zircon 91500 were used as secondary verification standards to monitor accuracy, instrumental drift, and matrix effects. The stoichiometric ^{29}Si content in zircon (15.32 wt.%) was used as an internal standard.

The LASS-ICP-MS weighted mean ^{176}Hf/^{177}Hf were compared to the reported values for each reference material are shown in Figures 3.1.6.17-3.1.6.20 and summarized in Tables 3.1.6.11-3.1.6.14. The mean LA-MC-ICP-MS ^{176}Hf/^{177}Hf results of Plešovice for each analytical

run (Table 3.1.6.11; Figure 3.1.6.17) agreed with published LA-ICP-MS and solution $^{176}Hf/^{177}Hf$ results (0.282482±13 (2σ); Sláma et al., 2008).

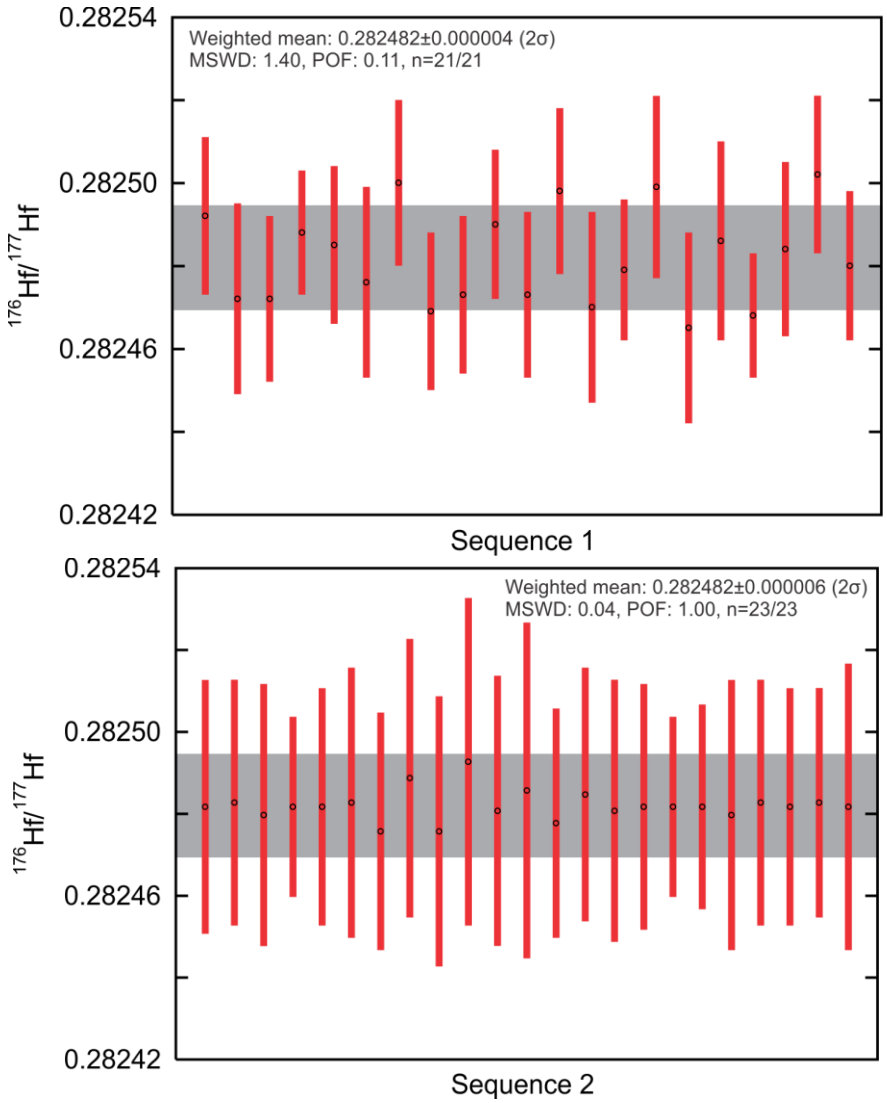

Figure 3.1.6.17. LASS-ICP-MS $^{176}Hf/^{177}Hf$ ratio result for primary calibration zircon reference material Plešovice. The grey line indicates the published RM value (0.282482±13; Sláma et al., 2008).

Table 3.1.6.11. Summary of LA-ICP-MS weighted $^{176}Hf/^{177}Hf$ ratio results for zircon reference material Plešovice.

Sample run	Session	Date	$^{176}Hf/^{177}Hf$ weighted mean (2SE)	No. analyses; MSWD; p(χ^2)	Difference from accepted $^{176}Hf/^{177}Hf$ (ppm)
18lo22-1d	1	May 4, 2021	0.282482±0.000004	21/21; 1.40; 0.11	0
19GJ12-3 19GJ16-2	2	May 5, 2021	0.282482±0.000006	23/23; 0.04; 1.00	0

The mean LASS-MC-ICP-MS $^{176}Hf/^{177}Hf$ results of RM zircon 91500 for each analytical run (Table 3.1.6.12; Figure 3.1.6.18) agreed with the published $^{176}Hf/^{177}Hf$ ratio of 0.282308±6 (solution chemistry and MC-ICP-MS, 2σ; Blichert-Toft, 2008). The measured 91500 $^{176}Hf/^{177}Hf$ ratios yield a less than 32 ppm difference from the accepted ratio, on average.

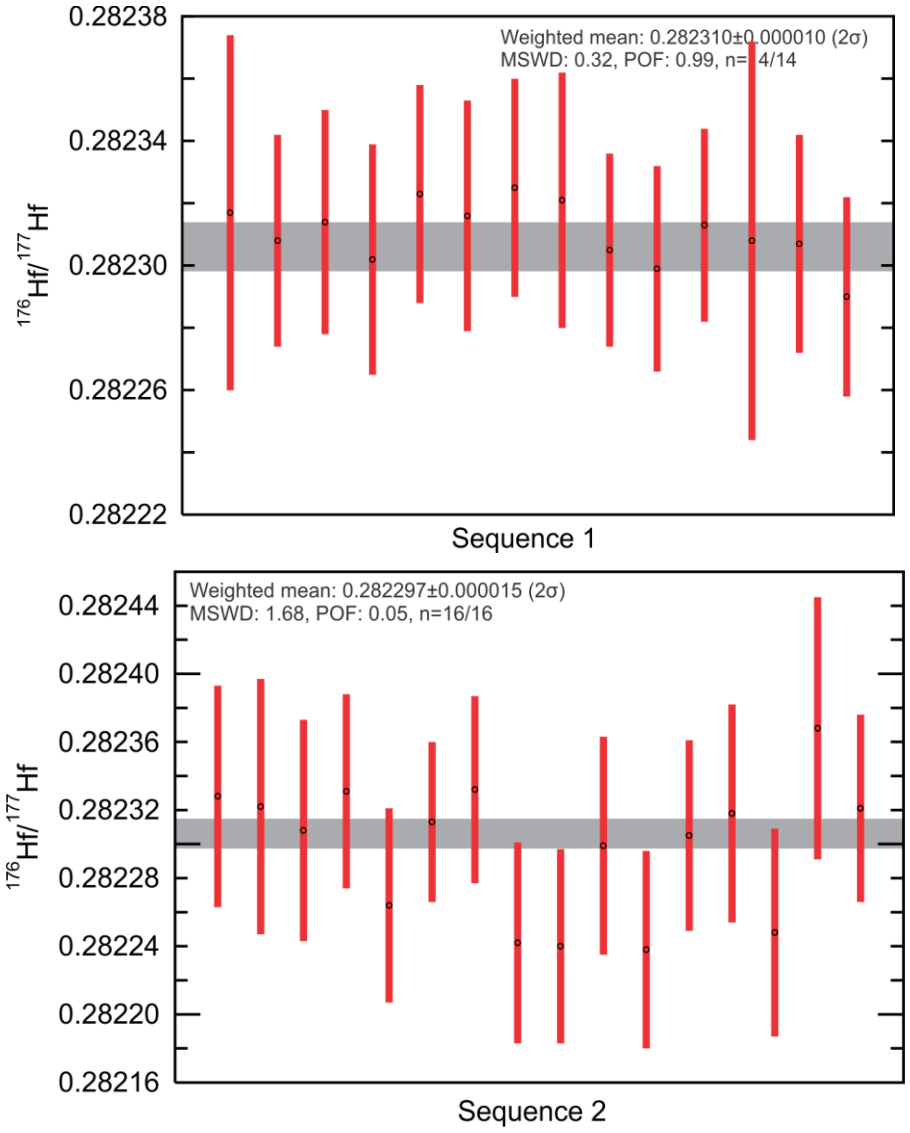

Figure 3.1.6.18. LASS-ICP-MS $^{176}Hf/^{177}Hf$ ratio results for zircon reference material 91500, analysed as a secondary standard. The grey line indicates the published RM value (0.282308±6; Blichert-Toft, 2008).

Table 3.1.6.12. Summary of LA-ICP-MS weighted $^{176}Hf/^{177}Hf$ ratio results for zircon reference material 91500.

Sample run	Session	Date	$^{176}Hf/^{177}Hf$ weighted mean (2SE)	No. analyses; MSWD; p(χ^2)	Difference from accepted $^{176}Hf/^{177}Hf$ (ppm)
18lo22-1d	1	May 4, 2021	0.282310 ±0.000010	14/14; 0.32; 0.99	14
19GJ12-3 19GJ16-2	2	May 5, 2021	0.282297 ±0.000015	16/16; 1.68; 0.05	32

The mean LA-MC-ICP-MS $^{176}Hf/^{177}Hf$ results of synthetic zircons MUN1 and MUN3 for each analytical run (Tables 3.1.6.13 and 3.1.6.14; Figures 3.1.6.19 and 3.1.6.20) agreed with published solution $^{176}Hf/^{177}Hf$ results (0.282135±7 (2σ); Fisher et al., 2011). The measured MUN1 and MUN3 $^{176}Hf/^{177}Hf$ ratios yielded less than an 89 ppm difference from the accepted ratio, on average.

Table 3.1.6.13. Summary of LA-ICP-MS weighted $^{176}Hf/^{177}Hf$ ratio results for synthetic zircon reference material MUN1.

Sample run	Session	Date	$^{176}Hf/^{177}Hf$ weighted mean (2SE)	No. analyses; MSWD; p(χ^2)	Difference from accepted $^{176}Hf/^{177}Hf$ (ppm)
18lo22-1d	1	May 4, 2021	0.282134 ±0.000009	7/7; 0.37; 0.9	4
19GJ12-3 19GJ16-2	2	May 5, 2021	0.282116 ±0.000018	8/8; 1.83; 0.08	67

Table 3.1.6.14. Summary of LA-ICP-MS weighted $^{176}Hf/^{177}Hf$ ratio results for synthetic zircon reference material MUN3.

Sample run	Session	Date	$^{176}Hf/^{177}Hf$ weighted mean (2SE)	No. analyses; MSWD; p(χ^2)	Difference from accepted $^{176}Hf/^{177}Hf$ (ppm)
18lo22-1d	1	May 4, 2021	0.282110 ±0.000015	7/7; 2.01; 0.06	89
19GJ12-3 19GJ16-2	2	May 5, 2021	0.282119 ±0.000016	8/8; 2.06; 0.05	57

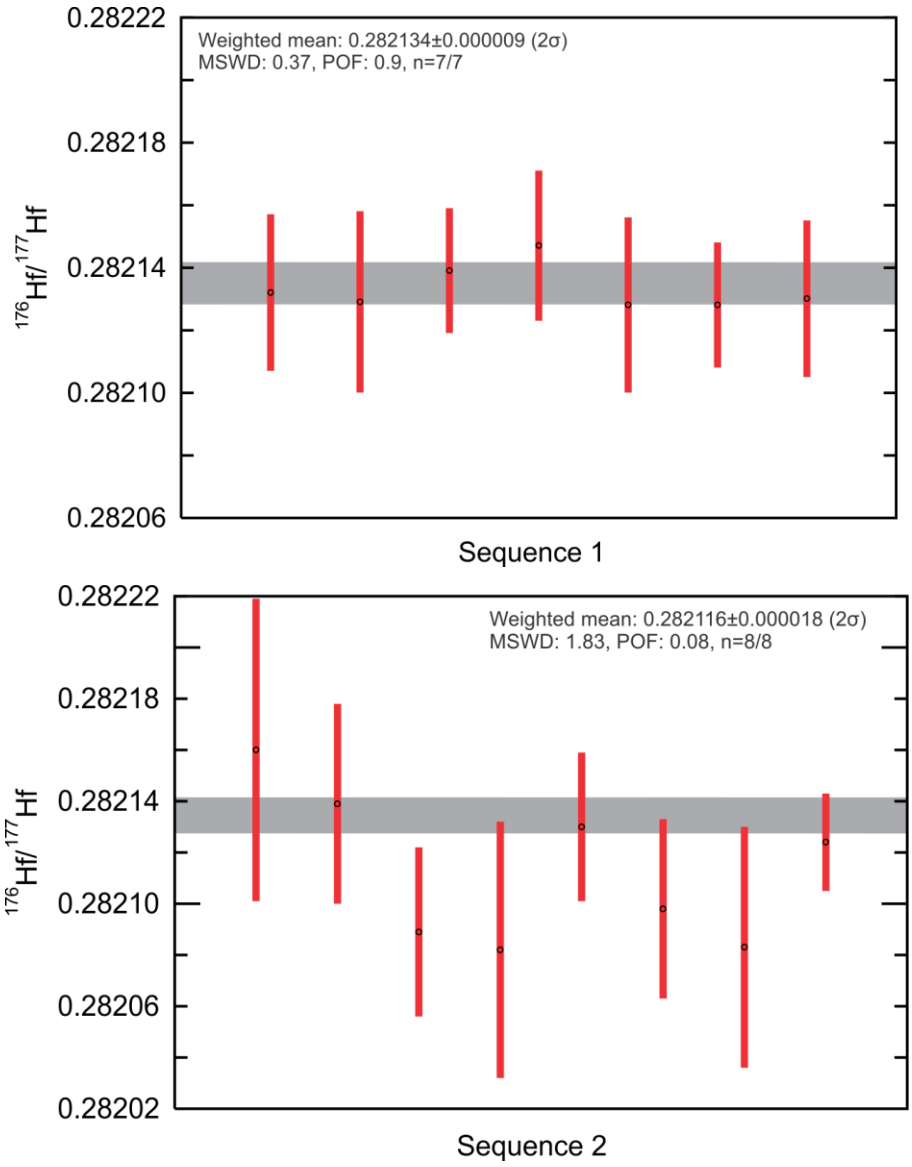

Figure 3.1.6.19. LASS-ICP-MS $^{176}Hf/^{177}Hf$ ratio results for synthetic zircon reference material MUN1, analysed as a secondary standard. The grey line indicates the published RM value (0.282135±7; Fisher et al., 2011).

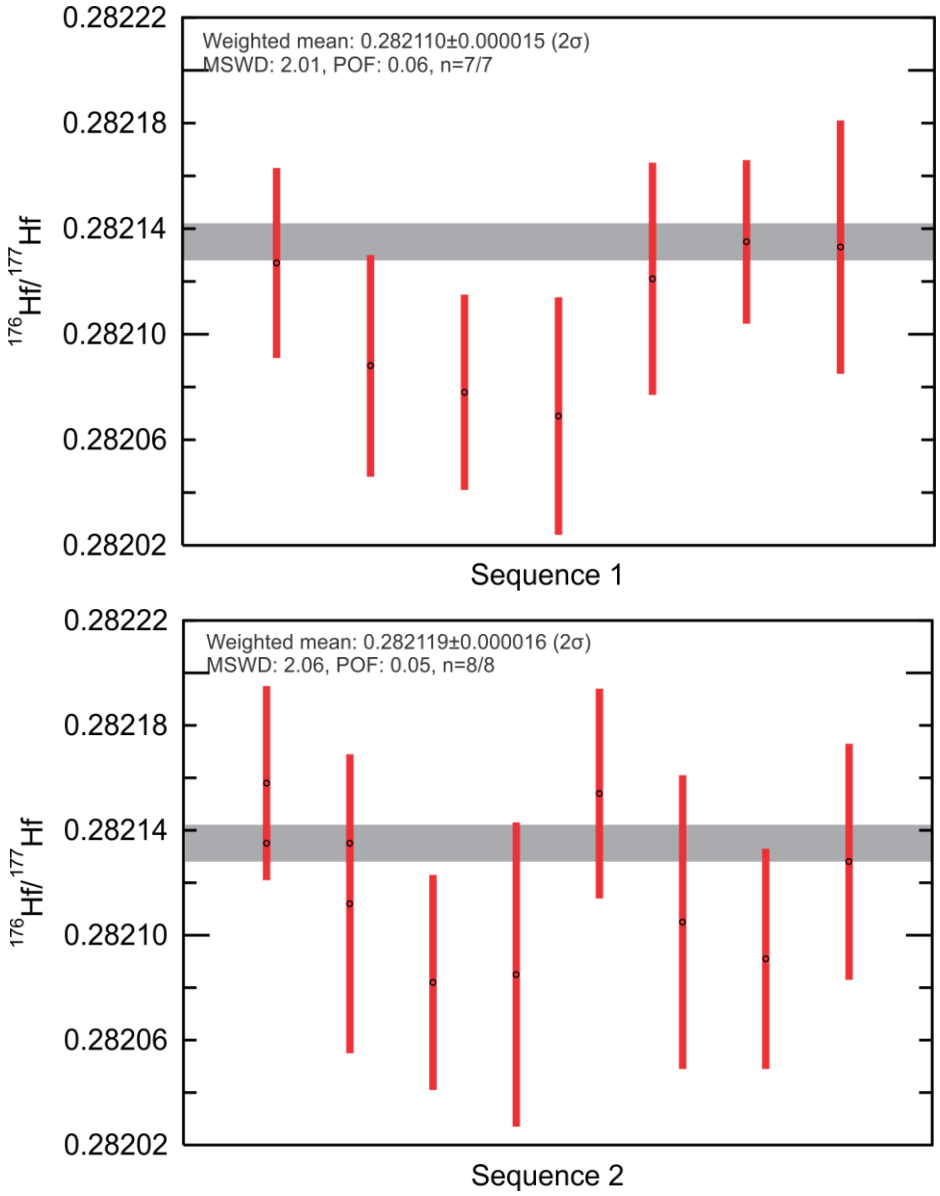

Figure 3.1.6.20. LASS-ICP-MS $^{176}Hf/^{177}Hf$ ratio results for synthetic zircon reference material MUN3, analysed as a secondary standard. The grey line indicates the published RM value (0.282135±7; Fisher et al., 2011).

Table 3.1.6.15 summarizes the average concentration, uncertainty, LOD, and LOQ results for the three trace element RMs, compared to accepted values. The NIST 612, NIST 614, and zircon 91500 reference values are from preferred GeoReM values (GeoReM 5211, Jochum et al., 2011; GeoReM 104, Wiedenbeck et al., 2004).

The trace element concentrations of NIST 612 from this study are within the 2 standard errors of GeoReM 5211 reported values (Figure 3.1.6.21; Jochum et al., 2011).

Table 3.1.6.15. Average trace element concentration, uncertainty, LOD, and LOQ for glass reference materials (RM) NIST612, 614 and zircon RM 91500.

Reference Material	Session	Element	^{31}P	^{43}Ca	^{45}Sc	^{49}Ti	^{55}Mn	^{57}Fe	^{89}Y	^{93}Nb
NIST612	1	Average concentration (ppm)	46.6	85035.7	39.9	44.0	38.7	51.2	38.3	38.9
		Uncertainty (2SE)	0.3	321.3	0.2	0.3	0.2	0.9	0.2	0.1
		Average LOD	1.1	127.3	0.2	0.4	1.6	4.6	0.0	0.02
		Average LOQ	3.2	381.9	0.6	1.2	4.7	13.8	0.1	0.05
	2	Average concentration (ppm)	46.6	85056.3	39.9	44.0	38.8	50.8	38.3	38.9
		Uncertainty (2SE)	0.4	411.5	0.2	0.4	0.4	1.4	0.2	0.2
		Average LOD	2.0	196.3	0.4	0.7	3.0	8.7	0.1	0.03
		Average LOQ	5.9	588.8	1.2	2.2	9.1	26.1	0.3	0.09
		Reference Value	46.6	85049	39.9	44.0	38.7	51	38.3	38.9
		Uncertainty	6.9		2.5	2.3	0.9	2	1.4	2.1
NIST614	1	Average concentration (ppm)	41.0	85131.4	BelowLOQ	3.2	BelowLOQ	BelowLOQ	0.79	0.80
		Uncertainty (2SE)	0.4	448.8	0.0	0.1	0.3	1.0	0.02	0.02
		Average LOD	1.1	98.9	0.4	0.5	1.4	5.1	0.04	0.08
		Average LOQ	3.2	296.6	1.2	1.6	4.2	15.4	0.13	0.25
	2	Average concentration (ppm)	40.7	84562.5	BelowLOQ	3.1	BelowLOD	BelowLOQ	0.78	0.79
		Uncertainty (2SE)	0.5	573.9	0.1	0.2	0.5	1.8	0.02	0.02
		Average LOD	1.9	191.3	0.4	0.7	2.9	8.7	0.09	0.03
		Average LOQ	5.7	573.8	1.2	2.1	8.6	26.1	0.26	0.09
		Reference Value	11.4	85061	0.74	3.61	1.42	18.8	0.790	0.824
		Uncertainty	3.9			0.25	0.07	6.0	0.032	0.030
91500	1	Average concentration (ppm)	29.7	BelowLOD	599.4	4.6	BelowLOQ	BelowLOD	122.0	BelowLOD
		Uncertainty (2SE)	0.2	12.5	3.7	0.1	0.19	0.6	0.7	0.01
		Average LOD	0.9	92.6	0.3	0.4	1.3	6.9	0.04	2.66
		Average LOQ	2.7	277.7	0.8	1.1	3.9	20.6	0.11	7.97
	2	Average concentration (ppm)	30.6	BelowLOD	593.6	4.5	BelowLOQ	BelowLOD	116.5	BelowLOD
		Uncertainty (2SE)	0.3	22.3	4.7	0.1	0.34	1.0	0.9	0.00
		Average LOD	1.8	157.3	0.3	0.6	2.4	7.0	0.07	0.02
		Average LOQ	5.3	472.0	1.0	1.9	7.1	20.9	0.22	0.07
		Reference Value	24	1.9	1.17	6	0.19	3.4	140	0.79
		Uncertainty	2	1.2	0.12	2	0.10	0.4	28	0.14

Table 3.1.6.15. continued.

Reference Material	Session	Element	^{137}Ba	^{139}La	^{140}Ce	^{141}Pr	^{146}Nd	^{147}Sm	^{153}Eu
NIST612	1	Average concentration (ppm)	39.3	36.0	38.4	37.9	35.5	37.7	35.6
		Uncertainty (2SE)	0.2	0.1	0.1	0.1	0.2	0.2	0.1
		Average LOD	0.1	0.00945	0.0152	0.01	0.05	0.05	0.03
		Average LOQ	0.4	0.0284	0.0456	0.04	0.16	0.15	0.08
	2	Average concentration (ppm)	39.3	36.0	38.4	37.9	35.5	37.7	35.6
		Uncertainty (2SE)	0.3	0.1	0.2	0.2	0.2	0.3	0.2
		Average LOD	0.2	0.0196	0.0306	0.03	0.11	0.10	0.05
		Average LOQ	0.7	0.0589	0.0917	0.09	0.34	0.30	0.16
		Reference Value	39.3	36.0	38.4	37.9	35.5	37.7	35.6
		Uncertainty	0.9	0.7	0.7	1.0	0.7	0.8	0.8
NIST614	1	Average concentration (ppm)	3.18	0.71	0.79	0.76	0.75	0.76	0.77
		Uncertainty (2SE)	0.09	0.01	0.01	0.01	0.03	0.03	0.02
		Average LOD	0.11	0.009	0.02	0.01	0.06	0.05	0.03
		Average LOQ	0.33	0.03	0.05	0.04	0.17	0.15	0.09
	2	Average concentration (ppm)	3.12	0.70	0.78	0.76	0.72	0.77	0.78
		Uncertainty (2SE)	0.10	0.01	0.02	0.02	0.04	0.04	0.02
		Average LOD	0.22	0.019	0.03	0.03	0.13	0.11	0.05
		Average LOQ	0.66	0.06	0.09	0.09	0.38	0.32	0.16
		Reference Value	3.20	0.720	0.813	0.768	0.752	0.754	0.770
		Uncertainty	0.09	0.013	0.025	0.015	0.014	0.013	0.016
91500	1	Average concentration (ppm)	BelowLOQ	BelowLOD	2.18	BelowLOQ	0.16	0.37	0.21
		Uncertainty (2SE)	0.01	0.001	0.02	0.002	0.01	0.02	0.01
		Average LOD	0.01	0.095	0.01	0.01	0.01	0.05	0.04
		Average LOQ	0.04	0.29	0.03	0.04	0.04	0.14	0.13
	2	Average concentration (ppm)	BelowLOD	BelowLOD	2.13	BelowLOD	BelowLOQ	0.36	0.19
		Uncertainty (2SE)	0.02	0.002	0.03	0.003	0.02	0.02	0.01
		Average LOD	0.18	0.015	0.02	0.02	0.10	0.09	0.04
		Average LOQ	0.55	0.04	0.07	0.07	0.31	0.27	0.13
		Reference Value	0.06	0.006	2.6	0.024	0.24	0.50	0.24
		Uncertainty	0.06	0.006	0.6	0.030	0.08	0.16	0.06

Table 3.1.6.15 continued.

Reference Material	Session	Element	^{157}Gd	^{159}Tb	^{163}Dy	^{165}Ho	^{166}Er	^{169}Tm	^{172}Yb	^{175}Lu	^{177}Hf	^{181}Ta
NIST612	1	Average concentration (ppm)	37.3	37.6	35.5	38.3	38.0	36.8	39.2	37.0	36.7	37.6
		Uncertainty (2SE)	0.2	0.2	0.2	0.2	0.2	0.2	0.2	0.2	0.2	0.1
		Average LOD	0.13	0.01	0.05	0.01	0.05	0.01	0.04	0.01	0.05	0.01
		Average LOQ	0.38	0.03	0.15	0.03	0.14	0.04	0.12	0.04	0.16	0.03
	2	Average concentration (ppm)	37.3	37.6	35.5	38.3	38.0	36.8	39.2	37.0	36.7	37.6
		Uncertainty (2SE)	0.3	0.2	0.2	0.2	0.2	0.2	0.3	0.2	0.2	0.2
		Average LOD	0.27	0.02	0.10	0.02	0.09	0.03	0.09	0.03	0.09	0.02
		Average LOQ	0.80	0.07	0.29	0.06	0.27	0.08	0.26	0.08	0.26	0.07
		Reference Value	37.3	37.6	35.5	38.3	38.0	36.8	39.2	37.0	36.7	37.6
		Uncertainty	0.9	1.1	0.7	0.8	0.9	0.6	0.9	0.9	1.2	1.9
NIST614	1	Average concentration (ppm)	0.77	0.74	0.75	0.75	0.75	0.72	0.78	0.73	0.72	0.75
		Uncertainty (2SE)	0.04	0.01	0.03	0.01	0.02	0.01	0.03	0.01	0.02	0.01
		Average LOD	0.14	0.01	0.05	0.01	0.04	0.01	0.04	0.01	0.05	0.01
		Average LOQ	0.42	0.03	0.16	0.03	0.13	0.04	0.13	0.04	0.14	0.03
	2	Average concentration (ppm)	BelowLOQ	0.73	0.77	0.75	0.74	0.72	0.78	0.73	0.72	0.75
		Uncertainty (2SE)	0.06	0.02	0.03	0.02	0.03	0.02	0.04	0.02	0.03	0.02
		Average LOD	0.28	0.02	0.10	0.02	0.10	0.03	0.08	0.03	0.10	0.02
		Average LOQ	0.84	0.07	0.29	0.07	0.29	0.08	0.25	0.08	0.29	0.07
		Reference Value	0.763	0.739	0.746	0.749	0.740	0.732	0.777	0.732	0.711	0.808
		Uncertainty	0.021	0.020	0.022	0.015	0.017	0.020	0.021	0.018	0.022	0.026
91500	1	Average concentration (ppm)	1.96	0.75	9.77	4.13	22.44	5.51	57.6	11.97	5076.0	0.34
		Uncertainty (2SE)	0.04	0.01	0.09	0.03	0.15	0.04	0.4	0.07	29.0	0.01
		Average LOD	0.02	0.11	0.01	0.04	0.01	0.04	0.01	0.04	0.01	0.04
		Average LOQ	0.07	0.34	0.03	0.12	0.03	0.12	0.03	0.13	0.03	0.11
	2	Average concentration (ppm)	1.89	0.72	9.36	3.95	21.57	5.25	55.2	11.37	4948.7	0.30
		Uncertainty (2SE)	0.06	0.01	0.11	0.04	0.20	0.05	0.5	0.10	38.6	0.01
		Average LOD	0.22	0.02	0.08	0.02	0.08	0.02	0.08	0.02	0.07	0.02
		Average LOQ	0.65	0.06	0.24	0.05	0.23	0.07	0.23	0.06	0.21	0.06
		Reference Value	2.2	0.86	12	4.8	25	6.9	74	13	5900	0.5
		Uncertainty	0.6	0.14	2	0.8	6	0.8	8	2	600	0.2

Table 3.1.6.15. continued.

Reference Material	Session	Element	^{204}Pb	^{206}Pb	^{207}Pb	^{208}Pb	^{Total}Pb*	^{232}Th	^{238}U
NIST612	1	Average concentration (ppm)	38.6	38.6	38.6	38.6	38.6	37.8	37.4
		Uncertainty (2SE)	0.6	0.1	0.1	0.1		0.1	0.1
		Average LOD	1.33	0.01	0.01	0.01		0.01	0.00
		Average LOQ	3.99	0.03	0.03	0.04		0.04	0.01
	2	Average concentration (ppm)	38.7	38.6	38.6	38.6	38.6	37.8	37.4
		Uncertainty (2SE)	0.8	0.2	0.2	0.2		0.2	0.2
		Average LOD	2.7	0.02	0.02	0.02		0.03	0.01
		Average LOQ	8.1	0.06	0.06	0.07		0.08	0.02
		Reference Value					38.57	37.79	37.38
		Uncertainty					0.20	0.08	0.08
NIST614	1	Average concentration (ppm)	BelowLOQ	2.38	2.28	2.32	2.33	0.75	0.81
		Uncertainty (2SE)	0.32	0.03	0.03	0.03		0.01	0.01
		Average LOD	1.33	0.01	0.01	0.01		0.01	0.00
		Average LOQ	3.99	0.04	0.03	0.04		0.04	0.01
	2	Average concentration (ppm)	BelowLOD	2.43	2.30	2.39	2.38	0.75	0.82
		Uncertainty (2SE)	0.56	0.04	0.03	0.04		0.02	0.02
		Average LOD	2.78	0.02	0.02	0.02		0.02	0.01
		Average LOQ	8.33	0.05	0.06	0.06		0.07	0.02
		Reference Value					2.32	0.748	0.823
		Uncertainty					0.04	0.006	0.002
91500	1	Average concentration (ppm)	1.00	52.40	4.27	2.55	14.9	23.4	66.7
		Uncertainty (2SE)	0.19	0.16	0.03	0.03		0.1	0.4
		Average LOD	0.01	1.16	0.01	0.01		0.03	0.01
		Average LOQ	0.03	3.49	0.03	0.03		0.10	0.03
	2	Average concentration (ppm)	BelowLOD	53.00	4.41	2.61	15.1	23.1	65.5
		Uncertainty (2SE)	0.31	0.19	0.04	0.03		0.2	0.5
		Average LOD	2.17	0.02	0.05	0.02		0.02	0.01
		Average LOQ	6.52	0.05	0.16	0.05		0.06	0.02
		Reference Value					15	30	80
		Uncertainty						6	16

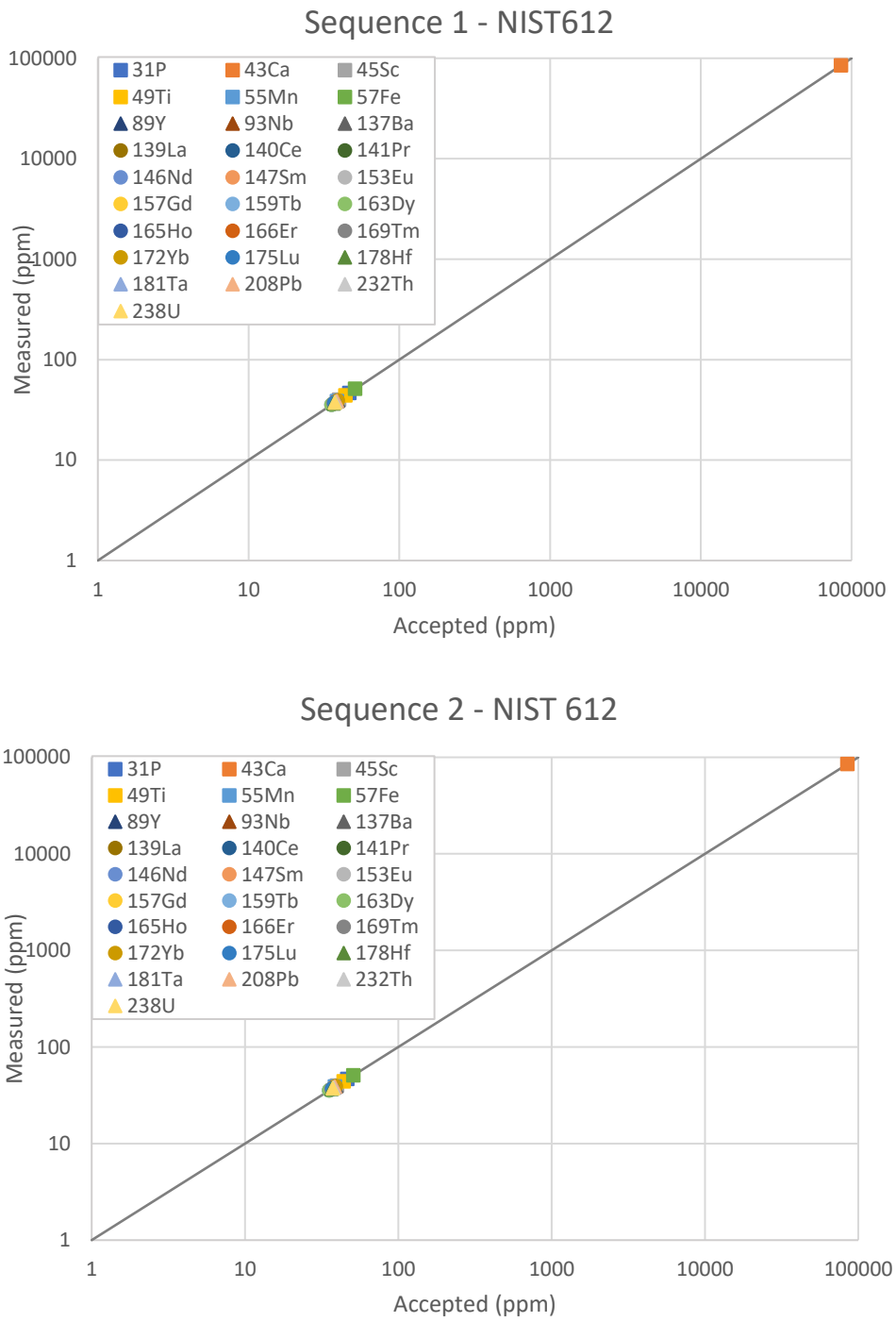

Figure 3.1.6.21. LASS-ICP-MS trace elements results for primary calibration glass reference material NIST612. The grey line indicates a 1:1 ratio of measured concentrations to the accepted RM values (Jochum et al., 2011). Deviation from this line indicates elements which do not agree with the accepted values.

The NIST 614 results generally agree with the GeoReM 5211 values (Table 3.1.6.15, Figure 3.1.6.22; Jochum et al., 2011). Exceptions include ^{31}P, with average concentrations of 41.0±0.4 ppm for session 1 and 40.7±0.5 for session 2, significantly higher than the reported 11.4±3.9 ppm. Scandium-45, ^{55}Mn and ^{57}Fe yielded concentrations below their respective limits of quantification. Additionally, the average concentration of ^{157}Gd was below the average limit of quantification in session 2 (Table 3.1.6.15).

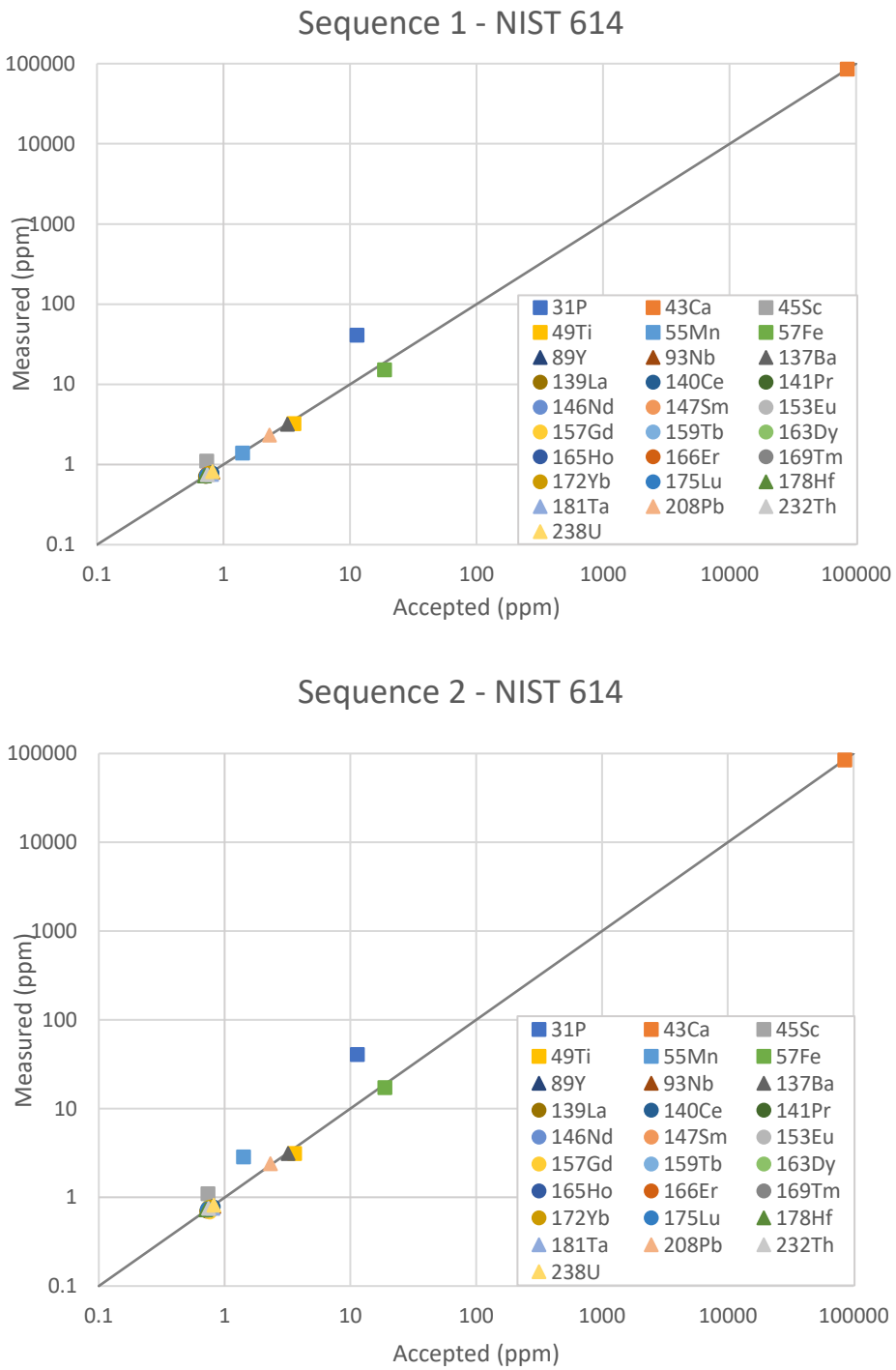

Figure 3.1.6.22. LASS-ICP-MS trace elements results for secondary glass reference material NIST614. The grey line indicates a 1:1 ratio of measured concentrations to the accepted RM values (Jochum et al., 2011). Deviation from this line indicates elements which do not agree with the accepted values.

The results of zircon 91500 are also generally within agreement of GeoReM 104 (Table 3.1.6.15, Figure 3.1.6.23; Wiedenbeck et al., 2004). Exceptions include ^{31}P and ^{45}Sc which had measured concentrations significantly greater than reported values (Table 3.1.6.15, Figure 3.1.6.23). The high concentrations of ^{45}Sc are likely due to interference with $^{29}Si^{16}O^{+}$ and Zr^{90++}, while ^{31}P has an interference with $^{15}N^{16}O$ and is difficult to ionize. Calcium-43, ^{55}Mn, ^{57}Fe, ^{93}Nb, ^{137}Ba,^{139}La, and ^{141}Pr yielded average concentrations below the limit of detections or quantification in both sessions 1 and 2. Additionally, the average concentration of ^{146}Nd was below the average LOQ in session 2. Concentrations of ^{169}Tm, ^{172}Yb, and ^{177}Hf were lower than the reported GeoReM 104 values (Figure 3.1.6.23; Wiedenbeck et al., 2004).

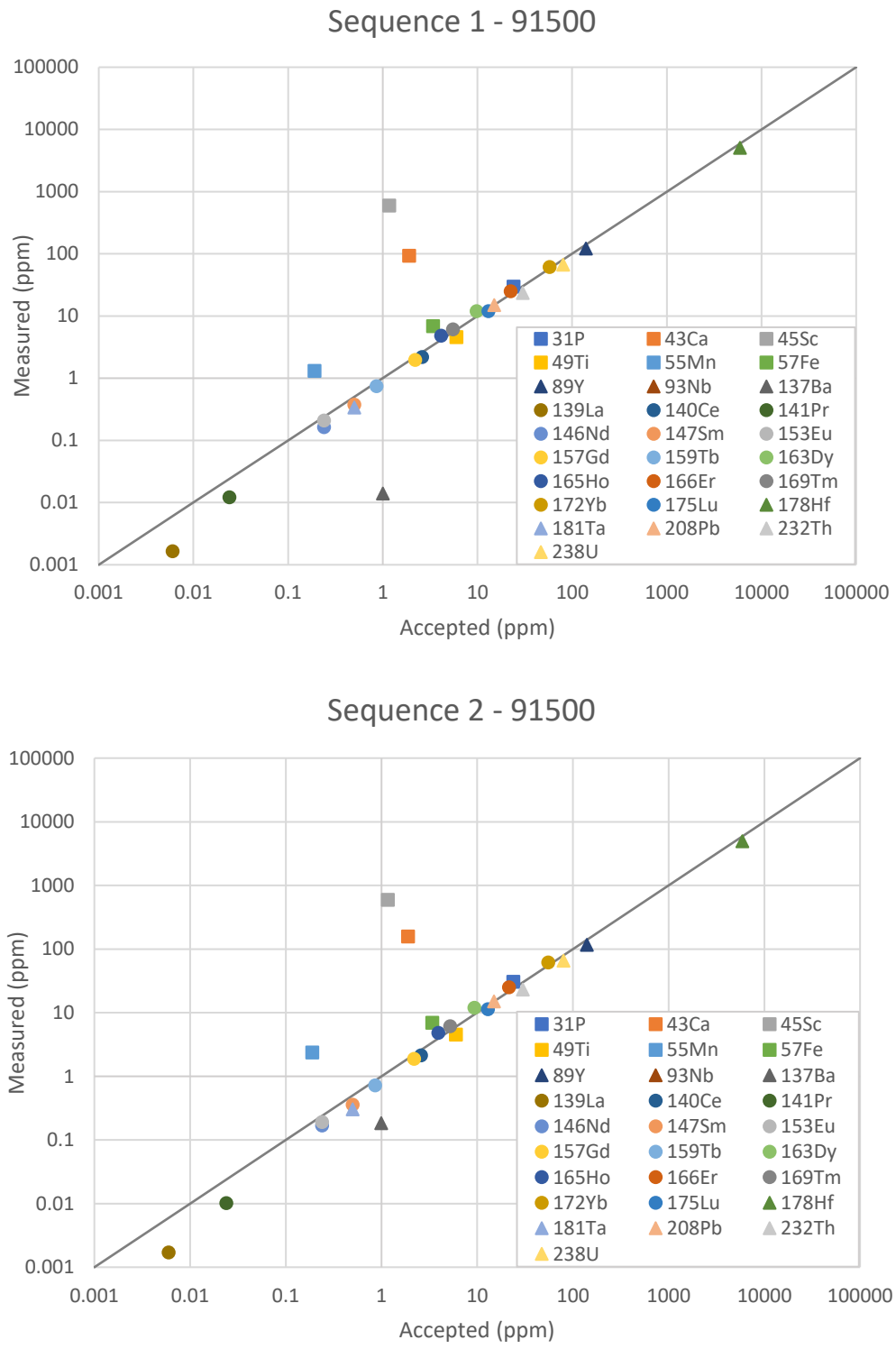

Figure 3.1.6.23. LASS-ICP-MS trace elements results for secondary zircon reference material 91500. The grey line indicates a 1:1 ratio of measured concentrations to the accepted RM values (Coble et al., 2018). Deviation from this line indicates elements which do not agree with the accepted values.

3.2 Results

3.2.1 LA-ICP-MS U-Pb Geochronology Results

3.2.1.1 Zircon U-Pb Geochronology

Zircon U-Pb LA-ICP-MS results are reported in the BCGS Geofile (in preparation) and summarized in Table 3.2.1.1. The majority of zircon LA-ICP-MS U-Pb crystallization ages presented in this thesis were previously reported in Jones et al. (2021). The ages have been further refined for this thesis, but do not differ significantly from Jones et al. (2021). Zircon LA-ICP-MS U-Pb ages for Thane Creek quartz diorite sample 18lo22-1d, Osilinka granite sample 19GJ12-3, and Mesilinka equigranular granite 19GJ16-2 were not previously reported.

Table 3.2.1.1. Summary of LA-ICP-MS $^{206}Pb/^{238}U$ weighted mean age results for unknown zircons.

Sample	Intrusive suite	$^{206}Pb/^{238}U$ weighted mean age, Ma (2SE)	No. of analyses	MSWD	$p(\chi^2)$	Excess scatter
19GJ12-4	Thane Creek	206.8±0.9	12/13	1.7	0.06	N/A
18lo22-1a	Thane Creek	191.4±0.7	33/42	0.87	0.68	N/A
18lo22-1d	Thane Creek	199.0±0.5	26/46	1.2	0.24	N/A
19GJ13-3	Thane Creek	194.0±1.0	38/50	1.3	0.11	3.25
18lo25-2a	Duckling Creek	179.0±1.0	20/44	1.0	0.46	1.63
19GJ13-5a	Duckling Creek	174.7±0.7	24/26	1.4	0.12	N/A
18lo17-1	Osilinka	159.2±4.0	1	N/A	N/A	N/A
19GJ12-3	Osilinka	187.7±3.8	1	N/A	N/A	N/A
18lo20-4	Osilinka	162.2±2.6	1	N/A	N/A	N/A
19GJ12-1	Mesilinka	134.1±0.5	18/23	1.5	0.09	N/A
18lo12-7	Mesilinka	135.4±0.9	20/33	1.4	0.11	2.18
18lo11-1	Mesilinka	127.7±0.8	34/48	1.5	0.02	2.31
19GJ16-2	Mesilinka	127.1±1.6	13/33	1.4	0.18	2.58

Thane Creek suite

Quartz diorite: 19GJ12-4

Zircons from Thane Creek quartz diorite sample 19GJ12-4 are typically brown, euhedral, fractured, 70 to 280 µm long, and dark in CL images. Internal textures are poorly preserved, with growth zones mostly obscured (Appendix C). The $^{206}Pb/^{204}Pb$ ratio in zircon ranges between 830 and 190000.

Thirteen spots from 11 zircons were analyzed for U-Pb from sample 19GJ12-4. After analysis and data reduction, one zircon was rejected for $f^{206}Pb_C$ >1%. Twelve remaining zircons range in age from 204.0±3.1 to 208.9±3.3 Ma. These results yield a weighted mean $^{206}Pb/^{238}U$ date of 206.8±0.9 Ma (mean squared weighted deviation; MSWD =1.7; probability of fit; ($p(\chi^2)$)=0.06). This weighted mean, and its associated MSWD, is consistent with the analysed zircons being derived from a single age population (Spencer et al., 2016), and is interpreted as the best estimate for the crystallization age for quartz diorite sample 19GJ12-4 (Figure 3.2.1.1; Table 3.2.1.1).

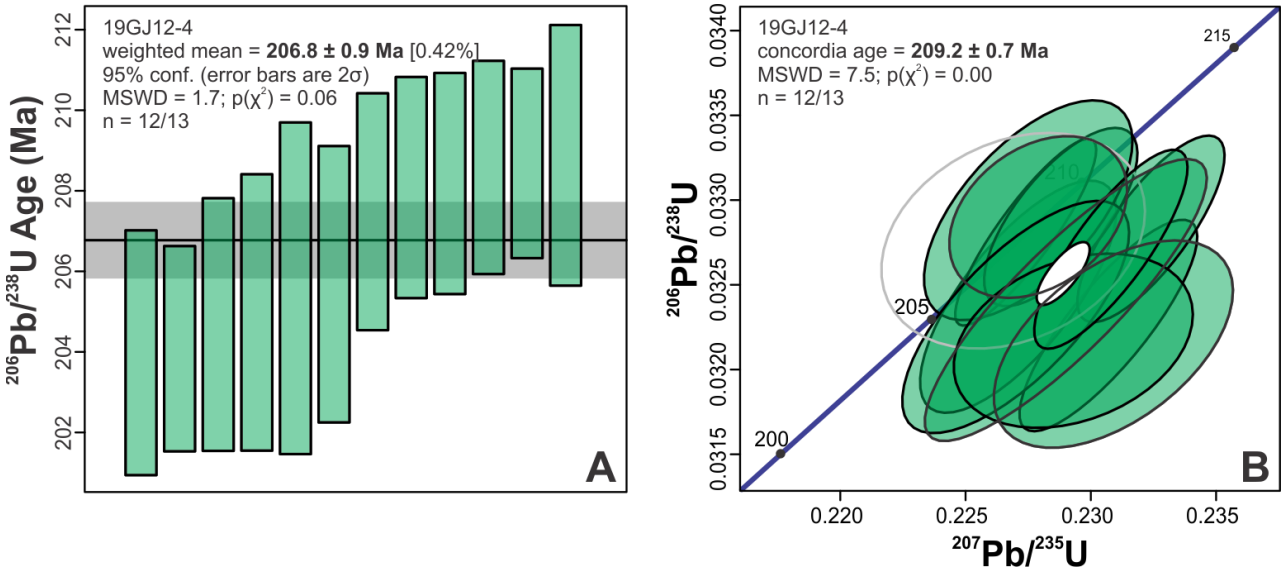

Figure 3.2.1.1. A) The weighted mean of zircon $^{206}Pb/^{238}U$ dates, interpreted as the crystallization age, of Thane Creek quartz diorite sample 19GJ12-4. The black line is the weighted mean, and the grey bar is the 2σ uncertainty of the mean. **B)** Wetherhill concordia plot of zircon $^{206}Pb/^{238}U$ and $^{207}Pb/^{235}U$ ratio results for 19GJ12-4. Open grey ellipses were screened out for $f^{206}Pb_C$ >1% and were not included in the concordia age calculation. The white ellipse is the concordia age result. Uncertainties and ages are reported at the 95.4% confidence level (2σ).

Hornblendite: 18lo22-1a

Zircons from Thane Creek hornblendite sample 18lo22-1a are typically light pink, euhedral, and 250 to 900 µm long. Internal textures are well preserved, with oscillatory and sector growth zoning (Appendix C). The $^{206}Pb/^{204}Pb$ ratio in zircon ranges between 400 and 1800000.

Forty-two spots from 32 zircons were analyzed for U-Pb from sample 18lo22-1a. After analysis and data reduction, nine results were rejected for $f^{206}Pb_c$ >1%. Thirty-three remaining zircons range in age from 187.5±3.8 to 195.5±4.1 Ma. These results have a $^{206}Pb/^{238}U$ weighted mean date of 191.4±0.7 Ma (MSWD=0.87; $p(\chi^2)$=0.68) (Figure 3.2.1.2; Table 3.2.1.1). This weighted mean, and its associated MSWD, is consistent with the analysed zircons being derived from a single age population (Spencer et al., 2016).

A zircon CA-TIMS U-Pb age of 197.6±0.1 Ma for sample 18lo22-1a was previously determined (Ootes et al., 2020b). The discrepancy between the LA-ICP-MS weighted mean $^{206}Pb/^{238}U$ date (191.4±0.7 Ma) and the reported CA-TIMS $^{206}Pb/^{238}U$ date (197.6±0.1 Ma) may be due to differences in the calibration techniques between the LA-ICP-MS and CA-TIMS methods. Although both the LA-ICP-MS and CA-TIMS U-Pb dates of the hornblendite are considered valid, the CA-TIMS date (197.6±0.1 Ma) is interpreted to be more accurate and the best estimate of the crystallization age.

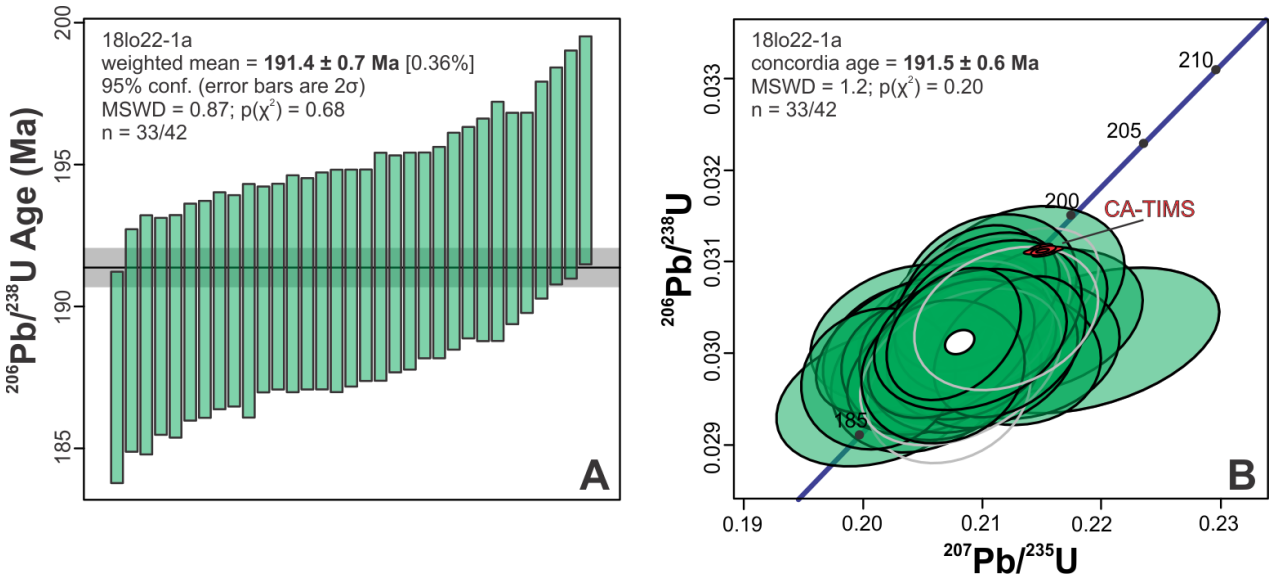

Figure 3.2.1.2. A) The weighted mean of zircon $^{206}Pb/^{238}U$ dates from Thane Creek hornblendite sample 18lo22-1a. The black line is the weighted mean, and the grey bar is the 2σ uncertainty of the mean. **B)** Wetherhill concordia plot of zircon $^{206}Pb/^{238}U$ and $^{207}Pb/^{235}U$ ratio results, shown by green ellipses, for hornblendite sample 18lo22-1a. Red ellipses indicate the CA-TIMS U-Pb age results for 18lo22-1a, interpreted as 197.5±0.1 Ma by Ootes et al. (2020b) and determined as the best estimate of the crystallization age for this sample. Open grey ellipses were screened out for $f^{206}Pb_C$ >1% and were not included in the concordia age calculation. The white ellipse is the concordia age result. Uncertainties and ages are reported at the 95.4% confidence level (2σ).

Quartz diorite: 18lo22-1d

Zircons from Thane Creek quartz diorite sample 18lo22-1d are typically light pink, euhedral, and 250 to 600 µm long. Internal textures are well preserved, with oscillatory and sector growth zoning (Appendix C). The $^{206}Pb/^{204}Pb$ ratio in zircon ranges between 500 and 26000. Forty-six spots from 38 zircons were analyzed from sample 18lo22-1d. After analysis and data reduction, 16 analyses were rejected for exceeding >5% discordance and/or $f^{206}Pb_c$ >1%.

Thirty remaining zircon spots range in $^{206}Pb/^{238}U$ apparent age from 196.5±2.6 to 203.3±2.2 Ma. These results have a weighted mean $^{206}Pb/^{238}U$ date of 199.6±0.7 Ma (MSWD=2.5). The high MSWD indicates the data may not represent a single population, using the MSWD versus sample number cut-off guidelines from Spencer et al. (2016). The four oldest zircon results (zircon 27, 22@2, 29, 20@1), with ages ranging from 202.7±2.1 to 203.3±2.2 Ma, may represent antecrysts or early crystallized grains and are not representative of the population. These four data were removed and 26 remaining results yield a $^{206}Pb/^{238}U$ weighted mean date of 199.0±0.5 Ma (MSWD=1.2; $p(\chi^2)$=0.24) (Figure 3.2.1.3; Table 3.2.1.1).

A zircon CA-TIMS age of 196.61±0.19 Ma was previously determined for sample 18lo22-1d (Ootes et al., 2020b). The CA-TIMS age was interpreted using the youngest zircon result out of five grains, which range in $^{206}Pb/^{238}U$ age from 196.61±0.19 to 202.28±0.64 Ma (Ootes et al., 2020b). Although the CA-TIMS U-Pb age results are more precise than LA-ICP-MS U-Pb age results for individual zircon grains, the range of LA-ICP-MS ages agree with the range of CA-TIMS U-Pb results in that sample. The reported CA-TIMS age may not represent the main stage of zircon crystallization in this sample, as the youngest zircon may have crystallized later than the bulk of the population. The LA-ICP-MS age takes a greater range of dates into account and is more representative of the age range of the zircon population in this sample than the interpreted CA-TIMS age. We consider the LA-ICP-MS age (199.0±0.5 Ma) the best estimate of the crystallization age for quartz diorite sample 18lo22-1d.

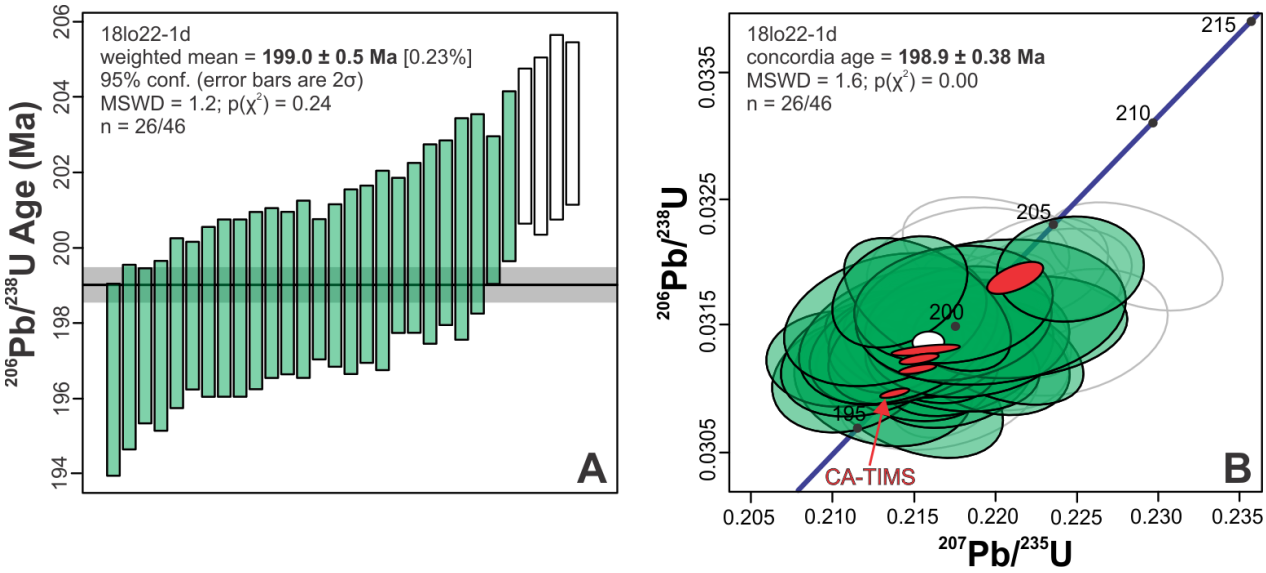

Figure 3.2.1.3. A) The weighted mean of zircon $^{206}Pb/^{238}U$ dates, interpreted as the crystallization age, of Thane Creek quartz diorite sample 18lo22-1d. White bars are zircon grains interpreted as antecrystic or early crystallized grain, and were not included in the weighted mean calculation. The black line is the weighted mean, and the grey bar is the 2σ uncertainty of the mean. **B)** Wetherhill concordia plot of zircon $^{206}Pb/^{238}U$ and $^{207}Pb/^{235}U$ ratio results, shown by green ellipses, for quartz diorite sample 18lo22-1a. Open grey ellipses are data filtered for >5% discordance, >1% $f^{206}Pb_C$, or interpreted to be antecrystic or xenocrystic zircons, and were not included in the concordia age calculation. The white ellipse is the concordia age result. Red ellipses are the CA-TIMS U-Pb results for 18lo22-1d, interpreted as 196.6±0.9 Ma by Ootes et al. (2020b) using the youngest zircon result. Uncertainties and ages are reported at the 95.4% confidence level (2σ).

Quartz monzodiorite: 19GJ13-3

Zircons from Thane Creek quartz monzodiorite sample 19GJ13-3 are typically clear to light pink, euhedral, and 150 to 425 μm long. Internal textures are well preserved, with oscillatory and sector growth zoning. Several zircons have rounded cores that are overgrown, but not crosscut, by later zonation (Appendix C). The $^{206}Pb/^{204}Pb$ ratio in zircon ranges between 400 and 87000.

Fifty spots from 35 zircons were analyzed from sample 19GJ13-3. After LA-ICP-MS analysis, six zircon data were rejected for $f^{206}Pb_C$ >1% and two zircons were rejected for >5% discordance. The remaining zircons range in apparent $^{206}Pb/^{238}U$ age from 182.9±3.2 to 201.4±2.9 Ma (MSWD=9.9). This high MSWD for this number of datapoints indicates the dataset includes multiple populations, using the MSWD versus sample number cut-off guidelines from Spencer et al. (2016). Only one rounded, possibly inherited, zircon core was identified using the CL image, and this result was removed from the weighted mean (Zircon 29@1).

Despite the high MSWD in the remaining zircon data, the zircon grains are interpreted as magmatic. It is possible the scatter in the age data is due to multiple magma pulses in a chamber over time, but individual pulse ages cannot be resolved at the level of analytical precision. Although the high MSWD indicates scatter in the age beyond that expected for a single data population controlled by random uncertainties (Spencer et al., 2016), further objective criteria (Hf, $\delta^{18}O$, trace element data) did not find any data outliers to remove and define a more accurate intrusion age. As such, the age presented must be viewed as an initial estimate of the age, pending further refinement.

Since the elevated MSWD of this age population is not commensurate with a single age population dominated by random uncertainties (Spencer et al., 2016), the overdispersed data were dealt with using the 'model-3' method outlined by Vermeesch (2018). In this method, data overdispersion is attributed to geologic scatter in the ages, and an overdispersion term (excess scatter; Table 3.2.1.1) is calculated to reduce the MSWD to unity (Vermeesch, 2018). This method did not change the resulting weighted mean $^{206}Pb/^{238}U$ age but increased the uncertainty of the weighted mean. An excess scatter constant of 3.25 was calculated and added to the standard error of the filtered data to decrease the MSWD of the weighted mean. The youngest three results (Zircon 5@1, 23@2, 3) were not included in the final weighted mean, as these may indicate undetected Pb-loss. Thirty-eight remaining results yield a weighted mean $^{206}Pb/^{238}U$ date

of 194.0±1.0 Ma (MSWD=1.3; p(χ^2)=0.11). This weighted mean is interpreted as the best estimate for the crystallization age for quartz monzodiorite sample 19GJ13-3 (Figure 3.2.1.4; Table 3.2.1.1).

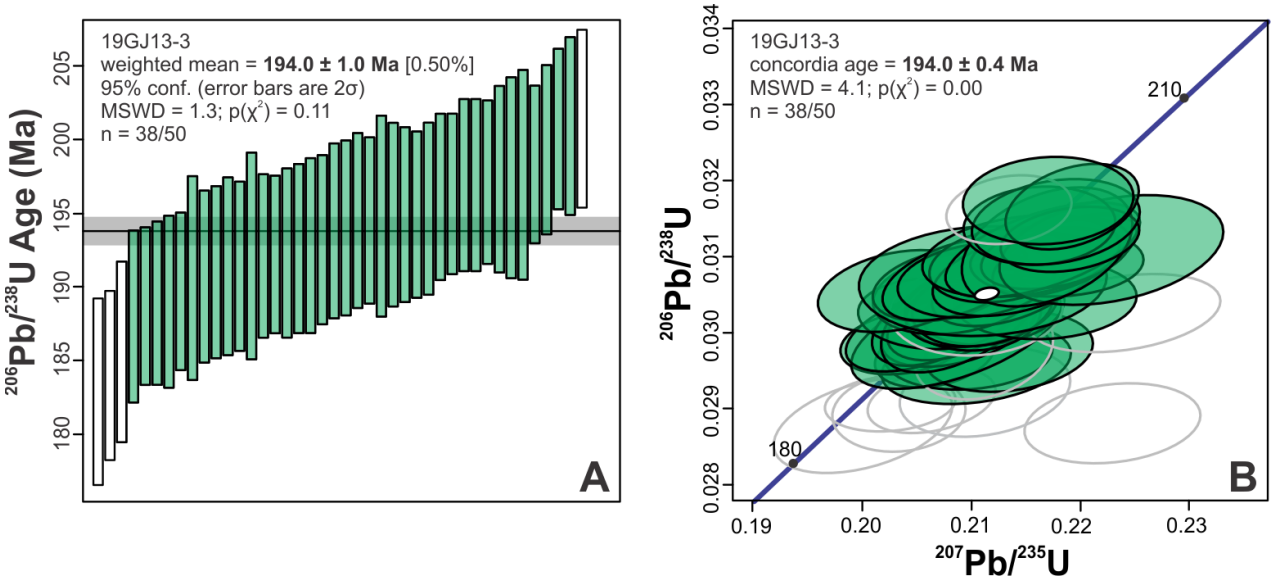

Figure 3.2.1.4. A) The weighted mean of zircon $^{206}Pb/^{238}U$ dates, interpreted as the crystallization age, of Thane Creek quartz monzodiorite sample 19GJ13-3. White bars are zircons interpreted to have potential Pb-loss or as xenocrystic, and were excluded from the weighted mean calculation. The black line is the interpreted weighted mean, and the grey bar is the 2σ uncertainty of the mean. **B)** Wetherhill concordia plot of zircon $^{206}Pb/^{238}U$ and $^{207}Pb/^{235}U$ ratio results for 19GJ13-3. Open grey ellipses indicate data filtered for >5% discordance, >1% $f^{206}Pb_C$, or interpreted to have Pb-loss or xenocrystic zircons, and were not included in the concordia age calculation. The white ellipse is the concordia age result. Uncertainties and ages are reported at the 95.4% confidence level (2σ).

Duckling Creek suite

Syenite: 18lo25-2a

Duckling Creek syenite sample 18lo25-2a bears two types of zircon. Type 'A' are clear-pink coloured zircon fragments between 100 to 200 mm. Type 'B' zircons are larger grains (300 to 400 mm) that are brown with good crystal habit, but with cores that are commonly metamict or highly fractured (Appendix C). The $^{206}Pb/^{204}Pb$ ratio in zircon ranges between 2100 and 35000. The U-Pb age interpretations were mostly determined from type A zircons, as only two type B zircon analyses passed data screenings.

Forty-four spots from 44 zircons were analyzed from sample 18lo25-2a. After LA-ICP-MS analysis, 17 type A and B zircons were rejected for >5% discordance, and three type B zircons were filtered for trace element results with Fe >300 ppm and/or Ca >300 ppm and La >1 ppm. One type B zircon analysis was rejected for excessive standard error of Ca.

After data screening, the remaining 23 zircons ranged in apparent $^{206}Pb/^{238}U$ age from 174.9±4.3 to 186.7±3.4 Ma (MSWD = 4.0). This high MSWD indicates the dataset likely includes multiple populations, using the MSWD versus sample number cut-off guidelines from Spencer et al. (2016). The three oldest zircon results (Zircon A6, A9, B7-1; Appendix C), with dates from 185.1±3.1 to 186.7±3.4 Ma, were removed from the weighted mean calculation, as these may represent antecrysts or early crystallized zircons and are not representative of the remaining grains. Excluding these older grains, the remaining 20 analyses ranged in apparent $^{206}Pb/^{238}U$ age from 174.9±4.3 Ma to 182.4±3.1 (MSWD = 2.3). The MSWD indicates the remaining data do not represent a single population; however, zircon BSE images and Hf, $\delta^{18}O$, and trace element data provide no further evidence that multiple zircon populations may be present. It is possible the age scatter is due to multiple magma pulses over time, but individual pulse ages cannot be resolved at the level of analytical precision. As such, the age presented must be viewed as an initial estimate of the age, pending further refinement.

Since the MSWD of this age population does not correspond with a single population dominated by random uncertainties (Spencer et al., 2016), the overdispersed data were dealt with using the model-3 method outlined by Vermeesch (2018). An excess scatter constant of 1.63 was calculated and added to the individual uncertainties of the remaining data to decrease the MSWD. This method did not change the resulting weighted mean $^{206}Pb/^{238}U$ age, nor significantly increase the uncertainty of the weighted mean. Twenty remaining zircons yield a weighted mean $^{206}Pb/^{238}U$ date of 179.0±1.0 Ma (MSWD=1.0; $p(\chi^2)$=0.46). This weighted mean is interpreted as the best estimate for the crystallization age of Duckling Creek syenite sample 18lo25-2a (Figure 3.2.1.5; Table 3.2.1.1).

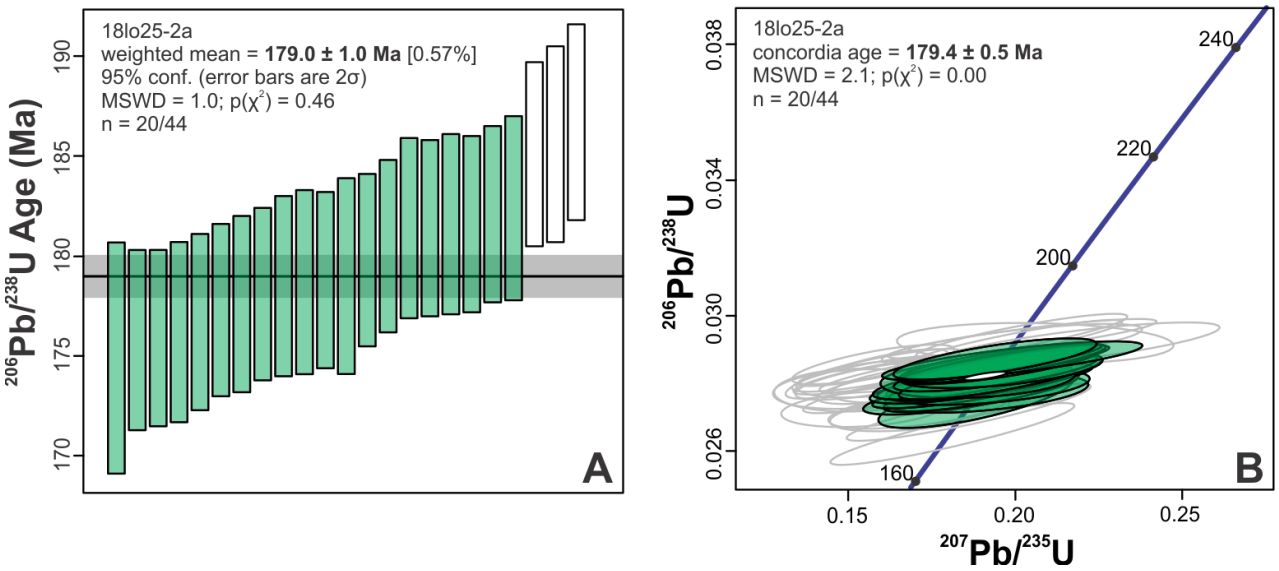

Figure 3.2.1.5. A) The weighted mean of zircon $^{206}Pb/^{238}U$ dates, interpreted as the crystallization age, of Duckling Creek syenite sample 18lo25-2a. White bars are zircons that may represent antecrysts and were excluded from the weighted mean. The black line is the weighted mean, and the grey bar is the 2σ uncertainty of the mean. **B)** Wetherhill concordia plot of zircon $^{206}Pb/^{238}U$ and $^{207}Pb/^{235}U$ ratio results for 18lo25-2a. Open grey ellipses are data filtered for >5% discordance, >1% $f^{206}Pb_C$, >300 ppm Fe, >300 ppm Ca, >1 ppm La, or interpreted to be antecrystic, and are not included in the concordia age calculation. The white ellipse is the concordia age. Uncertainties and ages are reported at the 95.4% confidence level (2σ).

Syenite: 19GJ13-5a

Zircons from Duckling Creek syenite sample 19GJ13-5a are typically clear-pink, euhedral, and 110 to 250 µm long. Internal textures are well preserved, with oscillatory, sector, and/or tabular growth zoning. The $^{206}Pb/^{204}Pb$ ratio in zircon ranges between 500 and 13000. Several zircons have cores with rounded rims that are overgrown, but not crosscut, by later zonation (Appendix C).

Twenty-six spots from 23 zircons were analyzed from sample 19GJ13-5a. After LA-ICP-MS analysis, two zircon U-Pb analyses were rejected for $f^{206}Pbc$ >1%. Twenty-four remaining zircons have apparent $^{206}Pb/^{238}U$ ages ranging from 170.7±3.3 to 178.0±3.7 Ma. These data yield a weighted mean $^{206}Pb/^{238}U$ date of 174.7±0.7 Ma (MSWD=1.4; $p(\chi^2)$=0.12). This weighted mean, and its associated MSWD, is consistent with the analysed zircons being derived from a single age population (Spencer et al., 2016), and is interpreted as the best estimate for the crystallization age for Duckling Creek syenite sample 19GJ13-5a (Figure 3.2.1.6; Table 3.2.1.1).

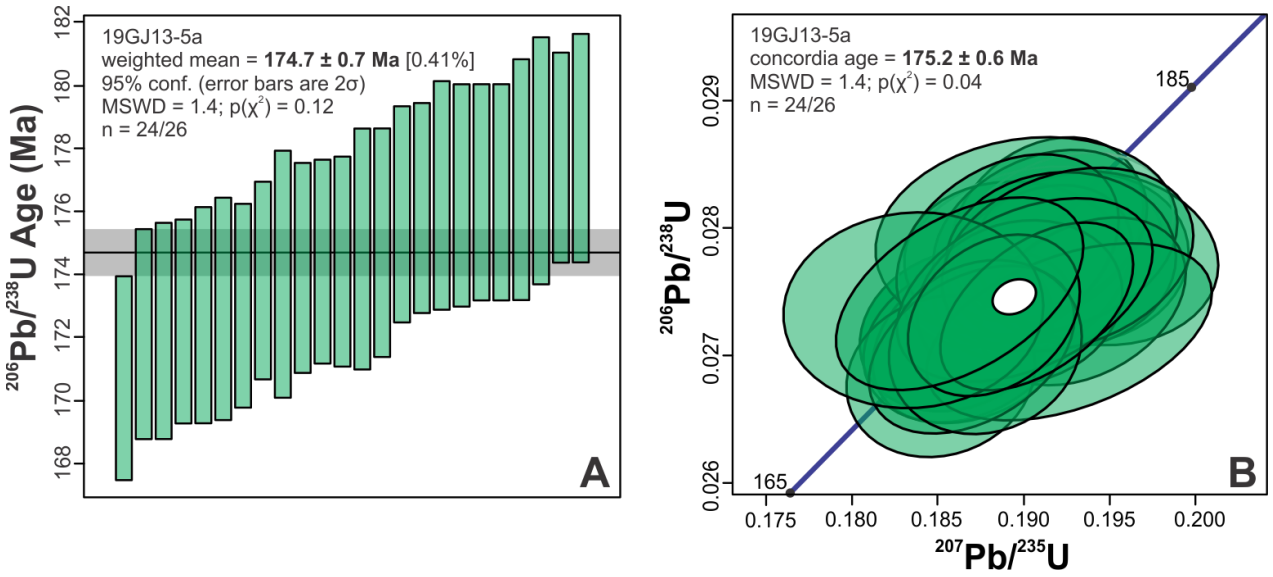

Figure 3.2.1.6. A) The weighted mean of zircon $^{206}Pb/^{238}U$ dates, interpreted as the crystallization age, of Duckling Creek syenite sample 19GJ13-5a. The black line is the weighted mean, and the grey bar is the 2σ uncertainty of the mean. **B)** Wetherhill concordia plot of zircon $^{206}Pb/^{238}U$ and $^{207}Pb/^{235}U$ ratio results for 19GJ13-5a. The white ellipse is the concordia age. Uncertainties and ages are reported at the 95.4% confidence level (2σ).

Osilinka suite

Granite: 18lo17-1

Zircons from Osilinka granite sample 18lo17-1 are typically clear, euhedral, fragmented, and 150 to 500 µm long. Internal textures are well preserved, with oscillatory growth zoning. The $^{206}Pb/^{204}Pb$ ratio in zircon ranges between 200 and 39000. Grains occasionally have overgrown rims (Appendix C).

Twenty-four spots from 21 zircons were analyzed from sample 18lo17-1. After LA-ICP-MS analysis, twelve results were rejected for $f^{206}Pb_c$ >1% and/or >5% discordance. The ten remaining zircons have a 36.1 million year spread in $^{206}Pb/^{238}U$ dates and are interpreted as inherited. The youngest zircon has a $^{206}Pb/^{238}U$ date of 159.2 ±4.0 Ma; it is unclear if this is a magmatic or inherited zircon and therefore this $^{206}Pb/^{238}U$ date is interpreted as the maximum crystallization age for Osilinka granite 18lo17-1 (Figure 3.2.1.7; Table 3.2.1.1).

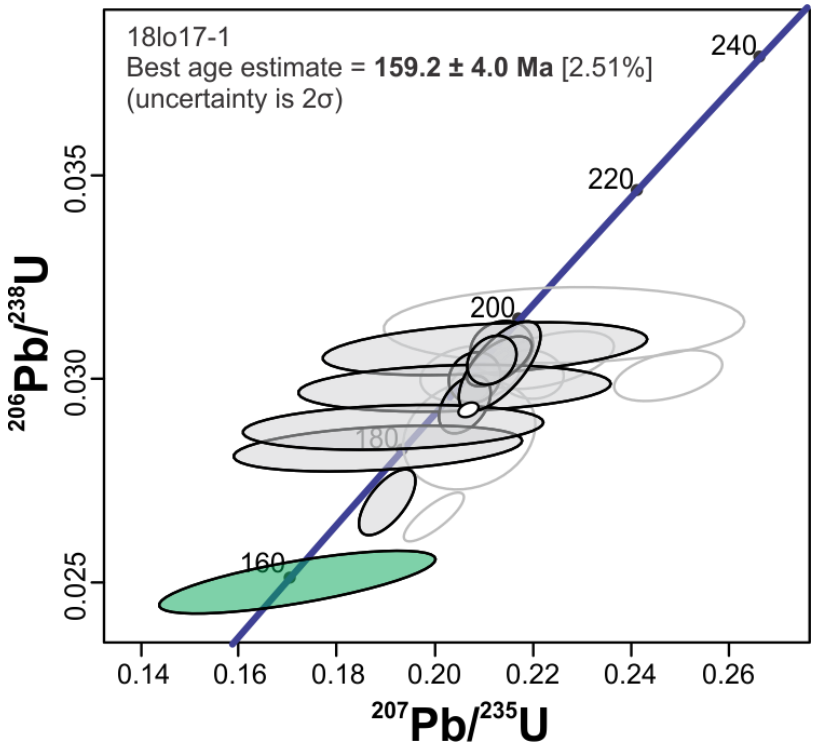

Figure 3.2.1.7. Wetherhill concordia plot of zircon $^{207}Pb/^{235}U$ and $^{206}Pb/^{238}U$ ratio results for Osilinka granite sample 18lo17-1. Open grey ellipses are data points screened for >5% discordance and/or >1% $f^{206}Pb_C$. Closed grey ellipses with black outlines are data that passed screenings, but are interpreted as inherited zircons. The green ellipse is the youngest zircon result, interpreted as the maximum crystallization age of the sample. Uncertainties and ages are reported at the 95.4% confidence level (2σ).

Granite: 19GJ12-3

Zircons from Osilinka granite sample 19GJ12-3 are typically colourless to pink, euhedral, 60 to 140 µm long. Approximately half the grains have well-preserved internal textures, while the remaining grains are metamict or irregularly zoned. The $^{206}Pb/^{204}Pb$ ratio in zircon ranges between 200 and 9000. Several grains have bright, rounded cores crosscut by later oscillatory zonation (Appendix C).

Sixteen spots from 16 zircons were analyzed from sample 19GJ12-3. After LA-ICP-MS analysis, ten zircon data points were rejected for >5% discordance and/or $f^{206}Pb_c$ >1%. The six remaining zircons yield a 42.6 million year spread in $^{206}Pb/^{238}U$ dates and are interpreted as inherited. The youngest zircon has a $^{206}Pb/^{238}U$ date of 187.7±3.8 Ma (Figure 3.2.1.8; Table 3.2.1.1). It is likely this zircon grain is also inherited, due to the presence of younger (ca. 160 Ma) zircons in Osilinka granite 18lo17-1 and porphyry sheet 18lo20-4. Additionally, Osilinka granite cross-cuts Duckling Creek syenite (ca. 179 to 174 Ma) in the field, so the Osilinka granite must be younger than at least ca. 174 Ma.

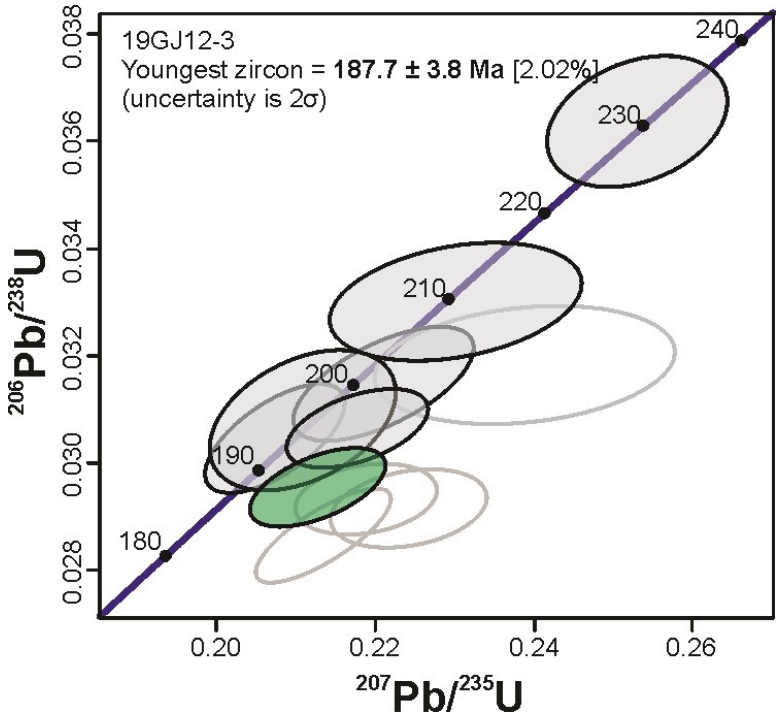

Figure 3.2.1.8. Wetherhill concordia plot of zircon $^{207}Pb/^{235}U$ and $^{206}Pb/^{238}U$ ratio results for Osilinka granite sample 19GJ12-3. Open grey ellipses are data points screened for >5% discordance and/or >1% f206PbC. Closed grey ellipses with black outlines are data that passed screenings, but are interpreted as inherited zircons. The green ellipse is the youngest zircon date result, which is also interpreted as inherited. Uncertainties and ages are reported at the 95.4% confidence level (2σ).

Porphyry sheet cutting granite: 18lo20-4

Zircons from porphyry sheet sample 18lo20-4 are typically euhedral, fragmented, and 85 to 425 µm long. Internal textures are generally well preserved with oscillatory growth zoning; however, some grains have metamict cores with overgrown rims. The $^{206}Pb/^{204}Pb$ ratio in zircon ranges between 300 and 97000. Several grains have rounded cores cross-cut by later zonation (Appendix C).

Seventeen spots from 14 zircons were analyzed from sample 18lo20-4. After LA-ICP-MS analysis, ten zircon data points were rejected for >5% discordance and/or $f^{206}Pb_c$ >1%. Seven remaining zircons have a 96.1 million year spread in $^{206}Pb/^{238}U$ dates and are interpreted as inherited. The youngest zircon has a $^{206}Pb/^{238}U$ date of 162.2±2.6 Ma; it is unclear if this is a magmatic or inherited zircon and therefore this $^{206}Pb/^{238}U$ date is interpreted as the maximum crystallization age (Figure 3.2.1.9; Table 3.2.1.1).

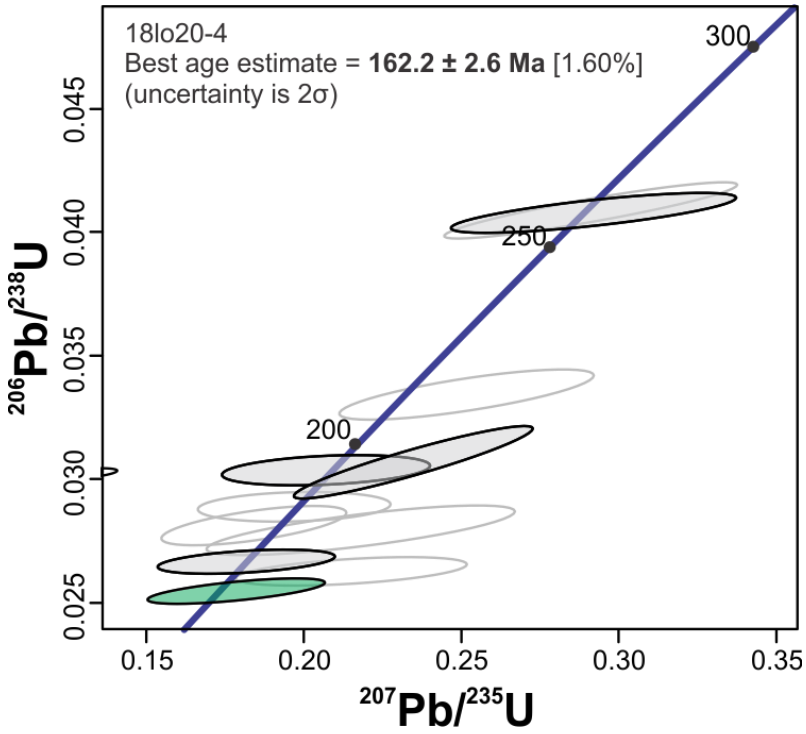

Figure 3.2.1.9. Wetherhill concordia plot of zircon $^{207}Pb/^{235}U$ and $^{206}Pb/^{238}U$ ratio results for Osilinka porphyry sheet sample 18lo20-4. Open grey ellipses are data points screened for >5% discordance and/or >1% $f^{206}Pb_C$. Closed grey ellipses with black outlines are data that passed screenings, but are interpreted as inherited zircons. The green ellipse is the youngest zircon date result, interpreted as the maximum crystallization age of the sample. Uncertainties and ages are reported at the 95.4% confidence level (2σ).

Mesilinka suite

Tonalite: 19GJ12-1

Zircons from Mesilinka tonalite sample 19GJ12-1 are typically clear-pink, euhedral, and 65 to 200 µm long. Internal textures are well preserved, with oscillatory growth zoning. The $^{206}Pb/^{204}Pb$ ratio in zircon ranges between 700 and 24000. Several grains have overgrown rims that disrupt previous zonation (Appendix C).

Twenty-three spots from 22 zircons were analyzed from sample 19GJ12-1. After LA-ICP-MS analysis, three zircon results were rejected for $f^{206}Pb_C$ >1%. After data screening, two results were rejected from the weighted mean calculation because the zircons are interpreted as xenocrysts or antecrysts. These grains have dark cores and disrupted rim growth in zircon CL images (Zircons 51 and 55; Appendix C). In addition, these zircons have higher $\delta^{18}O$ values relative to the remaining population (section 3.2.2). Trace element data was not available for this sample as an additional check for altered zircon grains.

Eighteen remaining analyses yield a weighted mean $^{206}Pb/^{238}U$ date of 134.1±0.5 Ma (MSWD=1.5; p(χ^2)=0.09). The weighted mean, and its associated MSWD, is consistent with the analysed zircons being derived from a single age population (Spencer et al., 2016), and is interpreted as the best estimate for the crystallization age of tonalite sample 19GJ12-1 (Figure 3.2.1.10; Table 3.2.1.1).

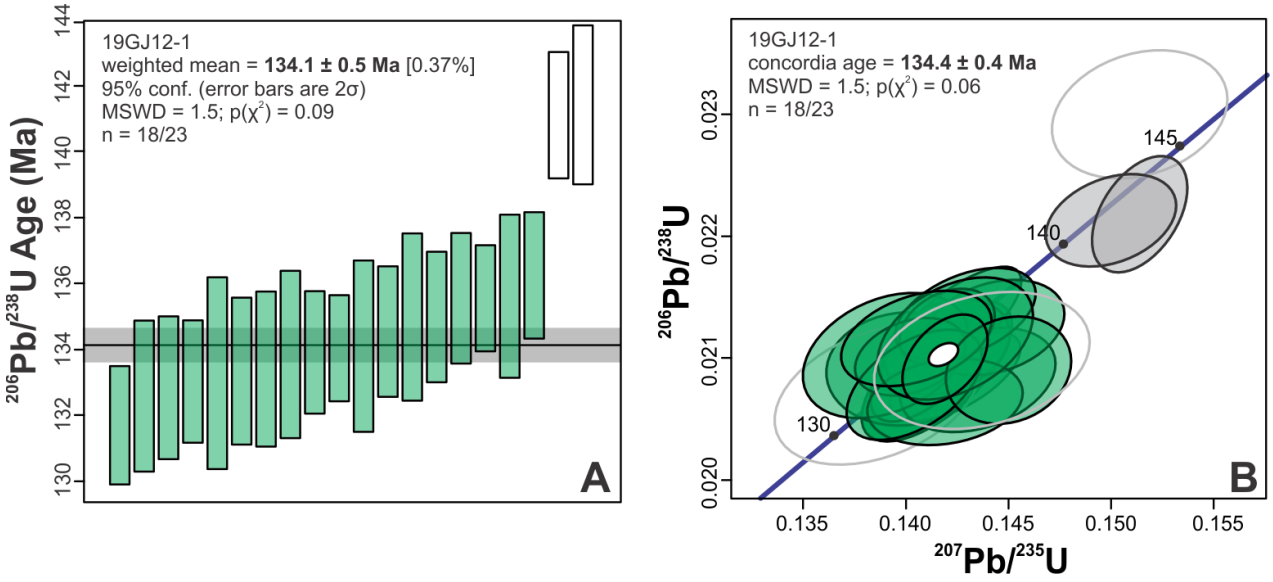

Figure 3.2.1.10. A) The weighted mean of zircon $^{206}Pb/^{238}U$ dates, interpreted as the crystallization age, of Mesilinka tonalite sample 19GJ12-1. White bars are zircon grains interpreted as xenocrystic or antecrystic and were excluded from the weighted mean calculation. The black line is the weighted mean, and the grey bar is the 2σ uncertainty of the mean. **B)** Wetherhill concordia plot of zircon $^{206}Pb/^{238}U$ and $^{207}Pb/^{235}U$ ratio results for 19GJ12-1. Closed grey ellipses with black outlines are zircon grains that passed data screenings, but are interpreted as antecrystic or xenocrystic. Open grey ellipses are data screened for >1% $f^{206}Pb_C$. Uncertainties and ages are reported at the 95.4% confidence level (2σ).

K-feldspar porphyritic granite: 18lo12-7

Zircons from Mesilinka K-feldspar porphyritic granite sample 18lo12-7 are typically clear-pink, euhedral, and 200 to 460 µm long. Internal textures are moderately preserved, with oscillatory growth zoning often surrounding irregularly zoned or metamict cores. The $^{206}Pb/^{204}Pb$ ratio in zircon ranges between 300 and 550000. Several grains have rims overgrowing rounded cores or crosscutting older growth zones (Appendix C).

Thirty-three spots from 22 zircons were analyzed from sample 18lo12-7. From the LA-ICP-MS results, seven analyses were rejected for $f^{206}Pbc$ >1% and/or >5% discordance. Two results were not included in the weighted mean, as the zircon was interpreted as inherited, displaying a bright, rounded core crosscut by later growth zoning in the CL image (Zircon 49-1 and -2; Appendix C). Two additional zircons (Zircons 45-1 and -2, 44-2) were interpreted as

antecrysts, as the $^{206}Pb/^{238}U$ dates (146.9±3.5, 147.3±2.7, 148.9±3.0 Ma) of the grains are several million years older than the mean date of the sample zircon population. The youngest zircon U-Pb result (zircon 30-2; 126.5±2.1 Ma) analytical spot was from a younger growth zone cross-cutting and rimming a core with >40% discordance (zircon 30-1). Zircon 30-2 was not included in the weighted mean as it may represent a later crystallized growth zone that is not representative of the zircon population, or it may have experienced undetected Pb-loss.

The remaining interpreted magmatic zircons range from 130.7±3.3 to 139.9±2.3 Ma (MSWD=6.3). This high MSWD indicates the data may not represent a single population; however, CL and BSE images, $\delta^{18}O$, Hf, and trace elements do not provide clear evidence of the presence of multiple populations. Lacking such discriminatory criteria, the remaining zircon were treated as a single population. As such, the age presented must be viewed as an initial estimate of the age, pending further refinement.

The higher-than-expected MSWD for the number of analyses (Spencer et al., 2016) was attributed to overdispersion due to geological scatter (Vermeesch, 2018). Using the model-3 method of dealing with overdispersion outlined by Vermeesch (2018), an excess scatter constant of 2.18 was calculated and added to the individual uncertainties of the remaining data to reduce the MSWD to unity. This method did not significantly change the resulting weighted mean $^{206}Pb/^{238}U$ age, nor the uncertainty of the weighted mean. Twenty zircon results have a weighted mean $^{206}Pb/^{238}U$ date of 135.4±0.9 Ma (MSWD=1.4; $p(\chi^2)=0.11$). The weighted mean is interpreted as the best estimate for the crystallization age of K-feldspar porphyritic granite sample 18lo12-7 (Figure 3.2.1.11; Table 3.2.1.1).

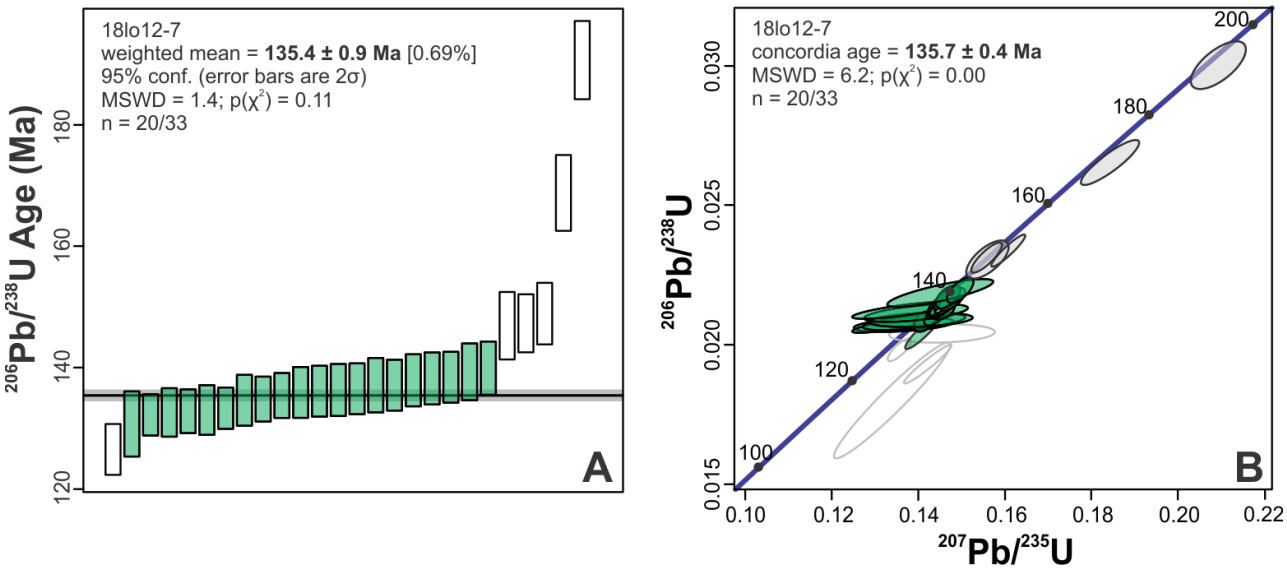

Figure 3.2.1.11. A) The weighted mean of zircon $^{206}Pb/^{238}U$ dates, interpreted as the crystallization age, of Mesilinka K-feldspar phenocrystic granite sample 18lo12-7. White bars are zircon grains interpreted as xenocrystic or antecrystic and were excluded from the weighted mean calculation. The black line is the weighted mean, and the grey bar is the 2σ uncertainty of the mean. **B)** Wetherhill concordia plot of zircon $^{206}Pb/^{238}U$ and $^{207}Pb/^{235}U$ ratio results for 18lo12-7. Closed grey ellipses are zircon grains that passed data screenings, but are interpreted as antecrystic or xenocrystic. Open grey ellipses are data screened for >5% discordance and/or >1% $f^{206}Pb_C$. Uncertainties and ages are reported at the 95.4% confidence level (2σ).

Equigranular granite: 18lo11-1

Zircons from Mesilinka equigranular granite sample 18lo11-1 are typically clear-pink, euhedral, and 100 to 430 µm long. Internal textures are well preserved, with oscillatory growth zoning. The $^{206}Pb/^{204}Pb$ ratio in zircon ranges between 700 and 840000. Several grains have overgrown rims that cross-cut older growth zones or cores (Appendix C). Forty-eight spots from 40 zircons were analyzed from sample 18lo11-1. Eleven analyses were rejected for $f^{206}Pb_c$ >1% and/or >5% discordance. Three zircons were not included in age calculations, as these grains are interpreted as antecrysts or xenocrysts. In CL images, these zircons have bright cores that are crosscut by darker rims (Zircons 8, 22, and 35; Appendix C). The youngest zircon (122.1±3.3 Ma; zircon 27) was rejected due to possible undetected Pb-loss and large uncertainty in the $^{206}Pb/^{238}U$ result.

The 34 remaining zircons range have $^{206}Pb/^{238}U$ dates from 123.3±1.7 to 132.2±2.0 Ma (MSWD=9.7). This high MSWD indicates the data may not represent a single population; however, CL and BSE images, $\delta^{18}O$, Hf, trace elements do not provide clear evidence of the presence of multiple zircon populations and the remaining zircons were treated as a single

population. As such, the age presented must be viewed as an initial estimate of the age, pending further refinement.

The higher-than-expected MSWD for the number of analyses (Spencer et al., 2016) was attributed to overdispersion due to geological scatter (Vermeesch, 2018). Using the model-3 method of dealing with overdispersion outlined by Vermeesch (2018), an excess scatter constant of 2.23 was calculated and added to the individual uncertainties of filtered data to reduce MSWD to unity. This method did not change the resulting weighted mean $^{206}Pb/^{238}U$ age, nor significantly increase the uncertainty of the weighted mean. Thirty-four remaining results have a weighted mean $^{206}Pb/^{238}U$ date of 127.7±0.8 Ma (MSWD=1.5; $p(\chi^2)$=0.02). The weighted mean is interpreted as the best estimate for the crystallization age of equigranular granite sample 18lo11-1 (Figure 3.2.1.12; Table 3.2.1.1).

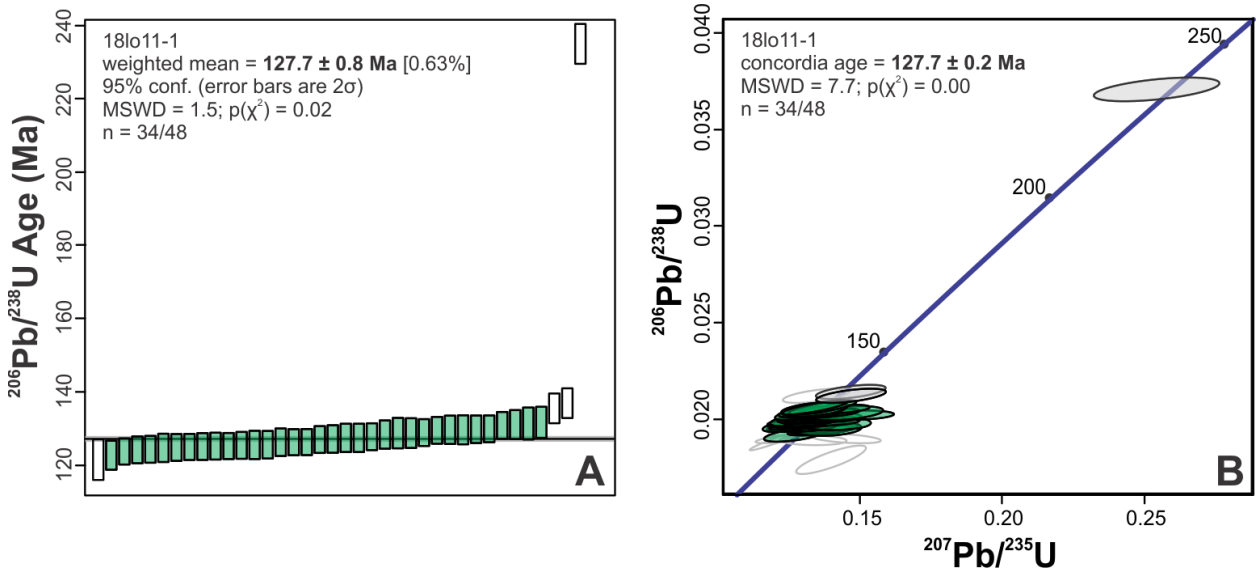

Figure 3.2.1.12. A) The weighted mean of zircon $^{206}Pb/^{238}U$ dates, interpreted as the crystallization age, of Mesilinka equigranular granite sample 18lo11-1. White bars are zircon grains interpreted as xenocrystic or antecrystic or data with potential Pb-loss, and were excluded from the weighted mean calculation. The black line is the weighted mean, and the grey bar is the 2σ uncertainty of the mean. **B)** Wetherhill concordia plot of zircon $^{206}Pb/^{238}U$ and $^{207}Pb/^{235}U$ ratio results for 18lo11-1. Closed grey ellipses are zircon grains that passed data screenings, but are interpreted as antecrystic or xenocrystic, or potentially have undetected Pb-loss. Open grey ellipses are data points screened for >5% discordance and/or >1% $f^{206}Pb_C$. Uncertainties and ages are reported at the 95.4% confidence level (2σ).

Equigranular granite: 19GJ16-2

Zircons from Mesilinka equigranular granite sample 19GJ16-2 are typically clear-pink, euhedral, and 80 to 160 μm long. Internal textures are well preserved, with generally oscillatory growth zoning. The $^{206}Pb/^{204}Pb$ ratio in zircon ranges between 400 and 70000. Several grains have overgrown rims that cross-cut core older zones or bright cores (Appendix C).

Thirty-three spots from 33 zircons were analyzed from sample 19GJ16-2. Seventeen analyses were rejected for $f^{206}Pb_c$ >1% and/or >5% discordance. Three zircons (Zircons 19, 46, and 56; Appendix C) were not included in age calculations. Zircon 56 was interpreted as an antecryst or xenocryst because the grain has a bright core crosscut by a darker rim in the CL image. Zircon 46 was interpreted as an antecryst or xenocryst, as the CL image shows the grain has a rounded, darker core embayed within a brighter growth zoned rim (Appendix C). The $^{206}Pb/^{238}U$ date result for zircon 19 (120.1±2.4 Ma) was screened out, as the analytical spot was located on a fracture. Zircon 19 was not analyzed for trace elements, so supplementary trace element data is unavailable to use as a check for alteration.

The thirteen remaining zircons range in apparent $^{206}Pb/^{238}U$ age from 122.8±2.0 to 131.5±2.5 Ma (MSWD=5.7). This high MSWD indicates the data may not represent a single population; however, CL and BSE images and $\delta^{18}O$ do not indicate multiple populations. Due to zircon grain size limitations in this sample, Hf and trace element data were collected wherever a LASS spot could fit on the grain. In most cases, Hf and trace element data were collected in overlapping or separate growth zones from U-Pb analytical spots. For this reason, the Hf and trace element data is not a high enough resolution to provide evidence of multiple U-Pb age populations in this sample. Lacking additional discriminatory data, the remaining zircons were treated as a single population. As such, the age presented must be viewed as an initial estimate of the age, pending further refinement.

The higher-than-expected MSWD for the number of analyses (Spencer et al., 2016) was attributed to overdispersion due to geological scatter (Vermeesch, 2018). Using the model-3 method of dealing with overdispersion outlined by Vermeesch (2018), an excess scatter constant of 2.58 was calculated and added to the individual uncertainties of the remaining data to decrease the MSWD of the weighted mean $^{206}Pb/^{238}U$ date. This method did not change the resulting weighted mean $^{206}Pb/^{238}U$ age, nor increase the uncertainty of the weighted mean. Thirteen remaining zircons have a weighted mean $^{206}Pb/^{238}U$ date of 127.1±1.6 Ma (MSWD=1.4;

p(χ^2)=0.18). This weighted mean is interpreted as the best estimate for the crystallization age of equigranular granite sample 19GJ16-2 (Figure 3.2.1.13; Table 3.2.1.1).

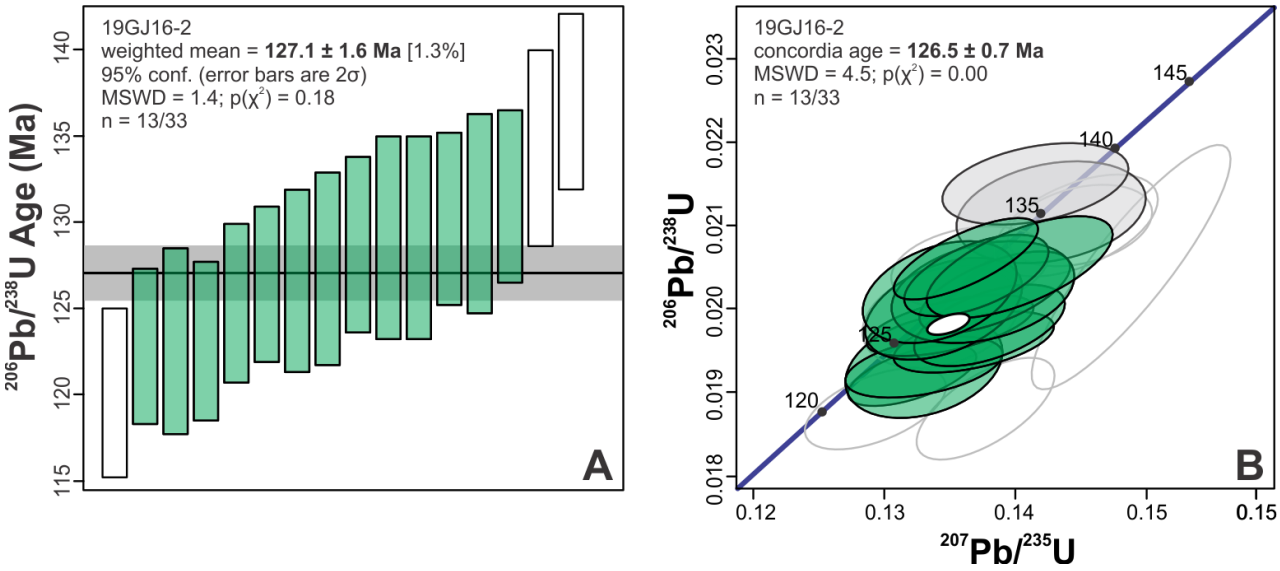

Figure 3.2.1.13. A) The weighted mean of zircon $^{206}Pb/^{238}U$ dates, interpreted as the crystallization age, of Mesilinka equigranular granite sample 19GJ16-2. White bars are zircon grains interpreted as xenocrystic or antecrystic, or potentially have Pb-loss, and were excluded from the weighted mean calculation. The black line is the weighted mean, and the grey bar is the 2σ uncertainty of the mean. **B)** Wetherhill concordia plot of $^{206}Pb/^{238}U$ and $^{207}Pb/^{235}U$ ratio results for 19GJ16-2. Closed grey ellipses are zircon grains that passed data screening, but are interpreted as antecrystic or xenocrystic, or potentially have Pb-loss. Open grey ellipses are data points screened for >5% discordance and/or >1% $f^{206}Pb_C$. Uncertainties and ages are reported at the 95.4% confidence level (2σ).

3.2.1.2 Titanite U-Pb Geochronology

Titanite U-Pb LA-ICP-MS results are reported in the BCGS Geofile (in preparation) and summarized in Table 3.2.1.2. Titanite LA-ICP-MS U-Pb results are plotted on Tera-Wasserburg diagrams, using uncorrected $^{238}U/^{206}Pb$ and $^{207}Pb/^{206}Pb$ ratios. A regression line was fit through the data for each sample to form an isochron. The lower intercept of the isochron with the concordia curve yields the approximate age of the titanite population for each sample. The upper intercept is indicative of the common Pb composition of the system. Individual data points which did not overlap with the regression line were excluded to reduce scatter, indicated by MSWD and p(χ^2) values closer to one.

Table 3.2.1.2. Summary of LA-ICP-MS U-Pb intercept age results for unknown titanite grains.

Sample	Intrusive Suite	U-Pb intercept age, Ma (2SE)	No. analyses	MSWD	p(χ^2)
19GJ13-3	Thane Creek	197.5±3.7	9/14	2.4	0.02
19GJ13-2	Duckling Creek	177.4±7.0	7/8	1.9	0.09
19GJ13-4	Duckling Creek	174.4±2.2	7/8	1.7	0.13
19GJ12-2	Mesilinka	145.8±4.6	7/9	1.5	0.17
19GJ12-1	Mesilinka	122.0±2.8	7/12	2.8	0.02

Thane Creek suite

Quartz monzodiorite: 19GJ13-3

Titanite grains from Thane Creek quartz monzodiorite sample 19GJ13-3 have a U-Pb intercept age of 197.5±3.7 Ma (Figure 3.2.1.14; Table 3.2.1.2). Five titanite results were excluded from the regression to reduce scatter, yielding an MSWD of 2.4 (n=9/14). This titanite U-Pb intercept age overlaps with the interpreted zircon crystallization age of the same sample (194.0±1.1 Ma; section 3.2.1.1). The titanite U-Pb intercept age is interpreted as the magmatic crystallization age of titanite, which occurred prior to and synchronous with zircon crystallization. Petrographic identification of zircon inclusions within titanite grains in sample 19GJ13-3 supports this interpretation (Appendix A2).

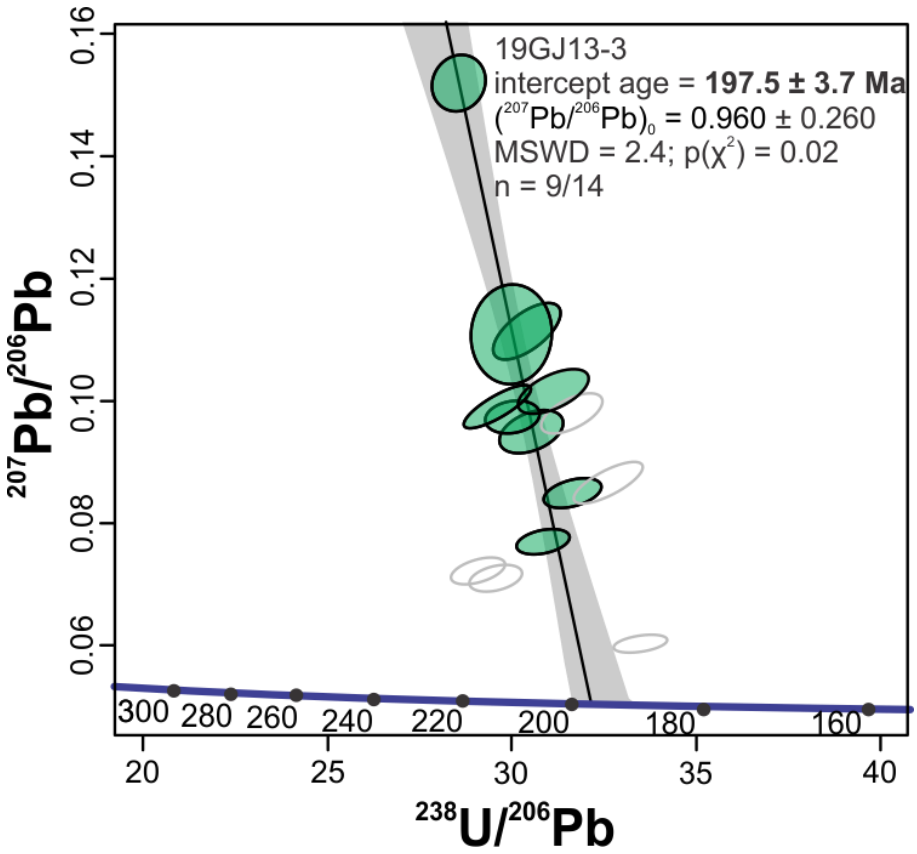

Figure 3.2.1.14. Tera-Wasserburg plot of $^{206}Pb/^{238}U$ versus $^{207}Pb/^{206}Pb$ results, with discordia U-Pb age lower intercept, for titanite grains from Thane Creek quartz monzodiorite sample 19GJ13-3. Grey ellipses were excluded from the regression to reduce scatter. Uncertainties and ages are reported at the 95.4% confidence level (2σ).

Duckling Creek suite

Syenite: 19GJ13-2

Titanite grains from Duckling Creek syenite sample 19GJ13-2 have a U-Pb intercept age of 177.4±7.0 Ma (Figure 3.2.1.15; Table 3.2.1.2). One titanite result was excluded from the regression to reduce scatter, yielding an MSWD of 1.9 and $p(\chi^2)$ of 0.09 (n=7/8). This titanite U-Pb intercept age may be interpreted as the magmatic crystallization age of titanite, due to the overlap with interpreted U-Pb zircon crystallization ages of two other Duckling Creek syenite samples (179.0±1.0 Ma and 174.7±0.7 Ma; section 3.2.1.1). It is unclear if titanite grains in sample 19GJ13-2 are magmatic as subhedral titanite grains are spatially associated with biotite inclusions in feldspar, and form intercumulus patches with magmatic biotite, magnetite, and secondary muscovite and epidote between K-feldspar phenocrysts (Figure 1.5.2).

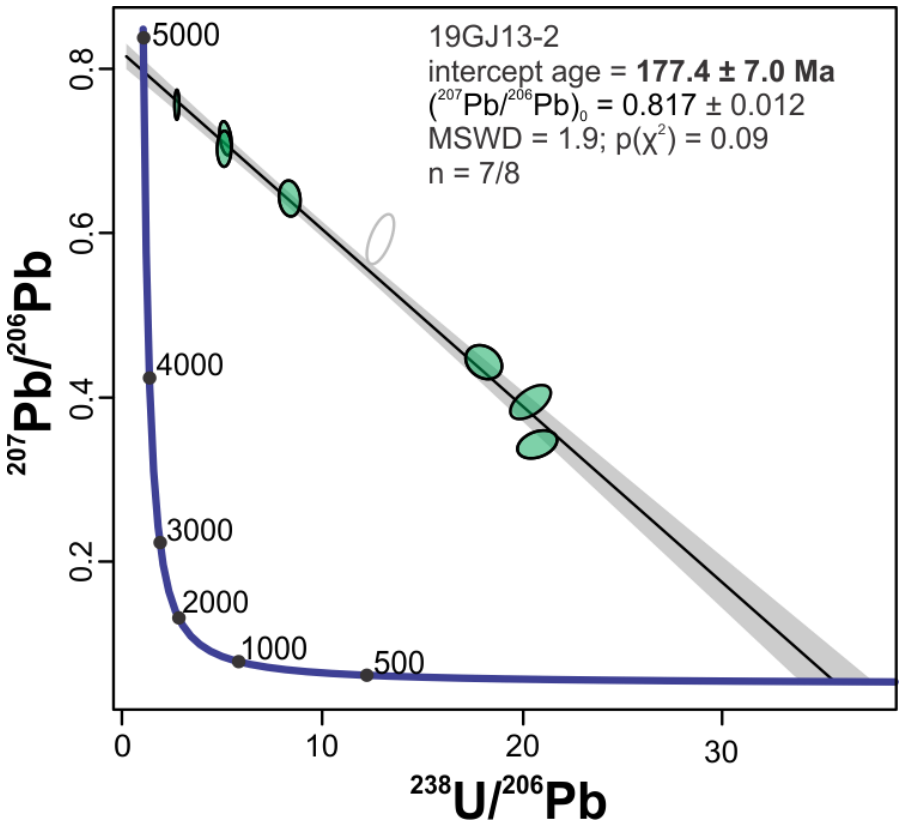

Figure 3.2.1.15. Tera-Wasserburg plot of $^{238}U/^{206}Pb$ versus $^{207}Pb/^{206}Pb$ results, with discordia U-Pb age lower intercept, for titanite grains from Duckling Creek syenite sample 19GJ13-2. Grey ellipses were excluded from the regression to reduce scatter. Uncertainties and ages are reported at the 95.4% confidence level (2σ).

Syenite: 19GJ13-4

Titanite grains from Duckling Creek syenite sample 19GJ13-4 have a U-Pb intercept age of 174.4±2.2 Ma (Figure 3.2.1.16; Table 3.2.1.2). One titanite result was excluded from the regression to reduce scatter, yielding an MSWD of 1.7 and probability of fit of 0.13 (n=7/8). This titanite U-Pb intercept age is interpreted as the magmatic crystallization age of titanite, due to the overlap and close agreement with the interpreted zircon U-Pb crystallization age of Duckling Creek syenite sample 19GJ13-5a (174.7±0.7 Ma; section 3.2.1.1). Titanite grains in sample 19GJ13-4 appear magmatic in thin section, as they form subhedral to euhedral, wedge-shaped crystals spatially associated with amphibole, biotite, and apatite (Figure 1.5.2G-H).

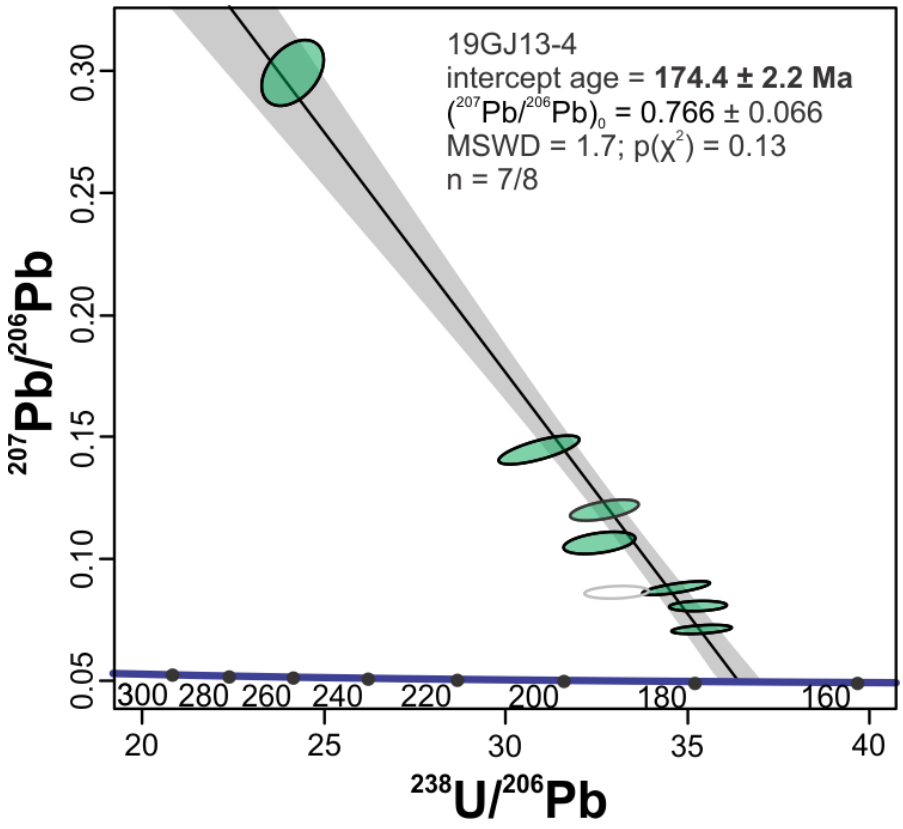

Figure 3.2.1.16. Tera-Wasserburg plot of $^{206}Pb/^{238}U$ versus $^{207}Pb/^{206}Pb$ results, with discordia U-Pb age lower intercept, for titanite grains from Duckling Creek syenite sample 19GJ13-4. Grey ellipses were excluded from the regression. Uncertainties and ages are reported at the 95.4% confidence level (2σ).

Mesilinka suite

Tonalite: 19GJ12-2

Titanite grains from Mesilinka tonalite sample 19GJ12-2 have a U-Pb intercept age of 145.8±4.6 Ma (Figure 3.2.1.17; Table 3.2.1.2). Two titanite data points were excluded from the regression to reduce scatter, yielding an MSWD of 1.5 and probability of fit of 0.17 (n=7/9). This titanite U-Pb intercept age is interpreted as the magmatic crystallization age of titanite. Sample 19GJ12-2 did not yield zircon grains, so there is not a zircon U-Pb age available for comparison and thus the titanite age is the best current estimate for the crystallisation age of this unit.

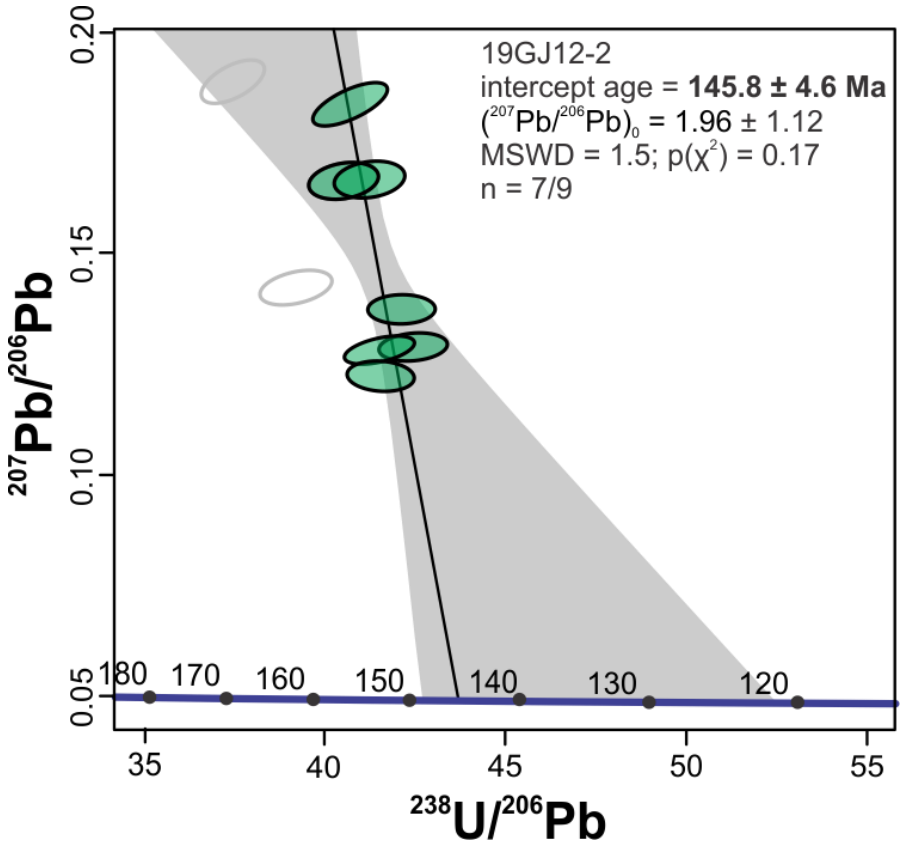

Figure 3.2.1.17. Tera-Wasserburg plot of $^{206}Pb/^{238}U$ versus $^{207}Pb/^{206}Pb$ results, with discordia U-Pb age intercept, for titanite grains from Mesilinka tonalite sample 19GJ12-2. Grey ellipses were excluded from the regression. Uncertainties and ages are reported at the 95.4% confidence level (2σ).

Tonalite: 19GJ12-1

Titanite grains from Mesilinka tonalite sample 19GJ12-1 have a U-Pb intercept age of 122.0±2.8 Ma (Figure 3.2.1.18; Table 3.2.1.2). Five titanite data points were excluded from the regression to reduce scatter, yielding an MSWD of 2.8 (n=7/12), which indicates there is some scatter in the data. Titanite grains in sample 19GJ12-1 are spatially associated with biotite, epidote, and apatite, and weakly define a foliation. As the titanite U-Pb intercept age is younger than the interpreted zircon crystallization age of sample 19GJ12-1 (134.1±0.5 Ma; section 3.2.1.1), this titanite U-Pb intercept age likely represents a post-deformation cooling age. However, the scatter in the data (MSWD >2) and exclusion of multiple results makes this titanite U-Pb intercept age difficult to confidently assess and further work would be needed to constrain this possibility more confidently.

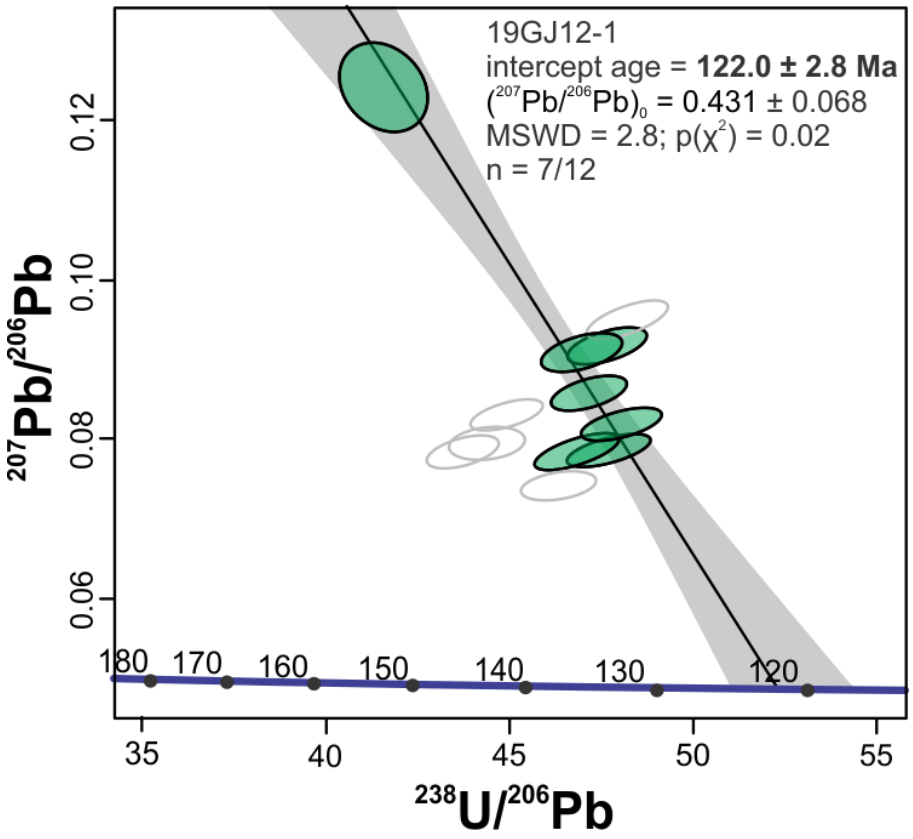

Figure 3.2.1.18. Tera-Wasserburg plot of $^{206}Pb/^{238}U$ versus $^{207}Pb/^{206}Pb$ results, with discordia U-Pb age intercept, for titanite grains from Mesilinka tonalite sample 19GJ12-1. Grey ellipses were excluded from the regression. Uncertainties and ages are reported at the 95.4% confidence level (2σ).

3.2.2 Zircon SIMS Oxygen Isotope Results

A total of 488 in situ $^{18}O/^{16}O$ analyses were conducted on zircon grains from 13 intrusive rock samples. These results are reported in the BCGS Geofile (in preparation). The average zircon oxygen-isotope compositions from each sample, reported as $\delta^{18}O_{VSMOW}$, are summarized in Table 3.2.2.1.

Table 3.2.2.1. Summary of mean $\delta^{18}O_{VSMOW}$ results for unknown zircons.

Sample	Intrusive Suite	$\delta^{18}O_{VSMOW}$ mean (‰)	2 SE	Median	No. analyses
19GJ12-4	Thane Creek	+5.89	0.36	+5.59	30
18lo22-1a	Thane Creek	+6.02	0.04	+6.02	43
18lo22-1d	Thane Creek	+6.30	0.03	+6.30	49
19GJ13-3	Thane Creek	+5.57	0.03	+5.58	55
18lo25-2a	Duckling Creek	+6.55	0.03	+6.56	45
19GJ13-5a	Duckling Creek	+6.12	0.07	+6.17	39
18lo17-1	Osilinka	+6.30	0.66	+6.02	23
19GJ12-3	Osilinka	+5.80	0.18	+5.77	23
18lo20-4	Osilinka	+5.32	0.31	+5.25	17
19GJ12-1	Mesilinka	+5.67	0.13	+5.58	43
18lo12-7	Mesilinka	+7.18	0.13	+7.25	32
18lo11-1	Mesilinka	+7.44	0.26	+7.38	47
19GJ16-2	Mesilinka	+6.49	0.47	+5.88	42

Thane Creek suite

Thane Creek zircon $\delta^{18}O$ compositions range from +4.95 to +8.52‰, with the majority (n=170/177) between +5.00 and +6.50‰ (Figures 3.2.2.1 and 3.2.2.2; Table 3.2.2.1).

Thane Creek intrusive suite rock samples 18lo22-1a, 18lo22-1d, and 19GJ13-3 have relatively similar zircon $\delta^{18}O$ ranges and means. Zircon from hornblendite (sample 18lo22-1a) have $\delta^{18}O$ from +5.77 to +6.30‰, with a mean of +6.02‰ (n=43). Quartz monzodiorite (sample 19GJ13-3) zircon have $\delta^{18}O$ from +5.22 to +6.05‰, with a mean of 5.57‰ (n=55). Zircon $\delta^{18}O$ results from quartz diorite (sample 18lo22-1d) range from +6.06 to +6.53‰, with a mean of +6.30‰ (n=49).

Zircons from quartz diorite (sample 19GJ12-4) have $\delta^{18}O$ from +4.95 to +8.52‰, with a mean of 5.89‰ (n=30). Most zircon $\delta^{18}O$ results are within a ~1‰, from +4.95 to +6.03‰. Four zircon grains have elevated $\delta^{18}O$ from +7.77 to +8.52‰.

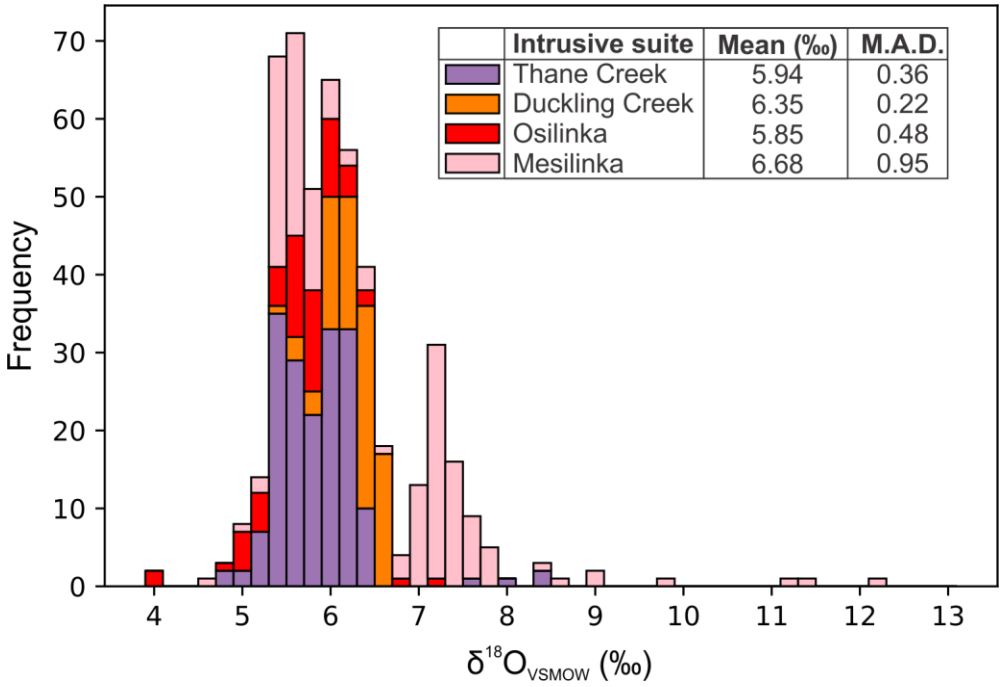

Figure 3.2.2.1. Frequency of zircon $\delta^{18}O_{VSMOW}$ (‰) results for Thane Creek, Duckling Creek, Osilinka, and Mesilinka suite intrusive rock samples. Bin size= 0.2. M.A.D.= mean absolute deviation.

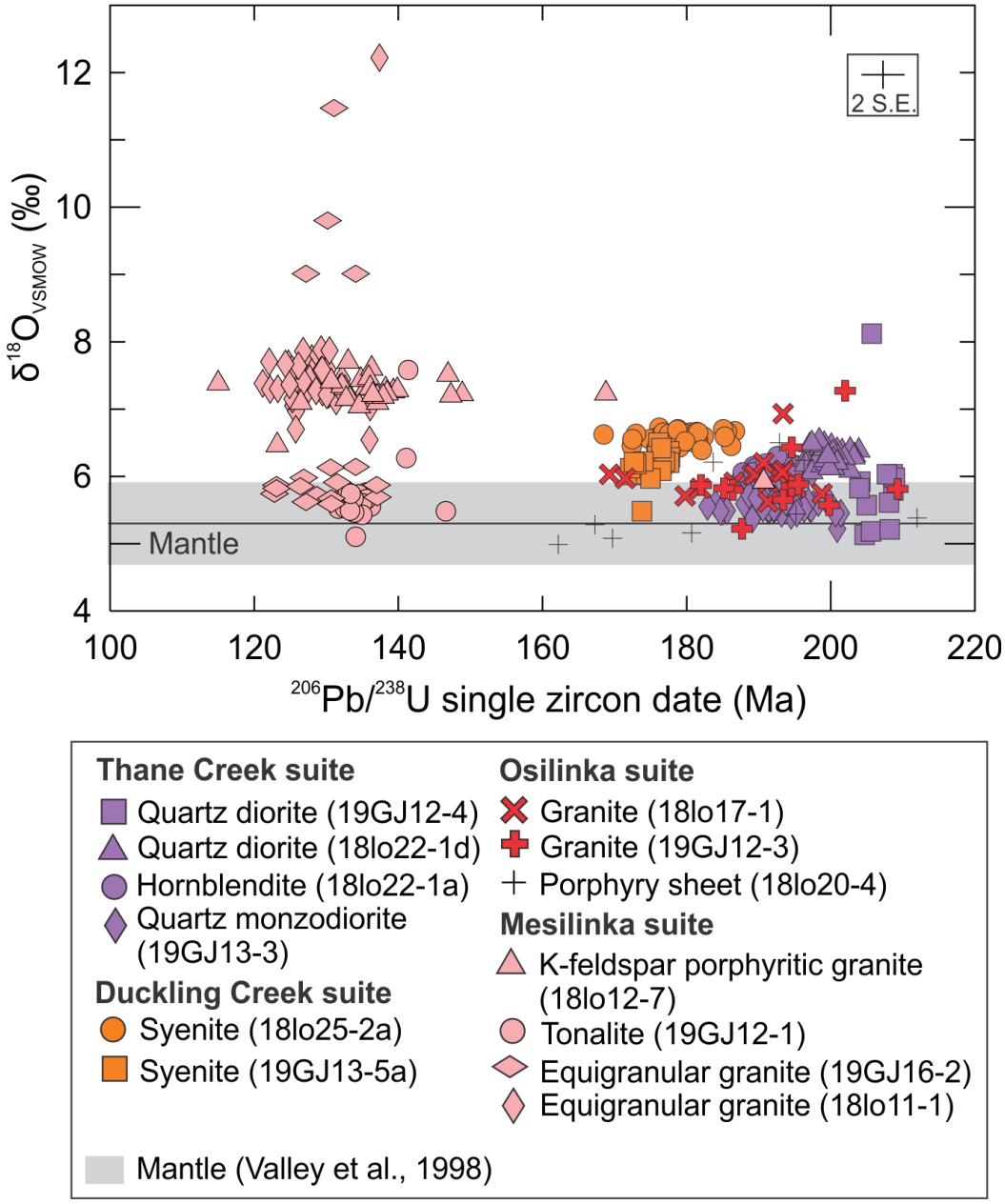

Figure 3.2.2.2. Single zircon $^{206}Pb/^{238}U$ dates versus corresponding $\delta^{18}O_{VSMOW}$ (‰) values for zircons from Hogem batholith intrusive rock samples. Zircon data was screened to exclude U-Pb results with >10% discordance. The grey bar represents the $\delta^{18}O$ range of the mantle (5.3±0.6 ‰; Valley et al., 1998). 2 S.E.= average 2σ standard error of all data points.

$$\delta^{18}O_{VSMOW} = \left(\frac{\left(^{18}O/^{16}O_{SAMPLE}\right)}{\left(^{18}O/^{16}O_{VSMOW}\right)} - 1\right) \times 1000$$, where $^{18}O/^{16}O_{VSMOW} = 0.0020052$ (Baertschi, 1976).

Duckling Creek suite

Duckling Creek zircon $\delta^{18}O$ compositions range from +5.48 to +6.72‰ with the majority (n=77/84) between +6.00 and +6.72‰ (Figure 3.2.2.1; Table 3.2.2.1).

Zircon from syenite (sample 18lo25-2a) have $\delta^{18}O$ ranging from +6.20 to +6.72‰, with a mean of +6.55‰ (n=45).

Zircon $\delta^{18}O$ results from syenite (sample 19GJ13-5a) range from +5.48 to +6.50‰, with a mean of +6.12‰ (n=39). Seven zircon grains have $\delta^{18}O$ from +5.48 to +6.00‰, while the remaining 32 zircons have $\delta^{18}O$ greater than +6.00‰ (Figure 3.2.2.2).

Osilinka suite

Osilinka zircon $\delta^{18}O$ compositions range from +4.11 to +13.45‰, but predominantly (n=41/63) from +5.00 to +6.00‰ (Figures 3.2.2.1 and 3.2.2.2; Table 3.2.2.1). As most Osilinka suite zircons are interpreted as inherited (section 3.2.1.1.), these $\delta^{18}O$ values represent the oxygen-isotope composition(s) of the primary magma source(s).

Zircon grains from granite (sample 18lo17-1) have $\delta^{18}O$ from +5.62 to +13.45‰, with a mean of +6.30‰ (n=23). Eleven zircon grains have $\delta^{18}O$ less than +6.00‰, and eleven zircon grains have $\delta^{18}O$ from +6.00‰ to +6.93‰. One zircon has an anomalously high $\delta^{18}O$ composition (+13.45‰). This grain shows no zonation in the CL image (zircon 17; Appendix C. Zircon SEM images and analytical spots) and has internal textures unlike any of the other zircons in the sample. Due to the otherwise relatively homogenous zircon $\delta^{18}O$ results in this sample, zircon 17 was interpreted as a contaminant grain included during crushing or mineral separation. No other discriminatory data (U-Pb, Lu-Hf, trace elements) were collected on this grain for further characterization.

Zircon grains from granite (sample 19GJ12-3) have $\delta^{18}O$ from +5.15 to +7.27‰, with a mean of +5.80‰ (n=23). Most zircon $\delta^{18}O$ results are less than +6.00‰ (n=19/23). Four zircons have slightly elevated $\delta^{18}O$ (+6.02 to +7.27‰).

Zircon grains from porphyry sheet (sample 18lo20-4) have $\delta^{18}O$ from +4.11 to +6.50‰, with a mean of +5.32‰ (n=17). Most zircons have $\delta^{18}O$ between +5.00 and +6.00‰ (n=11/17). Three zircons have slightly higher $\delta^{18}O$ (+6.21 to +6.50‰), and three zircons have slightly lower $\delta^{18}O$ (+4.11 to +4.99‰).

Mesilinka suite

Mesilinka zircon $\delta^{18}O$ compositions range from +4.68 to +12.22‰ (Figure 3.2.2.1; Table 3.2.2.1). There are two main distributions of zircon $\delta^{18}O$, with values from +5.00 to 6.00‰ (n=69/164) and from +7.00 to 8.00‰ (n=72/164).

Zircons from tonalite (sample 19GJ12-1) have $\delta^{18}O$ from +5.10 to +7.58‰, with a mean of 5.67‰ (n=43). Most zircons have $\delta^{18}O$ less than +6.00‰ (n=40/43). Three zircons have $\delta^{18}O$ greater than +6.00‰ (+6.27 to +7.58‰).

Zircon grains from granite (sample 18lo12-7) have $\delta^{18}O$ from +5.92 to +7.70‰, with a mean of 7.18‰ (n=32). Most zircons have $\delta^{18}O$ greater than +7.00‰ (n=29/34). Three zircons have $\delta^{18}O$ from +6.32 to +6.93‰, while only one zircon has $\delta^{18}O$ less than +6.00‰.

Zircons from granite (sample 18lo11-1) have $\delta^{18}O$ from +4.68 to +12.22‰, with a mean of 7.44‰ (n=47). Most zircons have $\delta^{18}O$ from +7.00 to +8.00‰ (n=40/47). Four zircons have $\delta^{18}O$ from +6.00 to +7.00‰. One zircon has an anomalously low $\delta^{18}O$ of +4.68‰ (zircon 22-1), and another grain has an anomalously high $\delta^{18}O$ of +12.22‰ (zircon 35-1). Both anomalous zircons were interpreted as antecrysts in section 3.2.1.1.

Zircons from granite (sample 19GJ16-2) have $\delta^{18}O$ from +5.43 to +11.47‰, with a mean of 6.49‰ (n=42). Most zircons have $\delta^{18}O$ between +5.00 and +6.00‰ (n=28/42). Six zircon grains have slightly elevated $\delta^{18}O$ (+6.02 to +6.53‰), and eight zircons have high $\delta^{18}O$ (+7.93 to +11.47‰).

3.2.3 Zircon Lu-Hf Results

Zircon LA-ICP-MS Lu-Hf results are reported in the BCGS Geofile (in preparation). These results are summarized in Table 3.2.3.1, and reported as εHf(t), as described in section 3.2.4. Zircon Lu-Hf results were screened by removing εHf(t) data with fully propagated 2σ uncertainties greater than 2ε units.

Thane Creek suite

Zircon from Thane Creek have εHf(t) from +8.2±1.6 to +12.1±1.5 (Figure 3.2.3.1). This is a relatively restricted range and is the most juvenile (mantle-like) zircon Hf range in the Hogem batholith (Figures 3.2.3.2 and 3.2.3.3).

Sixteen spots from 14 zircon grains from quartz diorite (sample 19GJ12-4) were analyzed for Lu-Hf isotopes (Figure 3.2.3.4A). After uncertainty screening, 11 spots from nine zircons remained. The remaining εHf(t) range from +9.8±1.5 to +12.1±1.5 (mean=+10.4; Table 3.2.3.1).

Forty-seven spots from 39 zircon grains from quartz diorite (sample 18lo22-1d) were analyzed for Lu-Hf isotopes (Figure 3.2.3.4B). Zircon εHf(t) range from +9.2±1.0 to +11.2±0.9 (mean=+10.0).

Forty-two Hf spots from 32 zircon grains from hornblendite (sample 18lo22-1a) were analyzed (Figure 3.2.3.4C). Zircon εHf(t) range from +8.2±1.6 to +11.1±1.5 (mean=+9.9).

Forty Hf spots from 31 zircon grains from quartz monzodiorite (sample 19GJ13-3) were analyzed (Figure 3.2.3.4D). The highest εHf(t) result was removed from the weighted mean, as the zircon grain was interpreted as antecrystic or xenocrystic using U-Pb data (section 3.2.1.1). The remaining zircon εHf(t) range from +9.1±1.4 to +11.2±1.2 (mean=+10.1).

Table 3.2.3.1. Summary of mean εHf(t) results and statistics for unknown zircon grains.

Sample	Intrusive Suite	Interpreted age (Ma)	εHf(t) weighted mean (±2SE)	No. analyses	MSWD	p(χ^2)
19GJ12-4	Thane Creek	206.8±0.9	+10.4±0.4	10/16	0.77	0.64
18lo22-1a	Thane Creek	191.4±0.7	+9.9±0.2	42/42	0.99	0.48
18lo22-1d	Thane Creek	199.6±0.7	+10.0±0.1	47/47	0.97	0.52
19GJ13-3	Thane Creek	194.0±1.1	+10.1±0.2	39/40	0.71	0.91
18lo25-2a	Duckling Creek	179.8±1.2	+9.1±0.1	44/45	1.1	0.38
19GJ13-5a	Duckling Creek	174.7±0.7	+9.3±0.3	25/29	0.92	0.57
18lo17-1	Osilinka	159.2±4.0	+9.3±0.2	23/24	1.3	0.19
19GJ12-3	Osilinka	159.2±4.0	+8.2±0.3	6/14	2.3	0.04
18lo20-4	Osilinka	162.2±2.6	+0.5±0.3	13/17	106	0.00
19GJ12-1	Mesilinka	134.1±0.5	+8.9±0.5	10/26	1.1	0.38
18lo12-7	Mesilinka	134.9±1.3	+5.7±0.2	24/33	0.90	0.60
18lo11-1	Mesilinka	127.7±0.7	+7.4±0.2	43/48	1.4	0.05
19GJ16-2	Mesilinka	127.1 ±1.6	+8.8±0.4	15/43	1.6	0.07

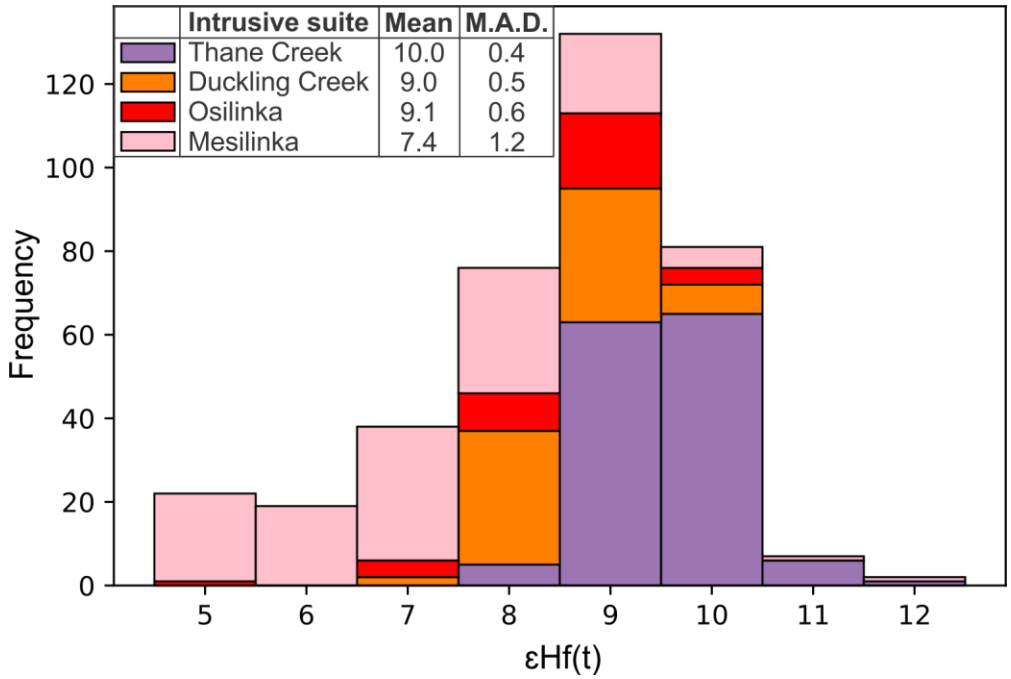

Figure 3.2.3.1. Frequency of zircon εHf(t) results for Thane Creek, Duckling Creek, Osilinka, and Mesilinka intrusive suite samples. Zircon data was screened to exclude εHf(t) results with propagated errors >2ε units. Bin size=1.0. M.A.D.= mean absolute deviation.

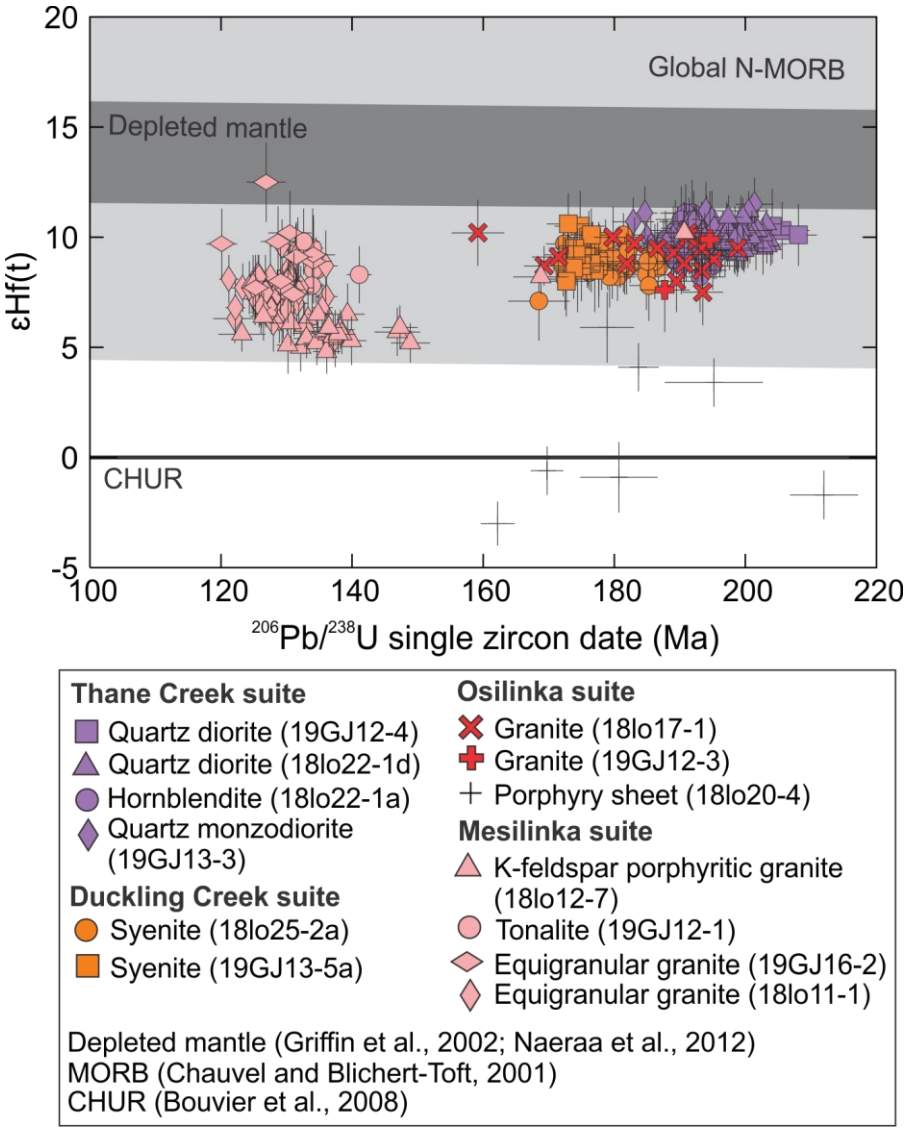

Figure 3.2.3.2. Single zircon $^{206}Pb/^{238}U$ dates versus corresponding εHf(t) values for zircons from Hogem batholith intrusive rock samples. Zircon data was screened to exclude εHf(t) results with propagated errors >2ε units and U-Pb results with >10% discordance. Uncertainties are at the 95.4% confidence level (2σ). CHUR= Chondritic uniform reservoir, after Bouvier et al. (2008). N-MORB= Normal mid ocean ridge basalt, after Chauvel and Blichert-Toft (2001). The upper depleted mantle limit is after Griffin et al. (2002) and lower depleted mantle limit is after Naeraa et al. (2012).

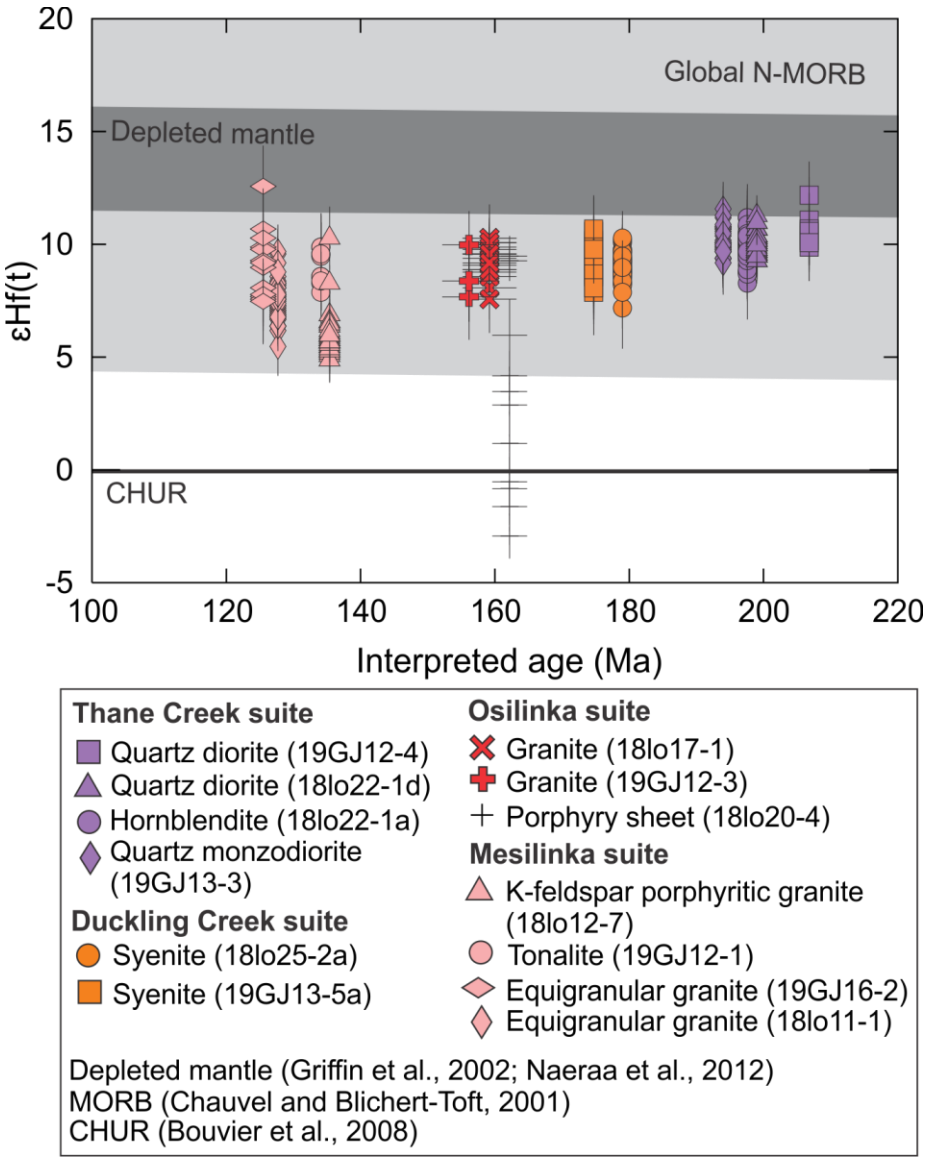

Figure 3.2.3.3. Interpreted crystallization age versus single zircon εHf(t) values of Hogem batholith intrusive rock samples. Zircon data was screened to exclude εHf(t) results with propagated errors >2ε units and U-Pb results with >10% discordance. Uncertainties are at the 95.4% confidence level (2σ). CHUR= Chondritic uniform reservoir, after Bouvier et al. (2008). N-MORB= Normal mid ocean ridge basalt, after Chauvel and Blichert-Toft (2001). The upper depleted mantle limit is after Griffin et al. (2002) and lower depleted mantle limit is after Naeraa et al. (2012).

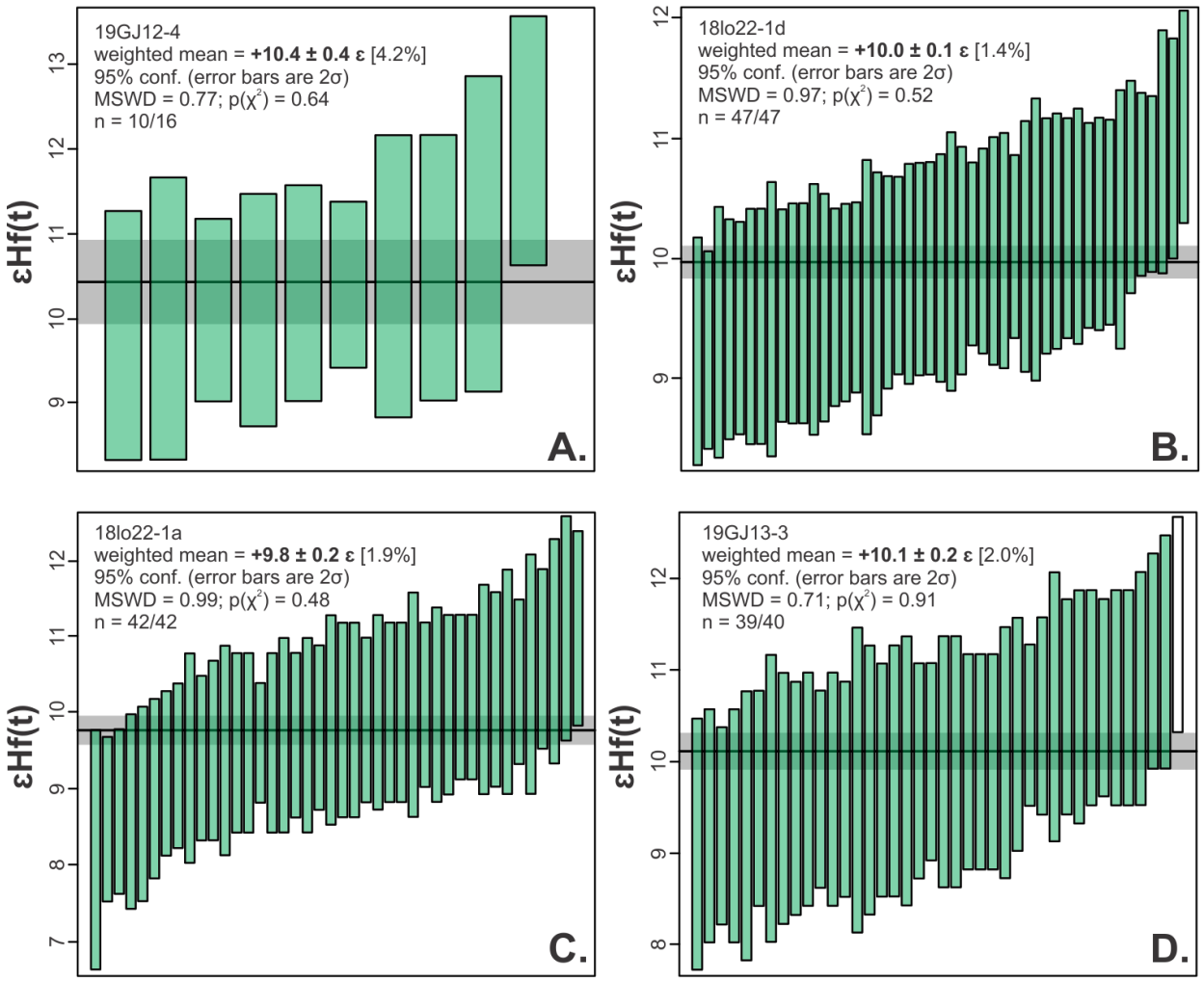

Figure 3.2.3.4. Weighted means of zircon εHf(t) results from Thane Creek intrusive suite **A)** Quartz diorite sample 19GJ12-4, **B)** Quartz diorite sample 18lo22-1d, **C)** Hornblendite sample 18lo22-1a, and **D)** Quartz monzodiorite sample 19GJ13-3. The white bar represents an antecrystic zircon and was not included in the weighted mean. Zircon data was screened to exclude εHf(t) results with propagated errors >2ε units. Uncertainties are displayed at the 95.4% confidence level (2σ). The black line is the weighted mean, and the grey bar is the 2σ uncertainty of the mean.

Duckling Creek suite

Zircon grains from Duckling Creek have εHf(0) compositions ranging from +3.9±1.9 to +6.7±1.4, corresponding to εHf(t) values of +7.8±1.9 to +10.6±1.4 (Figures 3.2.3.1-3.2.3.3).

Forty-six spots from 45 zircon grains from syenite (sample 18lo25-2a) were analyzed for Lu-Hf isotopes (Figure 3.2.3.5A). One zircon result (B-17) was removed from the weighted mean, as it had the lowest εHf(t) value and the greatest uncertainty. Additionally, the same analytical spot yielded a low $^{206}Pb/^{238}U$ date. The remaining 44 zircon results range in εHf(t) from +7.8±1.6 to +10.2±1.2 (mean=+9.1; Table 3.2.3.1).

Twenty-nine Hf spots from 28 zircon grains from syenite (sample 19GJ13-5a) were analyzed (Figure 3.2.3.5B). Four results were screened for yielding εHf(t) uncertainties greater than 2ε units. The remaining 25 results have εHf(t) from +7.8±1.9 to +10.6±1.4 (mean=+9.3).

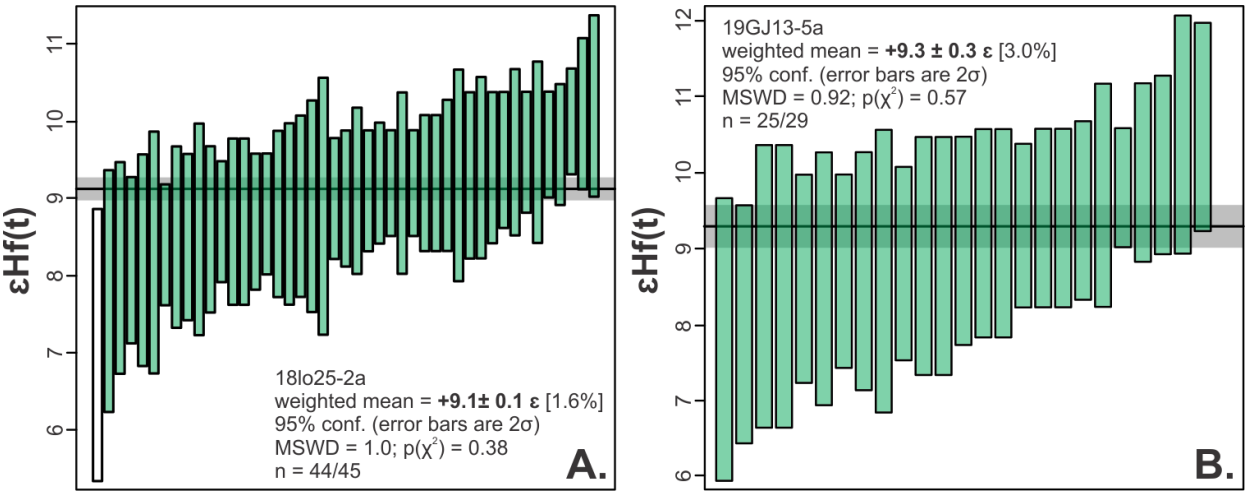

Figure 3.2.3.5. Weighted means of zircon εHf(t) results from Duckling Creek intrusive suite **A)** Syenite sample 18lo25-2a, and **B)** Syenite sample 19GJ13-5a. The white bar was not used in the weighted mean calculation, as this zircon had a lower εHf(t) and a greater uncertainty than other zircons in sample 18lo25-2a. Zircon data was screened to exclude εHf(t) results with propagated errors >2ε units. Uncertainties are displayed at the 95.4% confidence level (2σ). The black line is the weighted mean, and the grey bar is the 2σ uncertainty of the mean.

Osilinka Suite

Zircon grains from Osilinka suite have εHf(0) compositions ranging from -14.2±1.0 to +6.7±1.5, corresponding to εHf(t) values from -10.2±1.0 to +10.2±1.5 (Figures 3.2.3.1-3.2.3.3). Osilinka suite εHf(t) zircons have a ~10ε range, however the less radiogenic εHf(t) values (<+5.0ε) are strictly from the porphyry sheet sample 18lo20-4.

Twenty-four spots from 21 zircon grains from granite sample 18lo17-1 were analyzed for Lu-Hf isotopes (Figure 3.2.3.6A). One result was screened out from the weighted mean for εHf(t) uncertainty >2ε. The remaining 23 spots from 20 grains have εHf(t) from +7.5±1.5 to +10.2±1.5 (mean=+9.3; Table 3.2.3.1). Although the results cover a narrow spread (<3ε), the zircons were interpreted as inherited in this sample (section 3.2.1.1). The youngest zircon (159.2±4 Ma) has the second highest εHf(t) value (+10.2±1.5).

Fourteen spots from 14 zircon grains from granite sample 19GJ12-3 were analyzed for Lu-Hf isotopes (Figure 3.2.3.5B). Eight results were screened out for εHf(t) uncertainties >2ε. The remaining six results range in εHf(t) from +7.6±1.9 to +9.9±1.5 (mean=+8.2). Despite the narrow spread in the εHf(t) results, all the zircon grains in this sample were interpreted as inherited (section 3.2.1).

Seventeen spots from 13 zircon grains from porphyry sheet sample 18lo20-4 were analyzed for Lu-Hf isotopes (Figure 3.2.3.5C). The data range in εHf(t) from -10.2±1.0 to +9.4±0.9 and has a high degree of scatter (MSWD >100). The youngest interpreted zircon grain (162.2±2.6 Ma) has εHf(t) of -3.0±1.0.

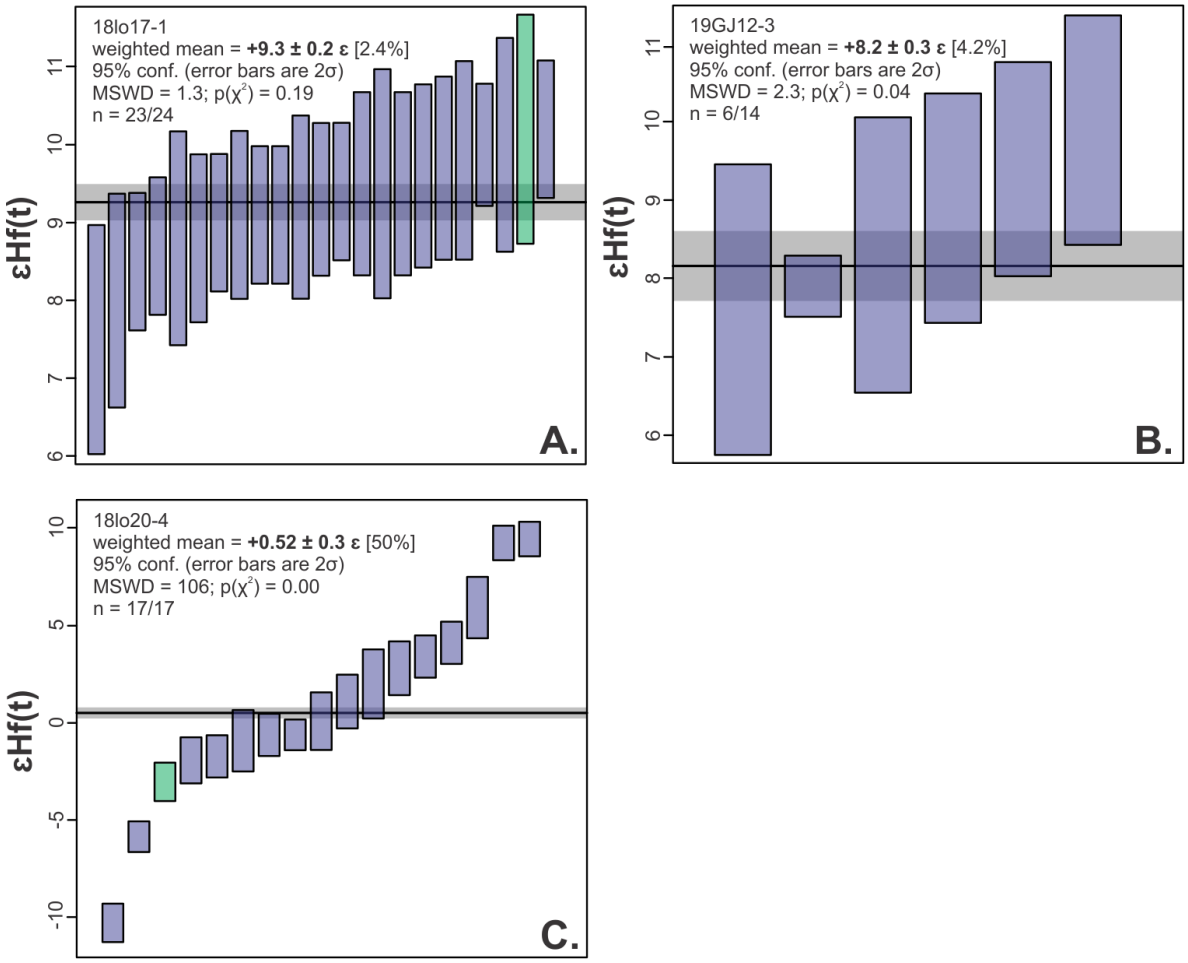

Figure 3.2.3.6. Weighted means of zircon εHf(t) results from Osilinka intrusive suite **A)** Granite sample 18lo17-1, **B)** Granite sample 19GJ12-3, and **C)** Porphyry sheet sample 18lo20-4. The blue bars represent zircons interpreted as inherited but were included in weighted mean calculations. The green bars represent the youngest zircon grains, which were used to determine the maximum crystallization ages of the rock samples. Zircon data was screened to exclude εHf(t) results with propagated errors >2ε units. Uncertainties are displayed at the 95.4% confidence level (2σ). The black line is the weighted mean, and the grey bar is the 2σ uncertainty of the mean.

Mesilinka suite

Zircon grains from Mesilinka suite have εHf(0) ranging from +1.8±1.0 to +9.7±1.8, corresponding to εHf(t) from +4.8±1.0 to +12.5±1.8 (Figure 3.2.3.1). Mesilinka suite has the least radiogenic εHf(t) values on average, but overall has relatively juvenile compositions (εHf(t) >+4; Figure 3.2.3.2 and 3.2.3.3).

Twenty-six spots from 26 zircon grains from tonalite (sample 19GJ12-1) were analyzed for Lu-Hf isotopes (Figure 3.2.3.6A). Fifteen results were screened for εHf(t) uncertainties >2ε. The lowest εHf(t) result (+7.6±1.1) was also screened, as this zircon was interpreted to be antecrystic or xenocrystic (zircon 51-1; section 3.2.1.1). The remaining ten zircons have εHf(t) from +7.8±1.4 to +9.8±1.5 (mean=+8.9).

Thirty-three spots from 22 zircon grains from K-feldspar porphyritic (sample 18lo12-7) were analyzed for Lu-Hf isotopes (Figure 3.2.3.6B). Two results were screened for εHf(t) uncertainties >2ε. Additionally, seven εHf(t) results from interpreted antecrystic or xenocrystic zircons (section 3.2.1.1) were screened out. The remaining 24 zircons have εHf(t) from +4.8±1.0 to +6.8±1.1 (mean=+5.7).

Forty-eight spots from 40 zircon grains from equigranular granite (sample 18lo11-1) were analyzed for Lu-Hf isotopes (Figure 3.2.3.6C). Four εHf(t) results from interpreted antecrystic or xenocrystic zircons, or zircons with suspect Pb-loss (section 3.2.1.1) were screened out. The highest εHf(t) result was treated as an outlier and excluded from the weighted mean. The remaining 43 results range in εHf(t) from +6.1±1.3 to +8.5±1.0 (mean=+7.4).

Forty-three spots from 43 zircon grains from equigranular granite sample (19GJ16-2) were analyzed for Lu-Hf isotopes (Figure 3.2.3.6D). Twenty-seven results were screened for εHf(t) uncertainties >2ε. The highest εHf(t) result (+12.5±1.8) was treated as an outlier and excluded from the weighted mean. The remaining 15 zircons have εHf(t) from +7.4±1.9 to +10.6±1.8 (mean=+8.8).

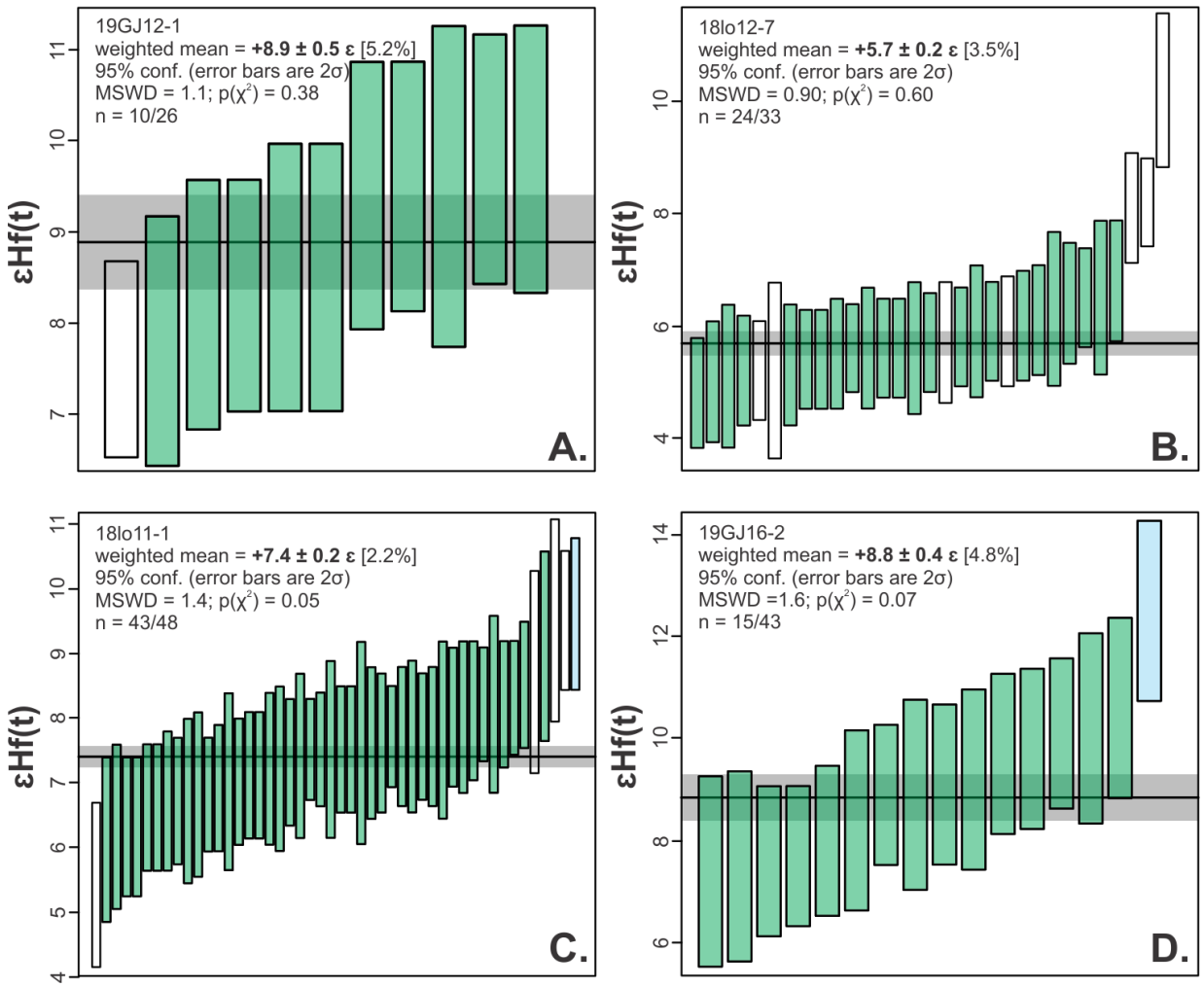

Figure 3.2.3.7. Weighted means of zircon εHf(t) results from Mesilinka intrusive suite **A)** Tonalite sample 19GJ12-1, **B)** K-feldspar phenocrystic granite sample 18lo12-7, **C)** Equigranular granite sample 18lo11-1, and **D)** Equigranular granite sample 19GJ16-2. The white bars are interpreted as inherited zircons, or zircons with potential Pb-loss issues, and were not included in the weighted means. The light blue bars represent outlier data and were not included in the weighted means. Zircon data was screened to exclude εHf(t) results with propagated errors >2ε units. Uncertainties are displayed at the 95.4% confidence level (2σ). The black line is the weighted mean, and the grey bar is the 2σ uncertainty of the mean.

3.2.4 Zircon Trace Element Results

Zircons from Hogem batholith intrusive rock samples have typical chondrite-normalized rare earth element trends with enriched HREEs relative to LREEs, positive Ce-anomalies, and negative Eu-anomalies (Figures 3.2.4.1-3.2.4.4). Duckling Creek syenite sample 18lo25-2a is an exception to these trends, as zircons from this sample have positive Ce-anomalies but lack Eu-anomalies (Figure 3.2.4.2).

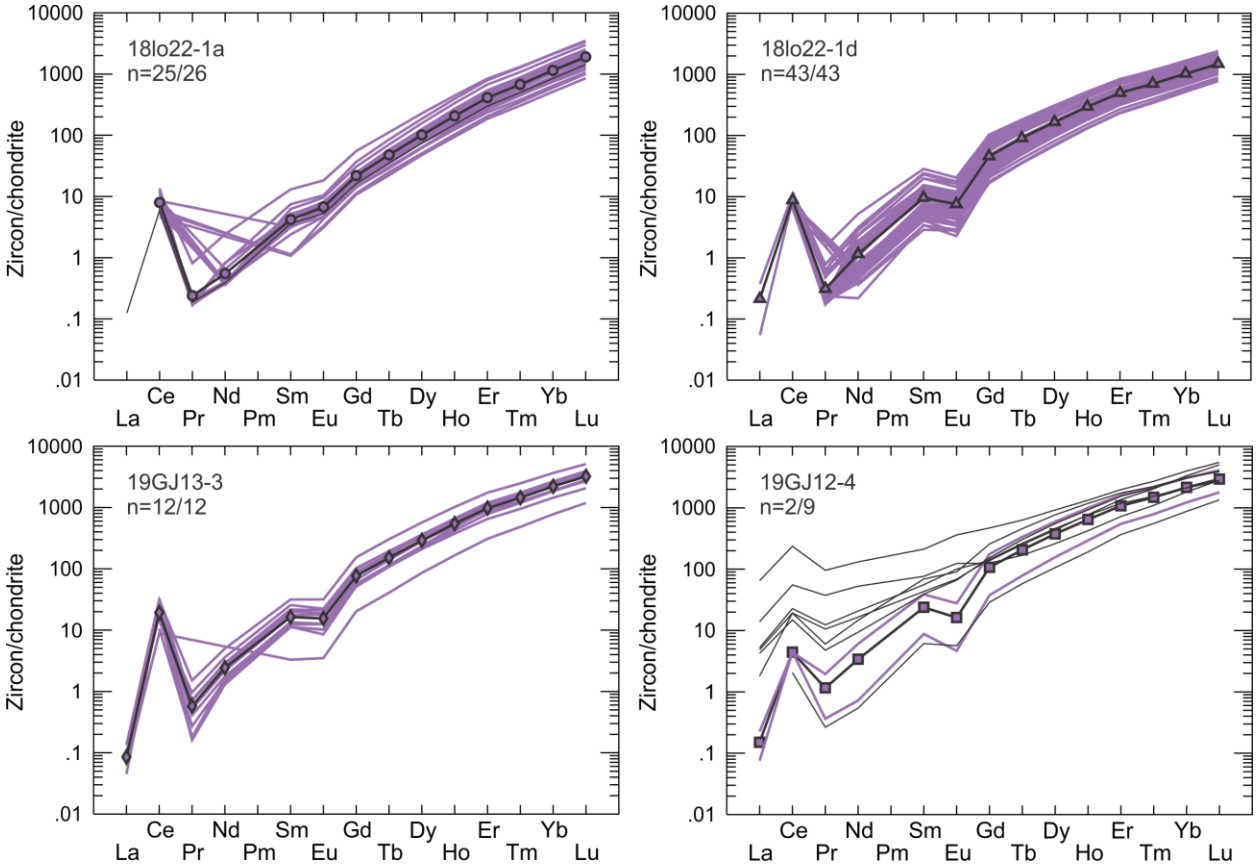

Figure 3.2.4.1. Chondrite-normalized rare earth element (REE) results of zircons from Thane Creek intrusive suite samples. Purple lines are individual zircon results. Black lines with symbols represent the averages of individual zircon results for each sample. Black lines without symbols represent zircon trace element results screened for Ca and/or Fe >300 ppm, Ti >20 ppm, and/or La >1 ppm. Normalizing values are from Sun and McDonough (1989).

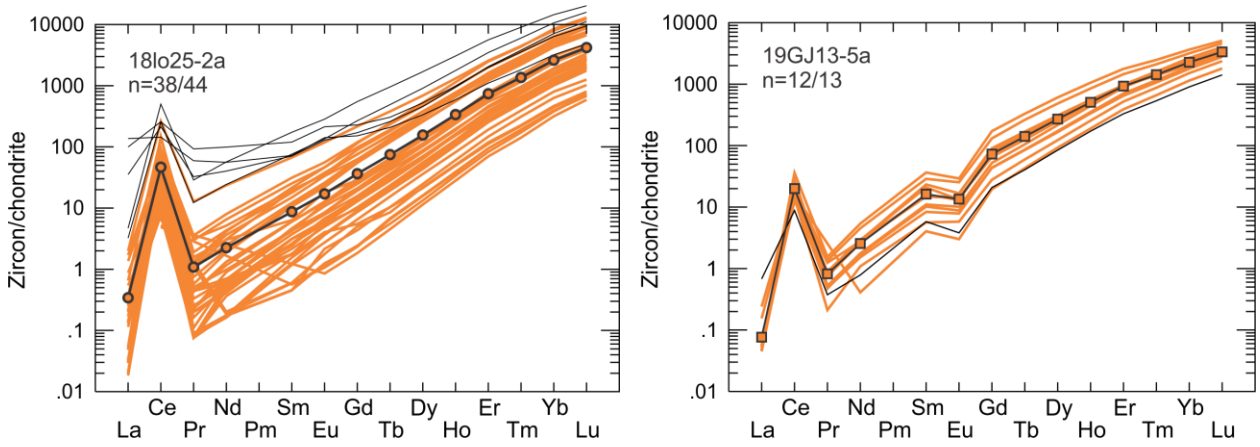

Figure 3.2.4.2. Chondrite-normalized rare earth element (REE) results of zircons from Duckling Creek intrusive suite samples. Orange lines are individual zircon results. Black lines with symbols represent the averages of individual zircon results for each sample. Black lines without symbols represent zircon trace element results screened for Ca and/or Fe >300 ppm, Ti >20 ppm, and/or La >1 ppm. Normalizing values are from Sun and McDonough (1989).

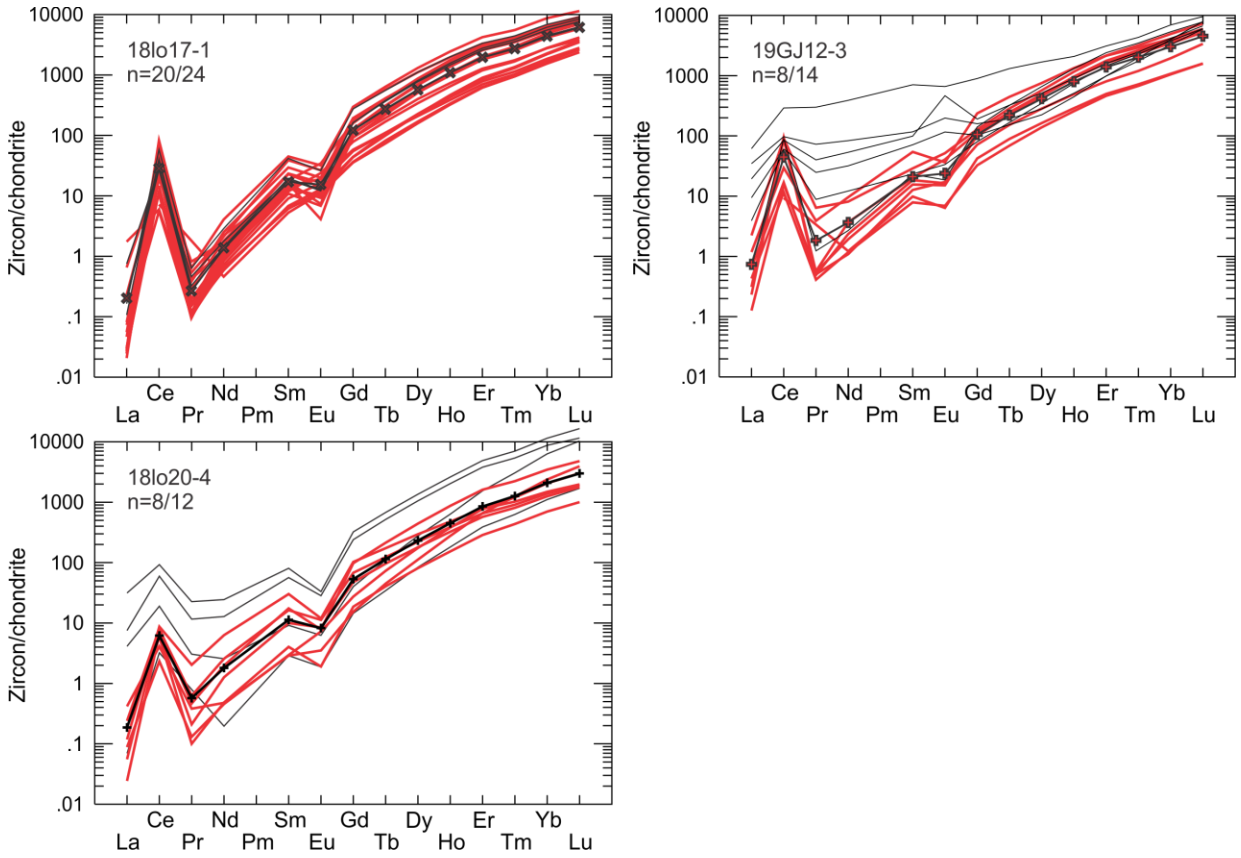

Figure 3.2.4.3. Chondrite-normalized rare earth element (REE) results of zircons from Osilinka intrusive suite samples. Red lines are individual zircon results. Black lines with symbols represent the averages of individual zircon results for each sample. Black lines without symbols represent zircon trace element results screened for Ca and/or Fe >300 ppm, Ti >20 ppm, and/or La >1 ppm. Normalizing values are from Sun and McDonough (1989).

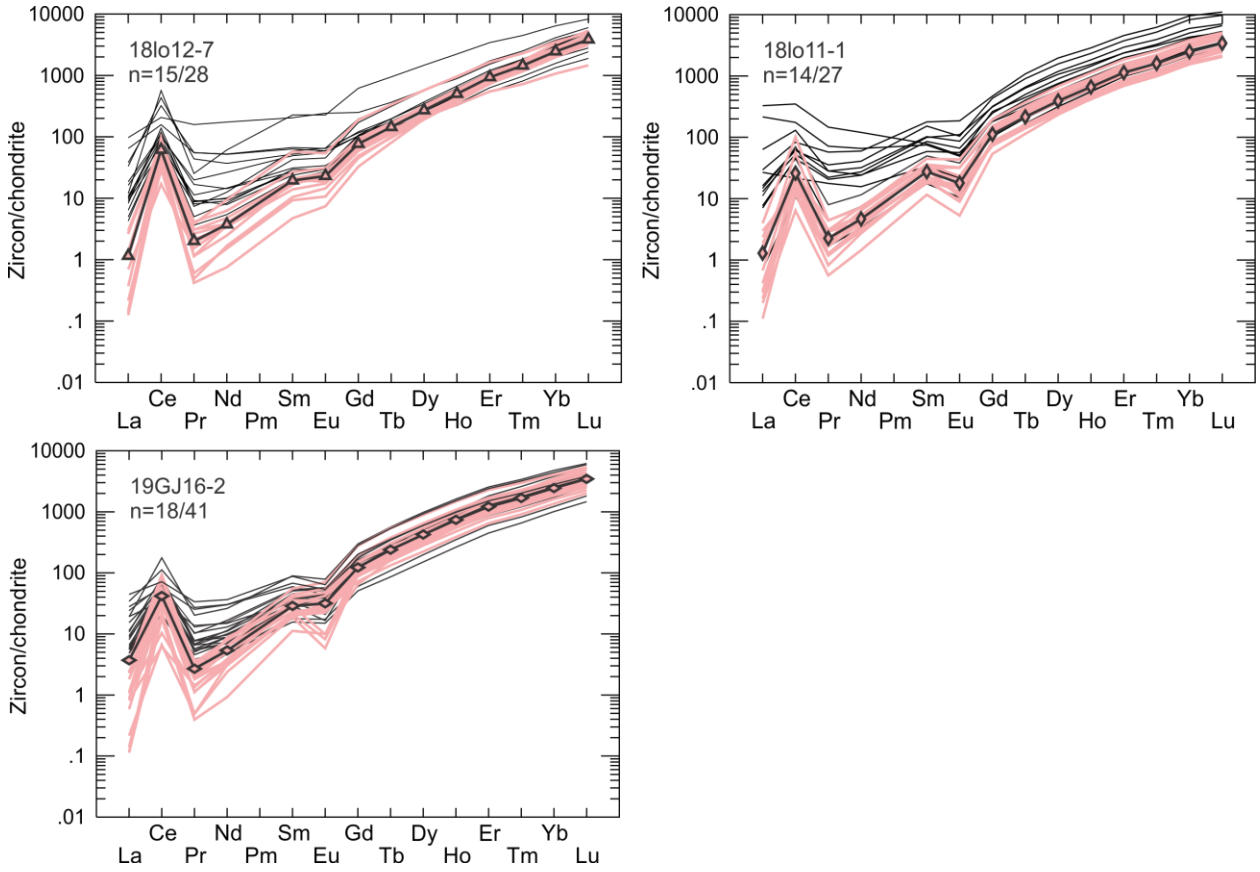

Figure 3.2.4.4. Chondrite-normalized rare earth element (REE) results of zircons from Mesilinka intrusive suite samples. Pink lines are individual zircon results. Black lines with symbols represent the averages of individual zircon results for each sample. Black lines without symbols represent zircon trace element results screened for Ca and/or Fe >300 ppm, Ti >20 ppm, and/or La >1 ppm. Normalizing values are from Sun and McDonough (1989).

Hogem zircon Hf concentrations range from 6000 to 20000 ppm and broadly positively correlate with U, Yb, and ∑REE concentrations (Figure 3.2.4.5). Thane Creek suite zircons have the lowest Hf concentrations, followed by Duckling Creek, Mesilinka, and Osilinka suites. Uranium concentrations in zircon vary greatly between intrusive suites, from 20 to 4000 ppm (Figure 3.2.4.6).

Zircons from Thane Creek, Duckling Creek, Osilinka suite sample 19GJ12-3, and Mesilinka suite have U concentrations that positively correlate with Yb, Nb, and ∑REE concentrations. Osilinka suite zircons from sample 18lo17-1 have the lowest U concentrations and form a separate positive trendline with Yb, Nb, and ∑REE.

Zircon Yb and Nb concentrations variably positively correlate within the four intrusive suites (Figure 3.2.4.7). Ytterbium concentrations vary widely in Thane Creek (88 to 521 ppm) and Duckling Creek (54 to 1438 ppm) suite zircons, whereas Nb concentrations have a narrow range (0.02 to 2.42 ppm in Thane Creek suite; 0.04 to 3.68 ppm in Duckling Creek suite). Osilinka suite zircons have moderate Nb concentrations (0.2 to 15.6 ppm), while Mesilinka suite zircons have the highest Nb concentrations (1.0 to 28.6 ppm).

Titanium concentrations in zircon have relatively constrained ranges in individual samples from Thane Creek and Duckling Creek suite (≤5 ppm range; Figure 3.2.4.8). In contrast, in Osilinka and Mesilinka suite, zircon Ti concentrations vary significantly within individual samples (8 to 15 ppm range).

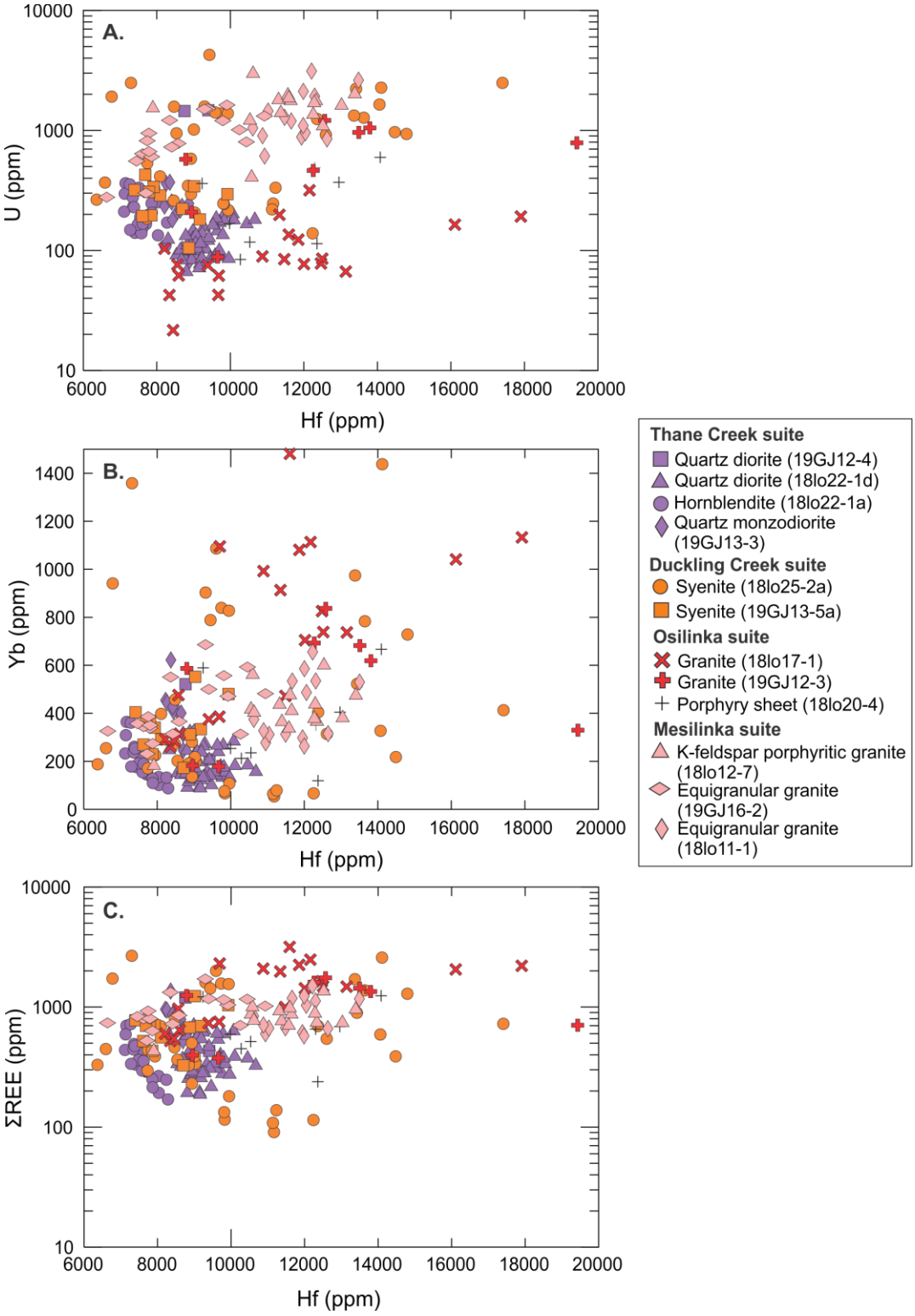

Figure 3.2.4.5. Zircon Hf concentration (ppm) versus **A)** U concentration (ppm), **B)** Yb concentration (ppm), **C)** Sum of rare earth element (REE) concentrations (ppm) for Thane Creek, Duckling Creek, Osilinka, and Mesilinka intrusive suite samples. Trace element data were screened for Ca and Fe >300 ppm, Ti >20ppm, and La >1 ppm. Uncertainties for U, Yb, and ∑REE are smaller than symbol widths. 2 S.E. = average 2σ uncertainty for all results.

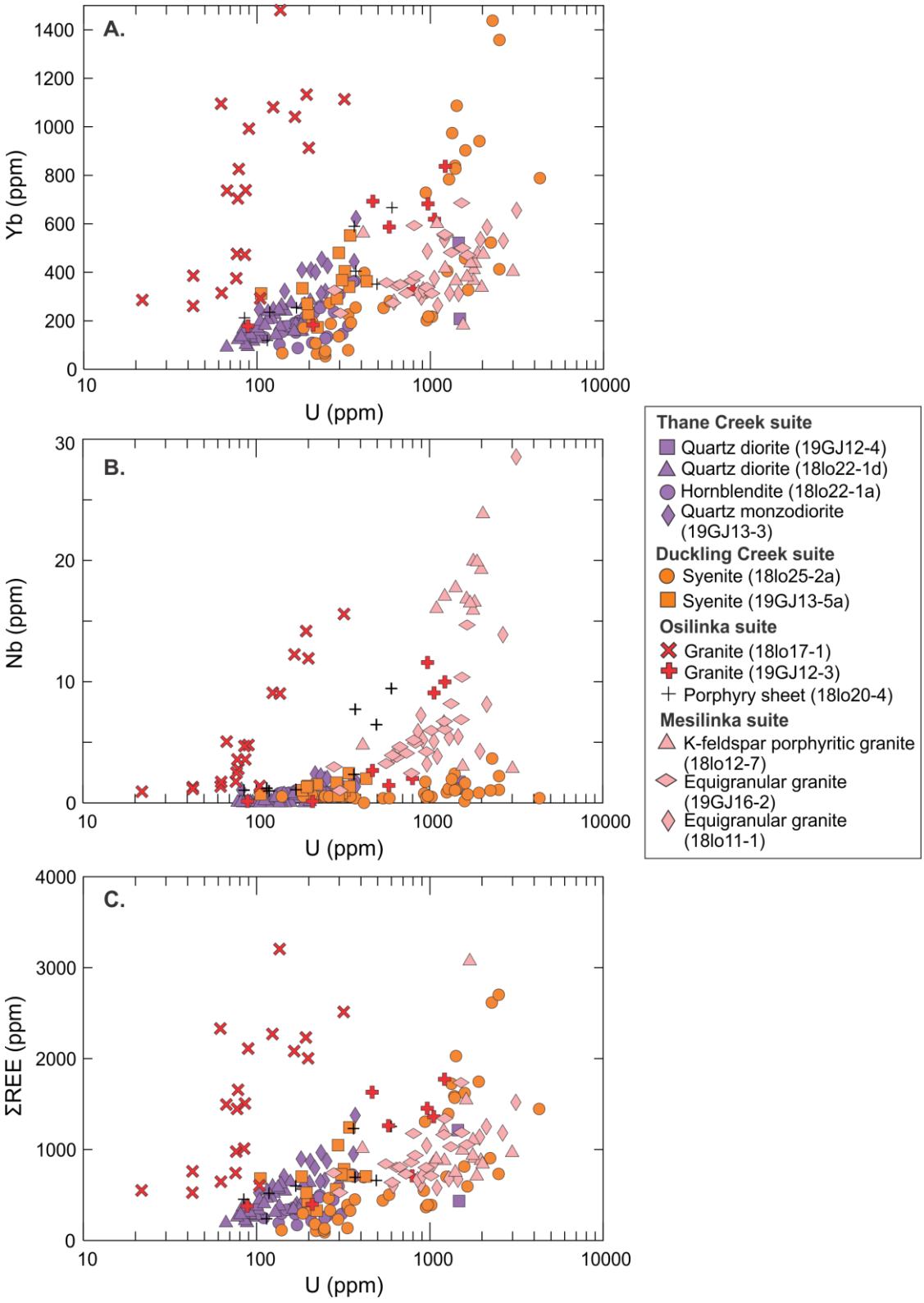

Figure 3.2.4.6. Zircon U concentration (ppm) versus **A)** Yb concentration (ppm), **B)** Nb concentration (ppm), **C)** sum of rare earth element (REE) concentrations (ppm) for Thane Creek, Duckling Creek, Osilinka, and Mesilinka intrusive suite samples.Trace element data were screened for Ca and Fe >300 ppm, Ti >20ppm, and La >1 ppm. Uncertainties are smaller than symbol widths.

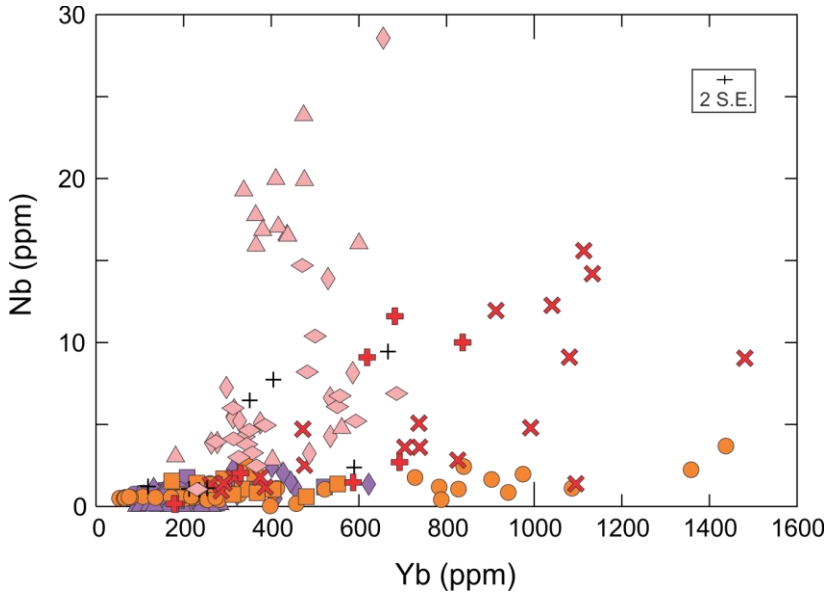

Figure 3.2.4.7. Zircon Yb concentration (ppm) versus Nb concentration (ppm) from Thane Creek, Duckling Creek, Osilinka, and Mesilinka intrusive suite samples. Trace element data were screened for Ca and Fe >300 ppm, Ti >20ppm, and La >1 ppm.

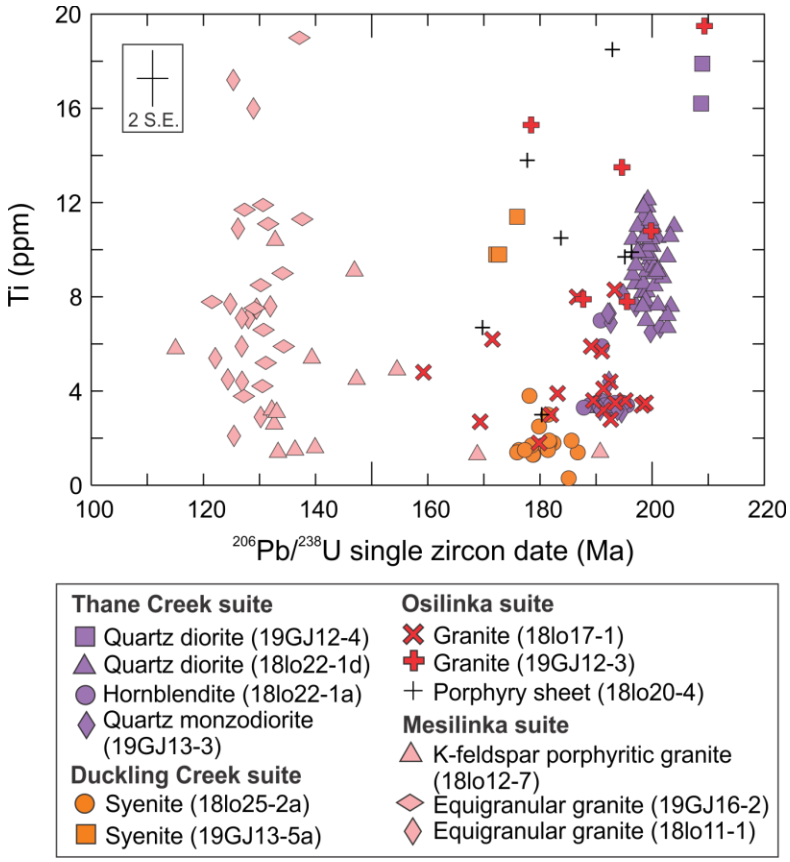

Figure 3.2.4.8. Single zircon $^{206}Pb/^{238}U$ date (Ma) versus corresponding Ti concentration (ppm) for Thane Creek, Duckling Creek, Osilinka, and Mesilinka intrusive suite samples. 2 S.E. = average 2σ uncertainty for all results.

3.2.5 Apatite and Titanite Sm-Nd Results

Apatite and titanite LA-ICP-MS Sm-Nd results are reported in the BCGS Geofile (in preparation). These results are summarized in Table 3.2.5.1 and 3.2.5.2, and reported as εNd(t), as well as converted εHf(t), using the calculation of Vervoort et al. (2011), as described in section 3.1.6. The εNd(t) results were filtered by removing data with propagated 2σ uncertainties greater than 2ε units.

Thane Creek suite

Apatite and titanite grains from Thane Creek intrusive suite samples have εNd(0) ranging from -3.4±1.8 to +1.0±1.7, corresponding to εNd(t) from +1.5±1.8 to +5.9±1.7 (Figure 3.2.5.1; Tables 3.2.5.1-3.2.5.2). These εNd(t) values convert to an εHf(t) range from +5.5 to +10.3.

Three apatite grains from quartz diorite (sample 19GJ12-4) range in εNd(t) from +3.3±1.2 to +4.4±0.9, with a weighted mean of +3.9±0.6 (Figure 3.2.5.2A). Converted εHf(t) range from +6.3 to +8.1.

Six apatite grains from quartz diorite (sample 18lo22-1d) range in εNd(t) from +4.0 ±1.0 to +5.7 ±1.1, with a weighted mean of +4.9±0.5 (Figure 3.2.5.2B). Converted εHf(t) range from +7.3 to +10.1.

Ten apatite grains from quartz monzodiorite (sample 19GJ13-3) range in εNd(t) from +3.3±1.3 to +5.9±1.7, with a weighted mean of +4.5±0.4 (Figure 3.2.5.2C). Three apatite εNd(t) results were screened for >2ε uncertainties. Converted εHf(t) range from +6.4 to +10.3.

Twelve titanite grains from quartz monzodiorite (sample 19GJ13-3) range in εNd(t) from +1.5±1.8 to +5.5±1.4, with a weighted mean of +4.3±0.4 (Figure 3.2.5.2D). Two titanite εNd(t) results were screened for >2ε uncertainty. Another titanite grain was screened due to a lower εNd(t) result than the remaining data. Converted εHf(t) range from +3.5 to +9.8.

Table 3.2.5.1. Summary of mean εNd(t) results and statistics for unknown titanite grains. Converted εHf(t) values were calculated from Sm-Nd results using the method of Vervoort et al. (2011).

Sample	Intrusive suite	Assumed age (Ma)	εNd(t) weighted mean (±2SE)	No. analyses	MSWD	$p(\chi^2)$	Average converted εHf(t)
19GJ13-3	Thane Creek	197.5	+4.3±0.4	11/14	1.6	0.11	+7.7
19GJ13-2	Duckling Creek	177.4	+4.0±0.5	6/8	2.4	0.03	+7.4
19GJ13-4	Duckling Creek	174.4	+4.3±0.4	6/8	1.2	0.31	+8.0
19GJ12-2	Mesilinka	145.8	+3.2±0.4	8/9	2.6	0.01	+6.2
19GJ12-1	Mesilinka	122.0	+3.8±0.5	8/12	1.6	0.14	+7.1

Table 3.2.5.2. Summary of mean εNd(t) results and statistics for unknown apatite grains. Converted εHf(t) values were calculated from Sm-Nd results using the method of Vervoort et al. (2011).

Sample	Intrusive suite	Assumed age (Ma)	εNd(t) weighted mean (±2SE)	No. analyses	MSWD	$p(\chi^2)$	Average converted εHf(t)
19GJ12-4	Thane Creek	206.6	+3.9±0.6	3/3	1.2	0.32	+7.3
18lo22-1d	Thane Creek	199.0	+4.9±0.5	6/7	1.2	0.32	+8.9
19GJ13-3	Thane Creek	194.0	+4.5±0.4	10/13	1.7	0.09	+8.2

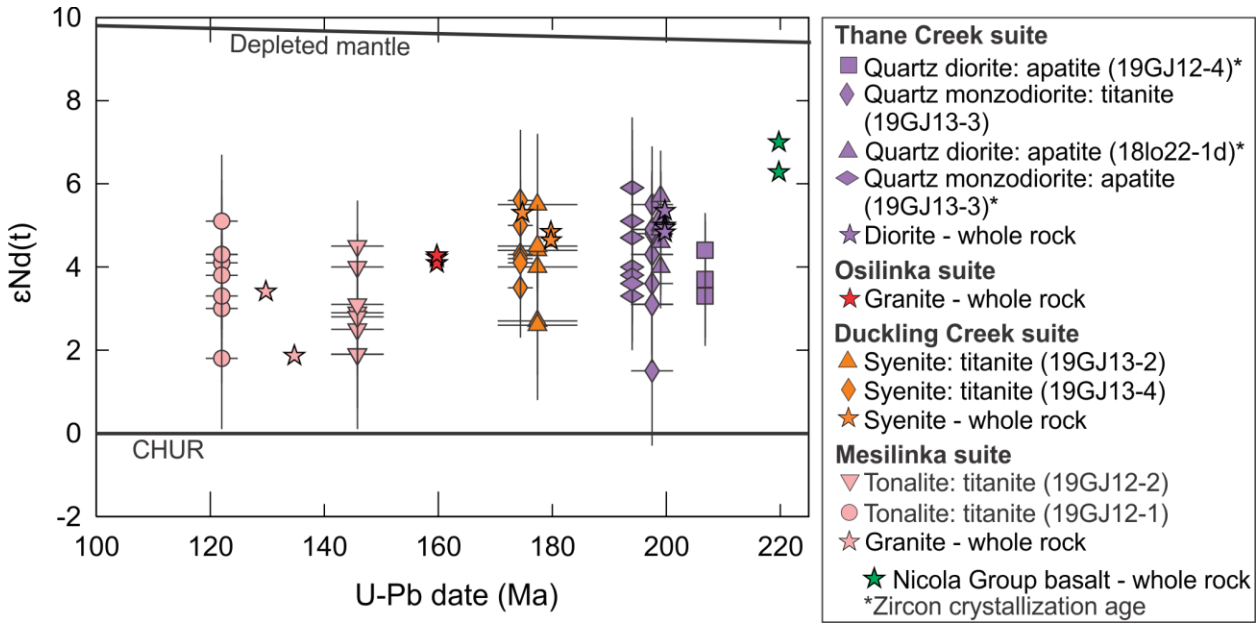

Figure 3.2.5.1. U-Pb date versus εNd(t) results for apatite and titanite grains from Thane Creek, Duckling Creek, and Mesilinka suite intrusive rock samples. Titanite dates are U-Pb intercept ages from the same grains (section 3.2.1.2). Apatite dates are zircon U-Pb ages from the same samples (section 3.2.1.1). Data has been screened for εNd(t) results with uncertainties >2ε. Star symbols represent Hogem batholith intrusive suite and Nicola Group basalt whole rock εNd(t) results, from Ootes et al. (2020a,c). Depleted mantle after Jacobsen and Wasserburg (1980). CHUR=Chondritic uniform reservoir, after Bouvier et al. (2008).

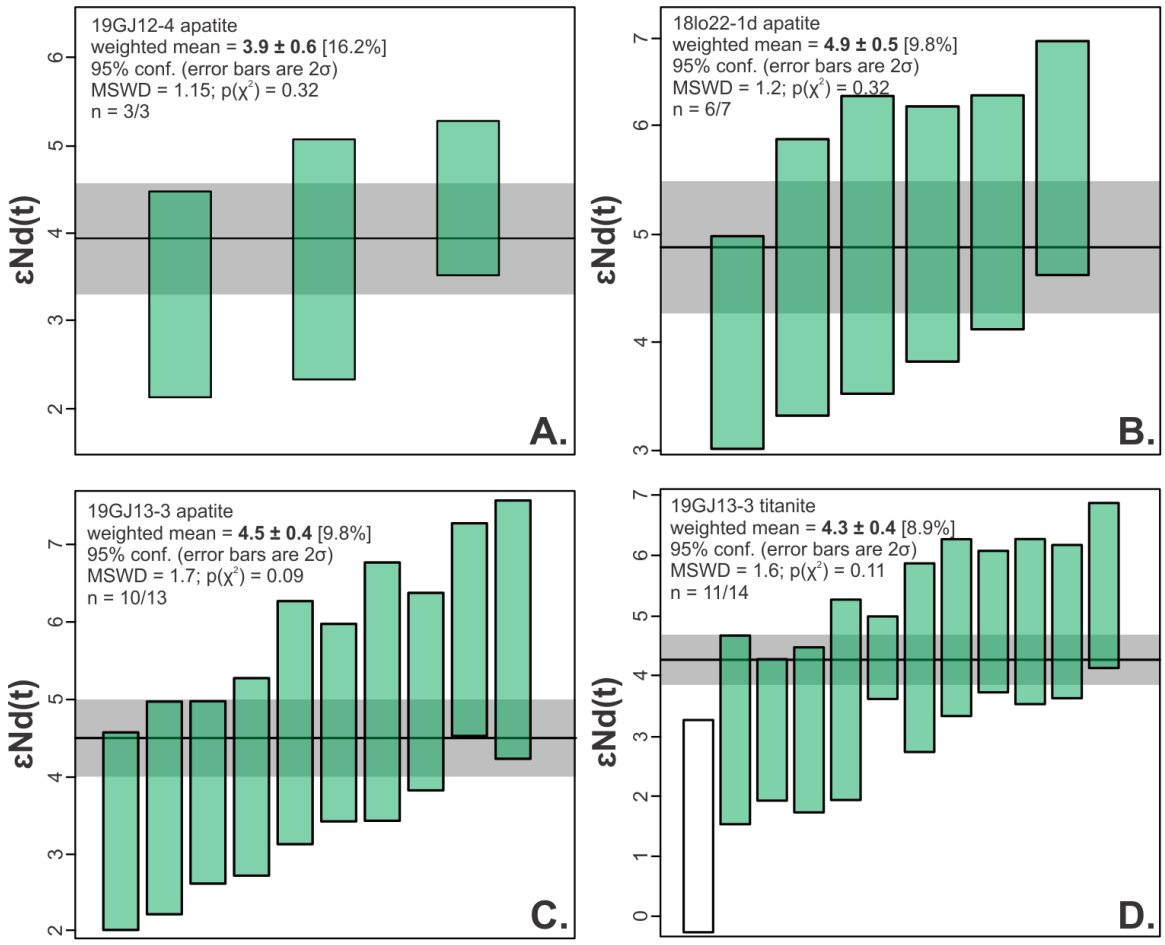

Figure 3.2.5.2. Weighted means of εNd(t) results for titanite and apatite grains from Thane Creek intrusive suite rock samples **A)** 19GJ12-4, **B)** 18lo22-1d, **C)** 19GJ13-3, and **D)** 19GJ13-3. Data were screened to exclude εNd(t) results with propagated uncertainties >2ε units. White bars represent outlier data and were excluded from weighted mean calculations. Uncertainties are reported at the 95.4% confidence level (2σ). The black line is the weighted mean, and the grey bar is the 2σ uncertainty of the mean.

Duckling Creek suite

Titanite grains from Duckling Creek intrusive suite samples have εNd(0) ranging from -1.8±1.2 to +1.2±1.7, corresponding to εNd(t) from +2.6±1.2 to +5.6±1.7 (Figure 3.2.5.1; Table 3.2.5.1). Converted εHf(t) range from +5.3 to +10.9.

Six titanite grains from syenite (sample 19GJ13-2) have εNd(t) from +2.6 ±1.2 to +5.5 ±1.7, with a weighted mean of +4.0±0.5 (Figure 3.2.5.3A). Two εNd(t) results were screened for >2ε uncertainty. Converted εHf(t) range from +5.3 to +9.7.

Seven titanite grains from syenite (sample 19GJ13-4) range in εNd(t) from +3.5±1.2 to +5.6±1.7, with a weighted mean of +4.3±0.4 (Figure 3.2.5.3B). One εNd(t) result was filtered for >2ε uncertainty. Converted εHf(t) range from +6.6 to +9.9.

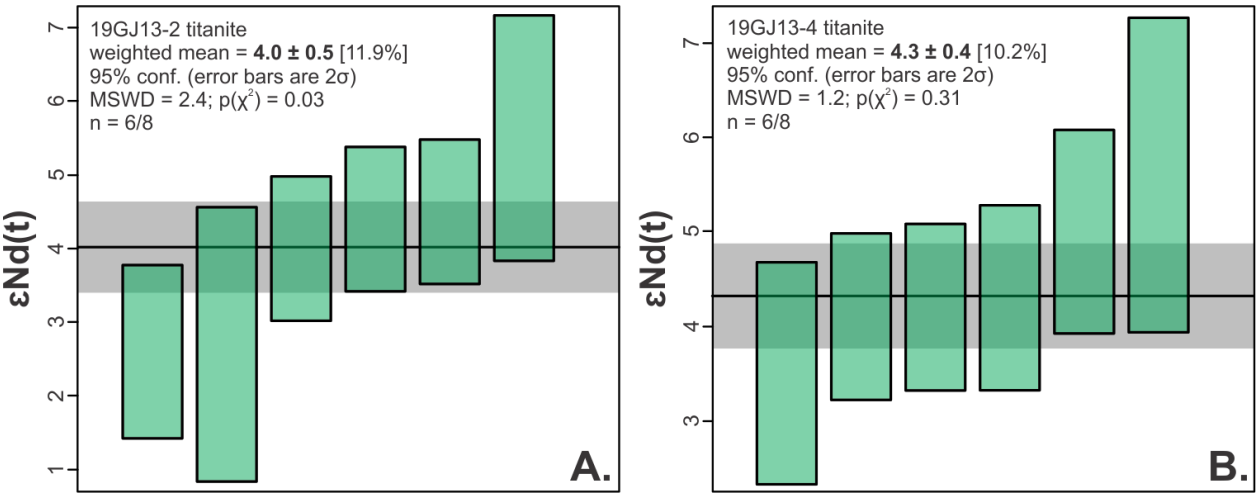

Figure 3.2.5.3. Weighted means of titanite εNd(t) results from Duckling Creek syenite samples **A)** 19GJ13-2 and **B)** 19GJ13-4. Data were screened to exclude εNd(t) results with propagated uncertainties >2ε units. White bars represent outlier data and were excluded from weighted mean calculations. Uncertainties are reported at the 95.4% confidence level (2σ). The black line is the weighted mean, and the grey bar is the 2σ uncertainty of the mean.

Mesilinka suite

Titanite grains from Mesilinka intrusive suite samples have εNd(0) ranging from -1.8±1.8 to +2.1±1.6, corresponding to εNd(t) from +1.9±1.8 to +5.1±1.6 (Figure 3.2.5.1; Table 3.2.5.1). These εNd(t) compositions convert to εHf(t) ranging from +4.1 to +9.2.

Eight titanite grains from tonalite (sample 19GJ12-2) have εNd(t) from +1.9±1.3 to +4.5±1.1, with a weighted mean of +3.2±0.4 (Figure 3.2.5.4A). One εNd(t) result was screened for >2ε uncertainty. Converted εHf(t) range from +4.1 to +8.1.

Eight titanite grains from tonalite (sample 19GJ12-1) have εNd(t) from +1.8±1.7 to +5.1±1.6, with a weighted mean of +3.8±0.5 (Figure 3.2.5.4B). Four εNd(t) results were screened for >2ε uncertainty. Converted εHf(t) range from +5.6 to +9.2.

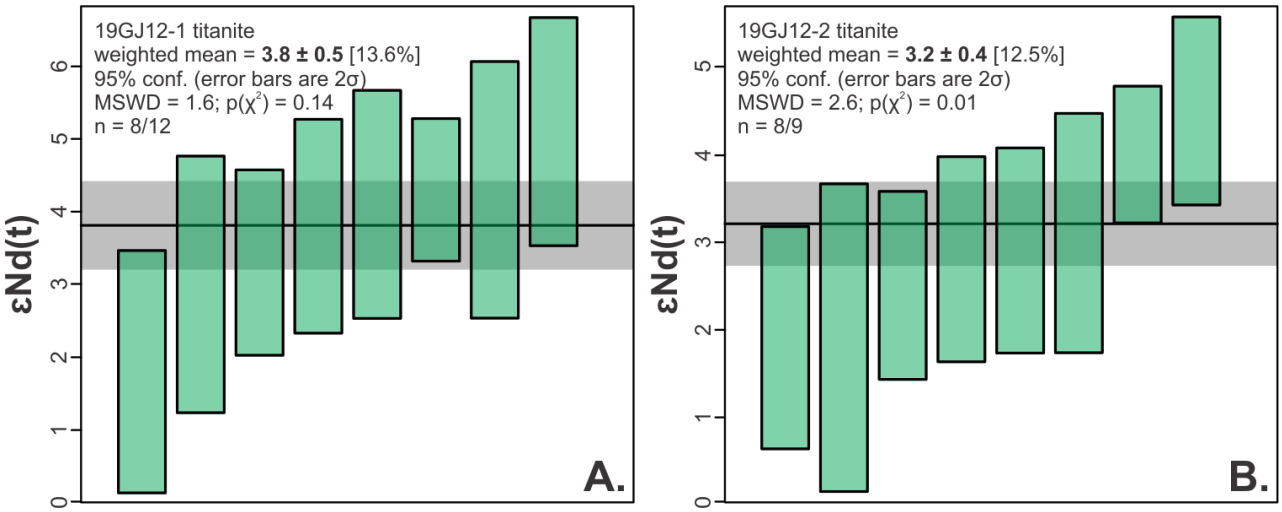

Figure 3.2.5.4. Weighted means of titanite εNd(t) results from Mesilinka tonalite samples A) 19GJ12-1 and B) 19GJ12-2. Data were screened to exclude εNd(t) results with propagated uncertainties >2ε units. White bars represent outlier data and were excluded from weighted mean calculations. Uncertainties are reported at the 95.4% confidence level (2σ). The black line is the weighted mean, and the grey bar is the 2σ uncertainty of the mean.

4 Zircon trace element geochemistry discussion

4.1 Zircon trace element constraints on oxidation and hydration state, temperature, and fractionation in Hogem magmas

The use of zircon trace elements has become an important tool in estimating the magmatic conditions (e.g., oxidation, hydration, temperature) in which zircon grains crystallized. Estimating these conditions not only helps constrain the evolution of a magma system, but also aids in evaluating magma fertility and potential for porphyry mineralization (e.g., Ballard et al., 2002; Dilles et al., 2015; Shen et al., 2015; Lu et al., 2016, Loader et al., 2017; Lee et al., 2017, 2020). As the Thane Creek and Duckling Creek suites have the most potential for porphyry mineralization in the Hogem batholith, zircon trace element results from these intrusive suites are the focus of the following sections. The Osilinka and Mesilinka intrusive suite zircon trace element results are combined into a single field and are used as a background reference.

4.1.1 Constraining magmatic oxidation and hydration states

Europium (Eu/Eu_N^*) and Ce (Ce/Ce_C^*) anomalies are suggested proxies for magma oxygen fugacity (fO_2), water content (Ballard et al., 2002; Burnham and Berry, 2012; Shen et al., 2015; Lu et al., 2016; Lee et al., 2017; Lee et al., 2020), and/or SO_2 degassing during zircon crystallization (Dilles et al., 2015). The ΔFMQ (fO_2 in log units relative to the fayalite-magnetite-quartz redox buffer) calculation of Loucks et al. (2020) uses zircon U-Pb age and Ce, Ti, and U concentrations to estimate the magma oxidation state during zircon crystallization.

Under normal magmatic differentiation, zircon Eu/Eu_N^* values will decrease progressively as plagioclase crystallizes and preferentially removes Eu from the melt (Streck and Dilles, 1998; Chambefort et al., 2008; Dilles et al., 2015; Lee et al., 2017; Lee et al., 2020). Elevated Eu/Eu_N^* (>0.4) in zircon may indicate increased water or fluid content caused by SO_2 degassing in the magma, which suppresses plagioclase crystallization and increases Eu availability in the melt (Ballard et al., 2002; Burnham et al., 2015; Dilles et al., 2015; Lu et al., 2016; Lee et al., 2017; Lee et al., 2021). Alternatively, a higher magma fO_2 will convert Eu^{2+} into Eu^{3+}, which is more compatible in zircon than Eu^{2+}, and will theoretically raise zircon Eu/Eu_N^* (Nathwani et al., 2021).

Hafnium concentration in zircon tracks magmatic evolution, as incompatible Hf progressively increases in the melt during crystallization; later crystallized zircons should have higher Hf concentrations relative to early crystallized grains from the same melt (Watson et al., 2006; Wooden et al., 2006; Clairborne et al., 2010; Dilles et al., 2015; Lee et al., 2017). In the Thane Creek suite, Eu/Eu_N*_{zircon} results are negatively correlated with Hf concentration, whereas the Duckling Creek suite zircons do not show any correlation between Eu/Eu_N* and Hf concentration (Figure 4.1.1.1A).

The negative correlation of zircon Eu/Eu_N* and Hf concentration in the Thane Creek suite may represent increased plagioclase concentration during magma differentiation. The higher Eu/Eu_N*_{zircon} and lower zircon Hf concentration in the Thane Creek hornblendites corresponds to the presence of only minor, interstitial plagioclase in these rocks. Zircon Eu/Eu_N* decreases with increased $Eu/Eu_N*_{whole\text{-}rock}$ in more felsic Thane Creek samples (Figure 4.1.1.2), consistent with higher plagioclase concentration. Additionally, Eu/Eu_N*_{zircon} is relatively invariant in the Thane Creek diorite compared to Ce/Ce_C* and ΔFMQ. Both zircon Ce/Ce_C* and ΔFMQ increase with progressive crystallization in the Thane Creek magmas, suggesting the oldest quartz diorite 19GJ12-4 is more reduced and the youngest quartz monzodiorite 19GJ13-3 is more oxidized (Figure 4.1.1.1B and 4.1.1.3B,C). However, ΔFMQ is calculated using measured Ce concentration in zircon so a correlation between Ce/Ce_C* and ΔFMQ is to be expected, regardless of the magma conditions.

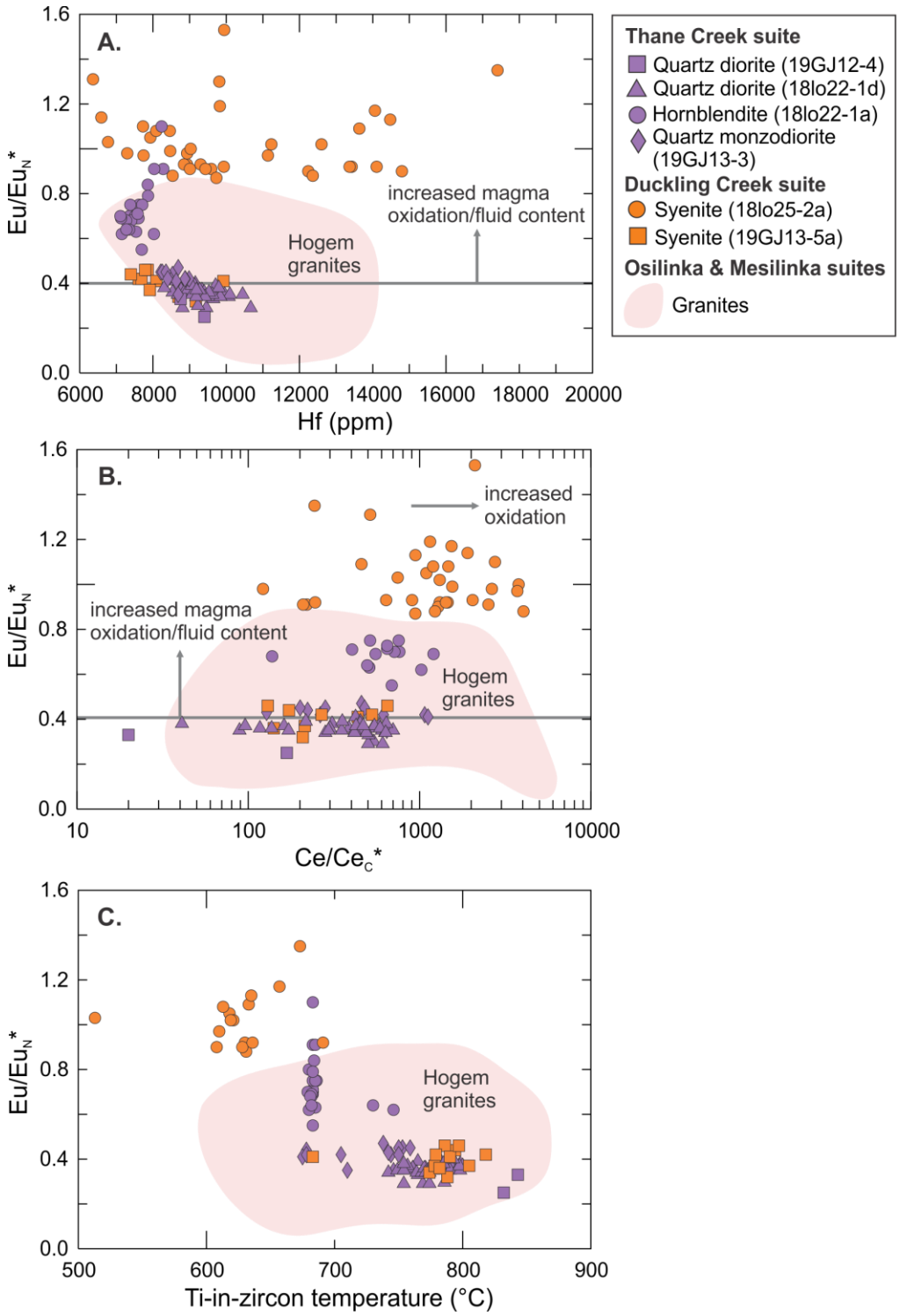

Figure 4.1.1.1. Zircon Europium anomaly (Eu/Eu_N^*) versus corresponding **A)** Hafnium concentration (ppm), **B)** Cerium anomaly (Ce/Ce_C^*), calculated using a curve fit line function through the zircon MREE and HREE concentrations to determine Ce* (Zhong et al., 2019; Lee et al., 2021), **C)** Calculated Ti-in-zircon temperature (°C), using an activity of Si=1.0 and Ti=0.7 (Ferry and Watson, 2007). Zircon trace element results were screened to exclude data with Ca, Fe >300 ppm, Ti >20 ppm, and La >1 ppm. $Eu/Eu_N^* = Eu_N/[(Sm_N*Gd_N)^{0.5}]$, where N indicates the element concentration normalized to chondrite (Sun and McDonough, 1989).

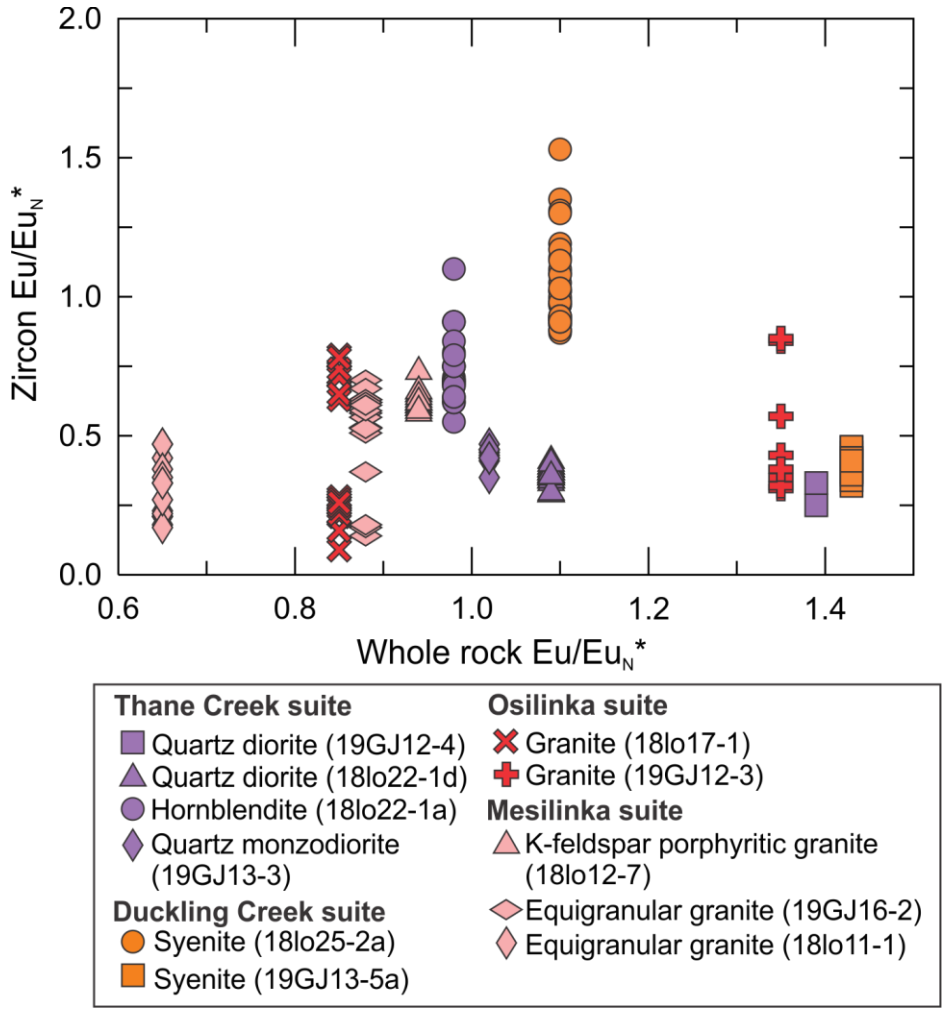

Figure 4.1.1.2. Zircon Europium anomaly (Eu/Eu$_N$*) versus corresponding whole rock Eu/Eu$_N$*. Zircon trace element results were screened to exclude data with Ca, Fe >300 ppm, Ti >20 ppm, and La >1 ppm. Eu/Eu$_N$* = Eu$_N$/[(Sm$_N$*Gd$_N$)0.5], where N indicates the element concentration in the whole-rock or zircon normalized to chondrite (Sun and McDonough, 1989).

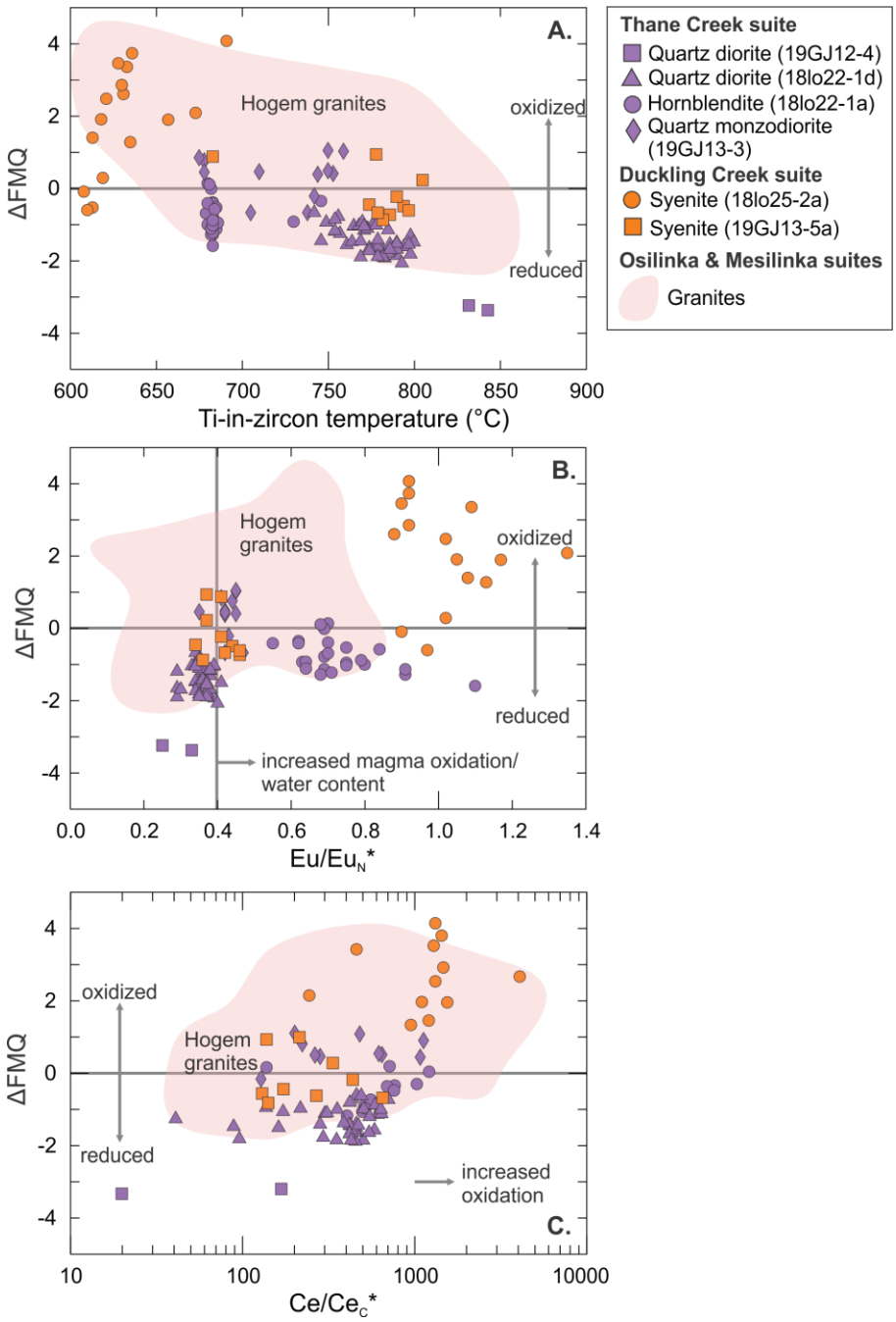

Figure 4.1.1.3. Change in the calculated zircon fayalite-magnetite-quartz redox buffer (ΔFMQ) versus corresponding **A)** Calculated Ti-in-zircon temperature (°C), using an activity of Si=1.0 and Ti=0.7 (Ferry and Watson, 2007), **B)** Europium anomaly (Eu/Eu$_N$*) calculated using chondrite-normalized Eu, Sm, and Gd values (Sun and McDonough, 1989), **C)** Cerium anomaly (Ce/Ce$_C$*) calculated using a curve fit line function through the zircon MREE and HREE concentrations to determine Ce* (Zhong et al., 2019; Lee et al., 2021). Zircon trace element results were screened to exclude data with Ca, Fe >300 ppm, Ti >20 ppm, and La >1 ppm.

ΔFMQ = 2.284 + 3.99 * LOG(Ce/SQRT(U(i)*Ti)), where U(i) = age * (EXP(U measured * 1.55125*10^{-4}) + 0.0072 * EXP(U measured * 9.8485*10^{-4})) (Loucks et al., 2020).
Eu/Eu$_N$* = Eu$_N$/(Sm$_N$^0.5*Gd$_N$^0.5), where N indicates the element concentration normalized to chondrite (Sun and McDonough, 1989).

The significant difference in $Eu/Eu_N^*_{zircon}$ between the two Duckling Creek syenite samples (18lo25-2a and 19GJ13-5a) is likely controlled by a factor other than the relative abundance of plagioclase, as both samples contain minor (<10%) plagioclase. Elevated $Eu/Eu_N^*_{zircon}$ values (≥0.9) from the Duckling Creek syenite 18lo25-2a indicate the magma may have been highly oxidized or vapour-rich. This corresponds to higher zircon Ce/Ce_C^* and positive ΔFMQ (Figure 4.1.1.1B and 4.1.1.3B,C) values in syenite 18lo25-2a, which both suggest elevated magmatic fO_2 during zircon crystallization. Notably, in the Duckling Creek syenite sample 18lo25-2a, all $Eu/Eu_N^*_{zircon}$ results are close to or greater than 1.0. Theoretically, a highly oxidized, primitive melt containing only Eu^{3+} would have an Eu/Eu_N^* of 1.0; therefore, a factor other than fO_2 must account for the zircon Eu/Eu_N^* values greater than 1.0 (Nathwani et al., 2021). Nathwani et al. (2021) suggests that melt fO_2 only has a minor control on $Eu/Eu_N^*_{zircon}$, and that $Eu/Eu_N^*_{zircon}$ is more strongly influenced by $Eu/Eu_N^*_{melt}$, which is affected by prior magmatic evolution (Trail et al., 2012; Buret et al., 2016; Loader et al., 2017; Rezeau et al., 2019). In their study, Nathwani et al. (2021) found $Eu/Eu_N^*_{zircon}$ increased in tandem with $Eu/Eu_N^*_{whole\text{-}rock}$, which the authors used as evidence of fractionation-dominated $Eu/Eu_N^*_{zircon}$ signatures, since an increase in melt fO_2 would not strongly affect the Eu concentration in the magma. However, in the two Duckling Creek syenites, this expected positive correlation between $Eu/Eu_N^*_{zircon}$ and $Eu/Eu_N^*_{whole\text{-}rock}$ is absent (Figure 4.1.1.2). The agreement between zircon Eu/Eu_N^*, Ce/Ce_C^*, and ΔFMQ suggests a higher magma oxidation state in syenite sample 18lo25-2a; however, magma fractionation likely also influenced the $Eu/Eu_N^*_{zircon}$ values, indicated by values greater than 1.0, which cannot be explained by fO_2 alone.

4.1.2 Relative zircon crystallization temperature estimates

Titanium concentration in zircon is used as a proxy for magma temperature during zircon crystallization (Ferry and Watson, 2007). Their Ti-in-zircon temperature calculation requires magmatic silica and titanium activity (quartz, αSiO_2; rutile, αTiO_2) to be estimated during zircon crystallization. Since most Hogem batholith intrusive samples contain quartz, titanite, and Fe-Ti oxides, but not rutile, αTiO_2=0.7 and αSiO_2=1.0 were assigned for all Ti-in-zircon temperature calculations. For the less Si-saturated Duckling Creek syenites, these zircon temperatures may be overestimated; lowering the αSiO_2 to 0.7 for these samples only decrease the temperature estimates by ~30°C.

The Duckling Creek syenite sample 18lo25-2a and the Thane Creek hornblendite sample 18lo22-1a have relatively low (<700°C) Ti-in-zircon temperatures compared to other rocks in the two suites (Figure 4.1.2.1). The hornblendite zircon crystallization temperature estimates are likely minimums, as the zircon Ti concentration results are almost all below the LOQ (average LOQ=7.0 ppm). The results below LOQ were substituted with 0.5*LOQ to calculate estimated crystallization temperatures. Using the original Ti results that were below LOQ, but above 0.5*LOQ, resulted in temperature estimates only ~30°C higher than using the substituted 0.5*LOQ values.

The relatively low temperatures of these syenite and hornblendite zircons correlate with higher $Eu/Eu_N^*{}_{zircon}$, possibly indicating higher magma fO_2 or hydration at lower temperatures. Alternatively, the low concentration of Ti in the hornblendite zircons may represent fractionation of Ti into amphibole and biotite, the major modal minerals in this Thane Creek phase. Further trace element work on amphibole and biotite is needed to address this possibility.

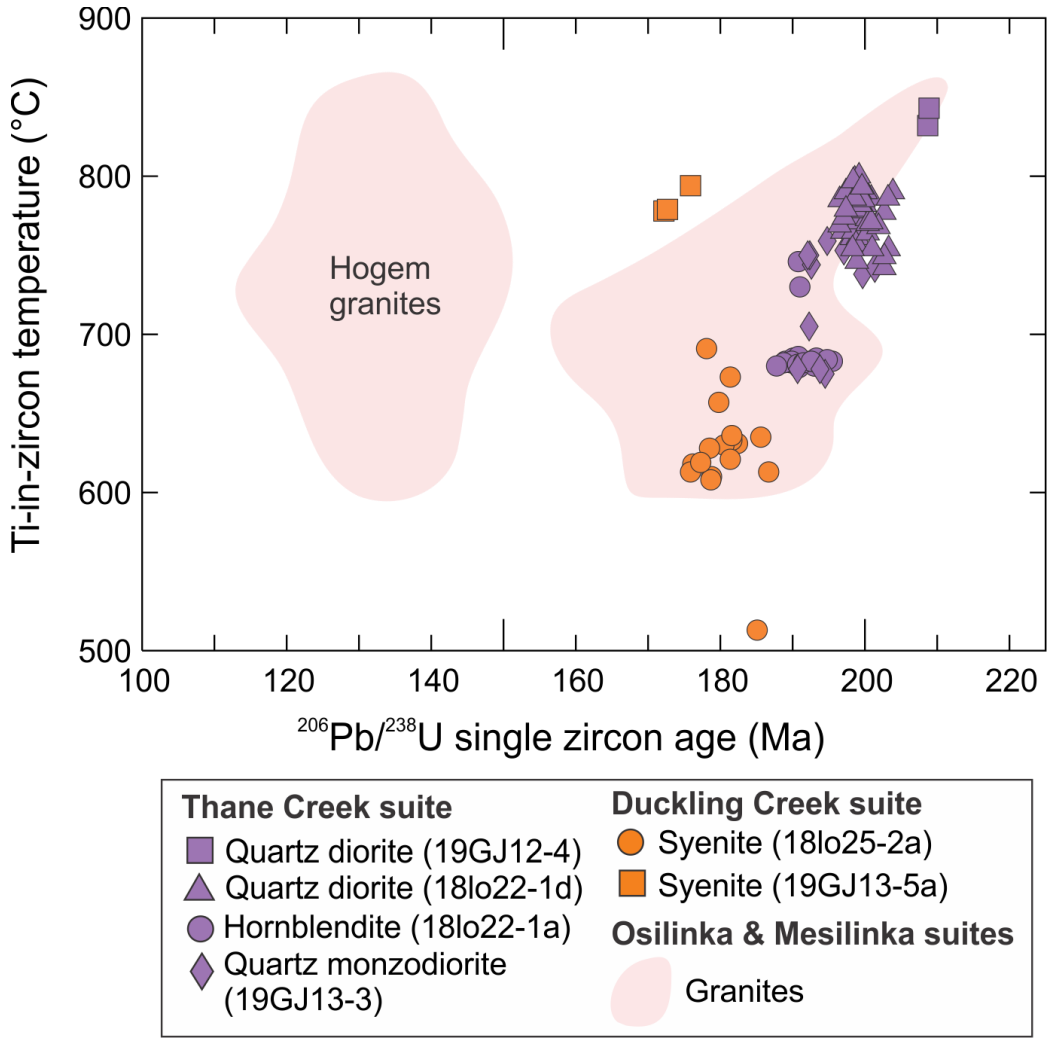

Figure 4.1.2.1. Single zircon $^{206}Pb/^{238}U$ age versus corresponding calculated Ti-in-zircon temperature (°C) results for zircons from Hogem batholith intrusive rock samples. Titanium temperatures were calculated using an activity of Si of 1.0 and activity of Ti of 0.7. Zircon trace element results were screened to exclude data with Ca, Fe >300 ppm, Ti >20 ppm, and La >1 ppm. Zircon U-Pb results were screened to exclude data with discordance >10%.

Ti temperature = -4800/[log(Ti49)+log(αSi)-log(αTi)-5.711]-273 (Ferry and Watson, 2007).

4.2 Zircon tectono-magmatic provenance using trace element geochemistry

Hafnium concentration and the U/Yb ratio in zircon increase progressively during magma differentiation. By correcting zircon U/Yb with Hf concentration, it is possible to estimate the initial U/Yb ratio of the magma source (Barth et al., 2017; Johnston and Kylander-Clark, 2021), which is useful in comparing the relative degree of fractionation of different aged intrusive suites (Figure 4.2.1). Higher U/Yb magmas are typical of enriched arc settings, while lower U/Yb magmas represent mid-ocean ridge or primitive island arc settings (Grimes et al., 2015; Barth et al., 2017; Johnston and Kylander-Clark, 2021). Zircons from the Thane Creek, Duckling Creek, and Mesilinka intrusive suites plot in the medium- to high- Hf-corrected U/Yb fields, consistent with arc magmatism (Figure 4.2.1). The Osilinka suite leucocratic zircons mostly plot in the low- to sub-low U/Yb fields, indicating these grains crystallized from a more depleted magma.

Previous studies have shown zircon trace element concentrations and ratios can be used to classify zircon provenance and tectono-magmatic setting (e.g., Hoskin and Ireland, 2000; Belousova et al., 2002; Grimes et al., 2007; Grimes et al., 2015). Using the zircon tectono-magmatic discrimination fields of Grimes et al. (2015), plots of U/Yb versus Nb/Yb and U/Yb versus Hf show most Hogem batholith zircons occur along the magmatic arc array (Figure 4.2.2A) and within the continental arc field (Figure 4.2.2B). Zircons from the Osilinka suite granites overlap into the mantle zircon array and the MORB field. These discriminations are consistent with zircon U-Pb, Lu-Hf, and oxygen isotope results, which suggest the Hogem batholith evolved from an island arc setting with juvenile magmatism (Thane Creek, Duckling Creek suites) into a post-accretionary setting with recycled, mixed magma sources (Osilinka, Mesilinka suites). The apparent depleted source of the Osilinka granite zircons also agrees with the interpreted inheritance of these zircons.

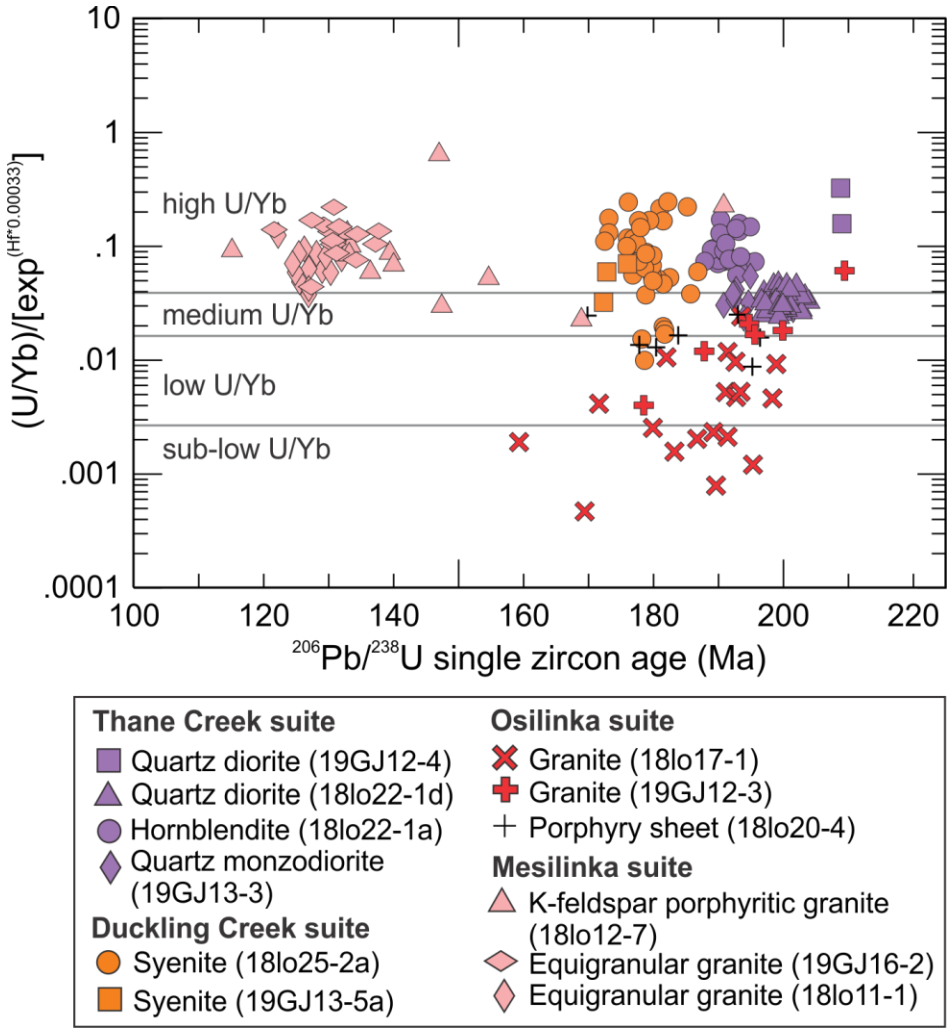

Figure 4.2.1. Single zircon $^{206}Pb/^{238}U$ age versus corresponding Hf-corrected U/Yb ratio for zircons from Hogem batholith intrusive samples. Zircon U/Yb ratios were corrected using zircon Hf concentrations to account for the enrichment in U relative to Yb in the melt as zircon progressively crystallizes. U-Yb fields are from Johnston and Kylander-Clark (2021), modified after Barth et al. (2017). Zircon trace element results were screened to exclude data with Ca, Fe >300 ppm, Ti >20 ppm, and La >1 ppm.

U/Yb (Hf-corrected) = [U/Yb]/[exp(Hf*0.00033)] (Johnston and Kylander-Clark, 2021).

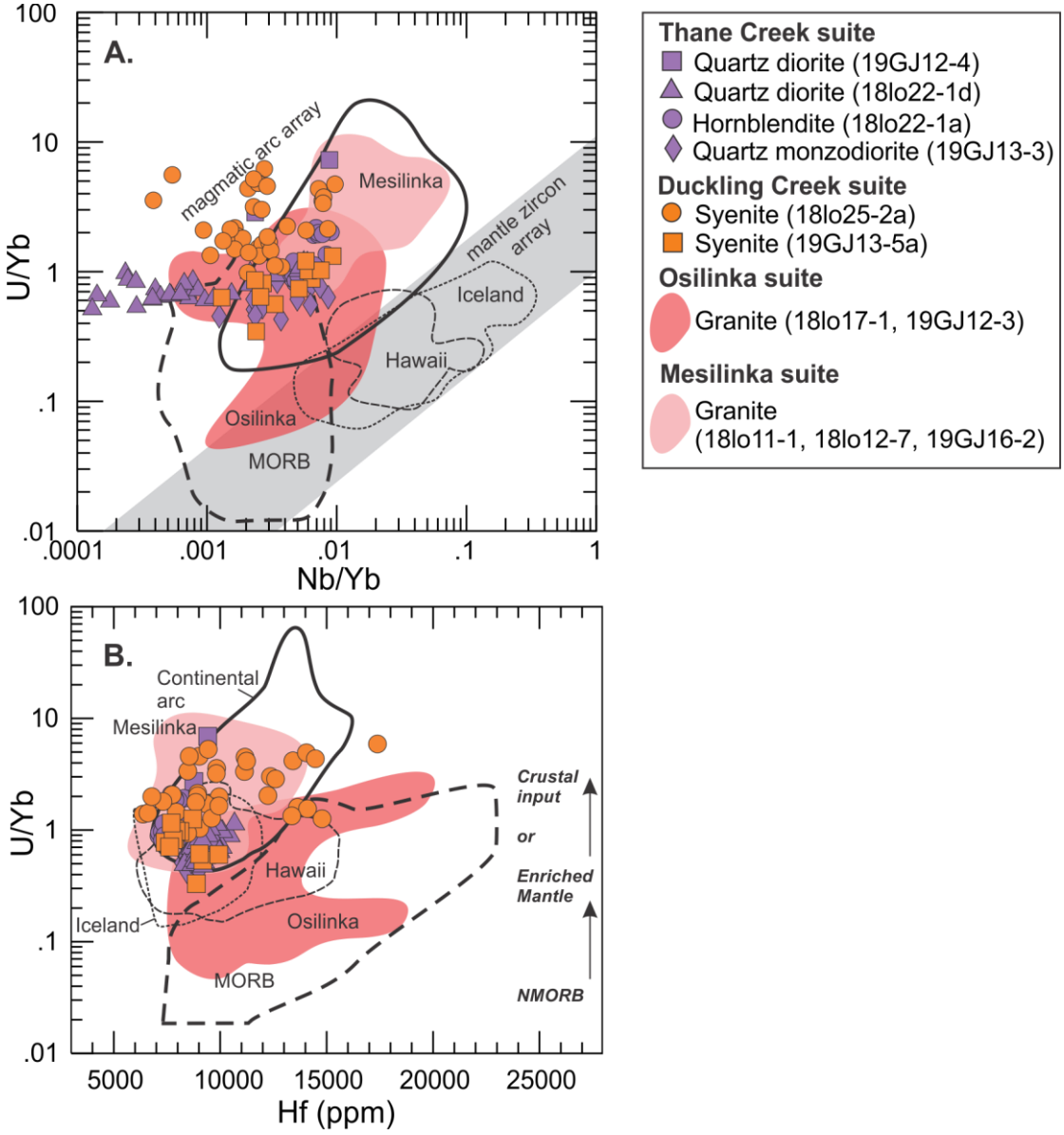

Figure 4.2.2. Tectono-magmatic provenance diagrams of **A)** Nb/Yb versus U/Yb and **B)** Hf concentration (ppm) versus U/Yb for zircons from Thane Creek, Duckling Creek, Osilinka, and Mesilinka intrusive suites. Discrimination fields are from Grimes et al. (2015). Zircon trace element results screened to exclude data with Ca, Fe >300 ppm, Ti >20 ppm, and La >1 ppm.

4.3 Implications for mineralization

Porphyry Cu±Au mineralization in the Hogem batholith is associated with the Thane Creek and Duckling Creek intrusive suites, which are interpreted to have predominantly juvenile magma sources with minor crustal influence. Magmatism of the Thane Creek suite coincides with the major 15-million-year period of porphyry Cu±Au-Mo-Ag mineralization at the Triassic-Jurassic boundary in the Quesnel and Stikine terranes (Logan and Mihalynuk, 2014). The earliest phase of Thane Creek magmatism (ca. 207 Ma) specifically overlaps the most prolific mineralization period, which deposited 90% of known porphyry mineralization in Quesnellia-Stikinia at 205±3 Ma (Logan and Mihalynuk, 2014). The Duckling Creek suite, which hosts the Lorraine Cu-Au porphyry deposit ~10 km south of the study area, is temporally associated with the latest stage of Quesnel-Stikine alkalic porphyry mineralization and corresponds to syn-accretion of Quesnel terrane to the ancestral western North American margin (Logan and Mihalynuk, 2014).

In the Thane Creek suite, whole rock Cu concentration is greatest in mafic hornblendites and decreases with increasing SiO_2 (Figure 2.2.2.6), which correlates to the global trend of decreasing Cu concentration with arc magma differentiation (Richards, 2015). Chang and Audétat (2018) suggest that lower crustal hornblendites sequester Cu and may either decrease the mineral potential of later-crystallized, upper crustal intrusive phases, or act as a Cu reservoir that can be remobilized during later magmatism. Despite evidence of Cu sequestration in lower crustal magmas, large porphyry deposits may still be generated in upper crustal arc magmas with average Cu concentrations of only 50-100 ppm (Cline and Bodnar, 1991; Richards, 2015), indicating factors other than Cu concentration of the magma play a greater role in porphyry fertility (e.g., oxidation, hydration, temperature).

Porphyry Cu±Au±Mo mineralization is typically associated with oxidized and hydrous arc magmas (Richards, 2015). Highly oxidized magmas are indicated by whole rock ΔFMQ values from +1 to +2 (Richards, 2015), and by proxy elevated $Eu/Eu_N{}^*_{zircon}$ (>0.4) and $Ce/Ce_C{}^*_{zircon}$ (>100; Lee et al., 2020). Nearly all the Thane Creek and Duckling Creek suite zircon results have $Eu/Eu_N{}^*_{zircon}$ values close to or ≥0.4 and $Ce/Ce_C{}^*_{zircon}$ values ≥100 (Figure 4.1.1.1), indicating the magmas potentially were oxidized and hydrous and thus favourable for porphyry mineralization. Zircon trace elements that indicate fO_2 conditions of ΔFMQ >0 suggest

the Thane Creek hornblendite and quartz monzodiorite and the Duckling Creek syenites crystallized from relatively more oxidized magmas and may have better porphyry mineralization potential than relatively reduced (ΔFMQ <0) Thane Creek quartz diorites (Figure 4.1.1.3). Although the Ti-in-zircon temperatures presented here are estimates due to the uncertainties in αSiO_2 and αTiO_2, most zircon results indicate temperatures close to the near-solidus temperature range (750 to 650°C), which is consistent with temperature estimates in previous studies of zircons associated with mineralized porphyries (Figures 4.1.1.1, 4.1.1.3, 4.1.2.1; Lee et al., 2017). Based on these criteria, zircon trace element results suggest the Thane Creek hornblendite and quartz monzodiorite phases and Duckling Creek syenites have the best potential for porphyry-favourable magma conditions in the Hogem batholith.

The younger, Cretaceous post-accretionary Mesilinka suite may be prospective for Mo mineralization. The oldest magmatic zircon U-Pb ages (ca. 145 Ma) of the Mesilinka tonalites and K-feldspar porphyritic granites correspond to the age of the Endako subsuite of the Francois Lake intrusive suite (149 to 145 Ma) in the Endako batholith, which hosts the oldest major molybdenite deposit in the Canadian Cordillera, the Endako Mo mine (Villeneuve et al., 2001). Villeneuve at al. (2001) proposed that molybdenite in Endako may have been concentrated due to long-lived episodic magmatism and emplaced into high level positions in the batholith, which was preserved from erosion by local post-mineralization extensional block faulting. Similar long-lived episodic magmatism is evident in Mesilinka suite, but further research is needed to evaluate if the tectonic setting was preferable for producing and preserving Mo mineralization. By analogy, if present, such a model would predict its occurrence in the youngest members of the suite.

5 Zircon U-Pb, Lu-Hf, and oxygen-isotope discussion

5.1 Timing and duration of Hogem batholith magmatism

New and previously published geochronological data clearly show that long-lived (80 million-year) magmatism during the Mesozoic produced the large, composite Hogem batholith in the north-central Quesnel terrane. New zircon LA-ICP-MS U-Pb results (section 3.2.1.1) better constrain the punctuated nature of the magmatism that constructed this batholith. Intermittent magmatism in northern Hogem batholith was initiated at least as early as Late Triassic (ca. 207 Ma) and continued to at least mid-Early Cretaceous times (ca. 127 Ma). This time span is separated into four main periods of activity that correspond to four mappable intrusive suites (Figure 5.1.1). The oldest pulse, from 206.8±0.9 to 194.0±1.0 Ma, corresponds to the Thane Creek intrusive suite. After a ~12-million-year hiatus, the next period of magmatism crystallized the Duckling Creek intrusive suite, from 181.7±1.0 (Devine et al., 2014) to 174.7±0.7 Ma. Another magmatic hiatus ensued until approximately 160 Ma, after which the Osilinka suite crystallized. The upper and lower age constraints of Osilinka suite magmatism are not well constrained due to the abundance of inherited zircons in the granite samples, but the youngest zircon U-Pb age from an Osilinka suite granite sample indicates an interpreted maximum crystallization age of 159.2±4.0 Ma. The final phase of magmatic activity in the Hogem batholith formed the Mesilinka intrusive suite, from at least 135.4±0.9 to 127.1±1.6 Ma. There is evidence that late-stage magmatism began earlier (ca. 145 Ma) in the Mesilinka suite, as several antecrystic zircons in Mesilinka tonalite 19GJ12-1, K-feldspar phenocrystic granite 18lo12-7, and equigranular granite 18lo11-1 have U-Pb ages from ~147 to 137 Ma. These antecrystic zircon dates also overlap a titanite U-Pb concordia intercept age of 145.8±4.6 Ma in Mesilinka tonalite 19GJ12-2. The three periods of magmatic quiescence apparent in the formation of the Hogem batholith were likely due to changes in the local and regional stress regimes in the Jurassic (Evenchick et al., 2007).

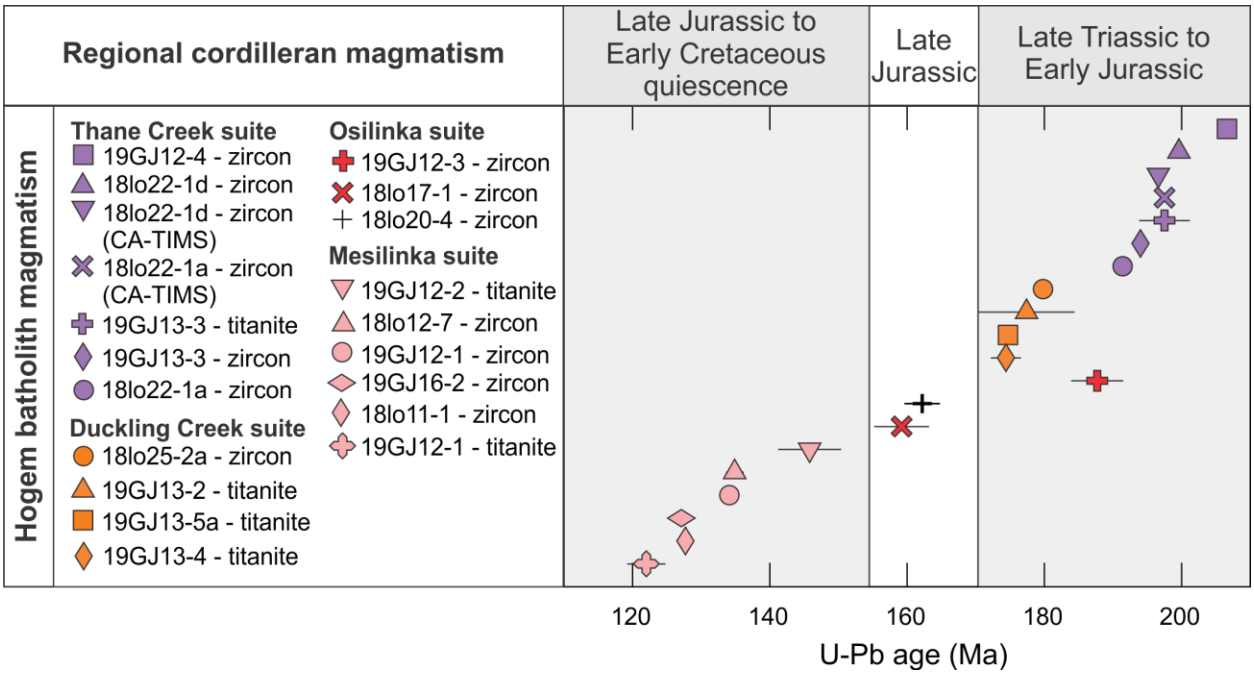

Figure 5.1.1. Summary timeline of mineral U-Pb age results from this study, compared to major time intervals of Canadian Cordilleran magmatism (after Woodsworth et al., 1991). Zircon ages were determined by $^{206}Pb/^{238}U$ age weighted means or the youngest inherited zircon age, unless specified as CA-TIMS in the legend. Zircon CA-TIMS ages from Ootes et al. (2020b). Titanite ages were determined by concordia lower intercepts on Tera-Wasserburg diagrams. Uncertainties are reported at the 95.4% confidence level (2σ).

Zircon LA-ICP-MS U-Pb dates from this study generally agree with previously published ages (Mortensen et al., 1995; Devine et al., 2014; Bath et al., 2014; Ootes et al., 2020b, 2020c; Jones et al., 2021); however, our new, expanded intrusive suite age ranges are more representative of protracted Hogem magmatism. This is evident in the Mesilinka suite, which prior to this study (and Ootes et al., 2020c and Jones et al., 2021), did not have any reported U-Pb ages. Ootes et al. (2020b) reported Ar-Ar ages of ca. 109 and 112 Ma for biotite from a Mesilinka granite and tonalite sample, which was interpreted as the age of post-deformation cooling during uplift. A Mesilinka grandiorite sample yielded Ar-Ar ages of ca. 123 Ma for biotite and ca. 139 Ma for hornblende, which possibly represent magmatic cooling prior to deformation (Ootes et al., 2020b). These Ar-Ar dates correlate with previously determined biotite and hornblende K-Ar dates from granite and granodiorite samples of the Mesilinka suite (Irvine, 1971; Garnett, 1978). The Osilinka intrusive suite was formerly interpreted as the youngest intrusive phase and correlative with the Cretaceous Cassiar batholith (ca. 100 Ma) to the north (Woodsworth et al., 1991). Although the crystallization age of the Osilinka suite is not

well constrained, the maximum zircon U-Pb crystallization age (Late Jurassic, ca. 160 Ma) presented here is approximately 60 Ma older than previously thought.

5.2 Timing of the crystallization of the Hogem batholith relative to Intermontane magmatism

The strikingly protracted and composite 80-million-year magmatic history of Hogem batholith has not been recognized elsewhere in Quesnel terrane and is unique within the Canadian Cordillera, which is one of the main outcomes of this study. Zircon U-Pb ages from the Thane Creek (Late Triassic to Early Jurassic) and Duckling Creek (late Early Jurassic) suites correspond to major periods of magmatism throughout the Canadian Cordillera (Figure 5.1.1; e.g., Woodsworth et al., 1991). However, the period in which the Mesilinka intrusive suite crystallized (135 to 127 Ma) has been linked to a major magmatic lull across western North America (Armstrong, 1988).

5.2.1 Comparison of Hogem batholith to select similar aged intrusions in Quesnel terrane

In the south-central Quesnel terrane, three parallel belts of calc-alkaline to alkaline intrusions have relatively narrow age ranges from Late Triassic to Early Jurassic (~229 to 193 Ma; Table 5.2.1.1; Schiarizza, 2019; Kobylinski et al., 2020). These intrusions progressively young from west to east and are associated with different phases of porphyry-style mineralization (Schiarizza, 2014). The older, western plutonic belt is composed of calc-alkaline intrusions (e.g., Guichon Creek batholith; Figure 5.2.1.1) which host Cu-Mo porphyry mineralization. The central plutonic belt comprises alkaline intrusions (e.g., Copper Mountain batholith; Figure 5.2.1.1) and hosts Cu-Au porphyry mineralization. The eastern plutonic belt is composed of younger (~202 to 193 Ma), Cu-Mo porphyry hosting calc-alkaline plutons (e.g., Pennask batholith; Figure 5.2.1.1). Similar intrusive age patterns are not recognized in northern Quesnel terrane (Nelson et al., 2013).

Table 5.2.1.1. Comparison of Hogem batholith to similar aged intrusions in the Quesnel (QT) and Stikine (ST) terranes. 1: this study; 2: Schiarizza, 2019; 3: Sack et al., 2020; 4: Woodsworth et al., 1991; 5: Villeneuve et al.., 2001.

Terrane	Batholith(s)	Age range (Ma)	Reference
north-central QT	Hogem	207 to 127	1
south-central QT	e.g., Guichon Creek, Copper Mountain, Pennask	229 to 193	2
northern QT	Tatchun McGregor	204 to 196 160 to 146	3
south-eastern QT	Kuskanax, Nelson	180 to 160	4
ST	Endako	220 to 145	5

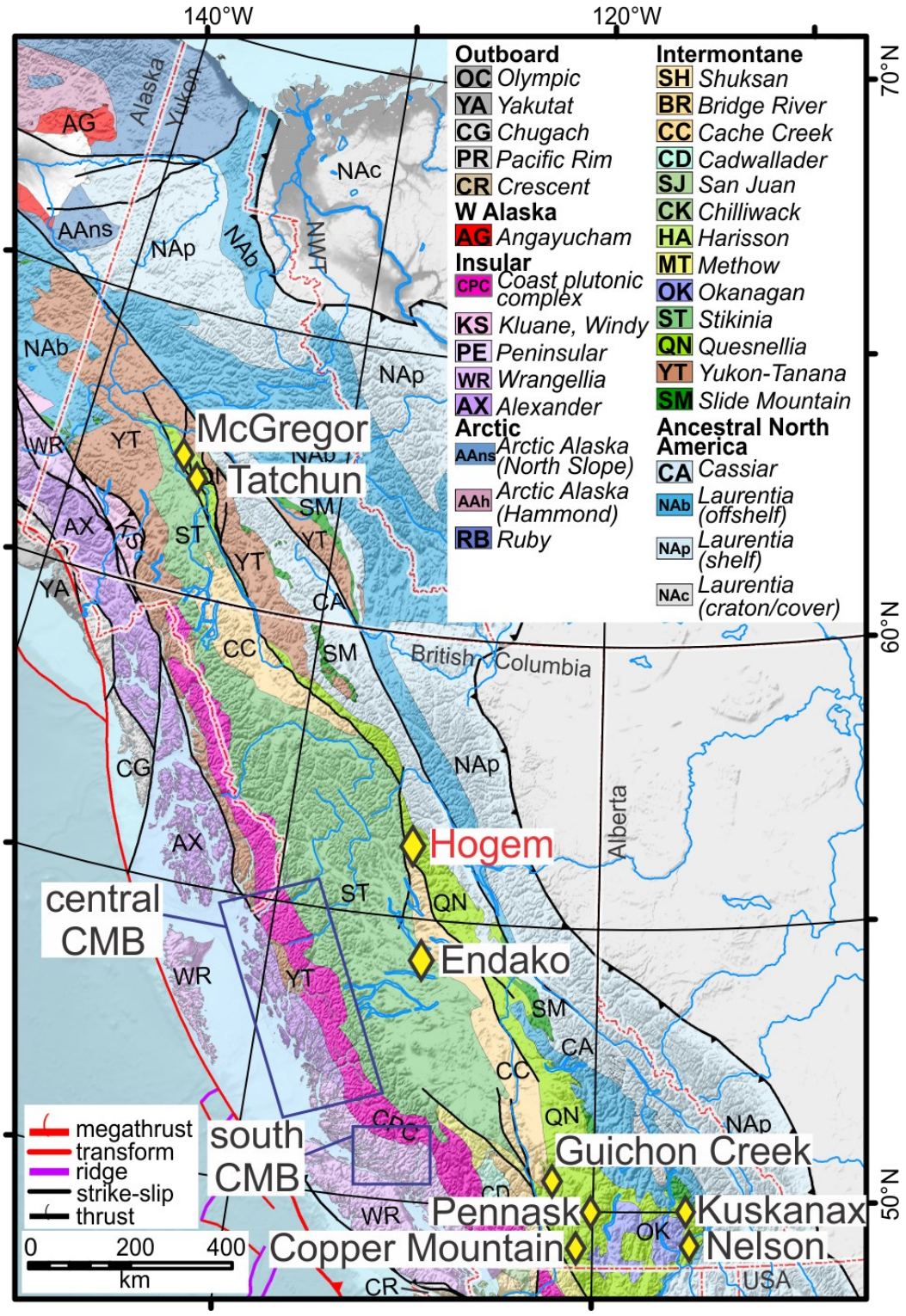

Figure 5.2.1.1. Terrane map of the Canadian Cordillera, northern Washington state, and eastern Alaska, modified after Colpron and Nelson (2020). Yellow diamonds indicate the locations of the Hogem batholith and other Cordilleran batholiths mentioned in the text. Blue squares show the central (Gehrels et al., 2009; Cecil et al., 2011) and southern (Homan, 2017; Cecil et al., 2021) areas of the Coast Mountains batholith (CMB).

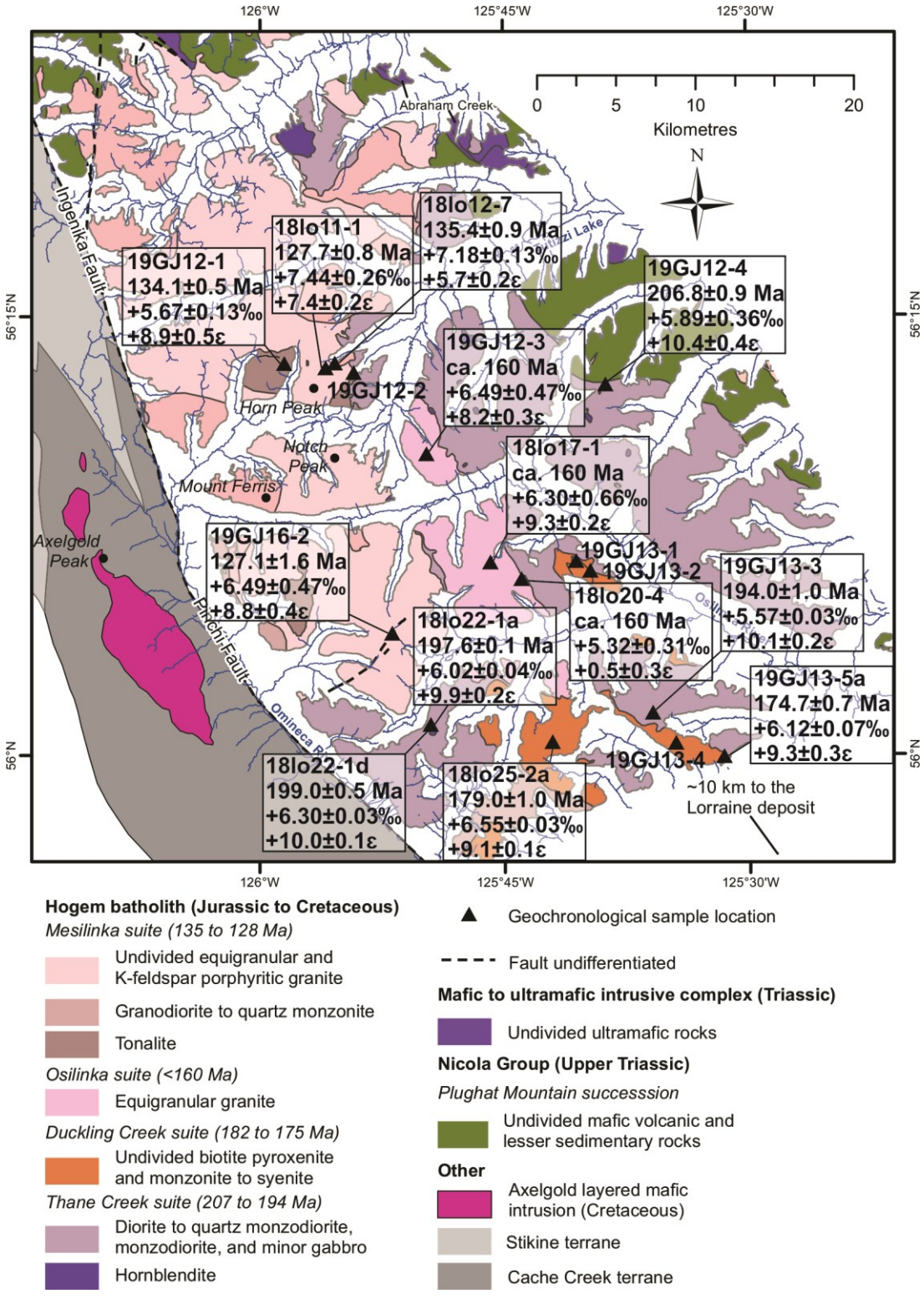

Figure 5.2.1.2. Sample location map of northern Hogem batholith showing weighted mean zircon LA-ICP-MS U-Pb ages (Ma), εHf(t), and SIMS $\delta^{18}O$ (‰) results for this study. Sample 18lo22-1a shows the zircon CA-TIMS U-Pb instead of LA-ICP-MS. Bedrock geology is after Ootes et al. (2020a). Black triangles represent geochronology and geochemistry intrusive rock samples taken for this study. Uncertainties are at the 95.4% confidence level (2σ).

In northern Quesnel terrane, Late Triassic to Jurassic plutons are represented by the Minto (205 to 194 Ma) and McGregor (163 to 146 Ma) suites (Sack et al., 2020). In southern Yukon, plutons of the Minto suite are interpreted to intrude across the boundaries of the Quesnel, Stikine, and Yukon-Tanana terranes (Sack et al., 2020), which has also been observed in similar-aged intrusions in the Cassiar Mountains of northern British Columbia (Nelson and Friedman, 2004), but has not been observed further south. The Tatchun batholith of the Minto suite intrudes the northern Quesnel terrane (Figure 5.2.1.1; Table 5.2.1.1) and has interpreted zircon TIMS U-Pb ages of granodiorite (196.13±0.09 Ma) and granite (203.32±0.06 Ma; Sack et al., 2020), which overlap with zircon ages from the Thane Creek suite in the Hogem batholith. However, inherited zircons with LA-ICP-MS U-Pb ages up to ~348 Ma are present in the Tatchun batholith intrusive samples, which have not been observed in the Thane Creek intrusions. Two diorite samples from the McGregor pluton intruding the northern Quesnel terrane in southern Yukon (Figure 5.2.1.1; Table 5.2.1.1) have zircon TIMS U-Pb ages of 163.42±0.05 Ma and 161.18±0.05 Ma (Sack et al., 2020). The McGregor batholith spans a unique magmatic period in Yukon (Sack et al., 2020), however, it is similar in age to the Osilinka suite in the Hogem batholith (ca. 160 Ma) and the Kuskanax and Nelson batholiths in southern BC (Table 5.2.1; Woodsworth et al., 1991). The Kuskanax and Nelson batholiths cross-cut ancestral North American rocks in the Omineca belt (Figure 5.2.1.1; Woodsworth et al., 1991; Nelson and Colpron, 2007) and have distinct continental crust-influenced isotopic signatures (Ghosh, 1995; Nelson et al., 2013).

5.2.2 Comparison of Hogem batholith to select similar aged intrusions in Stikine terrane

Similar to the Hogem batholith, the Endako batholith in eastern Stikine terrane, approximately 200 km south of northern Hogem batholith (Figure 5.2.1.1), has a protracted and composite magmatic history. Three separate Mesozoic intrusive suites form the Endako batholith and range in age from Late Triassic (ca. 220 Ma) to Early Cretaceous (ca. 145 Ma; Table 5.2.1.1; Villeneuve et al., 2001). The Francois Lake suite (~149 to 145 Ma; Villeneuve et al., 2001) is the youngest phase of the Endako batholith and is coincident with the oldest Mesilinka suite phases in the Hogem batholith. These intrusive phases occur in a period otherwise marked by magmatic quiescence across the Canadian Cordillera (Armstrong, 1988). The Hogem and Endako batholiths also have geochemical similarities, such as wide compositional ranges (SiO_2=44-80

wt.% for Endako and SiO_2=33-75 wt.% for Hogem), metaluminous to slightly peraluminous and low- to high-K granitoids, and juvenile isotopic signatures (Whalen et al., 2001; this study).

5.3 Zircon Hf-O constraints on relative juvenile and evolved components in Hogem magmas

Combined zircon Hf-O isotope data can help evaluate the relative amounts of mantle-derived and crustal components in the melts that crystallized a magmatic rock (e.g., Kemp et al., 2006). Initial Hf isotope ratios ($^{176}Hf/^{177}Hf$ initial, represented as εHf(t)) may indicate whether the melt source was isotopically juvenile (εHf >0) or evolved (εHf <0). Zircon oxygen isotope data help assess whether the magmatic source was derived from the mantle, such as that which characterises the asthenosphere ($\delta^{18}O$=+5.3±0.6‰; Valley et al., 1998), whether parts of it interacted with the low-temperature hydrosphere (i.e., recycled; $\delta^{18}O$ >+5.3±0.6‰), or with high-temperature hydrothermal fluids, which tend to drive oxygen isotopes to lower $\delta^{18}O$ values with increasing water-rock ratios. Later-stage interaction with lower temperature hydrothermal fluids have the potential to drive zircon $\delta^{18}O$ values higher (Valley et al., 2005). Mantle processes do not significantly fractionate oxygen-isotopes and the mantle $\delta^{18}O$ signature is stable through time (Valley et al., 2005). Extensive fractional crystallization of a magma can enrich ^{18}O in the residual melt, but only by ~1‰ (Matsuhisa, 1979; Muehlenbachs and Byerly, 1982; Hoefs, 2018). The combined Hf-O isotopes can resolve mixing of mantle-derived magmas with recycled crustal components, which may occur via contamination of the magma source, or assimilation of country rock during magma emplacement (Chapman et al., 2017).

Thane Creek intrusive suite

Zircons from the Thane Creek suite plutonic rocks have the most radiogenic εHf(t) compositions in the Hogem batholith. These are the oldest magmatic zircons, which have initial Hf isotopic values (εHf(t)= +8.2±1.6 to +12.1±1.5) consistent with derivation from a juvenile source, with little crustal input. The Thane Creek zircon data overlap with εHf(t) values for normal mid-ocean ridge basalts (Chauvel and Blichert-Toft, 2001; Figure 5.3.1), but only the most radiogenic Thane Creek data overlap with the estimated depleted mantle Hf range at ca. 207 to 194 Ma (εHf(t)= +11.3 to +15.8). Zircon oxygen isotope values are consistent with the juvenile Hf isotope compositions, as most $\delta^{18}O$ results are within the mantle zircon range (Figure 5.3.1). However, in the oldest interpreted Thane Creek diorite (19GJ12-4; 206.8±0.9 Ma), zircon

$\delta^{18}O$ values are up to 8.5‰. These elevated $\delta^{18}O_{zircon}$ values are thought to represent secondary low-temperature alteration and not the $\delta^{18}O$ of the melt, as these high $\delta^{18}O$ zircon grains are cracked and have altered growth zoning (Appendix C). This interaction with the hydrosphere did not involve significant input of other elements from the crust and is perhaps expected from the oldest end-member of a large composite batholith, which experienced the subsequent thermal and structural disruption by later intrusive episodes. Overall, the Thane Creek suite magmas are interpreted as predominantly depleted mantle-derived with minimal crustal influence.

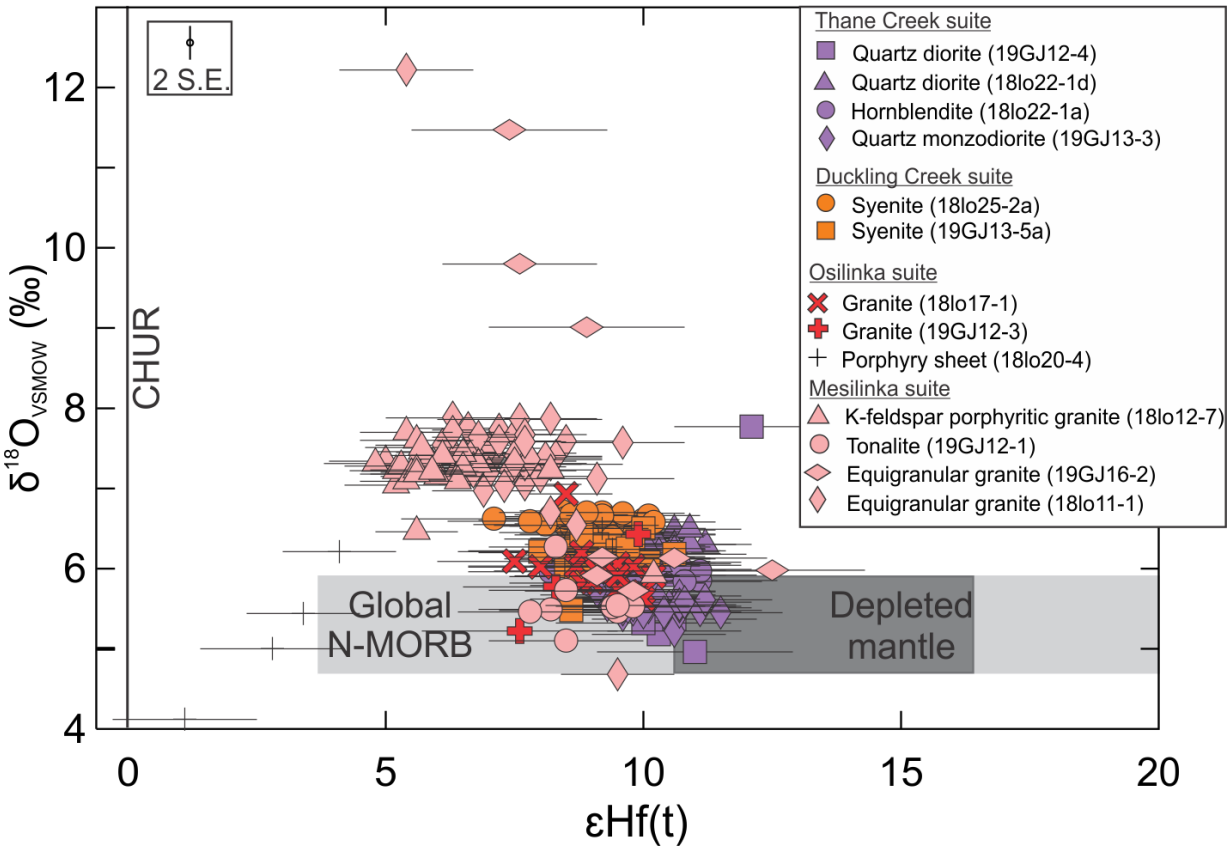

Figure 5.3.1. Single zircon εHf(t) versus corresponding $\delta^{18}O_{VSMOW}$ (‰) values for Hogem batholith intrusive rock samples. Zircon data were screened to exclude εHf(t) results with propagated errors >2ε units. Uncertainties are at the 95.4% confidence level (2σ). CHUR= Chondritic uniform reservoir, after Bouvier et al. (2008). N-MORB= Normal mid ocean ridge basalt, after Chauvel and Blichert-Toft (2001). The upper depleted mantle limit is after Griffin et al. (2002) and lower depleted mantle limit is after Naeraa et al. (2012). The mantle zircon $\delta^{18}O$ range (5.3±0.6‰) is from Valley et al. (1998). 2 S.E.= average 2σ standard error.

Duckling Creek intrusive suite

Positive zircon initial Hf results ($\varepsilon Hf_{(t)}$= +7.1±1.8 to +10.6±1.4) indicate the Duckling Creek suite magmas had a juvenile source. The Duckling Creek zircon $\delta^{18}O$ data (+5.48±0.19 to +6.72±0.18‰) overlap or are slightly heavier than mantle values (Figure 5.3.1). Zircons from the younger Duckling Creek syenite (19GJ13-5a) generally have lower, more mantle-like $\delta^{18}O$ values compared to older Duckling Creek syenite (18lo25-2a), which suggests a minor decrease in crustal recycling/interaction through time, if the higher values indicate derivation from a recycled component.

Osilinka intrusive suite

Zircons from the Osilinka suite leucocratic granite (ca. 160 Ma) have juvenile Hf-O signatures and overlap the Duckling Creek and Thane Creek suite results (Figure 5.3.1). In contrast to the exclusively magmatic zircons of the Thane Creek and Duckling Creek suites, U-Pb results (section 3.2.1.1) indicate that a significant proportion of the Osilinka granite zircons are inherited, with ages as much as 70 Ma older than the proposed intrusion age. The zircon grains inherited the relatively homogenous Hf-O signature of the melt source, which was possibly derived from re-melting of hybridized mantle-derived rocks of the Thane Creek suite, Duckling Creek suite, and/or Takla Group. Whole rock εNd(t) to εHf(t) results, calculated by exploiting the linearity of the mantle Hf-Nd isotope array, of Quesnel terrane Takla Group basalts (calculation of Vervoort et al., 2011; data after Dostal et al., 2009) range in $\varepsilon Hf_{(160\ Ma)}$ from +9.6±1.6 to +12.5±1.8, which overlap the most radiogenic Osilinka granite zircons (εHf(t)= +7.5±1.5 to +10.2±1.5).

The intrusive porphyry sheet (sample 18lo20-4) that cross-cuts the Osilinka intrusive suite (Ootes et al., 2019a,b) has an unconstrained minimum crystallization age, negative εHf(t) values, and high temperature hydrothermal (<5.3±0.6‰) $\delta^{18}O$ zircon values that indicate a significantly different magma source than the Osilinka granites and the other Hogem batholith suites. These porphyry sheets were likely partial melts from a distinct source that did not contribute to the magma sources of the Hogem batholith intrusive suites.

Mesilinka intrusive suite

Zircons from the Mesilinka suite have the widest range in Hf-O signatures in Hogem batholith. The Mesilinka K-feldspar porphyritic granite (135.4±0.9 Ma) has the least radiogenic zircon Hf compositions (εHf(t)= +4.8±1.0 to +6.8±1.1) and $\delta^{18}O$ values that are mostly >7‰ (Figure 5.3.1), indicating a significant recycled crustal component in the magma source. An older crustal component in the magma source is supported by the presence of xenocrystic zircons, with U-Pb results up to ~190 Ma.

In contrast, zircons from the Mesilinka tonalite (134.1±0.5 Ma) have homogenous, juvenile Hf-O values with no single zircon U-Pb ages >141 Ma. All tonalite zircon $\delta^{18}O$ compositions agree with the mantle range (Figure 5.3.1), except several antecrystic grains with higher $\delta^{18}O$ values (+6.27±0.20 to +7.58±0.20‰), which suggest only a minor crustal influence and indicate the melt source did not have significant interaction with the hydrosphere. The juvenile zircon Hf-O compositions for Mesilinka tonalites were possibly derived from partial melting of basalt or lower crustal mafic intrusive rocks.

The younger, Mesilinka equigranular granite (ca. 127 Ma) contains zircon Hf isotope compositions ranging from less radiogenic to juvenile (εHf(t)= +6.1±1.3 to +10.6±1.8) and mantle-like to low temperature hydrosphere-like $\delta^{18}O$ compositions (+4.68±0.20 to +12.22±0.24‰), which reflect a heterogeneous melt source. The presence of xenocrystic zircon ages up to ca. 235 Ma and $\delta^{18}O_{zircon}$ values commonly >7‰ indicate that an older recycled crustal component contributed to Mesilinka equigranular granite magmatism. However, more radiogenic Hf and mantle-like $\delta^{18}O$ zircon results in many of the zircons suggest that a juvenile melt source had a greater influence on the equigranular granite magmas than in the K-feldspar porphyritic granite, but less than in the tonalite.

The variation in zircon Hf-O populations between the magmatic phases in the Mesilinka suite likely represents a mix of juvenile and recycled crustal melt sources. As the Mesilinka intrusive suite crystallized after amalgamation of the Intermontane terranes and accretion to the continental margin, but synchronous with and prior to major cordilleran deformation, thrusting, and strike-slip faulting (Evenchick et al., 2007), the basement architecture and possible melt sources underlying the Hogem batholith at 135 to 127 Ma are cryptic.

5.4 Possible crustal sources and Hf-O contamination modelling

The relationship of the Quesnel terrane to rocks of Ancestral North American affinity has been a longstanding subject of debate. It is proposed that Quesnellia was built upon a portion of rifted North American crust or overlaps Yukon-Tanana terrane pericratonic crust (Colpron et al., 2006; Nelson et al., 2006; Colpron et al., 2007). Additionally, based on seismic-reflection profiles, it has been suggested that the Quesnel terrane is a thin (~2.5 km) klippe that was thrust over North American continental crust during accretion (Snyder et al., 2002; Cook et al., 2004; Evenchick et al., 2007). Zircon Hf-O isotope geochemistry provides an opportunity to address the extent of the North American basement beneath north-central Quesnel terrane by determining if North American crust contributed to Hogem batholith magmatism.

5.4.1 The role of North American crust and continental margin rocks in Hogem magmatism

The εHf(t) composition of western North American crust is modelled using detrital zircon data from the Hottah terrane, part of the Paleoproterozoic Wopmay orogen in the northwest Canadian Shield (Davis et al., 2015). A crustal evolution curve was calculated using the Hottah terrane average detrital zircon $^{176}Hf/^{177}Hf$ ratio (0.28151 after Davis et al., 2015; Figure 5.4.1.1) and the average $^{176}Lu/^{177}Hf$ ratio of bulk continental crust (0.011; Vervoort and Kemp, 2016). By 200 to 125 Ma, western North American Paleoproterozoic crust had εHf values from -57 to -33, far more evolved than the juvenile signatures in the Hogem batholith zircons (Figure 5.4.1.1). Hence, Paleoproterozoic North American crust had no role in the evolution of the Hogem batholith.

The Hottah terrane detrital zircon εHf(t) values partly overlap those of detrital zircons from Yukon-Tanana terrane (Figure 5.4.1.1; Pecha et al., 2016), consistent with the interpretation that Yukon-Tanana terrane (YTT) sediments were, in part, sourced from the northwestern Canadian shield (Tempelman-Kluit, 1976, 1979; Hansen, 1990; Mortensen, 1992; Dusel-Bacon et al., 2004, 2006, 2013; Nelson et al., 2006, 2013; Piercey and Colpron, 2009; Pecha et al., 2016). Detrital zircons from the Lay Range assemblage, the assumed north-central Quesnel terrane basement, also have a Precambrian zircon record that suggest partial continental derivation (Figure 5.4.1.1; Ferri, 1997; Ootes et al., unpublished data). A North American crustal influence in the YTT is evident from isotopic excursions from juvenile to lower εHf(t)

values of -20ε at 400 to 350 Ma, -18 ε at ca. 260 Ma, and -11ε at ca. 180 Ma (Figure 5.4.1.2; Pecha et al., 2016). The Lay Range assemblage appears to have a predominantly juvenile source, but a minor North American crustal influence caused isotopic excursions to evolved εHf(t) values of -12 at ca. 425 Ma and -6 from 360 to 299 Ma. Similar isotopic excursions towards negative εHf(t) values would be expected in magmas contaminated by evolved country rocks but are absent in zircons from the Hogem batholith. This indicates clearly that older, evolved crustal rocks did not significantly contribute to Hogem batholith magmas.

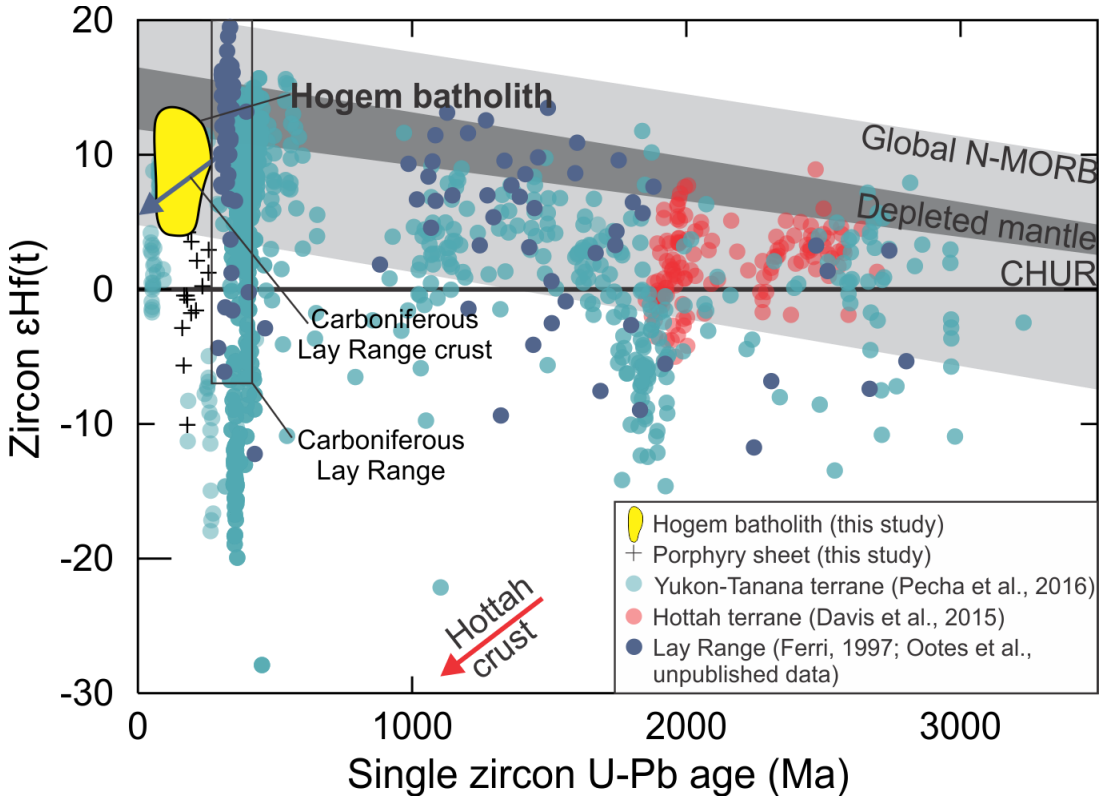

Figure 5.4.1.1. Single zircon U-Pb age (Ma) versus corresponding εHf(t) from Hogem batholith igneous zircons (this study), Lay Range detrital zircons (Ferri, 1997; Ootes et al., unpublished data), Yukon-Tanana terrane detrital zircons (Pecha et al., 2016), and Hottah terrane detrital zircons (Davis et al., 2015). Lay Range average crust was modelled using the average $^{176}Hf/^{177}Hf$ value from the range of Carboniferous-aged (358 to 299 Ma) detrital zircon LA-ICP-MS results, (0.282936; after Ferri, 1997 and Ootes et al., unpublished data), and $^{176}Lu/^{177}Hf$ of bulk continental crust (0.011; Vervoort and Kemp, 2016). Hottah terrane average crust was modelled using the average $^{176}Hf/^{177}Hf$ value from the range of detrital zircon results (0.28151; after Davis et al., 2015), and $^{176}Lu/^{177}Hf$ of bulk continental crust (0.011; Vervoort and Kemp, 2016). Hogem zircon data was screened to exclude εHf(t) results with propagated errors >2ε units and U-Pb results with >10% discordance. CHUR= Chondritic uniform reservoir, after Bouvier et al. (2008). N-MORB= Normal mid ocean ridge basalt, after Chauvel and Blichert-Toft (2001). The upper depleted mantle limit is after Griffin et al. (2002) and lower depleted mantle limit is after Naeraa et al. (2012).

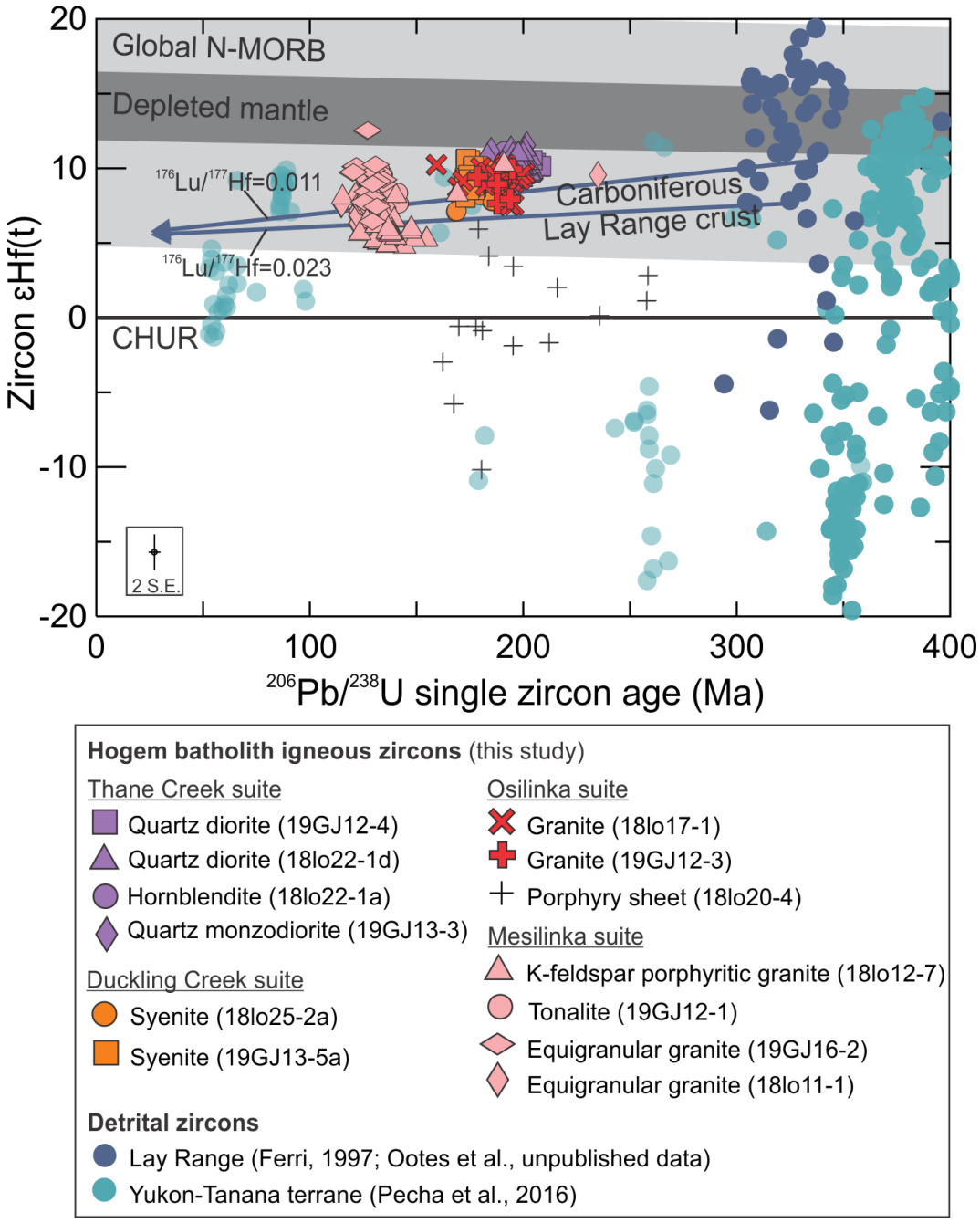

Figure 5.4.1.2. Single zircon $^{206}Pb/^{238}U$ age (Ma) versus corresponding εHf(t) from Hogem batholith igneous zircons (this study), Lay Range detrital zircons (Ferri, 1997; Ootes et al., unpublished data), and Yukon-Tanana terrane detrital zircons (Pecha et al., 2016). Lay Range average crust was modelled using the average $^{176}Hf/^{177}Hf$ value from the range of Carboniferous aged (358 to 299 Ma) detrital zircon LA-ICP-MS results (0.282936; after Ferri, 1997 and Ootes et al., unpublished data) and $^{176}Lu/^{177}Hf$ of bulk continental crust (0.011; Vervoort and Kemp, 2016) and mafic crust (0.023; Vervoort and Kemp, 2016). Hogem zircon data was screened to exclude εHf(t) results with propagated errors >2ε units and U-Pb results with >10% discordance. CHUR= Chondritic uniform reservoir, after Bouvier et al. (2008). N-MORB= Normal mid ocean ridge basalt, after Chauvel and Blichert-Toft (2001). The upper depleted mantle limit is after Griffin et al. (2002) and lower depleted mantle limit is after Naeraa et al. (2012).

5.4.2 Quesnel terrane basement contamination of Hogem magmas

The genetic relationship of Hogem batholith to the underlying Quesnel terrane basement was modelled using detrital zircon Lu-Hf data from the Lay Range assemblage (Ferri, 1997; Ootes et al., unpublished data). Although Precambrian-aged detrital zircons are present in the Lay Range assemblage, juvenile Hf isotope results of Carboniferous-aged (315 to 360 Ma) zircons are thought to be representative of the mantle source during development of the juvenile arc basement in the Quesnel terrane. Hafnium isotopic evolution curves for the mantle source region of the Carboniferous-aged Lay Range assemblage zircons were modelled using the average $^{176}Hf/^{177}Hf$ value of the detrital zircons (0.282936) and the average $^{176}Lu/^{177}Hf$ of the bulk continental crust and (0.011) and mafic crust (0.023; Vervoort and Kemp, 2016). It is evident that the Hf isotopic composition of the Lay Range source in the Carboniferous, projected through time to the main Hogem intrusive phases, overlap much of zircon εHf results of Hogem batholith (Figure 5.4.1.2). This indicates that the Hf compositions of zircon-crystallizing magmas across the Quesnel terrane did not significantly change from development of the juvenile island arc basement at ca. 350 Ma to post-accretion at ca. 127 Ma. There is a slight isotopic excursion to lower εHf(t) values in the Mesilinka suite at ca. 150 to 130 Ma (Figure 5.4.1.2) and suggests a minor influence of a less radiogenic, probably crustal component, in this phase of the batholith.

5.4.3 Modelling the extent of crustal contamination of Hogem magma sources

Though the depleted initial Hf isotope signatures of zircon from the Hogem magmas indicate little interaction with the continental crust through much of its evolution, the subtle isotopic differences between different phases might be due to this process. The overall radiogenic zircon Hf isotope compositions through the Hogem batholith's 80-million-year magmatic history can be mostly accounted for by juvenile crustal evolution (Figure 5.4.3.1). A regression through all the Thane Creek, Duckling Creek, and Osilinka suite zircon U-Pb age and εHf(t) results, but only the most radiogenic Hf results from the 135 to 127 Ma Mesilinka intrusive suite zircons (εHf(t) >8), results in a slope of εHf/Ma (0.0146) that corresponds to a $^{176}Lu/^{177}Hf$ ratio of 0.0118 (line 1 on Figure 5.4.3.1), which is the approximate average $^{176}Lu/^{177}Hf$ ratio of the bulk continental crust (0.011 of Vervoort and Kemp, 2016; 0.012 of Rudnick and Gao, 2003). However, regressing through the same Thane Creek, Duckling Creek, and Osilinka suite zircon results, but only the least radiogenic Hf results from the Mesilinka suite

zircons (εHf(t) <7) yields a steep εHf/Ma slope (0.05927) that corresponds to a $^{176}Lu/^{177}Hf$ ratio of -0.0560 (line 2 on Figure 5.4.3.1), which requires interaction with an isotopically evolved reservoir (Spencer et al., 2019). The average εHf/Ma slope (0.03467) of all Hogem batholith zircon results corresponds to a $^{176}Lu/^{177}Hf$ ratio of -0.0019 (line 3 on Fig. Figure 5.4.3.1) and likely reflects a mix of isotopically juvenile and evolved sources (Spencer et al., 2019). This average slope intersects the intermediate Mesilinka suite zircon Hf results (8> εHf(t) <7) and suggests these Mesilinka zircons crystallized from a mix of melt sources.

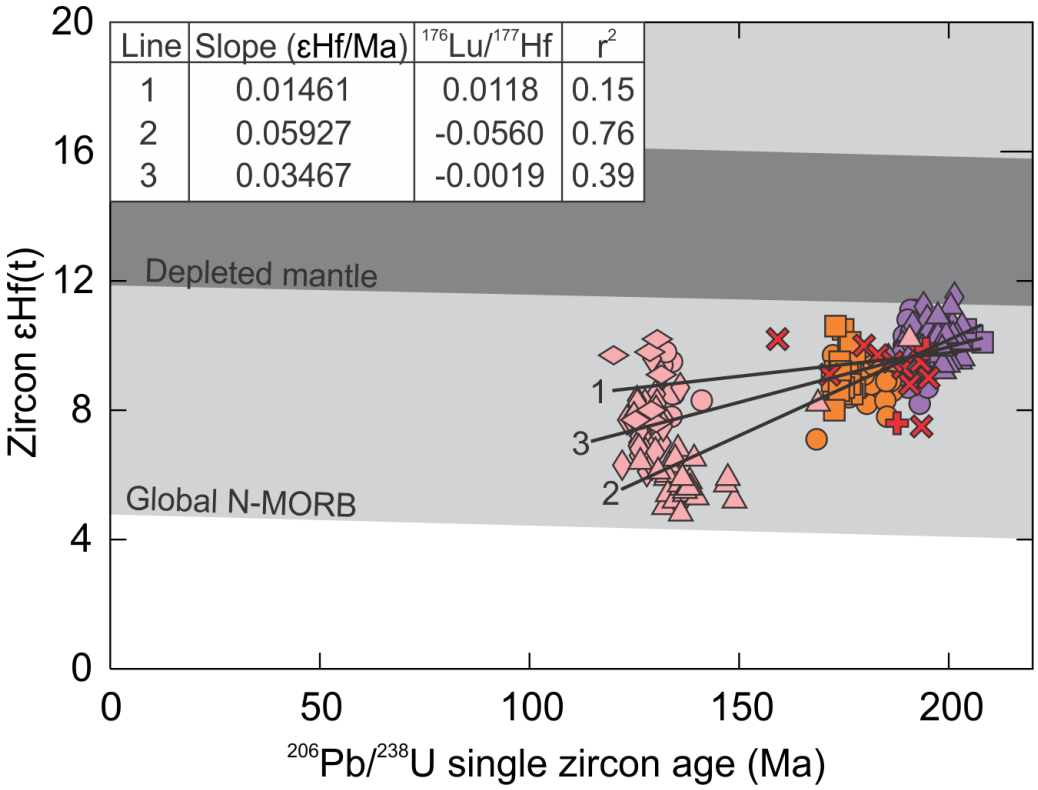

Figure 5.4.3.1. Single zircon $^{206}Pb/^{238}U$ age results versus corresponding εHf(t) values. Three different regressions define εHf/Ma slopes and corresponding $^{176}Lu/^{177}Hf$ values through all the Thane Creek (purple), Duckling Creek (orange), and Osilinka (red) data, but only the Mesilinka suite (pink) results with specific εHf(t) ranges. Line 1: Mesilinka suite zircon εHf(t) >8; Line 2: Mesilinka suite zircon εHf(t) <7; Line 3: All Mesilinka suite zircon εHf(t) results. N-MORB= Normal mid ocean ridge basalt, after Chauvel and Blichert-Toft (2001). The upper depleted mantle limit is after Griffin et al. (2002) and lower depleted mantle limit is after Naeraa et al. (2012).

Crustal contamination of Hogem batholith magmas were modelled using coupled zircon εHf(t) and $\delta^{18}O$ systematics on the basis that both these tracers are sensitive, at different levels, to interaction with crustal materials (Figure 5.4.3.2). The involvement of Quesnel terrane basement in contaminating mantle-derived or juvenile magmas was estimated using average Quesnellia Takla Group basalt as the parent melt (PM) and Lay Range assemblage as the

contaminant (C; Table 5.4.3.1). The average Takla Group field represents the approximate composition of the mantle source of the Thane Creek and Duckling Creek suite magmas, which was determined using whole-rock Sm-Nd results of eight Quesnel terrane Takla Group basalt samples (Dostal et al., 2009). The Takla Group average $\varepsilon Hf_{(190\ Ma)}$ (converted from $\varepsilon Nd_{(190\ Ma)}$ after Vervoort et al. (2011)) is 12.3±1.6, and was coupled with an assumed mantle $\delta^{18}O$ value (5.3±0.6‰; Valley et al., 1998). The average bulk Lay Range, <1.6 Ga Lay Range, and Carboniferous Lay Range fields represent the calculated εHf(t) values (Table 5.4.3.1) using the average Lu-Hf ratios of all Lay Range detrital zircons ($^{176}Lu/^{177}Hf$=0.00101 and $^{176}Hf/^{177}Hf$=0.282411), <1.6 Ga old detrital zircon ($^{176}Lu/^{177}Hf$=0.00113 and $^{176}Hf/^{177}Hf$=0.282648), and only Carboniferous-aged detrital zircons ($^{176}Lu/^{177}Hf$=0.00119 and $^{176}Hf/^{177}Hf$=0.282936; Ferri, 1997; Ootes et al., unpublished data). A $\delta^{18}O$ value of 9‰ was assumed for the Lay Range assemblage, after the approximate $\delta^{18}O$ of the upper oceanic crust (Valley, 2003). Binary mixing curves between the end-members were modelled assuming the Hf concentration of the contaminant was twice that of the parent melt (Hf_{PM}/Hf_C=0.5).

Mixing of the Carboniferous and <1.6 Ga Lay Range end-members with the Hogem mantle source constrains most Thane Creek and Duckling Creek suite zircon Hf-O results that fall outside of the mantle range (Figure 5.4.3.2A). This model shows up to 40% contamination of juvenile, mantle-derived magmas by juvenile Quesnel terrane basement may account for heavier $\delta^{18}O$ values (>5.3±0.6‰) and less radiogenic Hf results of Thane Creek and Duckling Creek zircons.

Table 5.4.3.1. End-member compositions used for binary mixing lines in Figures 5.4.4 to 5.4.5.

End-member	Material	$\varepsilon Hf_{(190\ Ma)}$	$\varepsilon Hf_{(130\ Ma)}$	$\delta^{18}O$ (‰)
Takla Group/Hogem mantle source	Basalt (whole rock)	12.3	-	5.3
Bulk Lay Range assemblage	Detrital zircon	-9.1	-10.4	9
Carboniferous Lay Range assemblage	Detrital zircon	8.2	7.3	9
<1.6 Ga Lay Range assemblage	Detrital zircon	-0.8	-2.1	9
Juvenile Mesilinka suite	Igneous zircon	-	9.8	5.5

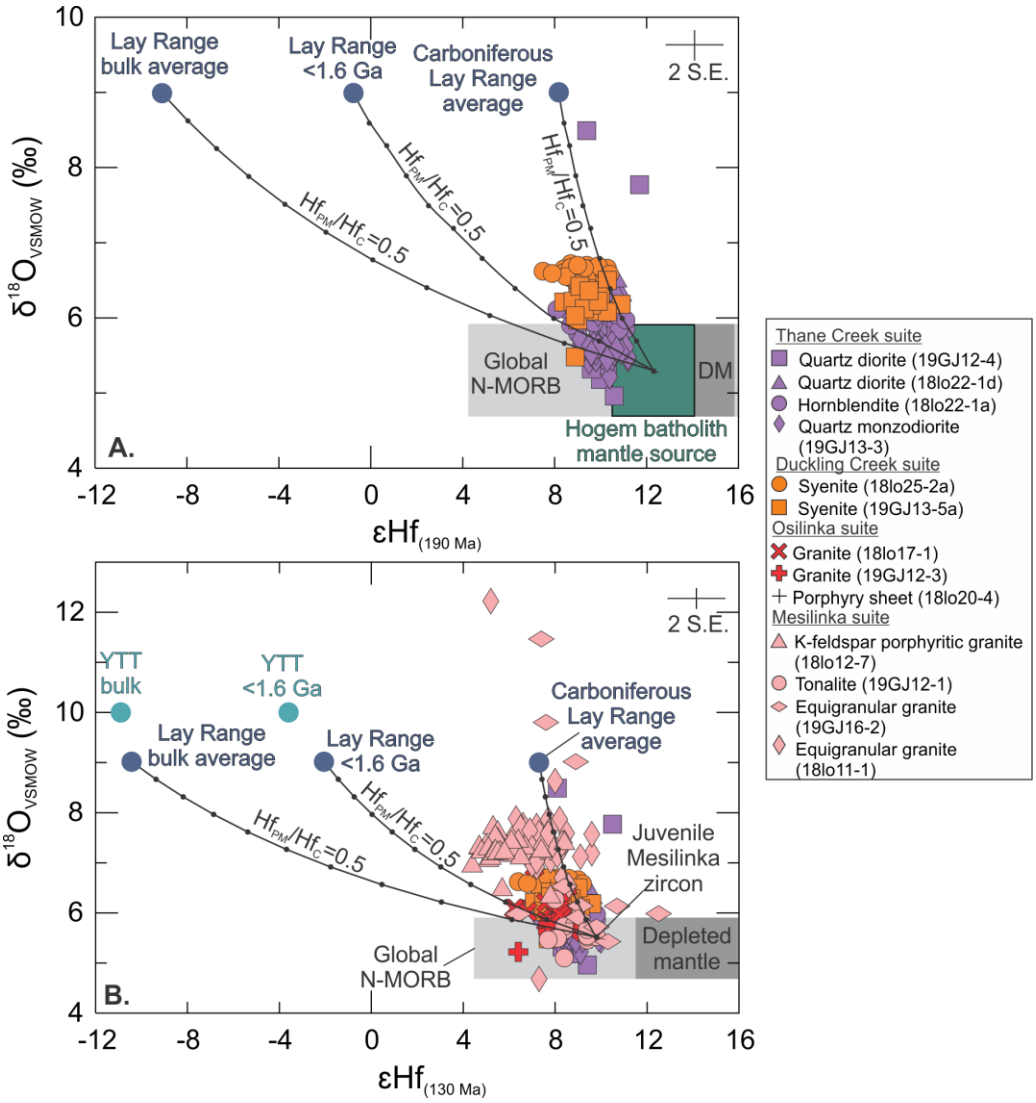

Figure 5.4.3.2. Zircon εHf(t) and $\delta^{18}O_{VSMOW}$ (‰) binary mixing curves, with end members: **A)** Hogem batholith depleted mantle source, represented by average Quesnel terrane Takla Group basalt ($\varepsilon Hf_{(190\ Ma)}$=+12.3, $\delta^{18}O$=+5.3‰) as the parent melt and average bulk, <1.6 Ga, and Carboniferous-aged Lay Range detrital zircon (after Ferri, 1997 and Ootes et al., in publication) as the contaminants. The average Quesnel terrane Takla Group basalt εHf(t) value was determined by calculating the average whole-rock $\varepsilon Nd_{(190\ Ma)}$ of eight basalt samples (Dostal et al., 2009), and converted to average $\varepsilon Hf_{(190\ Ma)}$ using the calculation of Vervoort et al. (2011). The Hogem batholith mantle source was assumed to have mantle $\delta^{18}O$ (+5.3±0.6‰; Valley et al., 1998). The average bulk Lay Range detrital zircon $\varepsilon Hf_{(190\ Ma)}$ value was calculated using $^{176}Lu/^{177}Hf$=0.00101 and $^{176}Hf/^{177}Hf$=0.282411. The average <1.6 Ga Lay Range detrital zircon $\varepsilon Hf_{(190\ Ma)}$ value was calculated using $^{176}Lu/^{177}Hf$=0.00113 and $^{176}Hf/^{177}Hf$=0.282648. The average Carboniferous Lay Range detrital zircon $\varepsilon Hf_{(190\ Ma)}$ value was calculated using $^{176}Lu/^{177}Hf$=0.00119 and $^{176}Hf/^{177}Hf$=0.282936. The Lay Range $\delta^{18}O$ composition is assumed to be 9‰, the approximate $\delta^{18}O$ value for the upper oceanic crust (Valley, 2003). **B)** Juvenile Mesilinka suite zircon (εHf(130 Ma)=+9.8, $\delta^{18}O$=+5.5‰) and average bulk Lay Range ($\varepsilon Hf_{(130\ Ma)}$= -10.4, $\delta^{18}O$= +9.0‰), average <1.6 Ga Lay Range ($\varepsilon Hf_{(130\ Ma)}$= -2.1, $\delta^{18}O$= +9.0‰), and average Carboniferous Lay Range ($\varepsilon Hf_{(130\ Ma)}$=+7.3, $\delta^{18}O$=+9.0‰). Binary mixing model curves after Langmuir et al. (1978), assuming Hf concentration of parent melt to contaminant ratios (Hf_{PM}/Hf_C) of 0.5. Points along the mixing curves indicate 10% mixing increments. N-MORB= Normal mid ocean ridge basalt, after Chauvel and Blichert-Toft (2001). The upper depleted mantle limit is after Griffin et al. (2002) and lower depleted mantle limit is after Naeraa et al. (2012). 2 S.E.= average 2σ standard error.

Using the same methods as at t=190 Ma, a binary mixing model was produced at t=130 Ma using the most juvenile Mesilinka suite zircon result ($\varepsilon Hf_{(130\ Ma)}$=9.8, $\delta^{18}O$=5.5‰) as the parent melt composition and the average bulk Lay Range, <1.6 Ga Lay Range, and Carboniferous Lay Range detrital zircon values as the contaminant melt compositions (Table 5.4.3.1; Figures 5.4.3.2B and 5.4.3.3). Most Mesilinka suite zircon $\varepsilon Hf_{(130\ Ma)}$ results are also constrained by the Carboniferous and <1.6 Ga Lay Range binary mixing lines and suggests up to 70% melting of predominantly juvenile Quesnel terrane basement formed the Mesilinka intrusive suite. The Mesilinka suite zircon data do not overlap with the bulk Lay Range Hf-O mixing curve (Figures 5.4.3.2B and 5.4.3.3).

Although binary mixing is an over-simplification of these magma systems and does not account for heterogeneous mantle sources, multiple contaminants, variable parent melt to contaminant Hf concentration ratios, or fractional crystallization, it is clear the Hogem batholith was generated from predominantly juvenile melts. The average North American crust at 130 Ma, indicated by any of the average Hottah terrane, >1.6 Ga Lay Range, or >1.6 Ga YTT detrital zircon compositions, is highly evolved. Mixing with the ancient crust pulls the bulk Lay Range $\varepsilon Hf_{(130\ Ma)}$ composition down ~8 epsilon units (Figure 5.4.3.3). There is a trend to lower εHf(t) values (+4.4) in the Mesilinka suite, but this isotopic excursion is only ~5 epsilon units lower than the most juvenile Mesilinka suite zircons. This variability could, in-part be due to mantle source heterogeneity; however, in cases where less radiogenic zircon εHf(t) values correspond with elevated $\delta^{18}O$ results, the involvement of an enriched mantle source may be excluded as this would not account for elevated $\delta^{18}O$ compositions. Even if the εHf(t) variability in the Mesilinka suite is driven by crustal assimilation, this is a more limited range that is still within the NMORB field. Hence, the Hf isotope data indicate that the melt source of the Mesilinka intrusive suite did not have a significant evolved North American crust component but may have experienced minor crustal contamination from pre-existing Quesnellia.

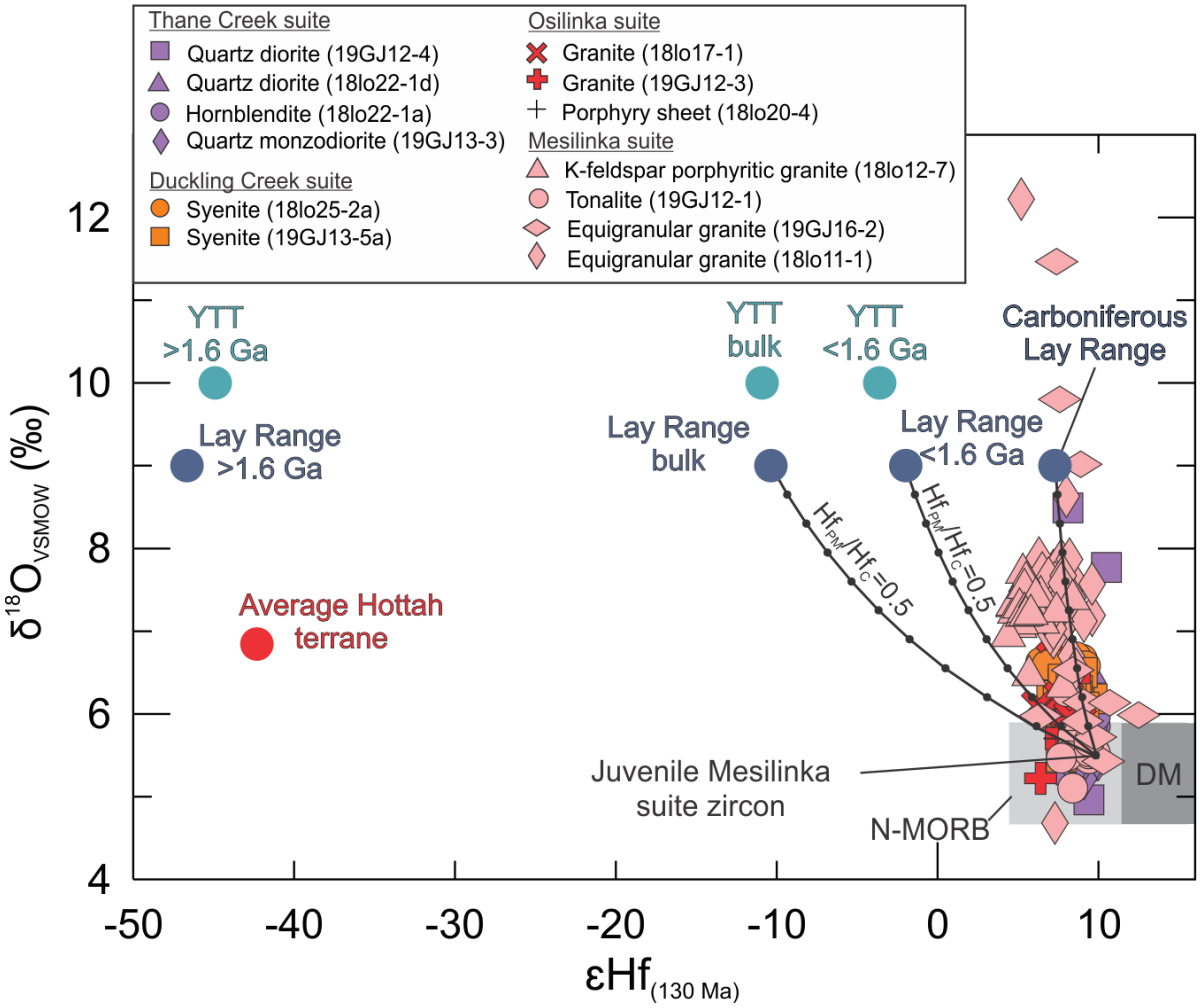

Figure 5.4.3.3. Zircon εHf(t), calculated at t=130 Ma versus corresponding zircon δ18OVSMOW (‰). Binary mixing curves are modelled using the most juvenile Mesilinka suite zircon (εHf(130 Ma)=+9.8, δ18O=+5.5‰) as the parent melt and average bulk, <1.6 Ga, and Carboniferous-aged Lay Range detrital zircon (Ferri, 1997; Ootes et al., unpublished data) as the contaminant melt. The average bulk Lay Range detrital zircon $\varepsilon Hf_{(190\ Ma)}$ value was calculated using $^{176}Lu/^{177}Hf$=0.00101 and $^{176}Hf/^{177}Hf$=0.282411. The average <1.6 Ga Lay Range detrital zircon $\varepsilon Hf_{(190\ Ma)}$ value was calculated using $^{176}Lu/^{177}Hf$=0.00113 and $^{176}Hf/^{177}Hf$=0.282648. The average Carboniferous Lay Range detrital zircon $\varepsilon Hf_{(190\ Ma)}$ value was calculated using $^{176}Lu/^{177}Hf$=0.00119 and $^{176}Hf/^{177}Hf$=0.282936. The Lay Range $\delta^{18}O$ composition is assumed to be 9‰, the approximate $\delta^{18}O$ value for the upper oceanic crust (Valley, 2003). Binary mixing model curves after Langmuir et al. (1978), assuming Hf concentration of parent melt to contaminant ratios (Hf_{PM}/Hf_C) of 0.5. Points along the mixing curves indicate 10% mixing increments. Average Hottah terrane detrital zircon composition after Davis et al. (2015). Bulk, >1.6 Ga, and <1.6 Ga YTT average detrital zircon $\varepsilon Hf_{(130\ Ma)}$ values after Pecha et al. (2016). N-MORB= Normal mid ocean ridge basalt, after Chauvel and Blichert-Toft (2001). The upper depleted mantle limit is after Griffin et al. (2002) and lower depleted mantle limit is after Naeraa et al. (2012). The mantle zircon $\delta^{18}O$ range (5.3±0.6 ‰) is from Valley et al., (1998).

5.5 Hogem batholith magmatism in context to the Canadian Cordilleran orogen

5.5.1 Pre- to syn-accretionary magmatism of Thane Creek and Duckling Creek intrusive suites

Late Triassic to Early Jurassic arc magmatism in the Quesnel terrane is likely attributed to westward subduction of oceanic crust beneath Quesnellia apparently prior to accretion of the Intermontane terranes to the North America margin and closure of the Cache Creek back-arc ocean (Mihalynuk et al., 1994; Nelson et al., 2013; Zagorevski, 2015; Sigloch and Mihalynuk, 2017). Relative depletion in HFSE (Nb, Ta, Zr, Ti) and enrichment in LILE (Cs, Rb, Ba, K, Sr) on primitive mantle normalized whole-rock multi-element plots (Figure 2.2.2.4) reflect subduction-related magmatism in the Thane Creek and Duckling Creek intrusive suites.

The metaluminous, calc-alkaline, and magnesian signatures of the Thane Creek intrusive rocks are typical of Cordilleran arc magmas (Frost et al., 2001). The zircon U-Pb crystallization age of the youngest phase of the Thane Creek suite (sample 19GJ13-3; 194.0±1.0 Ma) precedes the interpreted start of Quesnel terrane accretion. When combined with the relatively juvenile zircon Hf-O results, these support that the Thane Creek magmas were generated in an island arc setting. Amphibole and biotite are ubiquitous in all the Thane Creek suite phases and suggest the magmas were hydrous, possibly due to dehydration melting caused by volatile input into the mantle wedge from the subducting oceanic lithosphere (Gill, 1981; Tatsumi et al., 1986; Davies and Stevenson, 1992; Gaetani and Grove, 2003; Grove et al., 2006, 2012). Amphibole fractionation formed the Thane Creek suite hornblendite cumulates, indicated by whole-rock MREE enrichment (Figure 2.2.2.1; Dessimoz et al., 2012) and an abundance of euhedral, coarse amphibole and apatite grains that are surrounded by interstitial plagioclase (Vernon and Collins, 2011). Field relationships indicate that hornblendite is the oldest phase of the Thane Creek suite (Ootes et al. 2019b); however, hornblendite cumulate zircons are interpreted as slightly younger (sample 18lo22-1a; 197.6±0.1 Ma) than spatially associated dioritic rocks (sample 18lo22-1d; 199.0±0.5 Ma), which is likely due to late-stage crystallization of zircon intergrown with interstitial plagioclase in hornblendite. The early crystallized Thane Creek diorites and cumulate hornblendites are thought to be co-magmatic due to co-mingling texture recorded in outcrop (Figure 1.3.1.2) and similar zircon Hf-O results. Crystallization of quartz diorites to quartz

monzodiorites continued without a significant change in trace element signatures (Figure 2.2.2.1 and 2.2.2.4) or zircon Hf-O results until magmatism ceased at approximately 194 Ma.

The Duckling Creek intrusive suite is alkaline, metaluminous, and iron-rich. Mafic intrusions accumulated clinopyroxene rather than amphibole and are interpreted as the oldest magmatic phase in the Duckling Creek suite (181.68±0.95 Ma biotite pyroxenite of Devine et al., 2014). Clinopyroxene fractionation is reflected by MREE enrichment (Figure 2.2.2.1), rhythmically layered felsic- and mafic-syenites in outcrop (Figure 1.3.1.3), and interlocked, euhedral clinopyroxene grains which are spatially associated with apatite and magnetite in thin section (Figure 1.5.2C-D; Vernon and Collins, 2011). The presence of clinopyroxene rather than amphibole may indicate the Duckling Creek suite magmas were less hydrous, or more degassed, than the Thane Creek suite magmas, possibly due to decreased volatile influx from the subducting oceanic lithosphere or increased distance from the arc front (Grove et al., 2012). Overall, the Duckling Creek suite zircons have juvenile Hf-O results, but less radiogenic εHf(t) and higher $\delta^{18}O$ results relative to the Thane Creek suite zircons, which may indicate increased country rock contamination of the Duckling Creek magmas. The crystallization age of the youngest phase of the Duckling Creek syenite (sample 19GJ13-5a; 174.7±0.7 Ma) corresponds with the termination of Cache Creek subduction and accretion of Quesnel terrane with the continental margin at ca. 175 to 172 Ma (Mihalynuk et al., 2004; Nelson et al., 2013). The alkalic and shoshonitic signature of the Duckling Creek intrusive suite (Figure 2.2.1.2) may reflect syn-accretion arc extension in north-central Quesnel terrane, as shoshonitic rocks are associated with arc deformation during subduction termination or polarity change in unstable island arc regions during the transition between two different subduction regimes (Morrison, 1980).

5.5.2 Post-accretionary magmatism of Osilinka and Mesilinka intrusive suites

The post-accretionary Osilinka and Mesilinka intrusive suites were crystallized after accretion of the Intermontane terranes and are not direct products of subduction-related magmatism. Compared to the metaluminous Thane Creek and Duckling Creek suites, Osilinka and Mesilinka granites are silica-rich and weakly peraluminous (Figure 2.2.1.7). Peraluminous granites are traditionally thought to be formed by melting of pelitic rocks (‘S-type’; Chappell and White, 1974; Holtz and Johannes, 1991), or by hydrous melting of mafic source rocks (Ellis and Thompson, 1986). Trace garnet, muscovite, and allanite are variably present in Mesilinka

granites and represent aluminous trace mineral phases associated with S-type granites (Chappell and White, 1974). Positive zircon εHf(t) results of the post-accretionary Osilinka intrusive suite suggest the magma sources were relatively juvenile and supports hydrous melting of mafic source rocks (e.g., the Thane and Duckling Creek suites or Takla Group volcanics). However, Mesilinka zircon $\delta^{18}O$ values above the mantle range (>5.3±0.6‰) and less radiogenic zircon εHf(t) results (~+5) suggest the magma source had mixed recycled crustal components. Both Osilinka and Mesilinka suite rocks have high field strength element depletion (Zr, Nb, Ta, Ti) and LILE enrichment (Ba, Pb, K) patterns that were inherited from the crust they melted from, which suggests the crustal sources were formed in a subduction-related environment (Figure 2.2.2.4; e.g., Stern, 2002).

The Osilinka leucocratic granites have depleted, concave-up chondrite-normalized REE patterns (Figure 2.2.2.1), possibly due to low degree partial melting of a protolith with a high concentration of amphibole, clinopyroxene, or other MREE-rich mineral phase, which did not involve amphibole or clinopyroxene re-melting. The Osilinka suite is interpreted to have crystallized at approximately 160 Ma, after a ~15 Ma magmatic hiatus in the Hogem batholith. This gap in magmatism followed the syn-accretionary Duckling Creek suite magmatism, corresponding to the end of Quesnel arc magmatism. After 160 Ma, the Canadian Cordilleran western margin was in a compressional state due to westward-growing North American margin and accretion of the Insular belt (Evenchick et al., 2007; Nelson et al., 2013). Evidence of compression includes intrusion, deformation, and metamorphism at ca. 160 to 155 Ma in the central Coast plutonic belt (van der Heyden, 1992; Nelson et al., 2013), deformation recorded by the earliest thrust fault gouge ages in the southern Canadian Rocky Mountains (ca. 163 to 146 Ma; Pană and van der Pluijm, 2015), and magma cessation, uplift, and deposition of conglomerates at ca. 160 in the Talkeetna arc in southwestern Alaska (Clift et al., 2005; Nelson et al., 2013). The maximum crystallization age of the Osilinka suite leucocratic granite (ca. 160 Ma) coincides with this period of compression, and magmatism was likely in response to crustal thickening in north-central Quesnellia. The Osilinka suite inherited zircon ages and Hf-O signatures overlap with those of the Thane Creek and Duckling Creek suites (Figure 5.3.1 and 5.4.1.2) and suggests the Osilinka suite was derived from a hybrid Thane Creek and Duckling Creek suite crustal melt.

The oldest phases of the Mesilinka intrusive suite crystallized by at least ca. 135 Ma, and possibly as early as ca. 145 Ma. The Mesilinka tonalite generally has less fractionated chondrite-normalized REE patterns (Figure 2.2.2.1), while K-feldspar porphyritic granite has more fractionated REE patterns indicated by higher chondrite-normalized La/Yb ratios (Figure 2.2.2.2). The ca. 127 Ma equigranular granite has similar fractionated REE patterns to the K-feldspar porphyrytic granites, which suggests the granites experienced a lower degree of partial melting than the tonalites. Additionally, both Mesilinka granite phases have relatively high-K calc-alkaline compositions, while tonalites are sodic (Na_2O/K_2O >2), low- to mid-K calc-alkaline. The tonalites may have been generated by direct partial melting of pre-existing mafic crust within the Hogem batholith or the country rocks to the batholith, like processes that have been suggested for generation of Archean tonalite-trondjhemite-granodiorite (TTG) suites (e.g., Smithies, 2000; Moyen and Stevens, 2006; Nagel et al., 2012). Such processes would have facilitated the juvenile εHf(t) and mantle-like $\delta^{18}O$ zircon values in the Mesilinka suite tonalites. It has been suggested high-K calc-alkaline granites may be generated through crustal recycling (Roberts and Clemens, 1993), which supports the peraluminous compositions of most Mesilinka suite granites. Roberts and Clemens (1993) modelled high-K granites as derived from partial melts of hydrous, mafic to intermediate, transitional to high-K calc-alkaline igneous crustal protoliths. Zircon Hf-O modelling indicate Hogem batholith melts contaminated by various amounts of juvenile Lay Range assemblage may have been a possible source for Mesilinka suite magmas (Figure 5.4.3.3). Partial melting resulted in variable REE fractionation and U and Th concentrations in the different magmatic phases of the Mesilinka suite (Figures 2.2.2.1, 2.2.2.2, 2.2.2.5), which may have been triggered by compression resulting from continued build up of the Canadian Cordillera, indicated by the development of the Skeena Fold Belt in the Intermontane terranes from 145 to 135 Ma (Evenchick et al., 2007). Although magmatism was relatively absent across the rest of the Cordillera from 140 to 120 Ma, compression is also recorded in eastern Cordilleran terranes in southeastern BC and central Yukon during this time frame (Monger and Gibson, 2019). Compressional structures are recorded in metamorphic rocks in central Yukon (Staples et al., 2014, 2016), in the Selkirk allochthon and Cariboo Mountains (Currie, 1988; Crowley et al., 2000; Reid, 2002; Gibson et al., 2005, 2008), and the Kootenay arc (Webster et al., 2017; Webster and Pattison, 2018).

5.6 Preservation of long-lived juvenile magmatism in the Hogem batholith and its implication on Cordilleran accretionary models

5.6.1 A model for generation and emplacement of juvenile magmas of the Hogem batholith

Pulsed, juvenile magmatism occurred in the Hogem batholith for >30 million years during the crystallization of the Thane Creek and Duckling Creek suites (ca. 207 to 174 Ma) without a significant change in the zircon Hf-O isotope compositions of the magmas, despite whole rock compositional differences. Likely, these zircon isotope compositions were controlled by melting, assimilation, storage, and homogenization (MASH; Hildreth and Moorbath, 1988) processes in the deep crustal hot zone (Figure 5.6.1.1; Annen et al., 2006). During subduction, melting in the mantle wedge occurs due to a mix of decompression and dehydration melting via influx of volatiles from the downgoing slab, producing basaltic magmas (Annen et al., 2006). These basaltic magmas are incrementally emplaced into the lower arc crust or at the lower crust/mantle interface and accumulate in a volatile-rich deep crustal hot zone (Hildreth and Moorbath, 1988; Annen et al., 2006). Annen et al. (2006) suggest much of the geochemical variation in arc magmas develops in the hot zone due to varying levels of temperature, pressure, H_2O, and melt fraction, in tandem with minor assimilation of older country rock, which may impact the isotopic signature of the magmas (Hildreth and Moorbath, 1988).

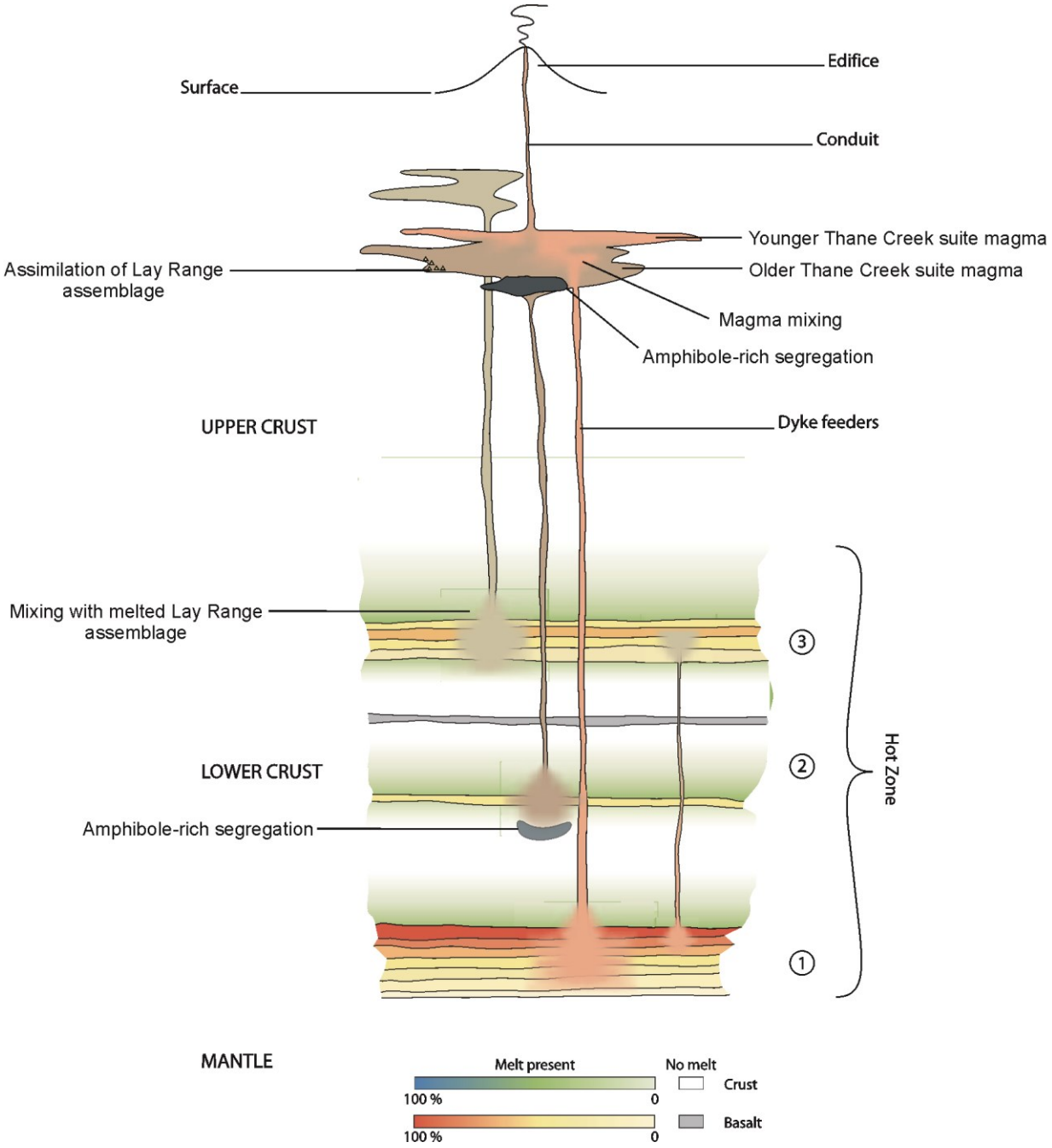

Figure 5.6.1.1. Generalized schematic diagram of MASH zone processes (Hildreth and Moorbath, 1988) and the deep crustal hot zone (Annen et al., 2006) that affected magmas of the Thane Creek intrusive suite from 207 to 194 Ma in the Hogem batholith. Similar processes are proposed for the Duckling Creek intrusive suite from 182 to 174 Ma. Figure is modified after Annen et al. (2006).

A deep crustal hot zone model is consistent with geochemistry, geochronology, and field observations in the Thane Creek and Duckling Creek intrusive suites of Hogem batholith. Incremental hydrous basaltic intrusions in the lower crust may have produced residual H_2O-rich intermediate melts of the Thane Creek suite. These melts segregated and crystallized over millions of years, time spans plausible in H_2O-rich, viscous melts (Annen et al., 2006), to produce amphibole-rich cumulates and dioritic residual melts (Figure 5.6.1.1). Multiple generations of basaltic magma input over the ~13-million-year span of the Thane Creek suite likely caused entrainment of older magmas and cumulates in younger magma phases, evidenced by magma mixing observed in outcrop (Figures 1.3.1.2 and 5.6.1.1) and the wide range in zircon U-Pb ages within the Thane Creek intrusive suite and single Thane Creek plutonic samples (e.g., sample 19GJ13-3; section 3.2.1.1). As the deep crustal hot zone evolved, along with compressional thickening due to build up of the Cordilleran orogen, a thickened arc crust would have caused a greater range in emplacement depths of the basalt intrusions and a wider range of melt compositions (Annen et al., 2006), such as the melts that crystallized the alkaline Duckling Creek intrusive suite from ca. 182 to 174 Ma. The Duckling Creek intrusive suite was likely generated under similar magma conditions to those of the Thane Creek suite, indicated by similar trace element concentrations (Figures 2.2.2.1-2.2.2.11) and zircon Hf-O results of the two suites (Figure 5.4.1.1); however, magma conditions may have been less hydrous in the Duckling Creek suite, which resulted in the formation of clinopyroxene cumulates rather than hornblendites. Drier, less viscous magmas could have segregated faster than the comparatively wet Thane Creek magmas and formed the rhythmic magmatic layering observed in the Duckling Creek suite (Figure 1.3.1.3). Minor thermal and mass transfer through mixing with melts of juvenile basement rocks of the Quesnel terrane (Lay Range assemblage) at lower crustal levels and assimilation at higher crustal levels may have imparted the heavier $\delta^{18}O$ signatures, but the overall juvenile εHf values, observed in both the Thane Creek suite and Duckling Creek suite zircons (Figure 5.6.1.1). Similar long-lived, pulsed juvenile magmatism is also observed in the Coast Mountains Batholith, which has little evidence of melt contribution by Precambrian crust, but may have been contaminated by minor Phanerozoic crust (Gehrels et al., 2009; Homan, 2017; Cecil et al., 2011, 2021).

5.6.2 Establishing the zircon Hf-O record of northern Cordilleran batholiths

At present, the zircon Hf-O record for Canadian Cordilleran batholiths is relatively limited. In the Intermontane terranes, igneous zircon U-Pb/Hf isotope studies have only been carried out on Triassic to Jurassic plutons in southern Yukon (Sack et al., 2020) and the Hogem batholith in north-central BC (Figure 5.6.2.1). Late Triassic to Jurassic-aged plutons in the northern Intermontane terranes in southern Yukon have more variability in zircon εHf(t) and overall, more evolved compositions than the juvenile zircon εHf(t) results of the Hogem batholith (Table 5.6.2.1; Figure 5.6.2.1).

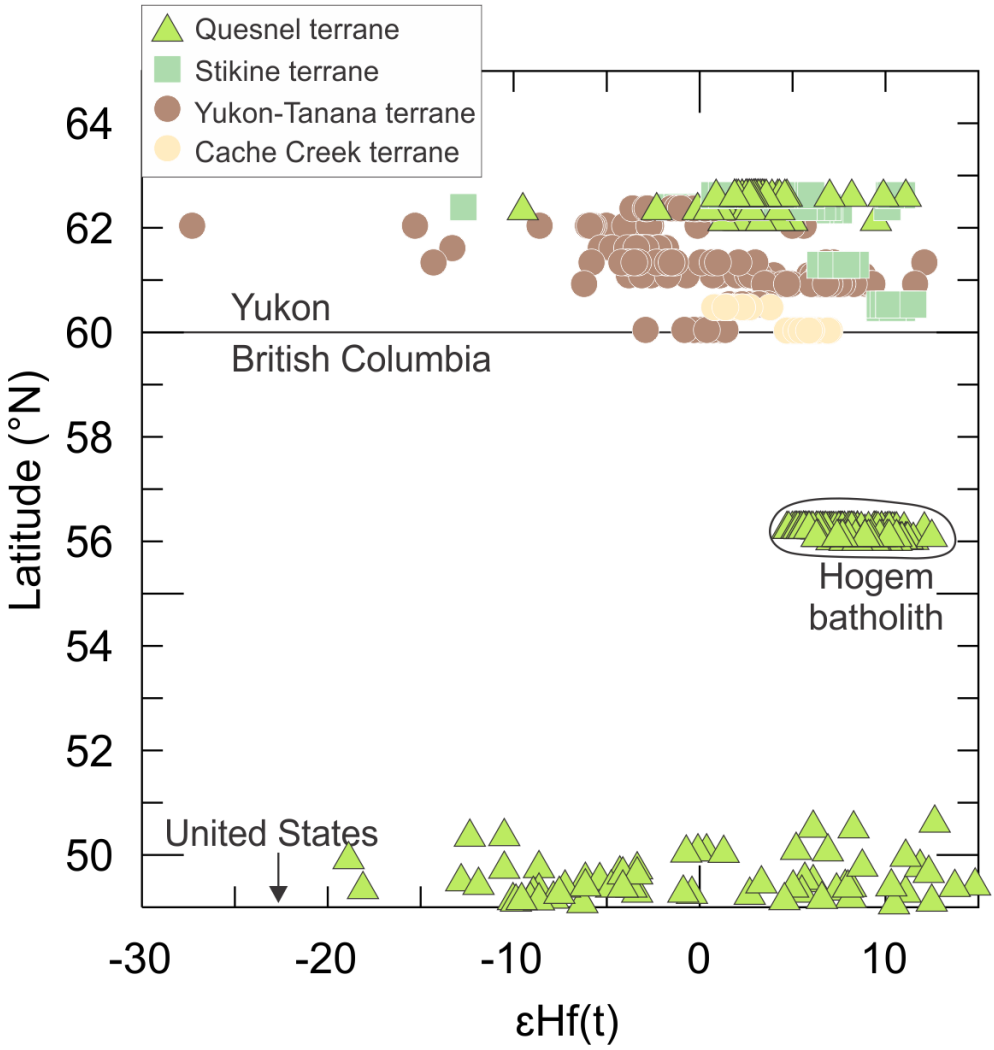

Figure 5.6.2.1. εHf(t) ranges of Mesozoic-aged Intermontane terrane plutons versus latitude. Northern and central Intermontane terrane Hf(t) data are from igneous zircons (this study; Sack et al., 2020). Southern Quesnel terrane Hf(t) values were converted from whole rock Sm-Nd data (Ghosh, 1995).

Table 5.6.2.1. Age, εHf(t), and $\delta^{18}O_{zircon}$ ranges from Mesozoic batholiths in northern Cordilleran batholiths. QT: Quesnel terrane; ST: Stikine terrane; YTT: Yukon-Tanana terrane; CC: Cache Creek terrane; CMB: Coast Mountains batholith; WT: Wrangellia terrane; AT: Alexander terrane. 1: this study; 2: Sack et al. (2020); 3: Ghosh (1995); 4: Cecil et al. (2011); 5: Homan (2017); 6: Cecil et al. (2021).

Batholith/Area	Terrane(s)	Age range (Ma)	Range of εHf(t)	$\delta^{18}O$ (‰)	Reference
Hogem batholith	north-central QT	207 – 127	+4.4 to +12.5	+4.7 to +12.2	1
southern Yukon	northern QT	203 – 196, 160 – 146	-9.5 to +9.5, +0.9 to +11.1	-	2
	northern ST	215 – 172	-12.7 to +10.1		
	northern YTT	198 – 183	-27.3 to +12.1		
	northern CC	173 – 168	+0.8 to +7.0		
southern BC	south-western QT	210 – 99	+6.0 to +14.7	-	3
	south-central QT	185 – 97	-18.2 to +13.6		
	south-eastern QT	195 – 79	-18.9 to +11.0		
central CMB	WT, ST, YTT, AT	153 – 53	+1.5 to +12.3	-	4
southern CMB		167 – 52	+6.1 to +16.2	+4.2 to +8.3	5, 6

Ghosh (1995) published whole-rock Sm-Nd geochemistry of plutonic rocks across the southern Quesnel terrane. Utilizing the linearity of the Hf-Nd array (Vervoort et al., 2011), these εNd(t) results were converted to εHf(t) (Table 5.6.2.1; Figure 5.6.2.1). The εHf(t) values trend from juvenile compositions in the western plutons to evolved compositions in the east. Ghosh (1995) interpreted this trend, along with younger intrusive ages to the east, as recording the progression from an offshore arc in the Late Triassic and Early Jurassic to obduction of the eastern Quesnel terrane onto the North American continent in the Middle Jurassic to Cretaceous. In the Hogem batholith, the εHf(t) record is closely coincident with the isotopic compositions of the south-western Quesnel terrane plutons (Table 5.6.2.1), but there is no observed shift to evolved εHf(t) compositions to the east like in the south-central and south-eastern Quesnel terrane intrusions.

A zircon U-Pb/Hf/O record has been established in the Coast Mountains batholith (CMB; Gehrels et al., 2009; Homan, 2017; Cecil et al., 2011, 2021), the Jurassic to Eocene plutonic complex along the west coast of British Columbia, southeast Alaska, and southwest Yukon (Table 5.6.2.1; Figure 5.2.1.1). In the central CMB, Cecil et al. (2011) determined a range of zircon εHf(t) values across the width of batholith, with the most radiogenic zircon εHf(t) values interpreted as crystallizing from the juvenile Alexander (εHf(t)=+5.4 to +8.1) and Stikine (εHf(t)=+9.2 to +12.3) terrane lower crusts and/or direct melting of the mantle. The authors interpreted the trend to less radiogenic εHf(t) zircon values (εHf(t)=+1.5 to +11.6) in the eastern CMB as the involvement of evolved Yukon Tanana terrane continental margin rocks in juvenile CMB magmatism. Homan (2017) and Cecil et al. (2021) found similar juvenile zircon Hf values, coupled with predominantly mantle-like zircon $\delta^{18}O$ results, in the southern CMB (Table 5.6.2.1), but did not find evidence of significant incorporation of evolved crust in the southern CMB magmas. Cecil et al. (2021) proposed that voluminous, episodic Cordilleran batholiths can be generated without significant crustal recycling if the mantle has variable hydration and melt fertility. The southern CMB zircon Hf-O results overlap with the Thane Creek and Duckling Creek suite zircon results (Figure 5.6.2.2), which supports the interpretation that Late Triassic to Early Jurassic (207 to 174 Ma) Hogem plutonic rocks were predominantly mantle-sourced, with little significant input from evolved basement.

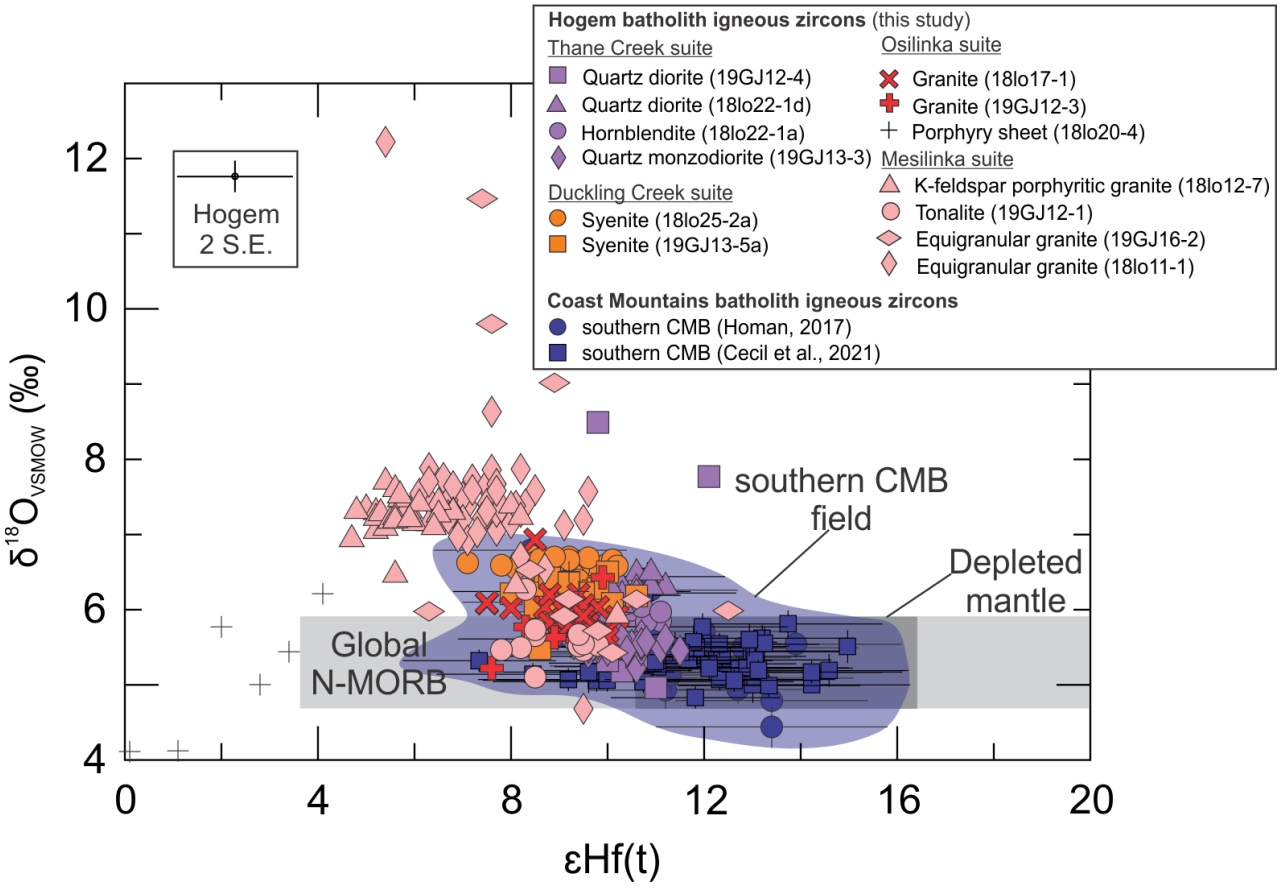

Figure 5.6.2.2. Zircon εHf(t) versus $\delta^{18}O_{VSMOW}$ results from the Hogem batholith in north-central Quesnel terrane, north-central BC and southern Coast Mountains batholith in southwestern BC. Southern Coast Mountains batholith data after Homan (2017) and Cecil et al. (2021). N-MORB= Normal mid ocean ridge basalt, after Chauvel and Blichert-Toft (2001). The upper depleted mantle limit is after Griffin et al. (2002) and lower depleted mantle limit is after Naeraa et al. (2012). Mantle zircon δ18O range (5.3±0.6‰) is from Valley et al., (1998). 2 S.E.= average 2σ standard error.

5.6.3 Variable basement compositions and crust contributions to Quesnel terrane magmatism

There is a disparity in the relative involvement of old crust in plutonic rocks of the Quesnel terrane, which suggests there are compositional differences in the Quesnellia basement. The similarity of the zircon εHf(t) range of the Hogem batholith to the εHf(t) ranges in the CMB and south-western Quesnel terrane, but their distinctiveness from similar aged-plutons in the northern and south-central to south-eastern Quesnel terrane, implies that contributions from ancient basement and the relative crustal contribution to magmatism significantly differed in time and space across northern, north-central, and southern Quesnel terrane. These discrepancies may also be due to diachronous accretion or different accretionary styles within the Intermontane terranes.

The lack of evolved zircon Hf results (εHf(t) <0) in the latest Triassic to early Cretaceous (207 to 127 Ma) intrusions of the Hogem batholith indicates the north-central Quesnel terrane was not developed on a substrate of rifted North American basement or thrust entirely onto the western margin of North America during Jurassic accretion, as suggested by some previous authors (e.g., Monger et al., 1982; Colpron et al., 2006, 2007; Nelson et al., 2006; Evenchick et al., 2007). However, it is plausible that compression resulted in minor imbrication of more evolved crustal material beneath north-central Quesnel terrane by ca. 135 Ma, and interaction of juvenile magma with this material resulted in excursions to less radiogenic zircon Hf results in the Hogem batholith at that time (Figure 5.6.3.1).

In contrast to the juvenile Hogem batholith zircon Hf results in north-central Quesnellia, evolved zircon Hf isotope results from Mesozoic Intermontane plutons in the northern Cordillera suggest significant involvement of older crust during magma genesis (Table 5.6.2.1; Sack et al., 2020). The basement to the Yukon-Tanana terrane is the pre-Late Devonian Snowcap assemblage, which comprises metasedimentary rocks that were sourced predominantly from northwestern Laurentia (Piercey and Colpron, 2009) and were likely involved in the production of the evolved plutonic rocks. Whether the northern Quesnel and Stikine terranes overly the same basement is uncertain, however, the presence of evolved zircon Hf isotope compositions (εHf ~ -10) in the otherwise juvenile (εHf >0) northern Quesnel and Stikine plutons (Figure 5.6.2.1; Table 5.6.2.1; Sack et al., 2020) suggest the presence of underlying Snowcap assemblage, or a similar continental-derived basement (Figure 5.6.3.2A). Alternatively, the presence of evolved zircon εHf signatures from the northern Intermontane plutons could indicate North American crystalline basement did underly these accreted terranes at the time of magmatism, as Ghosh (1995) interpreted for the evolved isotope signatures of plutonic rocks in south-eastern Quesnel terrane (Figure 5.6.3.2C).

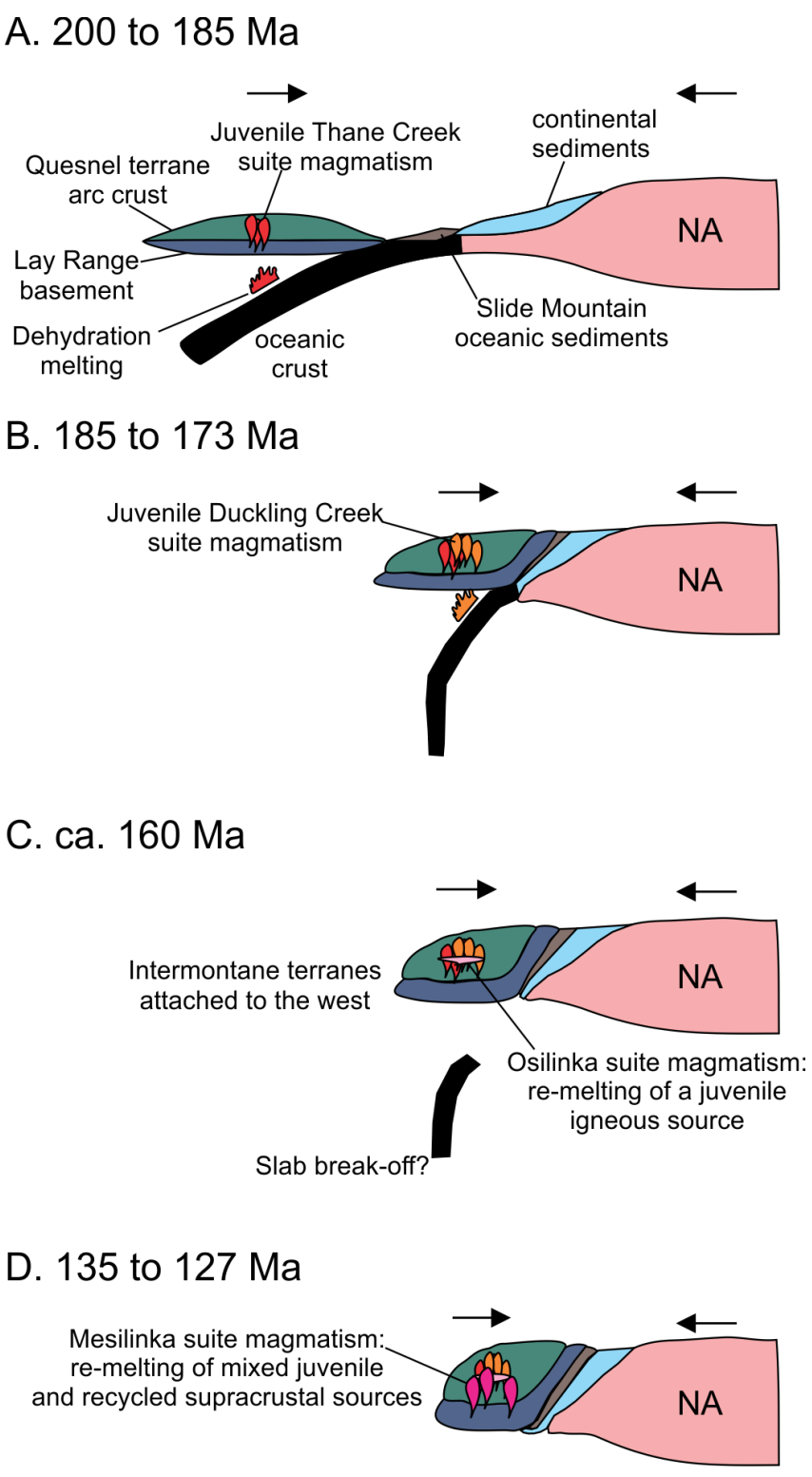

Figure 5.6.3.1. Schematic diagram for juvenile magmatism of the Hogem batholith and accretion of the north-central Quesnel terrane to the continental margin during the Mesozoic. Subduction geometry after Sigloch and Mihalynuk (2017). NA: North American crust. Figure is not to scale.

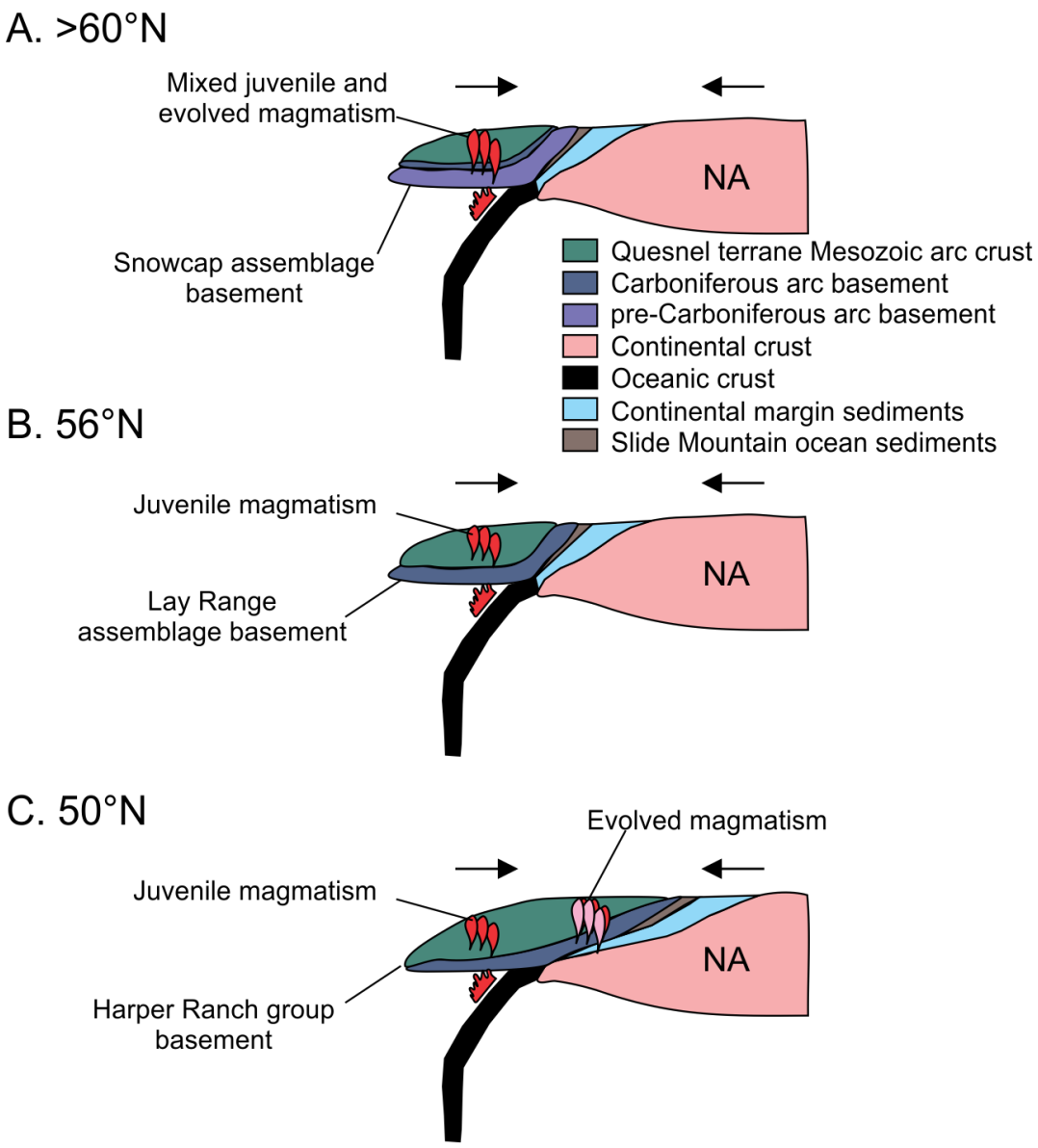

Figure 5.6.3.2. Schematic diagram for the magmatism and accretion of Quesnel terrane to the continental margin from 185 to 170 Ma at latitudes: **A)** >60°N, the latitude of the northern Quesnel terrane plutons; **B)** 56°N, the latitude of the juvenile Hogem batholith in north-central Quesnel terrane; **C)** 50°N, the latitude of the south-western to south-eastern Quesnel terrane plutons. Subduction geometry after Sigloch and Mihalynuk (2017). NA: North American crust. Figure is not to scale.

5.6.4 Models of production and preservation of juvenile crust in accreted terranes

Accretionary orogens play an important role in the production and preservation of juvenile continental crust of oceanic and continental arcs (Cawood et al., 2009; Collins et al., 2011). The relative importance of oceanic arcs in the production of juvenile crust is debated, because although it appears that accretion of oceanic arcs has contributed to the growth of Phanerozoic continental crust (Sengör et al, 1995; Kusky and Polat, 1999; Lee et al., 2007; Kemp et al., 2009), it is unclear how oceanic arcs are preserved from subduction beneath overriding buoyant continental crust (Hawkesworth et al., 2009; Condie and Kröner, 2013). The Canadian Cordillera a type example of accretionary orogenesis (Cawood et al., 2009) and provides an opportunity to study the relative roles of the contribution from juvenile material versus reworked crust in the continental crust. It also provides a window into how juvenile crust is produced and preserved in accretionary orogenic belts. However, uncertainties regarding the relationships of the accreted terranes to the North American continental margin have significant impact on the extent and mechanism of juvenile crust production.

It has been speculated that allocthonous or pericratonic Cordilleran terranes were thrust over the ancient North American continental margin or were built upon rifted fragments of ancient North American continental lithosphere (e.g., Monger et al., 1982; Colpron et al., 2006, 2007; Nelson et al., 2006; Evenchick et al., 2007). The presence of North American basement beneath the accreted terranes as far west as the Coast Belt has been supported by interpretations of Lithoprobe seismic reflection data in the northern and southern Canadian Cordillera (Cook et al., 1992, 2004; Clowes et al., 1995, 2005; Cook and Erdmer, 2005). These interpretations would suggest that Precambrian North American crust underlies the Paleozoic to Mesozoic basement of the Quesnel terrane. In contrast, the juvenile zircon Hf isotope signatures of the Hogem batholith presented in this study do not support the presence of underlying evolved North American continental crust, suggesting that north-central Quesnel terrane preserves oceanic arc-generated juvenile crust.

The speculation that ancient North American crust underlies the accreted Cordilleran terranes also contrasts with models of juvenile crustal growth in accretionary orogens (Collins et al., 2011). In their model, progressive removal of older crust and sub-continental lithospheric mantle (SCLM) during subduction in Phanerozoic accretionary, or ‘external’, systems are

responsible for the generation of new juvenile crust and increasingly radiogenic εHf values after 550 Ma in Gondwana, eastern Australia, New Zealand, South America, and Japan (Collins et al., 2011). The juvenile Hogem batholith zircon Hf-O results of this study indicate that accretion occurred in the north-central Quesnel terrane without any significant influence of evolved continental material and agrees with general εHf trends from circum-Pacific orogens (e.g., Collins et al., 2011), but the interpreted westward subduction of oceanic crust beneath the Intermontane terranes (Sigloch and Mihalynuk, 2017) does not require, nor provide a mechanism for, the removal and recycling of evolved continental crust into the mantle (Figure 5.6.3.1). Additionally, the Phanerozoic circum-Pacific accretionary orogen model does not appear to be supported in the northern and southern-eastern Quesnel terrane, where intrusions record interaction with continental crust (Figure 5.6.3.2). Evolved isotopic signatures in the northern and south-eastern Quesnel terrane plutons indicate magmas were generated by crustal re-working and are more coincident with observations and models in collisional orogenic systems (Collins et al., 2011).

The production of juvenile oceanic arc crust, in part, depends on the arc basement composition, as observed in the juvenile Hogem batholith in north-central Quesnel terrane compared to evolved plutonic rocks in the northern and south-eastern Quesnel terranes. Preservation of juvenile oceanic arc crust from being subducted during arc-continent collision remains enigmatic, since theoretically oceanic arcs and crust should be less buoyant and be overridden by continental crust (Condie and Kröner, 2013). Oceanic arc crust is thought to escape subduction through a combination of density, arc crust thickness, and subduction angle and direction (Hawkesworth et al, 2009; Brown and Ryan, 2011; Condie and Kröner, 2013). In the case of Quesnel terrane oceanic arc crust, the main factor in controlling preservation was likely the westward subduction of oceanic crust attached to the continental margin beneath the Intermontane terranes (Figure 5.6.3.2; Sigloch and Mihalynuk, 2017). Buoyant oceanic arc crust formed in favourable conditions (e.g., less dense and/or thicker arc crust) may have led to the apparent obduction of southern Quesnel terrane onto the North American margin (Figure 5.6.3.2A; Ghosh, 1995). In contrast, the north-central Quesnel terrane does not appear to have obducted onto the North American margin but was also preserved from subduction (Figure 5.6.3.2B). This lack of obduction may have resulted from relatively denser and/or thinner

oceanic arc crust that created a near equal buoyancy of the north-central Quesnel terrane relative to the North American margin.

Although the contribution of new juvenile continental crust by oceanic arcs is thought to be minor relative to continental arcs (Condie and Kröner, 2013), the preservation of juvenile oceanic arc crust at accretionary margins plays an important role in acting as a nucleus for more voluminous continental arc magmatism (e.g., Lee et al., 2007). This is observed in the large volumes of new juvenile continental crust in the central and southern CMB that intruded the juvenile Alexander and Stikine terranes (Cecil et al., 2011, 2021; Homan, 2017). These accreted terranes that serve as the juvenile basement to the CMB may have been preserved from subduction and interaction with evolved continental crust due to similar factors as interpreted in the north-central Quesnel terrane.

Accretionary orogenic systems are complex and cannot be fully explained by simple tectonic models, as suggested by the interpreted tectonic variation along strike of the Quesnel terrane in the Canadian Cordillera. The zircon Hf-O interpretations of the north-central Quesnel terrane imply a basement architecture that contrasts with geophysical models of the underlying North American basement in the Cordillera. These interpretations identify the need for similar zircon Hf-O studies in batholiths across the Canadian Cordillera to better understand the latitudinal and longitudinal changes in isotope signatures, the amount of juvenile crust generation versus re-working of old crust, and the possible implications of these on the Cordilleran tectonic history. Additionally, further studies in the Cordillera may constrain the controlling factors on accreted oceanic arc buoyancy, including arc crust thickness and density. This may help gain a better understanding of the generation and preservation of juvenile continental crust in these accreted Cordilleran terranes and have implications on the models of modern continental crust growth.

6 Conclusions

6.1 Key findings

New zircon U-Pb geochronology, paired with zircon Hf-O isotopes and trace element geochemistry, better constrain the ages and petrogenesis of protracted, episodic magmatism that formed the Hogem batholith. Key findings of this study include:

- Zircon trace element geochemistry ($Eu/Eu_N^* \geq 0.4$, $Ce/Ce_C^* > 100$, $\Delta FMQ > 0$) results suggest Thane Creek hornblendite and quartz monzodiorite and Duckling Creek syenites have oxidized and hydrous magma conditions that are more favourable for porphyry mineralization relative to other phases in these suites.
- The Thane Creek and Duckling Creek intrusive suites overlap significant periods of Cu±Au porphyry mineralization in the Late Triassic to Early Jurassic in the Quesnel and Stikine terranes. Similarities between the Mesilinka suite and the Endako Mo deposit hosting-rocks of the Endako batholith in Stikine terrane suggest that the Mesilinka suite may be prospective for Mo mineralization.
- The intrusive suites have distinct whole-rock geochemistry signatures that suggest petrogenetic differences, such as the calc-alkaline and magnesian Thane Creek suite versus alkaline and ferroan Duckling Creek suite, and the metaluminous Thane Creek and Duckling Creek suites versus the weakly peraluminous Osilinka and Mesilinka suites.
- New zircon U-Pb geochronology constrains the crystallization ages of:
    1) Thane Creek suite from 207 to 194 Ma.
    2) Duckling Creek suite from 182 to 175 Ma.
    3) Osilinka suite at ca. 160 Ma.
    4) Mesilinka suite from 135 to 127 Ma.
- Combined zircon Hf-O isotopes indicate the Thane Creek, Duckling Creek, and Osilinka suite magmas had juvenile and depleted mantle-like sources, while the Mesilinka suite magmas had mixed isotope composition sources indicating a larger contribution from recycled evolved crust.
- Zircon Hf-O modelling shows North American crust likely had little influence on Hogem batholith magmatism. Mixing models show up to 40% mixing of juvenile Quesnel terrane

basement with primary mantle-derived magmas may account for less radiogenic εHf_{zircon} and $\delta^{18}O_{zircon} > 5.3\pm0.6‰$ results in the Thane Creek and Duckling Creek suite intrusive rocks. Up to 70% contribution of juvenile Quesnel terrane basement to the Mesilinka suite melts can account for $\varepsilon Hf_{zircon} <\sim5.0$ and $\delta^{18}O_{zircon} >7.0‰$ results in Mesilinka intrusive rocks.

- It is clearly possible to generate large batholiths in accretionary orogens with minimal input from evolved ancient basement.
- Juvenile zircon Hf results from the Hogem batholith do not support the proposed presence of a rifted continental crust arc basement or western tapering ancient North American crust beneath the accreted north-central Quesnel terrane at the time of magmatism.

6.2 Future work

The LA-ICP-MS zircon U-Pb crystallization dates presented in this study achieved the aim to better constrain the ages of protracted, episodic magmatism in the Hogem batholith. Further studies may use higher resolution techniques (e.g., CA-TIMS) to determine specific zircon growth zone ages in intrusive samples with highly scattered individual zircon U-Pb ages. This may better resolve the timing of individual magma pulses and have implications for magma residence times.

To better constrain the evolution of Hogem batholith source rocks and contamination models using zircon Hf-O isotopes, further research will benefit from collecting zircon Hf-O data from country and host rocks (Lay Range assemblage, Takla Group) surrounding the Hogem batholith.

Using longer background times on future LA-ICP-MS trace element analyses to lower the LOD of elements such as La, Pr, Sm, and Ti will benefit zircon trace element interpretations by better constraining Eu- and Ce-anomalies and Ti-in-zircon temperatures.

This study has identified a need to develop a zircon Hf-O record for plutons across the Cordillera to better understand the relative contribution of juvenile and evolved crustal sources in magmas that intruded accreted terranes. This will help constrain the basement assemblages underlying these intrusions and has implications for the tectonic history of the Cordillera.

Additionally, better understanding of the density and thickness of the accreted terrane crusts and subduction geometry with the continental margin may have an impact on models of production and preservation of modern juvenile continental crust.

References

Aleinikoff, J.N., Wintsch, R.P., Tollo, R.P., Unruh, D.M., Fanning, C.M., Schmitz, M.D., 2007. Ages and origins of rocks of the Killingworth dome, south-central Connecticut: implications for the tectonic evolution of southern New England. American Journal of Science, 307:1, p. 63-119, https://doi.org/10.2475/01.2007.04.

Annen, C., Blundy, J.D., and Sparks, R.S.J., 2006. The Genesis of Intermediate and Silicic Magmas in Deep Crustal Hot Zones. Journal of Petrology, 47:3, p. 505-539, doi:10.1093/petrology/egi084.

Armstrong, J.E., 1949. Fort St. James Map-Area, Cassiar and Coast Districts, British Columbia. Geological Survey of Canada, Memoir 252, 231 p.

Armstrong, R. L., 1988. Mesozoic and early Cenozoic magmatic evolution of the Canadian Cordillera. Geological Society of America Special Papers, 218, p. 55-92.

Baertschi, P., 1976. Absolute 18O content of standard mean ocean water. Earth and Planetary Science Letters, 31:3, p. 341-344, https://doi.org/10.1016/0012-821X(76)90115-1.

Ballard, J.R., Palin, M.J., Campbell, I.H., 2002. Relative oxidation states of magmas inferred from Ce(IV)/Ce(III) in zircon: application to porphyry copper deposits of northern Chile. Contributions to Mineralogy and Petrology, 144, p. 347-364.

Barth, A.P., Tani, K., Meffre, S., Wooden, J.L., Coble, M.A., Arculus, R.J., Ishizuka, O., and Shukle, J.T., 2017. Generation of silicic melts in the early Izu-Bonin arc recorded by detrital zircons in proximal arc volcaniclastic rocks from the Philippine Sea. Geochemistry Geophysics Geosystems, 18, p. 3576–3591, https//doi.org/10.1002/2017GC006948.

Bath, A.B., Cooke, D.R., Friedman, R.M., Faure, K., Kamenetsky, V.S., Tosdal, R.M., and Berry, R.F., 2014. Mineralization, U-Pb geochronology, stable isotope geochemistry of the Lower Main Zone of the Lorraine deposit, north-central British Columbia: A replacement-style alkalic Cu-Au porphyry. Economic Geology, 109, p. 979-1004.

BC Geological Survey, 2020. MapPlace, Ministry of Energy, Mines, and Low Carbon Innovation, https://www2.gov.bc.ca/gov/content/industry/mineral-exploration-mining/british-columbia-geological-survey/mapplace.

Beck, M.E., Jr., 1991. Case for northward transport of Baja and coastal southern California: paleomagnetic data, analysis, and alternatives. Geology, 19, p. 506–509.

Beck, M.E., Jr., 1992. Tectonic significance of paleomagnetic results for the western conterminous United States. In: Burchfiel, B.C., Lipman, P.W., and Zoback, M.L. (eds). The Cordilleran Orogen: Conterminous US. (The Geology of North America). Geological Society of America, G-3, p. 683–697.

Belasky, P., and Stevens, C.H., 2006. Permian faunas of westernmost North America: Paleobiogeographic constraints on the Permian positions of Cordilleran terranes. In: Haggart, J.W., Enkin, R.J., and Monger, J.W.H. (eds.). Paleogeography of the North American Cordillera: Evidence for and Against Large-Scale Displacements. Geological Association of Canada, Special Paper 46, p. 71–80.

Belousova, E., Griffin, W., O'Reilly, S.Y., Fisher, N.I., 2002. Igneous zircon: trace element composition as an indicator of source rock type. Contributions to Mineralogy and Petrology, 143, p. 602–622, https://doi.org/10.1007/s00410-002-0364-7.

Black, L.P., Kamo, S.L., Allen, C.M., Davis, D.W., Aleinikoff, J.N., Valley, J.W., Mundil, R.,

Campbell. I.H., Korsch, R.J., Williams, I.S., Foudoulis, C., 2004. Improved 206Pb/238U microprobe geochronology by the monitoring of a trace-element-related matrix effect; SHRIMP, ID-TIMS, ELA-ICP-MS and oxygen isotope documentation for a series of zircon standards. Chemical Geology, 205:1-2, p. 115-140, https://doi.org/10.1016/j.chemgeo.2004.01.003.

Blichert-Toft, J., 2008. The Hf isotopic composition of zircon reference material 91500. Chemical Geology, 253:3-4, p. 252-257, https://doi.org/10.1016/j.chemgeo.2008.05.014.

Bouvier, A., Vervoort, J.D., Patchett, P.J., 2008. The Lu–Hf and Sm–Nd isotopic composition of CHUR: Constraints from unequilibrated chondrites and implications for the bulk composition of terrestrial planets. Earth and Planetary Science Letters, 273:1–2, p. 48-57, https://doi.org/10.1016/j.epsl.2008.06.010.

Bradley, D.C., Dumoulin, J., Layer, P., Sunderlin, D., Roeske, S., McClelland, W., Harris, A.G., Abbott, G., Bundtzen, T., and Kusky, T., 2003. Late Paleozoic orogeny in Alaska's Farewell terrane. Tectonophysics, 372, p. 23–40, doi:10.1016/S0040-1951(03)00238-5.

Brown D., and Ryan, P. D., 2011. Arc–Continent Collision. Springer, Berlin Heidelberg, pp. 1–493.

Buret, Y., von Quadt, A., Heinrich, C., Selby, D., Walle, M., and Peytchev, I., 2016. From a long-lived upper-crustal magma chamber to rapid porphyry copper emplacement: Reading the geochemistry of zircon crystals at Bajo de la Alumbrera (NW Argentina). Earth and Planetary Science Letters, 450, p. 120–131, https://doi.org/10.1016/j.epsl.2016.06.017.

Burnham A.D., and Berry A.J., 2012. An experimental study of trace element partitioning between zircon and melt as a function of oxygen fugacity. Geochimica et Cosmochimica Acta, 120, p. 196–212, https://doi.org/10.1016/j.gca.2012.07.034.

Burnham A.D., and Berry A.J., Halse, H.R., Schofield, P.F., Cibin, G., and Mosselmans, J.F.W., 2015. The oxidation state of europium in silicate melts as a function of oxygen fugacity, composition and temperature. Chemical Geology, 411:14, p. 248-259, https://doi.org/10.1016/j.chemgeo.2015.07.002.

Cawood, P.A., Kroner, A., Collins, W.J., Kusky, T.M., Mooney, W.D., and Windley, B.F., 2009. In: Cawood, P.A., and Kroner, A. (eds.), Earth Accretionary Systems in Space and Time, The Geological Society of London, Special Publications, 318, p. 1-36, doi: 10.1144/SP318.1.

Cecil, M.R., Gehrels, G., Ducea, M.N., and Patchett, P.J., 2011. U-Pb-Hf characterization of the central Coast Mountains batholith: Implications for petrogenesis and crustal architecture. Lithosphere, 3:4, p. 247-260, doi: 10.1130/L134.1.

Cecil, M.R., Gehrels, G., Rusmore, M.E., Woodsworth, G.J., Stowell, H.H., Yokelson, I.N., Homan, E., Kitajima, K., Valley, J.W., 2021. Mantle control on magmatic flare-ups in the southern Coast Mountains batholith, British Columbia. Geosphere, p. 1-15, https://doi.org/10.1130/GES02361.1.

Chambefort, I., Dilles, J.H., and Kent, A.J.R., 2008. Anhydrite-bearing andesite and dacite as a source for sulfur in magmatic-hydrothermal mineral deposits. Geology, 36:9, p. 719–722, doi:https://doi.org/10.1130/G24920A.1.

Chang, J., and Audétat, A., 2018. Petrogenesis and Metal Content of Hornblende-Rich Xenoliths from Two Laramide-age Magma Systems in Southwestern USA: Insights into the Metal Budget of Arc Magmas. Journal of Petrology, 59:10, p. 1869–1898, https://doi.org/10.1093/petrology/egy083.

Chapman, J.B., Ducea, M.N., Kapp, P., Gehrels, G.E., and DeCelles, P.G., 2017. Spatial and temporal radiogenic isotopic trends of magmatism in Cordilleran orogens. Gondwana Research, 48, p. 189-204, https://doi.org/10.1016/j.gr.2017.04.019.

Chappell, B.W. and White, A.J.R., 1974. Two Contrasting Granite Types. Pacific Geology, 8, p. 173-174.

Chauvel, C., and Blichert-Toft, J., 2001. A hafnium isotope and trace element perspective on melting of the depleted mantle. Earth and Planetary Science Letters, 190, p. 137-151.

Christopher, P. A., and Carter, N. C., 1976. Metallogeny and metallogenic epochs for porphyry mineral deposits in the Canadian Cordillera. Canadian Institute of Mining and Metallurgy, Special Volume 15, p. 64-71.

Church, B.N., 1975. Geology of the Sustut Area. British Columbia Department of Mines and Petroleum Resources, Geology, Exploration and Mining in British Columbia, 1974, p. 305–309.

Clairborne, L.L., Miller, C.F., and Wooden, J.L., 2010. Trace element composition of igneous zircon: a thermal and compositional record of the accumulation and evolution of a large silicic batholith, Spirit Mountain, Nevada. Contributions to Mineralogy and Petrology, 160, p. 511–531, https://doi.org/10.1007/s00410-010-0491-5.

Clennett, E. J., Sigloch, K., Mihalynuk, M. G., Seton, M., Henderson, M. A., Hosseini, K., Mohammadzaheri, A., Johnston, S.T., and Müller, R.D., 2020. A quantitative tomotectonic plate reconstruction of western North America and the eastern Pacific basin. Geochemistry, Geophysics, Geosystems, 21, e2020GC009117, https://doi.org/10.1029/2020GC009117.

Clift, P.D., Pavlis, T., DeBari, S.M., Draut, A.E., Rioux, M., and Kelemen, P.B., 2005. Subduction erosion of the Jurassic Talkeetna-Bonanza arc and the Mesozoic accretionary tectonics of western North America. Geology, 33: 11, p. 881–884, doi: https://doi.org/10.1130/G21822.1.

Cline, J. S., and Bodnar, R. J., 1991. Can economic porphyry copper mineralization be generated by a typical calc-alkaline melt? Journal of Geophysical Research, 96, p. 8113– 8126, doi:10.1029/91JB00053.

Clowes, R.M., Zelt, C.A., Amor, J.R., and Ellis, R.M., 1995. Lithospheric structure in the southern Canadian Cordillera from a network of seismic refraction lines. Canadian Journal of Earth Sciences, 32, p. 1485–1513.

Clowes, R.M., Hammer, P.T.C., Fernández-Viejo, G., and Welford, J.K., 2005. Lithospheric structure in northwestern Canada from Lithoprobe seismic refraction and related studies: a synthesis. Canadian Journal of Earth Sciences, 42, p. 1277–1293.

Collins, W.J., Belousova, E.A., Kemp, A.I.S., and Murphy, J.B., 2011. Two contrasting Phanerozoic orogenic systems revealed by hafnium isotope data. Nature Geoscience, 4, p. 333-337, doi:10.1038/NGEO1127.

Colpron, M., Nelson, J.L., and Murphy, D.C., 2006. A tectonostratigraphic framework for the pericratonic terranes of the northern Canadian Cordillera. Geological Association of Canada, Special Paper 45, p. 1–23.

Colpron, M., Nelson, J.L., and Murphy, D.C., 2007. Northern Cordilleran terranes and their interactions through time: GSA Today, 17: 4-5, p. 4–10.

Colpron, M. and Nelson, J.L., 2020. A Digital Atlas of Terranes for the Northern Cordillera. Yukon Geological Survey, http://data.geology.gov.yk.ca/Compilation/2.

Condie, K.C., and Kröner, A., 2013. The building blocks of continental crust: Evidence for a major change in the tectonic setting of continental growth at the end of the Archean. Gondwana and Research, 23, p. 394-402, doi:10.1016/j.gr.2011.09.011.

Coney, P. J., Jones, D. L., and Monger, J.W.H., 1980. Cordilleran suspect terranes. Nature, 288, p. 329-333.

Cook, F.A., and Erdmer, P., 2005. An 1800 km cross section of the lithosphere through the northwestern North American plate: lessons from 4.0 billion years of Earth's history. Canadian Journal of Earth Sciences, 42, p. 1295-1311, doi: 10.1139/E04-106.

Cook, F.A., Varsek, J.L., Clowes, R.M., Kanasewich, E.R., Spencer, C.S., Parrish, R.R., Brown, R.L., Carr, S.D., Johnson, B.J., Price, R.A., 1992. Lithoprobe crustal reflection cross section of the southern Canadian Cordillera, 1, Foreland Thrust and Fold Belt to Fraser River Fault. Tectonics, 11:1, p. 12-35.

Cook, F.A., Clowes, R.M., Snyder, D.B., van der Velden, A.J., Hall, K.W., Erdmer, P., and Evenchick, C.A., 2004. Precambrian crust beneath the Mesozoic northern Canadian Cordillera discovered by Lithoprobe seismic reflection profiling. Tectonics, 23:2, doi:10.1029/2002TC001412.

Cordey, F., Mortimer, N., DeWever, P., and Monger, J.W.H., 1987. Significance of Jurassic radiolarians from the Cache Creek terrane, British Columbia. Geology, 15, p. 1151-1154.

Crowley, J.L., Ghent, E.D., Carr, S.D., Simony, P.S., and Hamilton, M.A., 2000. Multiple thermotectonic events in a continuous metamorphic sequence, Mica Creek area, southeastern Canadian Cordillera. Geological Materials Research, 2:2, p. 1-45. http://www.minsocam.org/gmr/papers/v2/v2n2/v2n2.pdf

Currie, L.A., 1968. Limits for qualitative detection and quantitative determination. Application to radiochemistry. Analytical Chemistry, 40:3, p. 586–593, https://doi.org/10.1021/ac60259a007.

Currie, L.D., 1988. Geology of the Allan Creek area, Cariboo Mountains, British Columbia (MSc Thesis). University of Calgary, pp. 152.

Davies, J.H., and Stevenson, D.J., 1992. Physical model of source region of subduction zone volcanics. Journal of Geophysical Research, 97, p. 2037-70.

Davis, G.A., Monger, J.W.H., and Burchfiel, B.C., 1978. Mesozoic construction of the Cordilleran 'collage,' central British Columbia to central California. In: Howell, D. G., and McDougall, K. A. (eds.), Mesozoic paleogeography of the western United States. Society of Economic Paleontologists and Mineralogists, Pacific Section, Pacific Coast Paleogeography Symposium 2, p. 1-32.

Davis, W.J., Ootes, L., Newton, L., Jackson, V., and Stern, R.A., 2015. Characterization of the Paleoproterozoic Hottah terrane, Wopmay Orogen using multi-isotopic (U-Pb, Hf and O) detrital zircon analyses: An evaluation of linkages to northwest Laurentian Paleoproterozoic domains. Precambrian Research, 269, p. 296-310, http://dx.doi.org/10.1016/j.precamres.2015.08.012.

Dessimoz, M., Müntener, O., and Ulmer, P., 2012. A case for hornblende dominated fractionation of arc magmas: the Chelan Complex (Washington Cascades). Contributions to Mineralogy and Petrology 163, p. 567-589, https://doi.org/10.1007/s00410-011-0685-5.

Devine, F.A.M., Chamberlain, C.M., Davies, A.G.S., Friedman, R., and Baxter, P., 2014. Geology and district-scale setting of tilted alkalic porphyry Cu-Au mineralization at the Lorraine deposit, British Columbia. Economic Geology, 109, p. 939-977.

Dilles, J.H., Kent, A.J.R., Wooden, J.L., Tosdal, R.M., Koleszar, A., Lee, R.G., and Farmer, L.P., 2015. Zircon compositional evidence for sulfur-degassing from ore-forming arc magmas. Economic Geology, 110:1, p. 241–251, https://doi.org/10.2113/econgeo.110.1.241.

Dostal, J., Keppie, J.D., and Ferri, F., 2009. Extrusion of high-pressure Cache Creek rock into the Triassic Stikinia-Quesnellia arc of the Canadian Cordillera: implications for terrane analysis of ancient orogens and palaeogeography. In: Murphy, J.B., Keppie, J.D., and Hynes, A.J. (eds.), Ancient Orogens and Modern Analogues, Geological Society, London, Special Publications, 327, p. 71–87.

Dusel-Bacon, C., Wooden, J.L., and Hopkins, M.J., 2004. U-Pb zircon and geochemical evidence for bimodal mid-Paleozoic magmatism and syngenetic base-metal mineralization in the Yukon-Tanana terrane, Alaska. GSA Bulletin, 116: 7-8, p. 989–101, https://doi.org/10.1130/B25342.1.

Dusel-Bacon, C., Hopkins, M.J., Mortensen, J.K., Dashevsky, S.S., Bressler, J.R., and Day, W.C., 2006. Paleozoic tectonic and metallogenic evolution of the pericratonic rocks of east-central Alaska and adjacent Yukon. In: Colpron, M., and Nelson, J.L. (eds.), Paleozoic Evolution and Metallogeny of Pericratonic Terranes at the Ancient Pacific Margin of North America, Canadian and Alaskan Cordillera, Geological Association of Canada, Special Paper 45, p. 25–74.

Dusel-Bacon, C., Day, W.C., and Aleinikoff, J.N., 2013. Geochemistry, petrography, and zircon U-Pb geochronology of Paleozoic metaigneous rocks in the Mount Veta area of east-central Alaska: Implications for the evolution of the westernmost part of the Yukon-Tanana terrane. Canadian Journal of Earth Sciences, 50:8, p. 826–846, https://doi.org/10.1139/cjes-2013-0004.

Ellis, D.J., and Thompson, A.B., 1984. Subsolidus and Partial Melting Reactions in the Quartz-excess CaO + MgO+Al2O3 + SiO2 + H2O System under Water-excess and Water deficient Conditions to 10 kb: Some Implications for the Origin of Peraluminous Melts from Mafic Rocks. Journal of Petrology, 27:1, p. 91-121.

Evenchick, C.A., Gabrielse, H., and Snyder, D.B., 2005. Crustal structure and lithology of the northern Canadian Cordillera: alternative interpretations of SNORCLE seismic reflection lines 2a and 2b. Canadian Journal of Earth Sciences, 42, p. 1149–1161.

Evenchick, C.A., McMechan, M.E., McNicoll, V.J., and Carr, S.D., 2007, A synthesis of the Jurassic–Cretaceous tectonic evolution of the central and southeastern Canadian Cordillera: Exploring links across the orogen. In: Sears, J.W., Harms, T.A., and Evenchick, C.A., eds., Whence the Mountains? Inquiries into the Evolution of Orogenic Systems: A Volume in Honor of Raymond A. Price, Geological Society of America Special Paper 433, p. 117–145, doi: 10.1130/2007.2433(06).

Ferri, F., 1997. Nina Creek Group and Lay Range Assemblage, north-central British Columbia: remnants of late Paleozoic oceanic and arc terranes. Canadian Journal of Earth Sciences, 34, p. 854–874.

Ferri, F., Dudka, S., Rees, C., and Meldrum, D.G., 1993. Geology of the Aiken Lake and Osilinka River areas, Northern Quesnel Trough (94 C/2, 3,5, 6 and 12). In: Geological Fieldwork 1992. British Columbia Ministry of Energy, Mines and Petroleum Resources, Paper 1993-1, p. 109-134.

Ferry, J.M, and Watson, E.B., 2007. New thermodynamic models and revised calibrations for the

Ti-in-zircon and Zr-in-rutile thermometers. Contributions to Mineralogy and Petrology, 154, p. 429–437, doi:10.1007/s00410-007-0201-0.
Fisher, C.M., Hanchar, J.M., Samson, S.D., Dhuime, B., Blichert-Toft, J., Vervoort, J.D., and Lam, R., 2011. Synthetic zircon doped with hafnium and rare earth elements: A reference material for in situ hafnium isotope analysis. Chemical Geology, 286, 1-2, p. 32-47, https://doi.org/10.1016/j.chemgeo.2011.04.013.
Fisher, C. M., Vervoort, J. D., and DuFrane, S. A., 2014. Accurate Hf isotope determinations of complex zircons using the ‘‘laser ablation split stream’’ method. Geochemistry, Geophysics, Geosystems, 15, p. 121-139, doi:10.1002/2013GC004962.
Fisher, C.M., Paton, C., Pearson, D.G., Sarkar, C., Luo, Y., Tersmette, D.B., and Chacko, T., 2017. Data reduction of laser ablation split-stream (LASS) analyses using newly developed features within iolite: With applications to Lu-Hf+U-Pb in detrital zircon and Sm-Nd+U-Pb in igneous monazite. Geochemistry, Geophysics, Geosystems, 18, p. 4604-4622, https://doi.org/10. 1002/2017GC007187.
Fisher, C.M., Bauer, A.M., Luo, Y., Sarkar, C., Hanchar, J.M., Vervoort, J.D., Tapster, S.R., Horstwood, M., Pearson, D.G., 2020. Laser ablation split-stream analysis of the Sm-Nd and U-Pb isotope compositions of monazite, titanite, and apatite – Improvements, potential reference materials, and application to the Archean Saglek Block gneisses. Chemical Geology, 539, 119493, https://doi.org/10.1016/j.chemgeo.2020.119493.
Frost, B.R., Barnes, C.G., Collins, W.J., Arculus, R.J., Ellis, D.J., and Frost, C.D., 2001. A Geochemical Classification for Granitic Rocks. Journal of Petrology, 42:11, p. 2033–2048, https://doi.org/10.1093/petrology/42.11.2033.
Frost, B.R., and Frost, C.D., 2008. A Geochemical Classification for Feldspathic Igneous Rocks. Journal of Petrology, 49:11, p. 1955-1969, doi:10.1093/petrology/egn054.
Gaetani G.A., and Grove T.L., 2003. Experimental constraints on melt generation in the mantle wedge. In: Eiler, J., Abers, G. (eds.), Inside the Subduction Factory, American Geophysical Union, Monograph Series 138, p. 107-134.
Gain, S.E.M, Greau, Y., Henry, H., Belousova, E., Dainis, I., Griffin, W.L., and O’Reilly, S.Y., 2019. Mud Tank Zircon: Long Term Evaluation of a Reference Material for U-Pb Dating, Hf-isotope Analysis and Trace Element Analysis. Geostandards and Geoanalytical Research, 43:3, p. 339-345. doi: 10.1111/ggr.12265.
Garnett, J.A., 1972. Duckling Creek Area, Hogem Batholith. In: Geology, Exploration and Mining in British Columbia 1971, British Columbia Department of Mines and Petroleum Resources, p. 203-220.
Garnett, J.A., 1978. Geology and mineral occurrences of the southern Hogem batholith. British Columbia Ministry of Mines and Petroleum Resources, British Columbia Geological Survey Bulletin 70, 75 p.
Gehrels, G.E., McClelland, W.C., Samson, S.D., and Patchett, P.J., 1991. U-Pb geochronology of detrital zircons from a continental margin assemblage in the northern Coast Mountains, southeastern Alaska. Canadian Journal of Earth Sciences, 28, p. 1285–1300.
Gehrels, G., Rusmore, M., Woodsworth, G., Crawford, M., Andronicos, C., Hollister, L., Patchett, J., Ducea, M., Butler, R., Klepeis, K., Davidson, C., Friedman, R., Haggart, J., Mahoney, B., Crawford, W., Pearson, D., and Girardi, J., 2009. U-Th-Pb geochronology of the Coast Mountains batholith in north-coastal British Columbia: Constrains on age and tectonic evolution. GSA Bulletin, 121:9-10, p. 1341-1361, doi: 10.1130/B26404.1.
Ghosh, D.K., 1995. Nd-Sr isotopic constraints on the interactions of the Intermontane

Superterrane with the western edge of North America in the southern Canadian Cordillera. Canadian Journal of Earth Sciences, 32, p. 1740-1758, https://doi.org/10.1139/e95-136.
Gibson, H.D., Brown, R.L., and Carr, S.D., 2005. U-Th-Pb geochronologic constraints on the structural evolution of the Selkirk fan, northern Selkirk Mountains, southern Canadian Cordillera. Journal of Structural Geology, 27, p. 1899-1924. https://doi.org/10.1016/j.jsg.2005.05.014.
Gibson, H.D., Brown, R.L., and Carr, S.D., 2008. Tectonic evolution of the Selkirk fan, southeastern Canadian Cordillera: a composite Middle Jurassic–Cretaceous orogenic structure. Tectonics, 27:6, TC6007, https://doi.org/10.1029/2007TC002160.
Gill, J.B., 1981. Orogenic Andesites and Plate Tectonics. New York: Springer-Verlag. 390 p.
Griffin, W.L., Wang X., Jackson, S.E., Pearson, N.J., O'Reilly, S.Y., Xu, X., and Zhou, X., 2002. Zircon chemistry and magma mixing, SE China: In-situ analysis of Hf isotopes, Tonglu and Pingtan igneous complexes. Lithos, 61, p. 237-269.
Grimes, C.B., John, B.E., Kelemen, P.B., Mazdab, F.K., Wooden, J.L., Cheadle, M.J., Hanghøj, K., and Schwartz, J.J., 2007. Trace element chemistry of zircons from oceanic crust: A method for distinguishing detrital zircon provenance. Geology, 35:7, p. 643-646, https://doi.org/10.1130/G23603A.1.
Grimes, C.B., Wooden, J.L., Cheadle, M.J., and John, B.E., 2015. “Fingerprinting” tectono-magmatic provenance using trace elements in igneous zircon. Contributions to Mineralogy and Petrology, 170:46, p. 1-26, https//doi.org/10.1007/s00410-015-1199-3.
Grove, T.L., Chatterjee, N., Parman, S.W., and Médard, E., 2006. The influence of H2O on mantle wedge melting. Earth and Planetary Science Letters, 249:1-2, p. 74-89, https://doi.org/10.1016/j.epsl.2006.06.043.
Grove, T.L., Till, C.B., and Krawczynski, M.J., 2012. The Role of H2O in Subduction Zone Magmatism. Annual Review of Earth and Planetary Sciences, 40:1, p. 413-439, https://doi.org/10.1146/annurev-earth-042711-105310.
Hansen, V.L., 1990. Yukon-Tanana terrane: A partial acquittal. Geology, 18, p. 365–369, doi:10.1130/0091-7613(1990)018<0365:YTTAPA>2.3.CO;2.
Hawkesworth, C., Cawood, P., Kemp, T., Sorey, C., and Dhuime, B., 2009. A Matter of Preservation. Science, 323, p. 49-50, doi: 10.1126/science.1168549.
Hildreth, W., and Moorbath, S., 1988. Crustal contributions to arc magmatism in the Andes of Central Chile. Contributions to Mineralogy and Petrology, 98, p. 455-489, https://doi.org/10.1007/BF00372365.
Hoefs, J., 2018. Variations of stable isotope ratios in nature. In: Hoefs, J. (ed.), Stable Isotope Geochemistry, Springer, p. 229–432, https://doi.org/10.1007/978-3-319-78527-1.
Holtz, F., and Johannes, W., 1991. Genesis of Peraluminous Granites I. Experimental Investigation of Melt Compositions at 3 and 5 kb and Various H2O Activities. Journal of Petrology, 32:5, p. 935-958.
Homan, C., 2017. Investigating Causes of Magmatic Episodicity in the Southern Coast Mountains Batholith, British Columbia: Insights from Hafnium and Oxygen Isotopes in Magmatic Zircon (M.Sc Thesis). California State University, Northridge, 128p.
Horstwood, M.S.A., Košler, J., Gehrels, G., Jackson, S.E., McLean, N.M., Paton, C., Pearson, N.J., Sircombe, K., Sylvester, P., Vermeesch, P., Bowring, J.F., Condon, D.J. and Schoene, B., 2016. Community-Derived Standards for LA-ICP-MS U-(Th-)Pb Geochronology – Uncertainty Propagation, Age Interpretation and Data Reporting.

Geostandards and Geoanalytical Research, 40, p. 311-332, https://doi.org/10.1111/j.1751-908X.2016.00379.x.
Hoskin, P.W.O., and Ireland, T.R., 2000. Rare earth element chemistry of zircon and its use as a provenance indicator. Geology, 28:7, p. 627-630, https://doi.org/10.1130/0091-7613(2000)28<627:REECOZ>2.0.CO;2.
Ickert, R.B., 2013. Algorithms for estimating uncertainties in initial radiogenic isotope ratios and model ages. Chemical Geology, 340, p. 131-138, http://dx.doi.org/10.1016/j.chemgeo.2013.01.001.
Irvine, T.N., 1971. Age determinations and geological studies, K-Ar isotopic ages, Report 10. Geological Survey of Canada, Paper 71-2, p. 11.
Irvine, T.N, and Baragar, W.R.A., 1971. A Guide to the Chemical Classification of the Common Volcanic Rocks. Canadian Journal of Earth Sciences, p. 523-548.
Irving, E., Wynne, P.J., Thorkelson, D.J., and Schiarizza, P., 1996. Large (1000 to 4000 km) northward movements of tectonic domains in the northern Cordillera, 83 to 45 Ma. Journal of Geophysical Research, 101: B8, p. 17901-17916.
Jackson, S.E., Pearson, N.J., Griffin, W.L., and Belousova, E.A., 2004. The application of laser ablation-inductively coupled plasma-mass spectrometry to in situ U–Pb zircon geochronology. Chemical Geology, 211, p. 47-69, doi:10.1016/j.chemgeo.2004.06.017.
Jacobsen, S.B., and Wasserburg, G.J., 1980. Sm-Nd isotopic evolution of chondrites. Earth and Planetary Science Letters, 50:1, p. 139-155. ISSN 0012-821X.
Jaffey, A.H., Flynn, K.F., Glendenin, L.E., Bentley, W.C., and Essling, A.M., 1971. Precision measurements of half-lives and specific activities of 235U and 238U. Physical Reviews, C4, p. 1889-1906.
Jochum, K.P., Nohl, U., Herwig, K., Lammel, E., Stoll, B., and Hofmann, A.W., 2005. GeoReM: A New Geochemical Database for Reference Materials and Isotopic Standards. Geostandards and Geoanalytical Research, 29, p. 333-338. https://doi.org/10.1111/j.1751-908X.2005.tb00904.x.
Jochum, K.P., Weis, U., Stoll, B., Kuzmin, D., Yang, Qichao, Raczek, I., Jacob, D.E., Stracke, A., Birbaum, K., Frick, D.A., Günther, D., Enzweiler, J., 2011. Determination of Reference Values for NIST SRM 610-617 Glasses Following ISO Guidelines. Geostandards and Geoanalytical Research, 35:4, p. 397-429, doi: 10.1111/j.1751-908X.2011.00120.x.
Johnston, S.T., 2008. The Cordilleran Ribbon Continent of North America. Annual Review of Earth and Planetary Sciences, 36:1, p. 495-530, 10.1146/annurev.earth.36.031207.124331.
Johnston, S.M., and Kylander-Clark, A.R.C., 2021. Outer forearc uplift and exhumation during high-flux magmatism: Evidence from detrital zircon geochemistry of the Nacimiento forearc basin, California, USA. Geology, 49:7, p. 832-836, https://doi.org/10.1130/G48627.1.
Jones, D.L., Silberling, N. J., and Hillhouse, J., 1977. Wrangellia; a displaced terrane in northwestern North America. Canadian Journal of Earth Sciences, 14, p. 2565-2577.
Jones, D.L., Howell, D.G., Coney, P.J., and Monger, J.W.H., 1983. Recognition, character and analysis of tectonostratigraphic terranes in western North America. In: Hashimoto, M., and Uyeda, S. (eds.), Accretion Tectonics in the Circum-Pacific Regions: Tokyo, Terra Scientific Publishing Company, p. 21–35.
Jones, G., Ootes, L., Milidragovic, D., Friedman, R., Camacho, A., Luo, Y., Vezinet, A.,

Pearson, D.G., and Schiarizza, P., 2021. Geochronology of northern Hogem batholith, Quesnel terrane, north-central British Columbia. In: Geological Fieldwork 2020, British Columbia Ministry of Energy, Mines and Low Carbon Innovation, British Columbia Geological Survey Paper 2021-01, p. 37-56.

Kemp, A.I.S., Hawkesworth, C.J., Paterson, B.A., and Kinny, P.D., 2006. Episodic growth of the Gondwana supercontinent from hafnium and oxygen isotopes in zircon. Nature, 439, p. 580-583, https://doi.org/10.1038/nature04505.

Kemp, A.I.S., Hawkesworth, C.J., Collins, W.J., Gray, C.M., Blevin, P.L., and EIMF, 2009. Isotopic evidence for rapid continental growth in an extensional accretionary orogen: The Tasmanides, eastern Australia. Earth and Planetary Science Letters, 284, p. 455-466, doi:10.1016/j.epsl.2009.05.011.

Klepeis, K.A., Crawford, M.L., and Gehrels, G., 1998. Structural history of the crustal-scale Coast shear zone north of Portland Canal, southeast Alaska and British Columbia. Journal of Structural Geology, 20:7, p. 883-904, https://doi.org/10.1016/S0191-8141(98)00020-0.

Kobylinski, C., Hattori, K., Smith, S. and Plouffe, A., 2020. Protracted magmatism and mineralized hydrothermal activity at the Gibraltar porphyry copper-molybdenum deposit, British Columbia, Economic Geology, 115:5, p. 1119-1136, doi:10.5382/econgeo.4724.

Koo, Ja Hak, 1968. Geology and mineralization in the Lorraine Property area, Omineca Mining Division, B.C. University of British Columbia, Unpublished BSc. Thesis, 107 p.

Kusky, T.M., and Polat, A., 1999. Growth of granite–greenstone terranes at convergent margins, and stabilization of Archean cratons. Tectonophysics, 305, p. 43-73, https://doi.org/10.1016/S0040-1951(99)00014-1.

Langmuir, C.H., Vocke Jr., R.D., Hanson, G.N., and Hart, S.R., 1978. A general mixing equation with applications to Icelandic basalts. Earth and Planetary Science Letters, 37, p. 380-392.

Lebas, M.J., Lemaitre, R.W., Streckeisen, A., and Zanettin, B., 1986. A Chemical Classification of Volcanic-Rocks Based on the Total Alkali Silica Diagram. Journal of Petrology, 27:3, p. 745-750.

Lee, C.-T.A., Morton, D.M., Kistler, R.W., and Baird, A.K., 2007. Petrology and tectonics of Phanerozoic continent formation: From island arcs to accretion and continental arc magmatism. Earth and Planetary Science Letters, 263:3-4, p.3 70-387, https://doi.org/10.1016/j.epsl.2007.09.025.

Lee, R.G., Dilles, J.H., Tosdal, R.M., Wooden, J.L., and Mazdab, F.K., 2017. Magmatic Evolution of Granodiorite Intrusions at the El Salvador Porphyry Copper Deposit, Chile, Based on Trace Element Composition and U/Pb Age of Zircons. Economic Geology, 112:2, p. 245-273. https://doi.org/10.2113/econgeo.112.2.245

Lee, R.G., Byrne, K., D'Angelo, M., Hart, C.J.R., Hollings, P., Gleeson, S.A., and Alfaro, M., 2020. Using zircon trace element composition to assess porphyry copper potential of the Guichon Creek batholith and Highland Valley Copper deposit, south-central British Columbia. Mineralium Deposita, 56, p. 215-238, https://doi-org.login.ezproxy.library.ualberta.ca/10.1007/s00126-020-00961-1.

Lee, R.G., Plouffe, A., Ferbey, T., Hart, C.J.R., Hollings, P., and Gleeson, S.A., 2021. Recognizing porphyry copper potential from till zircon composition: A case study from the Highland Valley porphyry discrict, south-cental British Columbia. Economic Geology,116:4, p. 1035-1045, https://doi.org/10.5382/econgeo.4808.

Loader, M.A., Wilkinson, J.J., Armstrong, R.N., 2017. The effect of titanite crystallisation on Eu

and Ce anomalies in zircon and its implications for the assessment of porphyry Cu deposit fertility. Earth and Planetary Science Letters, 472, p. 107-119.
Logan, J.M., and Mihalynuk, M.G., 2014. Tectonic Controls on Early Mesozoic Paired Alkaline Porphyry Deposit Belts (Cu-Au±Ag-Pt-Pd-Mo) within the Canadian Cordillera. Economic Geology, 109:4, p. 827-858, https://doi.org/10.2113/econgeo.109.4.827.
Longerich, H.P., Jackson, S.E., Günther, D., 1996. Laser ablation inductively coupled plasma mass spectrometric transient signal data acquisition and analyte concentration calculation. Journal of Analytical Atomic Spectrometry, 11:9, p. 899-904.
Lord, C.S., 1948. McConnell Creek map-area, Cassiar District, British Columbia. Geological Survey of Canada, Memoir 251, 82 p.
Loucks, R.R., Fiorentini, M.L., and Henríquez, G.J., 2020. New magmatic oxybarometer using trace elements in zircon. Journal of Petrology, 61:3, p. 1-30, doi:10.1093/petrology/egaa034.
Lu, Y., Loucks, R.R., Fiorentini, M., McCuaig, T.C., Evans, N.J., Yang, Z.M., Hou, Z.Q., Kirkland, C.L., Parra-Avila, L.A., Kobussen, A., 2016. Zircon compositions as a pathfinder for porphyry Cu ± Mo ± Au deposits. In: Richards, J.P. (ed.), Tectonic and Metallogeny of the Tethyan Orogenic Belt, Economic Geology Special Publication 19, p. 329-347, https://doi.org/10.5382/SP.19.13.
Lugmair, G.W., and Marti, K., 1978. Lunar initial 143Nd/144Nd: differential evolution of the lunar crust and mantle. Earth and Planetary Science Letters, 39, p. 349-357, doi:10.1016/0012-821X(78)90021-3.
Malkowski, M.A., and Hampton, B.A., 2014. Sedimentology, U-Pb detrital geochronology, and Hf isotopic analyses from Mississippian–Permian stratigraphy of the Mystic subterrane, Farewell terrane, Alaska. Lithosphere, 6:5, p. 383-398, https://doi.org/10.1130/L365.1.
Matsuhisa, Y., 1979. Oxygen isotopic compositions of volcanic rocks from the east Japan island arcs and their bearing on petrogenesis. Journal of Volcanology and Geothermal Research, 5, p. 271–296.
Meade, H.D., 1977. Petrology and Metal Occurrences of the Takla Group and Hogem and Germansen Batholiths, North Central British Columbia. University of Western Ontario Digitized Theses, 1046, 349p. https://ir.lib.uwo.ca/digitizedtheses/1046.
Middlemost, E.A.K., 1994. Naming materials in the magma / igneous rock system. Earth-Science Reviews, 37, p. 215-224.
Mihalynuk, M.G., Nelson, J.L., and Diakow, L.J., 1994. Cache Creek terrane: oroclinal paradox within the Canadian Cordillera. Tectonics, 13, p. 575–595.
Mihalynuk, M.G., Erdmer, P., Ghent, E.D., Cordey, F., Archibald, D.A., Friedman, R.M., and Johannson, G.G., 2004. Coherent French Range blueschist: Subduction to exhumation in <2.5 m.y.?. Geological Society of America Bulletin, 116: 7-8, p. 910-922. doi:10.1130/B25393.1.
Monger, J.W.H., 1977. Upper Paleozoic rocks of the western Canadian Cordillera and their bearing on Cordilleran evolution. Canadian Journal of Earth Sciences, 14, p. 1832-1859.
Monger, J.W.H., and Church, B.N., 1977. Revised stratigraphy of the Takla Group, north-central British Columbia. Canadian Journal of Earth Sciences, 14, p. 318–326.
Monger, J.W.H., Price, R.A., and Tempelman-Kluit, D.J., 1982. Tectonic accretion and the origin of the two major metamorphic and tectonic welts in the Canadian Cordillera. Geology, 10, p. 70–75.
Monger, J.W.H., Wheeler, J.O., Tipper, H.W., Gabrielse, H., Harms, T., Struik, L.C., Campbell,

R.B., Dodds, C.J., Gehrels, G.E., and O'Brien, J., 1991. Part B. Cordilleran terranes, Upper Devonian to Middle Jurassic assemblages (Chapter 8). In: Gabrielse, H., and Yorath, C.J. (eds.), Geology of the Cordilleran Orogen in Canada, Geological Survey of Canada, Geology of Canada 4, p. 281–327.

Monger, J.W.H., and Price, R.A., 2002. The Canadian Cordillera: Geology and tectonic evolution. Canadian Society of Exploration Geophysicists Recorder, p. 17–36.

Monger, J.W., 2014. Logan Medallist 1. Seeking the Suture: The Coast-Cascade Conundrum. Geoscience Canada, 41:4, p. 379–398, https://doi.org/10.12789/geocanj.2014.41.058

Monger, J.W.H, and Gibson, H.D., 2019. Mesozoic-Cenozoic deformation in the Canadian Cordillera: The record of a "Continental Bulldozer"?. Tectonophysics, 757, p. 153-169. https://doi.org/10.1016/j.tecto.2018.12.023

Morel, M.L.A., Nebel, O., Nebel-Jacobsen, Y.J., Miller J.S., Vroon, P.Z., 2008. Hafnium isotope characterization of the GJ-1 zircon reference material by solution and laser-ablation MC-ICPMS. Chemical Geology, 255, p. 231-235, doi:10.1016/j.chemgeo.2008.06.040.

Morrison, G.W., 1980. Characteristics and tectonic setting of the shoshonite rock association. Lithos, 13, p. 97-108.

Mortensen, J.K., 1992. Pre-mid-Mesozoic tectonic evolution of the Yukon-Tanana terrane, Yukon and Alaska. Tectonics, 11:4, p. 836-853.

Mortensen, J.K., Ghosh, D.K., and Ferri, F., 1995. U-Pb geochronology of intrusive rocks associated with copper-gold porphyry deposits in the Canadian Cordillera. Canadian Institute of Mining, Metallurgy and Petroleum, Special Volume 46, p. 142-158.

Mortimer, N., 1986. Late Triassic, arc-related potassic igneous rocks in the North American Cordillera. Geology, 14, p. 1035-1038.

Moyen, J.-F., and Stevens, G., 2006. Experimental Constraints on TTG Petrogenesis: Implications for Archean Geodynamics. In: Benn, K., Mareschal, J.-C., and Condie, K.C. (eds.), American Geophysical Union, Archean Geodynamics and Environments, Geophysical Monograph Series 164, p. 149-175, https://doi.org/10.1029/164GM11.

Muehlenbachs, K., and Byerly, G., 1982. 18O-Enrichment of silicic magmas caused by crystal fractionation at the Galapagos Spreading Center. Contributions to Mineralogy and Petrology, 79, p. 76-79, https://doi.org/10.1007/BF00376963.

Murakami, T., Chakoumakos, B.C., Ewing, R. C., Lumpkin, G.R., and Weber, W.J., 1991. Alpha-Decay Event Damage in Zircon. American Mineralogist, 76, p. 1510-1532.

Næraa, T., Scherstén, A., Rosing, M., Kemp, A.I.S., Hoffmann, J.E., Kokfelt, T.F., and Whitehouse, M.J., 2012. Hafnium isotope evidence for a transition in the dynamics of continental growth 3.2 Gyr ago. Nature, 485, p. 627-630, https://doi.org/10.1038/nature11140.

Nagel, T.J., Hoffmann, J.E., and Münker, C., 2012. Generation of Eoarchean tonalite-trondjhemite-granodiorite series from thickened mafic arc crust. Geology, 40:4, p. 375-378, doi:10.1130/G32729.1.

Nathwani, C.L., Simmons, A.T., Large, S.J.E, Wilkinson, J.J., Buret, Y., and Ihlenfeld C., 2021. From long-lived batholith construction to giant porphyry copper deposit formation: petrological and zircon chemical evolution of the Quellaveco District, Southern Peru. Contributions to Mineralogy and Petrology, 176:12, https://doi.org/10.1007/s00410-020-01766-1

Nelson, J.L., and Bellefontaine, K.A., 1996. The Geology and Mineral Deposits of North-Central

Quesnellia; Tezzeron Lake to Discovery Creek, Central British Columbia. British Columbia Ministry of Energy, Mines and Petroleum Resources, British Columbia Geological Survey Bulletin 99, 112 p.

Nelson, J.L., and Colpron, M., 2007. Tectonics and metallogeny of the Canadian and Alaskan Cordillera, 1.8 Ga to present. Mineral Deposit Division, Geological Association of Canada, Special Publication 5, p. 755–791.

Nelson, J.L., and Friedman, R.M., 2004. Superimposed Quesnel (late Paleozoic–Jurassic) and Yukon-Tanana (Devonian-Mississippian) arc assemblages, Cassiar Mountains, northern British Columbia: Field, U-Pb and igneous petrochemical evidence. Canadian Journal of Earth Sciences, 41, p.1201-1235, doi:10.1139/e04-028.

Nelson, J.L., and Mihalynuk, M., 1993. Cache Creek ocean: closure or enclosure. Geology, 21, p. 173-176.

Nelson, J., Carmichael, B., and Gray, M., 2003. Innovative gold targets in the Pinchi Fault/Hogem batholith area: The Hawk and Axelgold properties, central British Columbia (94C/4, 94N/13). In: Geological Fieldwork 2002, British Columbia Ministry of Energy and Mines, British Columbia Geological Survey Paper 2003-1, p. 97-114.

Nelson, J.L., Colpron, M., Piercey, S.J., Dusel-Bacon, C., Murphy, D.C., and Roots, C.F., 2006. Paleozoic tectonic and metallogenic evolution of the pericratonic terranes in Yukon, northern British Columbia and eastern Alaska. In: Colpron, M., and Nelson, J.L. (eds.), Paleozoic Evolution and Metallogeny of Pericratonic Terranes at the Ancient Pacific Margin of North America, Canadian and Alaskan Cordillera, Geological Association of Canada, Special Paper 45, p. 323–360.

Nelson, J.L., Colpron, M., and Israel, S., 2013. The Cordillera of British Columbia, Yukon, and Alaska: Tectonics and metallogeny. In: Colpron, M., Bissig, T., Rusk, B.G., and Thompson, J.F.H. (eds.), Tectonics, Metallogeny and Discovery: The North American Cordillera and Similar Accretionary Settings, Society of Economic Geologists, Special Publication 17, p. 53–103, https://doi.org/10.5382/SP.17.03.

Nixon, G.T., and Peatfield, G.R., 2003. Geological setting of the Lorraine Cu-Au porphyry deposit, Duckling Creek syenite complex, north-central British Columbia. British Columbia Ministry of Energy, Mines and Petroleum Resources, British Columbia Geological Survey Open File 2003-4, 24p.

Nokleberg, W.J., Bundtzen, T., Eremin, R.A., Ratkin, V.V., Dawson, K.M., Shpikerman, V.V., Goryachev, N.A., Byalobzhesky, S.G., Frolov, Y.F.,Khanchuck, A.I., Koch, R.D., Monger, J.W.H., Pozdeev, A.A.,Rozenblum, I.S., Rodionov, S.M., Parfenov, L.M., Scotese, C.R., and Sidorov, A.A., 2005. Metallogenesis and tectonics of the Russian Far East, Alaska and the Canadian Cordillera. U.S. Geological Survey Professional Paper 1697, 397 p.

Ootes, L., Bergen, A.L., Milidragovic, D., and Graham, B., 2019a. Preliminary geology of Notch Peak and Ogden Creek (parts of NTS 094C/04 and 093N/13), northern Hogem batholith, Quesnel terrane, north-central British Columbia. British Columbia Ministry of Energy, Mines and Petroleum Resources, British Columbia Geological Survey Open File 2019-02, scale 1:50,000.

Ootes, L., Bergen, A.L., Milidragovic, D., Graham, B. and Simmonds, R., 2019b. Preliminary geology of northern Hogem batholith, Quesnel terrane, north-central British Columbia. In: Geological Fieldwork 2018, BC Ministry of Energy, Mines and Petroleum Resources, BC Geological Survey, Paper 2019-01, p. 31–53,

http://cmscontent.nrs.gov.bc.ca/geoscience/PublicationCatalogue/Paper/BCGS_P2019-01-03_Ootes.pdf .

Ootes, L., Bergen, A.L., Milidragovic, D., Jones, G.O., 2020a. Bedrock geology of northern Hogem batholith and its surroundings, north-central British Columbia. BC Ministry Energy, Mines and Petroleum Resources, BC Geological Survey, Open File 2020-02, scale 1:50000.

Ootes, L., Bergen, A.L., Milidragovic, D., Jones, G.O., Camacho, A. and Friedman, R., 2020b. An update on the geology of northern Hogem batholith and its surroundings, north-central British Columbia. In: Geological Fieldwork 2019, BC Ministry of Energy, Mines and Petroleum Resources, BC Geological Survey Paper 2020-01, p. 25–47, http://cmscontent.nrs.gov.bc.ca/geoscience/PublicationCatalogue/Paper/BCGS_P2020-01-03_Ootes.pdf.

Ootes, L., Jones, G., Schiarizza, P., Milidragovic, D., Friedman, R., Camacho, A., Luo, Y., Vezinet, A., Pearson, D.G., and Zhang, S., 2020c. Geochronologic and geochemical data from northern Hogem batholith and its surroundings, north-central British Columbia. British Columbia Ministry of Energy, Mines and Low Carbon Innovation, British Columbia Geological Survey GeoFile 2020-01, 21 p., http://cmscontent.nrs.gov.bc.ca/geoscience/PublicationCatalogue/GeoFile/BCGS_GF2020-01.pdf.

Pană, D.I., van der Pluijm, B.A., 2015. Orogenic pulses in the Alberta Rocky Mountains: Radiometric dating of major faults and comparison with the regional tectono-stratigraphic record. GSA Bulletin, 127:3-4, p. 480–502, https://doi.org/10.1130/B31069.1.

Paton, C., Woodhead, J. D., Hellstrom, J. C., Hergt, J. M., Greig, A., and Maas, R., 2010. Improved laser ablation U-Pb zircon geochronology through robust downhole fractionation correction. Geochemistry, Geophysics, Geosystems, 11, Q0AA06, doi:10.1029/2009GC002618.

Paton, C., Hellstrom, J., Paul, B., Woodhead, J., and Hergt, J., 2011. Iolite: Freeware for the visualisation and processing of mass spectrometric data. Journal of Analytical Atomic Spectrometry, 26:12 , p. 2508-2518, doi:10.1039/c1ja10172b.

Pearce, J.A., Harris, N.B.W, and Tingle, A.G., 1984. Trace Element Discrimination Diagrams for the Tectonic Interpretation of Granitic Rocks. Journal of Petrology, 25:4, p. 956-983, https://doi.org/10.1093/petrology/25.4.956.

Peccerillo, A., and Taylor, S.R., 1976. Geochemistry of Eocene Calc-Alkaline Volcanic Rocks from the Kastamonu Area, Northern Turkey. Contributions to Mineralogy and Petrology, 58, p. 63-81, http://dx.doi.org/10.1007/BF00384745.

Pecha, M.E., Gehrels, G.E., McClelland, W.C., Giesler, D., White, C., and Yokelson, I., 2016. Detrital zircon U-Pb geochronology and Hf isotope geochemistry of the Yukon-Tanana terrane, Coast Mountains, southeast Alaska. Geosphere, 12:5, p. 1556–1574, https://doi.org/10.1130/GES01303.1.

Pettke, T., Oberli, F., Audetat, A., Guillong, M., Simon, A.C., Hanley, J.J., and Klemm, L.M., 2012. Recent developments in element concentration and isotope ratio analysis of individual fluid inclusions by laser ablation single and multiple collector ICP-MS. Ore Geology Reviews, 44, p. 10-38, https://doi.org/10.1016/j.oregeorev.2011.11.001.

Piercey, S.J., and Colpron, M., 2009. Composition and provenance of the Snowcap assemblage, basement to the Yukon-Tanana terrane, northern Cordillera: Implications for Cordilleran crustal growth. Geosphere, 5, p. 439-464, doi:10.1130 /GES00505.1.

Read, P.B., and Okulitch, A.V., 1977. The Triassic unconformity of south-central British Columbia. Canadian Journal of Earth Sciences, 14, p. 686-638.
Reid, L.F., 2002. Stratigraphy, Structure, Petrology, Geochronology and Geochemistry of the Hobson Lake area (Cariboo Mountains, British Columbia) in Relation to the Tectonic Evolution of the Southern Canadian Cordillera (Ph.D. Thesis). University of Calgary, 221 p.
Rezeau, H., Moritz, R., Wotzlaw, J.F., Hovakimyan, S., and Tayan, R., 2019. Zircon petrochronology of the Meghri-Ordubad pluton, lesser Caucasus: Fingerprinting igneous processes and implications for the exploration of porphyry Cu–Mo deposits. Economic Geology 114:7, p. 1365-1388, https://doi.org/10.5382/econgeo.4671.
Richards, J.P., 2015. The oxidation state, and sulfur and Cu contents of arc magmas: implications for metallogeny. Lithos, 233, p. 27-45, http://dx.doi.org/10.1016/j.lithos.2014.12.011.
Roberts, M.P., and Clemens, J.D., 1993. Origin of high-potassium, calc-alkaline, I-type granitoids. Geology, 21, p. 825-828.
Roots, E.F., 1954. Geology and mineral deposits of Aiken Lake map area, British Columbia: Geological Survey of Canada, Memoir 274, 246 p.
Rosman, K.J.R., and Taylor, P.D.P., 1998. Isotopic compositions of the elements 1997 (Technical Report). Pure and Applied Chemistry, 71:1, p. 217-235, https://doi.org/10.1351/pac199870010217.
Ross, P.-S., and Bédard, J.H., 2009. Magmatic affinity of modern and ancient subalkaline volcanic rocks determined from trace-element discriminant diagrams. Canadian Journal of Earth Sciences, 46:11, p. 823-839, https://doi.org/10.1139/E09-054.
Rudnick, R.L., and Gao, S.L., 2003. 3.01 – Composition of the Continental Crust. Treatise on Geochemistry, 3, p. 1-64, https://doi.org/10.1016/B0-08-043751-6/03016-4.
Rusmore, M.E., Potter, C.J., and Umhoefer, P.J., 1988. Middle Jurassic terrane accretion along the western edge of the Intermontane superterrane, southwestern British Columbia. Geology, 16:10, p. 891-894, https://doi.org/10.1130/0091-7613(1988)016<0891:MJTAAT>2.3.CO;2.
Russell, W., Papanastassiou, D., and Tombrello, T., 1978. Ca isotope fractionation on the Earth and other solar system materials. Geochimica et Cosmochimica Acta, 42, p. 1075-1090, https://doi.org/10.1016/0016-7037(78)90105-9.
Sack, P.J., Colpron, M., Crowley, J.L., Ryan, J.J., Allan, M.M., Beranek, L.P. and Joyce, N.L., 2020. Atlas of Late Triassic to Jurassic plutons in the Intermontane terranes of Yukon. Yukon Geological Survey, Open File 2020-1, 365 p.
Samson, S.D., Patchett, P.J., McClelland, W.C., and Gehrels, G.E., 1991. Nd isotopic characterization of metamorphic rocks in the Coast Mountains, Alaskan and Canadian Cordillera: ancient crust bounded by juvenile terranes. Tectonics, 10, p. 770-780.
Schiarizza, P., and Tan, S.H., 2005a. Geology and mineral occurrences of the Quesnel Terrane between the Mesilinka River and Wrede Creek (NTS 94D/8, 9), north-central British Columbia. British Columbia Ministry of Energy and Mines, British Columbia Geological Survey Paper 2005-1, p. 109-130.
Schiarizza, P., and Tan, S.H., 2005b. Geology of the Johanson Lake area, parts of NTS 94D/8 and 9. British Columbia Ministry of Energy, Mines and Petroleum Resources, British Columbia Geological Survey Open File 2005-4, scale 1:50,000.
Schiarizza, P., 2014. Geological setting of the Granite Mountain batholith, host to the Gibraltar

porphyry Cu-Mo deposit, south-central British Columbia. In: Geological Fieldwork 2013, British Columbia Ministry of Energy and Mines, British Columbia Geological Survey Paper 2014-01, p. 95-100.
Schiarizza, P., 2019. Geology of the Nicola Group in the Bridge Lake-Quesnel River area, south-central British Columbia. In: Geological Fieldwork 2018, British Columbia Ministry of Energy, Mines and Petroleum Resources, British Columbia Geological Survey Paper 2019-01, p. 15-30.
Şengör, A.M.C., Natal'in, B. A., and Burtman, V.S., 1995. Evolution of the Altaid tectonic collage and Palaeozoic crustal growth in Eurasia. Nature, 364, p. 299-307, https://doi.org/10.1038/364299a0.
Shen, P., Hattori, K., Pan, H., Jackson, S., and Seitmuratova, E., 2015. Oxidation condition and metal fertility of granitic magmas: Zircon trace-element data from porphyry Cu deposits in the Central Asian orogenic belt. Economic Geology, 110, p. 1861-1878.
Sigloch, K., and Mihalynuk, M.G., 2017. Mantle and geological evidence for a Late Jurassic–Cretaceous suture spanning North America. GSA Bulletin, 129:11-12, p. 1489-1520, https://doi.org/10.1130/B31529.1.
Simard, R.-L., Dostal, J., and Roots, C.F., 2003. Development of late Paleozoic volcanic arcs in the Canadian Cordillera: an example from the Klinkit Group, northern British Columbia and southern Yukon. Canadian Journal of Earth Sciences, 40, p. 907-924.
Sláma, J., Košler, J, Condon, D.J., Crowley, J.L., Gerdes, A., Hanchar, J.M., Horstwood, M.S.A., Morris, G.A., Nasdala, L., Norberg, N., Schaltegger, U., Schoene, B., Tubrett, M.N., and Whitehouse, M.J., 2008. Plešovice zircon – A new natural reference material for U–Pb and Hf isotopic microanalysis. Chemical Geology, 249, p. 1–35, doi:10.1016/j.chemgeo.2007.11.005.
Smithies, R.H., 2000. The Archean tonalite-trodjhemite-granodiorite (TTG) series is not an analogue of Cenozoic adakite. Earth and Planetary Science Letters, 182, p. 115-125.
Snyder, D.B., Clowes, R.M., Cook, F.A., Erdmer, P., Evenchick, C.A., van der Velden, A.J., and Hall, K.W., 2002. Proterozoic Prism Arrests Suspect Terranes: Insights into the Ancient Cordilleran Margin from Seismic Reflection Data. GSA Today, 12:10, p. 4-10. doi:10.1130/1052-5173(2002)012<0004:PPASTI>2.0.CO;2
Söderlund, U., Patchett, P.J., Vervoort, J.D. and Isachsen, C.E., 2004. The 176Lu decay constant determined by Lu-Hf and U-Pb isotope systematics of Precambrian mafic intrusions. Earth and Planetary Science Letters, 219:3-4, p. 311-324, https://doi.org/10.1016/S0012-821X(04)00012-3.
Spandler, C., Hammerli, J., Sha, P., Hilbert-Wolf, H., Hu, Y., Roberts, E., and Schmitz, M., 2016. MKED1: A new titanite standard for in situ analysis of Sm–Nd isotopes and U–Pb geochronology. Chemical Geology, 425, p. 110-126, https://doi.org/10.1016/j.chemgeo.2016.01.002.
Spencer, C.J., Kirkland, and Taylor, R.J.M., 2016. Strategies towards statistically robust interpretations of in situ U–Pb zircon geochronology. Geoscience Frontiers, 7:4, p. 581-589, https://doi.org/10.1016/j.gsf.2015.11.006.
Spencer, C.J., Kirkland, Prave, A.R., Strachan, R.A., and Pease, V., 2019. Crustal reworking and orogenic styles inferred from zircon Hf isotopes: Proterozoic examples from the North Atlantic region. Geoscience Frontiers, 10:2, p. 417-424, https://doi.org/10.1016/j.gsf.2018.09.008.
Stacey, J.S., and Kramers, J.D., 1975. Approximation of terrestrial lead isotope evolution by a

two-stage model. Earth and Planetary Science Letters, 26:2, p. 207-221, https://doi.org/10.1016/0012-821X(75)90088-6.
Stanley, C.R., 2003. Estimating sampling errors for major and trace elements in geological materials using a propagation of variance approach. Geochemistry: Exploration, Environment, Analysis, 3, p. 167-178, https://doi.org/10.1144/1467-7873/03-008.
Staples, R.D., Murphy, D.C., Gibson, H.D., Colpron, M., Berman, R.G., and Ryan, J.J., 2014. Middle Jurassic to earliest Cretaceous mid-crustal tectono-metamorphism in the northern Canadian Cordillera: Recording foreland-directed migration of an orogenic front. GSA Bulletin, 26, p. 1511-1530, https://doi.org/10.1130/b31037.1.
Staples, R.D., Gibson, H.D., Colpron, M., and Ryan, J., 2016. An orogenic wedge model for diachronous deformation, metamorphism and exhumation in the hinterland of the northern Canadian Cordillera. Lithosphere 8, p. 165-184, https://doi.org/10.1130/L472.1.
Stern, R.J., 2002. Subduction zones. Review of Geosphysics, 40:4, p. 3-1-3-38. doi:10.1029/2001RG000108.
Stern, R.A., 2020. CCIM O-isotope methods – zircon. Unpublished document.
Streck, M.J., and Dilles, J.H., 1998. Sulfur evolution of oxidized arc magmas as recorded in apatite from porphyry copper batholith. Geology, 26, p. 523-526.
Sun, S.S., and McDonough, W.F., 1989. Chemical and isotopic systematics of oceanic basalts; implications for mantle composition and processes. In: Magmatism in the ocean basins. Saunders, A.D. and Norry, M.J. (eds.), Geological Society of London, 42, p. 313-345.
Tatsumi, Y., Hamilton, D.L., Nesbitt, R.W., 1986. Chemical characteristics of fluid phase released from a subducted lithosphere and origin of arc magmas: evidence from high-pressure experiments and natural rocks. Journal of Volcanology and Geothermal Research, 29, p. 293-309.
Tempelman-Kluit, D.J., 1976. The Yukon Crystalline Terrane: Enigma in the Canadian Cordillera. GSA Bulletin, 87, p. 1343-1357.
Tempelman-Kluit, D.J., 1979. Transported cataclasite, ophiolite and granodiorite in Yukon: Evidence of arc-continent collision. Geological Survey of Canada, Paper 79-14, 27 p.
Trail, D., Warson, E.B., and Taiby, N.D., 2012. Ce and Eu anomalies in zircon as proxies for the oxidation state of magmas. Geochimica et Cosmochimica Acta, 97, p. 70-87.
Valley, J., Kinny, P., Schulze, D., and Spicuzza, M.J., 1998. Zircon megacrysts from kimberlite: oxygen isotope variability among mantle melts. Contributions to Mineralogy and Petrology, 133, p. 1-11, https://doi.org/10.1007/s004100050432.
Valley, J.W., 2003. Chapter 13: Oxygen isotopes in zircon. In: Hanchar, J.M., and Hoskin, P.W.O, (eds.), Mineralogical Society of America, Reviews in Mineralogy & Geochemistry, 53, Zircon, p. 343-386.
Valley, J.W., Lackey, J.S., Cavosie, A.J., Clechenko, C.C., Spicuzza, M.J., Basei, M.A.S., Bindeman, I.N., Ferreira, V.P., Sial, A.N., King, E.M., Peck, W.H., Sinha, A.K., and Wei, C.S., 2005. 4.4 billion years of crustal maturation: oxygen isotope ratios of magmatic zircon. Contributions to Mineralogy and Petrology, 150, p. 561-580, https://doi.org/10.1007/s00410-005-0025-8.
Van der Heyden, P., 1992. A middle Jurassic to early Tertiary Andean-Sierran arc model for the Coast Belt of British Columbia. Tectonics, 11:1, p. 82-97.
Vermeesch, P., 2018. IsoplotR: A free and open toolbox for geochronology. Geoscience Frontiers, 9, p. 1479-1493, https://doi.org/10.1016/j.gsf.2018.04.001.
Vernon, R.H., and Collins, W.J., 2011. Structural Criteria for Identifying Granitic Cumulates.

The Journal of Geology, 119, p. 127-142, doi:10.1086/658198.
Vervoort, J.D., Plank, T., and Prytulak, J., 2011. The Hf-Nd isotopic composition of marine sediments. Geochimica et Cosmochimica Acta, 75:20, p. 5903-5926, https://doi.org/10.1016/j.gca.2011.07.046.
Vervoort, J.D., and Kemp, A.I.S., 2016. Clarifying the zircon Hf isotope record of crust-mantle evolution. Chemical Geology, 425, p. 65-75, https://doi.org/10.1016/j.chemgeo.2016.01.023.
Vezinet, A., Pearson, D.G., Thomassot, E., Stern, R.A., Sarkar, C., Luo, Y., and Fisher, C.M., 2018. Hydrothermally-altered mafic crust as source for early Earth TTG: Pb/Hf/O isotope and trace element evidence from TTG of the Eoarchean Saglek Block, N. Labrador (electronic supplementary material). Earth and Planetary Science Letters, 503, p. 95-107, https://doi.org/10.1016/j.epsl.2018.09.015.
Villeneuve, M.N, Whalen, J.B., Anderson, R.G., and Struik, L.C., 2001. The Endako Batholith: Episodic Plutonism Culminating in Formation of the Endako Porphyry Molybdenite Deposit, North-Central British Columbia. Economic Geology, 96, p. 171-196.
Watson, E.B., Wark, D.A., and Thomas, J.B., 2006. Crystallization thermometers for zircon and rutile. Contributions to Mineralogy and Petrology, 151, p. 413-433.
Webster, E.R., and Pattison, D.R.M., 2018. Spatially overlapping episodes of deformation, metamorphism, and magmatism in the southern Omineca Belt, southeastern British Columbia. Canadian Journal of Earth Sciences, 55, p. 84-110, https://doi.org/10.1139/cjes-2017-0036.
Webster, E.R., Pattison, D., and DuFrane, S.A., 2017. Geochronological constraints on magmatism and polyphase deformation and metamorphism in the southern Omineca Belt, British Columbia. Canadian Journal of Earth Sciences, 54, p. 529-549, https://doi.org/10.1139/cjes-2016-0126.
Wernicke, B., and Klepacki, D.W., 1988. Escape hypothesis for the Stikine block. Geology, 16, p. 461-464.
Whalen, J.B., Anderson, R.G., Struik, L.C., and Villeneuve, M.E., 2001.Geochemistry and Nd isotopes of the Francois Lake plutonic suite, Endako batholith: host and progenitor to the Endako molybdenum camp, central British Columbia. Canadian Journal of Earth Sciences, 38:4, p. 603-618, https://doi.org/10.1139/e00-080.
Whalen, J.B., and Hildebrand, R.S., 2019. Trace element discrimination of arc, slab failure, and A-type granitic rocks. Lithos, 348-349, 105179, https://doi.org/10.1016/j.lithos.2019.105179.
Wheeler, J.O., Brookfield, A.J., Gabrielse, H., Monger, J.W.H., Tipper, H.W., and Woodsworth, G.J., 1991, Terrane map of the Canadian Cordillera: Geological Survey of Canada, Map 1713A, scale 1:2,000,000.
Widmann, P., Davies, J.H.F.L., Schaltegger, U., 2019. Calibrating chemical abrasion: Its effects on zircon crystal structure, chemical composition and U-Pb age. Chemical Geology, 511, p. 1-10, https://doi.org/10.1016/j.chemgeo.2019.02.026.
Wiedenbeck, M., Allé, P., Corfu, D., Griffin, W.L., Meier, M., Oberli, F., Von Quadt, A., Roddick, J.C., and Spiegel, W., 1995. Three natural zircon standards for U-Th-Pb, Lu-Hf, Trace Element and REE Analyses. Geostandards Newsletter, 19:1, p. 1-23.
Wiedenbeck, M., Hanchar, J.M., Peck, W.H., Sylvester, P., Valley, J., Whitehouse, M., Kronz, A., Morishita, Y., Nasdala, L., Fiebig, J., Franchi, I., Girard, J.-P., Greenwood, R.C., Hinton, R., Kita, N., Mason, P.R.D., Norman, M., Ogasawara, M., Piccoli, P.M., Rhede,

D., Satoh, H., Schulz-Dobrick, B., Skår, Ø., Spicuzza, M.J., Terada, K., Tindle, A., Togashi, S., Vennemann, T., Xie, Q., and Zheng, Y.-F., 2004. Further Characterisation of the 91500 Zircon Crystal. Geostandards and Geoanalytical Research, 28:1, p. 9-39, https://doi.org/10.1111/j.1751-908X.2004.tb01041.x.

Wooden, J.L., Mazdab, F.K., Barth, A.P., Miller, C.F., and Lowery, L.E., 2006. Temperatures (Ti) and compositional characteristics of zircon: early observations using high mass resolution on the USGS Stanford SHRIMP-RG. Geochimica et Cosmochimica Acta Supplement, 70:18, p. A707, https://doi.org/10.1016/j.gca.2006.06.1533.

Woodhead, J., Hergt, J., Shelley, M., Eggins, S., and Kemp, R., 2004. Zircon Hf-isotope analysis with an excimer laser, depth profiling, ablation of complex geometries, and concomitant age estimation. Chemical Geology, 209:1, p. 121-135.

Woodsworth, G.J., 1976. Plutonic rocks of McConnell Creek (94D west half) and Aiken Lake (94 C east half) map-areas, British Columbia. Geological Survey of Canada, Paper 76-1A, p. 69-73.

Woodsworth, G.J., Anderson, R.G., and Armstrong, R.L., 1991. Plutonic regimes, Chapter 15. In: Gabrielse, H., and Yorath, C.J., (eds.), Geology of the Cordilleran Orogen in Canada, Geological Survey of Canada, Geology of Canada, 4, p. 491-531.

Yuan, H., Gao, S., Liu, X., Li, H., Günther, D., and Wu, F., 2004. Accurate U-Pb Age and Trace Element Determinations of Zircon by Laser Ablation-Inductively Coupled Plasma-Mass Spectrometry. Geostandards and Geoanalytical Research, 28:3, p. 353-370, https://doi.org/10.1111/j.1751-908X.2004.tb00755.x.

Zagorevski, A., 2015. Gabbro-peridotite Interaction in the Northern Cache Creek Composite Terrane Ophiolite, British Columbia and Yukon. American Geophysical Union, Fall Meeting 2015, abstract V11D-3082.

Zhong, S., Seltmann, R., Qu, H., and Song, Y., 2019. Characterization of the zircon Ce anomaly for estimation of oxidation state of magmas: A revised Ce/Ce* method. Mineralogy and Petrology, 113, p. 755–763, doi: 10.1007/ s00710-019-00682-y.

Appendix A. Hogem batholith intrusive samples

Appendix A1. Sample Locations

Table A1. Locations and lithologies of plutonic rock samples collected for this study.

Sample	Latitude	Longitude	Intrusive suite	Lithology
19GJ12-4	56.211666	-125.646053	Thane Creek	Quartz diorite
18lo22-1a	56.024407	-125.598711	Thane Creek	Hornblendite
18lo22-1d	56.024407	-125.598711	Thane Creek	Quartz diorite
19GJ13-3	56.013314	-125.820707	Thane Creek	Quartz monzodiorite
19GJ13-1	56.102513	-125.659887	Duckling Creek	Biotite clinopyroxenite
18lo25-2a	56.007961	-125.701574	Duckling Creek	Syenite
19GJ13-5a	55.999451	-125.526168	Duckling Creek	Syenite
19GJ13-2	56.101539	-125.659247	Duckling Creek	Syenite
19GJ13-4	56.003737	-125.570508	Duckling Creek	Syenite
18lo17-1	56.110442	-125.764089	Osilinka	Granite
18lo20-4	56.100984	-125.732593	Osilinka	Dyke
19GJ12-3	56.169348	-125.826751	Osilinka	Granite
19GJ12-1	56.223775	-125.974787	Mesilinka	Tonalite
19GJ12-2	56.214498	-125.905444	Mesilinka	Tonalite
18lo11-1	56.221037	-125.932380	Mesilinka	Equigranular granite
18lo12-7	56.223797	-125.923148	Mesilinka	K-feldspar porphyritic granite
19GJ16-2	56.072374	-125.859092	Mesilinka	Equigranular granite

Appendix A2. Sample Descriptions and Petrography

Sample: 18lo22-1a

Intrusive suite: Thane Creek

Rock Name: Plagioclase-bearing hornblendite

Hand sample description: Black with white patches, coarse-grained to pegmatitic plagioclase-bearing hornblendite.

Outcrop description: ~100 m wide well exposed hornblendite body within diorite with areas of copper sulphide mineralization and weathering. Crosscut by subparallel Osilinka granite sheets ~200 m away.

Textures: Medium-coarse grained, cumulate

Alteration: Biotite, chlorite

Mineralization: Minor Cu-sulphide

Normalized to QAP: N/A

Mineral Name	Abundance	Description
Hornblende	72%	Subhedral, ragged grain boundaries, ~2-8mm, average ~5mm, mostly equigranular, dirty looking from biotite and chlorite alteration, especially along cleavage
Biotite	9%	Subhedral, generally ~1mm, concentrated along amphibole grain boundaries, light green to brown pleochroism, chlorite alteration
Plagioclase	7%	Anhedral, intercumulus texture interstitial to amphibole, ~2-3mm grain size, twinning visible where relatively fresh, some grains sericitized
Magnetite	6%	Anhedral, ~0.6-2mm,, interstitial to amphibole, concentrated with titanite, apatite
Epidote	2%	Subhedral, associated with plagioclase and magnetite, ~1-2mm grain size
Chalcopyrite	1%	Anhedral, fine-grained, disseminated
Titanite	1%	Anhedral to subhedral, ~0.5-1.7mm, associated with magnetite. Anhedral grains have abundant opaque inclusions, titanite rims on magnetite
Apatite	Trace	Anhedral to subhedral, <0.1-0.4mm, concentrated with magnetite, contained as inclusions within apatite, amphibole
Zircon	Trace	~100-200 µm long inclusions in feldspar intercumulate patches

Sample: 18lo22-1d

Intrusive suite: Thane Creek

Rock Name: Medium-grained quartz diorite

Hand sample description: Black and white, medium-grained equigranular diorite with moderate foliation.

Outcrop description: Exposed diorite outcrop surrounding hornblendite body.

Textures: Medium grained, equigranular

Alteration: Sericite/clay

Mineralization: Chalcopyrite

Normalized to QAP:

Quartz: 6

Alkali feldspar: 9

Plagioclase: 85

Mineral Name	Abundance	Description
Plagioclase	65%	Anhedral, generally ~1-3mm, very clay altered and dirty looking
Biotite	12%	Anhedral, generally ~0.2-0.6mm, associated with amphibole and chlorite, some magnetite inclusions
Alkali feldspar	7%	Relict grain, 0.7-1.7mm, extensively clay altered
Hornblende	6%	Subhedral, ragged grain boundaries, ~0.75-3.5mm, chlorite and biotite alteration
Chlorite	5%	Anhedral, generally ~0.1-0.4mm, alteration product of amphibole and biotite, associated with magnetite
Quartz	5%	Anhedral, 0.4-1.5mm, strained, undulose extinction, interstitial to altered plagioclase
Magnetite	1%	Anhedral to subhedral, <0.1-0.5mm, disseminated, concentrated with mafic phases
Apatite	Trace	Subhedral, 0.3-0.5mm, associated with biotite, magnetite, epidote
Epidote	Trace	Anhedral, ~0.2-0.4mm, associated with biotite, chlorite, and magnetite concentrated around mafic phases
Chalcopyrite	Trace	Anhedral, Disseminated, ~0.1-0.25 mm
Zircon	Trace	0.005 mm inclusions in biotite; euhedral

Sample: 19GJ12-4

Intrusive suite: Thane Creek

Rock Name: Quartz diorite

Hand sample description: Grey-weathering, grey coarse-grained, equigranular relatively fresh diorite to monzodiorite.

Outcrop description: Well exposed, fresh diorite outcrop. Raining and thunder at sample location, so brief description and collection.

Textures: fine-grained, equigranular

Alteration: Clay alteration of plagioclase

Mineralization: minor chalcopyrite

Normalized to QAP:

Quartz: 8

Alkali feldspar: 9

Plagioclase: 83

Mineral Name	Abundance	Description
Plagioclase	62%	~0.2-0.5 mm; semi euhedral; Cores are clay altered; some grains within K-feldspar patches with microcline twinning
Amphibole	8%	0.1-0.6mm, green yellow pleochroic, occurs in patches with biotite, contains inclusions of magnetite and magnetite along fractures and cleavage, occasionally Rims on clinopyroxene
Biotite	8%	~0.025-0.2 mm wide; Brown, some green, associated with altered amphibole; intergrown in patches with amphibole
Alkali feldspar	7%	0.2-0.4mm, interstitial to plagioclase.,most Extremely clay altered; some less altered grains are zoned and microcline twinning
Clinopyroxene	7%	~0.1-0.3 mm wide cores in amphibole; altered and dirty looking, anhedral
Quartz	6%	~0.1-0.2 mm, interstitial to plagioclase grains; strained undulatory extinction
Magnetite	1%	Very fine grained (<0.01mm) to ~0.05 mm wide; Anhedral to euhedral; Disseminated; Inclusions in amphibole, “leopard spots”
Muscovite	Trace	~0.01 mm shreddy grain within feldspar (sericite)
Epidote	Trace	~0.02-0.05 wide patches that occur with altered feldspar and within fractures in magnetite
Chalcopyrite	Trace	Very fine inclusion in magnetite
Apatite	Trace	~0.02-0.04 wide, euhedral; Inclusions in feldspar and magnetite with epidote
Titanite	Trace	~0.2-0.5 mm; euhedral grains Occurs with amphibole; fine rims on magnetite
Zircon	Trace	~50-100 µm, rare euhedral inclusions in amphibole, cpx

Sample: 19GJ13-3

Intrusive suite: Thane Creek

Rock Name: Quartz monzodiorite

Hand sample description: Grey weathering, black and white, medium- to coarse-grained, equigranular diorite with abundant titanite.

Outcrop description: ~20 m wide exposure of relatively fresh Thane Creek diorite.

Textures: Fine to medium grained equigranular

Alteration: Chlorite

Mineralization: N/A

Normalized to QAP:

Quartz: 17

Alkali feldspar: 38

Plagioclase: 45

Mineral Name	Abundance	Description
Plagioclase	39%	Euhedral, 0.25-4mm, generally ~1mm, some myrmekitic grains
K-feldspar	33%	Microcline twinned, medium grained, 1.3- 2.2mm wide, Poikilitic, inclusions of plagioclase, amphibole, magnetite, quartz
Quartz	15%	Anhedral, 0.25-1mm subgrains, strained, undulose extinction
Amphibole	8%	Anhedral to subhedral, Generally ~1mm, up to 3mm, occasionally twinned, grain boundaries slightly altered to chlorite
Biotite	2%	Anhedral, generally 0.5mm, up to 2mm, inclusions of magnetite, poikilitic, growing around k-feldspar, and interstitially, slightly altered to chlorite
Titanite	2%	Subhedral, ~1.5mm, subpoikilitic, growing around K-feldspar and plagioclase. Contains inclusions of apatite and zircon.
Magnetite	1%	Anhedral, disseminated, interstitial grains up to 0.9mm, generally ~0.1mm, minor titanite rims
Apatite	Trace	Euhedral, ~0.12 mm, inclusions in magnetite and titanite
Zircon	Trace	Euhedral, fine grained (~80 µm long), inclusions in quartz, feldspar, biotite, titanite

Sample: 18lo25-2a

Intrusive suite: Duckling Creek

Rock Name: Syenite

Hand sample description: Pink-white, medium-grained, equigranular syenite

Outcrop description: Medium-coarse grained syenite-monzonite with pink/white weathering, with two feldspars and hornblende or pyroxene. Malachite staining in wall.

Textures: Medium-grained, equigranular

Alteration: Clay, chlorite

Mineralization: N/A

Normalized to QAP:

Quartz: 0

Alkali feldspar: 97

Plagioclase: 3

Mineral Name	Abundance	Description
Alkali feldspar	88%	Subhedral, ~1-4mm grain size, microcline twinning and perthitic, clay alteration
Clinopyroxene	5%	Subhedral, 0.4-1.2mm, fractured, associated with magnetite, chlorite alteration
Plagioclase	3%	Subheadral, twinned, intergrown with K-feldspar
Magnetite	2%	Subhedral, <0.1mm-0.5mm, associated with clinopyroxene, titanite, diseminated in feldspar, ilmenite exsolution
Titanite	1%	Euhedral, wedge shaped, ~0.7-1.6mm, intergrown with clinopyroxene
Chlorite	1%	Fine-grained, alteration product of clinopyroxene and fine grained inclusions in feldspar
Zircon	Trace	0.006 to 0.022 mm; subhedral to euhedral grains in feldspar, cpx

Sample: 19GJ13-1

Intrusive suite: Duckling Creek

Rock Name: Biotite clinopyroxenite

Hand sample description: Black-weathering, black with white coarse-grained, equigranular biotite pyroxenite.

Outcrop description: ~20 m wide exposure, cut by quartz veins up to 3 cm wide. Azurite is present in secondary veins. Highly magnetic. ~500 m from syenite contact.

Textures: Medium-grained, equigranular, cumulate texture

Alteration: none

Mineralization: N/A

Normalized to QAP: N/A

Mineral Name	Abundance	Description
Clinopyroxene	82%	Subhedral, ~1-3mm, cumulate texture, contains inclusions of magnetite, occasional biotite and apatite
Biotite	10%	Anhedral, ~0.25-0.5mm, subpoikilitic surrounding clinopyroxene and magnetite grains, sagenitic (acicular inclusions, possibly of Ti-phase)
Magnetite	5%	Anhedral to subhedral, 0.3-0.6mm, disseminated or intercumulus, contains inclusions of apatite, rims of titanite
Apatite	3%	Subhedral to anhedral, bimodal, range in grain size from 0.1-2mm, larger grains visible in hand sample, occurs mostly interstitially to clinopyroxene or inclusions in magnetite
Amphibole	Trace	Anhedral, ~2mm, contains apatite inclusions
Epidote	Trace	Within cross cutting veinlet (~0.2mm wide) with minor calcite
Titanite	Trace	Fine rims on magnetite

Sample: 19GJ13-2

Intrusive suite: Duckling Creek

Rock Name: K-feldspar phenocrystic syenite

Hand sample description: Light pink-weathering, pink fresh K-feldspar phenocrystic, coarse-grained syenite.

Outcrop description: ~50 m wide exposure of syenite on steep slope, ~500 m from biotite clinopyroxenite. Malachite/azurite staining present in outcrop.

Textures: Phenocrystic alkali feldspar with interstitial patches of alteration minerals

Alteration: Clay/sericite, epidote and biotite

Mineralization: Minor chalcopyrite

Normalized to QAP:

Quartz: 0

Alkali feldspar: 100

Plagioclase: 0

Mineral Name	Abundance	Description
Alkali feldspar	85%	Phenocrystic, euhedral, 3-6mm wide, >20mm long, microcline tartan twinning, moderate clay alteration affecting grain boundaries and in grain mid sections
Muscovite	10%	Anhedral to subhedral, fine-grained (<0.1mm-0.2mm), intergrown with quartz, epidote, biotite
Epidote	2%	Anhedral, Generally ~0.25-0.5mm wide, occurs interstital to k-feldspar phenocrysts, intergrown with biotite, muscovite, magnetite, titanite
Magnetite	1%	Subhedral to euhedral, Up to 2mm wide, mainly <0.1mm , occurs interstitial to k-feldspar, concentrated zones could indicate a relict grain boundary (cannot identify mineral). Occasional titanite rims.
Biotite	1%	Anhedral, fine grained, green in PPL, reddish-brown alteration along cleavage
Quartz	Trace	Anhedral, fine-grained (~0.05mm) strained grains occurring intergrown together (~0.2mm) within interstitial intergrowths of muscovite, biotite, and epidote
Apatite	Trace	Subhedral, fine grained (0.06-0.12mm long), high relief grains occurring in interstitial zones with concentrated magnetite
Titanite	Trace	Rare, disseminated, subhedral, fine grained (~60 µm), spatially associated with biotite inclusions in feldspar. Also within interstitial zones between alkali feldspar grains, with epidote, muscovite, and magnetite.
Chalcopyrite	Trace	

Sample: 19GJ13-4

Intrusive suite: Duckling Creek

Rock Name: Clinopyroxene bearing syenite

Hand sample description: Pink-weathering, pink and black medium-grained K-feldspar phenocrystic syenite.

Outcrop description: ~50 m wide well exposed, weathered syenite on steep slope. Weathering crust ~1 cm wide was chipped off to expose fresh surface.

Textures: Foliated, medium-grained

Alteration: Clay/sericite, biotite, chlorite

Mineralization: N/A

Normalized to QAP:

Quartz:0

Alkali feldspar: 100

Plagioclase: 0

Mineral Name	Abundance	Description
Alkali feldspar	80%	Mainly anhedral, diffuse grain boundaries, ~1-3mm wide, extensive clay alteration, "dirty" apperance
Clinopyroxene	8%	Anhedral, Emerald green, highly fractured, 0.5-1mm, diffused grain boundaries with surrounding altered k-feldspar
Amphibole	5%	Anhedral, fractured, fine to medium grained ~0.4-1 mm, associated with clinopyroxene, magnetite, and apatite, and biotite and chlorite alteration
Chlorite	2%	Anhedral, associated with areas of concentrated mafic minerals, alteration of biotite and clinopyroxene
Biotite	2%	Anhedral, ~0.25-0.45mm, appears to be altering clinopyroxene, which also has chlorite alteration, magnetite inclusions along cleavage
Apatite	1%	Euhedral, fine grained (~0.1-0.2 mm), associated with areas of concentrated mafics (clinopyroxene, amphibole, magnetite)
Magnetite	1%	Subhedral, some larger grains rounded, generally very fine grained and disseminated, up to 0.25 mm, associated with mafic minerals
Muscovite	1%	Anhedral, very fine grained, concentrated intergrowths, occasionally associated with epidote, biotite, and chlorite alteration
Epidote	Trace	Anhedral, ~0.3-0.5mm, intergrown with biotite, chlorite, titanite, apatite, and magnetite
Titanite	Trace	Subhedral to euhedral, ~0.1-0.15mm, intergrown with biotite, amphibole, and apatite, interstitial to K-feldspar

Sample: 19GJ13-5a

Intrusive suite: Duckling Creek

Rock Name: medium grained syenite

Hand sample description: Grey-weathering, white and greenish-black slightly foliated, equigranular syenite.

Outcrop description: ~100 m wide well exposed syenite. ~2 m wide zone of brown weathering, carbonate altered and copper sulphide mineralization approximately 20 m from sample location.

Textures: Fine to medium grained, equigranular

Alteration: Clay/sericite, biotite, chlorite

Mineralization: minor chalcopyrite

Normalized to QAP:

Quartz: 0

Alkali feldspar: 90

Plagioclase: 10

Mineral Name	Abundance	Description
Alkali feldspar	72%	Subhedral, ~1-4mm, some of centers of grains extensively sericitic altered, some grains have Carlsbad twinning
Amphibole	9%	Anhedral, ~0.9-1.2mm, some grains have Carlsbad twinning, associated with epidote and chlorite
Plagioclase	8%	Subhedral, generally ~0.9-1mm, twinned plagioclase overgrown by untwinned zones (k-spar?)
Clinopyroxene	5%	Subhedral, 0.1-1mm, generally ~0.5mm, associated with amphibole, biotite, epidote
Magnetite	2%	Anhedral, generally very fine grained disseminated grains, up to 0.4mm, some grains overgrown by titanite (ilmenite?)
Titanite	Trace	Subhedral, ~0.2mm, high relief some grains have wedge shape
Biotite	2%	Subhedral, ~0.25-0.4mm, associated with amphibole, titanite, magnetite, apatite
Chlorite	1%	Anhedral, ~0.2-0.3mm, associated with epidote, magnetite, alteration of biotite, clinopyroxene, amphibole
Apatite	Trace	Sub to euhedral, ~0.1mm-0.2mm, inclusions in amphibole, biotite, associated with magnetite, titanite
Epidote	Trace	Anhedral, ~0.1mm, high relief, associated with chlorite
Chalcopyrite	Trace	Rare, fine grained (~20 µm), disseminated, rimmed by titanite(?)
Zircon	Trace	Euhedral, rare, fine grained (~100 µm long), inclusion in feldspar, biotite

Sample: 18lo17-1

Intrusive suite: Osilinka

Rock Name: Granite

Hand sample description: White, medium-grained, equigranular granite with very low mafic content.

Outcrop description: Medium-grained equigranular granite with no foliation and little mafic minerals. Outcrop has abundant decimetre-scale joints in rock.

Textures: Medium-grained, equigranular

Alteration: Clay/sericite, chlorite

Mineralization: N/A

Normalized to QAP:

Quartz: 39

Alkali feldspar: 34

Plagioclase: 27

Mineral Name	Abundance	Description
Quartz	37%	Anhedral, ~1-4mm, strained, undulose extinction
Alkali feldspar	32%	Subhedral, ~1.2-2mm, some grains have microcline tartan twinning, clay alteration present in grain cores
Plagioclase	26%	Subhedral, ~0.8-3mm, some grains zoned
Biotite/chlorite	2%	Anhedral, ~0.2-0.9mm, associated with magnetite, interstitial to feldspar
Muscovite/sericite	2%	Anhedral, fine grained, present in feldspar cores and along grain boundaries
Magnetite	1%	Subhedral, <0.1mm-0.4mm, disseminated, concentrated with chlorite, exsolution of ?
Epidote	Trace	Subhedral, ~0.25-0.5mm, associated with biotite/chlorite
Zircon	Trace	~20-40 µm wide; euhedral; inclusions in quartz, K-feldspar

Sample: 18lo20-4

Intrusive suite: Osilinka

Rock Name: Feldspar porphyry

Hand sample description: White, feldspar porphyry from flat-lying dyke (sheet) with plagioclase phenocrysts up to 0.5 cm.

Outcrop description: Feldspar porphyry dyke with fine-grained groundmass and plagioclase phenocrysts up to 0.5 cm. Sheared and undulating contact with granite, low in mafic mineral except pyrite. Sill-like that is at least 4m thick, but top not observed.

Textures: Feldspar porphyrytic

Alteration: Chlorite, sericite

Mineralization: Chalcopyrite

Normalized to QAP:

Quartz: 56

Alkali feldspar: 0

Plagioclase: 44

Mineral Name	Abundance	Description
Quartz	50%	Very fine grained matrix
Plagioclase	40%	Euhedral, porphyritic, 2-3mm, completely sericitized Very fine grained matrix, sericitized
Calcite	3%	Vein (0.6 mm wide), strained, and in matrix
Chlorite	2%	Anhedral, ~0.2-1mm wide, associated with calcite
Epidote	2%	Subhedral, fine grained, ~0.2-0.4mm, associated with calcite
Magnetite	1%	Disseminated, very fine grained, up to 1.8mm, exsolution of ?
Muscovite	1%	Muscovite grains anhedral ~0.2-0.3mm. Sericite <0.25mm associated with altered feldspars
Chalcopyrite	Trace	Rare, euhedral, ~2.5mm wide

Sample: 19GJ12-3

Intrusive suite: Osilinka

Rock Name: Equigranular, fine to medium grained granite

Hand sample description: White-weathering, white fine-grained equigranular granite with very low mafic content and rare ~1 mm pyrite grains.

Outcrop description: Well exposed granite, ~200 m away from contact with Thane Creek diorite. Rain and thunder were approaching helicopter, therefore brief description and collection.

Textures: Fine to medium grained, equigranular

Alteration: Sericite, chlorite

Mineralization: N/A

Normalized to QAP:

Quartz: 32

Alkali feldspar: 31

Plagioclase: 37

Mineral Name	Abundance	Description
Plagioclase	35%	Subhedral, ~1mm average, polysynthetic twinning, extensive clay/sericite alteration
Quartz	30%	Anhedral, undulose extinction, strained, finer grained domains
Alkali feldspar	29%	Subhedral, ~1mm average, zonation, minor clay alteration, variable tartan twinning
Muscovite/sericite	5%	Muscovite grains anhedral ~0.2-0.3mm Sericite <0.25mm associated with altered feldspars
Biotite	1%	Anhedral, very fine grained ~0.1-0.2mm, chloritized
Epidote	Trace	Anhedral, fine grained, 0.5-1mm, fractured
Magnetite	Trace	Subhedral, very fine grained, ~0.05-0.2mm, disseminated, concentrated with biotite
Pyrite	Trace	Rare, anhedral, ~0.5-1mm, disseminated, rimmed by hematite
Zircon	Trace	Rare, euhedral, ~100 µm long, inclusions in feldspar and quartz

Sample: 18lo11-1

Intrusive suite: Mesilinka

Rock Name: Fine to medium grained granite

Hand sample description: White and black, fine to medium-grained equigranular granite with foliation defined by biotite.

Outcrop description: Homogenous yellow weathering and pinkish fresh coloured equigranular granite, with large (~2mx5m) grey xenoliths with white feldspar grains. Folitation defined by biotite, sparse magnetite crystals.

Textures: Fine-medium grained, equigranular

Alteration: sericite/muscovite, chlorite

Mineralization:

Normalized to QAP:

Quartz: 42

Alkali feldspar: 32

Plagioclase: 26

Mineral Name	Abundance	Description
Quartz	40%	Anhedral, ~1mm domains comprised of fine sub grains, strained, undulose extinction
Alkali feldspar	30%	Anhedral, 0.2-2mm, average ~1.6mm, minor clay alteration, some grains have microcline twinning
Plagioclase	25%	Anhedral-subhedral, ~0.4-1.6mm, average ~1.2mm, variable sericite (muscovite) alteration
Muscovite	2%	Anhedral, fine grained, occurs within feldspar cores and along grain boundaries
Biotite	1%	Anhedral, fine-grained, occurs interstitial to feldspars
Chlorite	1%	Anhedral, fine-grained, occurs interstitial to feldspars, with muscovite and biotite
Magnetite	1%	Anhedral, ~0.25-0.8mm, disseminated, rimmed by titanite?
Zircon	Trace	Euhedral, ~50 µm long, inclusions in feldspar

Sample: 18lo12-7

Intrusive suite: Mesilinka

Rock Name: K-feldspar porphyritic granite

Hand sample description: Pinkish-black, medium-grained K-feldspar porphyritic granite with a foliation defined by biotite.

Outcrop description: Predominantly K-feldspar phenocrystic granite with minor equigranular granite.

Textures: Medium grained, equigranular, myrmekitic

Alteration: Clay

Mineralization: N/A

Normalized to QAP:

Quartz: 32

Alkali feldspar: 43

Plagioclase: 25

Mineral Name	Abundance	Description
Alkali feldspar	38%	Subhedral, up to 16mm, average ~3mm, "dirty" appearance, quartz and biotite/chlorite inclusions
Quartz	28%	Anhedral, fine sub-grains making up domains ~3-6mm, undulose extinction
Plagioclase	22%	Anhedral-subhedral, 0.4-2.3mm, average ~1.5mm, some grains myrmekitic, "dirty" appearance but relatively unaltered
Biotite	10%	Subhedral, generally ~0.75-2mm, occurs interstitial to quartz and feldspar, slight chlorite alteration
Chlorite	1%	Anhedral, fine grained, occurs as inclusions in k-feldspar and as biotite alteration
Magnetite	1%	Subhedral, <0.1-0.6mm, disseminated, concentrated with biotite, exsolution of ?
Epidote	1%	Subhedral, ~0.25mm, associated with biotite
Apatite	Trace	Anhedral, ~0.1mm, inclusions in feldspar
Allanite	Trace	Euhedral, ~0.25mm, rimmed by epidote, zoned, orangey-brown
Zircon	Trace	0.02 mm long; inclusion in quartz, K-feldspar

Sample: 19GJ12-1

Intrusive suite: Mesilinka

Rock Name: Biotite tonalite

Hand sample description: White weathering, grey fresh, medium-grained, equigranular biotite-rich tonalite, with foliation defined by biotite.

Outcrop description: 5 m wide outcrop, with equigranular granite outcrop in proximity (~30-50 m), associated with pegmatitic dykes cutting tonalite.

Textures: Fine- to medium-grained, equigranular, with interstitial mafic minerals to plagioclase and quartz.

Alteration: Sericitic alteration of feldspar, associated with biotite and epidote.

Mineralization: N/A

Normalized to QAP:

Quartz: 40

Alkali feldspar: 0

Plagioclase: 60

Mineral Name	Abundance	Description
Plagioclase	48%	Subhedral, 0.75-2mm, average 1 mm grains. Twinned, generally weak sericite alteration (~5%), more strongly altered near zones of epidote and biotite. Some grains have zonation.
Biotite	13%	Anhedral to subhedral, "shreddy" 0.25-2mm, average 1 mm. Green to yellow pleochroism, preferentially aligned to foliation, minor alteration to chlorite on rims.
Quartz	32%	Anhedral, 0.25-2mm, average 0.5 mm. Fine grained domains with strained edges, undulose extinction.
Amphibole	2%	Subhedral, 0.5-1mm, spatially associated with biotite (alteration?).
Epidote	5%	Anhedral, ~0.5mm wide. Spatially associated with biotite along feldspar grain boundaries (alteration?).
Titanite	1%	Subhedral to anhedral, 0.2-0.4mm wide. Interstitial to feldspar and quartz. Spatially associated with biotite, epidote, and apatite, defining foliation. Inclusions of apatite and possibly zircon.
Apatite	Trace	Euhedral, ~0.05 mm wide. Spatially associated with zones of biotite and epidote, more altered and foliared areas. Occurs as inclusions in biotite.
Zircon	Trace	Euhedral, ~100 µm long and ~20 µm wide. Occurs as inclusions in biotite, quartz, and titanite.
Chlorite	Trace	Minor, fine-grained, some freestanding, some as alteration of biotite.
Magnetite	Trace	Minor, subhedral, fine-grained inclusions in plagioclase.

Sample: 19GJ12-2

Intrusive suite: Mesilinka

Rock Name: Biotite tonalite

Hand sample description: White weathering, grey fresh, fine-grained equigranular biotite-rich tonalite.

Outcrop description: Large exposure of tonalite (~50 m), in contact with equigranular granite and cut by pegmatite dykes. Xenoliths of extremely foliated diorite are present within the tonalite, but the tonalite is not foliated.

Textures: Fine-grained, equigranular, myrmekitic

Alteration: Chlorite, sericitization

Mineralization: N/A

Normalized to QAP:

Quartz: 40

Alkali feldspar: 0

Plagioclase: 60

Mineral Name	Abundance	Description
Plagioclase	48%	Subhedral, <3 mm, average ~0.5mm wide. Polysynthetic twinning, zonation, minor clay alteration in grain mid sections and along boundaries.
Quartz	33%	Anhedral, 0.1-0.2mm. Occasionally forms myrmekitic intergrowths with plagioclase. Fine-grained domains with strained edges, undulose extinction.
Biotite	16%	Euhedral, fine-grained, up to 0.5mm, average ~0.15mm. Bimodal in grain size. Coarser grain size has chlorite alteration.
Amphibole	2%	Subhedral, ~0.25mm wide. Twinned grains. Associated with biotite and epidote.
Apatite	Trace	Euhedral, ~0.04 mm wide, inclusions in feldspar, quartz, and biotite.
Epidote	1%	Anhedral, Associated with biotite. May have rare allanite cores
Magnetite	trace	Minor, fine-grained, subhedral, inclusions in plagioclase and biotite
Titanite	Trace	Anhedral, average ~0.25mm, accessory trace mineral. Spatially associated with biotite, amphibole and apatite, interstitial to plagioclase and quartz.

Sample: 19GJ16-2

Intrusive suite: Mesilinka

Rock Name: Granite

Hand sample description: Brown-weathering, whitish-pink and black, foliated, biotite-bearing equigranular granite.

Outcrop description: Very well-exposed (>500 m wide area), relatively fresh exposure of granite.

Textures: myrmekitic

Alteration: Minor chlorite, epidote

Mineralization: Very minor bornite, chalcopyrite

Normalized to QAP:

Quartz: 23

Alkali feldspar: 42

Plagioclase: 34

Mineral Name	Abundance	Description
Alkali feldspar	40%	Anhedral, 0.25-0.6mm, clay altered, "dirty" grain interiors, some microcline tartan twinned grains
Plagioclase	32%	Subhedral, 0.6-1mm, occasional myrmekitic texture, some grains have zoning
Quartz	22%	Anhedral, 0.8-2mm, Strained, undulose extinction
Biotite	3%	Anhedral, 0.2-0.5mm, Brown, inclusions of magnetite
Magnetite	1%	Subhedral, very fine grained, up to 0.5mm, mostly associated with biotite, Fe-Ti oxide exsolution
Apatite	1%	Euhedral, <0.05mm, inclusions in biotite
Chlorite	1%	0.4-0.6mm, alteration of biotite, associated with magnetite and epidote
Epidote	Trace	Anhedral, 0.2mm, associated with biotite
Allanite	Trace	Euhedral to subhedral, ~0.5mm long, orangey-brown grains, zoned, rimmed by epidote, associated with biotite
Titanite	Trace	Anhedral, ~0.5 mm, associated with biotite, magnetite
Muscovite	Trace	Fine grained, rare, associated with biotite
Zircon	Trace	Euhedral, very fine grained (~50-60 µm long), inclusion in biotite, quartz, feldspar
Chalcopyrite	Trace	Rare, very fine grained inclusion in magnetite, with bornite
Bornite	Trace	Rare, very fine grained inclusion in magnetite, with chalcopyrite

Appendix B. Whole rock Geochemistry

Appendix B1. 2018 whole rock geochemistry analysis reference material results

Table B1.1. Major oxide accuracy results of bulk rock reference materials analyzed in 2018.

	Analyte	SiO_2	Al_2O_3	$Fe_2O_3(T)$	MnO	MgO	CaO	Na_2O	K_2O	TiO_2	P_2O_5
		%	%	%	%	%	%	%	%	%	%
	Detection Limit	0.01	0.01	0.01	0.001	0.01	0.01	0.01	0.01	0.001	0.01
Year	Measurement										
2018	NIST 694 Meas	11.34	1.87	0.76	0.017	0.34	42.75	0.85	0.52	0.120	30.20
	NIST 694 Cert	11.20	1.80	0.79	0.012	0.33	43.60	0.86	0.51	0.110	30.20
	Percent Error	1.25	3.89	3.80	46.552	3.03	1.95	1.16	1.96	9.091	0.00
2018	DNC-1 Meas	47.36	18.12	9.76	0.147	10.11	11.53	1.83	0.21	0.487	0.07
	DNC-1 Cert	47.15	18.34	9.97	0.150	10.13	11.49	1.89	0.23	0.480	0.07
	Percent Error	0.45	1.20	2.11	2.000	0.20	0.35	3.17	10.26	1.458	0.00
2018	W-2a Meas	52.12	14.88	10.53	0.161	6.27	10.95	2.10	0.59	1.064	0.11
	W-2a Cert	52.40	15.40	10.70	0.163	6.37	10.90	2.14	0.63	1.060	0.14
	Percent Error	0.53	3.38	1.59	1.227	1.57	0.46	1.87	5.75	0.377	21.43
2018	SY-4 Meas	50.85	21.46	6.36	0.109	0.50	8.07	7.29	1.77	0.303	0.14
	SY-4 Cert	49.90	20.69	6.21	0.108	0.54	8.05	7.10	1.66	0.287	0.13
	Percent Error	1.90	3.72	2.42	0.926	7.41	0.25	2.68	6.63	5.575	6.87
2018	BIR-1a Meas	48.89	15.59	11.16	0.174	9.61	13.62	1.79	0.02	0.988	0.03
	BIR-1a Cert	47.96	15.50	11.30	0.175	9.70	13.30	1.82	0.03	0.960	0.02
	Percent Error	1.94	0.58	1.24	0.571	0.93	2.41	1.65	33.33	2.917	42.86
2018	Method Blank	< 0.01	< 0.01	< 0.01	0.001	< 0.01	< 0.01	< 0.01	< 0.01	< 0.001	< 0.01
2018	Method Blank	< 0.01	< 0.01	< 0.01	0.001	< 0.01	< 0.01	< 0.01	< 0.01	< 0.001	< 0.01
2018	Method Blank	< 0.01	< 0.01	< 0.01	0.001	< 0.01	< 0.01	< 0.01	< 0.01	0.001	< 0.01
2018	Method Blank	< 0.01	< 0.01	< 0.01	0.001	< 0.01	0.01	< 0.01	< 0.01	< 0.001	< 0.01

Table B1.2. Major oxide precision results of bulk rock reference materials analyzed in 2018.

	Analyte	SiO_2	Al_2O_3	$Fe_2O_3(T)$	MnO	MgO	CaO	Na_2O	K_2O	TiO_2	P_2O_5
		%	%	%	%	%	%	%	%	%	%
	Detection Limit	0.01	0.01	0.01	0.001	0.01	0.01	0.01	0.01	0.001	0.01
Year	Measurement										
2018	**18ab50 Orig**	53.08	15.05	12.40	0.219	5.98	1.42	2.43	1.22	1.839	0.35
	18ab50 Dup	53.40	15.03	11.93	0.216	5.96	1.40	2.43	1.21	1.824	0.33
	RSD	0.43	0.09	2.73	0.975	0.24	1.00	0.00	0.58	0.579	4.16
2018	**18bg20-3-2 Orig**	50.31	19.00	9.22	0.181	3.84	9.42	3.95	1.31	0.838	0.49
	18bg20-3-2 Dup	49.92	19.20	9.28	0.182	3.87	9.48	3.92	1.32	0.834	0.48
	RSD	0.55	0.74	0.46	0.390	0.55	0.45	0.54	0.54	0.338	1.46
2018	**18lo12-1 Orig**	68.11	15.93	3.41	0.087	0.86	2.61	4.36	2.94	0.401	0.22
	18lo12-1 Dup	69.53	15.67	3.34	0.084	0.85	2.64	4.42	2.72	0.387	0.22
	RSD	1.46	1.16	1.47	2.481	0.83	0.81	0.97	5.50	2.513	0.00
2018	**18lo22-5 Orig**	44.47	10.53	14.00	0.193	12.10	11.28	1.38	1.73	1.800	0.81
	18lo22-5 Dup	45.04	10.24	13.90	0.190	11.98	11.41	1.39	1.73	1.764	0.78
	RSD	0.90	1.97	0.51	1.108	0.70	0.81	0.51	0.00	1.428	2.67
2018	**18ab7-3a? Orig**	66.94	18.79	3.17	0.143	0.36	1.35	0.64	5.84	0.114	0.02
	18ab7-3a? Dup	66.72	19.72	3.26	0.146	0.36	1.35	0.63	5.78	0.116	0.01
	RSD	0.23	3.42	1.98	1.468	0.00	0.00	1.11	0.73	1.230	47.14

Table B1.3. Trace element accuracy results of bulk rock reference materials analyzed in 2018.

	Analyte	Sc ppm	Be ppm	V ppm	Cr ppm	Co ppm	Ni ppm	Cu ppm	Zn ppm	Ga ppm	Ge ppm	As ppm	Rb ppm	Sr ppm
	Detection Limit	1	1	5	20	1	20	10	30	1	0.5	5	1	2
Year	Measurement													
2018	NIST 694 Meas			1588										
	NIST 694 Cert			1740										
	Percent Error	-	-	8.74	-	-	-	-	-	-	-			
2018	DNC-1 Meas	31		146	300	55	250	100	70	14	-		4	134
	DNC-1 Cert	31		148	270	57	247	100	70	15			5	144
	Percent Error	0.0		1.4	11.1	3.5	1.2	0.0	0.0	6.7			20.0	6.9
2018	LKSD-3 Meas				80	29	50	30	160			30	75	
	LKSD-3 Cert				87	30	47	35	152			27	78	
	Percent Error				8.0	3.3	6.4	14.3	5.3			11.1	3.8	
2018	TDB-1 Meas				250		90	320	150					
	TDB-1 Cert				251		92	323	155					
	Percent Error				0.4		2.2	0.9	3.2					
2018	W-2a Meas	35	<1	257	90	43	70	110	80	18	1.5		19	184
	W-2a Cert	36	1.3	262	92	43	70	110	80	17	1.0		21	190
	Percent Error	2.8	N/A	1.9	2.2	0.0	0.0	0.0	0.0	5.9	50.0		9.5	3.2
2018	SY-4 Meas	<1	3	3										1254
	SY-4 Cert	1.1	2.6	8										1191
	Percent Error	N/A	15.4	N/A										5.3
2018	CTA-AC-1 Meas							50	40					
	CTA-AC-1 Cert							54	38					
	Percent Error							7.4	5.3					
2018	BIR-1a Meas	44	<1	321	380		170	120	70	15		2.5		105
	BIR-1a Cert	44	0.58	310	370		170	125	70	16		0.44		110

	Percent Error	0.0	N/A	3.5	2.7		0.0	4.0	0.0	6.3		N/A		4.5
2018	**NCS DC86312 Meas**													
	NCS DC86312 Cert													
	Percent Error													
2018	**NCS DC70009 (GBW07241) Meas**					3	10	1050	90	16	10.3	67	507	
	NCS DC70009 (GBW07241) Cert					3.7	2.8	960	100	16.5	11.2	69.9	500	
	Percent Error					18.9	N/A	9.4	10.0	3.0	8.0	4.1	1.4	
2018	**OREAS 100a (Fusion) Meas**					17		160						
	OREAS 100a (Fusion) Cert					18.1		169						
	Percent Error					6.1		5.3						
2018	**OREAS 101a (Fusion) Meas**					47		430						
	OREAS 101a (Fusion) Cert					49		430						
	Percent Error					3.7		0.0						
2018	**OREAS 101b (Fusion) Meas**					45	10	410						
	OREAS 101b (Fusion) Cert					47	9	420						
	Percent Error					4.3	N/A	2.4						
2018	**JR-1 Meas**					1	10			15	2.1	15	260	
	JR-1 Cert					0.83	1.67			16.1	1.88	16.3	257	
	Percent Error					20.5	N/A			6.8	11.7	8.0	1.2	
2018	**Method Blank**	< 1	< 1	< 5	< 20	< 1	< 20	< 10	< 30	< 1	< 0.5	< 5	< 1	< 2
2018	**Method Blank**	< 1	< 1	< 5										< 2
2018	**Method Blank**	< 1	< 1	< 5										< 2
2018	**Method Blank**	< 1	< 1	< 5										< 2

Table B1.3. continued.

	Analyte	Y ppm	Zr ppm	Nb ppm	Mo ppm	Ag ppm	In ppm	Sn ppm	Sb ppm	Cs ppm	Ba ppm	La ppm	Ce ppm	Pr ppm
	Detection Limit	**0.5**	**1**	**0.2**	**2**	**0.5**	**0.1**	**1**	**0.2**	**0.1**	**2**	**0.05**	**0.05**	**0.01**
Year	**Measurement**													
2018	**NIST 694 Meas**													1588
	NIST 694 Cert													1740
	Percent Error											-	-	8.74
2018	**DNC-1 Meas**	18.8	32						1		106	3.9		
	DNC-1 Cert	18	38						0.96		118	3.6		
	Percent Error	4.4	15.8						4.2		10.2	8.3		
2018	**LKSD-3 Meas**	28.9			< 2	2.8				2.3		47.3	89.7	
	LKSD-3 Cert	30			2	2.7				2.3		52	90	
	Percent Error	3.7			N/A	3.7				0.0		9.0	0.3	
2018	**TDB-1 Meas**	32.6										16.1	37.8	
	TDB-1 Cert	36										17	41	
	Percent Error	9.4										5.3	7.8	
2018	**W-2a Meas**	25	78	7.5	1				0.9		170	10.7	22.9	
	W-2a Cert	24	94	7.9	0.6				0.79		182	10	23	
	Percent Error	4.2	17.0	5.1	N/A				13.9		6.6	7.0	0.4	
2018	**SY-4 Meas**		535								368	1	3	3
	SY-4 Cert		517								340	1.1	2.6	8
	Percent Error		3.5								8.2	N/A	15.4	N/A
2018	**CTA-AC-1 Meas**	268										>2000	>3000	
	CTA-AC-1 Cert	272										2176	3326	
	Percent Error	1.5										N/A	N/A	
2018	**BIR-1a Meas**	15.8	13								12		1.8	
	BIR-1a Cert	16	18								6		1.9	

	Percent Error	1.3	27.8							100.0		5.3		
2018	**NCS DC86312 Meas**	955									>2000	172		
	NCS DC86312 Cert	976									2360	190		
	Percent Error	2.2									N/A	9.5		
2018	**NCS DC70009 (GBW07241) Meas**	129			1.4	1	>1000	3	41		24	61	8.1	
	NCS DC70009 (GBW07241) Cert	128			1.8	1.3	1700	3.1	41		23.7	60.3	7.9	
	Percent Error	0.8			22.2	23.1	N/A	3.2	0.0		1.3	1.2	2.5	
2018	**OREAS 100a (Fusion) Meas**	131		25							270	493	47.8	
	OREAS 100a (Fusion) Cert	142		24.1							260	463	47.1	
	Percent Error	7.7		3.7							3.8	6.5	1.5	
2018	**OREAS 101a (Fusion) Meas**	175		23							828	1400	132	
	OREAS 101a (Fusion) Cert	183		21.9							816	1396	134	
	Percent Error	4.4		5.0							1.5	0.3	1.5	
2018	**OREAS 101b (Fusion) Meas**	171		20							801	1410	123	
	OREAS 101b (Fusion) Cert	178		21							789	1331	127	
	Percent Error	3.9		4.8							1.5	5.9	3.1	
2018	**JR-1 Meas**	42.4		16.2			0.05	3	1.2	20.3		19.9	48.2	5.4
	JR-1 Cert	45.1		15.2			0.028	2.86	1.19	20.8		19.7	47.2	5.58
	Percent Error	6.0		6.6			N/A	4.9	0.8	2.4		1.0	2.1	3.2
2018	**Method Blank**	< 0.5	1	< 0.2	< 2	< 0.5	< 0.1	< 1	< 0.2	< 0.1	< 2	< 0.05	< 0.05	< 0.01
2018	**Method Blank**		< 1								< 2			
2018	**Method Blank**		< 1								< 2			
2018	**Method Blank**		< 1								< 2			

Table B1.3. continued.

	Analyte	Nd	Sm	Eu	Gd	Tb	Dy	Ho	Er	Tm	Yb
		ppm	ppm	ppm	ppm	ppm	ppm	ppm	ppm	ppm	ppm
	Detection Limit	0.05	0.01	0.005	0.01	0.01	0.01	0.01	0.01	0.005	0.01
Year	Measurement										
2018	NIST 694 Meas										
	NIST 694 Cert										
	Percent Error	-	-	-	-	-	-	-			
2018	DNC-1 Meas	5.6		0.62				-			2.1
	DNC-1 Cert	5.2		0.59							2
	Percent Error	7.7		5.1							5.0
2018	LKSD-3 Meas	45.9	8.7	1.5			5.2				3
	LKSD-3 Cert	44	8	1.5			4.9				2.7
	Percent Error	4.3	8.7	0.0			6.1				11.1
2018	TDB-1 Meas	24.3		2.1							3.3
	TDB-1 Cert	23		2.1							3.4
	Percent Error	5.7		0.0							2.9
2018	W-2a Meas	13.3	3.4	1.1		0.6	3.8	0.78			2.1
	W-2a Cert	13	3.3	1		0.63	3.6	0.76			2.1
	Percent Error	2.3	3.0	10.0		4.8	5.6	2.6			0.0
2018	SY-4 Meas										1254
	SY-4 Cert										1191
	Percent Error										5.3
2018	CTA-AC-1 Meas	1130	161	43.1	116						10.6
	CTA-AC-1 Cert	1087	162	46.7	124						11.4
	Percent Error	4.0	0.6	7.7	6.5						7.0
2018	BIR-1a Meas	2.3			2						1.8
	BIR-1a Cert	2.5			2						1.7

	Percent Error	8.0			0.0						5.9
2018	**NCS DC86312 Meas**	1580			234		189	35.8	101	13.9	89.7
	NCS DC86312 Cert	1600			225		183	36	96.2	15.1	87.79
	Percent Error	1.3			4.0		3.3	0.6	5.0	7.9	2.2
2018	**NCS DC70009 (GBW07241) Meas**	34	13		16	3.6	22	5	14	2	
	NCS DC70009 (GBW07241) Cert	32.9	12.5		14.8	3	20.7	4.5	13.4	2.2	
	Percent Error	3.3	4.0		8.1	9.1	6.3	11.1	4.5	9.1	
2018	**OREAS 100a (Fusion) Meas**	165	25.9	3.73	22.7	3.64	25.4	4.75	14.9	2.29	15.2
	OREAS 100a (Fusion) Cert	152	23.6	3.71	23.6	3.8	23.2	4.81	14.9	2.31	14.9
	Percent Error	8.6	9.7	0.5	3.8	4.2	9.5	1.2	0.0	0.9	2.0
2018	**OREAS 101a (Fusion) Meas**	404	49.9	8.22	40.3		33.9	6.85	20.6	3	18
	OREAS 101a (Fusion) Cert	403	48.8	8.06	43.4		33.3	6.46	19.5	2.9	17.5
	Percent Error	0.2	2.3	2.0	7.1		1.8	6.0	5.6	3.4	2.9
2018	**OREAS 101b (Fusion) Meas**	387	50	8		5	31	6.3	19.2	2.79	18.4
	OREAS 101b (Fusion) Cert	378	48	8		5	32	6.3	18.7	2.66	17.6
	Percent Error	2.4	4.2	4.0		7.3	2.5	0.3	2.7	4.9	4.5
2018	**JR-1 Meas**	25	6.59	0.31		0.92	5.66		3.79	0.68	4.78
	JR-1 Cert	23.3	6.03	0.3		1.01	5.69		3.61	0.67	4.55
	Percent Error	7.3	9.3	3.3		8.9	0.5		5.0	1.5	5.1
2018	**Method Blank**	< 0.05	< 0.01	< 0.005	< 0.01	< 0.01	< 0.01	< 0.01	< 0.01	< 0.005	< 0.01
2018	**Method Blank**										
2018	**Method Blank**										
2018	**Method Blank**										

Table B1.3. continued.

	Analyte	Lu	Hf	Ta	W	Tl	Pb	Bi	Th	U
		ppm	ppm	ppm	ppm	ppm	ppm	ppm	ppm	ppm
	Detection Limit	0.002	0.1	0.01	0.5	0.05	5	0.1	0.05	0.01
Year	Measurement									
2018	NIST 694 Meas									
	NIST 694 Cert									
	Percent Error									
2018	DNC-1 Meas						6			
	DNC-1 Cert						6.3			
	Percent Error						4.8			
2018	LKSD-3 Meas		4.5	0.8					11	4.5
	LKSD-3 Cert		4.8	0.7					11.4	4.6
	Percent Error		6.3	14.3					3.5	
2018	TDB-1 Meas								2.6	
	TDB-1 Cert								2.7	
	Percent Error								3.7	
2018	W-2a Meas	0.32		0.47	<0.5	0.06	10	<0.1		0.52
	W-2a Cert	0.33		0.5	0.3	0.2	9.3	0.03		0.53
	Percent Error	3.0		6.0	N/A	70.0	7.5	N/A		
2018	SY-4 Meas									
	SY-4 Cert									
	Percent Error									
2018	CTA-AC-1 Meas	1.06	1.2	2.41					21.3	4.1
	CTA-AC-1 Cert	1.08	1.13	2.65					21.8	4.4
	Percent Error	1.9	6.2	9.1					2.3	
2018	BIR-1a Meas		0.5				<5			
	BIR-1a Cert		0.6				3			

	Percent Error		16.7				N/A			
2018	**NCS DC86312 Meas**	12.5							24.9	
	NCS DC86312 Cert	11.96							23.6	
	Percent Error	4.5							5.5	
2018	**NCS DC70009 (GBW07241) Meas**	2			2410	1.93				
	NCS DC70009 (GBW07241) Cert	2.4			2200	1.8				
	Percent Error	16.7			9.5	7.2				
2018	**OREAS 100a (Fusion) Meas**	2.33							48.4	131
	OREAS 100a (Fusion) Cert	2.26							51.6	135
	Percent Error	3.1							6.2	
2018	**OREAS 101a (Fusion) Meas**	2.64							35.9	445
	OREAS 101a (Fusion) Cert	2.66							36.6	422
	Percent Error	0.8							1.9	5.5
2018	**OREAS 101b (Fusion) Meas**	2.67							35.8	415
	OREAS 101b (Fusion) Cert	2.58							37.1	396
	Percent Error	3.5							3.5	4.8
2018	**JR-1 Meas**		4.4	1.96	1.9		19	0.6	28.1	9.1
	JR-1 Cert		4.51	1.86	1.59		19.3	0.56	26.7	8.88
	Percent Error		2.4	5.4	19.5		1.6	7.1	5.2	2.5
2018	**Method Blank**	< 0.002	< 0.1	< 0.01	< 0.5	< 0.05	< 5	< 0.1	< 0.05	< 0.01
2018	**Method Blank**									
2018	**Method Blank**									
2018	**Method Blank**									

Table B1.4. Trace element precision results of whole rock reference materials analyzed in 2018.

	Analyte	Sc	Be	V	Cr	Co	Ni	Cu	Zn	Ga	Ge	As	Rb	Sr	Y	Zr
		ppm	ppm	ppm	ppm	ppm	ppm	ppm	ppm	ppm	ppm	ppm	ppm	ppm	ppm	ppm
	Detection Limit	1	1	5	20	1	20	10	30	1	0.5	5	1	2	0.5	1
Year	Measurement															
2018	**18ab50 Orig**	33	1	209	400	55	250	170	390	18	1.2	68	38	105	26.9	118
	18ab50 Dup	32	1	208	400	55	260	180	380	19	1.5	71	38	106	28.3	112
	RSD	2.18	0.00	0.34	0.00	0.00	2.77	4.04	1.84	3.82	15.71	3.05	0.00	0.67	3.59	3.69
2018	**18bg20-3-2 Orig**	19	1	235	< 20	20	< 20	60	90	24	1.3	< 5	24	1302	19.7	32
	18bg20-3-2 Dup	19	1	235	< 20	20	< 20	60	90	23	0.9	< 5	24	1328	19.7	35
	RSD	0.00	0.00	0.00		0.00		0.00	0.00	3.01	25.71		0.00	1.40	0.00	6.33
2018	**18lo12-1 Orig**	4	2	38	< 20	3	< 20	< 10	60	20	1.1	< 5	82	936	18.1	169
	18lo12-1 Dup	4	2	37	< 20	3	30	< 10	60	19	1.3	< 5	79	877	17.2	163
	RSD	0.00	0.00	1.89		0.00			0.00	3.63	11.79		2.64	4.60	3.61	2.56
2018	**18lo22-5 Orig**	60	< 1	490	340	56	110	< 10	130	18	1.9	< 5	38	273	23.7	49
	18lo22-5 Dup	59	< 1	495	340	56	110	< 10	130	18	1.9	< 5	39	264	23.8	49
	RSD	1.19	#DIV/0!	0.72	0.00	0.00	0.00		0.00	0.00	0.00		1.84	2.37	0.30	0.00
2018	**18ab7-3a? Orig**	1	2	14	< 20	1	< 20	< 10	40	25	1.6	< 5	193	148	1.5	63
	18ab7-3a? Dup	1	3	14	< 20	1	< 20	< 10	40	25	1.9	< 5	197	151	1.6	61
	RSD	0.00	28.28	0.00		0.00			0.00	0.00	12.12		1.45	1.42	4.56	2.28

Table B1.4. continued.

	Analyte	Nb	Mo	Ag	In	Sn	Sb	Cs	Ba	La	Ce	Pr	Nd	Sm	Eu	Gd
		ppm	ppm	ppm	ppm	ppm	ppm	ppm	ppm	ppm	ppm	ppm	ppm	ppm	ppm	ppm
	Detection Limit	0.2	2	0.5	0.1	1	0.2	0.1	2	0.05	0.05	0.01	0.05	0.01	0.005	0.01
Year	Measurement															
2018	**18ab50 Orig**	20.9	< 2	1.6	0.1	1	14.1	1.7	974	26.5	51.4	6.36	26.3	5.99	1.78	5.76
	18ab50 Dup	20.3	< 2	1.9	0.1	2	14.4	1.7	972	26.5	50.8	6.38	26.3	6.09	1.89	5.68
	RSD	2.06		12.12	0.00	47.14	1.49	0.00	0.15	0.00	0.83	0.22	0.00	1.17	4.24	0.99
2018	**18bg20-3-2 Orig**	3.6	< 2	< 0.5	0.1	1	0.2	3.8	1106	15.7	33	4.31	18	4.4	1.41	4.05
	18bg20-3-2 Dup	3.4	< 2	< 0.5	< 0.1	1	0.2	3.7	1111	15.9	33.7	4.34	19.4	4.69	1.31	4.22
	RSD	4.04				0.00	0.00	1.89	0.32	0.90	1.48	0.49	5.29	4.51	5.20	2.91
2018	**18lo12-1 Orig**	34.8	< 2	0.7	< 0.1	1	< 0.2	3.2	2749	104	159	17.2	55.5	7.85	1.91	5.15
	18lo12-1 Dup	34.8	< 2	0.8	< 0.1	1	< 0.2	3.1	2549	104	158	17	53.5	7.42	1.87	5
	RSD	0.00		9.43		0.00		2.24	5.34	0.00	0.45	0.83	2.59	3.98	1.50	2.09
2018	**18lo22-5 Orig**	3.9	< 2	< 0.5	0.1	1	0.3	17.3	452	12.8	34.3	5.15	26.1	6.78	1.82	6.83
	18lo22-5 Dup	4	< 2	< 0.5	0.1	1	0.3	17.1	451	13.1	34	5.19	25.7	6.74	1.9	6.84
	RSD	1.79			0.00	0.00	0.00	0.82	0.16	1.64	0.62	0.55	1.09	0.42	3.04	0.10
2018	**18ab7-3a? Orig**	0.6	2	< 0.5	0.2	< 1	< 0.2	2.2	2822	1.9	3.13	0.33	1.1	0.22	0.059	0.17
	18ab7-3a? Dup	0.8	2	< 0.5	0.2	< 1	< 0.2	2.3	2801	2.12	3.43	0.38	1.27	0.24	0.058	0.17
	RSD	20.20	0.00		0.00			3.14	0.53	7.74	6.47	9.96	10.14	6.15	1.21	0.00

Table B1.4. continued.

	Analyte	Tb ppm	Dy ppm	Ho ppm	Er ppm	Tm ppm	Yb ppm	Lu ppm	Hf ppm	Ta ppm	W ppm	Tl ppm	Pb ppm	Bi ppm	Th ppm	U ppm
	Detection Limit	0.01	0.01	0.01	0.01	0.005	0.01	0.002	0.1	0.01	0.5	0.05	5	0.1	0.05	0.01
Year	Measurement															
2018	**18ab50 Orig**	0.87	5.02	0.94	2.63	0.362	2.18	0.333	2.7	1.38	1.8	0.18	226	0.2	5.63	1.29
	18ab50 Dup	0.92	5.28	1	2.74	0.376	2.33	0.347	2.7	1.58	2.1	0.25	231	0.3	5.59	1.31
	RSD	3.95	3.57	4.37	2.90	2.68	4.70	2.91	0.00	9.56	10.88	23.02	1.55	28.28	0.50	1.09
2018	**18bg20-3-2 Orig**	0.61	3.64	0.74	2.03	0.287	1.96	0.299	1.1	0.15	< 0.5	< 0.05	6	< 0.1	0.36	0.17
	18bg20-3-2 Dup	0.61	3.54	0.71	2.06	0.299	2.05	0.329	1.2	0.18	< 0.5	< 0.05	6	0.3	0.34	0.17
	RSD	0.00	1.97	2.93	1.04	2.90	3.17	6.76	6.15	12.86			0.00		4.04	0.00
2018	**18lo12-1 Orig**	0.67	3.44	0.62	1.88	0.257	1.71	0.281	3.9	1.94	< 0.5	0.39	15	0.1	21.2	3.31
	18lo12-1 Dup	0.66	3.4	0.67	1.72	0.268	1.74	0.247	3.7	1.94	< 0.5	0.37	15	< 0.1	21	3.23
	RSD	1.06	0.83	5.48	6.29	2.96	1.23	9.11	3.72	0.00		3.72	0.00		0.67	1.73
2018	**18lo22-5 Orig**	0.85	5.02	0.97	2.54	0.332	1.98	0.296	1.9	0.33	< 0.5	< 0.05	< 5	0.4	1.07	0.49
	18lo22-5 Dup	0.95	5.06	0.92	2.53	0.343	2.05	0.319	1.9	0.37	< 0.5	< 0.05	< 5	0.3	1.08	0.49
	RSD	7.86	0.56	3.74	0.28	2.30	2.46	5.29	0.00	8.08				20.20	0.66	0.00
2018	**18ab7-3a? Orig**	0.03	0.18	0.05	0.18	0.029	0.25	0.043	2.2	0.11	8	0.37	< 5	0.8	0.25	0.19
	18ab7-3a? Dup	0.03	0.18	0.05	0.18	0.029	0.23	0.039	2	0.08	8.5	0.45	< 5	1	0.24	0.2
	RSD	0.00	0.00	0.00	0.00	0.00	5.89	6.90	6.73	22.33	4.29	13.80		15.71	2.89	3.63

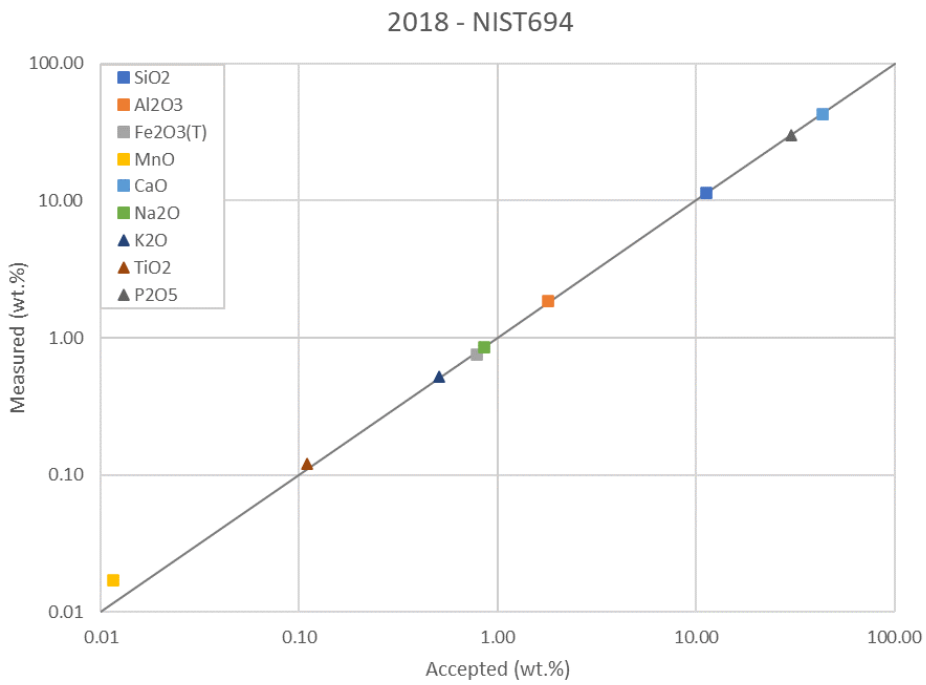

Figure B1.1. Measured major oxide results versus accepted values for reference material NIST694.

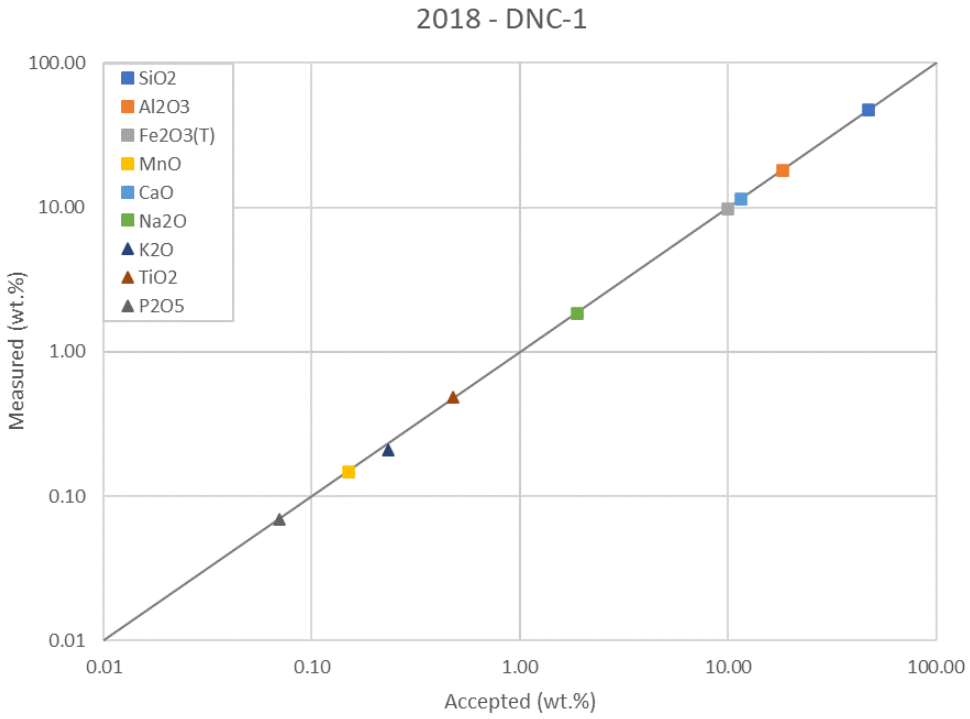

Figure B1.2. Measured major oxide results versus accepted values for reference material DNC-1.

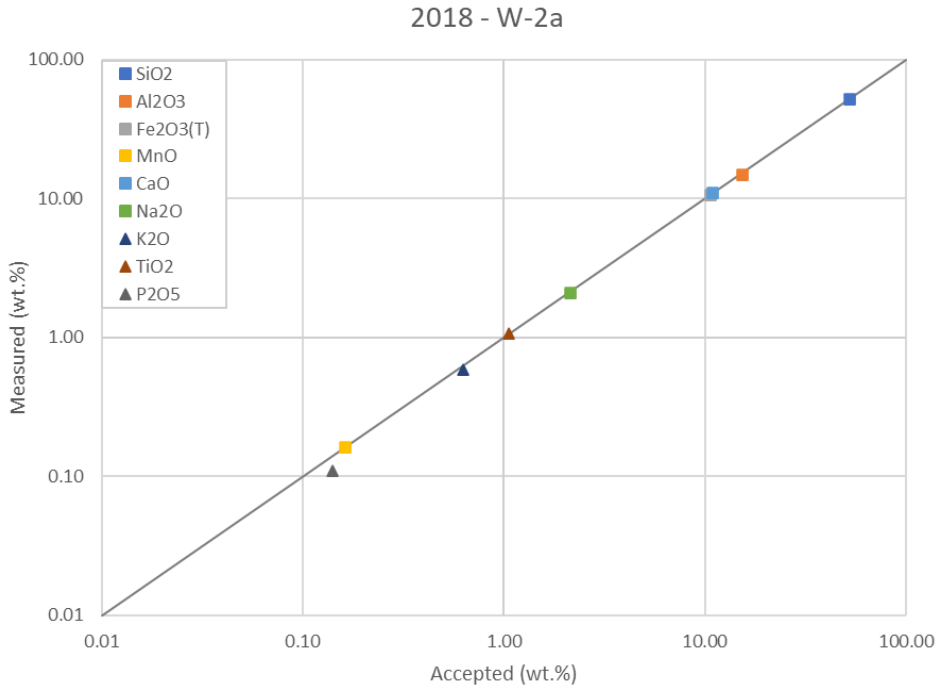

Figure B1.3. Measured major oxide results versus accepted values for reference material W-2a.

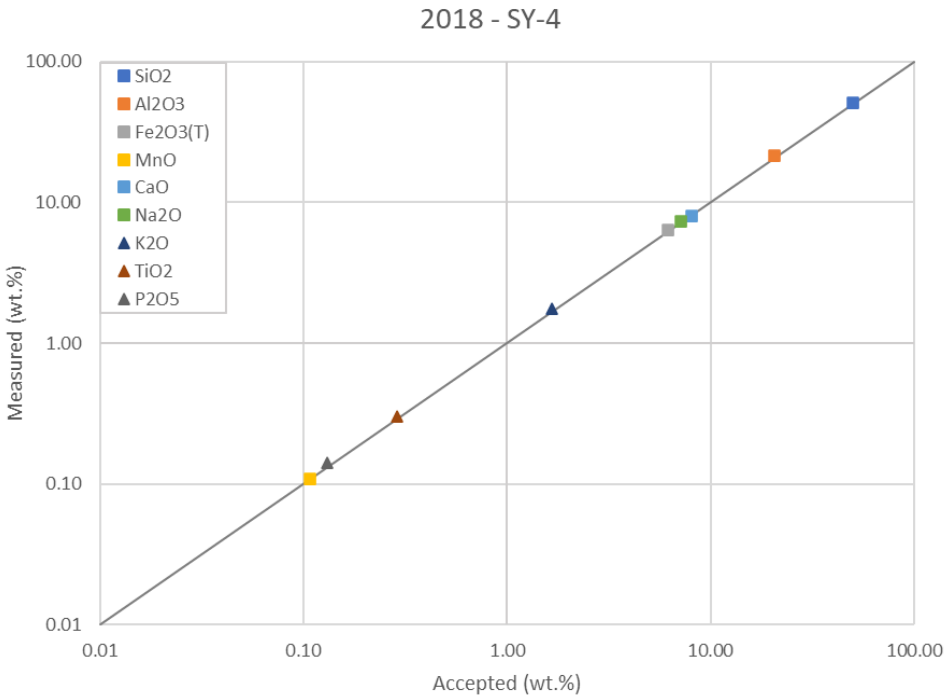

Figure B1.4. Measured major oxide results versus accepted values for reference material SY-4.

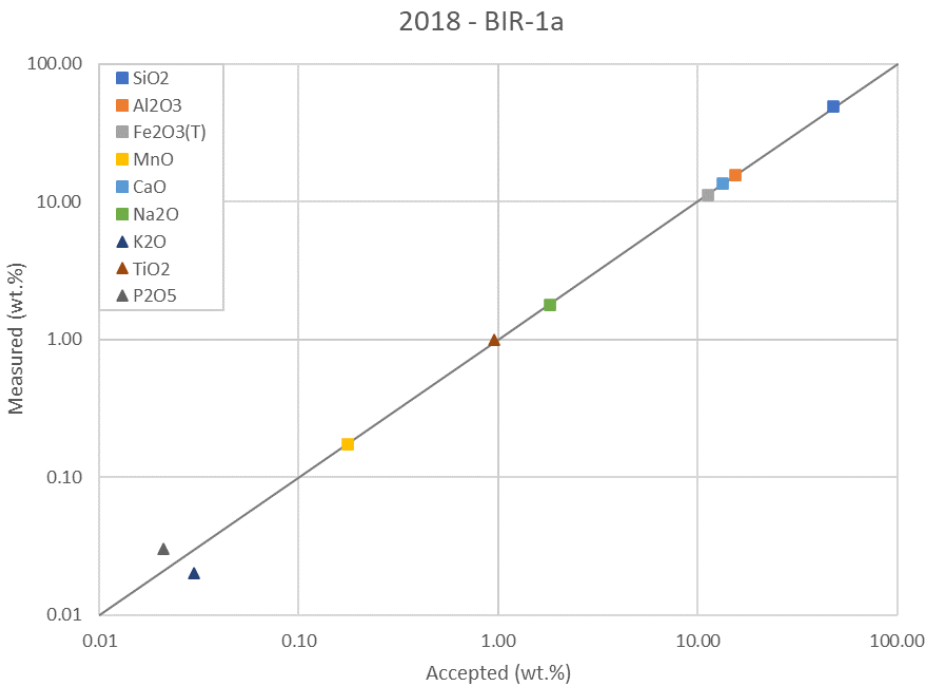

Figure B1.5. Measured major oxide results versus accepted values for reference material BIR-1a.

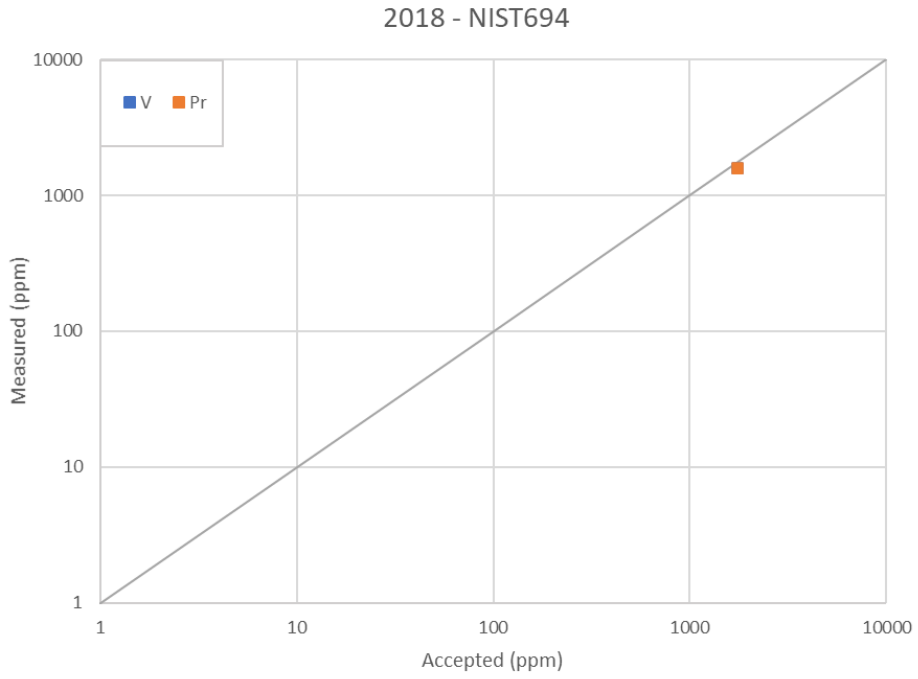

Figure B1.6. Measured trace element concentration results versus accepted values for reference material NIST694.

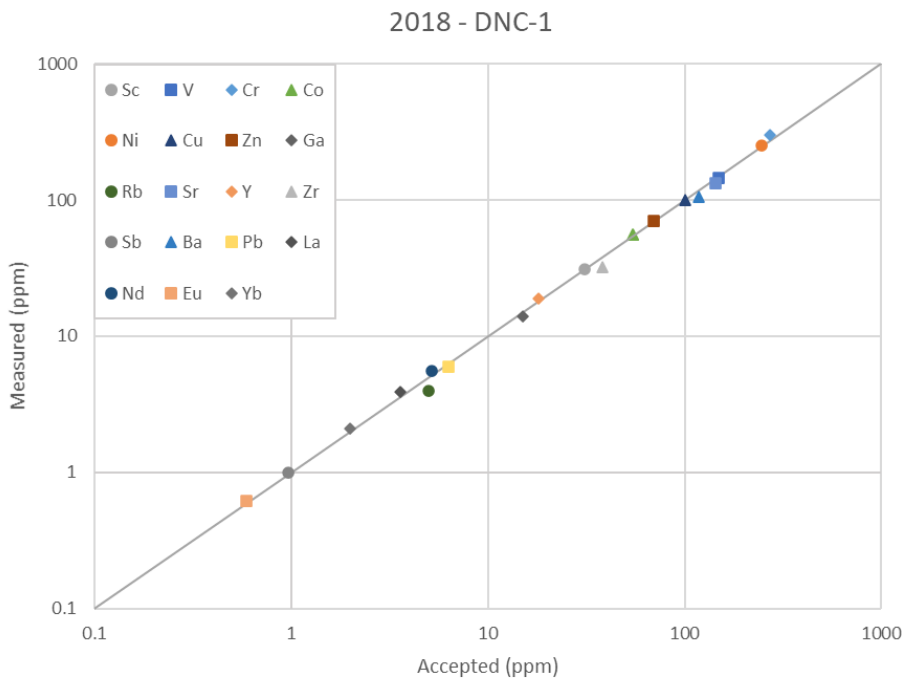

Figure B1.7. Measured trace element concentration results versus accepted values for reference material DNC-1.

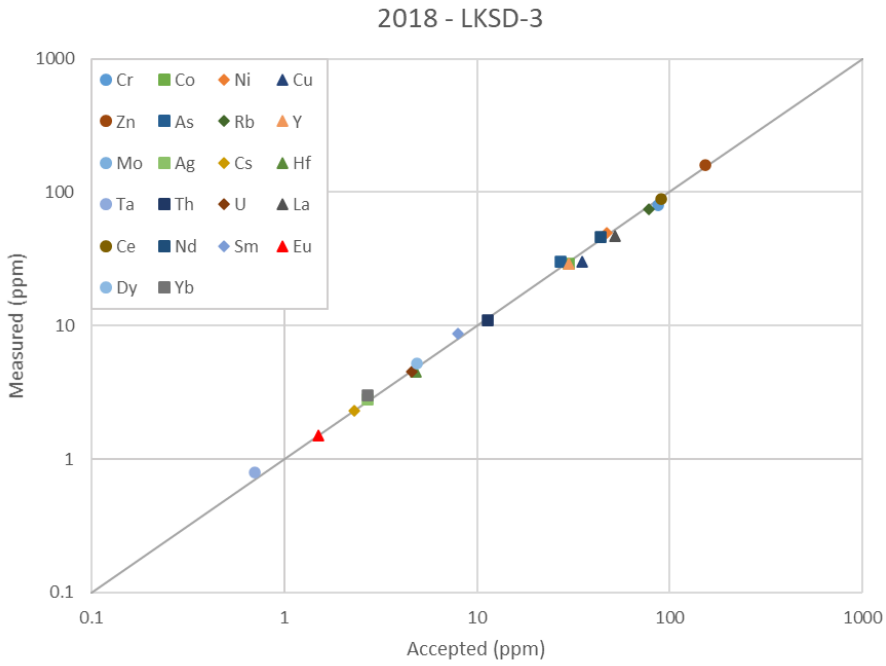

Figure B1.8. Measured trace element concentration results versus accepted values for reference material LKSD-3.

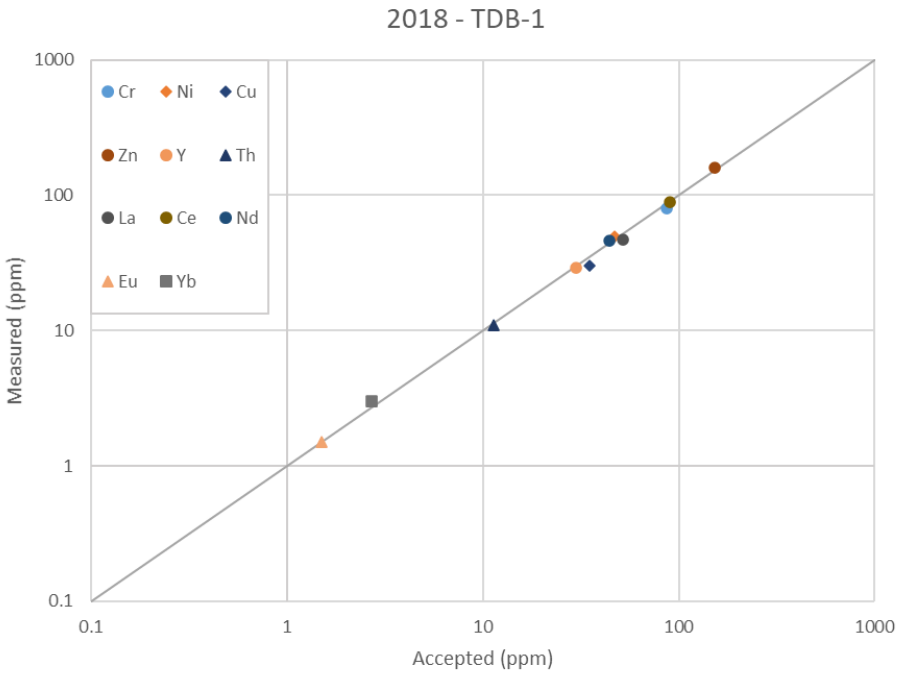

Figure B1.9. Measured trace element concentration results versus accepted values for reference material TDB-1.

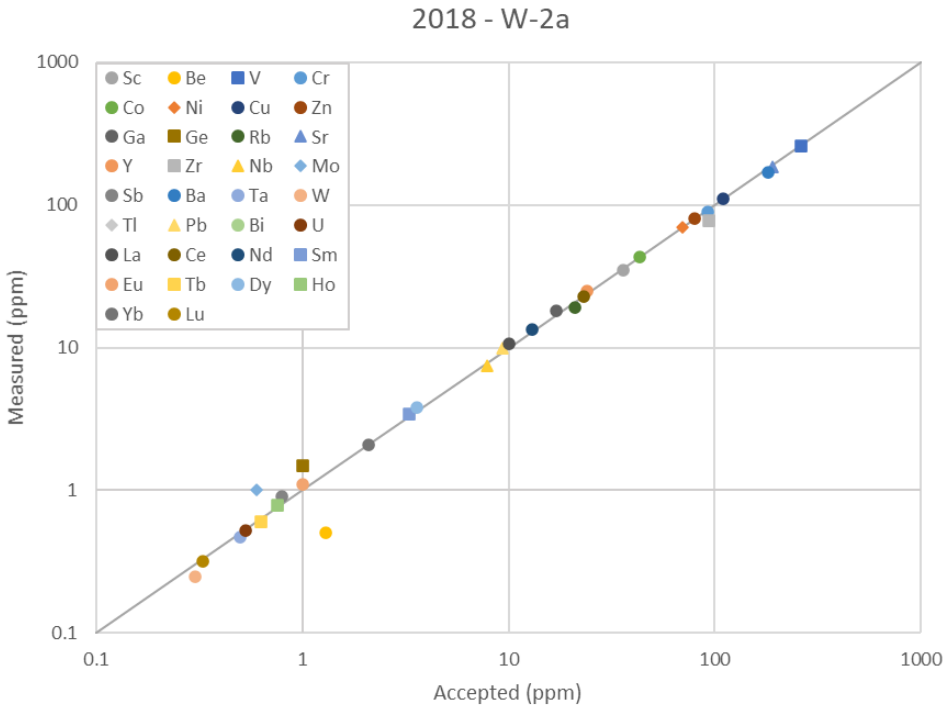

Figure B1.10. Measured trace element concentration results versus accepted values for reference material W-2a.

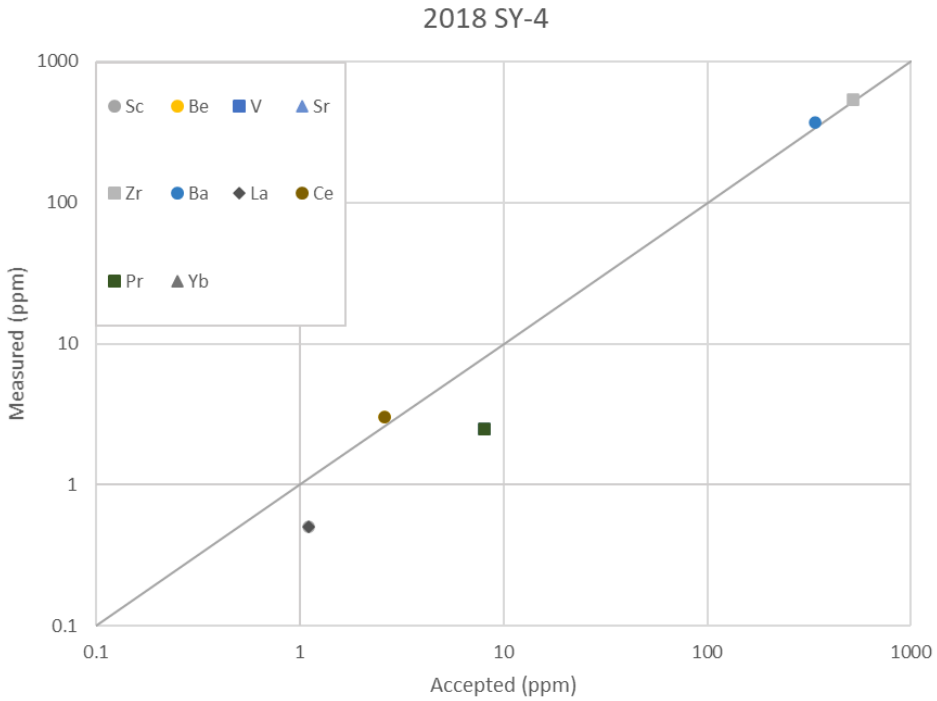

Figure B1.11. Measured trace element concentration results versus accepted values for reference material SY-4.

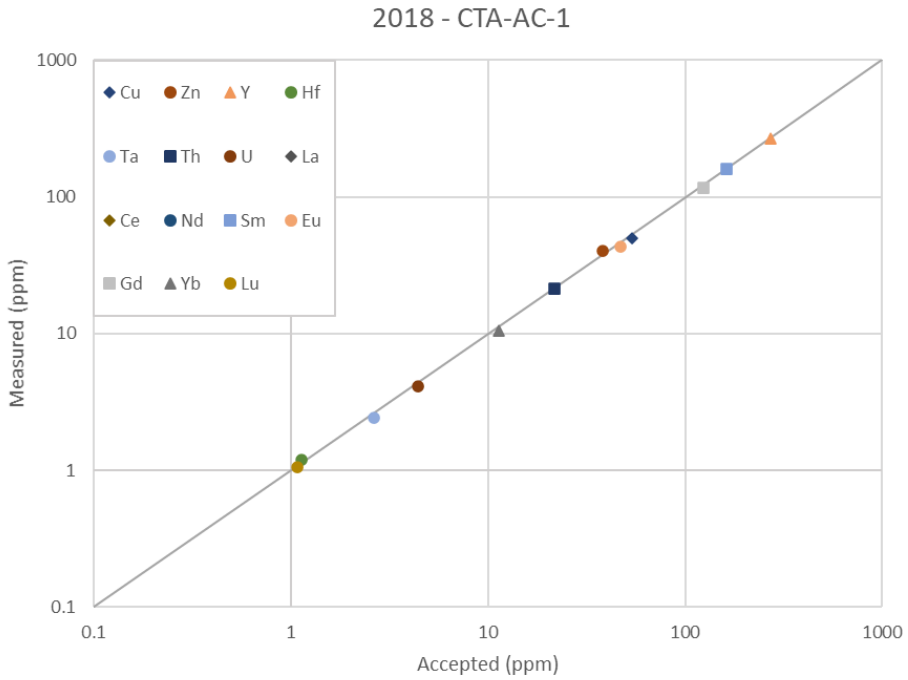

Figure B1.12. Measured trace element concentration results versus accepted values for reference material CTA-AC-1.

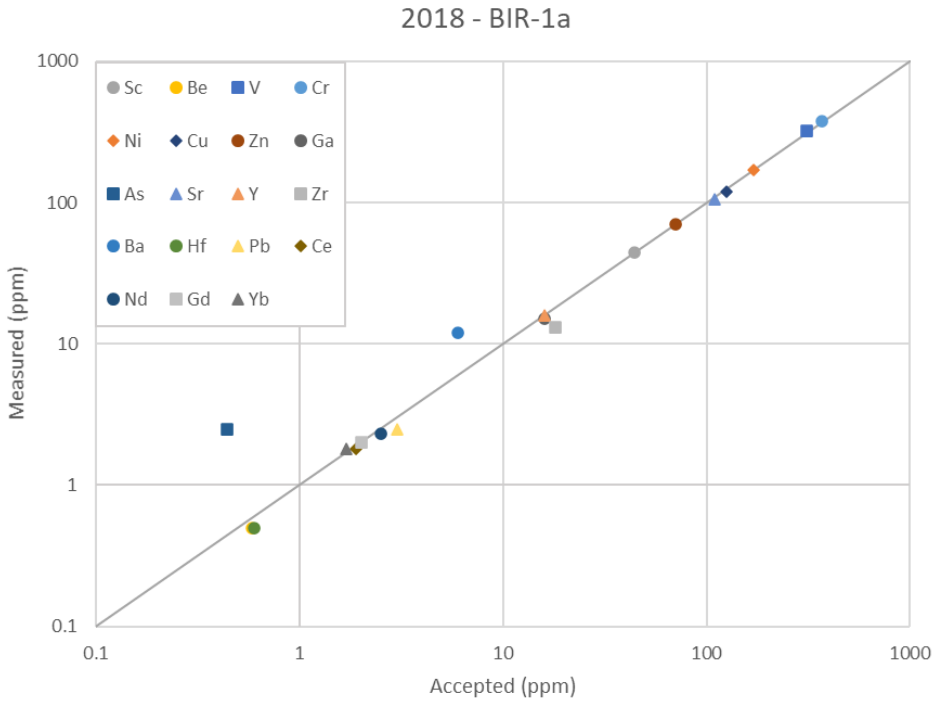

Figure B1.13. Measured trace element concentration results versus accepted values for reference material BIR-1a.

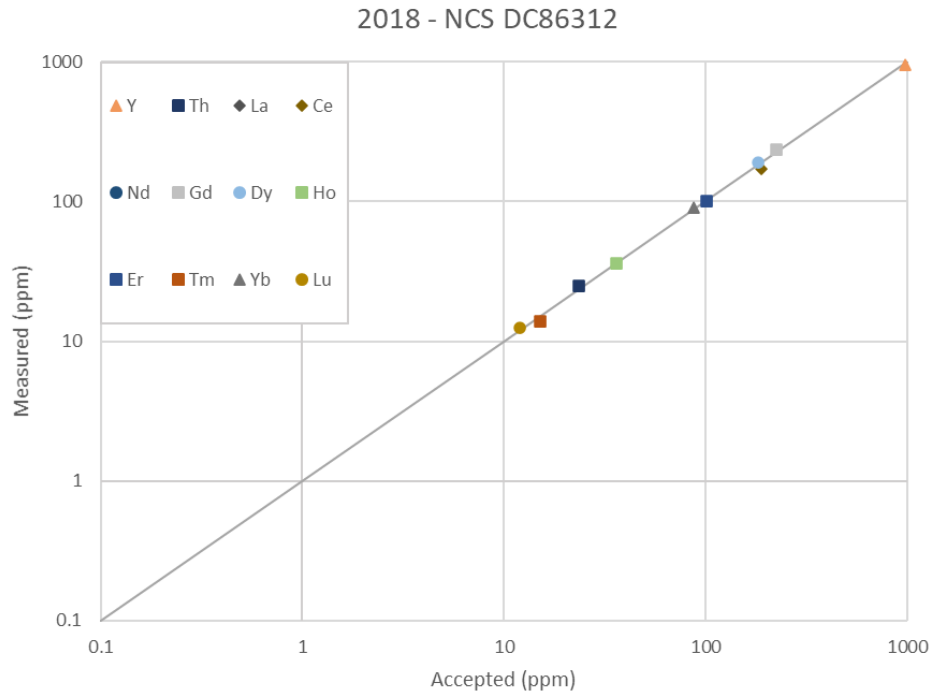

Figure B1.14. Measured trace element concentration results versus accepted values for reference material NCS DC86312.

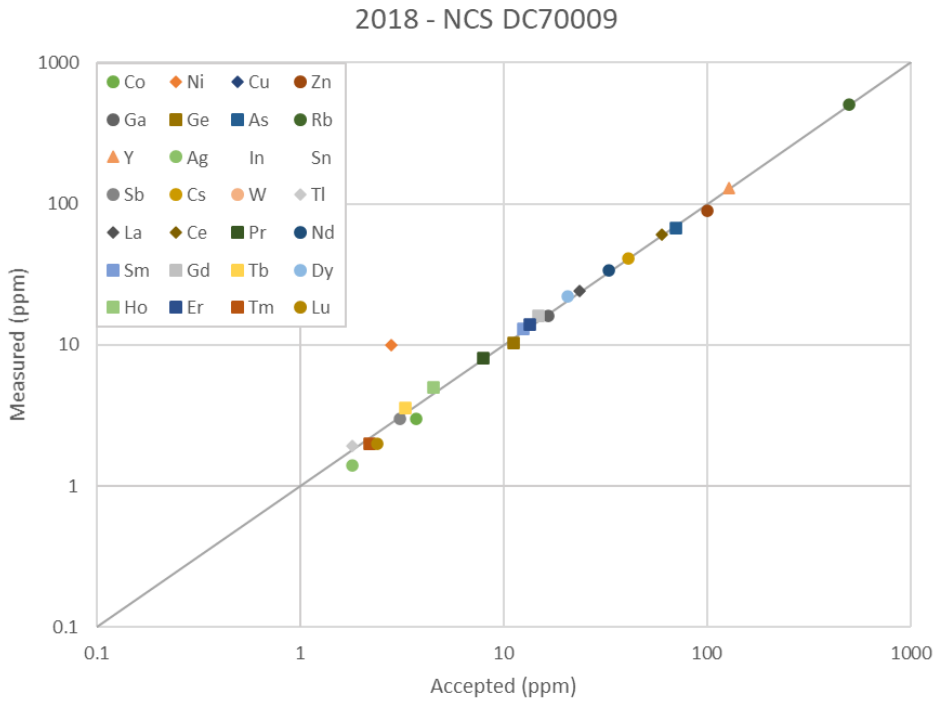

Figure B1.15. Measured trace element concentration results versus accepted values for reference material NCS DC70009.

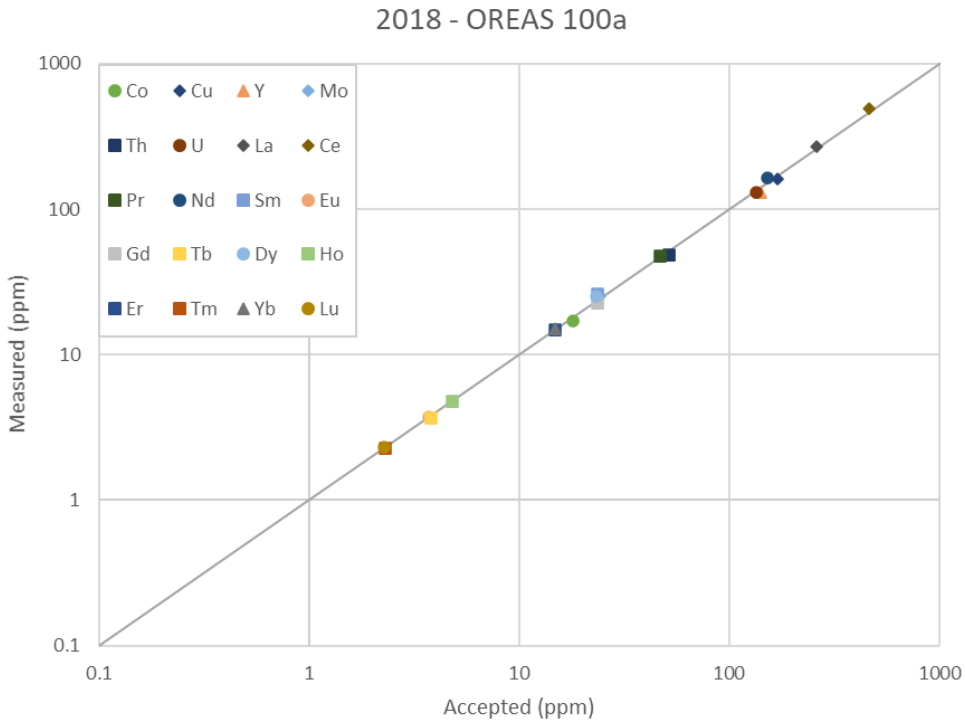

Figure B1.16. Measured trace element concentration results versus accepted values for reference material OREAS 100a.

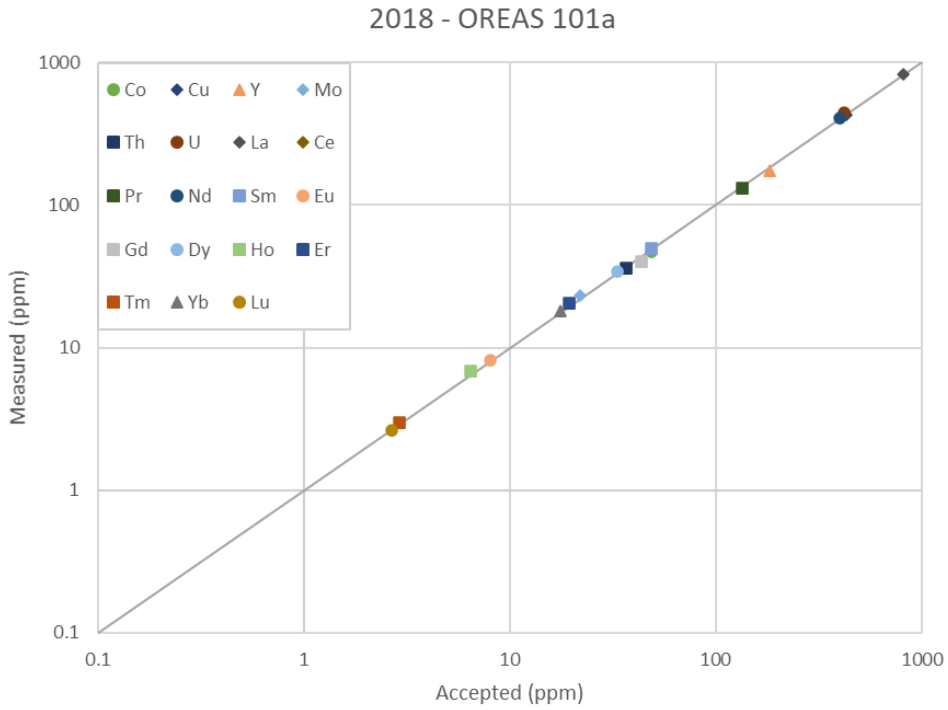

Figure B1.17. Measured trace element concentration results versus accepted values for reference material OREAS 101a.

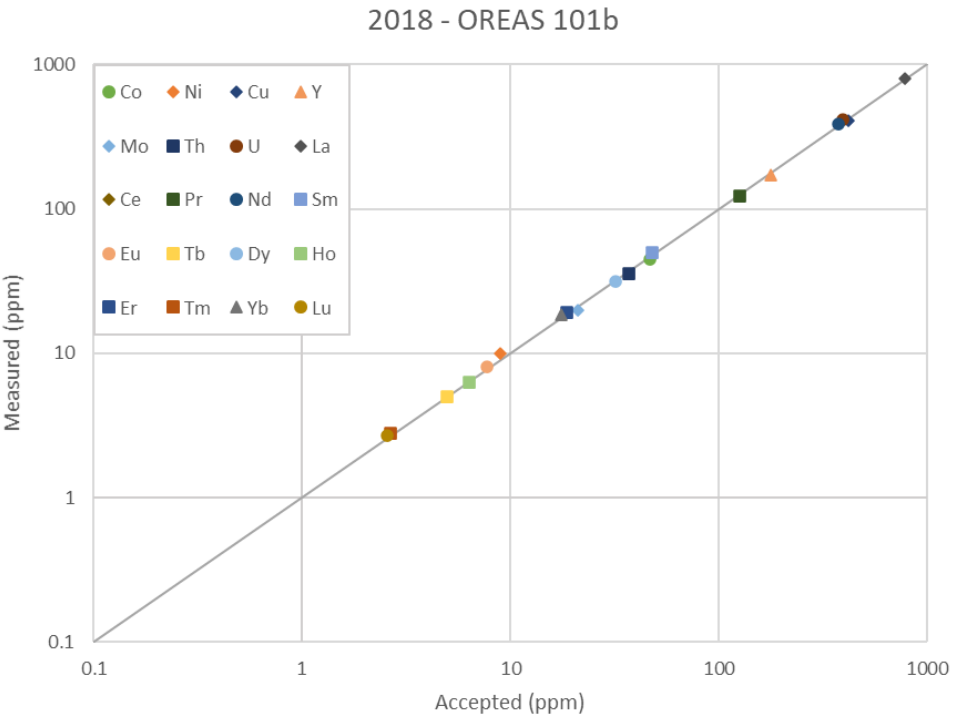

Figure B1.18. Measured trace element concentration results versus accepted values for reference material OREAS 101b.

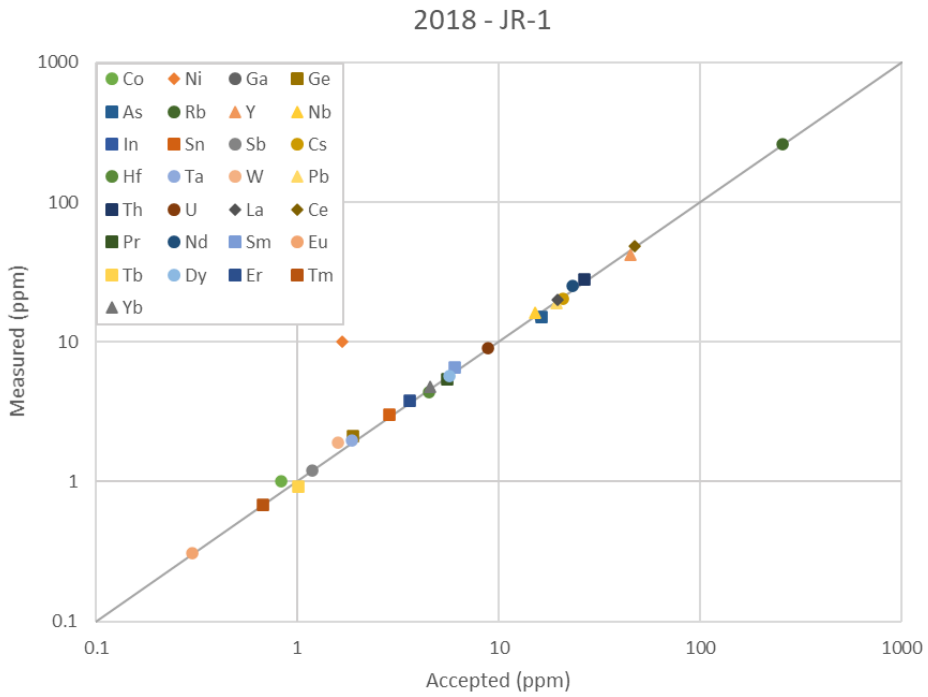

Figure B1.19. Measured trace element concentration results versus accepted values for reference material JR-1.

Appendix B2. 2019 whole rock geochemistry analysis reference material results

Table B2.1. Major oxide accuracy results of bulk rock reference materials analyzed in 2019.

	Analyte	SiO_2	Al_2O_3	$Fe_2O_3(T)$	MnO	MgO	CaO	Na_2O	K_2O	TiO_2	P_2O_5
		%	%	%	%	%	%	%	%	%	%
	Detection Limit	0.01	0.01	0.01	0.001	0.01	0.01	0.01	0.01	0.001	0.01
Year	Measurement										
2019	NIST 694 Meas	11.30	1.91	0.74	0.010	0.32	43.16	0.89	0.55	0.120	30.21
	NIST 694 Cert	11.20	1.80	0.79	0.012	0.33	43.60	0.86	0.51	0.110	30.20
	Percent Error	0.89	6.11	6.33	13.793	3.03	1.01	3.49	7.84	9.091	0.03
2019	DNC-1 Meas	46.64	18.25	10.00	0.150	10.03	11.45	1.85	0.22	0.490	0.07
	DNC-1 Cert	47.15	18.34	9.97	0.150	10.13	11.49	1.89	0.23	0.480	0.07
	Percent Error	1.08	0.49	0.30	0.000	0.99	0.35	2.12	5.98	2.083	0.00
2019	GSP-2 (AAA) - USGS Standard	65.64	14.68	4.89	0.043	0.90	2.04	2.84	5.47	0.654	0.28
	GSP-2 Cert.	66.60	14.90	4.90	0.041	0.96	2.10	2.78	5.38	0.660	0.29
	Percent Error	1.44	1.48	0.20	4.878	6.25	2.86	2.16	1.67	0.909	3.45
2019	TDB-1 Meas										
	TDB-1 (BBB) - Canmet STD	50.87	13.39	14.44	0.191	5.66	9.75	2.27	0.89	2.324	0.22
	TDB-1 Cert	50.20	13.60	14.40	0.200	5.9	9.60	2.20	0.89	2.300	0.23
	Percent Error	1.33	1.54	0.28	4.500	4.07	1.56	3.18	0.00	1.043	4.35
2019	W-2a Meas	52.38	15.32	10.81	0.160	6.26	10.91	2.23	0.64	1.070	0.13
	W-2a Cert	52.40	15.40	10.70	0.163	6.37	10.90	2.14	0.63	1.060	0.14
	Percent Error	0.04	0.52	1.03	1.840	1.73	0.09	4.21	2.24	0.943	7.14
2019	SY-4 Meas	50.26	20.53	6.09	0.110	0.5	7.97	7.00	1.70	0.290	0.12
	SY-4 (CCC) - Canmet STD	50.05	20.64	6.20	0.107	0.5	8.10	7.15	1.64	0.295	0.13
	SY-4 Cert	49.90	20.69	6.21	0.108	0.54	8.05	7.10	1.66	0.287	0.13
	Percent Error	0.72	0.77	1.93	1.852	7.41	0.99	1.41	2.41	1.045	8.40
2019	BIR-1a Meas	47.54	15.68	11.51	0.170	9.57	13.49	1.78	0.02	0.980	0.02

	BIR-1a Cert	47.96	15.50	11.30	0.175	9.7	13.30	1.82	0.03	0.960	0.02
	Percent Error	0.88	1.16	1.86	2.857	1.34	1.43	2.20	33.33	2.083	4.76
2019	**Method Blank**	< 0.01	< 0.01	< 0.01	0.004	< 0.01	< 0.01	< 0.01	< 0.01	< 0.001	< 0.01
2019	**Method Blank**	< 0.01	< 0.01	< 0.01	0.004	< 0.01	< 0.01	< 0.01	< 0.01	< 0.001	0.01

Table B2.2. Major oxide precision results of bulk rock reference materials analyzed in 2019.

	Analyte	**SiO_2**	**Al_2O_3**	**Fe_2O_3(T)**	**MnO**	**MgO**	**CaO**	**Na_2O**	**K_2O**	**TiO_2**	**P_2O_5**
		%	**%**	**%**	**%**	**%**	**%**	**%**	**%**	**%**	**%**
	Detection Limit	**0.01**	**0.01**	**0.01**	**0.001**	**0.01**	**0.01**	**0.01**	**0.01**	**0.001**	**0.01**
Year	**Measurement**										
2019	**TDB-1 Meas**										
	TDB-1 (BBB) - Canmet STD	50.87	13.39	14.44	0.191	5.66	9.75	2.27	0.89	2.324	0.22
	RSD	N/A	N/A	N/A	N/A	N/A	N/A	N/A	N/A	N/A	N/A
2019	**SY-4 Meas**	50.26	20.53	6.09	0.110	0.50	7.97	7.00	1.70	0.290	0.12
	SY-4 (CCC) - Canmet STD	50.05	20.64	6.20	0.107	0.50	8.10	7.15	1.64	0.295	0.13
	RSD	0.30	0.38	1.27	1.955	0.00	1.14	1.50	2.54	1.209	5.66
2019	**19GJ9-6 Orig**	48.03	12.27	13.26	0.200	8.73	11.50	2.25	0.08	1.163	0.27
	19GJ9-6 Dup	48.23	12.39	12.98	0.201	8.81	11.52	2.33	0.08	1.161	0.26
	RSD	0.29	0.69	1.51	0.353	0.65	0.12	2.47	0.00	0.122	2.67
2019	**19GJ15-10 Orig**	60.31	18.78	5.01	0.126	1.40	7.82	3.88	0.75	0.404	0.08
	19GJ15-10 Dup	60.69	19.02	5.12	0.127	1.42	7.84	3.90	0.75	0.408	0.09
	RSD	0.44	0.90	1.54	0.559	1.00	0.18	0.36	0.00	0.697	8.32
2019	**04PSC-329 Orig**	62.39	16.15	4.55	0.101	1.55	4.43	4.57	3.59	0.370	0.21
	04PSC-329 Dup	63.30	16.49	4.63	0.103	1.55	4.49	4.51	3.50	0.374	0.22
	RSD	1.02	1.47	1.23	1.386	0	0.95	0.93	1.80	0.760	3.29

Table B2.3. Trace element accuracy results of bulk rock reference materials analyzed in 2019.

	Analyte	Sc ppm	Be ppm	V ppm	Cr ppm	Co ppm	Ni ppm	Cu ppm	Zn ppm	Ga ppm	Ge ppm	As ppm	Rb ppm	Sr ppm
	Detection Limit	1	1	5	20	1	20	10	30	1	0.5	5	1	2
Year	Measurement													
2019	NIST 694 Meas			1656										
	NIST 694 Cert			1740										
	Percent Error			4.8										
2019	DNC-1 Meas	31		158										143
	DNC-1 Cert	31		148										144
	Percent Error	0.0		6.8										0.7
2019	GSP-2 (AAA) - USGS Standard	6	2	55	20	7	30	40	120	24	1.6	2.5	244	238
	GSP-2 Cert.	6.3	1.5	52	20	7.3	17	43	120	22	4.4	1.1	245	240
	Percent Error	4.8	33.3	5.8	0.0	4.1	76.5	7.0	0.0	9.1	63.6	N/A	0.4	0.8
2019	TDB-1 Meas				250		100	330	150				22	
	TDB-1 (BBB) - Canmet STD	37	2	485	250	42	100	300	160	22	1.8	< 5	20	221
	TDB-1 Cert	36	1.5	471	251	47	92	323	155	21	1.0	2.5	23	230
	Percent Error	2.8	33.3	3.0	0.4	10.6	8.7	7.1	3.2	4.8	80.0	N/A	13.0	3.9
2019	W-2a Meas	35	1	279	100	43	80	110	80	17	1.5	<5	19	194
	W-2a Cert	36	1.3	262	92	43	70	110	80	17	1.0	1.2	21	190
	Percent Error	2.8	23.1	6.5	8.7	0.0	14.3	0.0	0.0	0.0	50.0	N/A	9.5	2.1
2019	DTS-2b Meas				>10000	123	3760							
	DTS-2b Cert				15500	120	3780							
	Percent Error				N/A	2.5	0.5							
2019	SY-4 Meas	1	3	<5		2			100	34			52	1204
	SY-4 (CCC) - Canmet STD	1	3	3	< 20	2	< 20	< 10	100	36	1.3	< 5	52	1209
	SY-4 Cert	1.1	2.6	8		2.8			93	35			55	1191
	Percent Error	9.1	15.4	N/A		28.6			7.5	2.9			5.5	1.1

2019	**BIR-1a Meas**	44	1	339										109
	BIR-1a Cert	44	0.58	310										110
	Percent Error	0.0	N/A	9.4										0.9
2019	**ZW-C Meas**				60			1010	93			>1000		
	ZW-C Cert				56			1050	99			8500		
	Percent Error				7.1			3.8	6.1			N/A		
2019	**OREAS 101b (Fusion) Meas**					44	420							
	OREAS 101b (Fusion) Cert					47	420							
	Percent Error					6.4	0.0							
2019	**NCS DC86318 Meas**											378		
	NCS DC86318 Cert											369.42		
	Percent Error											2.3		
2019	**SARM 3 Meas**													
	SARM 3 Cert													
	Percent Error													
2019	**USZ 42-2006 Meas**						< 20	470						
	USZ 42-2006 Cert						13.18	469						
	Percent Error						N/A	0.2						
2019	**REE-1 Meas**				290	1	30	80				118		
	REE-1 Cert				277	1.58	24.7	79.7				124		
	Percent Error				4.7	36.7	21.5	0.4				4.8		
2019	**Method Blank**	< 1	< 1	< 5	< 20	< 1	< 20	< 10	< 30	< 1	< 0.5	< 5	< 1	< 2
2019	**Method Blank**	< 1	< 1	< 5										< 2

Table B2.3. continued.

	Analyte	Y ppm	Zr ppm	Nb ppm	Mo ppm	Ag ppm	In ppm	Sn ppm	Sb ppm	Cs ppm	Ba ppm	La ppm	Ce ppm
	Detection Limit	**0.5**	**1**	**0.2**	**2**	**0.5**	**0.1**	**1**	**0.2**	**0.1**	**2**	**0.05**	**0.05**
Year	**Measurement**												
2019	**NIST 694 Meas**												
	NIST 694 Cert												
	Percent Error												
2019	**DNC-1 Meas**		32								107		
	DNC-1 Cert		38								118		
	Percent Error		15.8								9.3		
2019	**GSP-2 (AAA) - USGS Standard**	27.1	534	24.7	2	2	0.05	7	0.5	1.2	1364	194	452
	GSP-2 Cert.	28	550	27	2.1		0.05	8.32	0.43	1.2	1340	180	410
	Percent Error	3.2	2.9	8.5	4.8		N/A	15.9	16.3	0.0	1.8	7.8	10.2
2019	**TDB-1 Meas**	33.6										16.1	37.1
	TDB-1 (BBB) - Canmet STD	34.9	153	12.4	< 2	0.6	0.1	2	0.8	0.5	240	16.9	39.6
	TDB-1 Cert	36	156	11	1.6	0.5	0.2	2	1		241	17	41
	Percent Error	3.1	1.9	12.7	N/A	20.0	50.0	0.0	20.0		0.4	0.6	3.4
2019	**W-2a Meas**	20.7	80		<2				0.8		179	10.4	22.2
	W-2a Cert	24	94		0.6				0.79		182	10	23
	Percent Error	13.8	14.9		N/A				1.3		1.6	4.0	3.5
2019	**DTS-2b Meas**												
	DTS-2b Cert												
	Percent Error												
2019	**SY-4 Meas**	118	533	13.2						1.5	355	58.5	121
	SY-4 (CCC) - Canmet STD	120	534	14.4	1	1.7	< 0.1	8	0.2	1.5	343	59.8	123
	SY-4 Cert	119	517	13						1.5	340	58	122
	Percent Error	0.8	3.1	1.5						0.0	4.4	0.9	0.8

2019	**BIR-1a Meas**		14								13		
	BIR-1a Cert		18								6		
	Percent Error		22.2								116.7		
2019	**ZW-C Meas**			202				>1000	4.4	265		28.9	97.2
	ZW-C Cert			198				1300	4.2	260		30	97
	Percent Error			2.0				N/A	4.8	1.9		3.7	0.2
2019	**OREAS 101b (Fusion) Meas**	172			19							771	1430
	OREAS 101b (Fusion) Cert	178			21							789	1331
	Percent Error	3.4			9.5							2.3	7.4
2019	**NCS DC86318 Meas**	>10000								11.5		>2000	400
	NCS DC86318 Cert	17008								10.28		1960	430
	Percent Error	N/A								11.9		N/A	7.0
2019	**SARM 3 Meas**			976									
	SARM 3 Cert			978									
	Percent Error			0.2									
2019	**USZ 42-2006 Meas**	170		34	36							>2000	>3000
	USZ 42-2006 Cert	167		31	34.4							21100	27600
	Percent Error	1.8		9.7	4.7							N/A	N/A
2019	**REE-1 Meas**									1.1		1640	3000
	REE-1 Cert									1.07		1661	3960
	Percent Error									2.8		1.3	24.2
2019	**Method Blank**	< 0.5	2	< 0.2	< 2	< 0.5	< 0.1	< 1	< 0.2	< 0.1	< 2	< 0.05	< 0.05
2019	**Method Blank**		2								< 2		

Table B2.3. continued.

	Analyte	Pr	Nd	Sm	Eu	Gd	Tb	Dy	Ho	Er	Tm
		ppm	ppm	ppm	ppm	ppm	ppm	ppm	ppm	ppm	ppm
	Detection Limit	0.01	0.05	0.01	0.005	0.01	0.01	0.01	0.01	0.01	0.005
Year	Measurement										
2019	NIST 694 Meas										
	NIST 694 Cert										
	Percent Error										
2019	DNC-1 Meas										
	DNC-1 Cert										
	Percent Error										
2019	GSP-2 (AAA) - USGS Standard	56.7	207	26.6	2.37	12	1.34	5.84	0.9	2.63	0.291
	GSP-2 Cert.	51	200	27	2.3	12	1.54	6.1	1	2.2	0.29
	Percent Error	11.2	3.5	1.5	3.0	3.3	13.0	4.3	10.0	20	0.3
2019	TDB-1 Meas		23.5		2						
	TDB-1 (BBB) - Canmet STD	5.38	24.7	6.37	2.1	6.76	1.18	6.95	1.31	3.59	0.502
	TDB-1 Cert	6	23	6	2.1	7	1.2	8	1.3	4	0.6
	Percent Error	10.3	7.4	6.2	2.4	3.4	1.7	13.1	0.8	10	16.3
2019	W-2a Meas		12.8	3.2	1.1		0.63	3.8	0.76		
	W-2a Cert		13	3.3	1		0.63	3.6	0.76		
	Percent Error		1.5	3.0	10.0		0.0	5.6	0.0		
2019	DTS-2b Meas										
	DTS-2b Cert										
	Percent Error										
2019	SY-4 Meas	15	58.6	13.2	2.03	14.9	2.86	19.3	4.49	14.6	2.31
	SY-4 (CCC) - Canmet STD	14.7	57.1	12.7	1.98	14	2.87	19.6	4.42	14.4	2.28
	SY-4 Cert	15	57	12.7	2	14	2.6	18.2	4.3	14.2	2.3
	Percent Error	0.0	2.8	3.9	1.5	6.4	10.0	6.0	4.4	2.8	0.4

2019	**BIR-1a Meas**										
	BIR-1a Cert										
	Percent Error										
2019	**ZW-C Meas**	9.4	25.0	6.7		4.7					
	ZW-C Cert	9.5	25.0	6.6		4.7					
	Percent Error	1.1	0.0	1.5		0.0					
2019	**OREAS 101b (Fusion) Meas**	124	378	48	8		5.41	31.4	6.28	18.9	2.71
	OREAS 101b (Fusion) Cert	127	378	48	7.8		5.37	32.1	6.34	18.7	2.66
	Percent Error	2.4	0.0	0.0	2.8		0.7	2.2	0.9	1.1	1.9
2019	**NCS DC86318 Meas**	773	>2000	>1000	19	>1000	506	>1000	583	>1000	262
	NCS DC86318 Cert	740	3430	1720	18.91	2095	470	3220	560	1750	270
	Percent Error	4.5	N/A	N/A	0.5	N/A	7.7	N/A	4.1	N/A	3.0
2019	**SARM 3 Meas**										
	SARM 3 Cert										
	Percent Error										
2019	**USZ 42-2006 Meas**	>1000	>2000	513	89						
	USZ 42-2006 Cert	2300	6500	539	87.22						
	Percent Error	N/A	N/A	4.8	2.0						
2019	**REE-1 Meas**		1450		24.2	439		854	206	691	
	REE-1 Cert		1456		23.5	433.0		847	208	701	
	Percent Error		0.4		3.0	1.4		0.8	1.0	1.4	
2019	**Method Blank**	< 0.01	< 0.05	< 0.01	< 0.005	< 0.01	< 0.01	< 0.01	< 0.01	< 0.01	< 0.005
2019	**Method Blank**										

Table B2.3. continued.

	Analyte	Yb	Lu	Hf	Ta	W	Tl	Pb	Bi	Th	U
		ppm	ppm	ppm	ppm	ppm	ppm	ppm	ppm	ppm	ppm
	Detection Limit	0.01	0.002	0.1	0.01	0.5	0.05	5	0.1	0.05	0.01
Year	Measurement										
2019	NIST 694 Meas										
	NIST 694 Cert										
	Percent Error										
2019	DNC-1 Meas										
	DNC-1 Cert										
	Percent Error										
2019	GSP-2 (AAA) - USGS Standard	1.59	0.239	15.7	0.86	0.7	1.18	35	0.05	108	2.68
	GSP-2 Cert.	1.6	0.23	14	1.01	0.39	1.1	42	0.028	105	2.4
	Percent Error	0.6	3.9	12.1	14.9	79.5	7.3	16.7	N/A	2.9	11.7
2019	TDB-1 Meas	3.2								2.6	
	TDB-1 (BBB) - Canmet STD	3.29	0.51	4.7	0.82	< 0.5	0.24	17	< 0.1	2.74	0.92
	TDB-1 Cert	3.4	0.52	5	0.8	0.6	<0.02	17	0.8	2.7	1
	Percent Error	3.2	1.9	6.0	2.5	N/A	N/A	0.0	N/A	1.5	8.0
2019	W-2a Meas	2.1	0.3	2.5	0.47		0.08	9	<0.1	2.3	0.51
	W-2a Cert	2.1	0.33	2.6	0.5		0.2	9.3	0.03	2.4	0.53
	Percent Error	0.0	9.1	3.8	6.0		60.0	3.2	N/A	4.2	3.8
2019	DTS-2b Meas										
	DTS-2b Cert										
	Percent Error										
2019	SY-4 Meas	15.5	2.26	9.8	0.85			11			
	SY-4 (CCC) - Canmet STD	15.6	2.26	11.6	0.78	0.5	0.3	11	< 0.1	1.09	0.82
	SY-4 Cert	14.8	2.1	10.6	0.9			10			
	Percent Error	4.7	7.6	7.5	5.6			10.0			

2019	**BIR-1a Meas**										
	BIR-1a Cert										
	Percent Error										
2019	**ZW-C Meas**				87.8	332	34.1				18.9
	ZW-C Cert				82	320	34				20
	Percent Error				7.1	3.8	0.3				5.5
2019	**OREAS 101b (Fusion) Meas**	17.8	2.65							34.1	395
	OREAS 101b (Fusion) Cert	17.6	2.58							37.1	396
	Percent Error	1.1	2.7							8.1	0.3
2019	**NCS DC86318 Meas**	>1000	253							66.8	
	NCS DC86318 Cert	1840	260							67	
	Percent Error	N/A	2.7							0.3	
2019	**SARM 3 Meas**										
	SARM 3 Cert										
	Percent Error										
2019	**USZ 42-2006 Meas**	16.9						1530		1090	
	USZ 42-2006 Cert	17.85						1600		946	
	Percent Error	5.3						4.4		15.2	
2019	**REE-1 Meas**			502							
	REE-1 Cert			479							
	Percent Error			4.8							
2019	**Method Blank**	< 0.01	< 0.002	< 0.05	< 0.01	< 0.5	< 0.05	< 5	< 0.1	< 0.05	< 0.01
2019	**Method Blank**										

Table B2.4. Trace element precision results of bulk rock reference materials analyzed in 2019.

	Analyte	Sc	Be	V	Cr	Co	Ni	Cu	Zn	Ga	Ge	As	Rb	Sr	Y	Zr
		ppm	ppm	ppm	ppm	ppm	ppm	ppm	ppm	ppm	ppm	ppm	ppm	ppm	ppm	ppm
	Detection Limit	1	1	5	20	1	20	10	30	1	0.5	5	1	2	0.5	1
Year	Measurement															
2019	**TDB-1 Meas**				250		100	330	150				22		33.6	
	TDB-1 (BBB) - Canmet STD	37	2	485	250	42	100	300	160	22	1.8	< 5	20	221	34.9	153
	RSD				0.00		0.00	6.73	7.07				2.72		0.77	
2019	**SY-4 Meas**	1	3	< 5		2			100	34			52	1204	118	533
	SY-4 (CCC) - Canmet STD	1	3	< 5	< 20	2	< 20	< 10	100	36	1.3	< 5	52	1209	120	534
	RSD	0.00	0.00			0.00			0.00	4.04			0.00	0.29	1.19	0.13
2019	**19GJ9-6 Orig**	37	1	328	370	52	90	170	100	15	2.1	< 5	1	373	20.1	60
	19GJ9-6 Dup	37	1	330	360	52	90	170	110	16	1.9	< 5	1	378	20.1	61
	RSD	0.00	0.00	0.43	1.94	0.00	0.00	0.00	6.73	4.56	7.07		0.00	0.94	0.00	1.17
2019	**19GJ15-10 Orig**	12	< 1	112	< 20	5	< 20	20	60	16	1.3	< 5	14	235	12.7	39
	19GJ15-10 Dup	12	< 1	114	< 20	5	< 20	20	60	16	1.4	< 5	15	234	13.2	39
	RSD	0.00		1.25		0.00		0.00	0.00	0.00	5.24		4.88	0.30	2.73	0.00
2019	**04PSC-329 Orig**	7	2	94	< 20	8	< 20	< 10	30	16	1.4	< 5	88	992	12	92
	04PSC-329 Dup	7	2	93	< 20	8	< 20	< 10	30	17	1.3	< 5	88	980	12.1	93
	RSD	0.00	0.00	0.76		0.00			0.00	4.29	5.24		0.00	0.86	0.59	0.76

Table B2.4. continued.

	Analyte	Nb	Mo	Ag	In	Sn	Sb	Cs	Ba	La	Ce	Pr	Nd	Sm	Eu	Gd
		ppm	ppm	ppm	ppm	ppm	ppm	ppm	ppm	ppm	ppm	ppm	ppm	ppm	ppm	ppm
	Detection Limit	0.2	2	0.5	0.1	1	0.2	0.1	2	0.05	0.05	0.01	0.05	0.01	0.005	0.01
Year	Measurement															
2019	TDB-1 Meas									16.1	37.1		23.5		2	
	TDB-1 (BBB) - Canmet STD	12.4	< 2	0.6	0.1	2	0.8	0.5	240	16.9	39.6	5.38	24.7	6.37	2.05	6.76
	RSD									0.96	1.45		1.47		1.76	
2019	SY-4 Meas	13.2						1.5	355	58.5	121	15	58.6	13.2	2.03	14.9
	SY-4 (CCC) - Canmet STD	14.4	< 2	1.7	< 0.1	8	0.2	1.5	343	59.8	123	14.7	57.1	12.7	1.98	14
	RSD	6.15						0.00	2.43	1.55	1.16	1.43	1.83	2.73	1.76	4.40
2019	19GJ9-6 Orig	1.9	< 2	< 0.5	0.1	1	0.6	0.1	85	7.86	17.7	2.68	13.1	3.6	1.13	4.2
	19GJ9-6 Dup	1.9	< 2	< 0.5	0.1	1	0.6	0.1	86	7.73	17.7	2.58	13.2	3.51	1.23	4.07
	RSD	0.00			0.00	0.00	0.00	0.00	0.83	1.18	0.00	2.69	0.54	1.79	5.99	2.22
2019	19GJ15-10 Orig	0.7	< 2	< 0.5	< 0.1	< 1	0.4	1.2	416	2.65	6.43	0.98	5.29	1.54	0.499	1.94
	19GJ15-10 Dup	0.8	< 2	< 0.5	< 0.1	< 1	0.3	1.2	418	2.56	6.42	1.01	5.17	1.44	0.485	2.04
	RSD	9.43					20.20	0.00	0.34	2.44	0.11	2.13	1.62	4.75	2.01	3.55
2019	04PSC-329 Orig	8.3	< 2	< 0.5	< 0.1	1	< 0.2	0.6	1100	16	28.9	3.2	12.3	2.39	0.692	2.28
	04PSC-329 Dup	8.7	< 2	< 0.5	< 0.1	1	< 0.2	0.6	1086	15.8	28.5	3.22	12.2	2.43	0.723	2.2
	RSD	3.33				0.00		0.00	0.91	0.89	0.99	0.44	0.58	1.17	3.10	2.53

Table B2.4. continued.

	Analyte	Tb ppm	Dy ppm	Ho ppm	Er ppm	Tm ppm	Yb ppm	Lu ppm	Hf ppm	Ta ppm	W ppm	Tl ppm	Pb ppm	Bi ppm	Th ppm	U ppm
	Detection Limit	0.01	0.01	0.01	0.01	0.005	0.01	0.002	0.1	0.01	0.5	0.05	5	0.1	0.05	0.01
Year	Measurement															
2019	**TDB-1 Meas**						3.2								2.6	
	TDB-1 (BBB) - Canmet STD	1.18	6.95	1.31	3.59	0.502	3.29	0.51	4.7	0.82	< 0.5	0.24	17	< 0.1	2.74	0.92
	RSD						0.41								9.08	
2019	**SY-4 Meas**	2.86	19.3	4.49	14.6	2.31	15.5	2.26	9.8	0.85			11			
	SY-4 (CCC) - Canmet STD	2.87	19.6	4.42	14.4	2.28	15.6	2.26	11.6	0.78	< 0.5	0.3	11	< 0.1	1.09	0.82
	RSD	0.25	1.09	1.11	0.98	0.92	0.45	0.00	11.90	6.07			0.00			
2019	**19GJ9-6 Orig**	0.67	3.89	0.72	2.15	0.318	1.95	0.291	1.7	0.15	< 0.5	< 0.05	< 5	< 0.1	0.91	0.59
	19GJ9-6 Dup	0.64	3.85	0.76	2.16	0.303	1.9	0.295	1.6	0.14	< 0.5	< 0.05	< 5	< 0.1	0.92	0.61
	RSD	3.24	0.73	3.82	0.33	3.42	1.84	0.97	4.29	4.88					0.77	2.36
2019	**19GJ15-10 Orig**	0.34	2.12	0.47	1.45	0.22	1.6	0.257	1.2	0.05	< 0.5	0.12	< 5	< 0.1	0.39	0.36
	19GJ15-10 Dup	0.36	2.24	0.44	1.44	0.222	1.5	0.237	1.3	0.07	0.5	0.11	< 5	< 0.1	0.4	0.36
	RSD	4.04	3.89	4.66	0.49	0.64	4.56	5.73	5.66	23.57		6.15			1.79	0.00
2019	**04PSC-329 Orig**	0.36	2.02	0.39	1.18	0.173	1.23	0.186	2.4	0.58	< 0.5	0.28	6	< 0.1	4.46	2.01
	04PSC-329 Dup	0.36	1.96	0.42	1.21	0.179	1.35	0.211	2.6	0.59	< 0.5	0.25	6	< 0.1	4.63	2.13
	RSD	0.00	2.13	5.24	1.78	2.41	6.58	8.91	5.66	1.21		8.00	0.00			

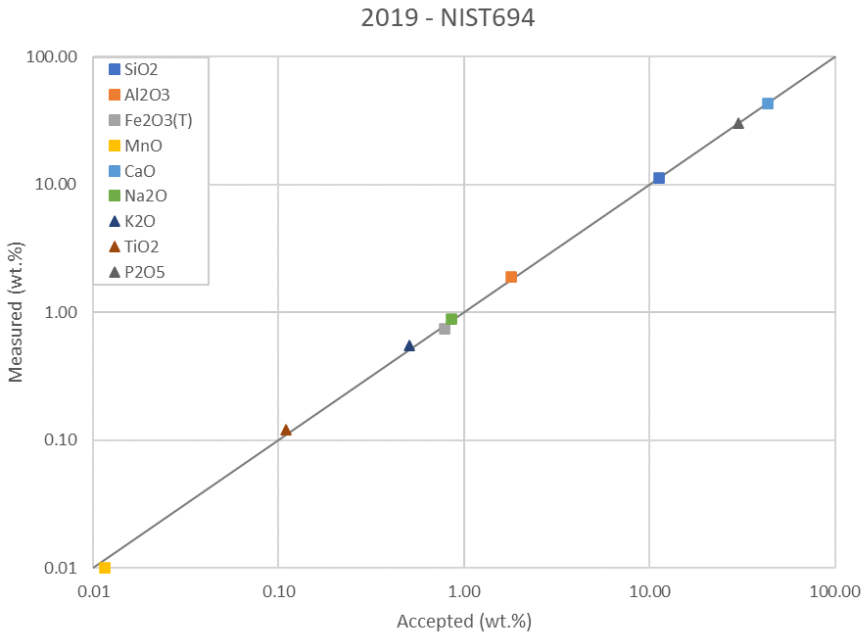

Figure B2.1. Measured major oxide results versus accepted values for reference material NIST-694.

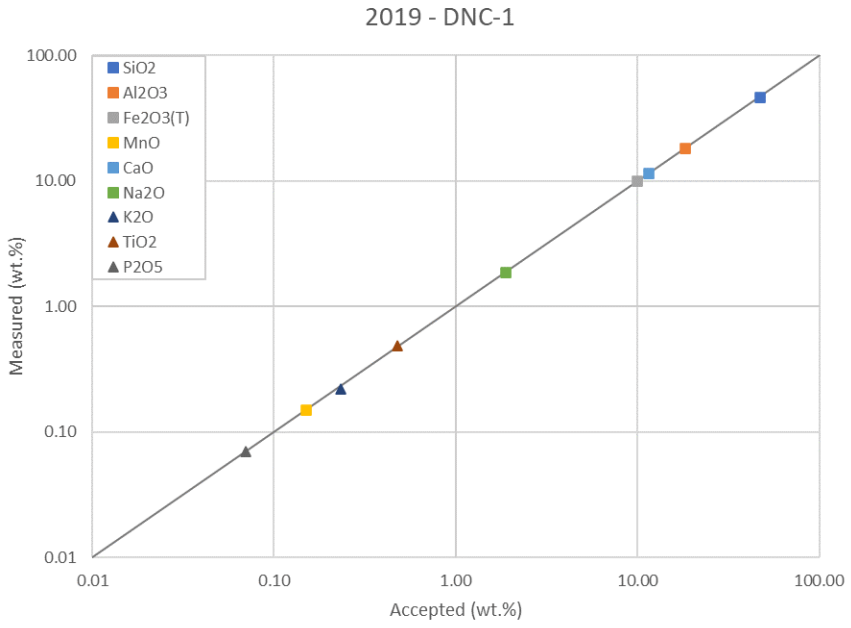

Figure B2.2. Measured major oxide results versus accepted values for reference material DNC-1.

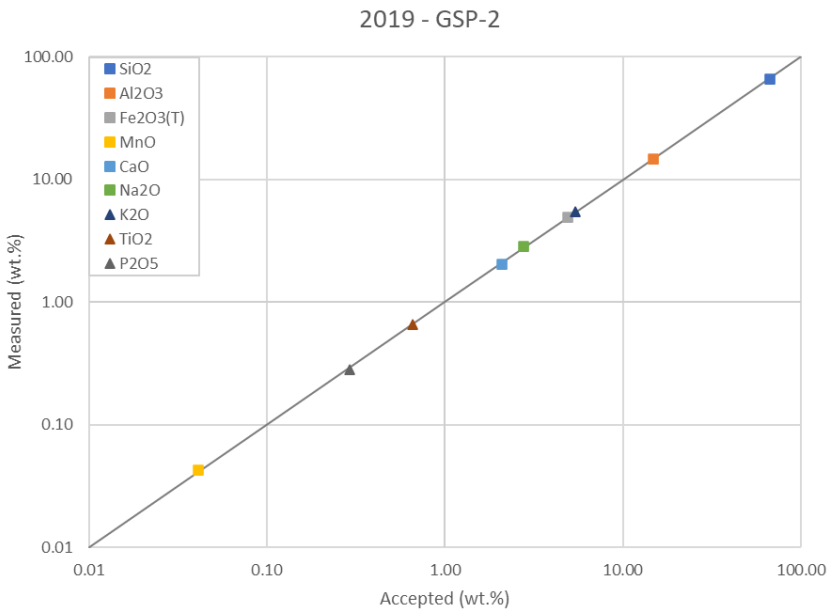

Figure B2.3. Measured major oxide results versus accepted values for reference material GSP-2.

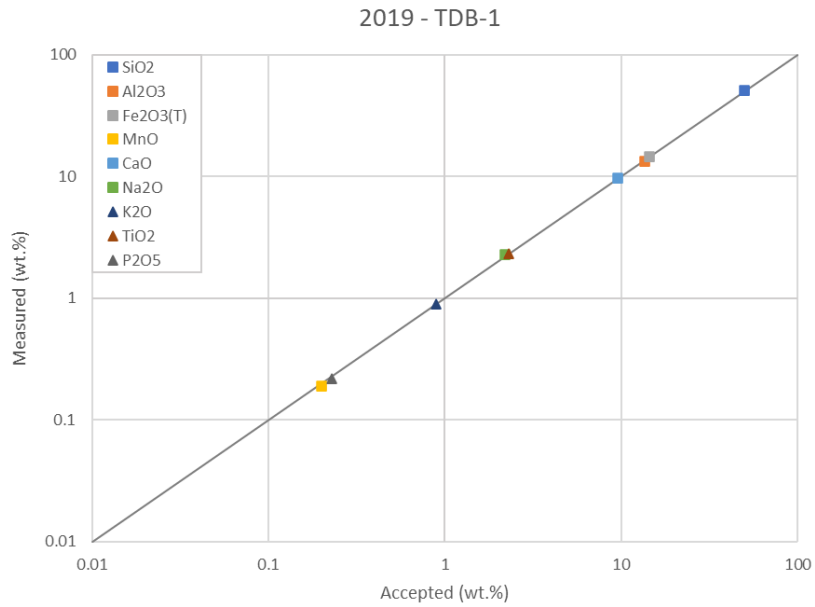

Figure B2.4. Measured major oxide results versus accepted values for reference material TDB-1.

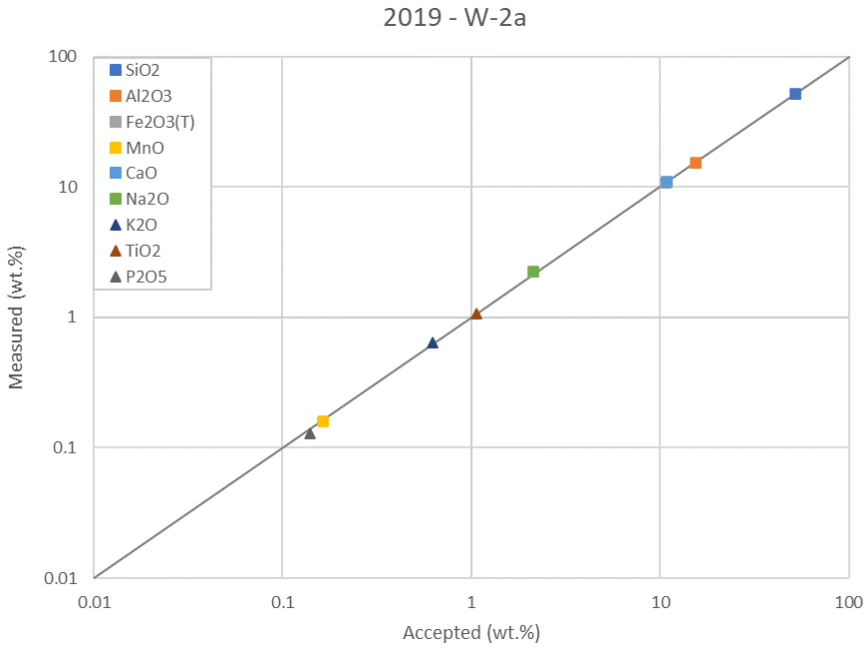

Figure B2.5. Measured major oxide results versus accepted values for reference material W-2a.

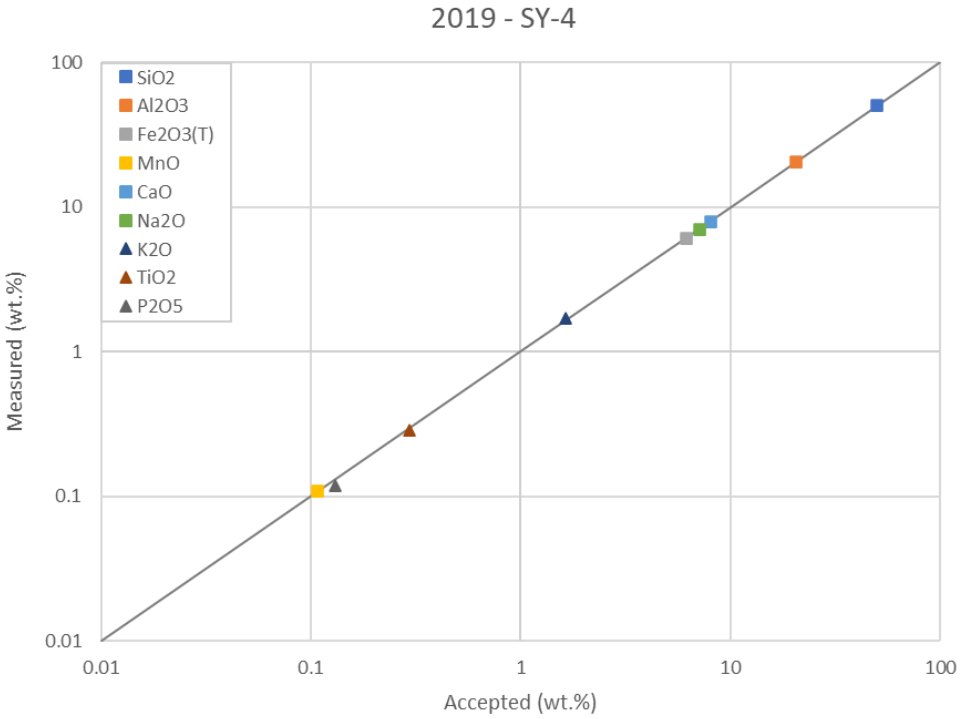

Figure B2.6. Measured major oxide results versus accepted values for reference material SY-4.

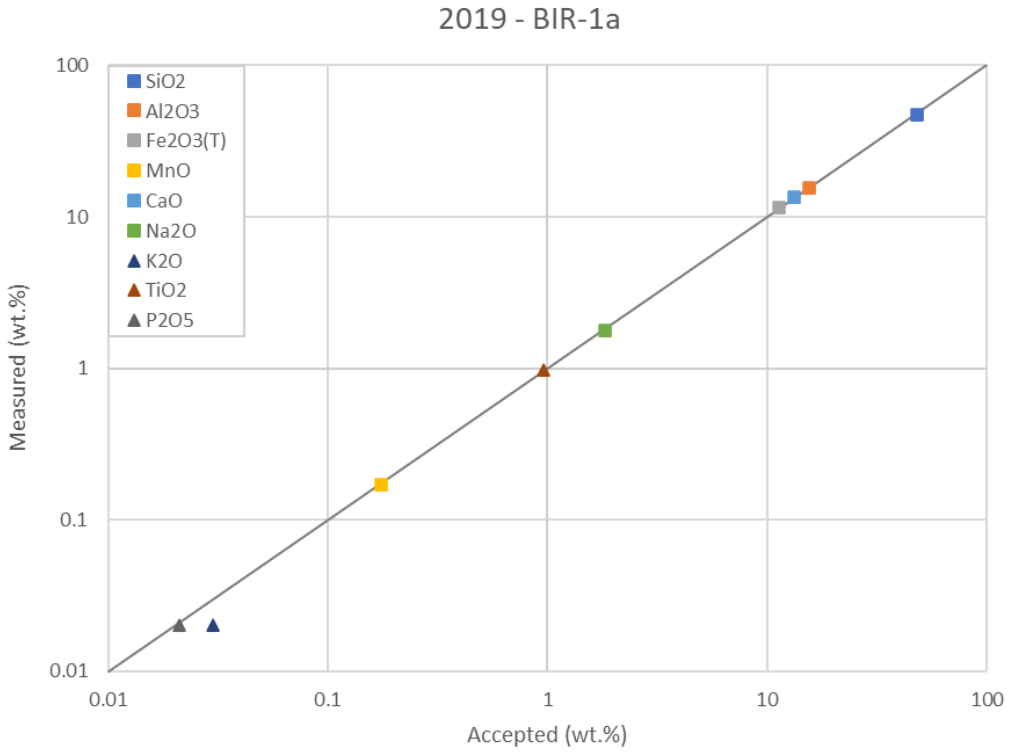

Figure B2.7. Measured major oxide results versus accepted values for reference material BIR-1a.

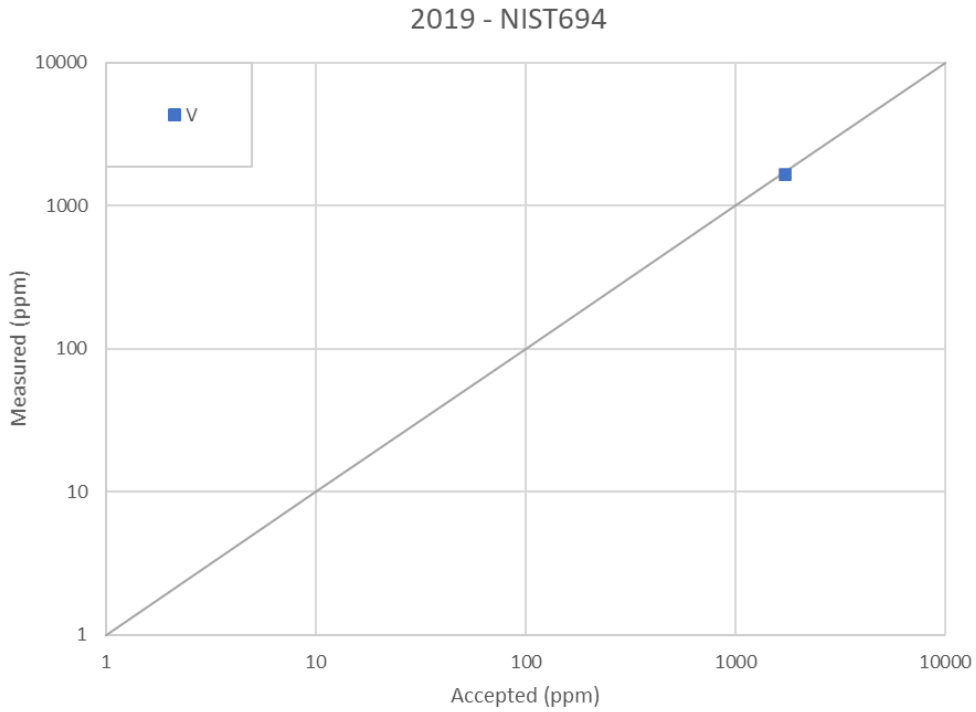

Figure B2.8. Measured trace element concentration results versus accepted values for reference material NIST694.

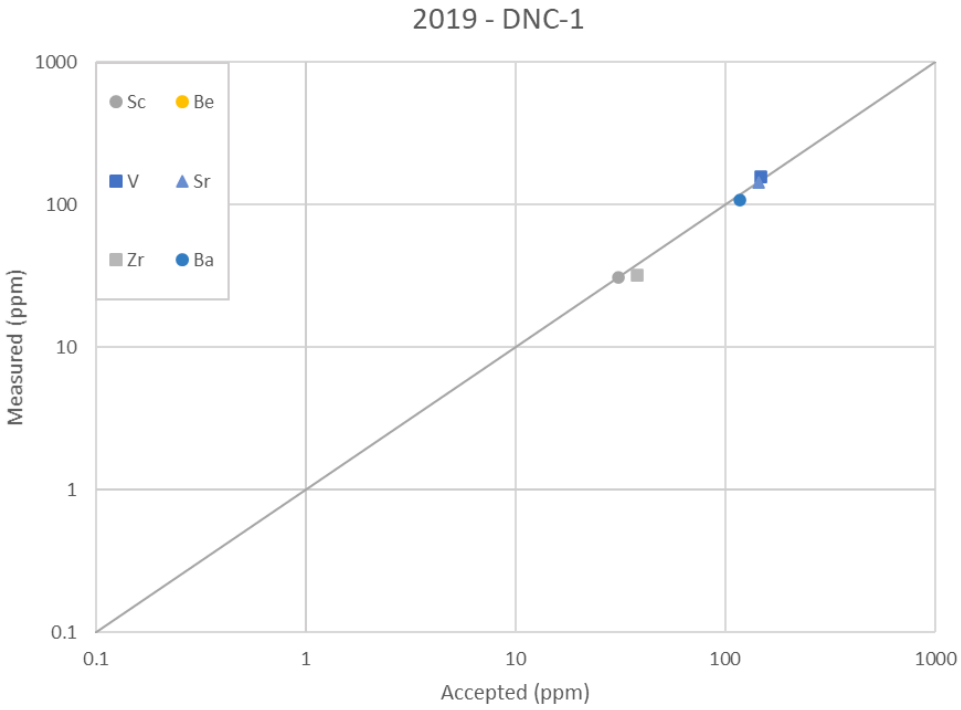

Figure B2.9. Measured trace element concentration results versus accepted values for reference material DNC-1.

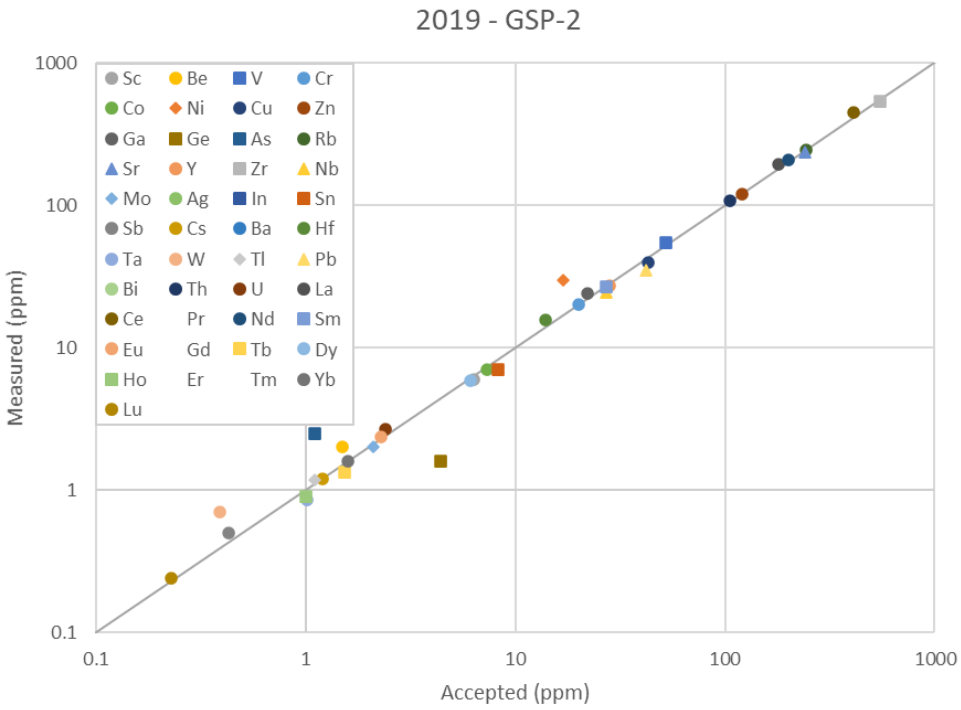

Figure B2.10. Measured trace element concentration results versus accepted values for reference material GSP-2.

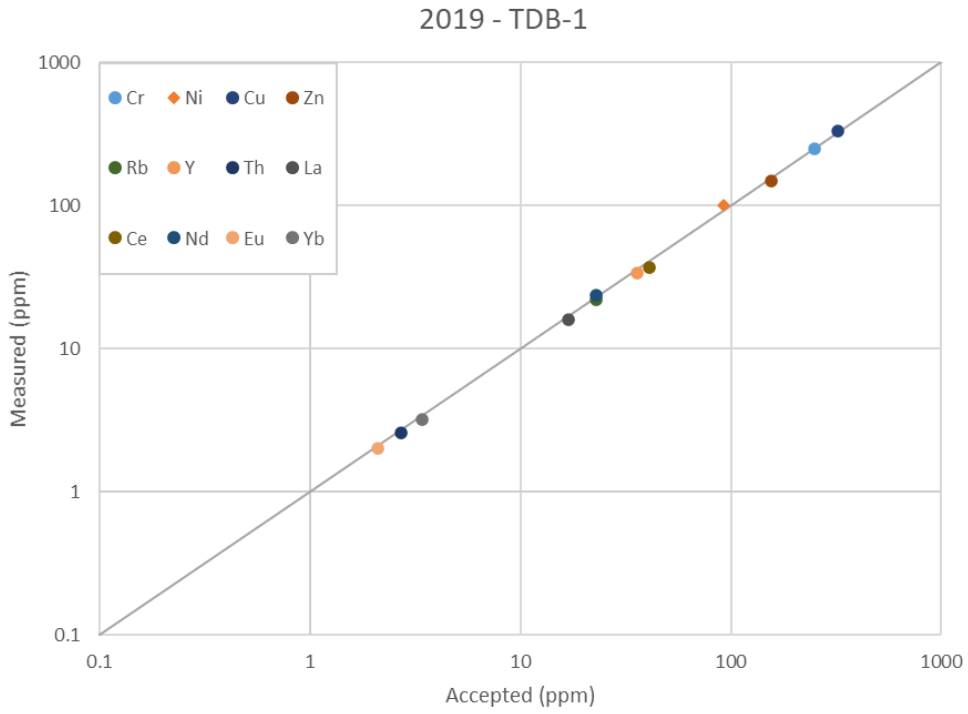

Figure B2.11. Measured trace element concentration results versus accepted values for reference material TDB-1.

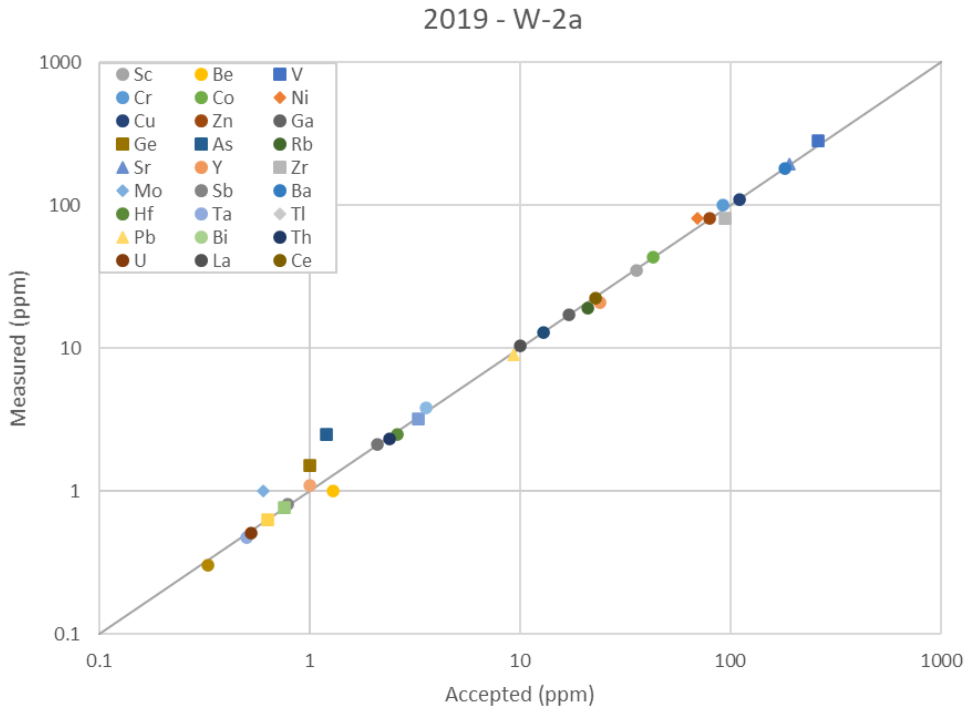

Figure B2.12. Measured trace element concentration results versus accepted values for reference material W-2a.

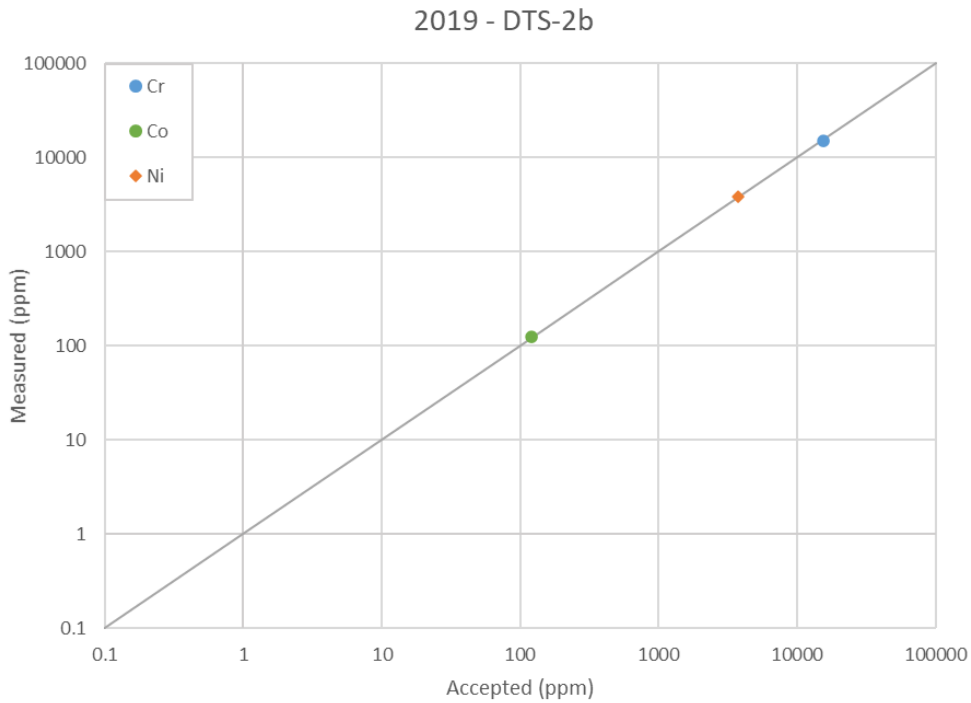

Figure B2.13. Measured trace element concentration results versus accepted values for reference material DTS-2b.

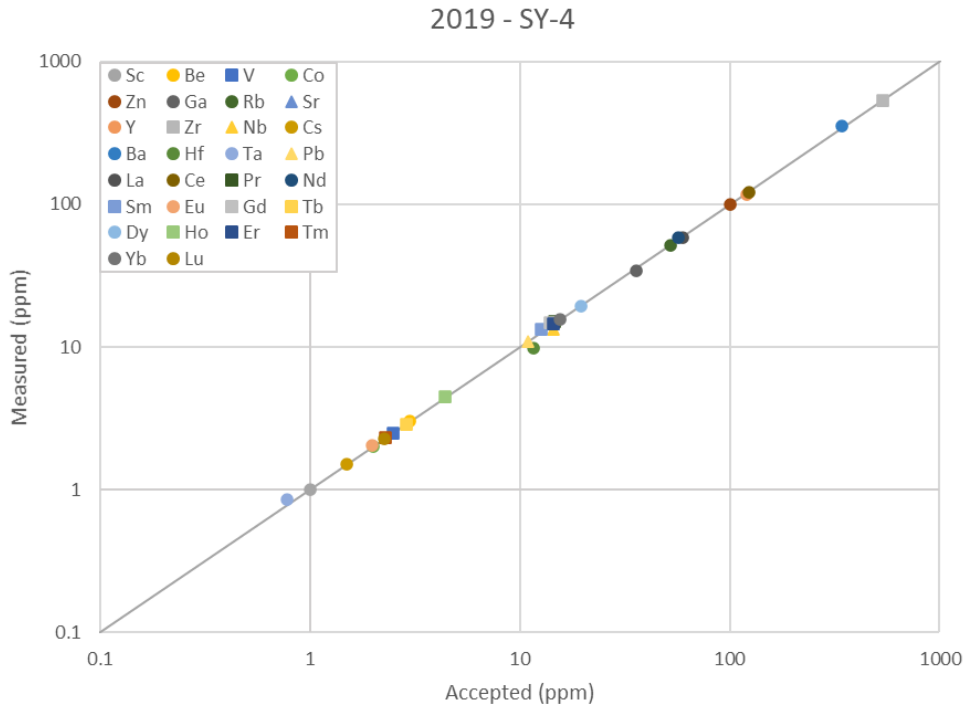

Figure B2.14. Measured trace element concentration results versus accepted values for reference material SY-4.

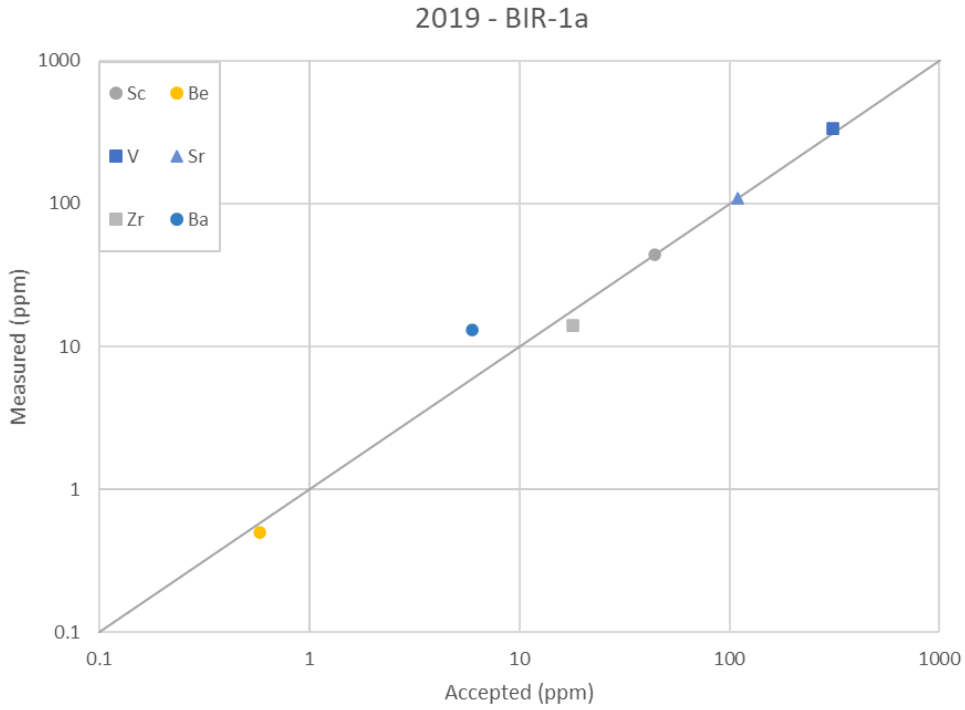

Figure B2.15. Measured trace element concentration results versus accepted values for reference material BIR-1a.

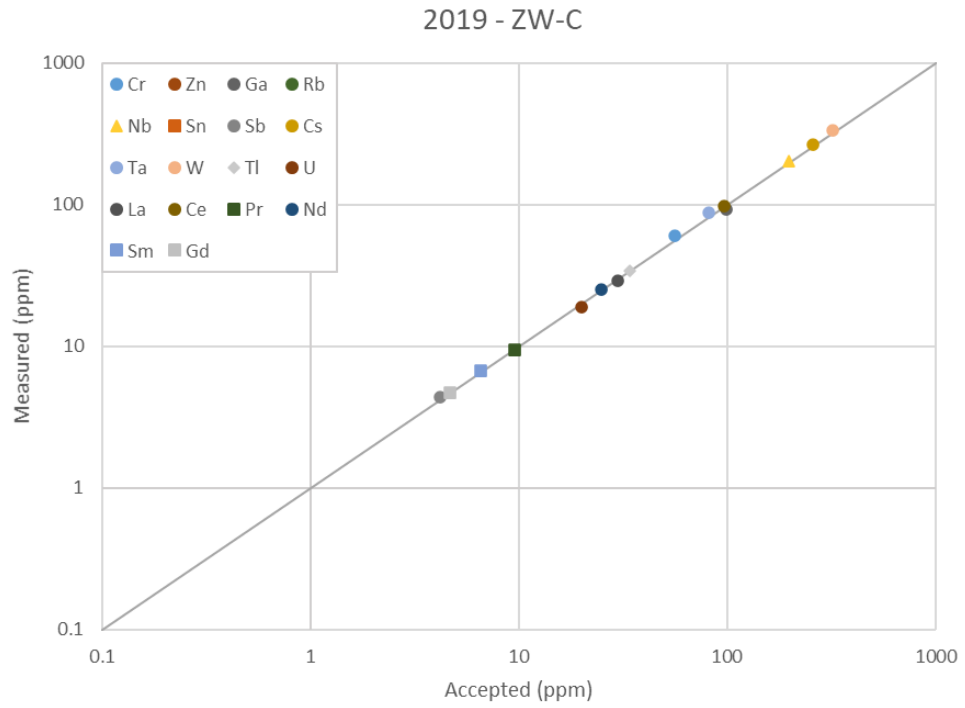

Figure B2.16. Measured trace element concentration results versus accepted values for reference material ZW-C.

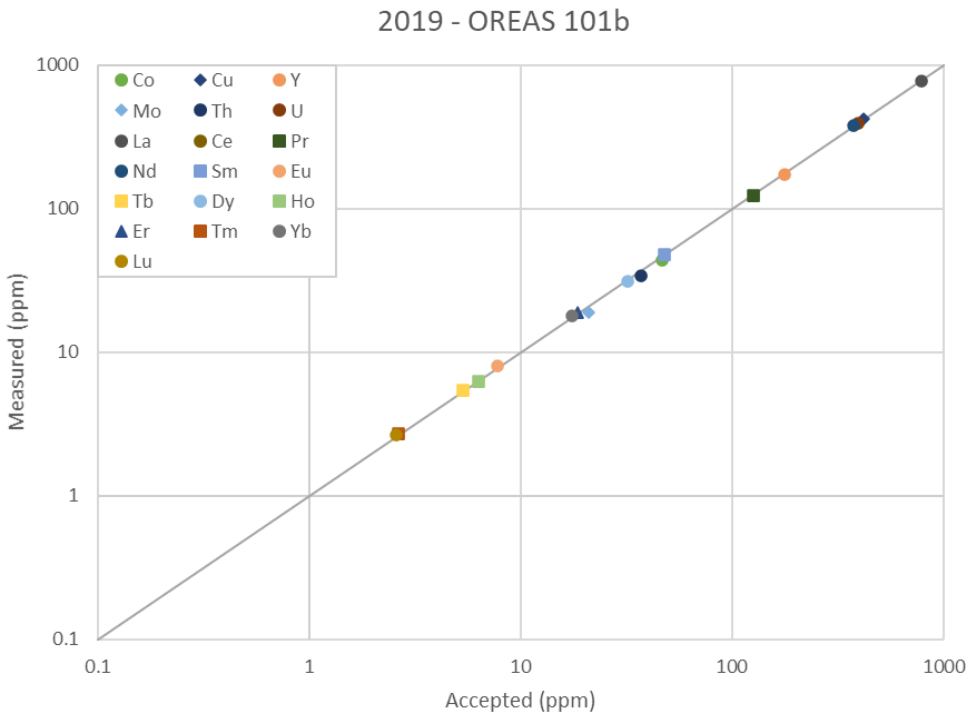

Figure B2.17. Measured trace element concentration results versus accepted values for reference material OREAS 101b.

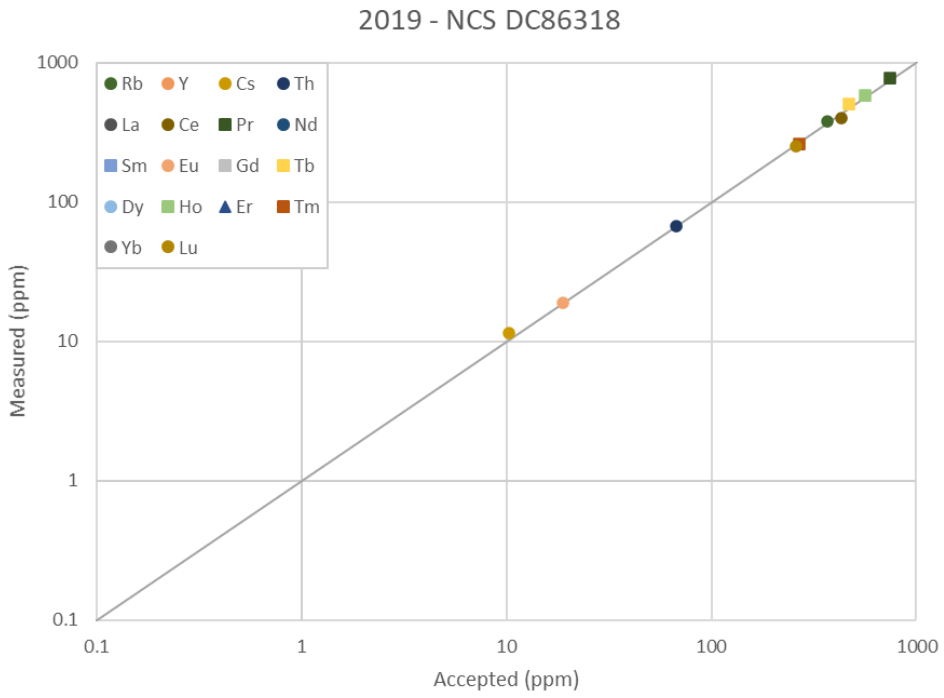

Figure B2.18. Measured trace element concentration results versus accepted values for reference material NCS DC86318.

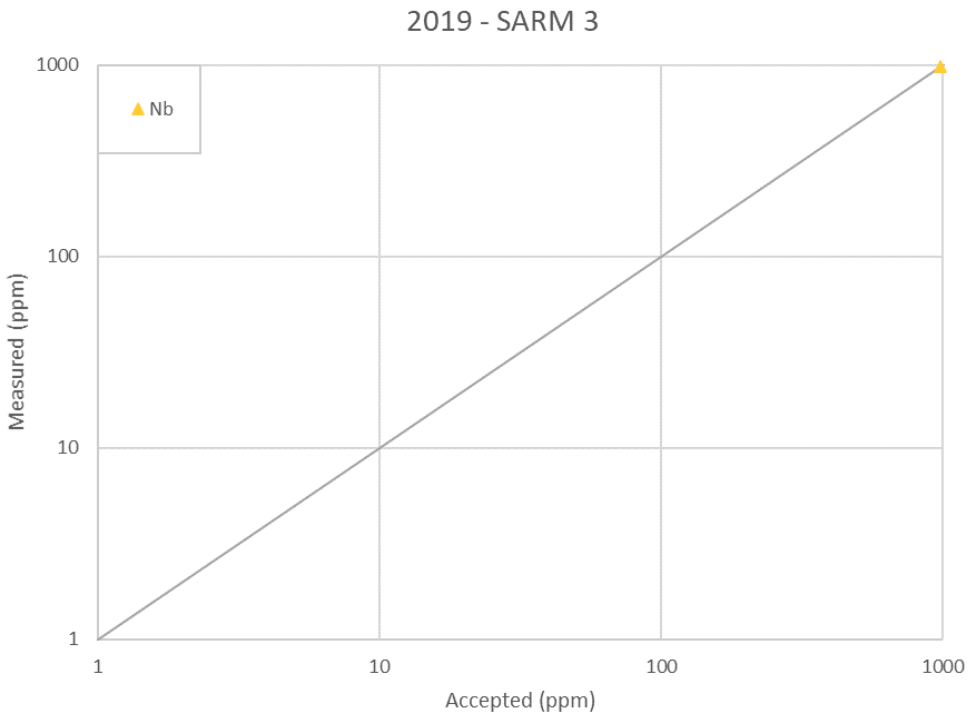

Figure B2.19. Measured trace element concentration results versus accepted values for reference material SARM 3.

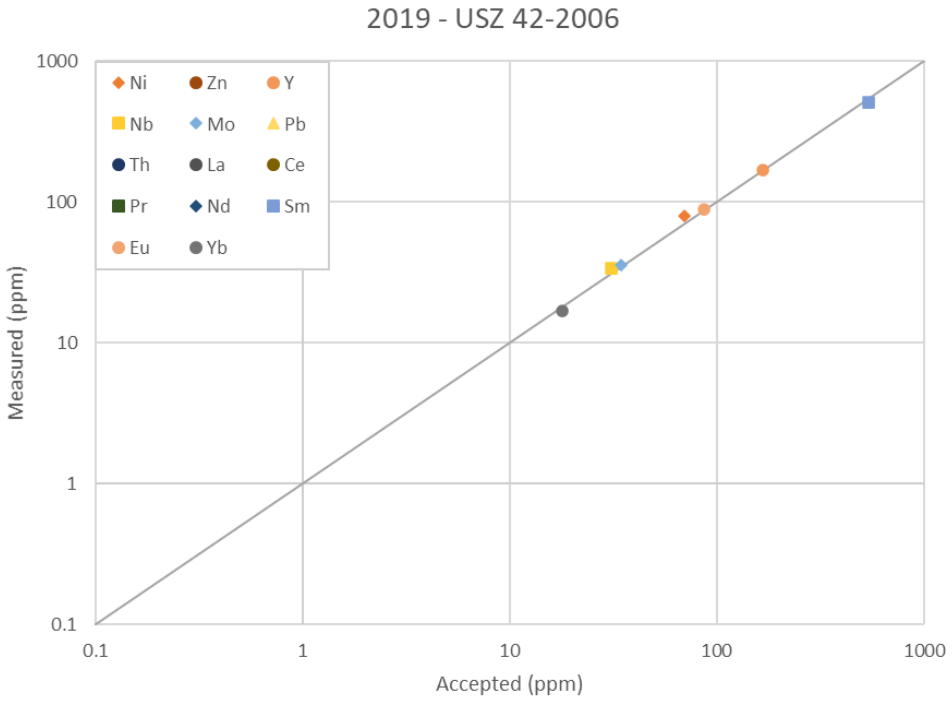

Figure B2.20. Measured trace element concentration results versus accepted values for reference material USZ 42-2006.

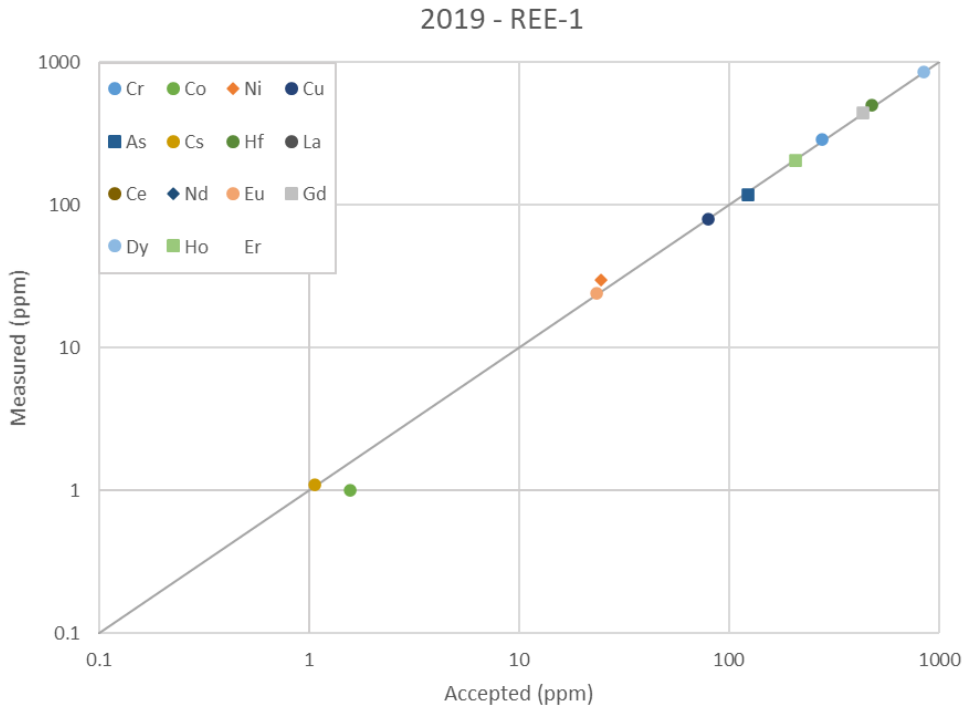

Figure B2.21. Measured trace element concentration results versus accepted values for reference material REE-1

Appendix B3. Whole rock geochemistry of Hogem batholith intrusive rock samples

Table B3.1. Whole rock major oxide (wt.%) results of Hogem batholith plutonic rock samples.

			Major oxides (wt.%)										
Sample	**Intrusive suite**	**Lithology**	**SiO_2**	**Al_2O_3**	**Fe_2O_3(T)**	**MnO**	**MgO**	**CaO**	**Na_2O**	**K_2O**	**TiO_2**	**P_2O_5**	**LOI**	**Total**
18lo22-1a	Thane Creek	hornblendite	40.99	13.04	17.61	0.215	10.27	10.23	1.46	1.87	1.790	0.23	1.26	98.97
18lo22-1d	Thane Creek	quartz diorite	54.19	18.14	8.53	0.161	3.46	7.59	3.75	1.7	0.717	0.37	1.51	100.1
19GJ12-4	Thane Creek	quartz diorite	53.46	17.75	8.98	0.154	3.91	8.23	4.08	1.79	0.760	0.41	0.81	100.3
19GJ13-3	Thane Creek	quartz monzodiorite	57.54	17.95	6.18	0.127	2.16	6.02	4.23	3.1	0.512	0.28	0.29	98.37
18lo25-2a	Duckling Creek	syenite	63.7	18.67	2.12	0.053	0.32	1.93	6.4	5.52	0.263	0.05	0.43	99.45
19GJ13-1	Duckling Creek	pyroxenite	35.65	8.36	22.77	0.300	9.19	19.16	0.56	1.14	1.981	1.3	0.23	100.6
19GJ13-2	Duckling Creek	syenite	60.43	20.5	1.41	0.039	0.09	0.71	4.08	10.41	0.123	0.02	0.7	98.52
19GJ13-4	Duckling Creek	Kspar phenocrystic syenite	52.38	17.67	7.64	0.193	2.57	6.63	4.03	5.84	0.676	0.43	1.79	99.85
19GJ13-5a	Duckling Creek	syenite	56.46	18.56	5.64	0.096	1.92	4.78	5.55	3.90	0.527	0.24	0.63	98.3
18lo17-1	Osilinka	granite	75.44	14.2	0.98	0.039	0.09	1.22	4.56	3.11	0.068	0.03	0.83	100.6
19GJ12-3	Osilinka	granite	73.11	14.93	1.16	0.033	0.15	1.54	5.23	2.95	0.085	0.03	0.82	100
18lo11-1	Mesilinka	equigranular granite	75.72	14.06	0.96	0.032	0.13	1.39	4.72	3.31	0.074	0.03	0.34	100.8
18lo12-7	Mesilinka	Kspar porphyritic granite	68.52	15.55	3.23	0.096	0.86	2.78	4.48	2.92	0.400	0.21	0.42	99.45
19GJ12-1	Mesilinka	tonalite	68.08	16.72	3.06	0.058	1.37	4.93	4.13	1.20	0.362	0.09	0.57	100.6
19GJ12-2	Mesilinka	tonalite	67.17	15.85	3.65	0.07	1.72	4.21	4.52	1.88	0.464	0.36	0.53	100.4
19GJ16-2	Mesilinka	equigranular granite	71.91	14.55	2.27	0.051	0.55	2.15	4.51	2.97	0.273	0.09	0.39	99.71

Table B3.2. Trace element results of Hogem batholith plutonic rock samples.

			Trace elements (ppm)														
Sample	**Intrusive suite**	**Lithology**	**Sc**	**Be**	**V**	**Cr**	**Co**	**Ni**	**Cu**	**Zn**	**Ga**	**Ge**	**As**	**Rb**	**Sr**	**Y**	**Zr**
18lo22-1a	Thane Creek	hornblendite	63	< 1	684	< 20	58	20	540	110	19	1.9	< 5	29	338	22.9	69
18lo22-1d	Thane Creek	quartz diorite	17	1	215	< 20	20	< 20	110	90	20	1.6	< 5	39	743	14.3	54
19GJ12-4	Thane Creek	quartz diorite	21	2	254	50	24	30	30	70	18	1.6	< 5	42	719	13.4	64
19GJ13-3	Thane Creek	quartz monzodiorite	10	2	145	< 20	14	< 20	20	60	18	1.3	< 5	66	815	12.6	118
18lo25-2a	Duckling Creek	syenite	2	< 1	59	< 20	3	< 20	< 10	< 30	16	1.2	< 5	66	2060	10.5	19
19GJ13-1	Duckling Creek	pyroxenite	54	1	709	50	63	40	< 10	140	19	2.0	< 5	31	394	22.9	47
19GJ13-2	Duckling Creek	syenite	1	2	59	< 20	1	< 20	110	< 30	16	1.1	< 5	168	2057	5.5	36
19GJ13-4	Duckling Creek	Kspar phenocrystic syenite	13	3	198	< 20	19	< 20	40	100	17	1.4	< 5	101	1580	18.4	70
19GJ13-5a	Duckling Creek	syenite	10	3	143	< 20	13	< 20	40	40	19	1.3	< 5	72	944	10.4	190
18lo17-1	Osilinka	granite	< 1	1	7	< 20	1	< 20	< 10	< 30	12	1.3	< 5	61	392	2.2	37
19GJ12-3	Osilinka	granite	1	2	11	< 20	1	< 20	< 10	< 30	16	0.9	< 5	49	661	1.3	45
18lo11-1	Mesilinka	equigranular granite	2	3	6	< 20	1	< 20	< 10	< 30	19	1.1	< 5	116	233	13.1	50
18lo12-7	Mesilinka	Kspar porphyritic granite	4	2	34	< 20	3	< 20	< 10	70	19	1.1	< 5	83	958	18.3	180
19GJ12-1	Mesilinka	tonalite	7	2	49	30	6	< 20	40	50	17	0.9	< 5	40	445	11.8	83
19GJ12-2	Mesilinka	tonalite	7	2	65	30	9	< 20	10	60	19	1.0	< 5	56	756	12.1	115
19GJ16-2	Mesilinka	equigranular granite	3	2	26	< 20	2	< 20	< 10	50	17	1.1	< 5	63	535	11.4	136

Table B3.2 continued.

			Trace elements (ppm)														
Sample	**Intrusive suite**	**Lithology**	**Nb**	**Mo**	**Ag**	**In**	**Sn**	**Sb**	**Cs**	**Ba**	**La**	**Ce**	**Pr**	**Nd**	**Sm**	**Eu**	**Gd**
18lo22-1a	Thane Creek	hornblendite	4.1	< 2	0.5	0.1	1	0.2	5.5	736	7.40	20.5	3.07	16.2	4.44	1.450	4.63
18lo22-1d	Thane Creek	quartz diorite	2.3	< 2	< 0.5	0.1	< 1	< 0.2	3.3	1360	11.7	24.0	3.06	13.4	3.24	1.140	3.13
19GJ12-4	Thane Creek	quartz diorite	3.3	< 2	< 0.5	< 0.1	1	< 0.2	1.2	1354	9.16	18.1	2.38	11.2	2.56	1.180	2.63
19GJ13-3	Thane Creek	quartz monzodiorite	4.3	< 2	< 0.5	< 0.1	1	< 0.2	0.7	2064	15.6	29.0	3.48	14.1	3.00	0.986	2.92
18lo25-2a	Duckling Creek	syenite	3.2	< 2	< 0.5	< 0.1	< 1	< 0.2	0.4	2749	10.7	23.0	2.92	11.7	2.56	0.845	2.15
19GJ13-1	Duckling Creek	pyroxenite	0.6	< 2	< 0.5	0.1	3	< 0.2	0.3	670	9.04	24.3	4.18	22.5	6.45	1.800	6.88
19GJ13-2	Duckling Creek	syenite	3.6	< 2	< 0.5	< 0.1	< 1	< 0.2	0.6	1365	5.52	10.2	1.36	5.86	1.07	0.359	0.93
19GJ13-4	Duckling Creek	Kspar phenocrystic syenite	5.3	< 2	< 0.5	0.1	1	0.2	0.6	1904	17.2	34.6	4.51	19.6	4.33	1.330	4.32
19GJ13-5a	Duckling Creek	syenite	2.7	< 2	< 0.5	< 0.1	1	< 0.2	0.6	2412	12.6	19.6	2.15	8.68	1.90	0.926	2.07
18lo17-1	Osilinka	granite	0.2	< 2	< 0.5	< 0.1	< 1	< 0.2	1.0	2645	1.60	2.78	0.33	1.33	0.27	0.075	0.27
19GJ12-3	Osilinka	granite	0.9	< 2	< 0.5	< 0.1	< 1	< 0.2	1.0	2270	2.18	3.24	0.35	1.19	0.22	0.088	0.18
18lo11-1	Mesilinka	equigranular granite	15.7	< 2	< 0.5	< 0.1	2	< 0.2	2.6	910	25.4	39.7	4.11	14	2.70	0.526	2.26
18lo12-7	Mesilinka	Kspar porphyritic granite	37.3	< 2	0.7	< 0.1	1	< 0.2	2.7	2751	98.1	160.0	15.9	51.7	7.23	1.770	4.57
19GJ12-1	Mesilinka	tonalite	7.8	< 2	< 0.5	< 0.1	1	0.4	1.6	583	5.84	10.9	1.35	6.13	1.57	0.562	1.9
19GJ12-2	Mesilinka	tonalite	15.8	< 2	< 0.5	< 0.1	1	< 0.2	3.2	1401	52.8	85.7	8.87	31.2	4.77	1.250	3.47
19GJ16-2	Mesilinka	equigranular granite	10.0	< 2	< 0.5	< 0.1	1	< 0.2	1.3	2219	41.8	66.5	6.79	22.9	3.44	0.847	2.54

Table B3.2 continued.

			Trace elements (ppm)							
Sample	**Intrusive suite**	**Lithology**	**Tb**	**Dy**	**Ho**	**Er**	**Tm**	**Yb**	**Lu**	**Hf**
18lo22-1a	Thane Creek	hornblendite	0.77	4.61	0.87	2.37	0.332	2.12	0.319	2.0
18lo22-1d	Thane Creek	quartz diorite	0.47	2.81	0.56	1.6	0.227	1.5	0.241	1.6
19GJ12-4	Thane Creek	quartz diorite	0.44	2.52	0.47	1.35	0.200	1.34	0.216	1.9
19GJ13-3	Thane Creek	quartz monzodiorite	0.42	2.44	0.46	1.37	0.205	1.37	0.230	3.1
18lo25-2a	Duckling Creek	syenite	0.34	2	0.4	1.11	0.154	0.88	0.138	0.5
19GJ13-1	Duckling Creek	pyroxenite	1.02	5.18	0.91	2.29	0.300	1.77	0.271	2.2
19GJ13-2	Duckling Creek	syenite	0.15	0.84	0.17	0.56	0.092	0.65	0.096	0.8
19GJ13-4	Duckling Creek	Kspar phenocrystic syenite	0.68	3.64	0.67	1.93	0.270	1.77	0.277	2.1
19GJ13-5a	Duckling Creek	syenite	0.29	1.77	0.36	1.12	0.181	1.26	0.203	4.4
18lo17-1	Osilinka	granite	0.05	0.33	0.07	0.24	0.046	0.35	0.068	1.1
19GJ12-3	Osilinka	granite	0.03	0.17	0.04	0.13	0.023	0.18	0.030	1.5
18lo11-1	Mesilinka	equigranular granite	0.37	2.06	0.4	1.27	0.190	1.31	0.190	1.7
18lo12-7	Mesilinka	Kspar porphyritic granite	0.6	3.28	0.65	1.76	0.248	1.7	0.267	4.0
19GJ12-1	Mesilinka	tonalite	0.37	2.12	0.43	1.26	0.181	1.15	0.181	2.0
19GJ12-2	Mesilinka	tonalite	0.49	2.46	0.42	1.18	0.172	1.06	0.153	2.8
19GJ16-2	Mesilinka	equigranular granite	0.35	1.94	0.38	1.11	0.159	1.05	0.175	3.3

Table B3.2 continued.

			Trace elements (ppm)						
Sample	**Intrusive suite**	**Lithology**	**Ta**	**W**	**Tl**	**Pb**	**Bi**	**Th**	**U**
18lo22-1a	Thane Creek	hornblendite	0.32	< 0.5	< 0.05	< 5	0.5	0.69	0.43
18lo22-1d	Thane Creek	quartz diorite	0.19	< 0.5	< 0.05	6	0.1	1.46	0.76
19GJ12-4	Thane Creek	quartz diorite	0.24	< 0.5	0.07	< 5	< 0.1	2.45	1.45
19GJ13-3	Thane Creek	quartz monzodiorite	0.33	< 0.5	0.30	< 5	< 0.1	3.59	1.87
18lo25-2a	Duckling Creek	syenite	0.30	< 0.5	< 0.05	8	< 0.1	0.73	0.31
19GJ13-1	Duckling Creek	pyroxenite	0.03	< 0.5	< 0.05	< 5	< 0.1	0.49	0.12
19GJ13-2	Duckling Creek	syenite	0.28	< 0.5	0.31	33	< 0.1	1.28	0.75
19GJ13-4	Duckling Creek	Kspar phenocrystic syenite	0.31	0.5	0.20	8	< 0.1	1.11	0.73
19GJ13-5a	Duckling Creek	syenite	0.14	< 0.5	0.17	< 5	< 0.1	1.67	1.19
18lo17-1	Osilinka	granite	0.10	< 0.5	< 0.05	12	0.1	0.11	0.07
19GJ12-3	Osilinka	granite	0.12	1.6	0.17	10	< 0.1	0.27	0.38
18lo11-1	Mesilinka	equigranular granite	2.38	1.0	0.80	23	< 0.1	16.0	10.4
18lo12-7	Mesilinka	Kspar porphyritic granite	2.03	< 0.5	0.37	15	< 0.1	21.3	4.15
19GJ12-1	Mesilinka	tonalite	0.73	< 0.5	0.36	7	< 0.1	2.22	1.66
19GJ12-2	Mesilinka	tonalite	1.34	< 0.5	0.56	11	0.1	11.1	5.71
19GJ16-2	Mesilinka	equigranular granite	0.84	< 0.5	0.58	16	< 0.1	13.7	4.36

Appendix C. Zircon SEM images and analytical spots

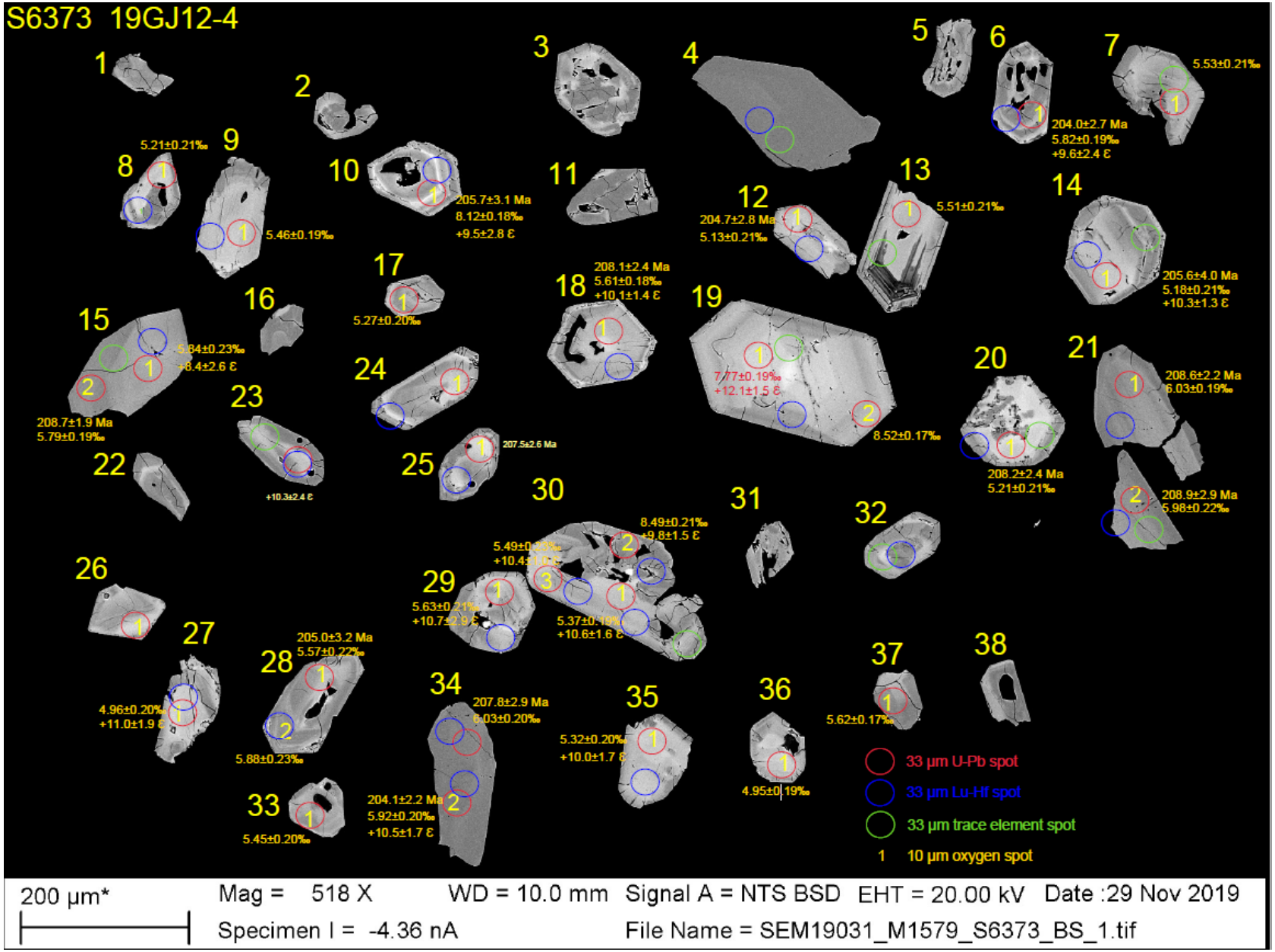
S6373 19GJ12-4
1
2
3
4
5
6
7
5.53±0.21‰
204.0±2.7 Ma
5.82±0.19‰
+9.6±2.4 ε
8
5.21±0.21‰
9
5.46±0.19‰
10
205.7±3.1 Ma
8.12±0.18‰
+9.5±2.8 ε
11
12
204.7±2.8 Ma
5.13±0.21‰
13
5.51±0.21‰
14
205.6±4.0 Ma
5.18±0.21‰
+10.3±1.3 ε
15
5.84±0.23‰
+8.4±2.6 ε
208.7±1.9 Ma
5.79±0.19‰
16
17
5.27±0.20‰
18
208.1±2.4 Ma
5.61±0.18‰
+10.1±1.4 ε
19
7.77±0.19‰
+12.1±1.5 ε
8.52±0.17‰
20
208.2±2.4 Ma
5.21±0.21‰
21
208.6±2.2 Ma
6.03±0.19‰
208.9±2.9 Ma
5.98±0.22‰
22
23
+10.3±2.4 ε
24
25
207.5±2.6 Ma
26
27
4.96±0.20‰
+11.0±1.9 ε
28
205.0±3.2 Ma
5.57±0.22‰
5.88±0.23‰
29
5.63±0.21‰
+10.7±2.9 ε
30
8.49±0.21‰
+9.8±1.5 ε
5.49±0.20‰
+10.4±1.0 ε
5.37±0.19‰
+10.6±1.6 ε
31
32
33
5.45±0.20‰
34
207.8±2.9 Ma
6.03±0.20‰
204.1±2.2 Ma
5.92±0.20‰
+10.5±1.7 ε
35
5.32±0.20‰
+10.0±1.7 ε
36
4.95±0.19‰
37
5.62±0.17‰
38
33 µm U-Pb spot
33 µm Lu-Hf spot
33 µm trace element spot
1 10 µm oxygen spot
200 µm*
Mag = 518 X
WD = 10.0 mm
Signal A = NTS BSD
EHT = 20.00 kV
Date :29 Nov 2019
Specimen I = -4.36 nA
File Name = SEM19031_M1579_S6373_BS_1.tif

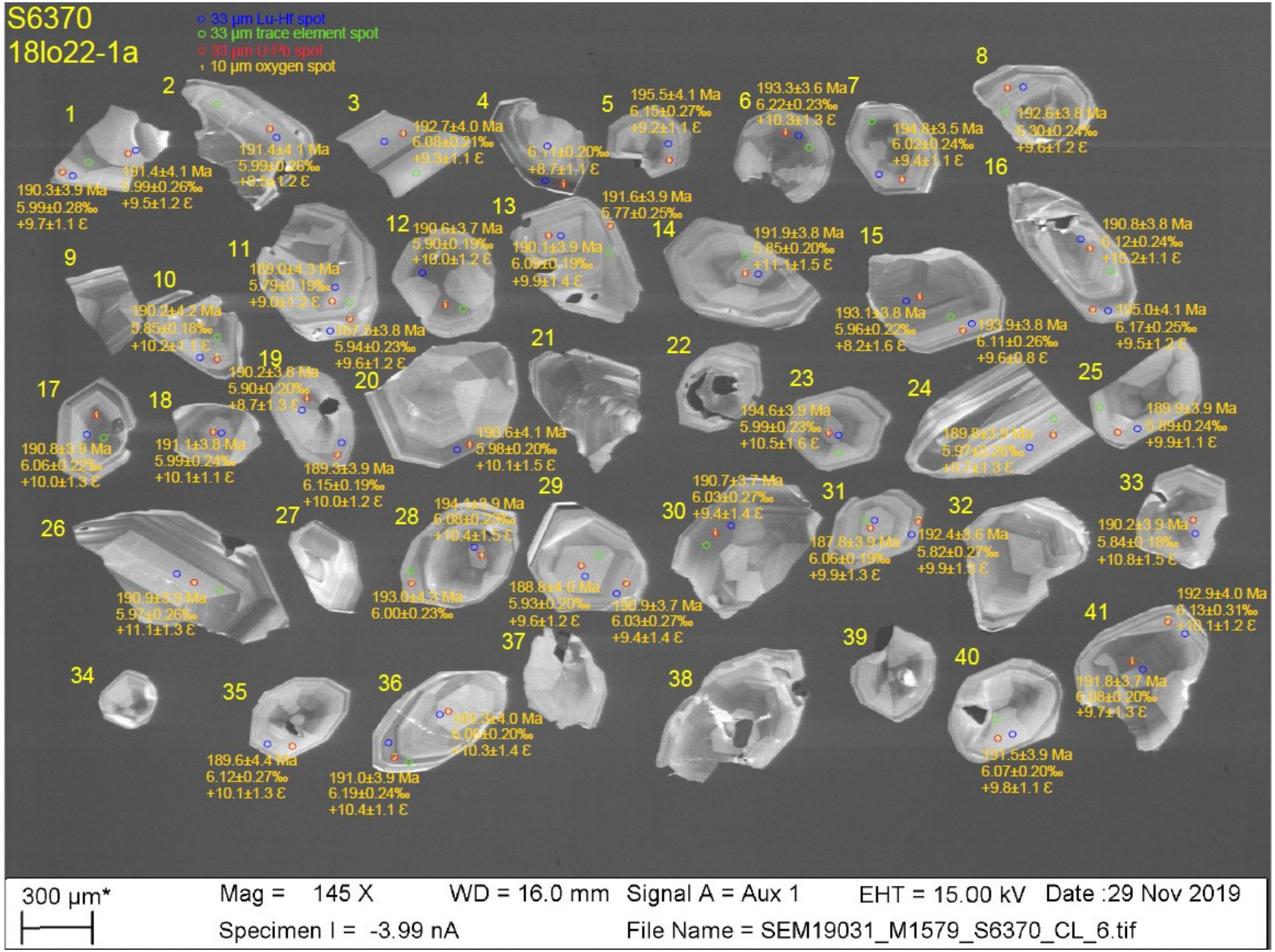
S6370
18lo22-1a
33 µm Lu-Hf spot
33 µm trace element spot
33 µm U-Pb spot
10 µm oxygen spot
1
190.3±3.9 Ma
5.99±0.28‰
+9.7±1.1 Ɛ
2
191.4±4.1 Ma
5.99±0.26‰
+9.5±1.2 Ɛ
3
191.4±4.1 Ma
5.99±0.26‰
+9.5±1.2 Ɛ
4
192.7±4.0 Ma
6.08±0.21‰
+9.3±1.1 Ɛ
5
195.5±4.1 Ma
6.15±0.27‰
+9.2±1.1 Ɛ
6
193.3±3.6 Ma
6.22±0.23‰
+10.3±1.3 Ɛ
7
194.8±3.5 Ma
6.02±0.24‰
+9.4±1.1 Ɛ
8
192.6±3.8 Ma
6.30±0.24‰
+9.6±1.2 Ɛ
9
10
190.2±4.2 Ma
5.85±0.18‰
+10.2±1.1 Ɛ
11
189.0±4.3 Ma
5.79±0.19‰
+9.0±1.2 Ɛ
12
190.6±3.7 Ma
5.90±0.19‰
+10.0±1.2 Ɛ
13
190.1±3.9 Ma
6.05±0.19‰
+9.9±1.4 Ɛ
14
191.6±3.9 Ma
5.77±0.25‰
15
191.9±3.8 Ma
5.85±0.20‰
+11.1±1.5 Ɛ
16
190.8±3.8 Ma
6.12±0.24‰
+10.2±1.1 Ɛ
17
190.8±3.9 Ma
6.06±0.22‰
+10.0±1.3 Ɛ
18
191.1±3.8 Ma
5.99±0.24‰
+10.1±1.1 Ɛ
19
190.2±3.8 Ma
5.90±0.20‰
+8.7±1.3 Ɛ
20
187.5±3.8 Ma
5.94±0.23‰
+9.6±1.2 Ɛ
21
190.6±4.1 Ma
5.98±0.20‰
+10.1±1.5 Ɛ
22
193.1±3.8 Ma
5.96±0.22‰
+8.2±1.6 Ɛ
23
194.6±3.9 Ma
5.99±0.23‰
+10.5±1.6 Ɛ
24
193.9±3.8 Ma
6.11±0.26‰
+9.6±0.8 Ɛ
25
195.0±4.1 Ma
6.17±0.25‰
+9.5±1.2 Ɛ
26
190.9±3.9 Ma
5.97±0.26‰
+11.1±1.3 Ɛ
27
189.3±3.9 Ma
6.15±0.19‰
+10.0±1.2 Ɛ
28
193.0±4.3 Ma
6.00±0.23‰
29
188.8±4.0 Ma
5.93±0.20‰
+9.6±1.2 Ɛ
30
190.7±3.7 Ma
6.03±0.27‰
+9.4±1.4 Ɛ
31
187.8±3.9 Ma
6.06±0.19‰
+9.9±1.3 Ɛ
32
192.4±3.6 Ma
5.82±0.27‰
+9.9±1.3 Ɛ
33
190.2±3.9 Ma
5.84±0.18‰
+10.8±1.5 Ɛ
34
35
189.6±4.4 Ma
6.12±0.27‰
+10.1±1.3 Ɛ
36
189.3±4.0 Ma
6.06±0.20‰
+10.3±1.4 Ɛ
37
191.0±3.9 Ma
6.19±0.24‰
+10.4±1.1 Ɛ
38
39
40
191.5±3.9 Ma
6.07±0.20‰
+9.8±1.1 Ɛ
41
191.8±3.7 Ma
6.08±0.20‰
+9.7±1.3 Ɛ
192.9±4.0 Ma
6.13±0.31‰
+10.1±1.2 Ɛ
300 µm*
Mag = 145 X
WD = 16.0 mm
Signal A = Aux 1
EHT = 15.00 kV
Date :29 Nov 2019
Specimen I = -3.99 nA
File Name = SEM19031_M1579_S6370_CL_6.tif

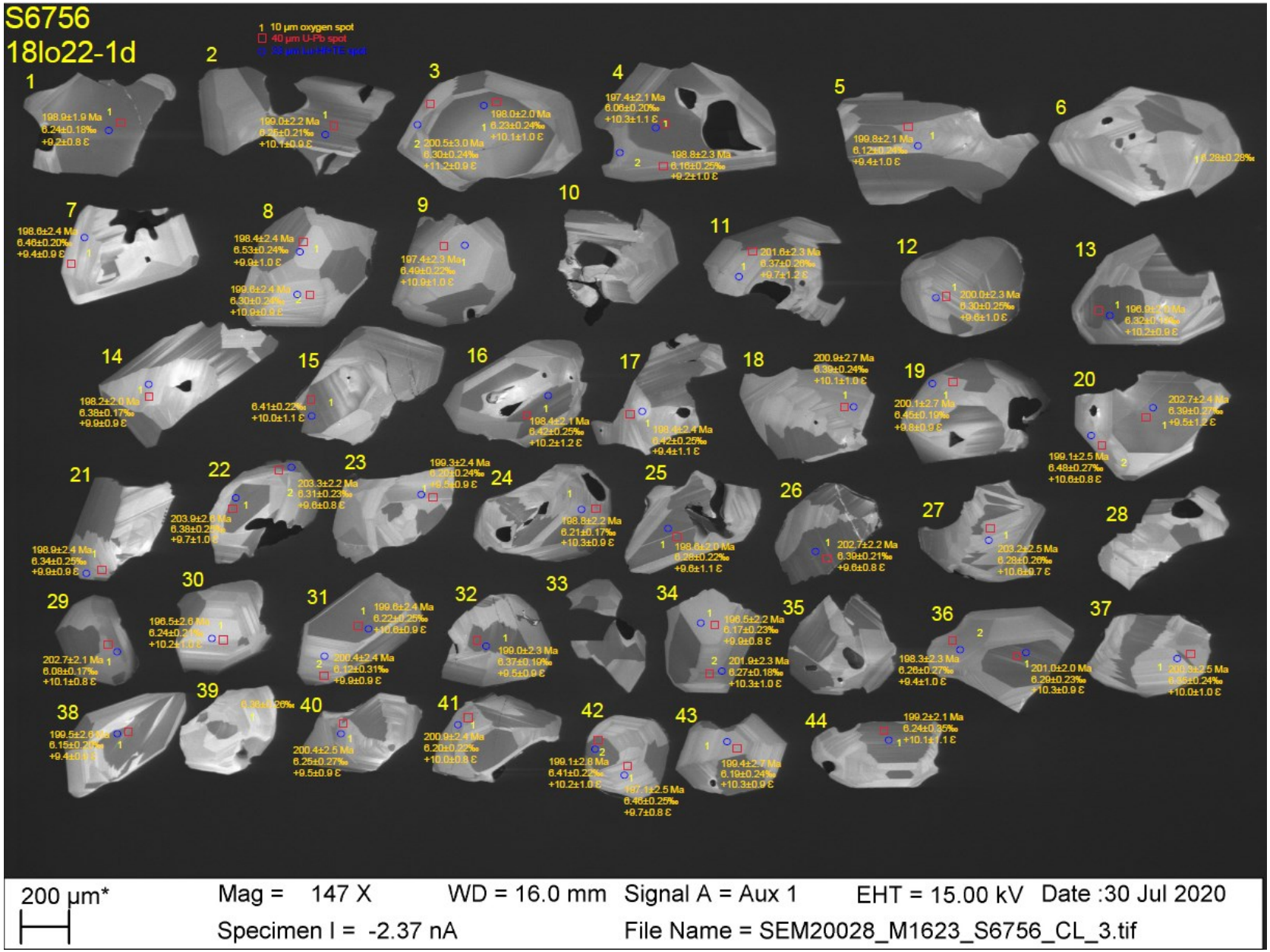
S6756
18lo22-1d
1 10 µm oxygen spot
40 µm U-Pb spot
33 µm LU-HREE spot
200 µm*
Mag = 147 X
WD = 16.0 mm
Signal A = Aux 1
EHT = 15.00 kV
Date :30 Jul 2020
Specimen I = -2.37 nA
File Name = SEM20028_M1623_S6756_CL_3.tif

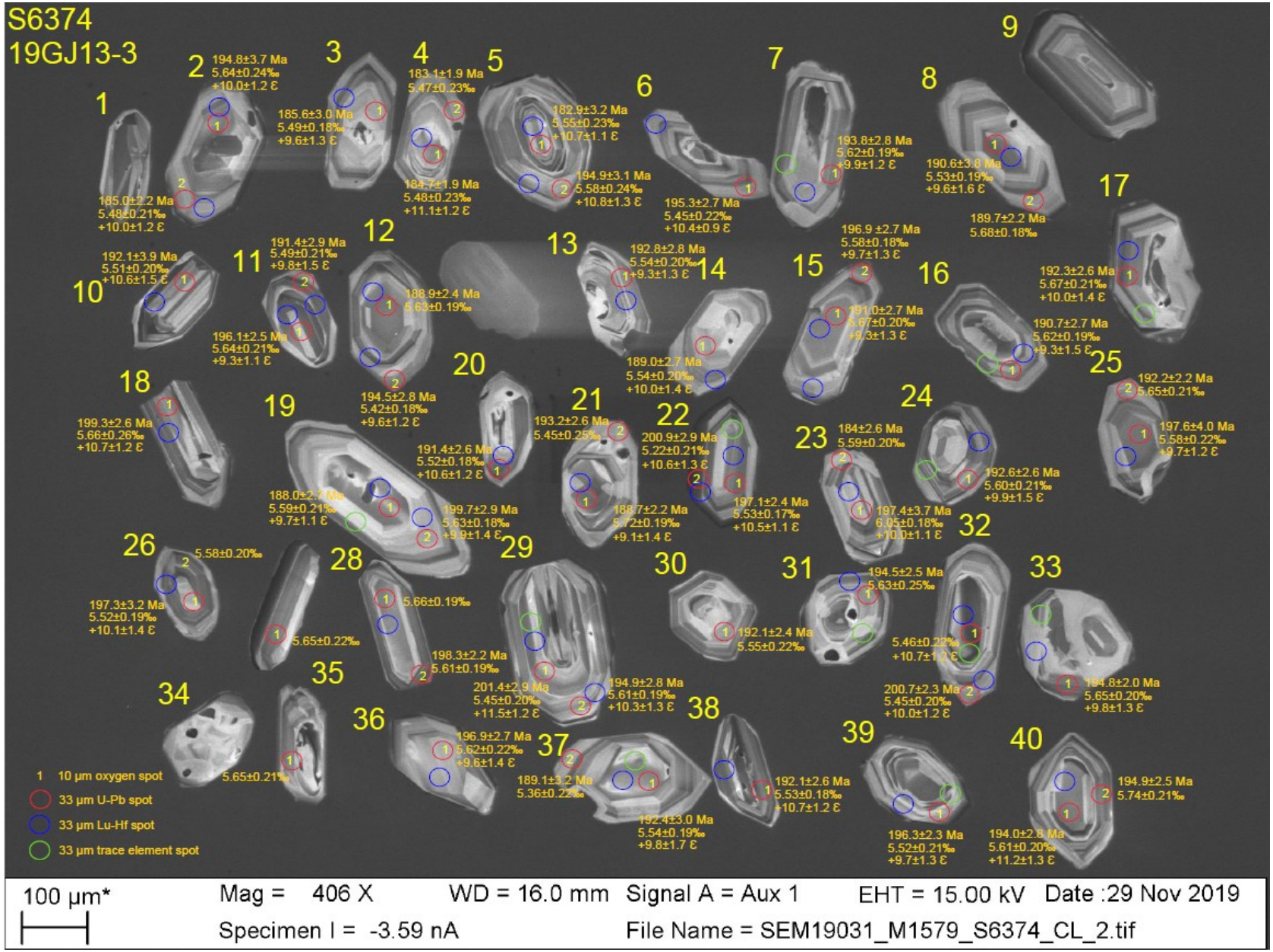
S6374
19GJ13-3
1
2 194.8±3.7 Ma 5.64±0.24‰ +10.0±1.2 ε
3
4 183.1±1.9 Ma 5.47±0.23‰
5
6
7
8
9
10
11 191.4±2.9 Ma 5.49±0.21‰ +9.8±1.5 ε
12
13
14
15
16
17
18
19
20
21
22
23
24
25
26
27
28
29
30
31
32
33
34
35
36
37
38
39
40
185.6±3.0 Ma 5.49±0.18‰ +9.6±1.3 ε
182.9±3.2 Ma 5.55±0.23‰ +10.7±1.1 ε
193.8±2.8 Ma 5.62±0.19‰ +9.9±1.2 ε
190.6±3.8 Ma 5.53±0.19‰ +9.6±1.6 ε
185.0±2.2 Ma 5.48±0.21‰ +10.0±1.2 ε
184.7±1.9 Ma 5.48±0.23‰ +11.1±1.2 ε
194.9±3.1 Ma 5.58±0.24‰ +10.8±1.3 ε
195.3±2.7 Ma 5.45±0.22‰ +10.4±0.9 ε
189.7±2.2 Ma 5.68±0.18‰
192.1±3.9 Ma 5.51±0.20‰ +10.6±1.5 ε
196.9 ±2.7 Ma 5.58±0.18‰ +9.7±1.3 ε
192.8±2.8 Ma 5.54±0.20‰ +9.3±1.3 ε
192.3±2.6 Ma 5.67±0.21‰ +10.0±1.4 ε
186.9±2.4 Ma 5.63±0.19‰
191.0±2.7 Ma 5.67±0.20‰ +9.3±1.3 ε
190.7±2.7 Ma 5.62±0.19‰ +9.3±1.5 ε
196.1±2.5 Ma 5.64±0.21‰ +9.3±1.1 ε
189.0±2.7 Ma 5.54±0.20‰ +10.0±1.4 ε
192.2±2.2 Ma 5.65±0.21‰
194.5±2.8 Ma 5.42±0.18‰ +9.6±1.2 ε
197.6±4.0 Ma 5.58±0.22‰ +9.7±1.2 ε
199.3±2.6 Ma 5.66±0.26‰ +10.7±1.2 ε
193.2±2.6 Ma 5.45±0.25‰
200.9±2.9 Ma 5.22±0.21‰ +10.6±1.3 ε
184±2.6 Ma 5.59±0.20‰
191.4±2.6 Ma 5.52±0.18‰ +10.6±1.2 ε
192.6±2.6 Ma 5.60±0.21‰ +9.9±1.5 ε
188.0±2.7 Ma 5.59±0.21‰ +9.7±1.1 ε
199.7±2.9 Ma 5.63±0.18‰ +9.9±1.4 ε
188.7±2.2 Ma 5.72±0.19‰ +9.1±1.4 ε
197.1±2.4 Ma 5.53±0.17‰ +10.5±1.1 ε
197.4±3.7 Ma 6.05±0.18‰ +10.0±1.1 ε
5.58±0.20‰
197.3±3.2 Ma 5.52±0.19‰ +10.1±1.4 ε
5.66±0.19‰
5.65±0.22‰
198.3±2.2 Ma 5.61±0.19‰
194.5±2.5 Ma 5.63±0.25‰
192.1±2.4 Ma 5.55±0.22‰
5.46±0.22‰ +10.7±1.2 ε
201.4±2.9 Ma 5.45±0.20‰ +11.5±1.2 ε
194.9±2.8 Ma 5.61±0.19‰ +10.3±1.3 ε
200.7±2.3 Ma 5.45±0.20‰ +10.0±1.2 ε
194.8±2.0 Ma 5.65±0.20‰ +9.8±1.3 ε
5.65±0.21‰
196.9±2.7 Ma 5.62±0.22‰ +9.6±1.4 ε
189.1±3.2 Ma 5.36±0.22‰
192.1±2.6 Ma 5.53±0.18‰ +10.7±1.2 ε
192.4±3.0 Ma 5.54±0.19‰ +9.8±1.7 ε
196.3±2.3 Ma 5.52±0.21‰ +9.7±1.3 ε
194.0±2.8 Ma 5.61±0.20‰ +11.2±1.3 ε
194.9±2.5 Ma 5.74±0.21‰
1 10 µm oxygen spot
33 µm U-Pb spot
33 µm Lu-Hf spot
33 µm trace element spot
100 µm*
Mag = 406 X
WD = 16.0 mm
Signal A = Aux 1
EHT = 15.00 kV
Date :29 Nov 2019
Specimen I = -3.59 nA
File Name = SEM19031_M1579_S6374_CL_2.tif

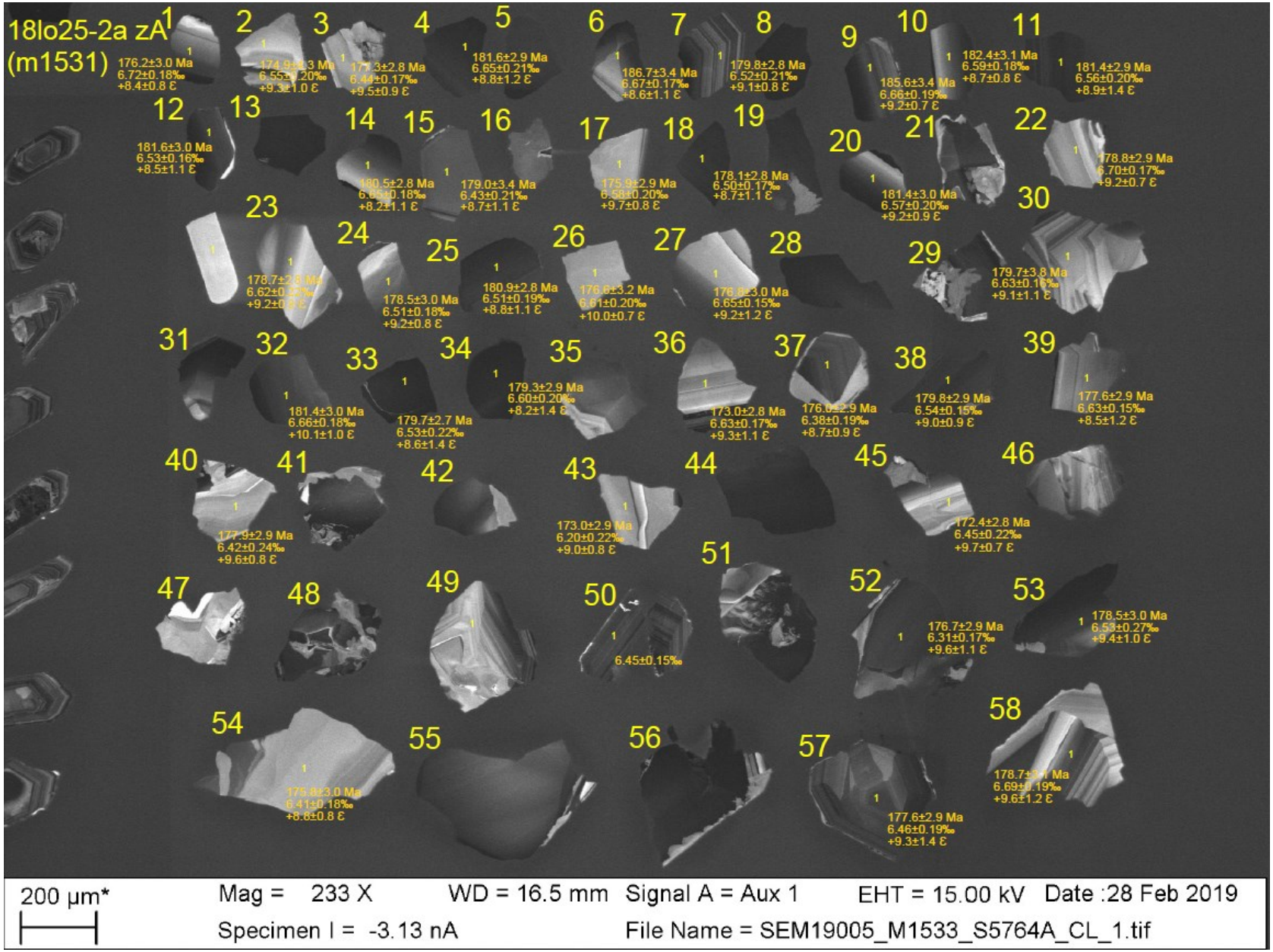
18lo25-2a zA
(m1531)
1 176.2±3.0 Ma 6.72±0.18‰ +8.4±0.8 ε
2
3
4
5 181.6±2.9 Ma 6.65±0.21‰ +8.8±1.2 ε
6
7 186.7±3.4 Ma 6.67±0.17‰ +8.6±1.1 ε
8 179.8±2.8 Ma 6.52±0.21‰ +9.1±0.8 ε
9
10 185.6±3.4 Ma 6.66±0.19‰ +9.2±0.7 ε
11 182.4±3.1 Ma 6.59±0.18‰ +8.7±0.8 ε
181.4±2.9 Ma 6.56±0.20‰ +8.9±1.4 ε
12 181.6±3.0 Ma 6.53±0.16‰ +8.5±1.1 ε
13
14 180.5±2.8 Ma 6.65±0.18‰ +8.2±1.1 ε
15 179.0±3.4 Ma 6.43±0.21‰ +8.7±1.1 ε
16
17 175.9±2.9 Ma 6.58±0.20‰ +9.7±0.8 ε
18
19 178.1±2.8 Ma 6.50±0.17‰ +8.7±1.1 ε
20 181.4±3.0 Ma 6.57±0.20‰ +9.2±0.9 ε
21
22 178.8±2.9 Ma 6.70±0.17‰ +9.2±0.7 ε
23
24
25 180.9±2.8 Ma 6.51±0.19‰ +8.8±1.1 ε
26 176.6±3.2 Ma 6.61±0.20‰ +10.0±0.7 ε
27
28 176.8±3.0 Ma 6.65±0.15‰ +9.2±1.2 ε
29 179.7±3.8 Ma 6.63±0.16‰ +9.1±1.1 ε
30
31
32 181.4±3.0 Ma 6.66±0.18‰ +10.1±1.0 ε
33 179.7±2.7 Ma 6.53±0.22‰ +8.6±1.4 ε
34
35 179.3±2.9 Ma 6.60±0.20‰ +8.2±1.4 ε
36 173.0±2.8 Ma 6.63±0.17‰ +9.3±1.1 ε
37 176.0±2.9 Ma 6.38±0.19‰ +8.7±0.9 ε
38 179.8±2.9 Ma 6.54±0.15‰ +9.0±0.9 ε
39 177.6±2.9 Ma 6.63±0.15‰ +8.5±1.2 ε
40 177.9±2.9 Ma 6.42±0.24‰ +9.6±0.8 ε
41
42
43 173.0±2.9 Ma 6.20±0.22‰ +9.0±0.8 ε
44
45 172.4±2.8 Ma 6.45±0.22‰ +9.7±0.7 ε
46
47
48
49
50 6.45±0.15‰
51
52 176.7±2.9 Ma 6.31±0.17‰ +9.6±1.1 ε
53 178.5±3.0 Ma 6.53±0.27‰ +9.4±1.0 ε
54 175.8±3.0 Ma 6.41±0.18‰ +8.8±0.8 ε
55
56
57 177.6±2.9 Ma 6.46±0.19‰ +9.3±1.4 ε
58 178.7±3.1 Ma 6.69±0.19‰ +9.6±1.2 ε
200 µm*
Mag = 233 X
WD = 16.5 mm
Signal A = Aux 1
EHT = 15.00 kV
Date :28 Feb 2019
Specimen I = -3.13 nA
File Name = SEM19005_M1533_S5764A_CL_1.tif

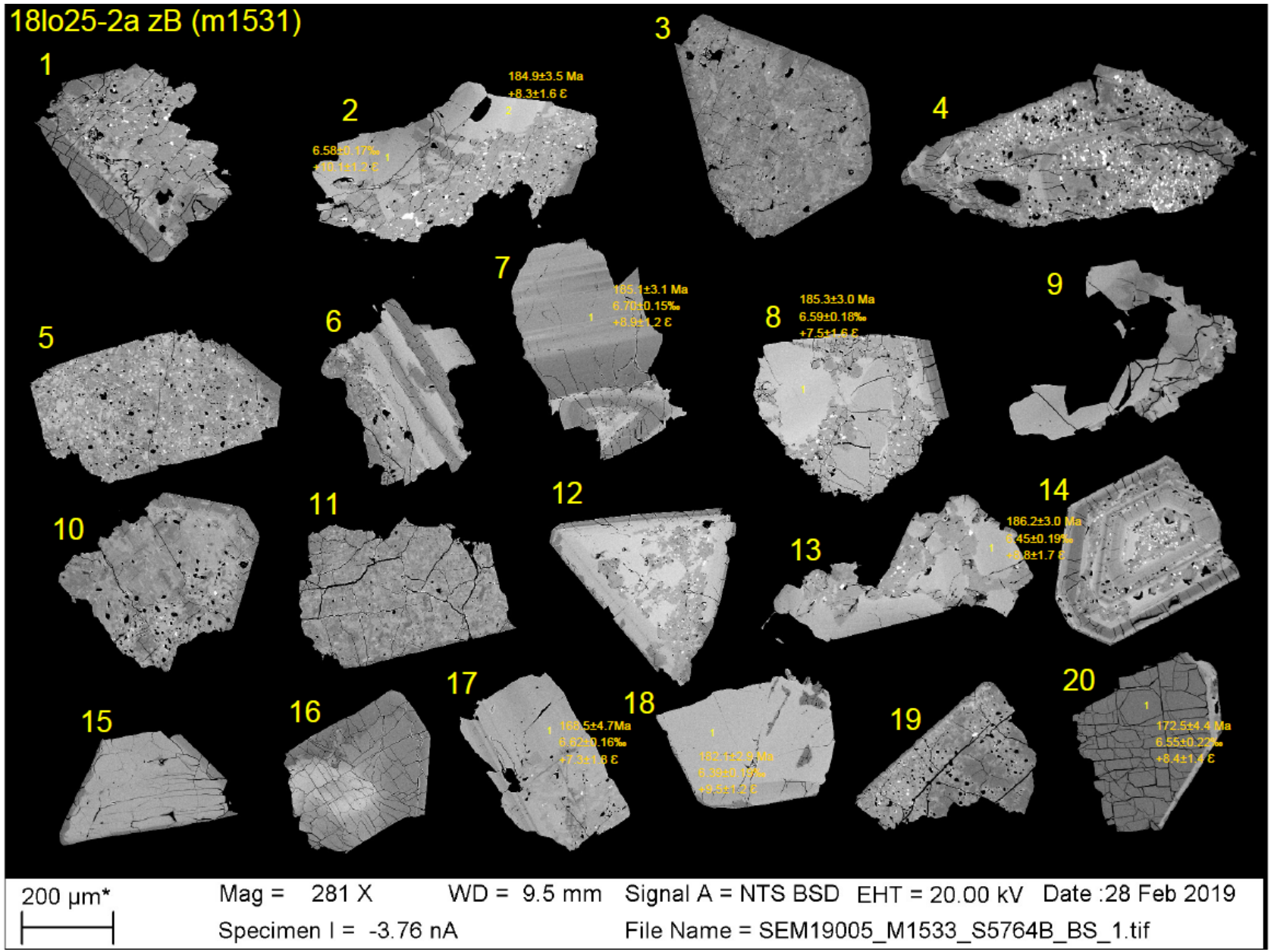
18lo25-2a zB (m1531)
1
2
184.9±3.5 Ma
+8.3±1.6 ε
6.58±0.17‰
+10.1±1.2 ε
3
4
5
6
7
185.1±3.1 Ma
6.70±0.15‰
+8.9±1.2 ε
8
185.3±3.0 Ma
6.59±0.18‰
+7.5±1.6 ε
9
10
11
12
13
14
186.2±3.0 Ma
6.45±0.19‰
+8.8±1.7 ε
15
16
17
168.5±4.7Ma
6.62±0.16‰
+7.3±1.8 ε
18
182.1±2.9 Ma
6.38±0.16‰
+9.5±1.2 ε
19
20
172.5±4.4 Ma
6.55±0.22‰
+8.4±1.4 ε
200 µm*
Mag = 281 X
WD = 9.5 mm
Signal A = NTS BSD
EHT = 20.00 kV
Date :28 Feb 2019
Specimen I = -3.76 nA
File Name = SEM19005_M1533_S5764B_BS_1.tif

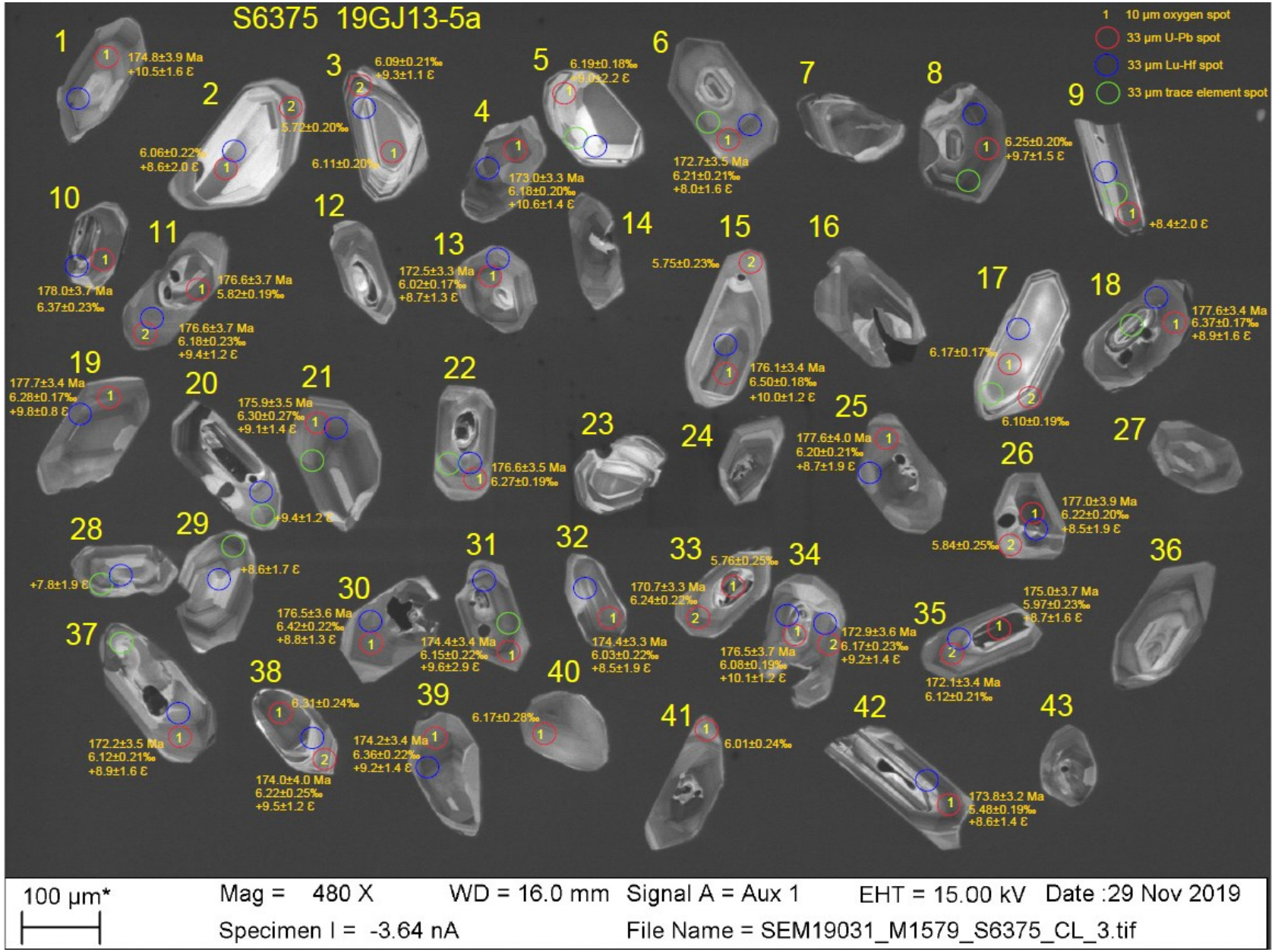
S6375 19GJ13-5a
1 10 µm oxygen spot
33 µm U-Pb spot
33 µm Lu-Hf spot
33 µm trace element spot
1 174.8±3.9 Ma +10.5±1.6 ε
2 5.72±0.20‰ 6.06±0.22‰ +8.6±2.0 ε
3 6.09±0.21‰ +9.3±1.1 ε 6.11±0.20‰
4 173.0±3.3 Ma 6.18±0.20‰ +10.6±1.4 ε
5 6.19±0.18‰ +9.0±2.2 ε
6 172.7±3.5 Ma 6.21±0.21‰ +8.0±1.6 ε
7
8 6.25±0.20‰ +9.7±1.5 ε
9 +8.4±2.0 ε
10 178.0±3.7 Ma 6.37±0.23‰
11 176.6±3.7 Ma 5.82±0.19‰ 176.6±3.7 Ma 6.18±0.23‰ +9.4±1.2 ε
12
13 172.5±3.3 Ma 6.02±0.17‰ +8.7±1.3 ε
14
15 5.75±0.23‰ 176.1±3.4 Ma 6.50±0.18‰ +10.0±1.2 ε
16
17 6.17±0.17‰ 6.10±0.19‰
18 177.6±3.4 Ma 6.37±0.17‰ +8.9±1.6 ε
19 177.7±3.4 Ma 6.28±0.17‰ +9.8±0.8 ε
20 +9.4±1.2 ε
21 175.9±3.5 Ma 6.30±0.27‰ +9.1±1.4 ε
22 176.6±3.5 Ma 6.27±0.19‰
23
24
25 177.6±4.0 Ma 6.20±0.21‰ +8.7±1.9 ε
26 177.0±3.9 Ma 6.22±0.20‰ +8.5±1.9 ε 5.84±0.25‰
27
28 +7.8±1.9 ε
29 +8.6±1.7 ε
30 176.5±3.6 Ma 6.42±0.22‰ +8.8±1.3 ε 174.4±3.4 Ma 6.15±0.22‰ +9.6±2.9 ε
31
32 174.4±3.3 Ma 6.03±0.22‰ +8.5±1.9 ε
33 5.76±0.25‰ 170.7±3.3 Ma 6.24±0.22‰
34 176.5±3.7 Ma 6.08±0.19‰ +10.1±1.2 ε 172.9±3.6 Ma 6.17±0.23‰ +9.2±1.4 ε
35 175.0±3.7 Ma 5.97±0.23‰ +8.7±1.6 ε 172.1±3.4 Ma 6.12±0.21‰
36
37 172.2±3.5 Ma 6.12±0.21‰ +8.9±1.6 ε
38 6.31±0.24‰ 174.0±4.0 Ma 6.22±0.25‰ +9.5±1.2 ε
39 174.2±3.4 Ma 6.36±0.22‰ +9.2±1.4 ε
40 6.17±0.28‰
41 6.01±0.24‰
42 173.8±3.2 Ma 5.48±0.19‰ +8.6±1.4 ε
43
100 µm*
Mag = 480 X WD = 16.0 mm Signal A = Aux 1 EHT = 15.00 kV Date :29 Nov 2019
Specimen I = -3.64 nA File Name = SEM19031_M1579_S6375_CL_3.tif

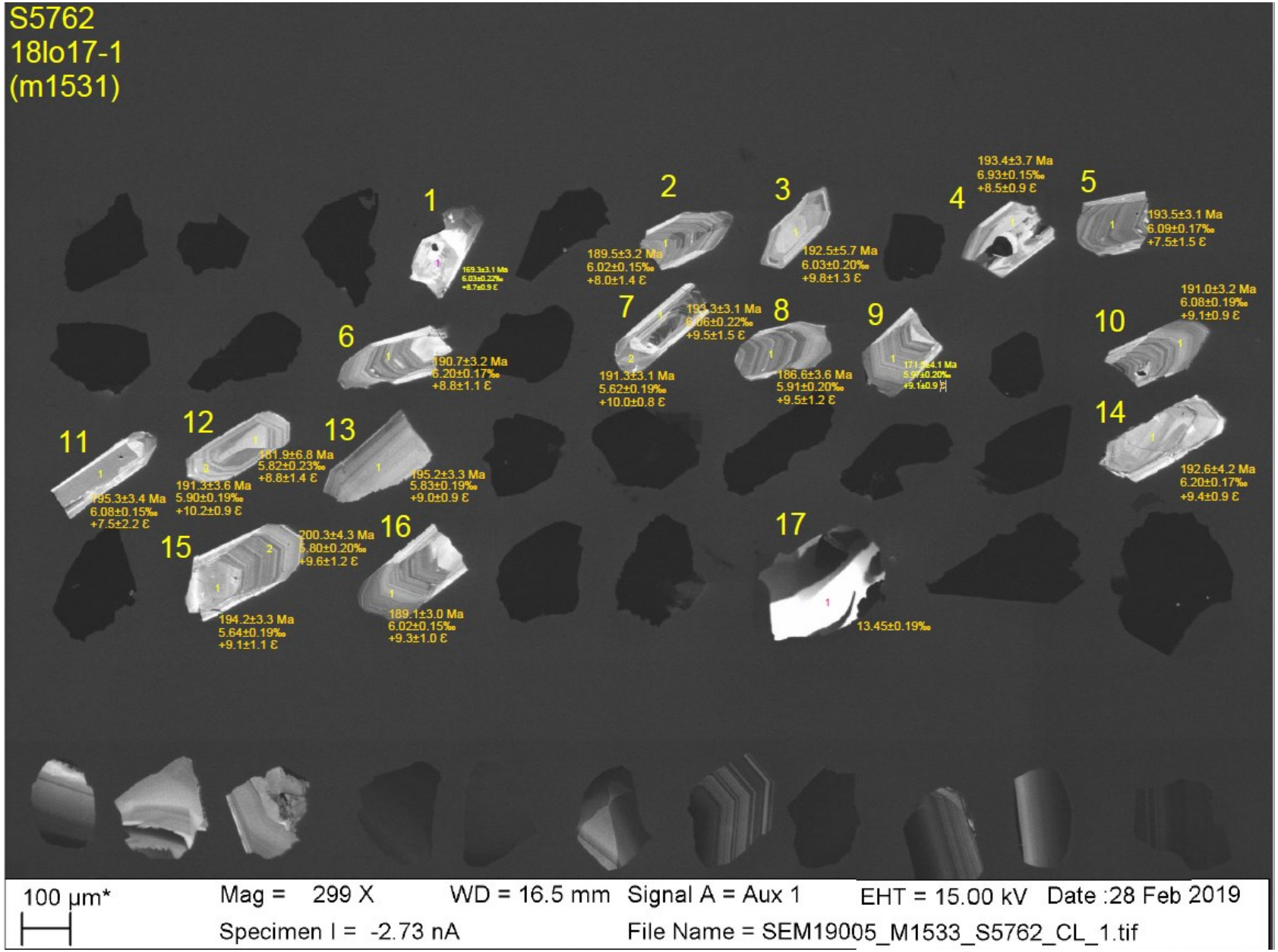
S5762
18lo17-1
(m1531)
1
2
189.5±3.2 Ma
6.02±0.15‰
+8.0±1.4 ε
3
192.5±5.7 Ma
6.03±0.20‰
+9.8±1.3 ε
4
193.4±3.7 Ma
6.93±0.15‰
+8.5±0.9 ε
5
193.5±3.1 Ma
6.09±0.17‰
+7.5±1.5 ε
6
190.7±3.2 Ma
6.20±0.17‰
+8.8±1.1 ε
7
193.3±3.1 Ma
191.3±3.1 Ma
5.62±0.19‰
+10.0±0.8 ε
8
186.6±3.6 Ma
5.91±0.20‰
+9.5±1.2 ε
9
10
191.0±3.2 Ma
6.08±0.19‰
+9.1±0.9 ε
11
195.3±3.4 Ma
6.08±0.15‰
+7.5±2.2 ε
12
191.3±3.6 Ma
5.90±0.19‰
+10.2±0.9 ε
181.9±6.8 Ma
5.82±0.23‰
+8.8±1.4 ε
13
195.2±3.3 Ma
5.83±0.19‰
+9.0±0.9 ε
14
192.6±4.2 Ma
6.20±0.17‰
+9.4±0.9 ε
15
200.3±4.3 Ma
5.80±0.20‰
+9.6±1.2 ε
194.2±3.3 Ma
5.64±0.19‰
+9.1±1.1 ε
16
189.1±3.0 Ma
6.02±0.15‰
+9.3±1.0 ε
17
13.45±0.19‰
100 µm*
Mag = 299 X
WD = 16.5 mm
Signal A = Aux 1
EHT = 15.00 kV
Date :28 Feb 2019
Specimen I = -2.73 nA
File Name = SEM19005_M1533_S5762_CL_1.tif

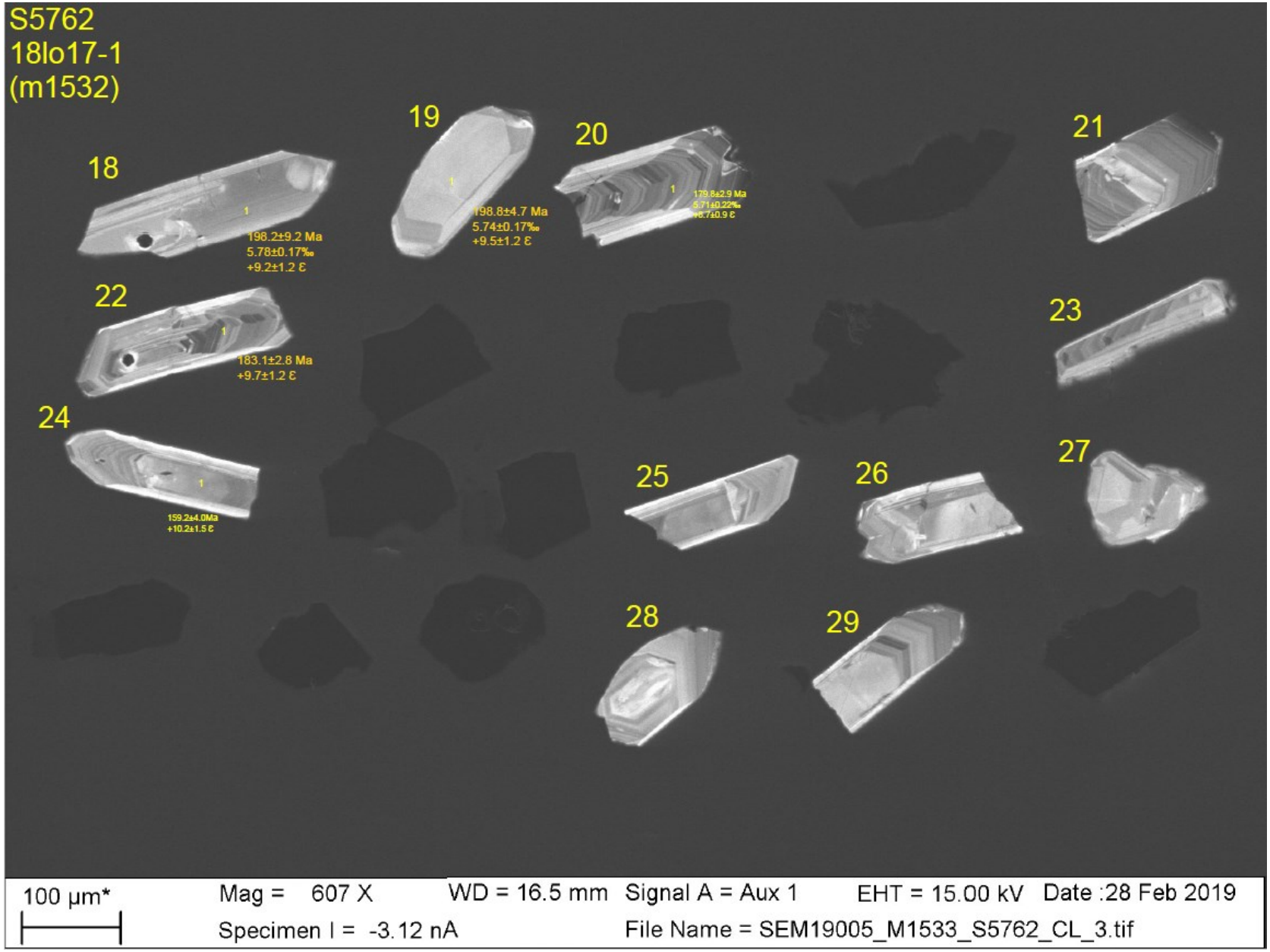
S5762
18lo17-1
(m1532)
18
198.2±9.2 Ma
5.78±0.17‰
+9.2±1.2 ε
19
198.8±4.7 Ma
5.74±0.17‰
+9.5±1.2 ε
20
179.8±2.9 Ma
5.71±0.22‰
+8.7±0.9 ε
21
22
183.1±2.8 Ma
+9.7±1.2 ε
23
24
159.2±4.0Ma
+10.2±1.5 ε
25
26
27
28
29
100 µm*
Mag = 607 X
WD = 16.5 mm
Signal A = Aux 1
EHT = 15.00 kV
Date :28 Feb 2019
Specimen I = -3.12 nA
File Name = SEM19005_M1533_S5762_CL_3.tif

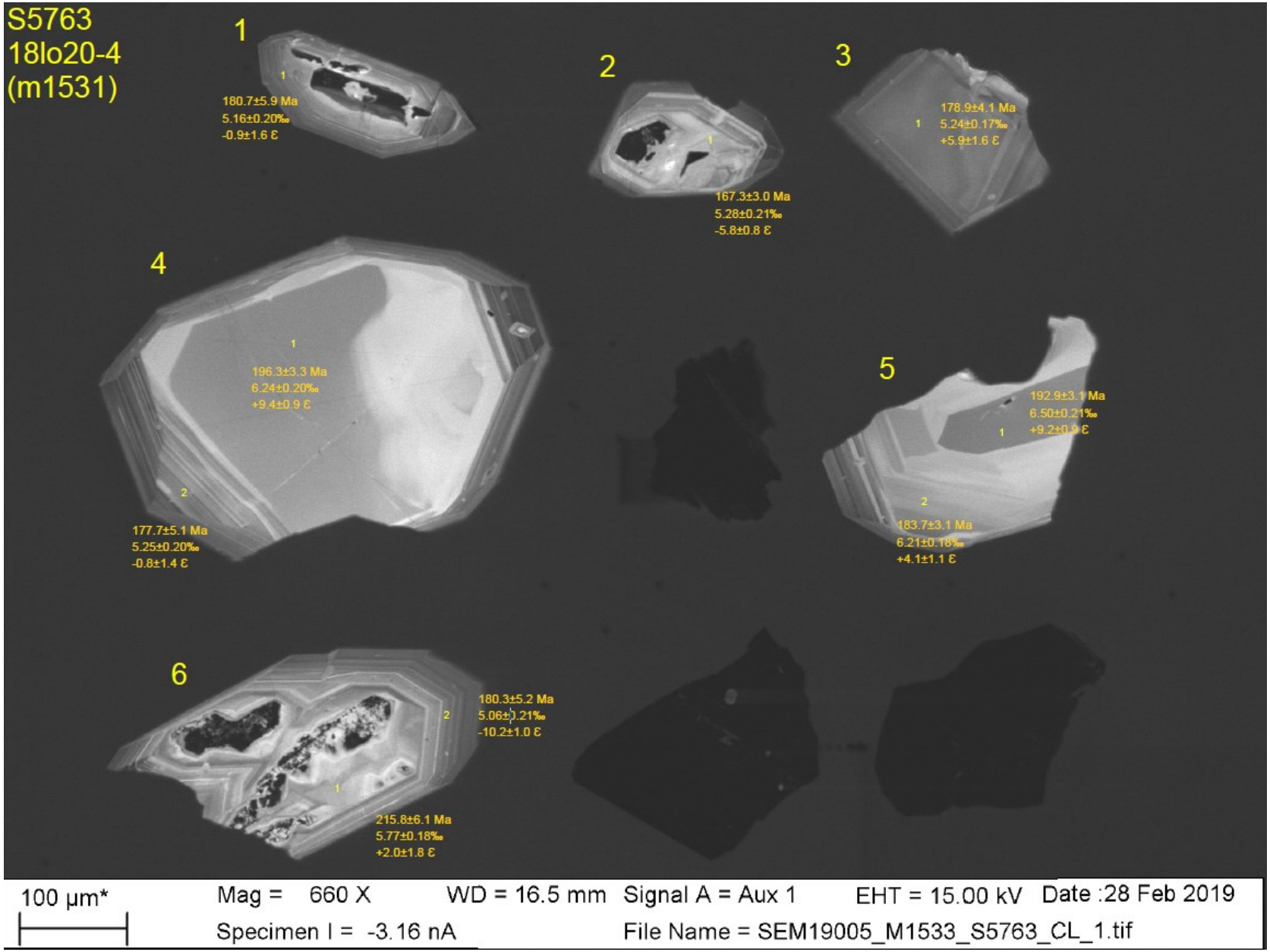
S5763
18lo20-4
(m1531)
1
180.7±5.9 Ma
5.16±0.20‰
-0.9±1.6 ε
2
167.3±3.0 Ma
5.28±0.21‰
-5.8±0.8 ε
3
178.9±4.1 Ma
5.24±0.17‰
+5.9±1.6 ε
4
196.3±3.3 Ma
6.24±0.20‰
+9.4±0.9 ε
177.7±5.1 Ma
5.25±0.20‰
-0.8±1.4 ε
5
192.9±3.1 Ma
6.50±0.21‰
+9.2±0.9 ε
183.7±3.1 Ma
6.21±0.18‰
+4.1±1.1 ε
6
180.3±5.2 Ma
5.06±0.21‰
-10.2±1.0 ε
215.8±6.1 Ma
5.77±0.18‰
+2.0±1.8 ε
100 µm*
Mag = 660 X
WD = 16.5 mm
Signal A = Aux 1
EHT = 15.00 kV
Date :28 Feb 2019
Specimen I = -3.16 nA
File Name = SEM19005_M1533_S5763_CL_1.tif

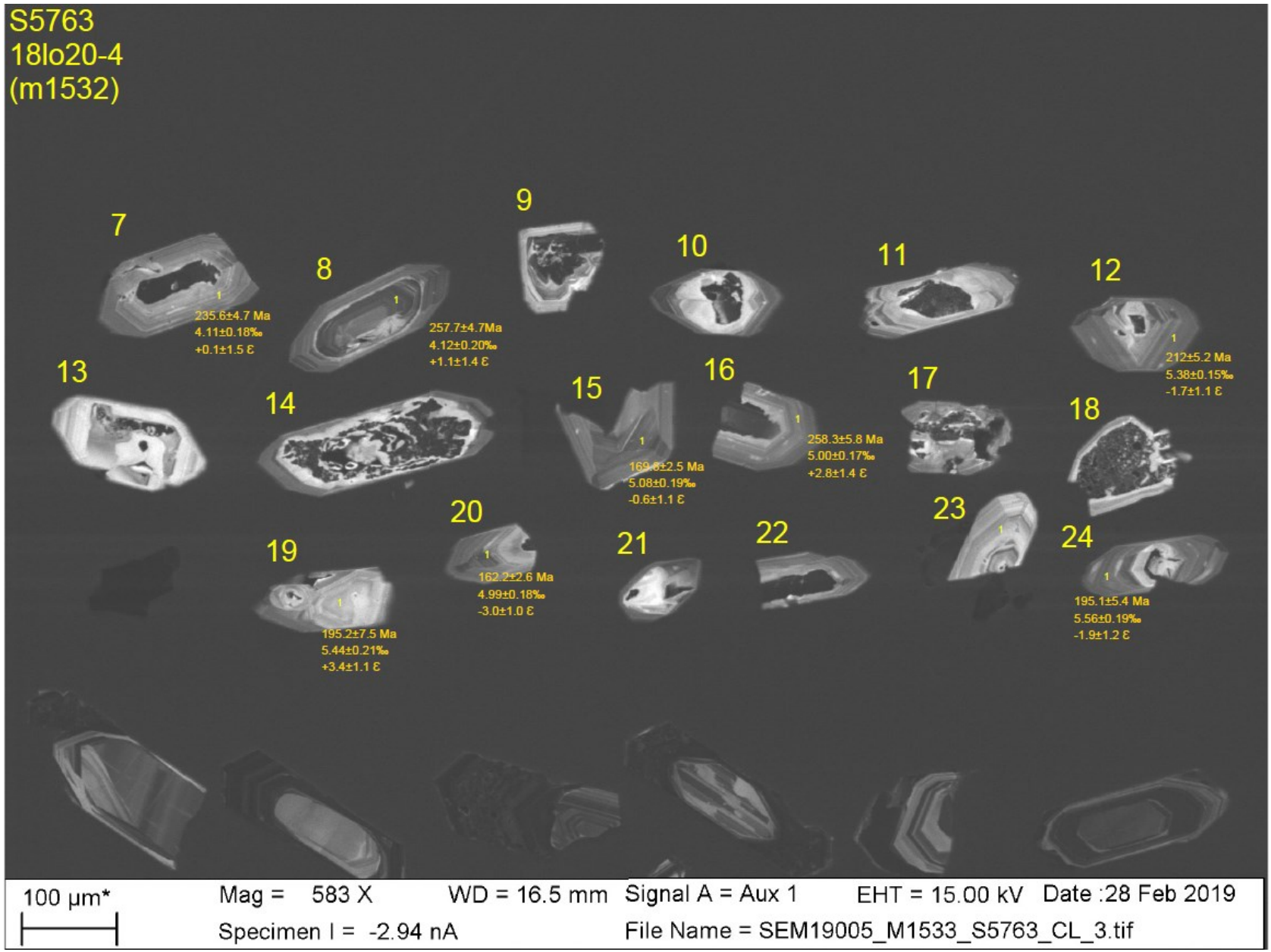
S5763
18lo20-4
(m1532)
7
235.6±4.7 Ma
4.11±0.18‰
+0.1±1.5 ε
8
257.7±4.7Ma
4.12±0.20‰
+1.1±1.4 ε
9
10
11
12
212±5.2 Ma
5.38±0.15‰
-1.7±1.1 ε
13
14
15
169.6±2.5 Ma
5.08±0.19‰
-0.6±1.1 ε
16
258.3±5.8 Ma
5.00±0.17‰
+2.8±1.4 ε
17
18
19
195.2±7.5 Ma
5.44±0.21‰
+3.4±1.1 ε
20
162.2±2.6 Ma
4.99±0.18‰
-3.0±1.0 ε
21
22
23
24
195.1±5.4 Ma
5.56±0.19‰
-1.9±1.2 ε
100 µm*
Mag = 583 X
WD = 16.5 mm
Signal A = Aux 1
EHT = 15.00 kV
Date :28 Feb 2019
Specimen I = -2.94 nA
File Name = SEM19005_M1533_S5763_CL_3.tif

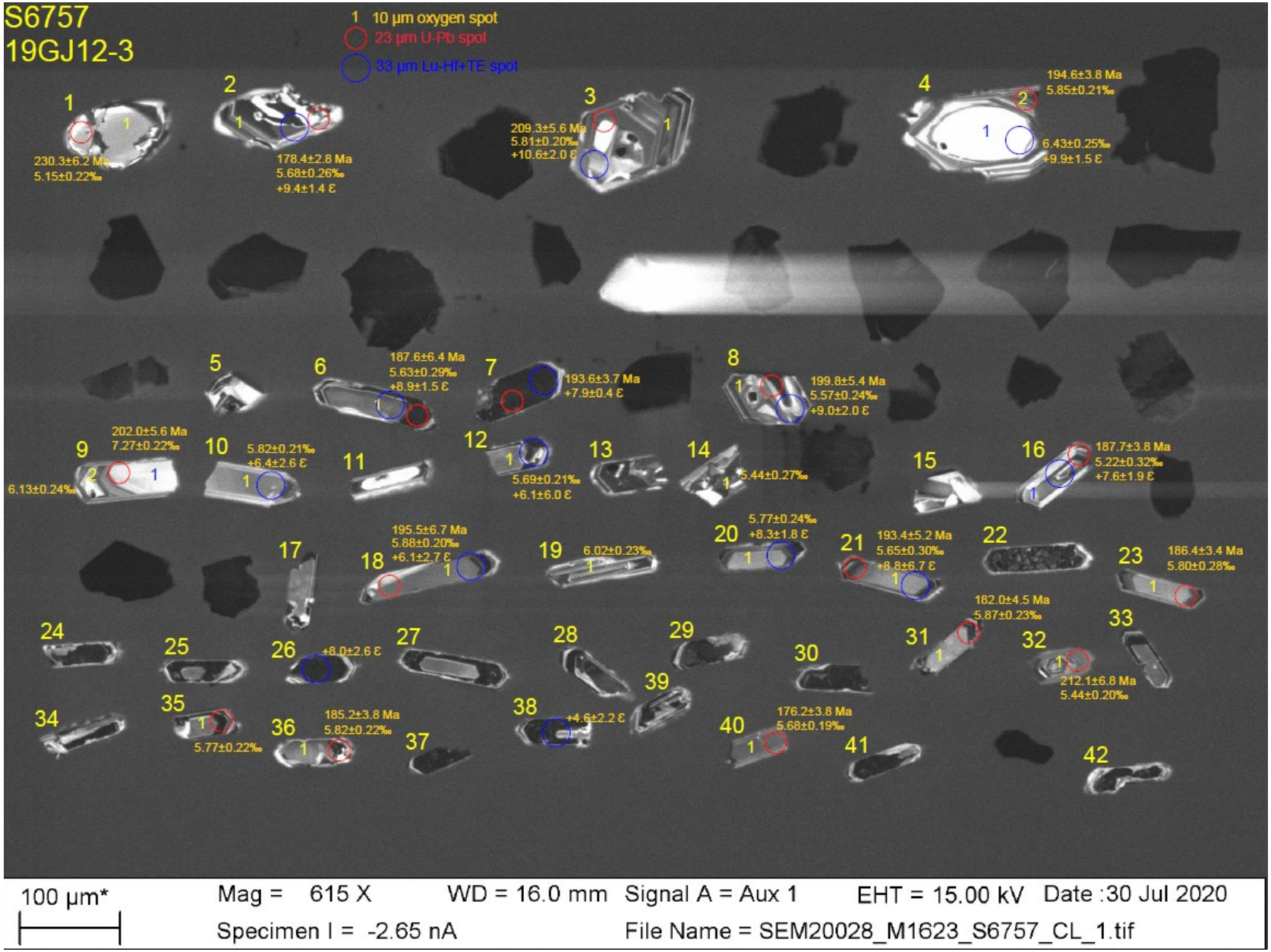
S6757
19GJ12-3
1 10 µm oxygen spot
23 µm U-Pb spot
33 µm Lu-Hf+TE spot
1
230.3±6.2 Ma
5.15±0.22‰
2
178.4±2.8 Ma
5.68±0.26‰
+9.4±1.4 ε
3
209.3±5.6 Ma
5.81±0.20‰
+10.6±2.0 ε
4
194.6±3.8 Ma
5.85±0.21‰
6.43±0.25‰
+9.9±1.5 ε
5
6
187.6±6.4 Ma
5.63±0.29‰
+8.9±1.5 ε
7
193.6±3.7 Ma
+7.9±0.4 ε
8
199.8±5.4 Ma
5.57±0.24‰
+9.0±2.0 ε
9
202.0±5.6 Ma
7.27±0.22‰
6.13±0.24‰
10
5.82±0.21‰
+6.4±2.6 ε
11
12
5.69±0.21‰
+6.1±6.0 ε
13
14
5.44±0.27‰
15
16
187.7±3.8 Ma
5.22±0.32‰
+7.6±1.9 ε
17
18
195.5±6.7 Ma
5.88±0.20‰
+6.1±2.7 ε
19
6.02±0.23‰
20
5.77±0.24‰
+8.3±1.8 ε
21
193.4±5.2 Ma
5.65±0.30‰
+8.8±6.7 ε
22
23
186.4±3.4 Ma
5.80±0.28‰
24
25
26
+8.0±2.6 ε
27
28
29
30
31
182.0±4.5 Ma
5.87±0.23‰
32
212.1±6.8 Ma
5.44±0.20‰
33
34
35
5.77±0.22‰
36
185.2±3.8 Ma
5.82±0.22‰
37
38
+4.6±2.2 ε
39
40
176.2±3.8 Ma
5.68±0.19‰
41
42
100 µm*
Mag = 615 X
WD = 16.0 mm
Signal A = Aux 1
EHT = 15.00 kV
Date :30 Jul 2020
Specimen I = -2.65 nA
File Name = SEM20028_M1623_S6757_CL_1.tif

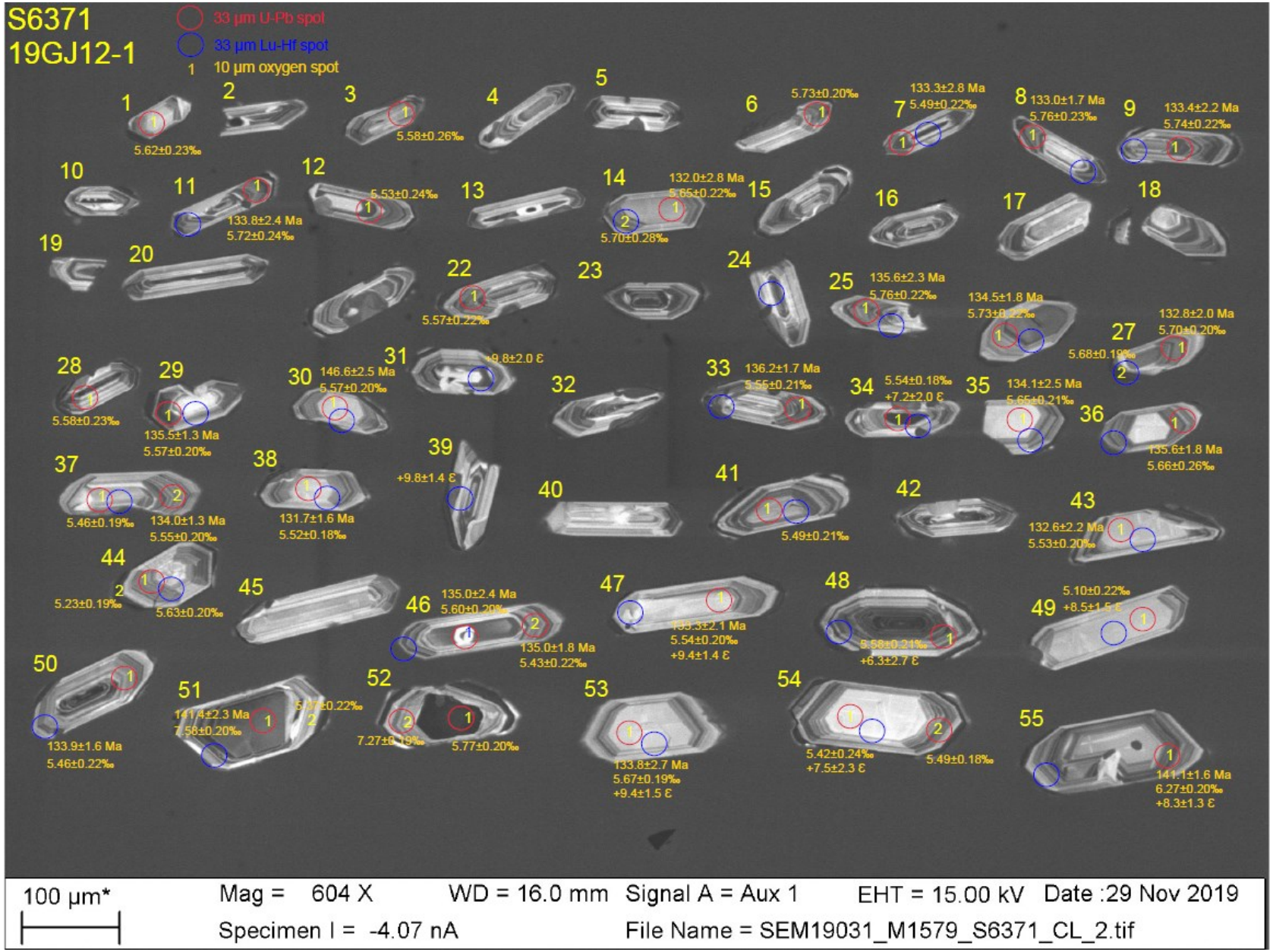
S6371
19GJ12-1
33 µm U-Pb spot
33 µm Lu-Hf spot
1 10 µm oxygen spot
1
5.62±0.23‰
2
3
5.58±0.26‰
4
5
6
5.73±0.20‰
7
133.3±2.8 Ma
5.49±0.22‰
8
133.0±1.7 Ma
5.76±0.23‰
9
133.4±2.2 Ma
5.74±0.22‰
10
11
133.8±2.4 Ma
5.72±0.24‰
12
5.53±0.24‰
13
14
132.0±2.8 Ma
5.65±0.22‰
5.70±0.28‰
15
16
17
18
19
20
22
5.57±0.22‰
23
24
25
135.6±2.3 Ma
5.76±0.22‰
134.5±1.8 Ma
5.73±0.22‰
27
132.8±2.0 Ma
5.70±0.20‰
5.68±0.19‰
28
5.58±0.23‰
29
135.5±1.3 Ma
5.57±0.20‰
30
146.6±2.5 Ma
5.57±0.20‰
31
+9.8±2.0 ε
32
33
136.2±1.7 Ma
5.55±0.21‰
34
5.54±0.18‰
+7.2±2.0 ε
35
134.1±2.5 Ma
5.65±0.21‰
36
135.6±1.8 Ma
5.66±0.26‰
37
5.46±0.19‰
134.0±1.3 Ma
5.55±0.20‰
38
131.7±1.6 Ma
5.52±0.18‰
39
+9.8±1.4 ε
40
41
5.49±0.21‰
42
43
132.6±2.2 Ma
5.53±0.20‰
44
5.23±0.19‰
5.63±0.20‰
45
46
135.0±2.4 Ma
5.60±0.20‰
135.0±1.8 Ma
5.43±0.22‰
47
135.3±2.1 Ma
5.54±0.20‰
+9.4±1.4 ε
48
5.58±0.21‰
+6.3±2.7 ε
49
5.10±0.22‰
+8.5±1.5 ε
50
133.9±1.6 Ma
5.46±0.22‰
51
141.4±2.3 Ma
7.58±0.20‰
52
7.27±0.19‰
5.77±0.20‰
53
133.8±2.7 Ma
5.67±0.19‰
+9.4±1.5 ε
54
5.42±0.24‰
+7.5±2.3 ε
5.49±0.18‰
55
141.1±1.6 Ma
6.27±0.20‰
+8.3±1.3 ε
100 µm*
Mag = 604 X
WD = 16.0 mm
Signal A = Aux 1
EHT = 15.00 kV
Date :29 Nov 2019
Specimen I = -4.07 nA
File Name = SEM19031_M1579_S6371_CL_2.tif

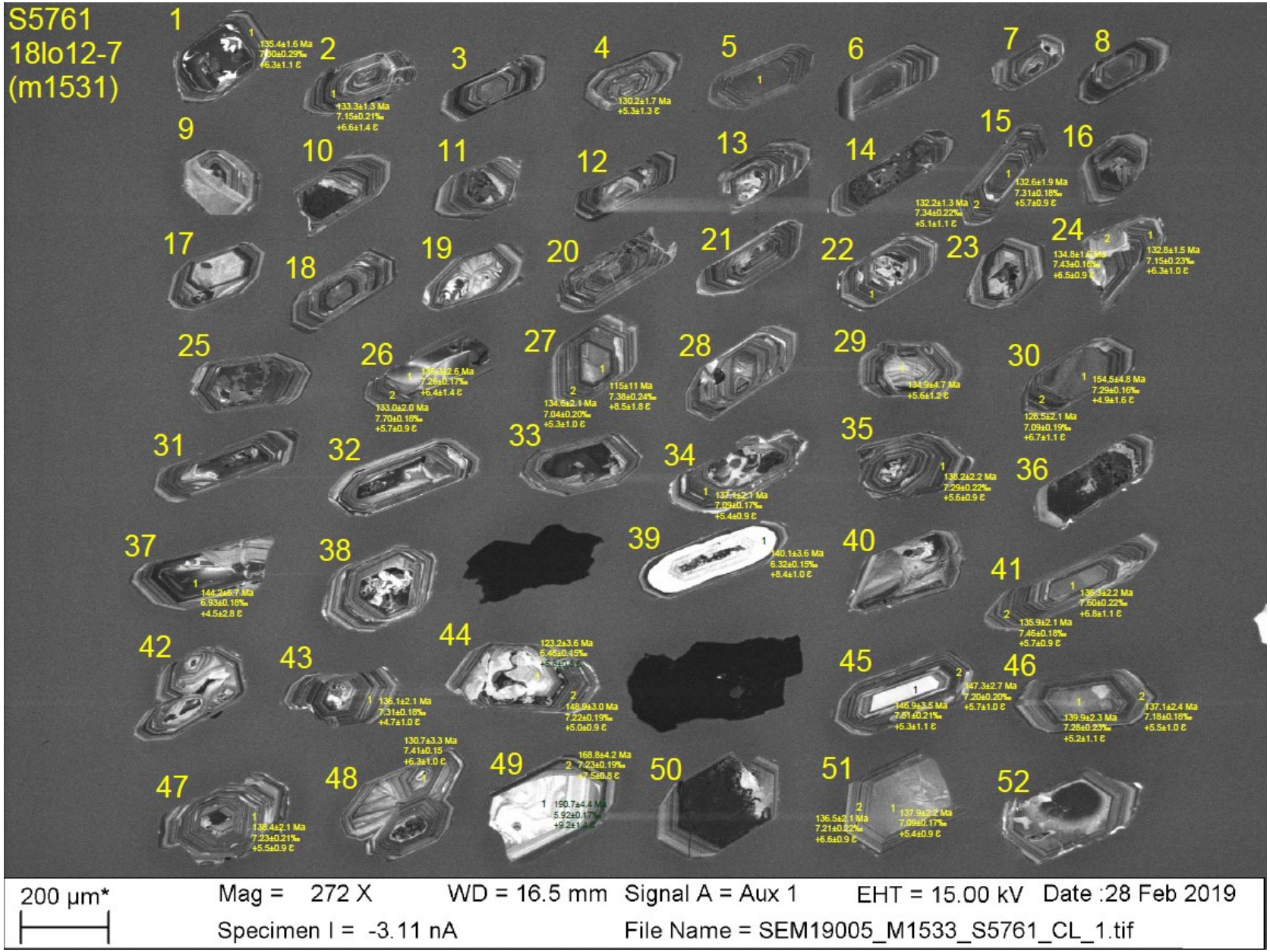
S5761
18lo12-7
(m1531)
1
135.4±1.6 Ma
7.00±0.29‰
+6.3±1.1 ε
2
+33.3±1.3 Ma
7.15±0.21‰
+6.6±1.4 ε
3
4
130.2±1.7 Ma
+5.3±1.3 ε
5
6
7
8
9
10
11
12
13
14
15
132.6±1.9 Ma
7.31±0.18‰
+5.7±0.9 ε
132.2±1.3 Ma
7.34±0.22‰
+5.1±1.1 ε
16
17
18
19
20
21
22
23
24
134.8±1.6 Ma
7.43±0.16‰
+6.5±0.9 ε
132.8±1.5 Ma
7.15±0.23‰
+6.3±1.0 ε
25
26
133.0±2.0 Ma
7.70±0.18‰
+5.7±0.9 ε
27
115±11 Ma
7.38±0.24‰
+8.5±1.8 ε
134.6±2.1 Ma
7.04±0.20‰
+5.3±1.0 ε
28
29
134.9±4.7 Ma
+5.6±1.2 ε
30
154.5±4.8 Ma
7.29±0.16‰
+4.9±1.6 ε
126.5±2.1 Ma
7.09±0.19‰
+6.7±1.1 ε
31
32
33
34
137.1±2.1 Ma
7.03±0.17‰
+5.4±0.9 ε
35
138.2±2.2 Ma
7.29±0.22‰
+5.6±0.9 ε
36
37
144.2±6.7 Ma
6.93±0.18‰
+4.5±2.8 ε
38
39
140.1±3.6 Ma
6.32±0.15‰
+8.4±1.0 ε
40
41
136.3±2.2 Ma
7.60±0.22‰
+6.8±1.1 ε
135.9±2.1 Ma
7.46±0.18‰
+5.7±0.9 ε
42
43
136.1±2.1 Ma
7.31±0.18‰
+4.7±1.0 ε
44
123.2±3.6 Ma
6.46±0.45‰
148.9±3.0 Ma
7.22±0.19‰
+5.0±0.9 ε
45
147.3±2.7 Ma
7.20±0.20‰
+5.7±1.0 ε
145.9±3.5 Ma
7.61±0.21‰
+5.3±1.1 ε
46
139.9±2.3 Ma
7.28±0.23‰
+5.2±1.1 ε
137.1±2.4 Ma
7.18±0.18‰
+5.5±1.0 ε
47
138.4±2.1 Ma
7.23±0.21‰
+5.5±0.9 ε
48
130.7±3.3 Ma
7.41±0.15
+6.3±1.0 ε
49
168.8±4.2 Ma
7.23±0.19‰
+7.5±0.8 ε
50
51
136.5±2.1 Ma
7.21±0.22‰
+6.6±0.9 ε
137.9±2.2 Ma
7.09±0.17‰
+5.4±0.9 ε
52
200 µm*
Mag = 272 X
WD = 16.5 mm
Signal A = Aux 1
EHT = 15.00 kV
Date :28 Feb 2019
Specimen I = -3.11 nA
File Name = SEM19005_M1533_S5761_CL_1.tif

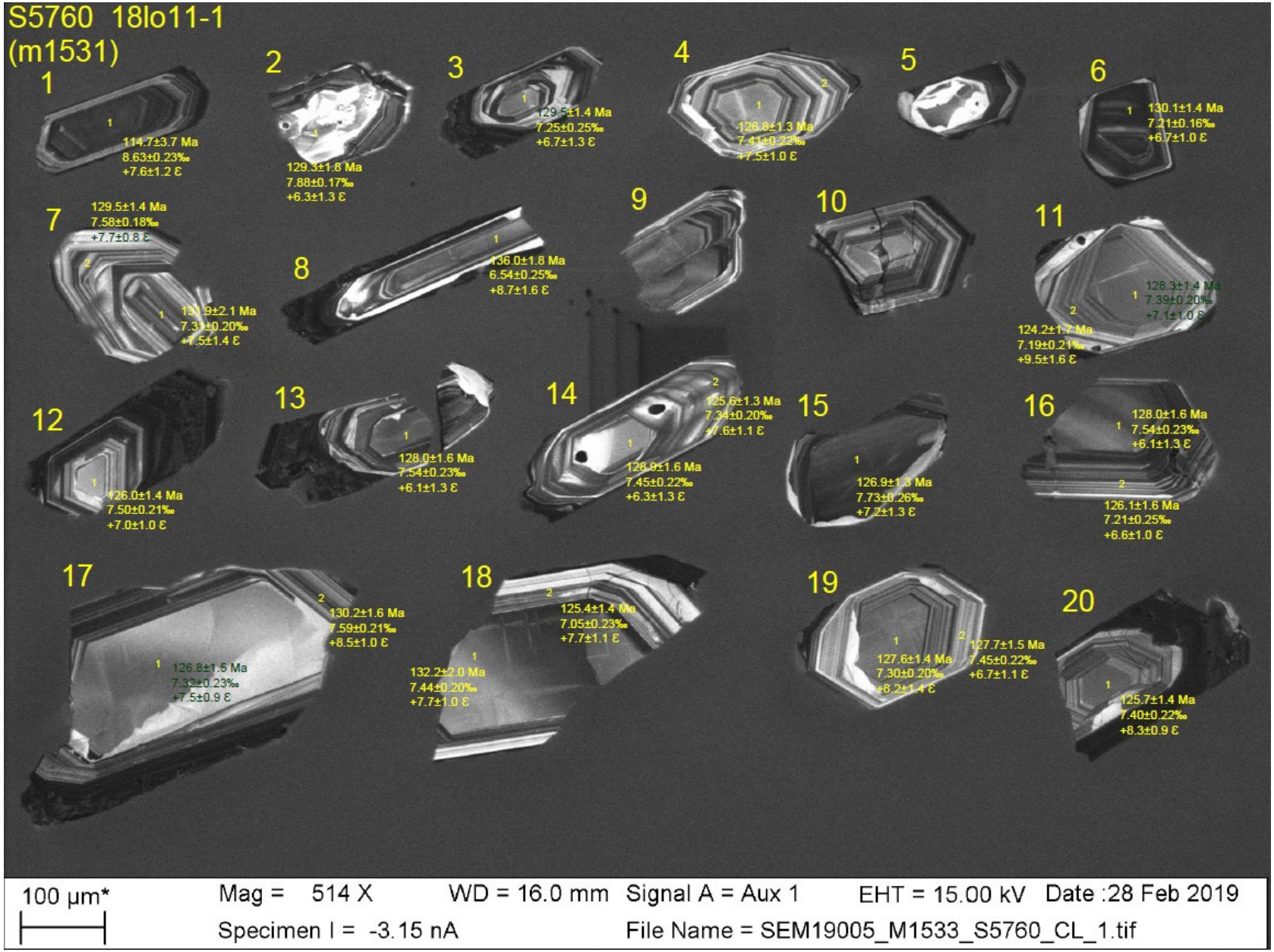
S5760 18lo11-1
(m1531)
1
114.7±3.7 Ma
8.63±0.23‰
+7.6±1.2 ε
2
129.3±1.8 Ma
7.88±0.17‰
+6.3±1.3 ε
3
129.5±1.4 Ma
7.25±0.25‰
+6.7±1.3 ε
4
126.8±1.3 Ma
7.41±0.22‰
+7.5±1.0 ε
5
6
130.1±1.4 Ma
7.21±0.16‰
+6.7±1.0 ε
7
129.5±1.4 Ma
7.58±0.18‰
+7.7±0.8 ε
8
136.0±1.8 Ma
6.54±0.25‰
+8.7±1.6 ε
9
10
11
128.3±1.4 Ma
7.39±0.20‰
+7.1±1.0 ε
124.2±1.7 Ma
7.19±0.21‰
+9.5±1.6 ε
12
126.0±1.4 Ma
7.50±0.21‰
+7.0±1.0 ε
13
128.0±1.6 Ma
7.54±0.23‰
+6.1±1.3 ε
14
125.6±1.3 Ma
7.34±0.20‰
+7.6±1.1 ε
128.9±1.6 Ma
7.45±0.22‰
+6.3±1.3 ε
15
126.9±1.3 Ma
7.73±0.26‰
+7.2±1.3 ε
16
128.0±1.6 Ma
7.54±0.23‰
+6.1±1.3 ε
126.1±1.6 Ma
7.21±0.25‰
+6.6±1.0 ε
17
130.2±1.6 Ma
7.59±0.21‰
+8.5±1.0 ε
126.8±1.5 Ma
7.32±0.23‰
+7.5±0.9 ε
18
125.4±1.4 Ma
7.05±0.23‰
+7.7±1.1 ε
132.2±2.0 Ma
7.44±0.20‰
+7.7±1.0 ε
19
127.6±1.4 Ma
7.30±0.20‰
+8.2±1.4 ε
127.7±1.5 Ma
7.45±0.22‰
+6.7±1.1 ε
20
125.7±1.4 Ma
7.40±0.22‰
+8.3±0.9 ε
100 µm*
Mag = 514 X
WD = 16.0 mm
Signal A = Aux 1
EHT = 15.00 kV
Date :28 Feb 2019
Specimen I = -3.15 nA
File Name = SEM19005_M1533_S5760_CL_1.tif

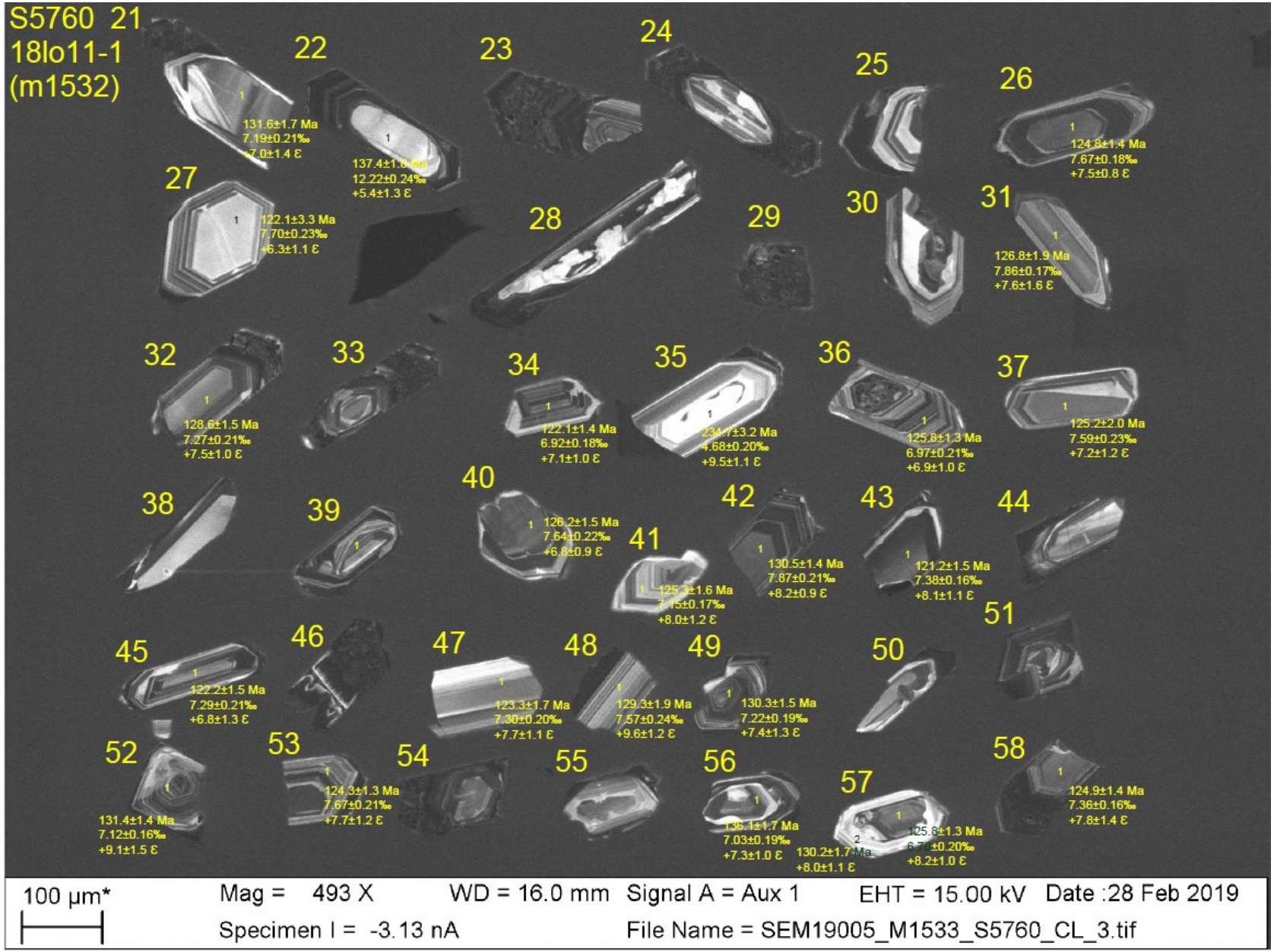
S5760 21
18lo11-1
(m1532)
22
131.6±1.7 Ma
7.19±0.21‰
+7.0±1.4 ε
137.4±1.8 Ma
12.22±0.24‰
+5.4±1.3 ε
23
24
25
26
124.8±1.4 Ma
7.67±0.18‰
+7.5±0.8 ε
27
122.1±3.3 Ma
7.70±0.23‰
+6.3±1.1 ε
28
29
30
31
126.8±1.9 Ma
7.86±0.17‰
+7.6±1.6 ε
32
128.6±1.5 Ma
7.27±0.21‰
+7.5±1.0 ε
33
34
122.1±1.4 Ma
6.92±0.18‰
+7.1±1.0 ε
35
234.7±3.2 Ma
4.68±0.20‰
+9.5±1.1 ε
36
125.8±1.3 Ma
6.97±0.21‰
+6.9±1.0 ε
37
125.2±2.0 Ma
7.59±0.23‰
+7.2±1.2 ε
38
39
40
126.2±1.5 Ma
7.64±0.22‰
+6.8±0.9 ε
41
125.3±1.6 Ma
7.15±0.17‰
+8.0±1.2 ε
42
130.5±1.4 Ma
7.87±0.21‰
+8.2±0.9 ε
43
121.2±1.5 Ma
7.38±0.16‰
+8.1±1.1 ε
44
45
122.2±1.5 Ma
7.29±0.21‰
+6.8±1.3 ε
46
47
123.3±1.7 Ma
7.30±0.20‰
+7.7±1.1 ε
48
129.3±1.9 Ma
7.57±0.24‰
+9.6±1.2 ε
49
130.3±1.5 Ma
7.22±0.19‰
+7.4±1.3 ε
50
51
52
131.4±1.4 Ma
7.12±0.16‰
+9.1±1.5 ε
53
124.3±1.3 Ma
7.67±0.21‰
+7.7±1.2 ε
54
55
56
136.1±1.7 Ma
7.03±0.19‰
+7.3±1.0 ε
57
130.2±1.7 Ma
+8.0±1.1 ε
125.6±1.3 Ma
+8.2±1.0 ε
58
124.9±1.4 Ma
7.36±0.16‰
+7.8±1.4 ε
100 µm*
Mag = 493 X
WD = 16.0 mm
Signal A = Aux 1
EHT = 15.00 kV
Date :28 Feb 2019
Specimen I = -3.13 nA
File Name = SEM19005_M1533_S5760_CL_3.tif

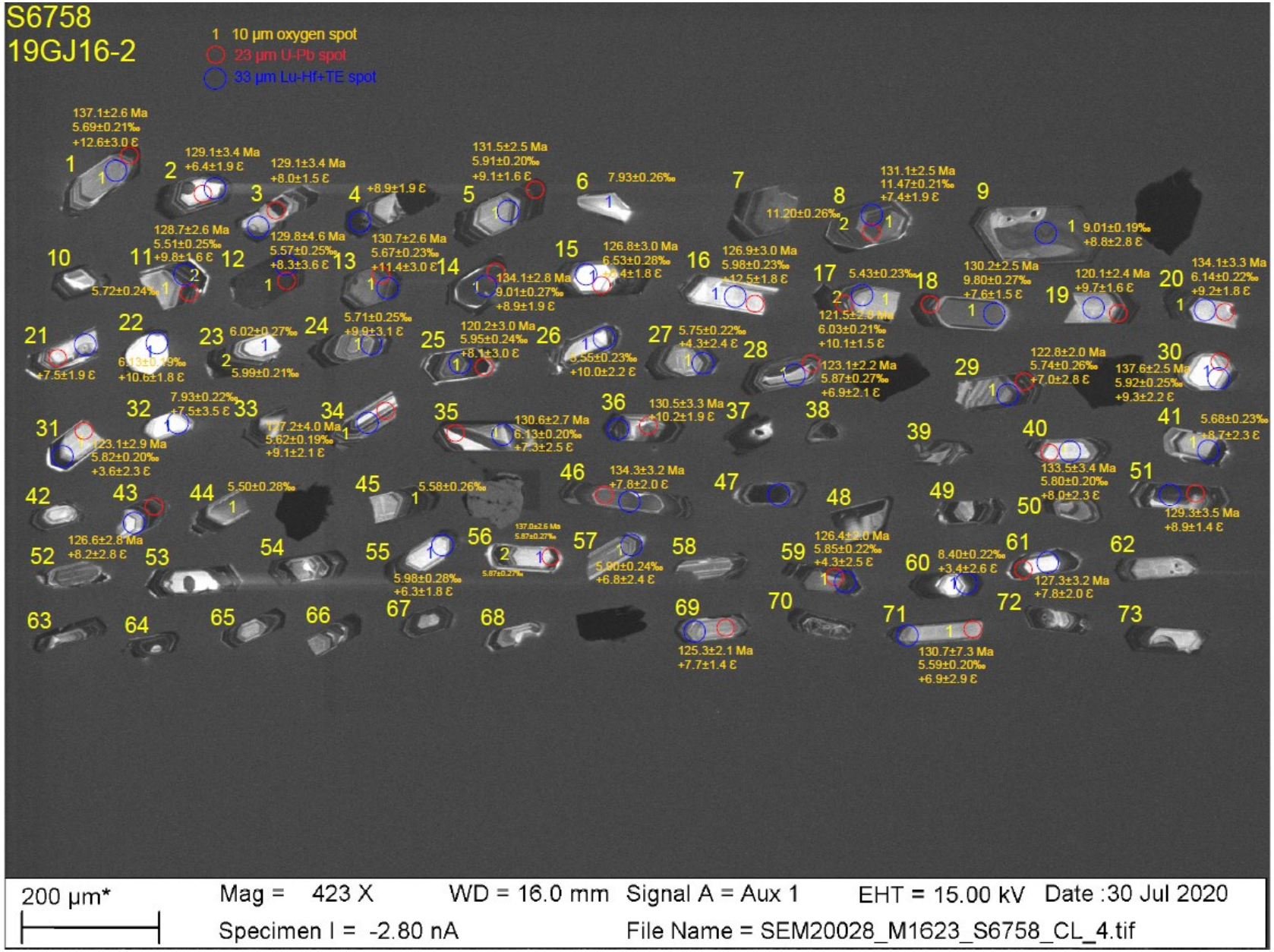
S6758
19GJ16-2
1 10 µm oxygen spot
23 µm U-Pb spot
33 µm Lu-Hf+TE spot
200 µm*
Mag = 423 X
WD = 16.0 mm
Signal A = Aux 1
EHT = 15.00 kV
Date :30 Jul 2020
Specimen I = -2.80 nA
File Name = SEM20028_M1623_S6758_CL_4.tif